

Molten Salt Synthesis of TiO_2 and $\text{Na}_2\text{Ti}_6\text{O}_{13}$ Crystals with Tailored Habit and Morphology

Salzschmelz-Synthese von TiO_2 und $\text{Na}_2\text{Ti}_6\text{O}_{13}$ Kristalle mit maßgeschneidertem Habitus und Morphologie

Zur Erlangung des akademischen Grades Doktor-Ingenieur (Dr.-Ing.)

Genehmigte Dissertation von Dario Mariano De Carolis aus Rom

Tag der Einreichung: 17. Januar 2023, Tag der Prüfung: 23. Februar 2023

1. Gutachten: Prof. Dr. Dr. h. c. Ralf Riedel
2. Gutachten: Prof. Dr. rer. nat. Wolfgang Donner
Darmstadt, Technische Universität Darmstadt



TECHNISCHE
UNIVERSITÄT
DARMSTADT

Materials and Earth
Sciences Department
Dispersive Solids

Molten Salt Synthesis of TiO_2 and $\text{Na}_2\text{Ti}_6\text{O}_{13}$ Crystals with Tailored Habit and Morphology
Salzschmelz-Synthese von TiO_2 und $\text{Na}_2\text{Ti}_6\text{O}_{13}$ Kristalle mit maßgeschneidertem Habitus und Morphologie

Accepted doctoral thesis by Dario Mariano De Carolis

Date of submission: 17. Januar 2023

Date of thesis defense: 23. Februar 2023

Darmstadt, Technische Universität Darmstadt

Bitte zitieren Sie dieses Dokument als:

URN: urn:nbn:de:tuda-tuprints-233223

URL: <http://tuprints.ulb.tu-darmstadt.de/23322>

Jahr der Veröffentlichung auf TUprints: 2023

Dieses Dokument wird bereitgestellt von tuprints,

E-Publishing-Service der TU Darmstadt

<http://tuprints.ulb.tu-darmstadt.de>

tuprints@ulb.tu-darmstadt.de

Die Veröffentlichung steht unter folgender Creative Commons Lizenz:

Namensnennung – Nicht kommerziell – Weitergabe unter gleichen Bedingungen 4.0 International

<https://creativecommons.org/licenses/by-nc-sa/4.0/>

This work is licensed under a Creative Commons License:

Attribution–NonCommercial–ShareAlike 4.0 International

<https://creativecommons.org/licenses/by-nc-sa/4.0/>

To my families: the first one in which I grew up (yes brother, you too) and the second one, still growing...

Erklärungen laut Promotionsordnung

§ 8 Abs. 1 lit. c PromO

Ich versichere hiermit, dass die elektronische Version meiner Dissertation mit der schriftlichen Version übereinstimmt.

§ 8 Abs. 1 lit. d PromO

Ich versichere hiermit, dass zu einem vorherigen Zeitpunkt noch keine Promotion versucht wurde. In diesem Fall sind nähere Angaben über Zeitpunkt, Hochschule, Dissertationsthema und Ergebnis dieses Versuchs mitzuteilen.

§ 9 Abs. 1 PromO

Ich versichere hiermit, dass die vorliegende Dissertation selbstständig und nur unter Verwendung der angegebenen Quellen verfasst wurde.

§ 9 Abs. 2 PromO

Die Arbeit hat bisher noch nicht zu Prüfungszwecken gedient.

Darmstadt, 17. Januar 2023

D. M. De Carolis

Abstract

Molten salt synthesis (MSS) is an efficient way to produce dispersed materials with a well-defined structure and morphology, ranging from the nano- to the micro-scale. This thesis presents a thorough analysis of the crystal growth of TiO₂ polymorphs (*i.e.* anatase and rutile) and sodium titanates by MSS, also known as flux growth. Metal chlorides and sulfates are investigated as high-temperature growth media. Two preparation methods of the precursor of the desired crystals have been followed: i) direct mixing of nanosized anatase with a salt (dry-mixed preparation (DMP)) and ii) wet-chemical preparation with TiOSO₄ and TiCl₄ as starting materials (wet chemical preparation (WCP)). The thesis has been concentrated on two subjects: i) tuning of the crystal habit and morphology of TiO₂ (rutile) and ii) the synthesis of highly pure Na₂Ti₆O₁₃ (NTO) nanorods. The samples obtained at temperatures ranging from 700 °C to 1200 °C are analyzed by means of X-ray diffraction (XRD), Raman spectroscopy, electron back-scatter diffraction (EBSD), scanning electron microscopy (SEM) and transmission electron microscopy (TEM) to investigate the correlation between the synthesis conditions and the obtained crystal habit, crystal size, composition and morphology. The variation of the structure and morphology of rutile is rationalized by the impact of the MSS parameters like the choice of the salt matrix, the precursor preparation and concentration, the temperature and atmosphere (air, argon, O₂). Hence, a central topic of this work is a thorough analysis of the MSS parameters influencing the anatase to rutile phase transition (ART) and the growth of NTO nanocrystals.

The MSS parameter salt matrix has a strong influence on the rutile morphology. The results mainly depend on the salt basicity, given by the O²⁻ activity in the salt (Lux-Flood theory). Chlorides generally favor the formation of rod-shaped rutile crystals. Their growth can be accelerated by an increase of the precursor concentration and of the synthesis temperature. The ART rate is fast in the chloride melt. The use of an inert atmosphere, *e.g.* synthesis under argon, increases the ART rate. The addition of NaF changes the rutile growth direction, hindering the formation of rod-shaped crystals at the expense of faceted bipyramidal octahedra. The replacement of Cl⁻ by SO₄²⁻-ions retards the ART, rutile being dominant only at temperatures ≥ 1000 °C. The ART is faster for the lowest precursor concentration (1 wt. % at 900 °C). Moreover, in the presence of SO₄²⁻, rutile crystals are not assuming the rod-shaped morphology as in chlorides. A study performed by varying the Cl⁻/SO₄²⁻ ratio in a NaCl-Na₂SO₄ mixture further confirms these correlations.

The WCP confirms the general trends observed by the DMP. However, WCP with TiCl₄ (or TiOSO₄) provides a faster ART rate. The addition of Na₃PO₄ — a strong Lux-Flood acid — to the TiOSO₄ precursor

solution strongly retards the ART at 1000 °C (and hinders the titanate formation). The retardation effect increases with Na₃PO₄ concentration, leading to an anatase quantity greater than rutile. WCP with 5 % Na₃PO₄ and treatment at 1100 °C under pure oxygen provides the most useful crystal habit for the TiO₂ application as pigment (pearl luster effect): "mosaic tile"-like rutile crystals. Higher Na₃PO₄ concentrations only lead to an increased formation of V-shaped rutile crystals.

WCP with Na₂SO₄ as salt component strongly enhances the formation of NTO in contrast to the DMP. Increasing the pH in the precipitation step by adding NaOH, promotes the formation of pure NTO. Therefore, this innovative MSS approach to obtain exceptionally pure Na₂Ti₆O₁₃ nanorods in high yield, opens a promising route for new applications, notably sodium batteries in stationary energy storage. In contrast to all the synthesis approaches reported in literature, no TiO₂ is found in the final specimen achieving an overall yield of Na₂Ti₆O₁₃ > 80 wt. %. The elaborated synthesis is fast, cost efficient and suitable for industrial up-scaling. The Na₂Ti₆O₁₃ nanorods generated at 900-1100 °C have an average length and diameter of about 30 μm and 200 nm, respectively, providing an average aspect ratio of 150. X-ray diffraction and Raman studies confirm the high purity of the material. The crystal growth direction of the nanorods has been determined by EBSD and selected area electron diffraction techniques, revealing a <010> growth direction. Moreover, Raman and electron energy-loss spectroscopy hint at slight changes in the Ti–O and Na bonding in the tunnel structure of NTO at > 900 °C. Electrochemical tests in Li and Na-half cells reveal stable performance providing capacities of about 100 mA h g⁻¹ (Li) and 40 mA h g⁻¹ (Na). Increase of the synthesis temperature of Na₂Ti₆O₁₃ to 1100 °C leads to a capacity decrease of ≈ 20 % most likely resulting from i) the morphology/volume change with temperature and ii) distortion of the Na₂Ti₆O₁₃ tunnel structure. Carbon coating and other activation processes enhance the performance establishing NTO nanorods as promising material for energy applications.

Zusammenfassung

Die Salzschnmelz-Synthese (MSS) ist eine effiziente Methode, nano- und mikro-disperse Materialien mit wohldefinierter Struktur und Morphologie herzustellen. Die vorliegende Arbeit berichtet über das Kristallwachstum von polymorphem TiO_2 (Anatas und Rutil) sowie Natriumtitanaten in Chloriden und Sulfaten als Hochtemperatur-Medien. Zwei unterschiedliche Präkursoren der o.e. Materialien wurden in der Salzschnmelz-Synthese eingesetzt: i) direkte Mischung von nanokristallinem Anatas und einem Salz (DMP) sowie ii) nass-chemische Präparation mit TiOSO_4 oder TiCl_4 und einem Salz als Ausgangsmaterialien (WCP). Die synthetischen Arbeiten konzentrierten sich auf: i) das Tuning des Habitus und der Morphologie von Rutil und ii) der Darstellung sehr reiner $\text{Na}_2\text{Ti}_6\text{O}_{13}$ (NTO) Nano-Stäbchen. Zur Untersuchung der Korrelation zwischen Synthesebedingungen und Kristallhabitus, der Kristallgröße sowie der Zusammensetzung und Morphologie wurden die in der MSS bei $700 < T < 1200$ °C erhaltenen Proben anhand von Raman und Röntgenbeugung (XRD), Elektronen-Rückstreu-Diffraktion (EBSD), Rasterelektronenmikroskopie (REM) und Transmissionselektronenmikroskopie (TEM) charakterisiert. Struktur und Morphologie der Proben sind stark vom Einfluss der MSS-Parameter wie die Wahl des Salzes, Herstellung und Konzentration des Präkursors, Synthesetemperatur und -atmosphäre (Luft, Argon, Sauerstoff) geprägt. Der Phasenübergang Anatas \rightarrow Rutil (ART) sowie das Wachstum von NTO Kristallen ist beispielsweise anhand geschickter Auswahl der MSS-Parameter steuerbar.

Der Parameter „Salzmatrix“ hat einen starken Einfluss auf die Morphologie des Rutils. Letztere wird im Wesentlichen durch die Basizität des Salzes bzw. seiner O^{2-} Aktivität bestimmt (Lux-Flood Theorie). Chloride favorisieren die Bildung stabförmiger Rutilkristalle. Ihr Wachstum kann durch die Erhöhung der Präkursorkonzentration und der Synthesetemperatur beschleunigt werden. Der ART erfolgt vergleichsweise schnell in Anwesenheit von Cl^- -Ionen und kann unter inerter Atmosphäre (e. g., Synthese unter Ar) weiter erhöht werden. Ersatz von Cl^- durch SO_4^{2-} verzögert den ART: Rutil dominiert die Phasenzusammensetzung erst ab $T \geq 1000$ °C. Weiterhin erfolgt eine deutliche Veränderung der Morphologie da keine stabförmigen Kristalle gebildet werden wie unter Präsenz von Cl^- . Variation des Verhältnisses $\text{Cl}^-/\text{SO}_4^{2-}$ bestätigt den spezifischen Einfluss von Cl^- und SO_4^{2-} . NaF verändert gleichfalls die Wachstumsrichtung von Rutilkristallen indem die Bildung stabförmiger Kristalle behindert wird, zugunsten facettenreicher bipyramidaler Oktaeder.

MSS mit WCP bestätigt generell die o.a. Ergebnisse mit DMP als Vorstufe. Allerdings ergibt sich mit TiCl_4 (oder TiOSO_4) als Ausgangsstoff eine deutlich erhöhte ART-Rate. Zugabe von Na_3PO_4 , eine starke Lux-Flood Säure, zu TiOSO_4 verzögert den ART sehr stark (bei $T = 1000$ °C) und verhindert

auch die Titanat-Bildung. Der Effekt nimmt mit der Konzentration von Na_3PO_4 zu und führt zu einer Phasenzusammensetzung Anatas > Rutil. WCP mit 5 mol% Na_3PO_4 und Synthese bei $1100\text{ }^\circ\text{C}$ unter reinem Sauerstoff ergibt einen Rutil -Habitus, der sich für eine Anwendung als Pigment mit Pearl Glanz Effekt eignet: mosaik-plattchenförmige Rutilkristalle (höhere Na_3PO_4 Konzentrationen als 5 mol% führen jedoch lediglich zu vermehrter Bildung von V-förmigen Rutilkristallen).

WCP mit Na_2SO_4 und anschließende Salzschnmelz-Synthese intensiviert die Bildung von NTO im Vergleich zur DMP. Zugabe von NaOH bzw. Erhöhung des pH bei der TiO_2 Fällung im WCP Schritt fördert die NTO Bildung weitaus stärker. Außergewöhnlich reine NTO-Nanokristalle in Stäbchenform können mit diesem innovativen Ansatz in hoher Ausbeute (> 80 wt. %) erhalten werden. Dies eröffnet aussichtsreiche neue Anwendungen, insbesondere als Na-Batterien für die stationäre Energiespeicherung. Im Vergleich zu allen in der Literatur beschriebenen Synthesen ist im Endprodukt kein TiO_2 vorhanden, die MSS ist einfach, kosteneffizient und geeignet für die industrielle Hochskalierung. Die NTO Nanokristalle, bei $900 < T < 1100\text{ }^\circ\text{C}$ synthetisiert, besitzen eine mittlere Länge und Durchmesser von $30\text{ }\mu\text{m}$ und 200 nm bzw. ein Aspektverhältnis von 150. Röntgen- und Raman-Untersuchungen bestätigen die Reinheit der Materialien. Die Richtung des Kristallwachstums wurde anhand von EBSD und Elektronenbeugung in ausgewählten Bereichen bestimmt und ergaben eine $\langle 010 \rangle$ Vorzugsrichtung. Raman und Elektronenenergieverlustspektroskopie weisen weiterhin auf (geringe) Änderungen in der Ti-O und Na-Bindung in der Tunnelstruktur von NTO bei $T \geq 900\text{ }^\circ\text{C}$ hin. Elektrochemische Tests von Li- und Na-Halbzellen belegen ein stabiles Verhalten mit Kapazitäten von ca. 100 mA h g^{-1} (Li) und 40 mA h g^{-1} (Na). Erhöhung der Synthesetemperatur auf $1100\text{ }^\circ\text{C}$ verursacht einen Kapazitätsverlust von ca. 20 %. Sehr wahrscheinliche Ursachen für dieses Ergebnis sind i) Volumen/Morphologie-Änderungen mit der Temperatur sowie ii) Distorsion der NTO Tunnelstruktur. Beschichtung von NTO mit Kohlenstoff und andere Aktivierungsprozesse sollten die Leistungsfähigkeit von NTO-basierten Batterien weiter verbessern und damit nanokristallinem NTO noch intensivere Aufmerksamkeit verleihen.

Contents

List of Figures	xv
List of Tables	xxvii
List of Abbreviations	xxix
1. Introduction and motivation of the work	1
2. Basic information	5
2.1. Properties of molten salts	5
2.1.1. Metal chlorides and sulfates as solvents in MSS	8
2.2. Crystal growth models	11
2.3. Crystal growth in molten salts	13
2.3.1. Habit of crystals grown from solutions	15
2.3.2. Supersaturation in molten salts	19
2.3.3. Salt matrix influence on crystal growth	21
2.3.4. Influence of acidity/basicity of melts on the crystallization process	23
2.3.5. Molten salt synthesis performed under O ₂ flow	25
3. Crystal structures and applications	27
3.1. TiO ₂ crystal structures	27
3.1.1. Anatase	28
3.1.2. Anatase to rutile phase transformation	30
3.1.3. Rutile	30
3.1.4. Rutile surfaces	32
3.2. TiO ₂ as pearl luster pigment	35
3.2.1. Pigments and the origin of color	35
3.2.2. Concept of pearl luster pigment	37
3.2.3. Manufacturing process of the TiO ₂ -based pearl luster pigment	41
3.3. A ₂ Ti ₆ O ₁₃ and A ₂ Ti ₃ O ₇ structures (A=Li ⁺ ,Na ⁺) and energy storage application	43
4. Experimental	47
4.1. Molten salt synthesis of samples	47
4.1.1. Dry-mixed precursor preparation in MSS (DMP)	47
4.1.2. Wet-chemical precursor preparation in MSS (WCP)	48
4.2. Experimental methods	48
4.2.1. Powder X-ray diffraction	48
4.2.2. DTA and TGA analysis	50
4.2.3. Scanning electron microscopy	50

4.2.4. Electron backscatter diffraction	51
4.2.5. Transmission electron microscopy and electron energy loss spectroscopy	51
4.2.6. Raman spectroscopy	51
4.3. Electrochemistry – battery performance of NTO	52
5. Results and discussion	53
5.1. Molten salt synthesis of TiO ₂ performed in chlorides	53
5.1.1. TiO ₂ crystal growth in NaCl flux	53
5.1.1.1. Influence of precursor content in the NaCl matrix on the crystal habit	57
5.1.1.2. Phase evolution followed by in-situ high-temperature XRD	62
5.1.2. TiO ₂ crystal growth in flux mixtures NaCl-X (X= AlCl ₃ ·6 H ₂ O, KCl, MgCl ₂ , NaF)	64
5.1.2.1. NaCl-KCl	64
5.1.2.2. NaCl-NaF	66
5.1.2.3. NaCl-MgCl ₂	69
5.1.2.4. NaCl-AlCl ₃	74
5.1.3. KCl-LiCl eutectic mixture with low melting point	75
5.1.4. Influence of the oxygen partial pressure on the crystal growth in NaCl	77
5.1.5. Addition of B ₂ O ₃ to NaCl synthesis	82
5.1.6. Wet chemical pretreatment in NaCl	84
5.1.7. Summary of MSS in chlorides	87
5.2. Molten salt synthesis of TiO ₂ performed in sulfates	91
5.2.1. TiO ₂ crystal growth in Na ₂ SO ₄ flux	91
5.2.2. TiO ₂ crystal growth in Na ₂ SO ₄ -NaCl mixture	96
5.2.2.1. Na ₂ SO ₄ -NaCl eutectic mixture	96
5.2.2.2. Effect of non-eutectic Na ₂ SO ₄ -NaCl mixtures	99
5.2.3. NaF addition to Na ₂ SO ₄	103
5.2.4. Influence of the oxygen partial pressure on the crystal growth in Na ₂ SO ₄	106
5.2.5. Addition of B ₂ O ₃ to the Na ₂ SO ₄ flux	110
5.2.6. Wet chemical precursor preparation for molten salt synthesis in sulfates	112
5.2.6.1. Wet chemical preparation with TiOSO ₄ precursor	112
5.2.6.2. Effect of Na ₃ PO ₄ addition in the molten salt synthesis	118
5.2.6.3. Heat-treatment under O ₂ flow	128
5.2.6.4. Wet chemical preparation at different temperatures and TiCl ₄ precursor	129
5.2.7. Summary of MSS in sulfates	133
5.3. Molten salt synthesis of sodium titanates in sulfates	135
5.3.1. Influence of the NaOH concentration on the phase composition	136
5.3.2. Synthesis of pure Na ₂ Ti ₆ O ₁₃	142
5.3.3. Raman investigation of Na ₂ Ti ₆ O ₁₃	148
5.3.4. TEM and EELS investigation of Na ₂ Ti ₆ O ₁₃	148
5.4. Electrochemical performance of sodium titanates	154
5.4.1. Galvanostatic cycling with potential limitation vs Li/Li ⁺	154
5.4.2. Galvanostatic cycling with potential limitation vs Na/Na ⁺	166
6. Conclusion and outlook	171
Bibliography	175
Acknowledgments	197

Appendix A. List of chemicals	199
Appendix B. Phase Diagrams	201
Appendix C. Additional XRD Data	207
Appendix D. Additional SEM results	221
Appendix E. Additional Raman results	245
Appendix F. List of publications	249
Appendix G. Curriculum Vitae	251

List of Figures

2.1.	Smoothed partial pair RDF of molten RbCl obtained by neutron diffraction, after [112].	8
2.2.	Enthalpy of mixing ΔH_{mix} (top row) and excess volume variation ΔV_{mix} (bottom row) of: a) NaCl (x_1) - KCl (x_2); b) NiCl ₂ (x_1) - CoCl ₂ (x_2); c) KCl (x_1) - CoCl ₂ (x_2) after [116].	10
2.3.	Representation of the PBCs and the F (100, 010, 001), S (110, 101, 011) and K (111) faces defined in the HP theory, after [124].	11
2.4.	Representation of the PBCs defining a F face within the HP theory, after [118].	12
2.5.	a) SEM images of BST powder synthesized at 1150 °C for 2 h by CSS reaction and b) at 900 °C for 2 h by MSS (reprinted from [128] Copyright © 2007, with permission from Elsevier).	14
2.6.	Schematic diagram of the a) dissolution-precipitation growth and b) of the template formation mechanism occurring in molten salt synthesis (MSS) (reproduced with permission from [91]. Copyright © 2020 Royal Society of Chemistry).	15
2.7.	Different habits originated from the same cubic system, but with the maximum growth rate along different directions (from left to right: [100], intermediate direction and [111]), after [81].	16
2.8.	ZnO crystal habit: a) grown along the <i>c</i> direction in strong basic solution as a long prism; b) grown perpendicular to the <i>c</i> -axis in a weak basic solution as a plate-like crystal, after [134].	17
2.9.	Attachment of impurities on the surface, after [123].	18
2.10.	Alumina flakes obtained via MSS reporting a flake like crystal habit.	18
2.11.	Growth habit of α -Al ₂ O ₃ crystal, after [139].	19
2.12.	Graph of the normal growth rate R versus the driving force $\Delta\mu/(K_B T)$ correlated to the expected crystal habit evolution, after [118, 124].	20
3.1.	Anatase single octahedron of a TiO ₆ unit a) and the anatase unit cell visualizing the connections between the octahedra in b). Both were designed with the VESTA 3D structure visualization software [172] (CIF file ICSD-63711 [173]).	28
3.2.	Equilibrium crystal shape of anatase by the Wulff construction (according to [174]) on the left hand side and the possible shapes that can evolve from it (reprinted with permission from [30]. Copyright © 2014 American Chemical Society).	29
3.3.	Rutile single octahedron in a) and rutile unit cell visualizing the connections between the octahedra in b). Both were designed with the VESTA 3D structure visualization software [172] (CIF file ICSD-202240 [171]).	31
3.4.	Equilibrium crystal shape of rutile by the Wulff construction (according to [203]) and the possible shapes that can evolve from it (reprinted with permission from [30]. Copyright © 2014 American Chemical Society)	32
3.5.	Lattice formation in rutile and anatase	33
3.6.	Relaxation of the surface atoms in a (110)-(1x1) TiO ₂ surface	34

3.7.	(100)-(1x1) TiO ₂ surface	34
3.8.	Left: side view of the rutile (001) surface. Right: only possibility to cut the rutile crystal in this direction (reprinted from [28] with permission from Elsevier Copyright © 2002).	35
3.9.	Reflectance curve of a blue absorption pigment (inspired by ref. [73]).	36
3.10.	Pigment classes and their characteristic interaction with the electromagnetic radiation (inspired by ref. [223]).	38
3.11.	Reflection from a) uneven and b) even surfaces (inspired by [223]).	38
3.12.	Interference occurring on a thin layer with refractive index $n_1 > n_0$ (inspired by [143]).	39
3.13.	Relative intensity distributions of reflections of two films with different thickness (taken from ref. [73]).	40
3.14.	The layer thickness of TiO ₂ generates the interference colors (taken from ref. [73]).	40
3.15.	Overview of mica substrates coated with anatase (left), and a cross-section of a pigment (right, reprinted with permission from [104]. Copyright © 2005 Wiley-VCH).	41
3.16.	Comparison between cross-sections of natural (left) and synthetic substrate (right).	42
3.17.	Manufacturing process for alumina flakes, after [104].	42
3.18.	Crystal structure of Na ₂ Ti ₆ O ₁₃ (NTO) with the Na ⁺ ions marked in yellow, filling the tunnel structure built up by the TiO ₆ framework. The red spheres represent the O atoms and the blue ones the Ti atoms. The orientation facilitates the view along the <010> direction. The structural model was realized using the 3D visualization software VESTA [172].	44
3.19.	Crystal structure of Na ₂ Ti ₃ O ₇ (realized by VESTA [172]) with the Na ⁺ ions marked in yellow, filling the interlayer spaces built up by the TiO ₆ octahedra. The red spheres are the O atoms and the blue ones the Ti atoms. The orientation facilitates the view along the <010> direction. The structural model was realized using the 3D visualization software VESTA [172].	45
4.1.	Huber 670.3 heater device for capillary measurement.	49
5.1.	SEM image of the anatase K1002 precursor manufactured by KRONOS INTERNATIONAL INC. showing an average particle size of about 100 nm.	54
5.2.	XRD patterns of titania samples obtained by MSS at 900 °C in NaCl with different wt. % of anatase precursor (1 %, 5 %, 10 %, 15 % and 20 %). Reference XRD patterns from the International Center for Diffraction Data (ICDD) for anatase and rutile are given at the bottom of the graph.	55
5.3.	XRD patterns of titania samples obtained by MSS in NaCl with a) 5 wt. % of anatase precursor at 850 °C, 900 °C and 1000 °C and b) 10 wt. % of precursor at 820 °C, 850 °C, 900 °C, 1000 °C and 1100 °C.	56
5.4.	SEM images of TiO ₂ particles obtained at 900 °C with 2 h of holding time with a) 1 wt. %, b) 10 wt. %, c) 20 wt. % and d) 50 wt. % of anatase precursor within NaCl. The rutile twin crystal in figure 5.4d is marked by a red circle.	58
5.5.	a) Raman spectra of the sample obtained at 900 °C with 1 wt. % anatase precursor in NaCl measured on spot b) S1, c) S2 and d) S3. The rutile spectrum of K2900 is added as reference.	59
5.6.	Raman spectra from two spots of the sample obtained by MSS in NaCl with 5 wt. % of titania at 1000 °C.	60
5.7.	Morphology of titania particles obtained at a) 820, b) 850, c) 900 and d) 1100 °C with 10 wt. % anatase precursor in NaCl, measured by SEM.	61

5.8.	High temperature XRD pattern of NaCl-10 wt. % TiO ₂ measured <i>in-situ</i> (up to 900 °C). Legend: A = anatase; R = rutile; Cl = NaCl; * = artifact from the device. Note the melting point of NaCl: T = 801 °C.	63
5.9.	XRD patterns of titania samples obtained by MSS in NaCl-KCl eutectic mixture at 800 °C, 900 °C, 1000 °C and 1100 °C with a) 5 and b) 10 wt. % of anatase precursor.	65
5.10.	SEM images of titania particles obtained with 10 wt. % of anatase precursor at 900 °C in NaCl-KCl eutectic mixture a) and NaCl b) respectively and with 20 wt. % of anatase precursor at 1000 °C in NaCl-KCl eutectic mixture c) and NaCl d).	66
5.11.	XRD patterns of titania samples obtained by MSS at 900 °C in NaCl/NaF with ≈ 20 wt. % of anatase precursor (0.1 %, 5 %, 10 % and 20 % NaF/TiO ₂ mol %).	67
5.12.	SEM images of titania crystals obtained at 900 °C with 20 wt. % of TiO ₂ precursor in NaCl. Additionally were added: a) 5 % b) 10 %, c) 20 % and d) 30 % F/Ti mol.	68
5.13.	SEM images of titania particles obtained at a) 900, c) 1000 and e) 1100 °C with 20 wt. % TiO ₂ in NaCl with the addition of 5 % F/Ti mol. In b), d) and f) the same synthesis temperatures were applied in pure NaCl.	70
5.14.	XRD patterns of titania samples obtained by MSS at 900 °C in 0.67 NaCl-0.33 NaF with 10 wt. % of anatase precursor. Reference patterns from the ICDD are reported for comparison.	71
5.15.	SEM images of titania crystals obtained in 0.77 NaCl-0.33 NaF eutectic mixture at a) 900 °C and b) 1000 °C with 10 wt. % of TiO ₂ precursor.	71
5.16.	XRD patterns of titania samples obtained by MSS in NaCl-MgCl ₂ at 900 °C, 1000 °C and 1100 °C with (a) 5 and (b) 20 wt. % of TiO ₂ precursor. Reference patterns from the ICDD are listed.	72
5.17.	SEM images of titania particles obtained at a) 900, b) 1000 and c) 1100 °C: 20 wt. % TiO ₂ in 0.8NaCl-0.2MgCl ₂ mixture.	73
5.18.	XRD patterns of titania samples obtained by MSS in 0.7 NaCl - 0.3 AlCl ₃ mixture with 2 hours holding time and 10 wt. % of titania.	74
5.19.	SEM images of titania and alumina particles obtained at a) 900, b) 1000, c) and d) 1100 °C, 10 wt. % TiO ₂ in 0.7 NaCl-0.3 AlCl ₃ mixture.	76
5.20.	XRD patterns of titania samples obtained by MSS between 400 and 700 °C in 0.41 KCl-0.59 LiCl with 10 wt. % of anatase precursor. Reference patterns from the ICDD are reported for comparison.	77
5.21.	SEM images of titania particles obtained at a) 400, b) 500, c) 600 and d) 700 °C with 10 wt. % TiO ₂ precursor in 0.41 KCl-0.59 LiCl.	78
5.22.	SEM images of titania particles obtained at a) and b) 500 °C and c) and d) 600 °C with 10 wt. % TiO ₂ precursor in 0.41 KCl-0.59 LiCl. a) and c) report the addition of 10 mol % NaF and b) and d) of 20 mol % NaF respect to TiO ₂	79
5.23.	Comparison between samples with 1 wt. % anatase precursor in NaCl heat-treated under ambient atmosphere and under argon at 900 °C; reference patterns from the ICDD are reported for comparison.	81
5.24.	Morphology of titania particles obtained at 900 °C for 1 wt. % anatase precursor in NaCl under: a) ambient atmosphere (same picture as in figure 5.4 a) and b) argon flow, measured by SEM.	81
5.25.	Comparison between samples heat-treated under ambient atmosphere and under O ₂ flow at 1100 °C with 10 wt. % anatase precursor in NaCl. A reference pattern from the ICDD is reported for comparison.	82

5.26. Morphology of titania particles obtained at 1100 °C with 10 wt. % anatase precursor in NaCl under: a) ambient atmosphere and b) pure oxygen, measured by SEM.	83
5.27. XRD patterns of titania samples obtained by MSS at 900 °C for NaCl/20 wt. % anatase precursor (red dashed line) and the addition of 0.8 mol % B ₂ O ₃ (black solid line). The rutile reference pattern from the ICDD is added at the bottom.	84
5.28. SEM images of titania particles obtained at 900 °C, 1000 °C and 1100 °C: 20 wt. % TiO ₂ precursor in NaCl (b, d and f) and with the addition of 0.8 mol % B ₂ O ₃ (a, c and e). .	85
5.29. SEM images of titania particles obtained at 900 °C: 20 wt. % TiO ₂ precursor in NaCl with the addition of 0.8 mol % B ₂ O ₃ in a) ambient atmosphere and b) under argon. .	86
5.30. XRD patterns of titania samples obtained by MSS in NaCl with 5 wt. % TiCl ₄ as precursor. Reference XRD patterns from the ICDD for anatase and rutile are present at the bottom of the graph.	87
5.31. SEM images of titania particles synthesized by MSS in NaCl with 5 wt. % TiCl ₄ precursor.	88
5.32. SEM images showing the comparison between titania particles obtained in NaCl by WCP (with 5 wt. % TiCl ₄ precursor) (figure a and c) and by DMP with 5 wt. % anatase precursor (figure b and d).	89
5.33. MSS in NaCl: schematic representation of the change of a) the rutile crystals morphology with temperature, precursor concentration, the addition of NaF and B ₂ O ₃ by DMP; b) the rutile and NTO particle size and morphology by WCP with TiCl ₄	90
5.34. XRD patterns of titania samples obtained by MSS at 900 °C in Na ₂ SO ₄ with 5 different wt. % of anatase precursor (1 %, 5 %, 10 %, 15 % and 20 %). Reference XRD patterns from the ICDD for anatase and rutile are given at the bottom of the graph.	92
5.35. SEM images of TiO ₂ particles obtained at 900 °C and 2 h of holding time: a) 1 wt. %, b) 5 wt. %, c) 10 wt. %, d) 15 wt. %, and e) 20 wt. % of TiO ₂ in Na ₂ SO ₄	94
5.36. SEM images of TiO ₂ particles obtained at 900 °C, 1000 °C and 2 h of holding time with 20 wt. % of precursor in Na ₂ SO ₄ (a and c) and in NaCl (b and d).	95
5.37. XRD patterns of titania samples obtained by MSS at 1000 °C in Na ₂ SO ₄ with 5 different wt. % of anatase precursor (1 %, 5 %, 10 %, 15 % and 20 %). Reference XRD patterns from the ICDD for anatase and rutile are given at the bottom of the graph.	96
5.38. SEM images of TiO ₂ particles obtained at 1000 °C and 2 hours of holding time with a) 1 wt. %, b) 5 wt. %, c) 10 wt. % and d) 15 wt. % of anatase precursor in Na ₂ SO ₄	97
5.39. XRD patterns of titania samples obtained by MSS at 900 °C in Na ₂ SO ₄ , NaCl and in 0.47 Na ₂ SO ₄ -0.53 NaCl with 10 wt. % of precursor. Reference XRD patterns from the ICDD for anatase and rutile are given at the bottom of the graph.	99
5.40. SEM images of TiO ₂ particles obtained at 900 °C and 2 hours of holding time with a) 1 wt. %, b) 5 wt. % and c) 10 wt. % of TiO ₂ in 0.47 Na ₂ SO ₄ -0.53 NaCl.	100
5.41. High temperature XRD pattern of 10 wt. % TiO ₂ mixed in 0.47 Na ₂ SO ₄ -0.53 NaCl measured <i>in-situ</i> (up to 850 °C). Legend: A = anatase; R = rutile; Cl = NaCl; S = Na ₂ SO ₄ ; SS = Na ₂ SO ₄ V-I; Q = quartz capillary.	101
5.42. XRD patterns of titania samples obtained by MSS at 900 °C in 4 different Na ₂ SO ₄ - NaCl combinations with 10 wt. % of precursor. Reference XRD patterns from the ICDD for anatase and rutile are given at the bottom of the graph.	102
5.43. SEM images of TiO ₂ particles obtained at 900 °C and 2 hours of holding time with 10 wt. % of TiO ₂ in: a) 0.2 NaCl-0.8 Na ₂ SO ₄ , b) 0.4 NaCl-0.6 Na ₂ SO ₄ , c) 0.53 NaCl-0.47 Na ₂ SO ₄ , d) 0.6 NaCl-0.4 Na ₂ SO ₄ and e) 0.8 NaCl-0.2 Na ₂ SO ₄	104

5.44.	XRD patterns of titania samples obtained by MSS at 1100 °C in Na ₂ SO ₄ , with different moles of NaF added. The precursor amount is 10 wt. %. Reference XRD patterns from the ICDD for Na ₂ Ti ₆ O ₁₃ and rutile are given at the bottom of the graph.	105
5.45.	SEM images of TiO ₂ particles obtained at 1100 °C and 2 h of holding time, 10 wt. % of TiO ₂ with: a) 0.1 NaF mol %, b) 0.5 NaF mol %, c) 5 NaF mol %, d) 10 NaF mol %, e) 20 NaF mol % and f) 30 NaF mol %.	107
5.46.	SEM images showing the comparison between a) TiO ₂ particles obtained in Na ₂ SO ₄ at 1100 °C, 2 h of holding time and 10 wt. % of anatase precursor and those with the addition of b) 0.5 NaF mol %, c) 30 NaF mol % and d) 40 NaF mol %.	108
5.47.	Comparison between samples heat-treated under ambient atmosphere and under argon at 900 °C with 1 wt. % anatase precursor in Na ₂ SO ₄ and NaCl. Reference XRD patterns from the ICDD for anatase and rutile are given at the bottom of the graph.	109
5.48.	SEM images of TiO ₂ particles obtained at 900 °C and 2 h of holding time with 1 wt. % of TiO ₂ in Na ₂ SO ₄ under: a) ambient atmosphere and b) argon. The terraced growth is highlighted by a red circle.	110
5.49.	Comparison between samples heat-treated under ambient atmosphere and under O ₂ flow at 1100 °C with 10 wt. % anatase precursor in Na ₂ SO ₄ . Reference XRD pattern from the ICDD for rutile is given at the bottom of the graph.	111
5.50.	SEM images of TiO ₂ particles obtained at 1100 °C and 2 h of holding time in Na ₂ SO ₄ with 10 wt. % of TiO ₂ under: a) ambient atmosphere and b) O ₂ flow (red circles: truncated bifrustum habit).	111
5.51.	Comparison between samples heat-treated at 1100 °C with 10 wt. % anatase precursor in Na ₂ SO ₄ (red solid line) and the addition of 0.8 (green dashed line) and 1.2 mol % (black dotted line) of B ₂ O ₃ to Na ₂ SO ₄	112
5.52.	SEM images showing the comparison between TiO ₂ particles obtained at 1100 °C and 2 h of holding time, 10 wt. % of TiO ₂ with: a) any B ₂ O ₃ , b) 0.5 B ₂ O ₃ mol %, c) 0.8 B ₂ O ₃ mol % and d) 1.2 B ₂ O ₃ mol %.	113
5.53.	XRD of samples obtained by WCP performed at 60 °C with 10 wt. % TiOSO ₄ precursor heat-treated at 1000 °C, 1100 °C and 1200 °C. Reference XRD patterns from the ICDD for Na ₂ Ti ₆ O ₁₃ and rutile are given at the bottom of the graph.	114
5.54.	SEM images of titania and NTO particles synthesized at a) 1000 °C and b) 1100 °C by MSS in Na ₂ SO ₄ via WCP at 60 °C with 10 wt. % TiOSO ₄ precursor.	115
5.55.	XRD of samples obtained by WCP performed at 60 °C with 5 wt. % TiOSO ₄ precursor, heat-treated at 850 °C, 900 °C, 1000 °C and 1100 °C. Reference XRD patterns from the ICDD for Na ₂ Ti ₆ O ₁₃ and rutile are given at the bottom of the graph.	115
5.56.	SEM images of titania and NTO particles synthesized at a) 1000 °C and b) 1100 °C by MSS in Na ₂ SO ₄ via WCP at 60 °C with 5 wt. % TiOSO ₄ precursor.	116
5.57.	XRD of samples obtained by WCP performed at 30 °C with 10 wt. % TiOSO ₄ precursor, heat-treated at 1000 °C, 1100 °C and 1200 °C. Reference XRD patterns from the ICDD for Na ₂ Ti ₆ O ₁₃ and rutile are given at the bottom of the graph.	117
5.58.	XRD of precipitates obtained by WCP performed at 30 °C and 60 °C with 10 wt. % TiOSO ₄ precursor. Reference XRD patterns from the ICDD for anatase is given at the bottom of the graph.	117
5.59.	SEM images of titania and NTO particles synthesized at a) 1000 °C and b) 1100 °C by MSS in Na ₂ SO ₄ via WCP at 30 °C with 10 wt. % TiOSO ₄ precursor.	118

5.60. XRD of samples obtained by WCP performed at 60 °C with 10 wt. % TiOSO ₄ precursor and the addition of 1 mol % of Na ₃ PO ₄ . The samples were heat-treated at 1000 °C, 1100 °C and 1200 °C. Reference XRD patterns from the ICDD for Na ₂ Ti ₆ O ₁₃ and rutile are given at the bottom of the graph.	119
5.61. SEM images of samples synthesized at a) 1000 °C, b) 1100 °C and c) 1200 °C by MSS in Na ₂ SO ₄ via WCP with 10 wt. % TiOSO ₄ precursor. 1 mol % of Na ₃ PO ₄ was added to the system.	120
5.62. XRD of samples obtained by WCP performed at 60 °C with 10 wt. % TiOSO ₄ precursor and the addition of 10 mol % of Na ₃ PO ₄ . Heat-treatments performed at: 1000 °C, 1100 °C and 1200 °C. Reference XRD patterns from the ICDD for Na ₂ Ti ₆ O ₁₃ and rutile are given at the bottom of the graph.	121
5.63. SEM images of samples synthesized by MSS in Na ₂ SO ₄ via WCP with 10 wt. % TiOSO ₄ precursor, heat-treated at a) 1000 °C, b) 1100 °C and c) 1200 °C. 10 mol % of Na ₃ PO ₄ were added to the system.	122
5.64. XRD of samples obtained by WCP performed at 60 °C with 5 wt. % TiOSO ₄ precursor and a) 2.7 % and b) 5 % of Na ₃ PO ₄ . Reference XRD patterns from the ICDD for Na ₂ Ti ₆ O ₁₃ , anatase and rutile are given at the bottom of the graph.	124
5.65. XRD of samples obtained by WCP performed at 60 °C with 5 wt. % TiOSO ₄ precursor and a) 10 % and b) 20 % of Na ₃ PO ₄ . Reference XRD patterns from the ICDD for anatase and rutile are given at the bottom of the graph.	125
5.66. SEM images of samples synthesized at a) 900 °C, b) 1000 °C and c) 1100 °C by MSS in Na ₂ SO ₄ via WCP with 5 wt. % TiOSO ₄ precursor. 2.7 mol % of Na ₃ PO ₄ were added to the system.	126
5.67. SEM images of samples synthesized by MSS in Na ₂ SO ₄ at 1000 °C and 1100 °C via WCP with 5 wt. % TiOSO ₄ precursor and the addition of respectively 5 % (a and b), 10 % (c and d) and 20 % of Na ₃ PO ₄ (e and f).	127
5.68. XRD of samples obtained by WCP performed at 60 °C with 5 wt. % TiOSO ₄ precursor and the addition of 5 wt. % of Na ₃ PO ₄ . Reference XRD patterns from the ICDD for anatase and rutile are given at the bottom of the graph.	129
5.69. XRD comparison of phases obtained by WCP and heat-treatment at 1100 °C under O ₂ flow or ambient condition and the addition of a) 10 % and b) 20 % of Na ₃ PO ₄ . Reference XRD patterns from the ICDD for rutile is given at the bottom of the graph.	130
5.70. SEM images of samples synthesized by MSS under different oxygen partial pressures in Na ₂ SO ₄ at 1100 °C via WCP with 5 wt. % TiOSO ₄ precursor and the addition of respectively 5 % (a and b) and 10 % (c and d) of Na ₃ PO ₄	131
5.71. XRD of samples obtained by WCP performed at 30, 60 and 95 °C with 10 wt. % TiCl ₄ precursor and the addition of 10 % of Na ₃ PO ₄ to Na ₂ SO ₄ . Reference XRD pattern from the ICDD for rutile is given at the bottom of the graph.	132
5.72. SEM images of samples synthesized by MSS in Na ₂ SO ₄ at 1100 °C via WCP with 10 wt. % TiCl ₄ precursor and the addition of 10 % Na ₃ PO ₄ at a) 30 °C, b) 60 °C and c) 95 °C.	133
5.73. MSS in Na ₂ SO ₄ : schematic representation of the change of a) the TiO ₂ crystals morphology with temperature, precursor concentration, the Cl ⁻ /SO ₄ ²⁻ ratio and the addition of NaF by DMP; b) the rutile and NTO particle size and morphology by WCP with TiOSO ₄ and the addition of Na ₃ PO ₄	134
5.74. SEM images of titania and NTO particles synthesized by MSS in Na ₂ SO ₄ via WCP with 5 wt. % TiOSO ₄ precursor at pH = 7 and heat-treated at a) 850 °C, b) 900 °C, c) 1000 °C and d) 1100 °C.	137

5.75.	XRD of samples obtained by WCP with a) pH = 10 and b) pH = 11 performed at 60 °C with 5 wt. % TiOSO ₄ precursor. Reference XRD patterns from the ICDD for rutile, anatase, NTO and Na ₂ Ti ₃ O ₇ are given at the bottom of the graph.	139
5.76.	SEM images of samples synthesized by MSS in Na ₂ SO ₄ via WCP with 5, 10 and 20 wt. % of TiOSO ₄ precursor at pH = 7, 10 and 11, all heat-treated at 850 °C.	140
5.77.	SEM images of samples synthesized by MSS in Na ₂ SO ₄ via WCP with 5 wt. % TiOSO ₄ precursor at pH = 10 and pH = 11 and heat-treated at a) and b) 900 °C, c) and d) 1000 °C and e) and f) 1100 °C.	141
5.78.	XRD of samples obtained by WCP with pH = 11 performed at 60 °C with 5 wt. % TiOSO ₄ precursor in the eutectic mixture 0.53 NaCl-0.47 Na ₂ SO ₄ synthesized at 700 °C < T < 1100 °C. Reference XRD patterns from the ICDD for rutile, anatase, NTO and Na ₂ Ti ₃ O ₇ are given at the bottom of the graph.	142
5.79.	SEM images of titanates particles synthesized by MSS in the eutectic mixture 0.53 NaCl-0.47 Na ₂ SO ₄ via WCP with 5 wt. % TiOSO ₄ precursor at pH = 11 and heat-treated at a) 700 °C, b) 800 °C, c) 900 °C, d) 1000 °C and e) 1100 °C.	143
5.80.	Samples obtained by WCP with pH = 10.3 performed at 60 °C with 5 wt. % TiOSO ₄ precursor in Na ₂ SO ₄ . Reference XRD pattern from the ICDD for NTO is given at the bottom of the graph.	144
5.81.	SEM images of Na ₂ Ti ₆ O ₁₃ rod-shaped particles synthesized by MSS in Na ₂ SO ₄ via WCP with 5 wt. % TiOSO ₄ precursor at pH = 10.3, heat-treated at a) 900 °C, c) 1000 °C and e) 1100 °C. A magnification of each is reported in b), d) and f) respectively.	145
5.82.	SEM image of NTO-1100 showing nanorods on a carbon pad (a) with raw Kikuchi pattern (b) and indexed pattern with Euler angles (c) acquired at the spot marked by a green cross in (a). The insert in (a) shows the orientation of the unit cell according to the indexed pattern.	146
5.83.	XRD diffractograms recorded <i>in-situ</i> during the heat-treatment up to 900 °C of the precursor mixed to Na ₂ SO ₄ . The phases are labeled as follows: S) Na ₂ SO ₄ with the recognizable structural change at T ≈ 240 °C; A) anatase; R) rutile.	147
5.84.	DTA (black line) and TG (blue line) measurement performed on the precursor powder mixed to Na ₂ SO ₄ . The DTA of Na ₂ SO ₄ is reported for comparison (red line). The inset shows a magnification of the exothermic peak at 463.7 °C with baseline correction. . .	147
5.85.	Raman spectra of NTO-900 (black curve), NTO-1000 (red curve) and NTO-1100 (blue curve). The most important bands discussed in the text are shaded and labeled with the respective wavenumber.	149
5.86.	TEM imaging and diffraction in sample NTO-900. a) Bright-field TEM image of an NTO nanorod oriented in [0-10] zone-axis orientation (red circle: SAED aperture) and b) selected area diffraction pattern. c) HRTEM phase contrast image and d) corresponding FFT to c). The inset in c) shows a magnified region of c).	150
5.87.	TEM imaging and diffraction in sample NTO-1100. a) Bright-field TEM image of an NTO nanorod oriented in [001] zone-axis orientation (red circle: SAED aperture) and b) selected area diffraction pattern. c) HRTEM phase contrast image and d) corresponding FFT. e) Noise-filtered STEM-HAADF Z-contrast image and f) magnified part of e) with an atomic model of NTO overlaid (Na: green, Ti: red, O: blue).	152

5.88.	a) Low-loss EELS spectra of rutile [312], anatase [312], sample NTO-900, NTO-1100, and araldite. b) Magnified view of a) to highlight the Na-L _{2,3} and Ti-M _{2,3} edges for sample NTO-900 and NTO-1100, respectively. c) Ti-L _{2,3} and O-K core-loss EELS spectra of rutile [312], anatase [312], sample NTO-900, and NTO-1100. (d) O-K ELNES of sample NTO-900 and NTO-1100, respectively.	153
5.89.	Charge-discharge capacities of NTO-900, NTO-900-60min, NTO-1000 and NTO-1100 electrodes assessed with 74.4 mA/g from 0.01 to 3 V vs. Li/Li ⁺ with their relative efficiencies.	155
5.90.	First cycle's charge and discharge profiles of NTO-900, NTO-1000 and NTO-1100 V vs. Li/Li ⁺ with 74.4 mA/g.	156
5.91.	CV performed on sample NTO-900. The half-cell is cycled from 0.01 to 3 V vs. Li/Li ⁺ at 20 μV s ⁻¹ for 5 cycles and at 10 μV s ⁻¹ during the 6th cycle.	158
5.92.	Rate capability of NTO-900 measured from 0.01 to 3 V vs. Li/Li ⁺ with different applied rates. The reference for the rate is a theoretical capacity of 297 mA h g ⁻¹	159
5.93.	Rate capability of NTO-1000 measured from 0.01 to 3 V vs. Li/Li ⁺ with different rates. The reference for the rate is the theoretical capacity of graphite: 372 mA h g ⁻¹	160
5.94.	Charge-discharge capacities of Na ₂ Ti ₆ O ₁₃ /Na ₂ Ti ₃ O ₇ electrodes heat-treated at different temperatures and with 5 and 20 wt. % precursor. The cells were cycled from 0.01 to 3 V vs. Li/Li ⁺ with 74.4 mA/g.	161
5.95.	SEM images of titanates particles synthesized by MSS in Na ₂ SO ₄ via WCP with a) 5 and b) 20 wt. % TiOSO ₄ precursor at pH = 11 and heat-treated at 900 °C.	162
5.96.	Charge-discharge capacities of Na ₂ Ti ₆ O ₁₃ /Na ₂ Ti ₃ O ₇ electrodes heat-treated at different temperatures in the NaCl-Na ₂ SO ₄ eutectic mixture. The cells were cycled from 0.01 to 3 V vs. Li/Li ⁺ with 74.4 mA/g.	162
5.97.	Charge-discharge capacities per cycle and corresponding efficiency of a rutile-dominated Na ₂ Ti ₆ O ₁₃ (NTO) sample, synthesized by WCP with TiCl ₄ precursor, assessed with 74.4 mA/g from 0.01 to 3 V vs. Li/Li ⁺	163
5.98.	First and second cycle's charge and discharge profiles of the sample obtained by WCP of TiCl ₄ precursor in NaCl, cycled from 0.01 to 3 V vs. Li/Li ⁺ with 74.4 mA/g. The first and second cycles of NTO-900 are added for comparison.	164
5.99.	CV of a combination of rutile and NTO phase, obtained by the WCP with 5 % of TiCl ₄ precursor.	165
5.100.	a) Charge-discharge capacities of NTO-900, NTO-900-60min, NTO-1000 and NTO-1100 assessed with 74.4 mA/g from 0.01 to 3 V vs. Na/Na ⁺ with their relative efficiencies. b) First cycle's charge and discharge profiles of NTO-900, NTO-1000 and NTO-1100 from 0.01 to 3 V vs. Na/Na ⁺	167
5.101.	CV performed on sample NTO-900. The half-cell is cycled from 0.01 to 3 V vs. Na/Na ⁺ at 200 μV s ⁻¹ for 5 cycles and at 10 μV s ⁻¹ during the 6th cycle.	168
5.102.	Rate capability of NTO-900 measured from 0.01 to 3 V vs. Na/Na ⁺ with different applied rates. The reference for the rate is a theoretical capacity of 297 mA h g ⁻¹	169
5.103.	Potential Na/Na ⁺ vs. specific capacity plot classifying materials having been reported to exhibit reversible sodium insertion (reprinted with permission from [234]. Copyright © 2011 American Chemical Society.)	170
B.1.	Phase diagram of the KCl-NaCl binary mixture.	201
B.2.	Phase diagram of the AlCl ₃ -NaCl binary mixture.	202
B.3.	Phase diagram of the MgCl ₂ -NaCl binary mixture.	202

B.4.	Phase diagram of the NaCl-NaF binary mixture.	203
B.5.	Phase diagram of the KCl-LiCl binary mixture.	203
B.6.	Phase diagram of the NaOH-Na ₂ SO ₄ binary mixture.	204
B.7.	Phase diagram of the NaCl-Na ₂ SO ₄ binary mixture.	204
B.8.	Phase diagram of the NaF-Na ₂ SO ₄ binary mixture.	205
C.1.	XRD patterns of a series of tests of titania samples obtained by MSS at 900 °C by mixing always 1 g of anatase precursor with 5 different NaCl masses (99 g, 19 g, 9 g, 5.67 g and 4 g).	207
C.2.	Magnification of XRD patterns reported in figure 5.2 on page 55. The marked area highlights the presence of a reflection belonging to NTO phase at 21.79°.	208
C.3.	Magnification of four XRD patterns reported in figure 5.3 on page 56. The reflection belonging to NTO phase at 21.79° is highlighted.	208
C.4.	XRD patterns of titania samples obtained by MSS in NaCl with 5 and 10 wt. % of titania at 850 °C.	210
C.5.	XRD patterns of titania samples obtained by MSS at 900 °C in NaCl with ≈ 20 wt. % of anatase precursor first without the addition of NaF and with different mol % of NaF (0.1 % and 20 %).	210
C.6.	XRD patterns of titania samples obtained by MSS at 1000 °C in NaCl with ≈ 20 wt. % of anatase precursor and the addition of different mol % of NaF (0.1 % to 50 %).	211
C.7.	XRD patterns of titania samples obtained by MSS at 1100 °C in NaCl with ≈ 20 wt. % of anatase precursor and the addition of different mol % of NaF (0.1 % to 20 %).	211
C.8.	XRD patterns of titania samples obtained by MSS at 900 °C with ≈ 20 wt. % of anatase precursor in pure NaCl and with the addition of 20 mol % of NaF.	212
C.9.	XRD patterns of titania samples obtained by MSS in 0.6 NaCl - 0.4 AlCl ₃ mixture with 2 hours holding time and 10 wt. % of titania.	212
C.10.	XRD patterns of titania samples obtained by MSS between up to 700 °C in 0.41 KCl-0.59 LiCl with 10 wt. % of anatase precursor and with and without the addition of 1 mol % NaF.	213
C.11.	XRD patterns of titania samples obtained by MSS at 500 and 600 °C in 0.41 KCl-0.59 LiCl with 10 wt. % of anatase precursor and the addition of 10 and 20 mol % NaF.	213
C.12.	XRD patterns of titania samples obtained by MSS at 900 °C in NaCl, 20 wt. % anatase precursor and the addition of 0.8 mol % and 1.2 mol % B ₂ O ₃	214
C.13.	Overlapped view of the diffractograms reported in figure 5.25, heat-treatment under ambient atmosphere and under O ₂ flow at 1100 °C with 10 wt. % anatase precursor in NaCl. A reference pattern from the ICDD is reported for comparison.	214
C.14.	Samples heat-treated at 1100 °C with different wt. % anatase precursor in Na ₂ SO ₄ . A reference pattern from the ICDD is reported for comparison.	215
C.15.	Samples heat-treated at 1000 °C with 10 wt. % anatase precursor in Na ₂ SO ₄ with the addition of 0.8 and 1.2 mol % of B ₂ O ₃ . Reference patterns from the ICDD are reported for comparison.	215
C.16.	Samples heat-treated at 1100 °C with 10 wt. % anatase precursor in Na ₂ SO ₄ with the addition of 0.1, 0.5, 0.8 and 1.2 mol % of B ₂ O ₃	216
C.17.	XRD comparison of samples obtained with 5 wt. % TiOSO ₄ precursor and different Na ₃ PO ₄ concentrations at a) 950 °C and b) 1000 °C. Reference XRD patterns from the ICDD for Na ₂ Ti ₆ O ₁₃ , anatase and rutile are given at the bottom of the graph.	217

C.18.	Comparison of phases obtained by WCP with a) 10 % and b) 20 % of TiOSO_4 . Reference XRD patterns from the ICDD for rutile, anatase and NTO are given at the bottom of the graph.	218
C.19.	Comparison of samples obtained by WCP performed at 60 °C with 5, 10 and 20 wt. % TiOSO_4 precursor in Na_2SO_4 at pH = 7, heat-treated at 850 °C.	219
C.20.	Comparison of samples obtained by WCP performed at 60 °C with 5 wt. % TiOSO_4 and a pH of a) 8 and b) 9. Reference XRD patterns from the ICDD for rutile, anatase and NTO are given at the bottom of the graph.	220
D.1.	SEM images showing the magnifications of the alumina flakes obtained via MSS reported in figure 2.10.	221
D.2.	SEM images of rutile particles obtained at a) 900, b) 1000 and c) 1100 °C with 20 wt. % anatase precursor in NaCl.	222
D.3.	SEM images of titania particles obtained with 10 wt. % of anatase precursor at 800 °C in NaCl-KCl eutectic mixture a) and at 820 °C in NaCl b).	222
D.4.	SEM images of titania particles obtained at 1000 °C in NaCl-KCl eutectic mixture with 5 wt. % a), 10 wt. % b) and 20 wt. % c) of anatase precursor respectively.	223
D.5.	SEM image of a detailed view of the terraced growth on titania crystals obtained at 900 °C with 20 wt. % of TiO_2 precursor in NaCl with 20 % F/Ti mol.	224
D.6.	SEM images showing the size comparison between titania particles obtained at 900 a) and b) 1000 °C: 20 wt. % TiO_2 in 0.8NaCl-0.2MgCl ₂ mixture.	224
D.7.	SEM images of titania particles obtained at 900 °C with 5 wt. % a) and 20 wt. % b) of TiO_2 in 0.8NaCl-0.2MgCl ₂ mixture.	225
D.8.	SEM images of alumina flakes mixed to rutile crystals (10 wt. % TiO_2 in 0.7 NaCl-0.3 AlCl ₃ mixture): a) magnification of figure 5.19b and b) magnification of figure 5.19d.	225
D.9.	SEM images showing the morphology of titania particles obtained at 1000 °C with 1 wt. % anatase precursor in NaCl under a) ambient atmosphere and b) under argon flow.	225
D.10.	Larger view of the samples reported in figure 5.26 on page 83. Morphology of titania particles obtained at 1100 °C with 10 wt. % anatase precursor in NaCl under: a) ambient atmosphere and b) under pure oxygen, measured by SEM.	226
D.11.	SEM images showing the morphology of titania particles obtained at 1100 °C with 10 wt. % anatase precursor in NaCl under: a) ambient atmosphere and b) pure oxygen. Enlarged view of the samples reported in figure 5.26.	227
D.12.	SEM images of titania particles obtained at 900 °C and 1000 °C: 20 wt. % TiO_2 precursor in NaCl with the addition of 0.8 mol % (a and c) and 1.2 mol % B_2O_3 (b and d).	228
D.13.	SEM images of samples obtained in NaCl by WCP with 5 wt. % TiCl_4 precursor (figure a) and by DMS (figure b) at 850 °C.	229
D.14.	SEM images of titania and NTO particles obtained in NaCl by WCP (with 5 wt. % TiCl_4 precursor) at 1000 °C (figure a) and 1100 °C (figure b).	230
D.15.	SEM image showing the enlarged view of the sample reported in figure 5.35d, with the typical bifrustum morphology of anatase particles: MSS at 900 °C with 15 wt. % precursor in Na_2SO_4	231
D.16.	SEM images of TiO_2 particles obtained at 1100 °C with 2 hours of holding time with a) 1 wt. %, b) 5 wt. %, c) 10 wt. %, d) 15 wt. % and e) 20 wt. % of TiO_2 in Na_2SO_4	232

D.17.	SEM images of TiO ₂ particles obtained at 1000 °C with 2 hours of holding time with a) 5 wt. % and c) 10 wt. % TiO ₂ precursor in 0.47 Na ₂ SO ₄ -0.53 NaCl and b) 5 wt. % and d) 10 wt. % of TiO ₂ precursor in Na ₂ SO ₄ . e) and f) report 10 wt. % of TiO ₂ precursor at 1100 °C in 0.47 Na ₂ SO ₄ -0.53 NaCl and Na ₂ SO ₄ , respectively.	233
D.18.	SEM images showing the magnification of figure 5.43. TiO ₂ particles obtained at 900 °C, 2 hours of holding time with 10 wt. % of TiO ₂ in: a) 0.2 NaCl-0.8 Na ₂ SO ₄ , b) 0.4 NaCl-0.6 Na ₂ SO ₄ , c) 0.6 NaCl-0.4 Na ₂ SO ₄ and d) 0.8 NaCl-0.2 Na ₂ SO ₄	234
D.19.	SEM images showing a broader view on TiO ₂ particles and Na ₂ Ti ₆ O ₁₃ "micro-belts" obtained at 1100 °C, 2 hours of holding time and 10 wt. % of TiO ₂ with the addition of a) 20 NaF mol%, b) 30 NaF mol% and c) 40 NaF mol%.	235
D.20.	SEM images showing the enlarged view of figure 5.52: a) TiO ₂ particles obtained at 1100 °C, 2 hours of holding time and 10 wt. % of TiO ₂ , b) with the addition of 0.8 B ₂ O ₃ mol% and c) with the addition of 1.2 B ₂ O ₃ mol%.	236
D.21.	SEM images showing the zoomed view of the particles in figure 5.56, synthesized by MSS in Na ₂ SO ₄ heat-treated at a) 1000 °C and b) 1100 °C.	236
D.22.	SEM image showing the zoomed view of a V-shaped crystal in figure 5.67c, synthesized by WCP in Na ₂ SO ₄ heat-treated at 1000 °C and with the addition of 10 % of Na ₃ PO ₄	237
D.23.	SEM image showing the zoomed view of crystals in figure 5.70f, synthesized by WCP in Na ₂ SO ₄ heat-treated under O ₂ flow at 1100 °C and with the addition of 20 % of Na ₃ PO ₄	237
D.24.	SEM images showing the zoomed view of the particles in figure 5.70a and b, synthesized by MSS in Na ₂ SO ₄ under a) ambient condition and b) oxygen flow.	238
D.25.	EBSD data of samples obtained by MSS under pure oxygen flow in Na ₂ SO ₄ at 1100 °C via WCP with 5 wt. % TiOSO ₄ precursor and the addition of 5 % Na ₃ PO ₄	239
D.26.	Additional EBSD data of samples obtained by MSS under pure oxygen flow in Na ₂ SO ₄ at 1100 °C via WCP with 5 wt. % TiOSO ₄ precursor and the addition of 5 % Na ₃ PO ₄	240
D.27.	EBSD data of samples NTO-900 (top) and NTO-1100 (bottom). The representation follows the pattern described in figure 5.82.	241
D.28.	Comparison of FFTs calculated from HRTEM images with calculated NTO spot patterns for samples NTO-900 a) and b) and NTO-1100 c) and d), respectively.	242
D.29.	SEM image of rutile and NTO particles obtained in NaCl by WCP (with 5 wt. % TiCl ₄ precursor) at 900 °C.	243
E.1.	Raman reference spectrum of anatase (Kronos K1002).	245
E.2.	Raman reference spectrum of Rutile (Kronos K2900).	245
E.3.	Raman spectra from two spots of the sample obtained by MSS in NaCl with 5 wt. % of titania at 900 °C.	246
E.4.	Raman spectra from three spots of the sample obtained by MSS in NaCl with 10 wt. % of titania at 1000 °C.	246
E.5.	Raman spectra from three spots of the sample obtained by MSS in NaCl with 10 wt. % of titania at 1100 °C.	247
E.6.	Enlarged view of figure 5.85, obtained with a break in the Raman shift. This allows a detailed view on the intensity variations in the Raman measurements depending on the temperature.	247

List of Tables

2.1. Coordination Number (CN) and cation-anion distance in solid and molten alkali halides according to W. Sundermeyer [108], G.J. Janz [109] and H. Bloom [78].	7
2.2. Combinations of binary and ternary mixtures of molten halides.	9
2.3. Melting temperature T_m of some commonly used salts and typical eutectic compositions used for the molten salt synthesis [4, 8].	22
3.1. Crystal structures of TiO_2 [167].	27
3.2. Classification of inorganic pigments [104].	36
5.1. Phase composition of samples after heat-treating different amounts of TiO_2 in NaCl in the range 820 °C to 1100 °C (A = Anatase, R = Rutile) calculated by Rietveld refinement.	57
5.2. Phase composition of samples synthesized in molten 0.5 NaCl-0.5 KCl. Synthesis temperature: 900 to 1100 °C, holding time: 2 hours (A = Anatase, R = Rutile).	64
5.3. Phase composition of samples heat-treated in two different NaCl- $AlCl_3$ ratios. Synthesis temperature: 900 to 1100 °C, 2 hours holding time (A = Anatase, R = Rutile).	75
5.4. Phase composition of samples obtained by MSS in NaCl with 5 wt. % $TiCl_4$ precursor calculated by Rietveld refinement. Synthesis temperature: 850 to 1100 °C, 2 hours holding time.	86
5.5. Phase composition of samples after heat-treating different amounts of TiO_2 in Na_2SO_4 in the range 900 °C to 1200 °C calculated by Rietveld refinement (A = Anatase, R = Rutile).	92
5.6. Phase composition of samples obtained by DMP in the 0.47 Na_2SO_4 -0.53 NaCl eutectic mixture calculated by Rietveld refinement. Synthesis temperature: 900 to 1100 °C and 2 hours holding time.	98
5.7. Phase composition of samples obtained by MSS in NaCl- Na_2SO_4 mixtures by DMP calculated by Rietveld refinement. Synthesis temperature: 900 to 1100 °C and 2 hours holding time.	102
5.8. Phase composition of samples obtained by WCP at 60 °C in Na_2SO_4 with $TiOSO_4$ precursor. Synthesis temperature: 1000 to 1200 °C and 2 hours holding time (A = Anatase, R = Rutile, NTO = $Na_2Ti_6O_{13}$).	113
5.9. Phase composition of samples obtained by WCP in Na_2SO_4 with 10 % $TiOSO_4$ precursor and the addition of Na_3PO_4 . Synthesis temperature: 1000 to 1200 °C and 2 hours holding time. (R = rutile, NTO = $Na_2Ti_6O_{13}$).	119
5.10. Phase composition of samples obtained by WCP in Na_2SO_4 with 5 % $TiOSO_4$ precursor and the addition of Na_3PO_4 . Synthesis temperature: 900 to 1100 °C and 2 hours holding time. (A = anatase, R = rutile, NTO = $Na_2Ti_6O_{13}$).	123
5.11. Phase composition of samples obtained by WCP of $TiOSO_4$ at different pH and MSS at 750 °C - 1100 °C. A = Anatase, R = Rutile, NTO = $Na_2Ti_6O_{13}$, NTO7 = $Na_2Ti_3O_7$	136

5.12. Quantification of EDX spectra acquired from a single $\text{Na}_2\text{Ti}_6\text{O}_{13}$ nanorod using the Cliff-Lorimer k-factor method.	154
A.1. List of the chemicals used for the synthesis of TiO_2 and sodium titanates powders.	199
C.1. Phase composition of samples after heat-treating different amounts of TiO_2 in 25 g of NaCl in the range 820 °C to 1100 °C (A = Anatase, R = Rutile, NTO = $\text{Na}_2\text{Ti}_6\text{O}_{13}$) and 2 hours of holding time calculated by Spurr's equation.	209
C.2. Phase composition of samples obtained by heat-treating 1 g of TiO_2 mixed in different NaCl amounts at 900 °C (A = Anatase, R = Rutile) and 2 hours of holding time calculated by Spurr's equation.	209

List of Abbreviations

ART	anatase to rutile phase transition
BCF	Burton-Cabrera-Frank
CFE	crystal facet engineering
CIF	Crystallographic Information File
CN	coordination number
CP	coordination polyhedron
CSS	conventional solid-state
CV	cyclic voltammetry
DIN	German Institute for Standardization
DMP	dry-mixed preparation
DTA	differential thermal analysis
EBS	electron backscatter diffraction
EELS	electron energy-loss spectroscopy
ELNES	energy loss near edge structure
FFT	fast Fourier transform
GCPL	galvanostatic cycling with potential limitation
GIC	graphite intercalation compound
GU	growth unit
HP	Hartman-Perdok
HAADF	high angle annular dark-field
ICDD	International Center for Diffraction Data
ICSD	Inorganic Crystal Structure Database
ISO	International Organisation for Standardization
KGaA	Kommanditgesellschaft auf Aktien
L-F	Lux-Flood

LIB	lithium-ion battery
MSS	molten salt synthesis
NTO	$\text{Na}_2\text{Ti}_6\text{O}_{13}$
OA	oriented attachment
PBC	periodic bond chain
PSD	particle size distribution
PLP	pearl luster pigment
RDF	radial distribution function
RT	room temperature
SAED	selected area electron diffraction
SEI	solid electrolyte interface
SEM	scanning electron microscope
SIB	sodium-ion battery
SSS	solid-state synthesis
TEM	transmission electron microscope
TPRE	twin-plane re-entrant edge
TMSS	topochemical molten salt synthesis
UV	ultraviolet
USP	ultrasonic spray pyrolysis
WCP	wet chemical preparation
XRD	X-Ray Diffraction

1. Introduction and motivation of the work

Introduction The present thesis deals with the crystal structure and morphology of TiO_2 and sodium titanates ($\text{Na}_2\text{O} \cdot n\text{TiO}_2$, $n = 3$ and 6) prepared by molten-salt synthesis (MSS). The research interest in the crystallization process of these materials resides mainly in their attractive physical and chemical properties and the advantage of the MSS as an easily up-scalable synthesis procedure. The MSS is a quite facile technique to produce, *e.g.*, ceramic powders and 1D nanostructures [1], using a molten salt as medium where the reactants dissolve and precipitate [1–9]. Crystallization occurs once the supersaturation condition is reached either by evaporating the solvent or by cooling the reactor. The ratio of reactant and salt matrix, the heat treatment and the type of precursor material affect the final product [10–15]. Molten salts especially facilitate the dissolution and precipitation of oxides [16, 17]. MSS is more effective at lower temperatures than the conventional solid-state reaction [4], allowing the control of the crystallinity and of the morphology of the products, all aspects increasing the environmental appeal of this method [8, 9, 18]. The control of the crystal structure, the morphology and the particle size of the synthesized materials are essential topics in the field of material science. The knowledge of the morphology can be of specific advantage for many applications, *e.g.*, the pigment industry [19] or the battery production (both topics explicitly considered in this thesis) [20]. The ability to shape crystal habits — defined as *crystal facet engineering (CFE)* — helps to establish the correlation between phase and morphology with other physical and chemical material properties. Recently CFE has emerged as a successful strategy to improve the design of materials for *e.g.*, catalysis, molecular adsorption, photoreactions [21] and electronics [22]. The synthesis routes, the choice of precursors and the use of capping agents, stabilizing highly reactive crystal facets during the crystal growth, lead to different crystal shapes allowing to tailor the crystal habit for the desired application. Hydrothermal synthesis and sol-gel synthesis are commonly used for CFE to obtain nanoparticles selectively grown along specific directions. Recently the formation of high-index facets by means of MSS was reported for several complex materials [23–26].

TiO_2 is one of the most investigated metal oxides because of its wide range of applications. It is used in heterogeneous catalysis, as photocatalyst, as gas sensor, as a corrosion-protective coating, in solar cells, as food additive [27] and as white pigment (for paints and cosmetic products) [28]. It is popular due to its clear white color and the strong hiding power and covers about 60% of the global pigment production with more than 4 million tons per year [29]. The two main polymorphs of titania, anatase and rutile, form both a tetragonal structure and belong to the space groups $I4_1/amd$ and $P4_2/mnm$, respectively [28]. Their equilibrium crystal shapes by the Wulff construction differ due to different

surface energies [30, 31]. Therefore, the growth of the particles is driven by different crystal facets ultimately defining the crystal habit. CFE can improve many of the application of TiO₂. Selecting the 001 facet of both anatase and rutile as most exposed surfaces, enhances the photocatalytic properties of TiO₂ for example [32–34].

The influence of the precursor type on TiO₂ formation is investigated in this thesis by using i) a nanosized anatase directly mixed to the salt or ii) a TiO₂ precursor (TiOSO₄ and TiCl₄) leading to the formation of titanium hydroxide after hydrolysis. Previous studies on TiO₂ in the literature compare the results of MSS with those obtained by solid state synthesis [35, 36]. Anatase nanoparticles obtained by MSS were investigated as anode material for lithium-ion batteries [37], or for dye-sensitized solar cells [38]. More recently, the O²⁻ activity in the salt melt was correlated with the rutile habit and the product composition [39]. Molten salt composition (chlorides, sulfates and eutectic mixtures), heating temperatures and atmospheres, and different molar ratio of titania in the salt matrix are causing different morphologies. Therefore, the influence of these parameters on the rutile and anatase dissolution rate, on their habits, and on the anatase to rutile phase transition (ART) are investigated in this work. Special attention is given here to the type of precursor and its preparation.

The second part of this work is concerned with the synthesis and application of Na₂Ti₆O₁₃ as a battery component. Alkali and alkali-earth titanates have recently attracted strong interest due to their excellent physical- chemical properties (*e.g.* an outstanding chemical stability and anomalously high ionic conductivity [40–43]). In particular, sodium titanates (Na₂O·nTiO₂) have been extensively investigated for the application as photocatalyst [44, 45] and zero-strain anode material for lithium-ion battery (LIB)s [46, 47] and sodium-ion battery (SIB)s [48, 49]. Batteries are increasingly gaining popularity among the plethora of energy storage technologies available for large-scale applications, due to their strong development driven by the conversion of combustion engine cars to electric vehicles powered by LIBs[50]. SIBs are expected to be increasingly important for stationary energy storage solutions, being a cheaper and environmental friendlier alternative to LIBs. SIBs have less strict requirements for the gravimetric and volumetric energy density [48, 51–54] and their redox potential (-2.71 V (Na/Na⁺) vs. SHE) is only 0.3 V above that of Li/Li⁺. Additionally, SIBs would decrease the safety issues typically for the LIB technology in "battery farms" [55, 56]. Indeed fires and explosions by highly inflammable gases (HF, H₂, CH₄, C₂H₄ and CO) are a common safety issue still not resolved for battery energy storage systems of several MWh [57]. Establishing SIBs in grid energy storage systems would have a positive effect on the capital costs, the grid reliability and on the integration of intermittent renewable energy sources, supporting the transition to a low-carbon economy [58, 59]. However, SIBs are less explored than LIBs and the research for promising electrode materials is still a fundamental concern, since the commonly used materials for LIBs, especially graphite, are less effective in SIBs assemblies [51–53, 60–63]. A stage-I Na graphite intercalation compound (GIC) is unstable due to a positive formation energy and higher redox potential of Na/Na⁺ with respect to Li/Li⁺ [64, 65]. The overall thermodynamic balance is thus unfavorable [66]. Non-graphitic disordered carbons have been intensively explored as potential anodes for sodium reversible storage [67–69]. However, their major drawback is a weak cycling stability,

a serious capacity fading upon prolonged cycling and a low-potential sodium insertion leading to the risk of dendritic plating. Thus, in particular for the application of grid storage, SIBs need stable and safe negative electrode materials. NTO has been shown to be electrochemically active in a lithium cell [70, 71]. With sodium NTO forms a plateau at around 0.8 V leading to a high-voltage SIB if coupled with an appropriate high-potential cathode material [72].

Several synthesis methods can be found in the literature for NTO. However, these approaches often lead to mixtures of NTO/TiO₂ and cannot be upscaled as MSS can. The MSS used for the growth of TiO₂ crystals can easily be adapted to the synthesis of NTO. Therefore, this thesis focuses also on the synthesis of titanates by the MSS method and their application as battery component, analyzing the parameters that influence the morphology, particle size and structure of the titanates. According to our knowledge, a systematic study of the crystal growth of TiO₂ and titanates by MSS is still missing.

Aim of the study Mono-crystalline lamellar TiO₂ could be very attractive for the pigment industry due to its high refractive index, its chemical and thermal resistance, its low price and low toxicity [73]. Many techniques have been investigated to achieve this habit: hydrothermal synthesis [74], dissolution of a TiO₂-mica pigment substrate in a strong acid [19], sol-gel syntheses [75], exfoliation of layered precursor combined with freeze-drying [76] and the use of surfactants as self-assembly template [77]. All these methods cause problems like coarse surfaces, twinning of crystals or poly-crystalline and slightly porous flakes. Implementing the MSS production method for flake-like titania pigments, like the well-known alumina-flakes (Xirallic®, Merck KGaA), would generate an enormous benefit of increasing the chromatic effects available for paints. Therefore it is intended to achieve rutile crystals with a very similar habit to the alumina flakes by means of the MSS.

Main aim of the second part of the thesis is making available an efficient and cost-effective synthesis of NTO in large yield. Control of the habit of the NTO crystals (nanorods with length of tenth of microns) and of the structure and composition by MSS (avoiding the formation of rutile) is expected to improve the performances of sodium-based batteries. Therefore, electrochemical tests of Na-half cells (and for comparison Li-half cells) with NTO nanorods, are foreseen. Such studies will answer the question whether NTO-based SIBs are well suited for grid storage application, compensating the low theoretical capacity of $\approx 50 \text{ mA h g}^{-1}$ (with respect to Na) with the high thermal stability, high rate capability and low synthesis costs. A high purity of the NTO nanorods leading to a high sodium ion mobility and stable capacity of the Na-half cell are an excellent starting point to achieve this goal.

Chapter 1 comprises the introduction and the motivation of the work. Basics of the MSS and the crystal growth are given in chapter 2. Chapter 3 describes complementary crystallographic information on TiO₂ and titanates. Chapter 4 summarizes the applied experimental investigation methods. The results are reported and discussed in chapter 5: how to control the crystal structure and habit of rutile particles by MSS in chlorides and sulfates is described in sections 5.1 and 5.2, respectively; how to

adopt the same process to obtain pure NTO is described in section 5.3; electrochemical studies of NTO are presented in section 5.4.

2. Basic information

Chapter 2 presents background information about MSS and the crystal structures of interest for the understanding of the forthcoming chapters.

2.1. Properties of molten salts

The main solvent in chemistry is water, but in several cases molten salts are a much better and more versatile solvent [78]. The latter allow chemical reactions not possible in water or organic solvents because of their high thermal stability, low viscosity and low vapor pressure. The choice of the salt — either a single one or a mixture of several salts — strongly affects the chemical reactions occurring during the MSS and defines the properties of the products, *e.g.*, their composition, morphology and crystal structure. Due to the large variety of available salts, it is possible to select among different melting temperatures, strongly oxidizing or reducing conditions and different acidities/basicities of the melt. A comparison between conventional solid-state synthesis (SSS) and MSS shows that lower temperatures (150 °C to 1100 °C) are needed for reactions in MSS. The liquid solvent guarantees a higher mobility of the reactant particles, leading to an increased reaction rate. Typically mobilities in MSS (of 10^{-5} to 10^{-8} $\text{cm}^2 \text{s}^{-1}$) are by several orders of magnitudes higher than conventional solid-state (CSS) mobilities [79]. Furthermore, MSS achieves high yields, reason why its importance grows as manufacturing process. Last but not least, the stability for red-ox systems in molten salts is much higher compared to aqueous solution (decomposition potential of, *e.g.*, 3.5 volts for LiCl-KCl at 700 °C compared to 1.2 volts for water at room temperature (RT)).

Molten salts attract the interest of scientists working in experimental and theoretical research fields, *e.g.* electrochemistry, transition metal chemistry, inorganic coordination chemistry, nuclear technology, corrosion science and catalysis. As a consequence, the electrolysis of metals has been one of the first applications gaining great commercial importance. Already at the end of the 19th century the Hall-Hérault process was the major industrial process for refining aluminum from bauxite ore dissolving it in molten cryolite (Na_3AlF_6) [80]. The energetic advantage of using a molten salt as solvent is obvious, since there is a decrease of the melting point of alumina from 2000–2500 °C to 940–980 °C. Alkali nitrates/nitrites are commonly used as molten flux for solar thermal power installations. Molten

fluoride melts are effective for the electrorefining of silicon [80]. In general, ionic melts are also used to perform high-temperature electrochemical synthesis, one of the promising methods for the deposition of refractory coatings, *e.g.* Mo₂C, W₂C and ZrB₂.

In the last two decades the use of molten salts reflowered, reporting on stable ternary, quaternary and higher order oxides [81]. The recently growing popularity of the MSS approach stems from the ease of producing anisometric particles, enlarging the prospect of free standing or hierarchical nanomaterials [17]. Additionally, the continuous interest for novel 1D nanomaterials provided new synthesis techniques, showing that the solution based routes are most promising [82–84]. Shaowei Zhang and W.E. Lee investigated the “*template growth*” mechanism [2, 85, 86], especially useful for coatings on ceramic powders [87–89]. This method is also known as the *topochemical molten salt synthesis (TMSS)* [90, 91]. On the other hand, the “*dissolution-precipitation*” mechanism was found to play a role in the formation of LaOCl [92]. A detailed explanation of both mechanisms can be found in section 2.3 on page 14 (see figure 2.6 for a representation of both). Recently, the review of Fu *et al.* [91] demonstrated that the TMSS is well suited for the synthesis of ferroelectrics. Nitrides and oxynitrides were studied as photocatalyst for water splitting under visible-light irradiation. Their formation via MSS was investigated, among others, by the research teams of Kazunari Domen and Katsuya Teshima [93–96]. The exposition of stable high-index facets appears to be relevant for catalytic reactions, since they lead to an increase of under-coordinated sites [26]. The research group of Hans-Conrad zur Loye [3, 81, 97] as well as the the group of Paul A. Maggard [7, 98–103], have been quite successful in synthesizing complex oxides, notably transition metals in reduced oxidation states. Concerning industrial application, the MSS process is also quite popular for the production of pigments. The MSS is also quite popular for the production of pigments [104] (for more details see chapter 3 on page 27). Finally, a recent work presents a new application for molten salts, reporting the manufacturing of non-oxide ceramics, whose synthesis is not performed under inert atmosphere, as it is usually done with oxidation-prone materials [105, 106].

Molten salt structure Molten salts share with liquids the property of fluidity. Above their melting point the salts are liquids having ions as structural units with a considerable freedom of movement. Their structure is characterized by an alternation of positively and negatively charged ionic solvation shell around a given ion [107]. Coulomb forces between anions and cations restrict the movement of ions guaranteeing short-range order. The ions can cluster into groups termed as *ion pairs* or *complex ions* [78]. They have the freedom to move and adopt an interparticle distance different from the original one in the solid state. Measurements performed on alkali halides (see data reported in table 2.1) have shown that the cation-anion distance as well as the average cation-anion *coordination number (CN)* decrease with the change of the state of matter [108]. At the same time the distance between like ions (cation-cation and anion-anion) increases. A volume expansion is observed during the melting of most of the salts, with an increase of around 20% in the case of the alkali halides [78]. This increase is given by the empty space introduced into the structure by the melting process, the so-called *free volume*. It

can be distinguished in two ways: *fluctuation volume* and *hole volume*.¹ All these changes lead to a loss of the long-range order present in the solid structure.

Table 2.1.: Coordination Number (CN) and cation-anion distance in solid and molten alkali halides according to W. Sundermeyer [108], G.J. Janz [109] and H. Bloom [78].

	Solid crystal			Molten salt		
	CN	Distance [Å] (cation-anion)	Distance [Å] (cation-cation, anion-anion)	Average CN	Distance [Å] (cation-anion)	Distance [Å] (cation-cation, anion-anion)
LiCl	6	2.66	3.76 ^[78]	3.7	2.46	3.85 ^[78]
LiBr	6	2.85	-	5.2	2.68	-
LiI	6	3.12	4.41 ^[78]	5.6	2.85	4.45 ^[78]
NaCl	6	2.95	-	4.7	2.80	-
NaF ^[109]	6	2.40	-	4.1	2.30	-
NaI ^[109]	6	3.35	4.74 ^[78]	4	3.15	4.80 ^[78]
KCl	6	3.26	-	3.6	3.10	-
CsCl	6	3.57	5.05 ^[78]	4.6	3.53	4.87 ^[78]
RbCl ^[109]	6	3.41	-	4.2	3.30	-

All this information was obtained by extended X-ray absorption fine structure providing structural data in the form of the pair *radial distribution function (RDF)*. The latter expresses the probability that pairs of ions exist within a certain distance. The maxima of a RDF present the average separation between the particles, the first peak refers to unlike ions while the second to like ions. For a single fused salt, three different partial RDFs have to be collected with at least three independent sets of diffraction measurements. They describe the cation-anion, anion-anion and cation-cation distribution (see the example reported in figure 2.1). The forces acting between the particles constituting the melt were first described by F.H. Stillinger using quantum mechanics [110].² The experimental data from the partial pair RDF match quite well with the results obtained by molecular dynamics [107, 111] and Monte Carlo simulations — employing a pair potential that included rigid and polarizable ions [112]. It is also possible to describe the electrical transport properties of a molten salt by such simulations [113].

Diffusion in molten salts Diffusion in molten salts is of great theoretical and practical importance. It is relevant especially for electrolysis, where the metal ions migrate to the surface of the electrodes. Diffusion promotes the growth of crystals in molten salts by increasing the contact between nucleating clusters. This topic will be described in more detail in the following section 2.3. Self-diffusion coefficients of the ions can be determined by Fick's second law of diffusion (equation 2.1). Considering a uniform

¹For details refer to section 2.1 of [78].

²For a more detailed description refer to chapter 1 of [110].

cross-section and unidirectional diffusion, one obtains

$$\frac{\partial C}{\partial t} = \frac{\partial}{\partial l} \left(D \frac{\partial C}{\partial l} \right) \quad (2.1)$$

with C being the ion concentration, t the diffusion time, D the diffusion coefficient and l the diffusion length. Diffusion coefficients of molten salts are of the order of $10^{-4} - 10^{-5} \text{ cm}^2 \text{ s}^{-1}$. The temperature dependence of the diffusion coefficient is given by the Arrhenius equation 2.2

$$D = D_{\infty} \exp \left(\frac{-E_D}{RT} \right) \quad (2.2)$$

where D_{∞} is a constant and E_D the activation energy for the diffusion.

Reaction types in MSS Chemical reactions in molten salts can be categorized in: i) those utilizing the molten salt — or a component of it — as reactant; ii) those using the molten salt as nonreactive solvent; iii) those for which the molten salt acts as a catalyst [78, 108]. A quite known example for i) is the deposition of a metal from its molten salt (e.g. Hall-Héroult Process). An example for type ii) is given by reaction 2.3, carried out in molten LiCl-KCl at 400 °C. The high solubility of LiH in the LiCl-KCl melt is the reason why the formation of SiH_4 is possible.

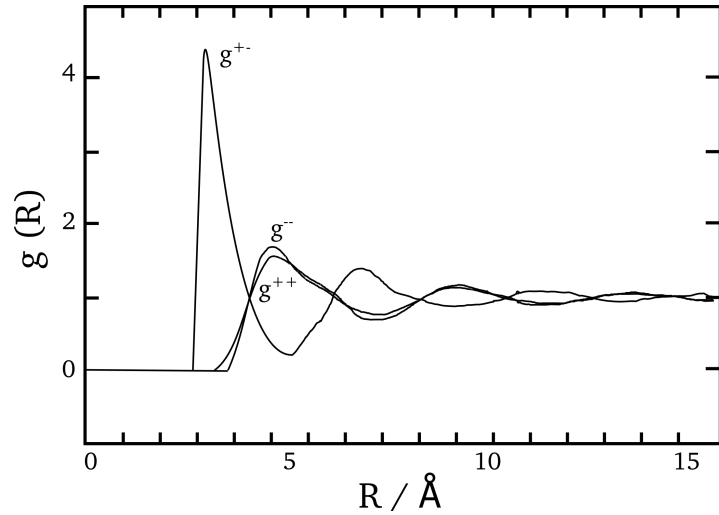
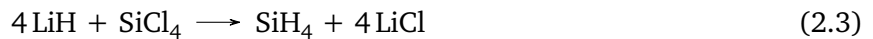


Figure 2.1.: Smoothed partial pair RDF of molten RbCl obtained by neutron diffraction, after [112].



Examples for the third case are chlorination reactions [108, 114] or thermal dehydrogenation [115], where a much faster development of the reactions is required. In this work the molten salt is mainly used as a nonreactive solvent (type ii) or as reactant (i).

2.1.1. Metal chlorides and sulfates as solvents in MSS

This section focuses on metal chlorides and sulfates (or mixture of both) as solvents. Table 2.2 lists some examples of binary and ternary combinations. Salt solutions are classified into groups determined by these variables. In the case of a two-salts mixture with no ion in common, the change of their proportion leads to a variation in composition with respect to all the ions [78]. This combination is known as

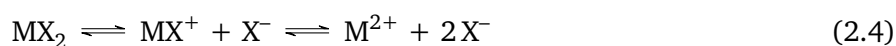
reciprocal system (see example 4 of table 2.2). Most of the salt systems are completely miscible but there exist systems with partial miscibility. Examples for partial miscibility are given by: i) binary mixtures between a covalent salt (with multivalent cations like: Al^{3+} , Sb^{3+} or Bi^{3+}) and a completely ionic character component (e.g. $\text{AlCl}_3 + \text{KCl}$); ii) binary mixtures with anions of considerably different size, e.g. NaCl mixed with sodium titanate, silicate or borate; iii) *reciprocal systems* made of one component with low polarity combined with a typical ionic salt like $\text{AlBr}_3\text{-NaCl}$ or AgBr-LiNO_3 .

Table 2.2.: Combinations of binary and ternary mixtures of molten halides.

Nr.	Description	Example
1	Symmetrically charged mixture with one ion in common	NaCl-KCl
2	Asymmetrically charged mixture with one ion in common	NaCl-AlCl_3
3	Symmetrically charged mixture	NaCl-KBr
4	Asymmetrically charged mixture	NaCl-AlBr_3
5	Ternary mixtures with just one anion in common	NaCl-KCl-AlCl_3

From a thermodynamical point of view a salt mixture is ideal when the enthalpy of mixing $\Delta H_{\text{mix}} = 0$. Correspondingly, also $\Delta V_{\text{mix}} = 0$. This condition is almost reached in the case of example 1 in table 2.2, showing a nearly ideal behavior due to the quite similar ionic radius and charge of Na and K. As the difference between the cations radii increases, the mixing enthalpy becomes more exothermic with $\Delta H_{\text{mix}} < 0$. Non-ideal mixtures are described in terms of *excess quantities*, which estimate the deviation from the ideal case. A detailed description is given by Bloom [78]. Transition metal chloride melts are prone to form dimers, trimers or polymers as molecular units. Figure 2.2 reports some examples of non-ideal mixtures. As shown, for a mixture between an alkali chloride and a transition metal chloride salt, the ΔH_{mix} and ΔV_{mix} follows an S-shaped trend. The addition of an alkali chloride to a transition metal chloride salt leads to complex ions, and even the formation of polymeric ions. The higher is the alkali chloride fraction, the more ionic becomes the melt.

The melting behavior of chlorides differs when the cation belongs either to the alkali or earth-alkali group. In the first case, the interaction between the ions is governed by coulombic forces, showing a strong attraction between oppositely charged ions. For the earth-alkali halides it is more complicated to define a structural pattern. Equation 2.4 reports the reaction path of IIA-chlorides (with the exception of BeCl_2 with a largely covalent character) forming some ion association complex at a first stage, dissociating completely in a second stage by increasing the temperature [78].



Sulfates are more complicated as reactants due to the high melting temperatures typical of these salts. Their acid/base and redox properties are of main importance [117]. The dissociation equilibrium

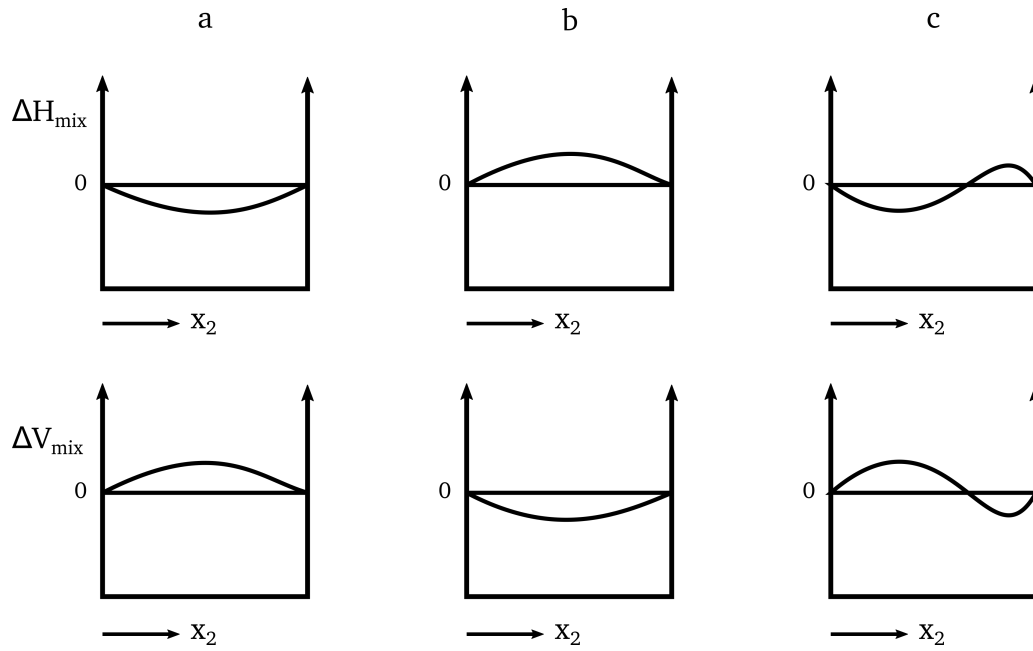


Figure 2.2.: Enthalpy of mixing ΔH_{mix} (top row) and excess volume variation ΔV_{mix} (bottom row) of: a) NaCl (x_1) - KCl (x_2); b) NiCl₂ (x_1) - CoCl₂ (x_2); c) KCl (x_1) - CoCl₂ (x_2) after [116].

for the sulfate anion in the melt determines the acid/base properties of the salt (equation 2.5).



Thus the acidity of the melt is determined by the SO₃ partial pressure, as well as the SO₂ and O₂ partial pressures, in equilibrium with the melt (equation 2.6).



An alternative is to estimate the concentration of the oxide ion in the melt, which is generally preferred for basic melts. These control parameters allow to understand the interaction between the sulfate melt and the oxide material, depending on the acidity of the first and the relative acidity of the second. If the flux is acidic enough to follow the path reported in equation 2.7,



metal and sulfate ions are formed in the melt. On the contrary, in a basic melt metal oxy-anions MO₂²⁻ are dissolved in the melt (equation 2.8).



2.2. Crystal growth models

Section 2.2 provides a brief overview of crystal growth models, specifically of the *Hartman-Perdok (HP)* theory. The equilibrium shape concept developed by Wulff (1901) allowed predictions on the morphology of crystals [118], essentially being a further development of the thermodynamical description given by Gibbs (1878). The *Burton-Cabrera-Frank (BCF)* theory is the first description (1951) of the growth mechanism of stepped crystal surfaces and successfully predicted the presence of growth spirals on the surfaces [119]. The BCF theory represented a revolutionary advance in the theory of crystal growth and its impact is still strong since it applies to any theory of crystal growth [120, 121]. This theory explained the facets' growth by means of the screw dislocations mechanism. In steadily growing state, a single dislocation exhibit a growth velocity of the same order of any distribution of dislocations [122].

The Hartman-Perdok Theory The BCF theory was followed by the HP theory (1955) giving interpretations about the crystal growth. The HP theory introduces a classification of the crystal facets forming during the growth of crystals. These can be classified as **F** (flat), **K** (kinked) or **S** (stepped) faces (as reported in figure 2.3). This classification is based on the strength of the chemical bonding inside the crystal. According to their direction, uninterrupted chains of strong bonds, known as *periodic bond chain (PBC)*, are defining the aforementioned faces. At least two PBCs crossing each other and oriented in parallel form a F face. S faces are oriented parallel to one PBC while K faces are not parallel to any PBC [123]. The PBCs are described as composed of *growth unit (GU)*s. To predict the morphology of the crystals, Hartman and Perdok introduced the attachment energy (broken bond energies) E_{att}^{hkl} and the energy of a slice of the crystal E_{sl}^{hkl} . They were able to show that the relative growth rate of (hkl) faces for spiral growth and two-dimensional nucleation is directly proportional to the attachment energy E_{att}^{hkl} [125]. Thus, it is possible to determine the growth morphology by calculating the E_{att}^{hkl} of all (hkl) . After sectioning a crystal in slices with thickness d_{hkl} , one has to determine how many PBCs are intersecting in this slice. In the case of an F face the intersection of two PBCs forms the area A_{hkl} (as shown in figure 2.4). The slice energy E_{sl}^{hkl} is defined as the half of the energy released when an infinite d_{hkl} slice is formed. It is determined by calculating the interaction energy per GU of the A_{hkl} and the half of the surrounding slice. Finally, E_{att}^{hkl} is defined by the interaction energy per GU of the A_{hkl} and the underlying

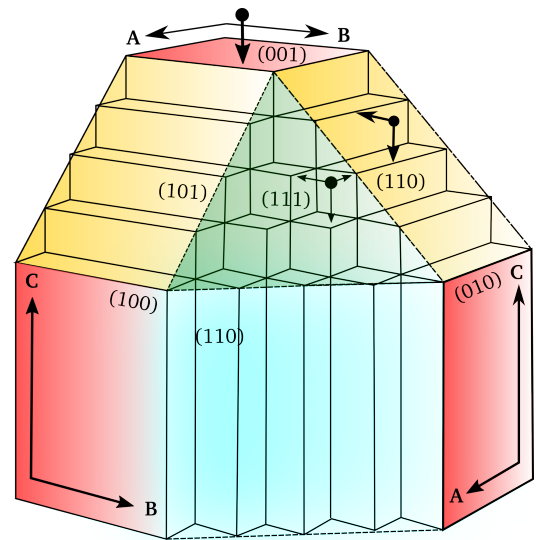


Figure 2.3.: Representation of the PBCs and the **F** (100, 010, 001), **S** (110, 101, 011) and **K** (111) faces defined in the HP theory, after [124].

slice [118]. As reported in equation 2.9, the energy released per GU is the crystallization energy E_{cr}

$$E_{cr} = E_{att}^{hkl} + E_{sl}^{hkl}, \quad (2.9)$$

constant for all the crystal faces of a crystal.

The proportionality of the growth rate R_{hkl} to the E_{hkl}^{att} is given by the fact that the probability of having a GU, remaining fixed to an (hkl) face, increases with E_{att}^{hkl} (equation 2.10).

$$R_{hkl} \propto E_{att}^{hkl} \quad (2.10)$$

Layered crystal forms, e.g., graphite and mica, are the most striking examples demonstrating the correlation between R_{hkl} and E_{att}^{hkl} .

To conclude, the choice of the GU is of fundamental importance in the HP theory to predict the growth and the equilibrium shape of a crystal. They determine the strength of the PBCs and of the E_{att}^{hkl} , respectively. For example in a crystal with more than one F face involved, their morphological importance is given by the strength of their PBCs following the order of the E_{att}^{hkl} . The morphological importance $MI(hkl)$ is defined as the relative size of an hkl form compared to the entirety of the morphology. The larger the lattice distance d_{hkl} , the larger is the morphological importance $MI(hkl)$ of the corresponding hkl form (Bravais–Friedel–Donnay–Harker (BFDH) law)

$$d_{h_1k_1l_1} > d_{h_2k_2l_2} \longrightarrow MI(h_1k_1l_1) > MI(h_2k_2l_2). \quad (2.11)$$

A difference in MI also provides a relative measure of the growth rate of a given form

$$R_{hkl} \propto \frac{1}{d_{hkl}} \quad (2.12)$$

once the effective d_{hkl} distances, due to the systematic extinction rules, are taken into account.

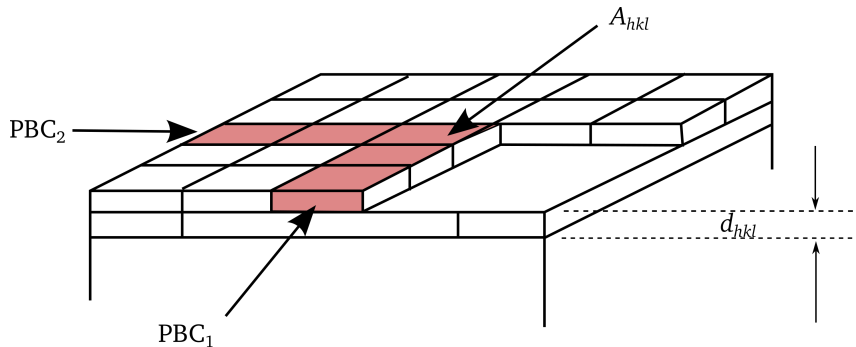


Figure 2.4.: Representation of the PBCs defining a F face within the HP theory, after [118].

2.3. Crystal growth in molten salts

The HP theory describes the crystal growth process without regard to experimental preconditions. Molten salts are commonly used to grow single crystals. The material applied as solute is dissolved into the flux and crystals grow via supersaturation. This happens either by lowering the solubility through a gradual temperature decrease of the melt or by reducing its volume through flux evaporation at a constant temperature [93]. When the molten salt at high temperatures acts as an inert solvent (reaction type II; see page 8), the crystal growth occurs by the following steps [4, 7]:

- (i) dissolution of reactants;
- (ii) diffusion in the molten salt;
- (iii) nucleation of reactants;
- (iv) clustering and growth into defined crystal structures and morphologies.

All these steps are influenced by parameters that are discussed in the following sections, *e.g.*, the supersaturation, the oxoacidity of molten salts (Lux-Flood theory) [126, 127] and the oxygen partial pressure P_{O_2} dictating the redox equilibria [81]. As a consequence, the crystal growth requires careful adjustment of the mentioned parameters. Furthermore, the use of additives or mineralizers (*e.g.* OH^- , F^- , Cl^-) can have a decisive role. Mineralizers *de facto* have a multitude of effects ranging from i) promoting the dissolution of the reagents by stabilizing metal complexes in solution, ii) increasing the width of the metastable region where supersaturation exists, iii) altering the viscosity of the melt, and iv) influencing nucleation and consequently crystal size. Halide salts such as NaCl, KF or BaCl_2 can promote the formation of metal complexes in solution and thereby increase the solubility of reagents [81]. Therefore, the molten flux has to be individually designed to initiate reactions of type II, or reactions between reactant and flux itself (type I). In MSS the salt has to be the predominant part of the mixture, in order to fulfill the control function on the size and the shape of the reaction product. Additions of only a few percent of the total weight limit the salt's function.

The advantage of growing crystals by the MSS approach becomes evident when comparing it to the SSS or to the crystals growth from the own melt [128]. Crystals grow within a molten salt in a shorter time and at much lower temperatures (see section 2.1 on page 5). The reason lies in the increased contact area of the reactant particles and in the higher mobility of the species within the molten salt [129]. Moreover, the absence of a temperature gradient in the MSS reduces the presence of defects such as vacancies or dislocations within the crystals, since they undergo a process of dissolution and subsequent recrystallization [81, 93]. Enhanced reaction kinetics have been detected at early stages of reaction by *in-situ* powder X-ray diffraction measurements. Typically, the reaction times for the formation of mixed-metal oxides (*e.g.* NaTi_2O_4 and CuNb_3O_8 [100]) are reduced from several days to as low as 15 minutes. The flux surrounding the growing units prevents agglomeration and sintering. As an example, Mao C. *et al.* [128] reports the comparison between $\text{Ba}_{0.70}\text{Sr}_{0.30}\text{TiO}_3$ (BST) powder

synthesized by MSS at 900 °C and BST powder synthesized by CSS reaction at 1150 °C (see figure 2.5). Figure 2.5a shows that the particles obtained by CSS reaction are forming big agglomerates. On the contrary the powder obtained by MSS is more homogeneous, with the crystals manifesting clearly a square-like morphology (figure 2.5b). The facets developed so clearly because the crystals could grow free from mechanical or thermal constraints in the salt melt [123].

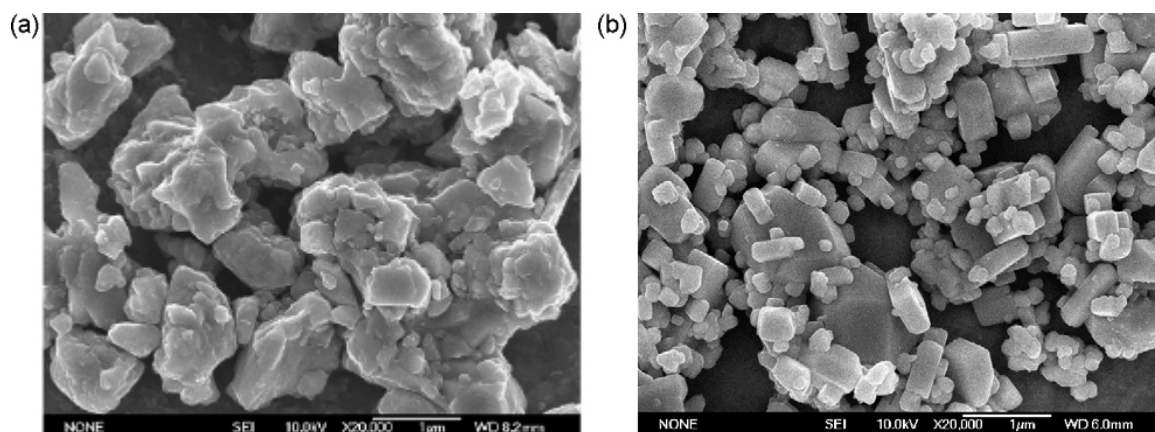


Figure 2.5.: a) SEM images of BST powder synthesized at 1150 °C for 2 h by CSS reaction and b) at 900 °C for 2 h by MSS (reprinted from [128] Copyright © 2007, with permission from Elsevier).

Influence of reactant solubility on crystal growth Two different interaction mechanisms were recognized in the case of an unreactive molten flux containing two reactants: the *template formation* and the *dissolution-precipitation* process [4, 130]³. If the reactants' solubilities are similar, the *dissolution-precipitation* process occurs, while the *template formation* mechanism takes place when they strongly differ. The morphologies of the product phases are heavily influenced by these mechanisms. In the case of a *dissolution-precipitation* process, the morphologies of the product particles generally differ from the reactants, while in the *template formation* the morphology remains similar to that of the less soluble reactant (see figure 2.6).

In MSS the surfaces of the reactants act as nucleation sites for the heterogeneous nucleation of the product particles [4]. The cooling rates are of minor influence in MSS, differently from the case of the growth of single crystals, where the cooling rate is of crucial importance for the nuclei concentration and crystals dimensions. As a matter of fact, a large number of particles already solidify before the cooling process starts. The reagent particles, still dissolved in the molten salt, precipitate without further influencing the particle sizes [4].

³Refer to chapter 25 of reference [130].

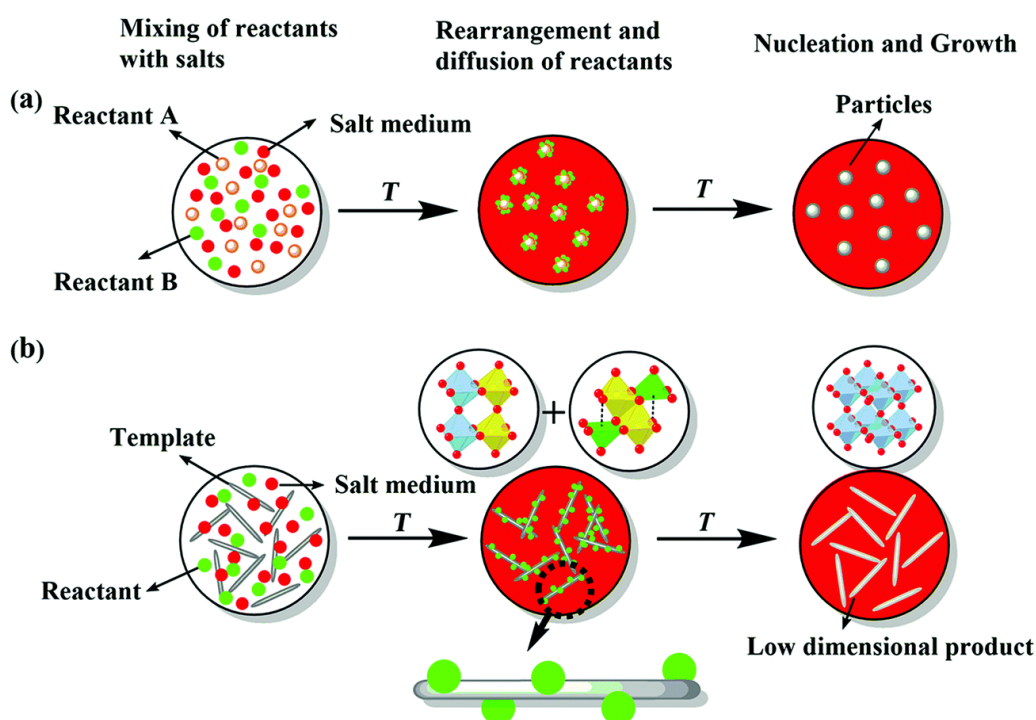


Figure 2.6.: Schematic diagram of the a) dissolution-precipitation growth and b) of the template formation mechanism occurring in MSS (reproduced with permission from [91]. Copyright © 2020 Royal Society of Chemistry).

2.3.1. Habit of crystals grown from solutions

Shaping the crystal habit For the sake of clarity it is important to specify the difference between *morphology* and *crystal habit*. *Morphology* refers to the set of $\{hkl\}$ crystal forms defining the *apparent shape*. The *crystal habit* describes the appearance as defined by the growth conditions [118]. Since crystal faces develop following the layer by layer growth,⁴ the selection between those remaining and those disappearing is determined by the growth rate. The fast-growing ones are the first to disappear and the *crystal habit* is defined by the faces with the slowest growth rate. This does not necessarily mean that new $\{h'k'l'\}$ forms have to appear, since already existing $\{hkl\}$ forms can develop [118].

The *crystal habit* relies on internal as well as external factors. The underlying crystal structure and the presence of defects are internal factors, whereas external factors are the supersaturation, the composition of the solution and other growth environment parameters [81]. Crystal growth is a process in which the change in one parameter affects all the others influencing thus growth and habit of the crystals. Figure 2.7 shows to which extent solution controlled kinetic factors can affect the habit. The different growth rate determines whether a cubic crystal takes a cubic or an octahedral habit. The $[100]$ face (and equivalent) is the fastest growing one in the cubic habit, whereas for the octahedron it is the $[111]$ face (and equivalent). Intermediate growth rates will lead to truncated structures,

⁴as already noticed by Niels Steensen in 1669 on quartz and hematite

such as a cubeoctahedron. Crystals belonging to lower-symmetry systems exhibit prismatic or platy habit. A marked difference in the axial length is of crucial importance. For example a much shorter c-axis than the a- and b-axes gives rise to a prismatic habit, whereas a much longer c-axis favors a platy habit perpendicular to the c-axis. The expected polyhedral form of a crystal is thus correlated with the symmetry elements involved in the unit cell. The morphology alone deduced from crystal structure is frequently called *structural form* [118] and can be calculated theoretically from symmetry elements, entirely neglecting the effect of thermodynamic or kinetic parameters. Best example is the Bravais-Friedel law [131], based on reticular spacing or reticular density of the unit-cell.

The previous discussion on the crystal habit is only relevant when the crystal grows unconstrained in a solution, *i.e.* when the crystal can form equilibrium faces. For this purpose an isotropic environment (an ambient phase with a concentric diffusion gradient toward the growing crystal) is mandatory. Methods like the traveling solvent zone, the liquid phase epitaxy or the pulling of crystals from a solution by a modified Czochralski technique do not meet this requirement [123]. Indeed crystals rarely reach the equilibrium form due to kinetic factors that can disturb the growth process [132]. However, the MSS offers an environment that permits to tune the crystal habits of the products. Susman *et al.* have recently shown that the control on the faceting of MgO [133] and NiO [26] crystals can be achieved by a shrewd selection of the salt matrix. This is rarely reported in literature, nevertheless the interest in getting crystals with exposed high-index facets is increasing in recent years [1, 133]. Also Mann *et al.* [6] reported the control of the crystal habit of $\alpha - \text{Fe}_2\text{O}_3$ and $\gamma - \text{Fe}_2\text{O}_3$, while Boltersdorf and coworkers [7, 101, 102] accomplished this with Sn_2TiO_4 and other complex oxides containing Ta, Nb and Sn. Earlier, Wang *et al.* [134] were able to control the growth habit of ZnO changing from a long hexagonal prism-like to an hexagonal plate-like single crystal by adjusting the basicity of the salt melt (see figure 2.8). Models based on calculations of the relative growth rate or on the internal crystal structure rather than on the interfacial free energies fail in foreseeing the variety of habits that can be obtained by MSS. However, a model based on growth units consisting of complexes made out of a cation and OH^- ions was proposed [135]. Here the growth rates of metal oxide facets are related to i) the growth units that

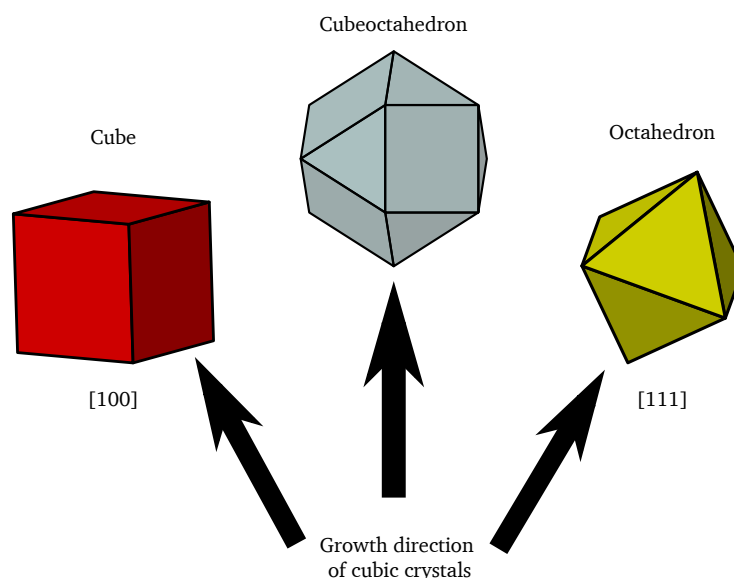


Figure 2.7.: Different habits originated from the same cubic system, but with the maximum growth rate along different directions (from left to right: [100], intermediate direction and [111]), after [81].

recently shown that the control on the faceting of MgO [133] and NiO [26] crystals can be achieved by a shrewd selection of the salt matrix. This is rarely reported in literature, nevertheless the interest in getting crystals with exposed high-index facets is increasing in recent years [1, 133]. Also Mann *et al.* [6] reported the control of the crystal habit of $\alpha - \text{Fe}_2\text{O}_3$ and $\gamma - \text{Fe}_2\text{O}_3$, while Boltersdorf and coworkers [7, 101, 102] accomplished this with Sn_2TiO_4 and other complex oxides containing Ta, Nb and Sn. Earlier, Wang *et al.* [134] were able to control the growth habit of ZnO changing from a long hexagonal prism-like to an hexagonal plate-like single crystal by adjusting the basicity of the salt melt (see figure 2.8). Models based on calculations of the relative growth rate or on the internal crystal structure rather than on the interfacial free energies fail in foreseeing the variety of habits that can be obtained by MSS. However, a model based on growth units consisting of complexes made out of a cation and OH^- ions was proposed [135]. Here the growth rates of metal oxide facets are related to i) the growth units that

have CNs identical to those of the metal in the oxide crystal and, more importantly, ii) to the orientation of the coordination polyhedron (CP) at the interface. The growth units interact with the interface of the crystal. The crystal face with the CP oriented with the corner towards the interface has the fastest growth rate; then follows the one with the edge exposed at the interface with the second fastest growth rate. Finally the crystal face with the face of the CP being part of the interface has the slowest growth rate [135, 136].

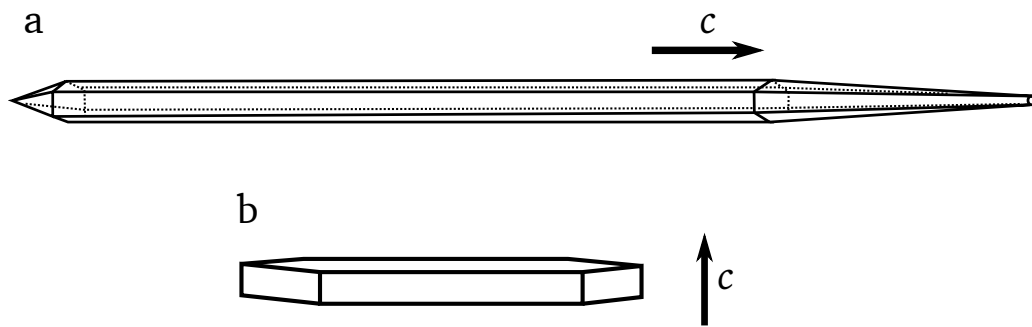


Figure 2.8.: ZnO crystal habit: a) grown along the c direction in strong basic solution as a long prism; b) grown perpendicular to the c -axis in a weak basic solution as a plate-like crystal, after [134].

The habit of a crystal growing in an isotropic environment is determined by the growth rate of the different faces present on the crystal surface (see figure 2.7). There are important parameters that have an impact on the driving force and the edge free energy of the crystals growing in an isotropic environment. Supercooling or supersaturation are decisive as driving forces. The solute-solvent interactions are also crucial since crystals of the same species show different growth forms when growing from different ambient phases or in systems with different solvent compositions. Finally the normal growth rate of non-smooth interfaces may be suppressed by impurity atoms since they modify the edge free energy by adsorbing on spiral growth steps (see figure 2.9).

Anisotropic growth can be induced by different processes. In this case polyhedral growth forms deviate from the ideal one and even equivalent faces (usually being equal in size) develop differently [118]. Possible factors are:

- (i) Anisotropy in mass transfer induced by convection or directional flow in the ambient phase.
- (ii) Seeds modifying the growth form. The surface of seeds (or substrate) affects the normal growth rates by generating dislocations on the interface.
- (iii) Preferential growth on re-entrant corners or dislocations in twin junctions.
- (iv) Anisotropic distribution of active growth centers, *i.e.* outcrops of screw-type dislocations.
- (v) Impurity elements selectively adsorbed along growth steps, foreign compounds that selectively cover the growing surface due to epitaxial relation, or selective adsorption that suppresses the normal growth rate.

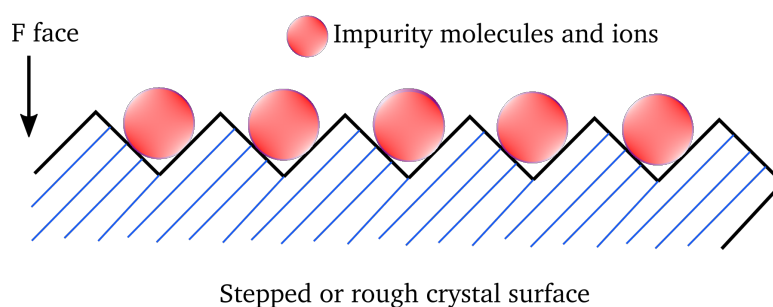


Figure 2.9.: Attachment of impurities on the surface, after [123].

Growth of Al_2O_3 crystals with flake morphology In view of one of the major aims of this thesis — creating special chromatic effects by pigments similar to the pearl luster and iridescent effect of nacre — it is important to discuss the typical habit of $\alpha\text{-Al}_2\text{O}_3$. Alumina is the example par excellence of crystals growing with a strong anisotropy (see figure 2.10). Slightly different crystal habits of alumina can appear, but due to the slowest growth rate of the 001 face it generally assumes a plate-like habit (growth along the c -axis is slow, see figure D.1 in the appendix).

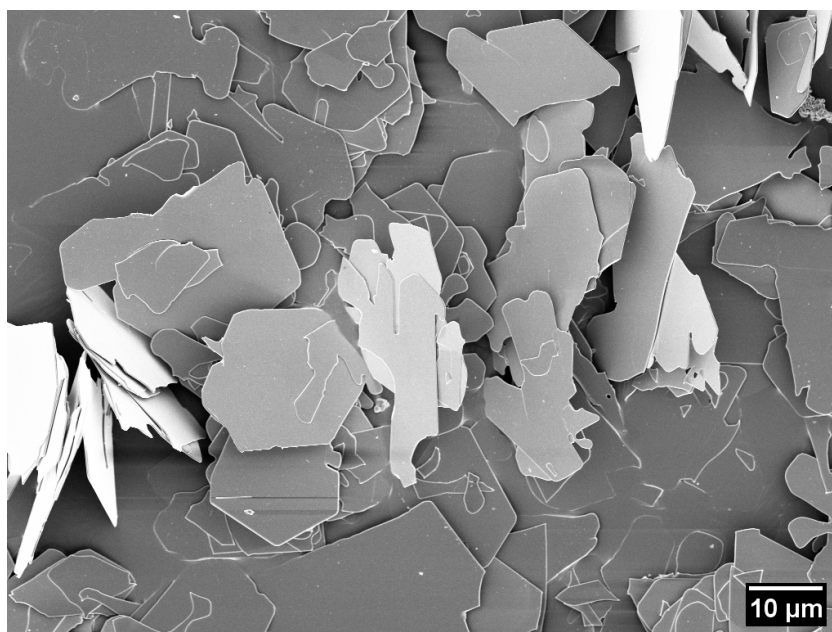


Figure 2.10.: Alumina flakes obtained via MSS reporting a flake like crystal habit.

The influence of the growth mechanism, impurities, type of solvent and temperature on the Al_2O_3 habit is not yet clearly understood. There are some growth mechanisms that were deduced to explain the formation of a platy habit. Among these is the twin growth mechanism of White and Brightwell (1965) [137]. Sunagawa (1967) observed hillocks, apparently originating from screw dislocations, on the (001) plane of an alumina plate. This indicates that alumina plates often grow rapidly perpendicular to the c -axis by the twin-plane re-entrant edge (TPRE) mechanism [138] and slowly along (001) by a

screw-dislocation mechanism. The TPRES growth mechanism seems to dominate the formation of the Al_2O_3 habit by rapid growth in the direction of the twin plane (perpendicular to the c -axis) at temperatures lower than 1250°C . The presence of twins act as a nucleation site with the twinning consisting of a rotation of 180° in the basal plane [123]. However, untwinned Al_2O_3 crystals, of equidimensional shape and low in impurity content, can be obtained from a flux free from inclusions by a proper choice of solvent, dopant, supersaturation and growth temperature

Li *et al.* [139] comprehensively discussed the habit of Al_2O_3 crystals, reporting the relationship between the growth rates of the various faces and the number of corners of the $[\text{AlO}_6]$ -octahedra present at the interface. The higher the number, the faster the growth. The growth rates of the various crystal faces are determined by the orientation of the CP at the interface and lead to the habit reported in figure 2.11. Kim B.Y. *et al.* [140] studied the control of the habit obtained in different molten salts, correlating the control of the growth rate of the different faces with the ionic strength of the salts ($\text{NaCl} > \text{Na}_2\text{SO}_4 > \text{Na}_3\text{PO}_4$). Billik *et al.* [141] and Messing *et al.* [142] reported that the diameter and thickness of the Al_2O_3 platelets are strongly depending on the molten salt used for the synthesis. Also the addition of Ti-containing precursors can lead to strong changes in the alumina habit [19, 143–145].

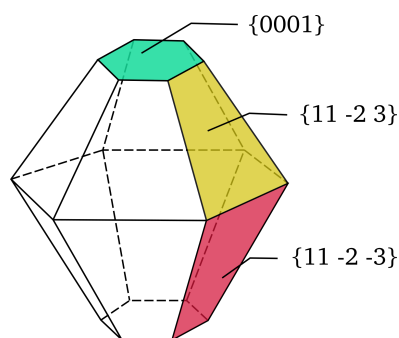


Figure 2.11.: Growth habit of $\alpha\text{-Al}_2\text{O}_3$ crystal, after [139].

2.3.2. Supersaturation in molten salts

Supersaturation, intimately connected with the formation of precipitates, can greatly affect the habit of crystalline particles. Supersaturation triggers the crystal growth out of the hot melt in MSS. The nucleation rate is practically equal to zero till reaching a critical chemical potential value $\Delta\mu_C$. The nucleation rate increases quickly by many orders of magnitudes beyond this threshold. A steady-state of super-saturation/cooling has to be ensured during the growth process in order to obtain high crystal quality. The growth rate of the different types of crystal faces depends on the supersaturation with a linear dependence for the S- and K-face (see page 11), while for an F-face it is determined by the growth mechanism (spiral mechanism or two-dimensional nucleation). The supersaturation in a solution is initially high when a crystal starts to nucleate but decreases during the growth along fast growing directions. Therefore, spontaneously nucleated crystals tend to grow dendritically branched. Part of

the dendrites are left in the areas with a different supersaturation when the growth rate slows down. This leads to the formation of stepped edges forming terraced structures. At this growth stage a *hopper* morphology is achieved. The growth will be unstable and turning in to a dendritic growth when further increasing the supersaturation gradient. This is reported in figure 2.12, presenting a rough scheme of the normal growth rate as a function of the driving force $\Delta\mu$ expressed as the chemical potential difference between the liquid and the solid phase, equation 2.13 [146].

$$\Delta\mu = k_B T \ln \beta \quad (2.13)$$

where $\beta = \frac{C}{C_\infty}$, with C_∞ being the equilibrium concentration, T the temperature and k_B the Boltzmann constant.

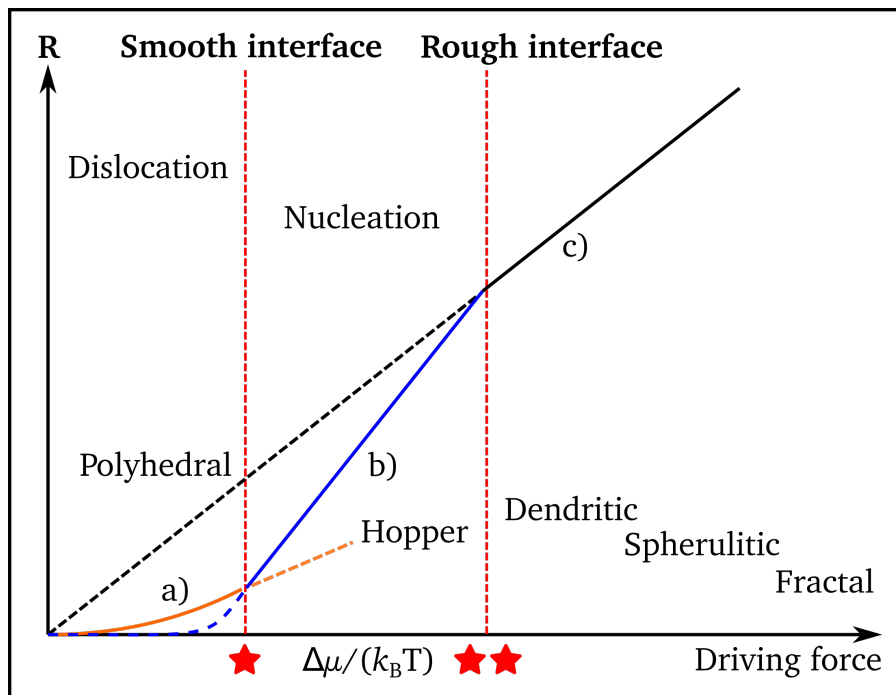


Figure 2.12.: Graph of the normal growth rate R versus the driving force $\Delta\mu/(k_B T)$ correlated to the expected crystal habit evolution, after [118, 124].

In figure 2.12 the different areas represent typical growth mechanisms for crystals, namely a) spiral growth, b) the 2D nucleation growth and c) the adhesive-type growth mechanism. Two critical conditions $\Delta\mu/(k_B T^*)$ and $\Delta\mu/(k_B T^{**})$ occur for a crystallographic face by increasing the driving force. Their values depend on the growing crystal faces, environmental phases and crystallographic directions [124]. Above $\Delta\mu/(k_B T^{**})$ the interface is rough and the growing mechanism is of adhesive type. The interface is smooth below that condition, following either the spiral growth mechanism or the 2D nucleation growth. Below $\Delta\mu/(k_B T^*)$ the growth is controlled by the spiral mechanism. The driving force is $\Delta\mu = 0$ once the equilibrium condition is reached.

In MSS the critical condition for supersaturation can be reached in two different ways: by evapora-

tion of the solvent, starting then the so-called evaporative crystallization, or by cooling the melt [5]. The latter mechanism is most common, leading to the formation of crystals during the cooling process. Molten salts are an excellent solvent for oxides and, according to Einarsrud *et al.* [17], this should permit a complete dissolution of the oxidic precursor in the molten salt and start crystallization once the cooling process begins. The evaporative crystallization increases the concentration of the reactants in the solution and initiate a fast growth rate. He *et al.* [5] observed how the change of the evaporation rate of a NaCl-KCl eutectic mixture effects the crystallization process and the obtained crystal size. Mann *et al.* [6] recently reported a further way of reaching different stages of supersaturation. They coupled the MSS with the ultrasonic spray pyrolysis (USP) in order to achieve a spatial and temporal confinement of MSS, limiting the growth of iron oxides. In this way they provided access to products obtained at different stages of supersaturation and growth, and thus to different sizes and shapes.

2.3.3. Salt matrix influence on crystal growth

The efficiency of the reaction process in MSS relies on specific features of the salt type. These can be summarized as: i) ability to dissolve the reagents, ii) significant change of the solubility with temperature, iii) low melting point, iv) low volatility, v) easy product isolation and vi) no or low corrosion with the crucible that contains the melt [81, 123]. The acidity or basicity of the melt is another important parameter, strongly depending on the chemistry of the salt involved in the synthesis (halides, sulfates, nitrates, carbonates). It determines the O^{2-} activity (for details see section 2.3.4). The use of additives can help to tune the O^{2-} activity. The pioneering works of Hermann Lux and Håkon Flood established the importance of this reaction parameter for MSS [126, 127, 147]. Sulfates and chlorides (and the eutectic mixtures) are the most commonly used salts in MSS [4] (see table 2.3).

The amount of salt is another important synthesis parameter in MSS. Usually, the ideal "reactant : salt matrix" ratio allows the filling of all the interstices between the reactant particles and to coat their surfaces. However, the ideal mixture is hard to find a priori. Usually, excess or too low salt quantities are introduced in the synthesis. In the first case sedimentation of the reactant particles occurs. Reactant particles differing in density and size have different sedimentation rates and tend to separate, leading thus to a reduction of the reaction rate. Kimura and coworkers [148] noticed this effect in a mixture of NiO and Fe_2O_3 reactants. If the salt quantity is too low, an inefficient product formation is noticed. Yoon *et al.* [10] found that the amount of salt determines the particle size via the heating rate. Equation 2.14 describes the particle growth with temperature:

$$d^2 - d_0^2 = k(t - t_0)exp(-E_a/RT) \quad (2.14)$$

with d being the average particle size at a time t , d_0 the initial particle size at t_0 , R the gas constant, E_a the activation energy, T the synthesis temperature and k the rate constant [149]. Danek *et al.* [150] reported an increase of the mean particle size with reaction time and temperature, although the growth rate at constant temperature slowed down with the time. Prolonged holding times increase the Ostwald

Table 2.3.: Melting temperature T_m of some commonly used salts and typical eutectic compositions used for the molten salt synthesis [4, 8].

Salt system	Salt 1	T_m [°C]	Salt 2	T_m [°C]	Composition [mol%]	T_m [°C]
Halides	NaCl	801	KCl	770	50 - 50	650
	NaCl	801	AlCl ₃	192.4	50 - 50	154
	LiCl	605	KCl	770	59 - 41	352
	ZnCl ₂	290	KCl	770	52 - 48	228
	LiI	469	KI	681	63 - 37	286
Oxosalts	Li ₂ SO ₄	859	Na ₂ SO ₄	884	63.5 - 36.5	594
	Li ₂ SO ₄	859	K ₂ SO ₄	1069	71.6 - 28.4	535
	K ₂ SO ₄	1069	Na ₂ SO ₄	884	63.5 - 36.5	594
	Li ₂ CO ₃	723	K ₂ CO ₃	891	50 - 50	503
	Li ₂ CO ₃	723	Na ₂ CO ₃	851	50 - 50	500
	LiNO ₃	255	KNO ₃	334	43 - 57	132
	NaNO ₃	308	KNO ₃	334	50 - 50	228
	LiBO ₂	849	KBO ₂	947	56 - 44	582
	NaOH	318	KOH	360	51 - 49	170
Without ions in common	NaCl	801	Na ₂ SO ₄	884	0.53 - 0.47	625.3

ripening rate, having thus an impact on the average particle size due to coarsening [18, 151–153]. Isotropic cubic crystal structures tend to form high-symmetry cubic-related morphologies in molten salts and crystallographic anisotropy governs the anisotropic crystal growth. As a consequence, the greater is the degree of structural anisotropy, the more likely the formation of 1D rods, 2D platelets, or more complex morphologies with differing exposed crystal facets [7, 17].

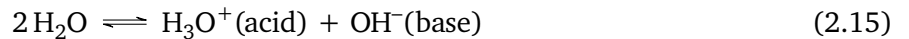
The MSS can be also successfully applied to the production of oxide powders [82], especially for the nanowires of the oxide of manganese [154], cobalt, magnesium [133], nickel and zinc [26]. One-dimensional single-crystalline nanowires of α -MnO₂ and β -MnO₂ were synthesized through the MSS, respectively, using KNO₃ and a mixture of NaNO₃ and LiNO₃ as salts. The smaller sodium and lithium ions appear to be easily incorporated into the larger β -MnO₂ crystal lattice [82]. Also, the choice of the anion present in the salt system is of relevance for the synthesis [155, 156]. Sodium ions of the Na₂SO₄ flux can be preferentially attached to the (001) face of β -Li₂TiO₃ crystals and combined with the solvation power of the O²⁻ ions in the sulfate-anion based flux, they strongly determine the crystal growth of the particles [157]. On the other hand Cortese and coworkers [97] found, experimentally and supported by calculations, that halide melts with large alkali metal cations (Rb, Cs) are superior in solvating O²⁻ compared to the smaller alkali metal cations such as sodium. This facilitates the growth of larger single crystals. Hayashi and coworkers [158], reported a greater solubility of the precursor oxides in sulfate-based fluxes compared to the halide-based fluxes, resulting in changes of the particle shape.

In summary, no unique crystal growth conditions exist in MSS, since each synthesis depends on

the reagents used, choice of flux solvent, and several other conditions. The properties of the salts are crucial for the crystallization process. The activity of O^{2-} in oxosalts melts strongly influences the crystal growth by increasing the basicity of the melt [7]. The formation of ternary or higher order oxides can be achieved by the MSS. $Na_2Ti_6O_{13}$ is presented in the second part of this work as an example.

2.3.4. Influence of acidity/basicity of melts on the crystallization process

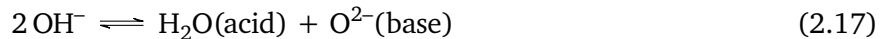
According to the Lux–Flood (L-F) theory the acidity or basicity of salts can be correlated with the activity of the O^{2-} ions in the melt [126, 127, 147, 159]. This applies to the oxosalts and the hydroxides. The L-F theory relies on the concept of a Lewis base (an electron-pair donor). In molten salts, the latter consist of anions, *i.e.* O^{2-} , Cl^- and F^- . Acids are the species combining with them. The scale of acidity/basicity varies according to the nature of the acid or base ("oxoacidity", "chloroacidity" and "fluoroacidity") [160]. The O^{2-} solubility is a relevant factor in MSS, since its interaction within the molten salt can promote the crystallization process or slow it down. Molten hydroxides, nitrates and sulfates can be counted as bases, by delivering O^{2-} ions to the melt. They have an oxidizing effect [1]. Concerning the hydroxides, they can dissolve oxides quite well and have a low melting point [161]. Their water content has to be taken into account, since it has a significant impact on the oxoacidity of the melt (being highly acidic for hydrated hydroxides and strongly basic for oxide anhydrides) [81]. For this reason the acidity of an hydroxide flux is usually represented as $pH_2O = -\log[H_2O]$. The solubility of the metal cations can be controlled in this way. For a better understanding, the commonly known auto-dissociation of water is reported in equation 2.15:



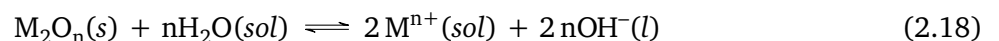
with $[H_3O^+] = [OH^-] = (K_w)^{1/2} = 1 \times 10^{-7}$, ($pH=7$). Analogously, the dissociation of hydroxides [3] follows equation 2.16



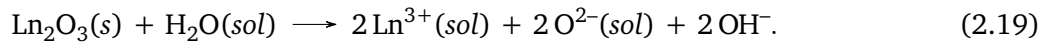
The further reaction step (equation 2.17) determines the oxoacidity of the melt [162, 163].



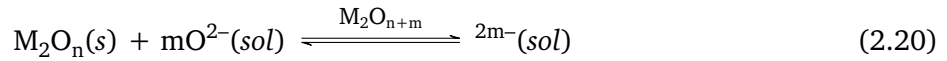
This equilibrium is given by the dissociation constant K_d of the salt, changing according to the metal cation. Among the alkali metal cations, Li^+ has the highest charge density and therefore $LiOH$ has the greatest degree of dissociation among the alkali metal hydroxides [3]. Furthermore, K_d increases with temperature since the auto-dissociation process is endothermic. The solubility of metal oxides in hydroxide melts is achieved by solvation or complexation. Under acidic conditions equation 2.18 holds,



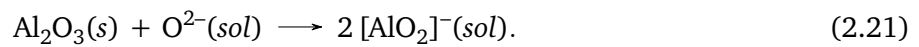
with an example (lanthanum oxide) represented in equation 2.19,



Under acidic conditions the metal cation is solvated, while under basic conditions the metal oxo-anion is solvated (equation 2.20)

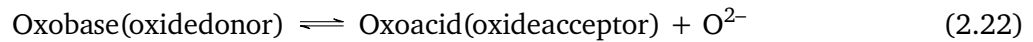


with an example being reported in equation 2.21



Thus, the solubility of a metal oxide in acidic or basic conditions can be controlled by changing the $p\text{H}_2\text{O}$.

Oxosalt systems (e.g. metal nitrate [26, 133] and sulphate) are an obvious choice for the synthesis of oxide ceramics. The L-F type acid–base equilibrium for molten oxides is represented by the reaction 2.22, that follows the definition of H. Lux [126] (later reformulated with respect to oxides and oxosalts by Flood and Förland [127]).



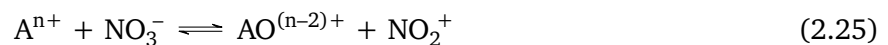
The oxide ion O^{2-} is the simplest base and the basicity of the melt is expressed as $p\text{O}^{2-} = -\log m(\text{O}^{2-})$, where m represents the molality of O^{2-} in solution. The $p\text{O}^{2-}$ value determines the reactions in the melt. As an example, the precipitation of TiO_2 occurs under moderate $p\text{O}^{2-}$:



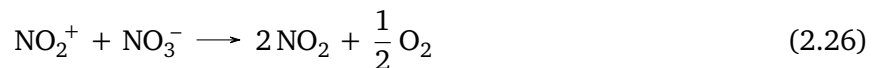
With further increase in basicity (lower $p\text{O}^{2-}$), the precipitated TiO_2 dissolves into titanate anions [7]



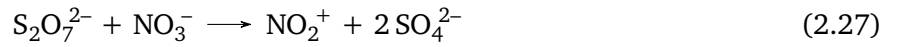
The following example shows how the equilibrium of a molten nitrate (equation 2.25) changes when an oxide acceptor A^{n+} is added (equation 2.26).



The system switches to a new state (equation 2.26) and with the oxygen atoms forming O_2 .



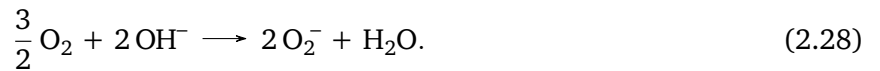
Next, adding the oxide acceptor $S_2O_7^{2-}$ to the $NaNO_3$ - KNO_3 melt, yields to reaction 2.27:



immediately followed by the reaction reported in equation 2.26 [78].

2.3.5. Molten salt synthesis performed under O_2 flow

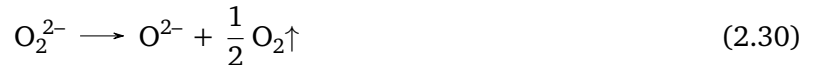
The gaseous atmosphere above the melt affects the reactions occurring in the molten salt. An example is given by the studies of H. Lux *et al.* [164], reporting the formation of peroxides and superoxides from hydroxides in the presence of water vapor. Their synthesis depends on the nature of the cation, the temperature and the partial pressures of oxygen and water. The reaction with NaOH leads to the formation of small quantities of peroxide, while higher alkali-metal hydroxides lead to the formation of superoxides. The hydroxide melt interacts with the oxygen atmosphere and accordingly the following reaction 2.28 occurs:



The formed superoxide decomposes into a peroxide and oxygen under an oxygen-free gaseous atmosphere [117] (equation 2.29).



The peroxide further decomposes to generate an oxide ion and oxygen (equation 2.30).



The pH_2O (mentioned in the previous section 2.3.4) that regulates the acidity of the melt is given by equation 2.31

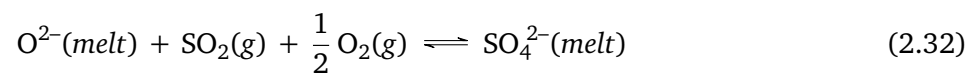
$$pH_2O = -\log P_{H_2O} - \log k_{H_2O} \quad (2.31)$$

where k_{H_2O} is the Henry's coefficient and P_{H_2O} the partial pressure of water. The water concentration can easily be controlled and — according to Henry's law — is proportional to the partial pressure of water in the gas.

In summary, all the redox equilibria that dictate the oxidation states of the metals in the melt are influenced by the gaseous atmosphere above the melt, which can be controlled by tuning the P_{O_2} choosing either an O_2 or an N_2 rather than a CO/CO_2 atmosphere [81, 165]. For instance, Bartholomew *et al.* [166] were able to grow intermediate oxides of titanium by controlling the P_{O_2} . Tiano and coworkers [155] investigated the effect on the morphology and product composition of $SrRuO_3$ in $NaCl/KCl$ melt.

The dissociation of sulfates in the melt present another example of the importance of partial

pressure in MSS



Studies with sulfates are the main part of the thesis and are described in the sections 5.2 and 5.3.

3. Crystal structures and applications

Chapter 3 deals with the crystal structures of the materials that are in the focus of this work, *i.e.* titanium dioxide and sodium titanate. The advantages of the MSS for their crystal growth are highlighted, allowing to synthesize $\text{Na}_2\text{Ti}_6\text{O}_{13}$ nanorods with exceptionally high aspect ratio. Further on, the properties of TiO_2 and its possible application as pigment are considered, followed by a brief description of $\text{Na}_2\text{Ti}_6\text{O}_{13}$ applied as anode material, with the prospect of application in grid storage batteries.

3.1. TiO_2 crystal structures

Titanium dioxide can crystallize in three main phases: rutile, anatase and brookite. Rutile and anatase are relevant for this work and thus will be described in detail. Both rutile and anatase have tetragonal unit cells, with titanium atoms sixfold coordinated with oxygen atoms giving rise to a slightly distorted octahedron. The oxygen atoms at the two vertices of the octahedron have bonds with the titanium atom which are longer than the other four Ti–O bonds. The bond angles in anatase are not exactly 90° like in the rutile octahedron and the different lattice constants and space group result [28] (see table 3.1 and figure 3.1a and 3.3a for a comparison between the anatase and rutile single octahedron). It is essential to know which titania phase forms at specific synthesis conditions, since this will allow different applications, *e.g.*, the generation of optical effects by specific crystal habit, photo-catalysis and energy storage, all influenced by the different crystal habits that anatase and rutile can assume.

Table 3.1.: Crystal structures of TiO_2 [167].

Phase	Crystal structure	Space group	Lattice constants (nm)			
			a	b	c	c/a
rutile	tetragonal	D_{4h}^{14} -P4 ₂ /mnm	0.4584	-	0.2953	0.644
anatase	tetragonal	D_{4h}^{19} -I4 ₁ /amd	0.3733	-	0.937	2.51
brookite	rhombohedral	D_{2h}^{15} -Pbca	0.5446	0.9166	0.5135	0.944

3.1.1. Anatase

Anatase is a metastable TiO_2 polymorph. It is the first phase formed when synthesizing TiO_2 [168] and it transforms into rutile by applying heat, pressure or varying other synthesis parameters, *e.g.* mineralizing agents, pH etc. (for details see section 3.1.2). It is more stable than brookite and rutile in strongly basic conditions [169] and it is the most stable phase in air for particle dimensions lower than 11 nm [170]. The bond lengths in a single octahedron at 295 K are 1.979 Å and 1.933 Å for apical and equatorial bonds [171], resulting in a more distorted octahedra compared to rutile. The bond angles correspond to 102.3° and 92.6°. The unit cell is reported in figure 3.1b and shows the arrangement between the octahedra. In the anatase structure each TiO_6 octahedron shares a corner with the neighboring one along the $\{001\}$ planes with the octahedra edges linking the planes [28]. Threefold coordinated oxygen atoms are involved in the stacking of the octahedra in both anatase, rutile and even in brookite.

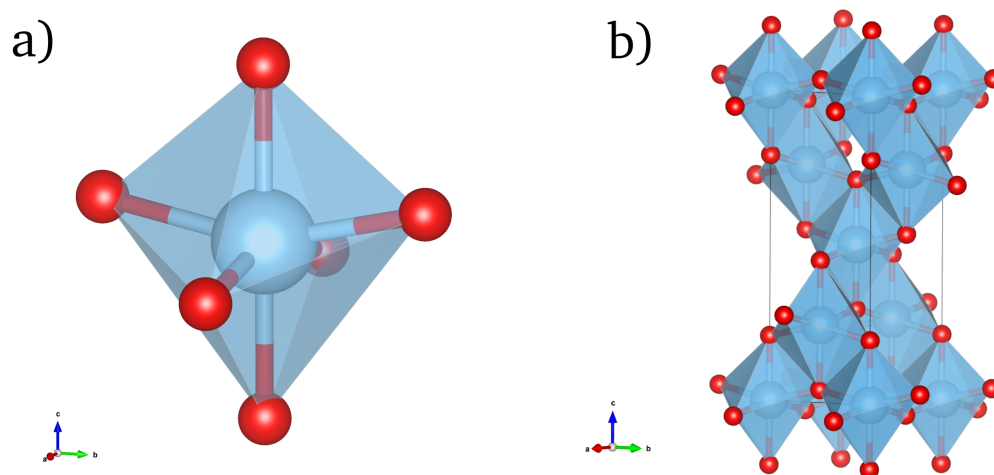


Figure 3.1.: Anatase single octahedron of a TiO_6 unit a) and the anatase unit cell visualizing the connections between the octahedra in b). Both were designed with the VESTA 3D structure visualization software [172] (CIF file ICSD-63711 [173]).

Figure 3.2 presents the equilibrium shapes adopted by anatase crystals. The calculated Wulff construction [174] consists of $\geq 94\%$ of $\{101\}$ facets with $\{001\}$ facets forming a truncated bipyramid. The surface energies of low-index facets are in the order $(110) > (001) > (010) > (101)$ with 1.09 J m^{-2} , 0.90 J m^{-2} , 0.53 J m^{-2} and 0.44 J m^{-2} , respectively [30, 175].^{1,2} The surface energy is strictly depending on the density of the undercoordinated Ti atoms. Therefore, the (110) surface with four-fold coordinated Ti atoms (Ti_{4c})³ results being the low-index facet with the highest surface energy. The facets (001) and (010) contain only five-fold coordinated Ti_{5c} atoms, while the (101) has 50% of Ti_{6c} and 50% of Ti_{5c}

¹Lazzeri *et al.* [174] calculated 0.53 J m^{-2} for (100) instead of (010) .

²Lazzeri *et al.* [175] recalculated the surface energies after having found an error in the approximation presented in [174].

³ Ti_{4c} represents an undercoordinated Ti atom that is four-fold coordinated.

atoms [176]. The lower are the surface energies, the more likely will these facets define the final habit of the crystal.

The (010) surfaces do not appear in the predicted shape in vacuum through the Wulff construction (figure 3.2), despite their low surface energy (lower than (001)). Barnard *et al.* [177, 178] predicted that O₂-rich surfaces stabilize the {010} facets in anatase crystals. These appear like a belt around the center (see the red area in the central line of figure 3.2) favoring the crystal growth along the ⟨001⟩ direction. As regards the {001} facets, they are only appearing when targeted synthesis stabilize them. Wet chemistry methods are commonly used to introduce capping agents stabilizing the {001} high-energy surfaces. Fluorine is the most common capping agent since the breakthrough by Yang *et al.* [179, 180]. The Ti–F bonds saturate the Ti_{5c} atoms leading to a higher stability of {001} with respect to {101}, reaching 47% of {001} facets (crystal habit as depicted in violet in the upper line of figure 3.2). Menzel *et al.* [181] made a systematic study providing a straightforward analysis of the 2D anisotropy of anatase and the competing role of HF and H₂O in the crystal formation. The interest in this kind of “facet engineering” increased because of the enhanced performance of anatase for energy conversion and other environmental applications [22, 34, 182, 183].

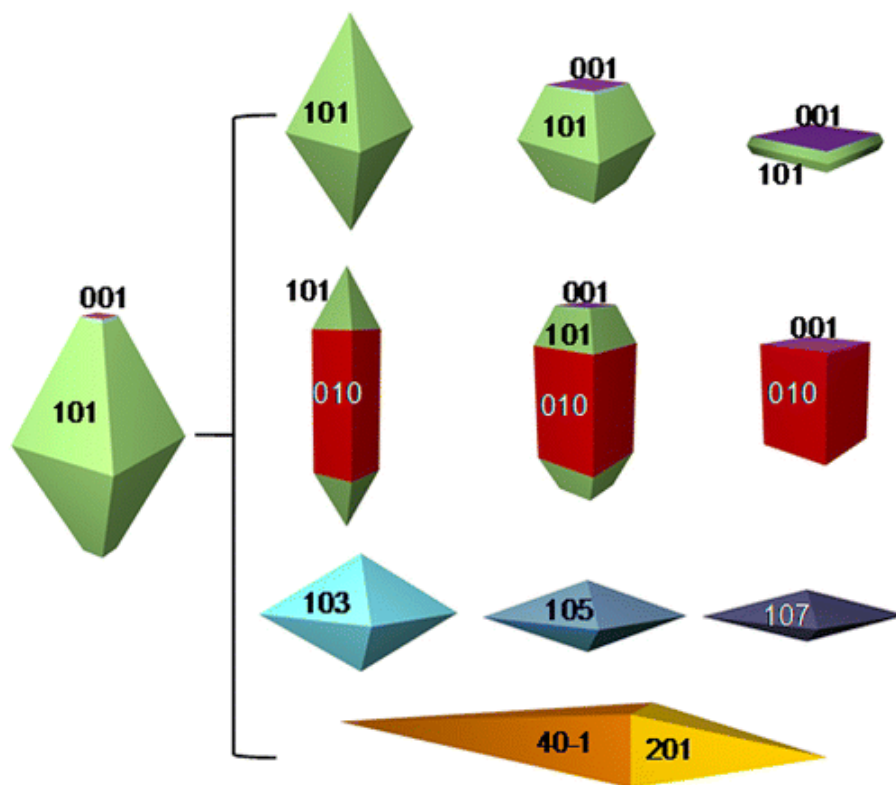


Figure 3.2.: Equilibrium crystal shape of anatase by the Wulff construction (according to [174]) on the left hand side and the possible shapes that can evolve from it (reprinted with permission from [30]. Copyright © 2014 American Chemical Society).

3.1.2. Anatase to rutile phase transformation

A precise understanding of the anatase to rutile transformation (ART) is a prerequisite for controlling the TiO₂ crystal shape. The ART happens irreversibly in a wide range of transition temperatures (400–1200 °C) [29, 184–186]. According to Hanaor *et al.* [168], the ART transition temperature is about 600 °C. Information from differential thermal analysis (DTA) indicates a slow start of the phase transformation at this temperature. The exothermic peak identifying the ART is located, however at higher temperatures. The less-constrained structure of anatase permits the TiO₆ octahedra to arrange into a long-range ordered structure with great easiness [187]. The lower surface free energy of anatase promotes a more rapid re-crystallization process than the one of rutile, although the last one has a lower Gibbs free energy [188, 189].

The ART is not instantaneous due to its reconstructive nature: bonds are broken and reformed in contrast to a displacive transformation (which distorts the bonds without breaking them) [190, 191]. The reconstruction leads to a volume reduction caused by the contraction of the c-axis of ~ 8% [191], which explains the higher density of rutile. An orientation relationship of [110]_A // (011)_R and (112)_A // (100)_R (A denoting anatase and R rutile) is suggested for the formation of rutile nano-needles within anatase particles by the (112) twinning plane [192]. Three paths were suggested to explain the coarsening of the rutile particles [192]. First, by sintering of anatase particles. Transforming, attaching and then rotating is the second way to obtain a single orientation. Third way, the most likely one, implies the attachment of an anatase particle on a rutile particle, which after the rotation into the correct orientation starts to transform into rutile.

Cationic dopants or other impurities strongly affect the kinetics of the ART, promoting or inhibiting it [193]. Selective doping, *e.g.*, with ZnO₂ or SnO₂, can retard or promote the transformation [194–196]. The use of SnCl₂ as rutile phase promoter is well known in the pigment industry and permits to obtain rutile crystals in aqueous solution already at 100 °C [197]. The presence of aliovalent dopant ions changes the oxygen vacancy concentration in the anatase lattice. In the case of interstitial dopants, the lattice constraint hinders or enhances the ART [198–201]. Reidy *et al.* [193] suggested that a rise in the ART transition temperature is due to a limited mass transport in the system. On the other hand a drop of the transition temperature is probably related to an increase of the defect sites able to provide mass transport with lower energy.

Summarizing the available results, it appears that up to date i) no generally accepted view exists for the ART and ii) that every synthesis method changes the conditions for the reconstructive transformation.

3.1.3. Rutile

Rutile is the thermodynamical stable phase of titania and its crystal growth is favorable in acidic environments [169]. This is strongly related to the type of Ti complex that is formed prior to the rutile

nucleation. The nucleation seems to be promoted in the presence of Cl^- ions [202]. The TiO_6 unit arranges in an octahedron whose two apical bonds measure 1.979 \AA while the four equatorial bonds are 1.948 \AA long (at 295 K), resulting in a less distorted octahedron compared to anatase (see figure 3.3a) [171]. In the rutile structure each TiO_6 octahedron shares a corner with the neighboring one along the $\langle 110 \rangle$ direction. Stacking occurs by alternating the long axis between the two vertices with the short axis through a 90° rotation (as reported in figure 3.3b) and more noticeable in figure 3.5a. The four equatorial Ti–O bonds lie on the same plane forming 90° angles with the two apical bonds [171].

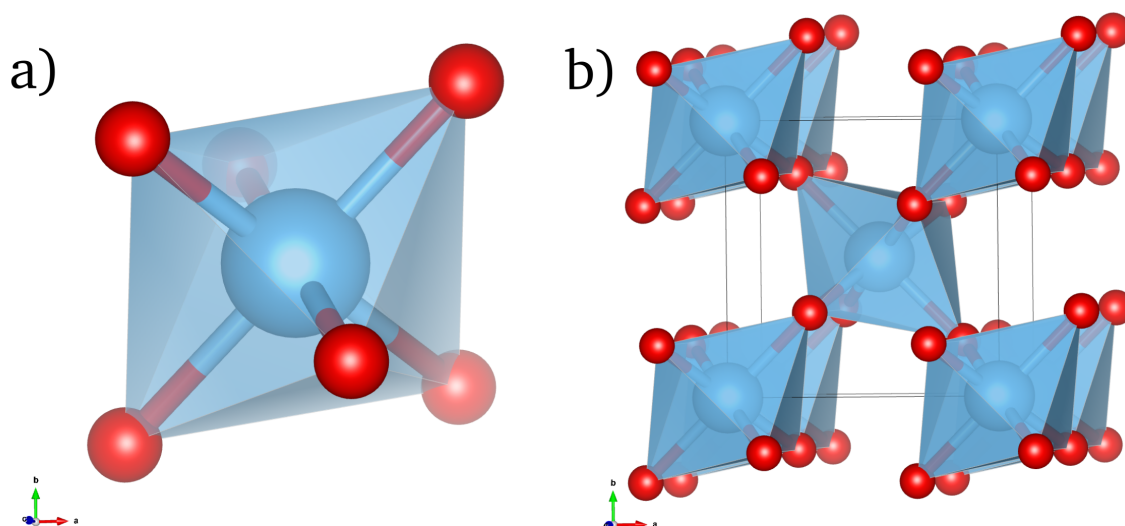


Figure 3.3.: Rutile single octahedron in a) and rutile unit cell visualizing the connections between the octahedra in b). Both were designed with the VESTA 3D structure visualization software [172] (CIF file ICSD-202240 [171]).

Figure 3.4 reports the Wulff construction of rutile (according to Ramamoorthy *et al.* [203]) with $\{110\}$, $\{101\}$, $\{011\}$ and $\{100\}$ as main exposed facets. The (110) facet has the lowest surface energy and a low density of dangling bonds, covering around 56% of the crystal surface. The surface energies of the low-index facets are in the order $(001) > (011) > (100) > (110)$ with 2.07 J m^{-2} , 1.75 J m^{-2} , 1.40 J m^{-2} and 1.12 J m^{-2} , respectively [203].⁴ Most of the synthetic routes end up with rutile crystals with nanowire- or nanorod-like shapes grown along the $[001]$ direction, even without the use of specific capping agents [30, 32, 204–207]. This trend can be explained with the surface energy balance, that promotes growth on the $\{111\}$ and $\{001\}$ facets instead of the $\{110\}$. Recent studies report additional information on rutile facets obtained by first-principles density functional theory combined with the Wulff principle [31, 208].

The systematic use of capping agents can determine the growth direction. The addition of NaF in the solvothermal synthesis permits to regulate the (110) , (111) and (001) facet ratio. Its effect is to

⁴Ramamoorthy *et al.* [203] report the surface energies in meV au^{-2} . The values were converted in J m^{-2} for an easier comparison with the values reported for the anatase in the previous section ($1 \text{ meV au}^{-2} = 7.16 \times 10^{-45} \text{ J m}^{-2}$).

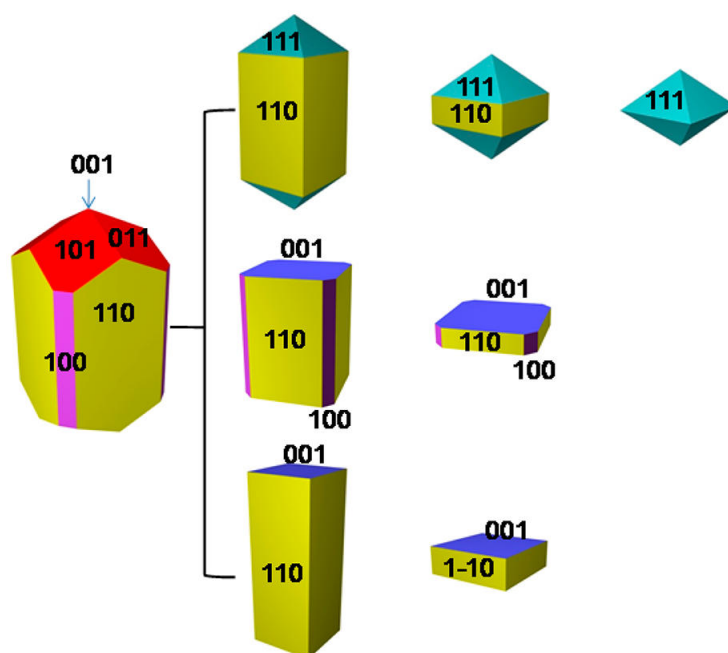


Figure 3.4.: Equilibrium crystal shape of rutile by the Wulff construction (according to [203]) and the possible shapes that can evolve from it (reprinted with permission from [30]. Copyright © 2014 American Chemical Society)

lower the energies of (111) and (001) surfaces promoting their preferential growth. The limitation of the (110) growth improves the photoreactivity just by a changed ratio of the surfaces with high energy facets [209]. The percentage of the {111} facet increases from 25 % to 98.5 %. Notably, curved surfaces appear in the rutile crystal with increase of the F^- concentration [210]. Strategies to increase the presence of {001} facets were also developed [211, 212].

3.1.4. Rutile surfaces

(110) surface According to the *ab initio* total-energy calculations of Ramamoorthy of periodic TiO_2 slices, the (110) surface has the lowest energy while the (001) one has the highest [203] (see section 3.1.3). This difference can be explained in terms of electrostatics [213] or by the influence of dangling bonds [214]. Both concepts express necessary but not universally valid conditions for stable surfaces. Despite being the surface with the highest stability, the (110) surface reconstructs at high temperature under both oxidizing and reducing conditions [28]. Tasker [213] analyzed the surface stability from an electrostatic point of view, while LaFemina [214] applied the concept of *auto-compensation* to the oxide surfaces, with two different types of dangling bonds compensating the (110) surface (see figure 3.5). Figure 3.5a suggest that the dipole moment of the repeating unit is zero because of being perpendicular to the surface. In figure 3.5b, the surface of the crystal, cut along line A, contains two types of Ti atoms: bulk Ti atoms sixfold coordinated, alternated with fivefold coordinated Ti atoms with a perpendicular

dangling bond. The situation of the oxygen atoms is similar, being threefold coordinated in the bulk and twofold coordinated in the proximity of the removed layer. These twofold coordinated "bridging" oxygen atoms, are of importance for the reactions taking place on the surfaces during annealing processes. They can be removed easily due to their weak bonding, generating point defects in the surface layer [215].

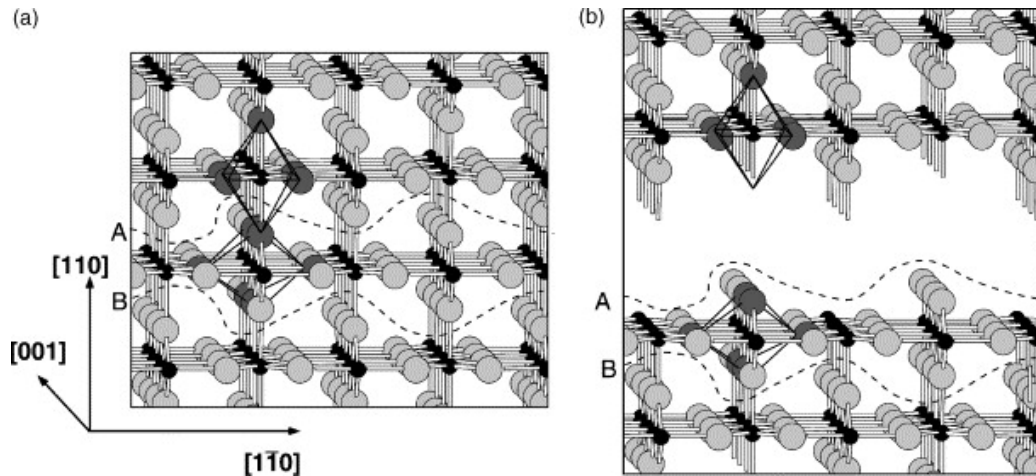


Figure 3.5.: a) 90° alternated stacking system in rutile. Open channels are visible in the [001] direction and the dashed lines A and B show the uncharged repeating unit. b) The crystal is ideally cut along A, showing that the same number of Ti-O and O-Ti bonds are broken auto-compensating the surface [214]. The (1x1)-terminated (110) surface is thus stabilized (reprinted from [28] with permission from Elsevier Copyright © 2002).

Surface relaxation causes atoms in the near surface layer to move perpendicular to the (110) surface, as reported in figure 3.6. The different atoms are labeled with numbers in this figure, e.g. the bridging oxygen atom labeled with "3", relaxing downwards. The sixfold coordinated Ti atom with "1" move upwards, whereas the fivefold coordinated Ti atom with "2" moves downwards. These relaxations do not induce an increase of the unit cell because they are symmetric [216].

(100) surface The concept of *auto-compensation* can also be applied to the (100)-(1x1) TiO₂ surface. When in a *Gedankenexperiment* the bulk material is cut along this surface, the same number of Ti → O and O → Ti bonds are broken (as highlighted by the dashed line in figure 3.7b)). A surface with (110) facets is generated by removal of a portion of surface atoms, as proposed by Zschak *et al.* [217]. Relaxations do not occur along the [001] direction but along the [100], where only the fivefold coordinated Ti atoms move downwards [203]. Along the [010] direction the twofold and threefold coordinated oxygen atoms move against the fivefold and sixfold coordinated Ti atoms, increasing thus the effective coordination of the fivefold coordinated Ti atoms [218].

(001) surface Figure 3.8 depicts the only way to cut the rutile crystal along the (001) direction. This surface is in a high energy configuration due to the fact that all the Ti atoms are fourfold coordinated

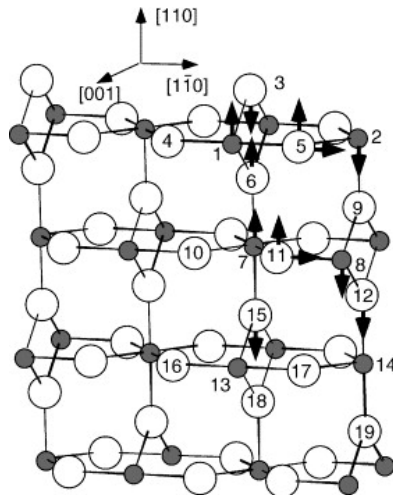


Figure 3.6.: Relaxation of the surface atoms in a (110)-(1x1) rutile surface calculated by [216] (reprinted from [28] with permission from Elsevier Copyright © 2002).

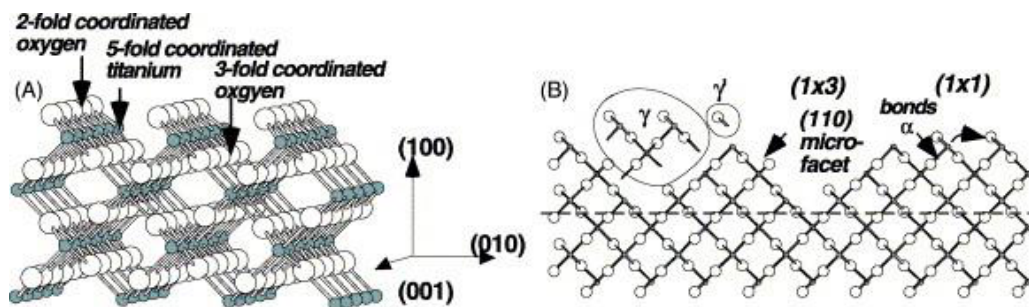


Figure 3.7.: a) Unreconstructed (100)-(1x1) rutile surface, resulting when the bonds are broken along the dashed line reported in b) (reprinted from [28] with permission from Elsevier Copyright © 2002).

and all the O atoms are twofold coordinated, resulting in a higher number of broken bonds with respect to the (110) and (100) surfaces described above. In this way it is possible to explain the high surface energy which causes the (001) surface to reconstruct [28].

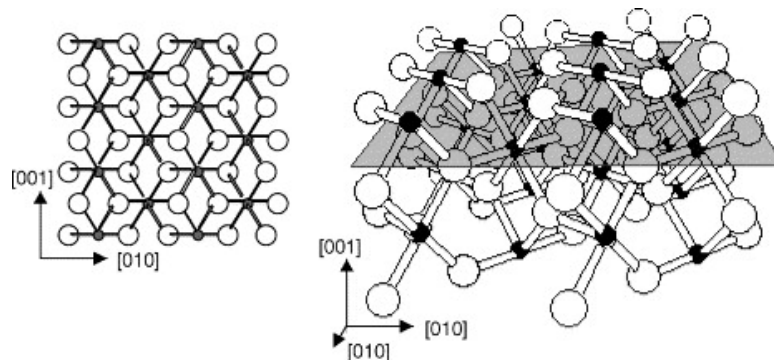


Figure 3.8.: Left: side view of the rutile (001) surface. Right: only possibility to cut the rutile crystal in this direction (reprinted from [28] with permission from Elsevier Copyright © 2002).

3.2. TiO₂ as pearl luster pigment

Pigments are one of the main applications of TiO₂. In this chapter basic information about pigments is provided and special attention is given to the optical phenomenon of the *interference effect* and to the crystal habit that is necessary for its generation.

3.2.1. Pigments and the origin of color

Originating from the Latin word "pigmentum", this class of material later adopted its modern meaning of a substance consisting of defined particles insoluble in the applied medium with coloring, protective and magnetic properties [104]. Pigments are distinguished from dyes exactly for their insolubility in solvents and binders. Table 3.2 reports a classification following the guidelines of the International Organisation for Standardization (ISO) and the German Institute for Standardization (DIN). There are other characteristics that allow to differentiate the range of available pigments, for instance the stability properties (retention of gloss, resistance towards corrosion, light, weather, chemicals and heat), the behavior in binders (dispersibility, compatibility and solidifying effect) or the general chemical and physical properties (hardness, chemical composition, density, particle size and content of water-soluble and acid-soluble matter). All these factors acquire different importance according to the application for which the pigment is chosen.

Color generation The typical interactions of a photon with a pigment particle are *absorption* and *scattering* [219]. Scattering will be observed as white color by the human eye. Black is the observed

Table 3.2.: Classification of inorganic pigments [104].

Term	Definition
White pigments	optical effect caused by non-selective light scattering (examples: titanium dioxide and zinc sulfide pigments, lithopone, zinc white)
Colored pigments	optical effect caused by selective light absorption and also to a large extent by selective light scattering (examples: red and yellow iron oxide, cadmium pigments, ultramarine pigments, chrome yellow, cobalt blue)
Black pigments	optical effect caused by non-selective light absorption (examples: carbon black pigment, iron oxide black)
Effect pigments	optical effect caused by regular reflection or interference
Metal effect pigments	regular reflection takes place on mainly flat and parallel metallic pigment particles (example: aluminum flakes)
Pearl luster pigments	regular reflection takes place on highly refractive parallel pigment platelets generating the phenomenon of interference (example: titanium dioxide on mica, iron oxide on mica)

color in case of absorption in the visible region. The perception of other colors is due to selective absorption and reflection. The reflectance curve reported in figure 3.9 shows how the photons interact with a blue body which absorbs the green spectral part. Yellow and red components only reflect the blue wavelength. Such a spectral reflectance curve is characteristic for every pigment. As regards the effect pigments — detailed information are given in section 3.2.2 on page 37 — it is the result of oriented reflection and interference phenomena.

Scattering and absorption of light in small particles can be described by the Mie theory which expresses the relationship between scattering and the particle size D . For a particular particle size there exists a specific wavelength that produces the maximum light scattering and, with respect to the lightening power, there is an optimum D [220, 221]. Knowing the particle size distribution (PSD), the complex refractive index ($\underline{n} = n + i\kappa$) and the concentration of a pigment, it is possible to calculate its reflectance spectrum [104]. There are some optical properties that provide important information about the pigment performance, like

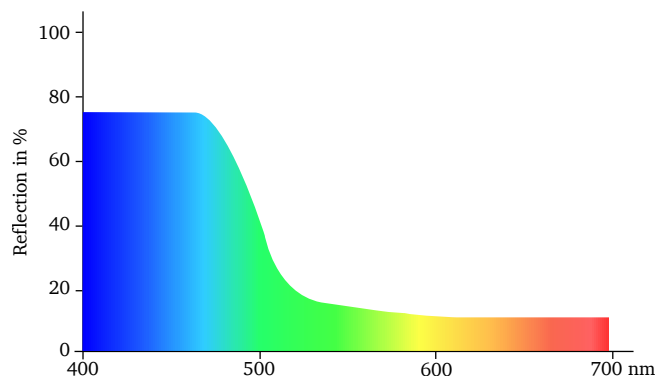


Figure 3.9.: Reflectance curve of a blue absorption pigment (inspired by ref. [73]).

the *tinging strength*, the *lightness* and the *hiding power*. The first one refers to the capacity of a pigment to add a color to a light-scattering material by means of its absorption property. The second one defines the ability of a pigment to increase the reflectance of a material which mostly absorbs [104]. As regards the third one, the *hiding power* is given by the reciprocal of the *hiding thickness*. The latter corresponds to the minimum thickness of a coating film deposited on a half black and half white support, that completely hide the contrast line formed at the junction between the black and the white part. The *hiding power* defines the area (m^2) that can be covered with 1 liter of paint.

TiO₂ absorption pigments TiO₂ absorbs in the ultraviolet (UV) part of the spectrum at $\lambda = 377$ nm (anatase) and $\lambda = 397$ nm (rutile). Light absorption in the near UV generates electrons in the conduction band and a positively charged hole p^+ in the valence band. Hydroxyl ions at the TiO₂ surface are oxidized by the holes p^+ , forming reactive radicals ($\bullet\text{OH}$ and $\text{HO}_2\bullet$) [222]. These radicals can oxidize a coating polymer on a TiO₂ pigment and deteriorate it by producing polymer radicals $\text{R}\bullet$. In this series of reactions Ti^{4+} reduces to Ti^{3+} , which can then be oxidised again by O_2 generating thus an oxygen anion radical. The chain of reactions can be limited by reducing the number of hydroxyl groups on the TiO₂, e.g. by doping with ZnO. This helps to reduce the loss of gloss, which is the first step of chalking. Also the refractive index ($n = 2.70$) is a fundamental property of TiO₂ (see following section) [29].

3.2.2. Concept of pearl luster pigment

Pearls generate their well known luster because of a series of alternating layers with different refractive indices, formed through a biomineralization process. In the oyster a foreign body like a grain of sand is encapsulated by CaCO₃ layers with a high refractive index, alternating with protein layers with a low refractive index. Light is partially reflected by the CaCO₃ layer, passes through a protein layer, and meets then the next CaCO₃ and so on [73]. This luster effect underlies the industrial luster pigments, recalling the natural counterpart.

Pigments could be divided in *absorption pigments* and *effect pigments* on the basis of their interaction with light (see table 3.2 on page 36). The luster, brilliance and gloss that distinguishes effect pigments from the absorption pigments are due to i) the thin platelet morphology of the crystals, and ii) their layer arrangement parallel to applied surface [104]. Figure 3.10 depicts the different types of pigments together with their characteristic interaction with electromagnetic radiation. The effect pigments can be divided in two main classes, the pearl luster pigment (PLP)s and the metal effect pigments. The latter reflect the total incident visible light on flat and parallel metallic particles, which act as mirrors generating thus a metallic gloss effect [223]. Typical materials for this group are aluminium, copper and copper/zinc alloys.

In order to explain the PLP effect, it is useful to recall the law of reflection with the angle of incidence ε equal to the angle of reflection ε' . Diffuse reflection results if the surface reflecting the

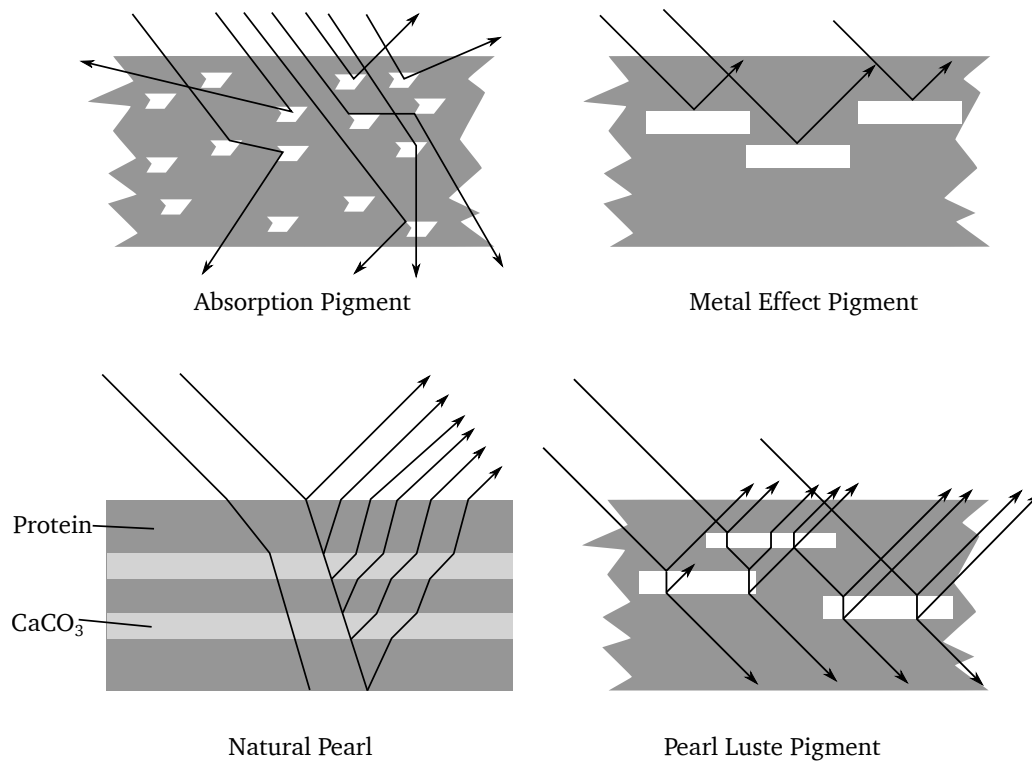


Figure 3.10.: Pigment classes and their characteristic interaction with the electromagnetic radiation (inspired by ref. [223]).

light is uneven (see figure 3.11). On smooth surfaces light finds an ideal condition to be reflected in a preferential direction. Reflection in one defined direction is the basis for luster, which can have different aspects according to the degree of illumination and the angle of observation.

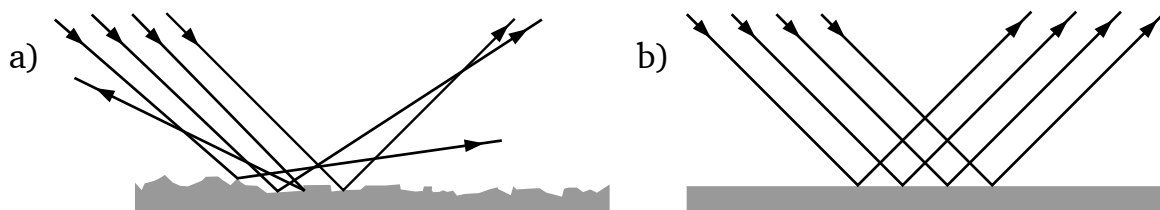


Figure 3.11.: Reflection from a) uneven and b) even surfaces (inspired by [223]).

Knowing the angle of incidence ε and the refractive indices of the media, it is possible to describe the relationship between reflected and incident light intensity. The larger the difference between the two refractive indices, the higher the intensity of the reflected light. The portion of light which is refracted from the medium forms a refraction angle ε'' towards the perpendicular of the interface between the media (Snell's law, equation 3.1). If the light enters a medium with a higher optical density (expressed by the refractive index n_1 in eq. 3.1), the ε'' decreases, otherwise it increases [223].

$$n_1 \cdot \sin \varepsilon = n_2 \cdot \sin \varepsilon'' \quad (3.1)$$

The reflection coefficient $r(\varepsilon)$ for non-polarized light can be obtained by applying the Fresnel equation (equation 3.2). It is defined by the ratio between the reflected luminous flux ϕ_r and the entering one ϕ_e .

$$r_\varepsilon = \frac{\phi_r}{\phi_e} = \frac{1}{2} \cdot \left[\frac{\tan^2(\varepsilon - \varepsilon'')}{\tan^2(\varepsilon + \varepsilon'')} + \frac{\sin^2(\varepsilon - \varepsilon'')}{\sin^2(\varepsilon + \varepsilon'')} \right] \quad (3.2)$$

For almost perpendicular light rays equation 3.2 simplifies to [223]:

$$r_\varepsilon = \left(\frac{n_2 - n_1}{n_2 + n_1} \right)^2 \quad (3.3)$$

According to equation 3.3, regardless whether the flux is coming from a less or more dense medium, only the difference between the two refractive indices n_1 and n_2 is decisive for the reflection coefficient. A phase shift of 180° in the reflected light results if the refractive index of the thin layer is higher than that of the medium. This shift corresponds to a length of $\lambda/2$. No shift is produced if the refractive index is lower or equal. Relation 3.2 and 3.3 are essential for the understanding of the phenomenon of interference. A light beam of intensity I_0 meeting a medium with a higher refractive index causes a phase shift in the reflected part of the light R_1 (point A in figure 3.12). The transmitted light R_2 , which is reflected at the second interface (point B in figure 3.12), shows no phase shift because it meets a medium with a lower refractive index. At point C, R_1 and R_2 can interact with each other in two possible ways, according to the optical path difference of R_1 and R_2 (which is equal to $2d \cdot n_1$ at vertical incidence, and n_1 as refractive index of the medium).

The rays R_1 and R_2 can interfere destructively or constructively when the conditions of equations 3.4) and 3.5) are fulfilled. In the first case colors are extinguished, while in the second case they are amplified. Considering different angles of incidence, the optical path will be longer and the formulas could not be simplified as in equation 3.3.

$$2d \cdot n_2 = \lambda \cdot x \quad x = 1, 2, 3 \dots \quad (3.4)$$

$$2d \cdot n_2 = \frac{\lambda(2x + 1)}{2} \quad x = 0, 1, 2, 3 \dots \quad (3.5)$$

According to the description given above, a high difference in the refractive indices is a pre-requisite to achieve well defined interference effects in pigments [143]. Additionally, undesired diffuse reflections caused by uneven surface of the platelets have to be minimized.

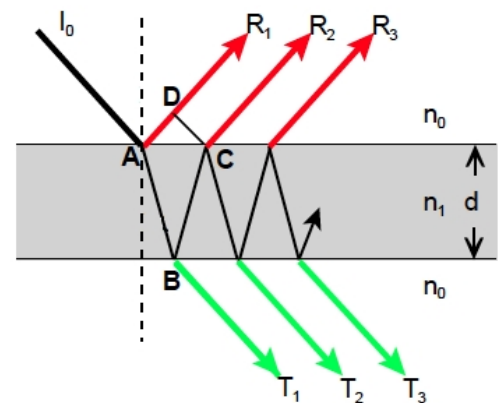


Figure 3.12.: Interference occurring on a thin layer with refractive index $n_1 > n_0$ (inspired by [143]).

Influence of platelet thickness on the color The thickness of the platelets is an essential factor in the color generation, the reflection maximum shifting to a higher wavelengths for an increasing thickness [224]. Consider a platelet of thickness x and a high refractive index in contact with low refractive index material. The maximum of the reflection is typically found in the UV range for a thickness below 85 nm, whereas one obtains the highest gloss and even white reflection for a thickness between 85–140 nm (as reported in figure 3.13).

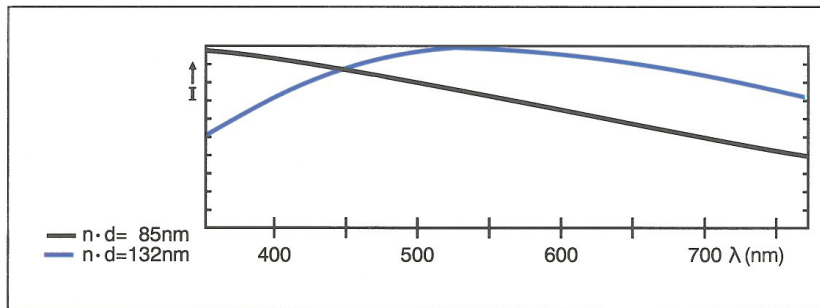


Figure 3.13.: Relative intensity distributions of reflections of two films with different thickness (taken from ref. [73]).

The intensity distributions reported in figure 3.13 change progressively with increasing thickness. The more the thickness increases, the more maxima and minima appear in the visible range, generating colors with different degree of shade and brilliance. This phenomenon finds its application in the layer-substrate system, where the film thickness is used to produce the colors. TiO_2 of different thickness, coated on mica provide a typical example. The interference color is reported in figure 3.14. More details about the preparation of layer-substrate systems are given in the next section.

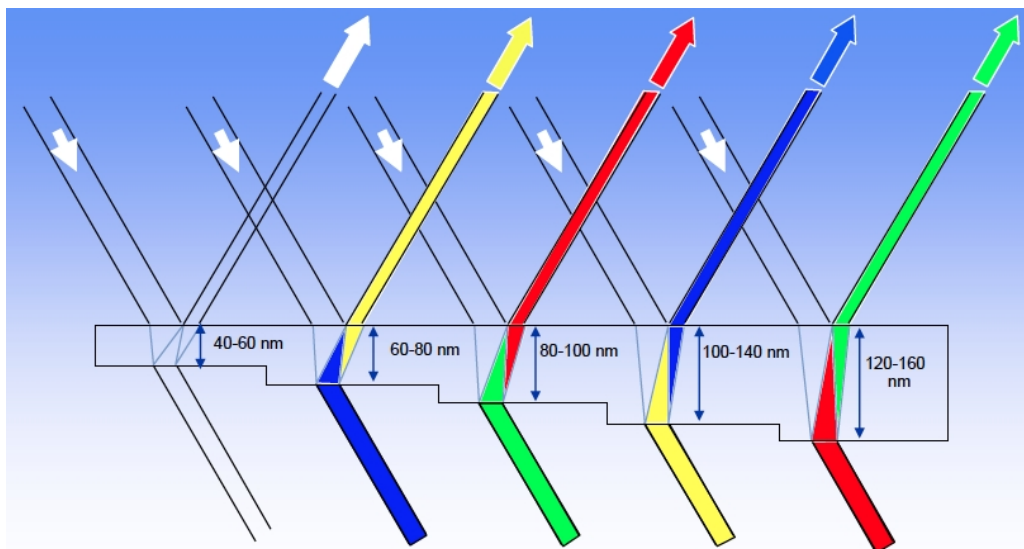


Figure 3.14.: The layer thickness of TiO_2 generates the interference colors (taken from ref. [73]).

3.2.3. Manufacturing process of the TiO₂-based pearl luster pigment

Commonly PLPs consist of platelets coated with a thin layer of a metal oxide [143, 144, 225, 226]. They are used for the production of substrate-based pigments. Mica substrates — a natural sheet layer silicate — act as a mechanical support for the coating layer for example. Typically the mica substrate is coated on both sides with TiO₂ of total thickness in the range of ≈ 150 nm (see figure 3.15). Such a configuration implies three different refractive indices (mica, TiO₂ and air) and four interfaces, generating interference through their possible combination [104]. By increasing the thickness of the metal oxide coating layer, it is possible to generate different interference effects (see figure 3.14), and the variety of possible interference colors can even be increased by coating the platelets in a sandwich-like arrangement by two different metal oxides with different indices of refraction.

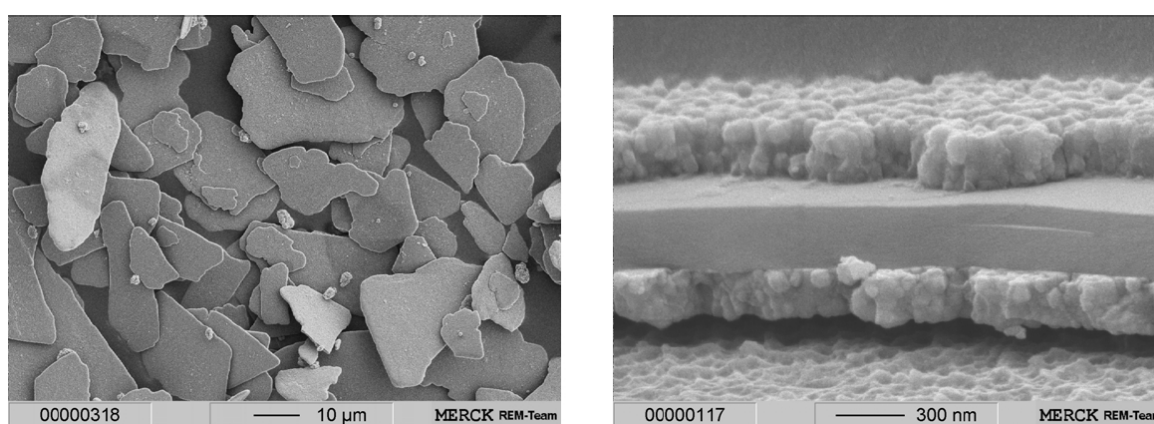
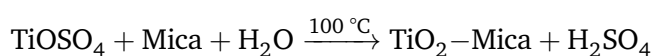


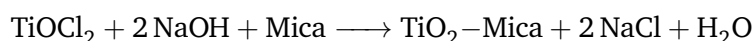
Figure 3.15.: Overview of mica substrates coated with anatase (left), and a cross-section of a pigment (right, reprinted with permission from [104]. Copyright © 2005 Wiley-VCH).

The process of coating mica with TiO₂ usually takes place in aqueous solution and two methods are used [104]:

1. Homogeneous hydrolysis



2. Titration



In the first case, titanium sulfate is added in a reactor containing the aqueous mica suspension, slowly hydrolyzing TiOSO₄ to insoluble titanium dioxide. The second method has the advantage to be easier to control, since the titanium dioxide hydrate precipitation occurs at a certain pH value that is held constant with NaOH addition [223]. After the coating step, the pigments are dried and calcined at 600–900 °C. Anatase is precipitated and covers the platelets in both production methods. No pure rutile phase is formed in combination with mica, even during calcination at 1000 °C. However, the rutile phase is preferred due to its higher refractive index. Hence, a process using SnO₂ as pre-coating

layer was developed [223], which induces the crystallization of TiO_2 rutile [197] (see section 3.1.2 on page 30). As a matter of fact, SnO_2 crystallizes in the rutile structure and its lattice parameters favor the formation of TiO_2 rutile [223]. Flat substrates with tailorable thickness are alternatives to mica opening new frontiers of interference color generation (see figure 3.16). SiO_2 and Al_2O_3 flakes provide smooth surfaces, but have too low indices of refraction. Therefore, they need coating with metal oxides. Figure 3.17 reports the scheme for the production of Al_2O_3 flakes, also known as Xirallic® (registered trademark of the company Merck Kommanditgesellschaft auf Aktien (KGaA), Darmstadt). Phosphates and other compounds (like TiCl_4), able to control the crystallization during heat-treatment [227], are added to a reactor containing an aqueous solution with an aluminium salt used as feedstock. After neutralization, the suspension is dried and calcined at 900–1400 °C. The corundum flakes obtained after washing exhibit a very narrow thickness distribution and a high aspect ratio [104].

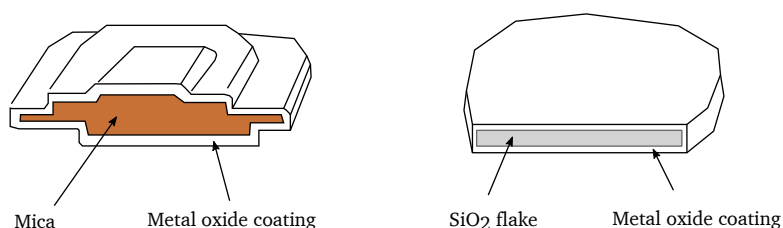


Figure 3.16.: Comparison between cross-sections of natural (left) and synthetic substrate (right).

The crystal habit of Al_2O_3 flakes inspired our studies (see section 2.3.1 on page 18), aiming to generate an iridescent effect (typical of nacre) directly from uncoated TiO_2 flakes. The refractive index of rutile is close to 2.9, much higher than that of alumina and silica, being thus of advantage for the PLP preparation. Additionally, a higher level of control will be possible if the thickness of the flakes could be adjusted by the synthesis parameters. Ideally, the TiO_2 flakes should be obtained with the MSS, as for the Al_2O_3 flakes.

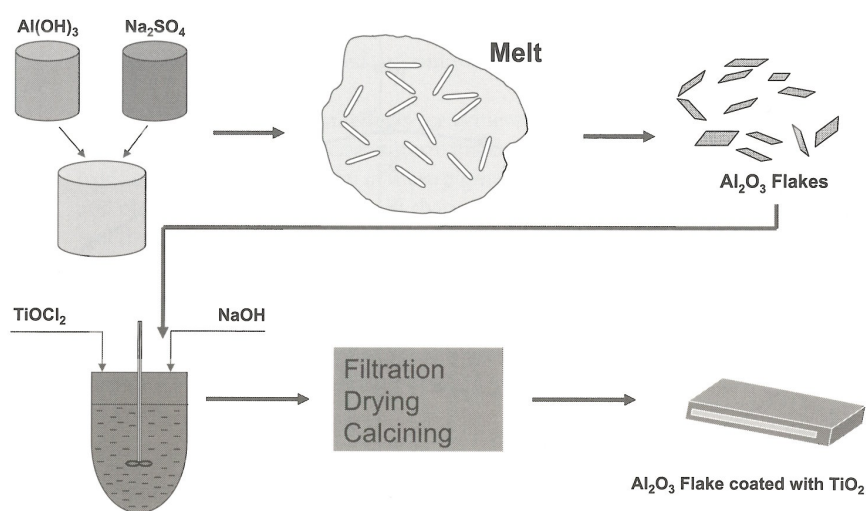


Figure 3.17.: Manufacturing process for alumina flakes, after [104].

3.3. $A_2Ti_6O_{13}$ and $A_2Ti_3O_7$ structures ($A=Li^+, Na^+$) and energy storage application

Sodium titanate is the second material synthesized in this work by molten-salt synthesis (MSS). Using MSS different structures can be obtained just by tuning the basicity of the molten oxosalt (see section 2.3.4 on page 23). Starting from a Ti-containing precursor either titania or titanates can be made. Moderate basicity leads to TiO_2 formation, as reported in equation 2.23. Titanate formation is promoted by a lower pO^{2-} following the reaction described in equation 2.24 (see section 2.3.4 for the definition of pO^{2-}). This parameter is also decisive for the type of titanate structure synthesized by MSS (see the results reported in chapter 5.3.1).

Titanate structures Monovalent cations A^+ are located in different sites of the alkali titanate lattice depending on the structure that is formed: either the tunnel structure $A_2Ti_6O_{13}$ made of the basic $[Ti_6O_{13}^{2-}]$ network [41, 228], or the layered structure $A_2Ti_3O_7$. As concerns the $A_2Ti_6O_{13}$ structure, the A^+ species inserted in the $[Ti_6O_{13}^{2-}]$ framework has an impact on the tunnel space size as reported by Kataoka *et al.* [229]. Exchanging Na^+ with Li^+ causes a tunnel space expansion, contrarily to the expectations based on the much smaller ionic radius of Li^+ [230]. Both Li and Na atoms stay on the 4i site⁵ but the occupation site of Li is shifted to $y = 0.5$ respect to the original site of Na in $Na_2Ti_6O_{13}$ (NTO) (forming thus a LiO_4 planar coordination) [229]. NTO and the ion-exchanged $Li_2Ti_6O_{13}$ both belong to the monoclinic crystal system, with space group $C2/m$. The TiO_6 octahedra share edges and corners in NTO forming corrugated sheets. Adjacent sheets build the tunnel by corner-cross-linked octahedra. The Na-ions occupy the interstitial sites. The NTO tunnel structure with a rectangular section developing along [010] (see figure 3.18) provides a free space where Li-ions or Na-ions can easily move. For this reason NTO attracted attention as battery component [44, 45, 228, 231]. A movement along a sinusoidal path was suggested for the intercalation of Li^+ in NTO to minimize the Li–Na electrostatic interaction [47]. Lithium (Li1) allocates in a square planar LiO_4 2c site (to decrease the electrostatic repulsion with Na ions) during the first intercalation step ($Li_{0.8}Na_2Ti_6O_{13}$) at a potential of 1.3 V. The further reduction step at 1.1 V ($Li_{1.7}Na_2Ti_6O_{13}$) forces the Li ions (Li2 and Li3) to the 4i sites. The Li-ion motion leads to a change of their coordination to minimize the Li–Li interactions [47]. Remaining Na ions force the Li ions to move along the sinusoidal path $Li1(2c) \rightarrow Li3(4i) \rightarrow Li1(2c)$ to reduce Li–Na electrostatic interactions. This suggestion is in contrast to reference [232], attributing the central site 2d between two Na ions to the Li ion intercalated in the second reduction step.

The structural features of NTO ensure a high ionic conductivity and cycling stability, whereas $Na_2Ti_3O_7$ owns a poor conductivity and low ionic mobility [233]. The $Na_2Ti_3O_7$ structure consists of zigzag layers of Ti–O octahedra forming interlayer spaces occupied by Na atoms (see figure 3.19). In contrast to NTO, this structure contains a higher amount of Na per formula unit which hinders the

⁵4i and 2c indicate the Wyckoff positions of the site which the single atoms occupy.

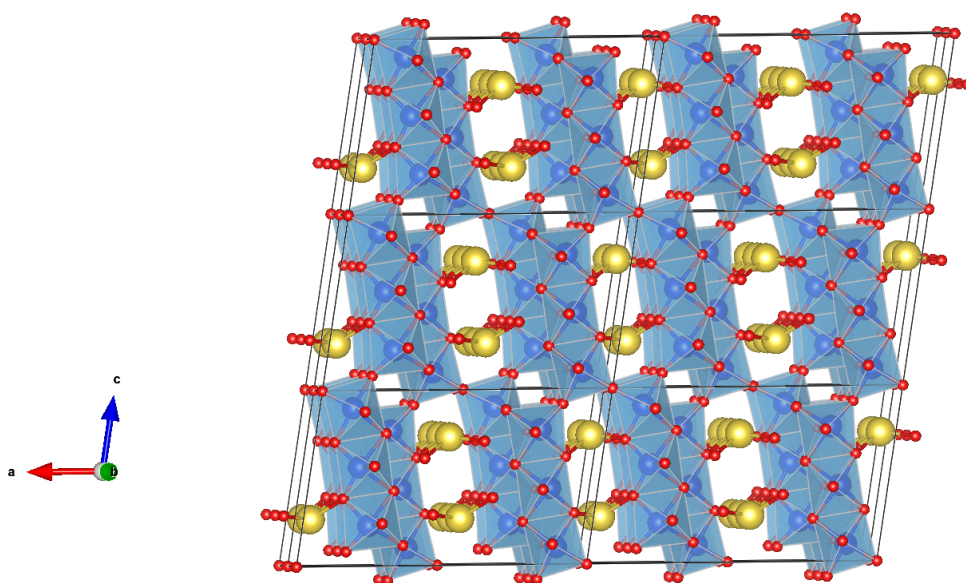


Figure 3.18.: Crystal structure of $\text{Na}_2\text{Ti}_6\text{O}_{13}$ (NTO) with the Na^+ ions marked in yellow, filling the tunnel structure built up by the TiO_6 framework. The red spheres represent the O atoms and the blue ones the Ti atoms. The orientation facilitates the view along the $\langle 010 \rangle$ direction. The structural model was realized using the 3D visualization software VESTA [172].

corner sharing between the TiO_6 octahedra [234]. The high interlayer space allows Na^+ storage with a theoretical capacity for Na at 310 mA h g^{-1} [235]. The layer distance is $\approx 8 \text{ \AA}$ and quite large in comparison to the $\approx 3.4 \text{ \AA}$ of graphite [49, 236]. The high theoretical capacity attracts research interest in energy storage despite the low conductivity and ionic mobility. Another advantage of $\text{Na}_2\text{Ti}_3\text{O}_7$ is the rather low Na^+ ion insertion potential (0.3 V vs. Na/Na^+), which allows a high energy density as well as a high operating potential window. As a consequence, sodium dendrite formation is excluded improving thus the electrochemical performances [46, 49, 233]. The two titanate structures can be combined in a hybrid $\text{Na}_2\text{Ti}_6\text{O}_{13}/\text{Na}_2\text{Ti}_3\text{O}_7$ electrode for both Li^+ and Na^+ insertion [233, 237–239]. This improves the electrochemical performances of $\text{Na}_2\text{Ti}_3\text{O}_7$. The above described electrochemical features make these materials potentially suitable for grid storage application. Nevertheless, a suitable synthesis method for such an application needs to fulfill the requirements for the large scale production.

Titanates synthesis methods Different synthesis routes have been applied in order to tailor the structure and morphology of sodium titanates with the aim of improving their electrochemical performance using solid-state reaction, hydrothermal [237, 238, 240–245] and sonochemical [246] synthesis. NTO was produced by solid-state reaction of anatase with Na_2CO_3 [46, 232, 247–249]. Also sol-gel synthesis [250, 251] and soft-template method were successfully implemented [72]. The latter obtained remarkable electrochemical performance at voltages between 3-2 V vs Na/Na^+ . Further improvement was achieved by prolonged hydration of $\text{Na}_2\text{Ti}_6\text{O}_{13}$ precursor, leading to a larger interlayer in the tunnel

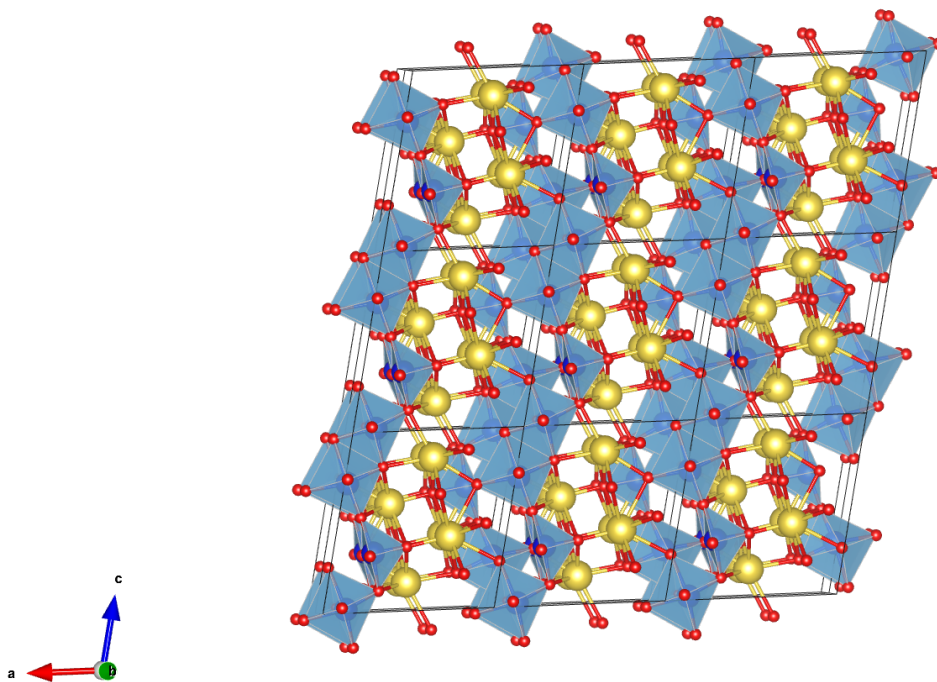


Figure 3.19.: Crystal structure of $\text{Na}_2\text{Ti}_3\text{O}_7$ (realized by VESTA [172]) with the Na^+ ions marked in yellow, filling the interlayer spaces built up by the TiO_6 octahedra. The red spheres are the O atoms and the blue ones the Ti atoms. The orientation facilitates the view along the $\langle 010 \rangle$ direction. The structural model was realized using the 3D visualization software VESTA [172].

structure of NTO [241]. An enhancement of the rate capability of lithium [245] and sodium [252] storage was reported for carbon coating of the $\text{Na}_2\text{Ti}_6\text{O}_{13}$ nanorods.

MSS was also already successfully implied for the synthesis of NTO. Teshima *et al.* [44, 45, 253] and Zhen *et al.* [254] synthesized NTO in NaCl flux, with anatase nanopowder mixed with Na_2CO_3 as reactants [13, 15]. He *et al.* [5] performed the synthesis in NaCl-KCl salt mixture containing anatase nanopowder and Na_2CO_3 . Very recently, the formation of sodium titanates was reported by molten salt electrochemical synthesis [255, 256]. Moreover, NTO synthesized by MSS was used as precursor to get $\text{Li}_2\text{Ti}_6\text{O}_{13}$ via ion exchange in molten lithium salt [231]. Compared to the other synthesis methods, MSS could quite better meet the requirements for a large scale production, providing a high yield per synthesis batch compared to *e.g.* hydrothermal or sol-gel synthesis [1, 16]. MSS also permits to achieve a unique morphology that could improve the electrochemical performance. Finally, it is a cost saving synthesis method [4, 8, 9].

4. Experimental

This chapter describes the experimental work on the molten salt synthesis of TiO₂ and sodium titanate. Their crystal structure, morphology and electrochemical properties have been characterized by a variety of investigation methods.

4.1. Molten salt synthesis of samples

Two paths have been followed for the preparation of the precursors of TiO₂ and sodium titanates as starting material for the MSS: i) the dry-mixed preparation (DMP) and ii) the wet-chemical preparation (WCP). In the first case, nanosized anatase powder ($d < 100$ nm) has been mixed with the salt species (chlorides and sulfates). On the other hand, the precursor is obtained by an hydrolysis reaction and then mixed with the salt in solution. The temperature for the MSS of the samples ranges from 400–1200 °C, with two hours of holding time if not stated differently. The precursor concentration is usually between 1 and 50% in terms of the weight fraction. The heat-treatment is mainly performed in ambient air, but also in argon or pure oxygen. The chemical compounds used for the experiments are listed in table A.1 (see appendix A on page 199).

4.1.1. Dry-mixed precursor preparation in MSS (DMP)

DMP has been mainly used for the preparation of rutile crystals. All the adopted reagents have analytical purity, as received from different manufacturers. Anatase (Kronos K1002) has been used as precursor and mixed with Na₂SO₄, NaCl, LiCl, KCl, MgCl₂, AlCl₃, NaF and B₂O₃. The amount of precursor mixed with the salt has been varied in order to assess the influence of the precursor concentration on the morphology and composition of the product. The chemicals have been thoroughly mixed for 20 min in an agate mortar and put in an alumina crucible closed with a lid. The calcination has been mainly performed under ambient conditions by varying the heating rate and the holding time. After cooling down to room temperature, the crucible has been immersed in 1 L deionized (DI) water at 85 °C in order to leach out the salt matrix. The solution has been filtered by means of a Büchner flask. The samples collected in the filter have been further rinsed with DI water in order to ensure the total removal of the

salt traces. The filtrates have been washed until no chloride ions (or sulfate ions) could be detected by silver nitrate solution. Finally, the samples have been dried at 110 °C in a drying oven. Typically, 2.78 g of anatase have been mixed with 25 g of salt (*e.g.* NaCl or Na₂SO₄) for 10 wt. % of TiO₂. The product yield is in average $\approx 95\%$. The amounts of added NaF and B₂O₃ are defined by the molar ratio respect to TiO₂.

4.1.2. Wet-chemical precursor preparation in MSS (WCP)

The WCP has been mainly applied for the synthesis of NTO nanorods. Pure NTO nanorods have been obtained through a two-step MSS: the preparation of the precursors by WCP, followed by heat-treatment in molten salts. The following reagents of analytical purity have been used as Ti-precursor: TiOSO₄ hydrated and TiCl₄. The acidic TiOSO₄ or TiCl₄ solution in deionized water (formed under moderate stirring) is heated up to 60 °C. Titration with 32 % NaOH monitored by a pH meter, neutralizes the solution. The salt (Na₂SO₄ or NaCl) has been added to the solution setting a typical ratio of 1 : 10 of precursor to salt matrix. The precursor mixture has been dried at 110 °C for 24 h and ground before heating-up in an alumina crucible under air (or other atmospheres). The following calcination temperatures have been investigated: 900 °C, 1000 °C, and 1100 °C. After 2 h of holding time and cooling to room temperature, the samples have been dissolved in DI water at 85 °C and filtrated by means of a Büchner flask. The crystalline powders collected in the filter have then been rinsed with DI water in order to remove remaining traces of the salt. No chloride ions (or sulfate ions) could be detected by silver nitrate solution. Finally, the obtained powder was dried at 110 °C in a drying oven. Typically, 20 g of TiOSO₄ have been added to 1 L of deionized water. About 130 g of salt (*e.g.* Na₂SO₄) have been mixed to the solution after the neutralization to perform the MSS with ≈ 5 wt. % of TiO₂. The product yield is in average $\geq 90\%$. The amount of added Na₃PO₄ are defined by the molar ratio respect to TiO₂.

4.2. Experimental methods

4.2.1. Powder X-ray diffraction

X-ray diffraction (XRD) has been mainly measured in flat-sample transmission geometry on a STOE STADI P diffractometer (STOE & Cia GmbH, Darmstadt, Germany) with monochromatic Mo-K α ($\lambda = 0.7093 \text{ \AA}$) radiation (emitted at 30 mA and 45 kV operation). The diffractometer is equipped with a Germanium 111 monochromator and a position sensitive detector with a 6° aperture. A 1 : 10 mixture of collodium and isoamylacetate was used to fix the powdered samples between two acetate foils for the measurement at the STOE STADI P.

In-situ high-temperature XRD The phase evolution during the MSS was investigated via high-temperature *in-situ* XRD with a HUBER G670-180 Guinier camera (Huber Diffraktionstechnik GmbH & Co. KG, Rimsting, Germany) using a position sensitive imaging plate method and a Guinier-Monochromator 611 with a focusing monochromator crystal of the Johansson-Guinier type. The X-ray source is Cu-K α ($\lambda = 1.5405 \text{ \AA}$) radiation. A quartz capillary (0.5 mm diameter) was filled with the specimen powder (less than 1 mg), then sealed with alumina paste and placed on the rotary stage. Sample heating was achieved by means of u-shaped ceramic heating fork (Huber heater device 670.3 represented in figure 4.1). Both oven and capillary were shielded by a cylindrical Kapton foil. The temperature is measured by a Pt-10Rh-Pt thermal element positioned directly above the rotating capillary. The device allows measurements up to 900 °C.

Rietveld refinement of the XRD results The phase composition of the obtained materials was determined by Rietveld refinement performed by statistical calculation on the measured powder diffraction data [257, 258]. The software GSAS II was used for this purpose [259, 260]. A NIST Si standard has been measured (SMR 640d) to improve the reliability of the refinements. The obtained diffractograms were refined using the Crystallographic Information File (CIF) provided by NIST (CIF generated by M. Suchomel at AP-S/ANL). This has the advantage to stabilize the parameters U , V and W that are related to the diffractometer (given set of experimental parameters that change with photon energy, beam size, thickness of the sample and sample-to-detector distance) and modeled with the Caglioti formula (see equation 4.1) [261]. This formula expresses the Gaussian component of the full width at half maximum (FWHM) as a function of the angle θ (U , V and W are free parameters) [262].



Figure 4.1.: Huber 670.3 heater device for capillary measurement.

$$FWHM^2 = U \tan^2 \theta + V \tan \theta + W \quad (4.1)$$

Equation 4.2 expresses the Lorentzian component of the XRD signal with the respective instrumental broadening coefficients X and Y .

$$FWHM = X \tan \theta + Y / \cos \theta \quad (4.2)$$

The resulting fitting has been saved as an instrumental parameter file, and loaded in the software GSAS II before refining further sample measurements collected with the same diffractometer [259, 260]. This procedure ensures a more reliable fitting of the data taking into account the device influence on the diffractogram. For the refinements, the CIFs with the following collection codes were downloaded from the Inorganic Crystal Structure Database (ICSD) database (FIZ Karlsruhe):

- anatase: 94566
- rutile: 33837
- Na₂Ti₆O₁₃: 186996
- Na₂Ti₃O₇: 187821

The Rwp (overall weighted profile R-factor in %), the chisq ($\sum \omega * (I_{obs} - I_{calc})^2$) and the goodness-of-fit (GOF), *i.e.* the square root of the reduced chi squared, are evaluated in order to control the fitting reliability.

4.2.2. DTA and TGA analysis

Thermogravimetric analysis and DTA of the precursor mixture were performed with a STA 429 (TGA/DTA-Sensor, Netzsch Gerätebau GmbH, Selb (Bavaria), Germany) under a continuous flow of synthetic air (75 mL/min). Typically, 100 mg of powder were placed into an Al₂O₃ crucible for the measurement and a heating rate of 5 °C/min has been set. The mass change of the sample was recorded with 100 points per minute during the heating ramp. The DTA has been conducted in order to identify phase transformations, notably the anatase to rutile transformation.

4.2.3. Scanning electron microscopy

Two microscopes were used to perform the morphological investigation of the samples. The first device is a Philips XL30 FEG (Philips, Netherlands) detecting low-energy secondary electrons emitted from the surface (10 - 100 nm) after the excitation by the primary high-energy electron beam. Low conductive samples were coated with a thin layer of gold using an EMITECH K950X (Quorum Technologies Ltd, Kent, UK) in order to avoid charging of the sample surfaces. Imaging and semi-quantitative elemental analysis have been performed by applying an acceleration voltage of 10 to 25 kV and the use of energy dispersive X-ray (EDX) module (CDU, EDAX Inc.). The second device is a JEOL JSM-7600F (Tokyo, Japan) equipped with a field emission cathode (Schottky Emitter) with acceleration voltage: 0.1 kV – 30 kV (resolution 1.0 nm at 15 kV and 1.5 nm at 1 kV), an InLens SE Detector, a Retractable BSE Detector (RBEI) and an EDS Detector (X-Max80, Oxford).

4.2.4. Electron backscatter diffraction

The electron backscatter diffraction (EBSD) experiments have been performed using a MIRA3-XMH (TESCAN, Brno, Czech Republic) high resolution scanning electron microscope (SEM), equipped with a DIGIVIEW 5 (EDAX, Mahwah, USA) EBSD system to identify the growth direction of the nanorods. The structure file for $\text{Na}_2\text{Ti}_6\text{O}_{13}$ was generated using the Wyckoff positions according to reference [228]. The nanorods were placed on an adhesive carbon pad and tilted to 70° . Kikuchi patterns were acquired in spot mode with an acceleration voltage of 15 keV on seven different nanorods that were aligned with their growth axis close to the vertical axis of the SEM.

4.2.5. Transmission electron microscopy and electron energy loss spectroscopy

The samples have been prepared for transmission electron microscope (TEM) by embedding the nanorods in araldite and subsequent sectioning using an ultramicrotome. TEM characterization was performed in a Thermofisher Talos F200X scanning transmission electron microscope (STEM) equipped with four energy-dispersive X-ray (EDX) detectors and a Gatan Enfium electron energy-loss (EEL) spectrometer with DualEELS capability. The microscope was operated at 200 kV, and the extraction voltage of the field emission electron source was lowered for the electron energy-loss spectroscopy (EELS) measurements from 4050 to 3400 V, resulting in an energy resolution of 0.7–0.8 eV. The convergence and the collection angle for the EELS experiments were 10.5 and 14.1 mrad, respectively. The beam current in STEM was kept in the range of 100-150 pA as a compromise between beam damage effects and signal intensity. In TEM mode an objective aperture was always inserted to protect the sample from destruction due to the electron beam. TEM images were acquired by using a Thermofisher Ceta 16M CCD camera.

4.2.6. Raman spectroscopy

Raman measurements were performed with a Horiba HR800 micro-Raman spectrometer (Horiba Jobin Yvon, Bensheim, Germany) equipped with a He-Ne laser (633 nm). The excitation line has its own interference filter (to filter out the plasma emission) and a Raman notch filter (for laser light rejection). The measurements were performed by using a grating of 600 g mm^{-1} and a confocal microscope (magnification 50 X, NA 0.5) with a $100\text{ }\mu\text{m}$ aperture, giving a resolution of approximately $2\text{ }\mu\text{m} - 4\text{ }\mu\text{m}$. Neutral density filters with optical density 0.6 have been applied to attenuate the laser power to 20 - 200 μW . Spectra were collected with 8 scans, each scan lasting 5 seconds. For each sample, several spectra have been collected on different spots in order to control the homogeneity of the samples.

4.3. Electrochemistry – battery performance of NTO

Concerning the electrochemical experiments, the samples have been first processed into a slurry mixed with polyvinylidene fluoride (PVDF) as binder and carbon black as conducting additive in a ratio of 85:10:5 wt. %. The binder consisted of 10 wt. % polyvinylidene fluoride and 90 wt. % N-methyl-2-pyrrolidone (NMP). NMP has been added to reduce the viscosity of the slurry. Subsequently, the slurry has been dispersed by an Ultra-Turrax dispersing instrument (IKA[®] T25) for 25 minutes in total at 8000 rpm and applied by a doctor blading device (Elcometer 4340) to a 20 µm thick copper foil (SE-Cu R360, Schlenk Metallfolien GmbH & Co. KG). The typical sample thickness is 120 µm. The Cu foils coated with the sample have been dried for 24 h at 40 °C. Then circular electrodes have been cut using a hollow punch with a diameter of 10 mm and the weights of the electrodes have been recorded. The electrodes have been inserted into the argon-filled glovebox after drying for 24 h under vacuum in a glass oven (Büchi, B-585) at 80 °C. For assembling Swagelok[®] half-cells, the working electrodes have been inserted with the copper side touching the current collector. The electrodes were tested for two different reference/counter electrodes - elementary sodium and lithium foil (0.75 mm thick, 99.9 % purity, Alfa Aesar). The hollow punch with a diameter of 10 mm has been also utilized for cutting the reference electrodes. 180 µL 1 M NaClO₄ (mixture of EC:PC:DMC 45:45:1 by weight) and 180 µL 1 M LiPF₆ (99.9 %, mixture of EC:DMC 1:1 by volume) have been used as electrolytes. A porous Whatman[™]-glass fiber membrane with a diameter of 14 mm served as separator. The cells have been stored for 24 h at a constant temperature of 25 °C in the cabinet of the potentiostat in order to ensure a sufficient wetting of the separator and the electrodes.

5. Results and discussion

The results discussed in chapter 5 have been obtained by using two different synthesis routes (section 4.1 on page 47). The results are arranged according to i) the main salt matrix used for the MSS and ii) the product phase, *i.e.*, titanium dioxide or titanates. Sections 5.1 and 5.2 present the results of the materials synthesized in chlorides and sulfates, respectively. Section 5.2.6.2 describes the influence of phosphates, here Na_3PO_4 , on the resulting phases, structure and morphology. Finally, section 5.3 reports the synthesis of sodium titanates, followed by the description of their electrochemical performance (section 5.4). Several different crystal structures were obtained as final products of the MSS, in multi-phase yield or as a single phase. This is related to the reactivity between reagents and salt matrix and is further discussed in detail in the entire chapter.

5.1. Molten salt synthesis of TiO_2 performed in chlorides

5.1.1. TiO_2 crystal growth in NaCl flux

Anatase nanopowder (Kronos Inc.: see table A.1 in the appendix) of average size $\simeq 100$ nm (figure 5.1) was mixed with NaCl powder in different ratios (or percentage by weight, *wt. %* of TiO_2 as precursor) in order to investigate the influence of the salt matrix on the TiO_2 crystal growth. All the samples have been obtained by heating the different mixtures to a given temperature that was kept for two hours. The phase composition and the habits of the obtained crystals change according to the anatase/NaCl ratio and the synthesis conditions. Table 5.1 reports the different phases that are obtained from the NaCl flux.

X-ray diffractograms allow to analyze the phase composition of samples synthesized at, *e.g.* 900°C , in NaCl (see figure 5.2). The TiO_2 /salt ratio, one of the main MSS parameters, evidently determines the phase composition. At low precursor concentrations (1 and 5 *wt. %* of TiO_2) it is still possible to observe the presence of anatase, rutile being the main phase. At 900°C a complete transformation of anatase into rutile can be expected according to reference [168]. This is the case for precursor contents > 5 *wt. %*. Further experiments have been carried out with TiO_2 contents up to 50 *wt. %* to investigate the correlation between the TiO_2 precursor concentration and the phase composition of the samples.

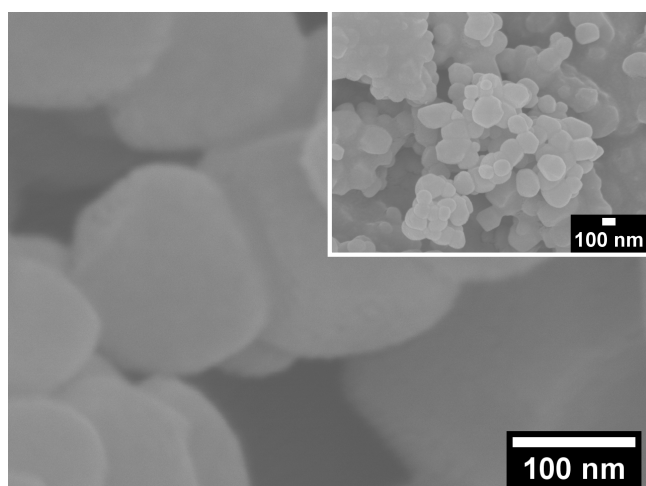


Figure 5.1.: SEM image of the anatase K1002 precursor manufactured by KRONOS INTERNATIONAL INC. showing an average particle size of about 100 nm.

This was done by varying the salt mass keeping the precursor amount constant (*i.e.* 1 g of TiO_2 mixed in a variable amount on NaCl). The results are reported in the appendix (see figure C.1 on page 207). The phase compositions reported in table C.2 confirm that the anatase fraction decreases by increasing the TiO_2 precursor content in the salt. The low XRD intensity at 21.79° indicates the presence of $\text{Na}_2\text{Ti}_6\text{O}_{13}$ (NTO) crystals (see also figure C.2 on page 208 in the appendix).

Low concentrations of precursor (anatase, ≤ 5 wt. %) within the salt matrix appear to slow down the anatase to rutile transformation (ART) for samples prepared at temperatures lower than 1000°C . Anatase is not detected in samples treated at $T \geq 1000^\circ\text{C}$ in NaCl melt (see figures 5.3a and b), indicating that the ART is complete at $T \approx 1000^\circ\text{C}$. The ART is a reconstructive transformation (see section 3.1.2 on page 30), meaning that it is not instantaneous since it involves breaking of bonds and formation of new ones (as reported by Shannon *et al.* [190, 191]). Therefore the transformation process can indeed be retarded in the molten salt at temperatures lower than 1000°C . At low precursor contents there exist a low probability of particles to get in contact. A higher number of particles and a high temperature favor the contact between the anatase particles, being thus an important aspect regulating the structural change. Zhang and Banfield [263] also consider the anatase-anatase interface nucleation and nuclei growth as determinant for the net phase transformation rate. Also the equilibrium oxygen vacancy concentration of anatase is slowing down the ART [36]. The amount of oxygen involved in the MSS is a fundamental quantity, confirmed by a recent study about the role of the oxygen activity modulated by additives [39]. The comparison with the samples containing a higher amount of precursor (5 and 10 wt. %) obtained at 850°C and 900°C confirm this description (see figure 5.3a and 5.3b).

However, rutile is not the only phase forming at temperatures higher than 1000°C , since a reflection (of weak intensity) that can be assigned to the $\text{Na}_2\text{Ti}_6\text{O}_{13}$ (NTO) phase is visible at 21.79° . A small part of the melt reacts to form the ternary compound NTO (for more details see section 3.3 on page

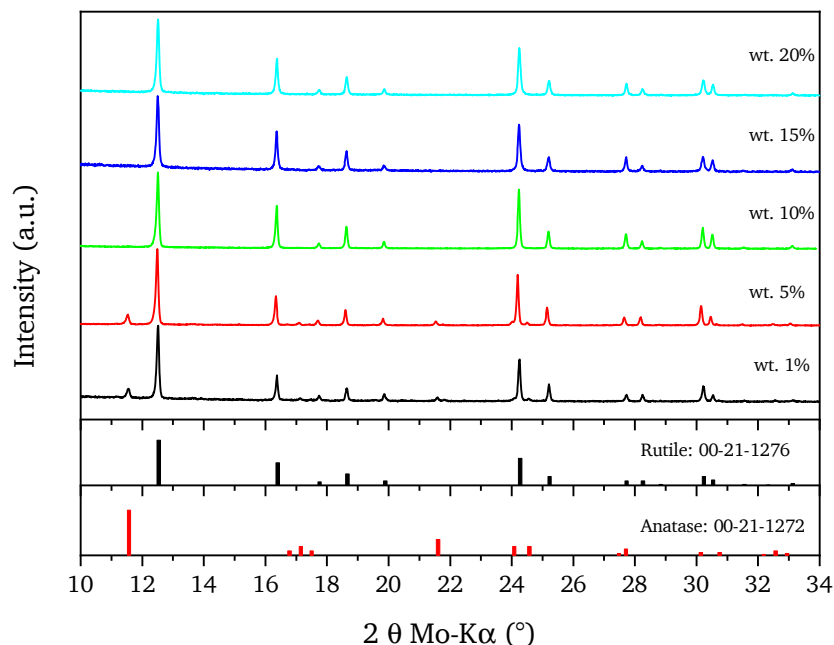


Figure 5.2.: XRD patterns of titania samples obtained by MSS at 900 °C in NaCl with different wt. % of anatase precursor (1 %, 5 %, 10 %, 15 % and 20 %). Reference XRD patterns from the ICDD for anatase and rutile are given at the bottom of the graph.

43 and figure C.3 on page 208 in the appendix with the magnified area showing the NTO reflection). The 21.79° reflection is caused by the (020) plane of the NTO and its intensity represents a deviation from the standard pattern, since the most intense reflection of the NTO should appear at 5.43° for the (200) planes. It indicates a preferential structural orientation. Raman results confirm this finding for the samples obtained under the following conditions: 900 °C with 1 and 5 wt. % (see figure 5.5 and in the appendix figure E.3), 1000 °C with 5 and 10 wt. % (see figure 5.6 and figure E.4) and 1100 °C with 10 wt. % (see figure E.5). Rietveld refinements (see table 5.1) were performed to estimate the phase fractions with a higher precision than by just comparing the ratios of the main reflection of anatase and rutile by using Spurr's equation [264] (see equation C.1 in appendix C on page 207 for more details). For a comparison, the phase fractions of anatase and rutile calculated by Spurr's equation are reported in table C.1 and table C.2 (see appendix C on page 207). As shown in table 5.1, the rutile phase dominates in all the samples at $T > 850$ °C for all TiO_2 weight fractions. At 900 °C the anatase content decreases with increasing TiO_2 weight fraction and vanishes for precursor contents higher than 5 wt. %, as it is with the samples obtained by keeping the TiO_2 mass constant (1 g) and varying the salt mass. The room temperature powder diffractograms of the samples with 5 and 10 wt. % of TiO_2 synthesized in the temperature range 800 to 1100 °C are reported in figure 5.3a and 5.3b, respectively. Comparing the two samples heated at 850 °C (see figure C.4 in the appendix), the one synthesized with 10 wt. % of TiO_2 reports a higher content of rutile (also confirmed by Spurr equation, see table C.1), confirming

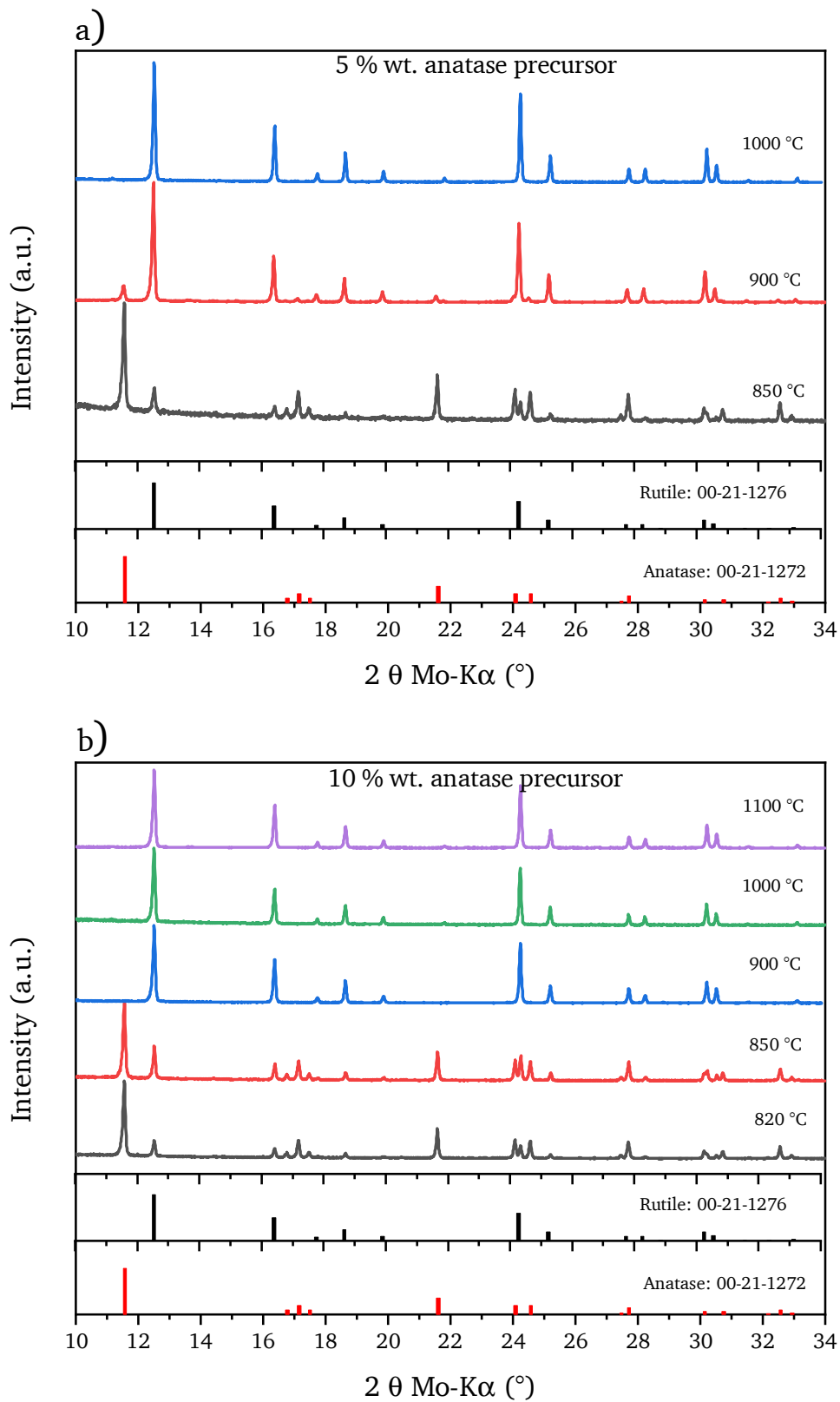


Figure 5.3.: XRD patterns of titania samples obtained by MSS in NaCl with a) 5 wt. % of anatase precursor at 850 °C, 900 °C and 1000 °C and b) 10 wt. % of precursor at 820 °C, 850 °C, 900 °C, 1000 °C and 1100 °C.

that a higher content of anatase precursor in the molten salt speeds up the ART. Anatase is, however, the main phase in both samples at temperatures lower than 900 °C.

Table 5.1.: Phase composition of samples after heat-treating different amounts of TiO₂ in NaCl in the range 820 °C to 1100 °C (A = Anatase, R = Rutile) calculated by Rietveld refinement.

wt. % TiO ₂	820 °C	850 °C	900 °C	1000 °C	1100 °C
1	n/a	n/a	10.3 % A, 89.7 % R	n/a	n/a
5	n/a	78.4 % A, 21.6 % R	10.2 % A, 89.8 % R	100 % R	n/a
10	76.9 % A, 23.1 % R	64.7 % A, 35.3 % R	100 % R	100 % R	100 % R
15	n/a	n/a	100 % R	n/a	n/a
20	n/a	n/a	100 % R	100 % R	100 % R
50	n/a	n/a	100 % R	n/a	n/a

5.1.1.1. Influence of precursor content in the NaCl matrix on the crystal habit

The crystal habit of titania particles is strongly affected by the initial precursor content in the NaCl flux. Figure 5.4 presents a SEM graph of the 1 wt. % sample showing rods with a length $\geq 20 \mu\text{m}$ and a diameter $\leq 500 \text{ nm}$. The habit change is more marked for samples with precursor contents $\geq 10 \text{ wt. \%}$ (TiO₂). Here, much thicker but shorter rods develop (length $\simeq 6 \mu\text{m}$ and diameter $\geq 1 \mu\text{m}$). This trend is confirmed for the samples reported in figure 5.4c and 5.4d. Additionally, figure 5.4d shows a twin crystal of rutile (marked with a red circle), indicating self-assembly and twinning [265–269]. The observed oriented attachment (OA) is supposed to be a part of the ART, with rutile nucleating at 112 twin-like anatase [270–272]. According to the X-Ray Diffraction (XRD) analysis (figure 5.2) all the samples mainly contain rutile crystals. Additional anatase particles are present only in the samples synthesized with 1 % and 5 % of TiO₂. The anatase particles can be identified by the small particulates around the nanorods (see figure 5.4a). As known from literature rutile crystals can grow in a rod-like shape under specific conditions [39, 266, 273–277].

Interestingly, long and thin nanorods can be obtained in MSS at moderate precursor concentrations ($\simeq 1 \text{ wt. \%}$) and temperatures around 900 °C. Raman measurements at different spots of the nanorods (S1 and S2) indicate the formation of NTO in addition to TiO₂ (see figure 5.5). The rutile spectrum taken on the spot S3 is reported in figure 5.5d for comparison. The low rod concentration explains the barely visible reflection of NTO in the XRD diffractogram in figure C.2. This reflection only appears due to oriented growth along the (020) axis.¹ The spectrum recorded from spot S3 on an agglomerate of small crystals (green curve) clearly reveals the presence of rutile and anatase. The reference spectra of anatase (Kronos K1002) and rutile (Kronos K2900) are given in the appendix in figure E.1 and E.2 and support this assignment. The NTO crystals increase in size at 1000 °C (see figure 5.6) and the morphology of the sample is similar to the one obtained at 900 °C.

¹These structural considerations about NTO are discussed in detail in section 5.3.2 on page 142. Figure 5.80 shows the indexed NTO planes.

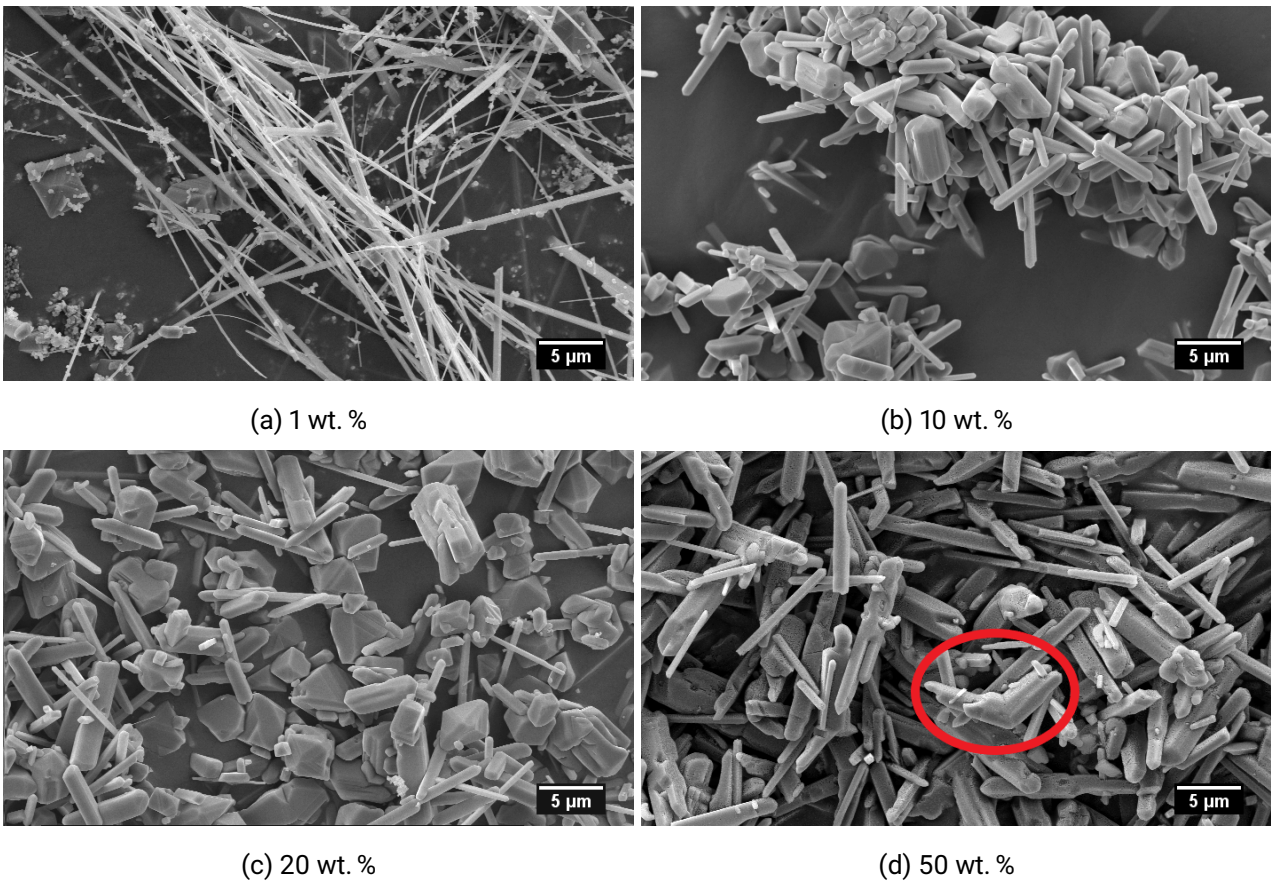
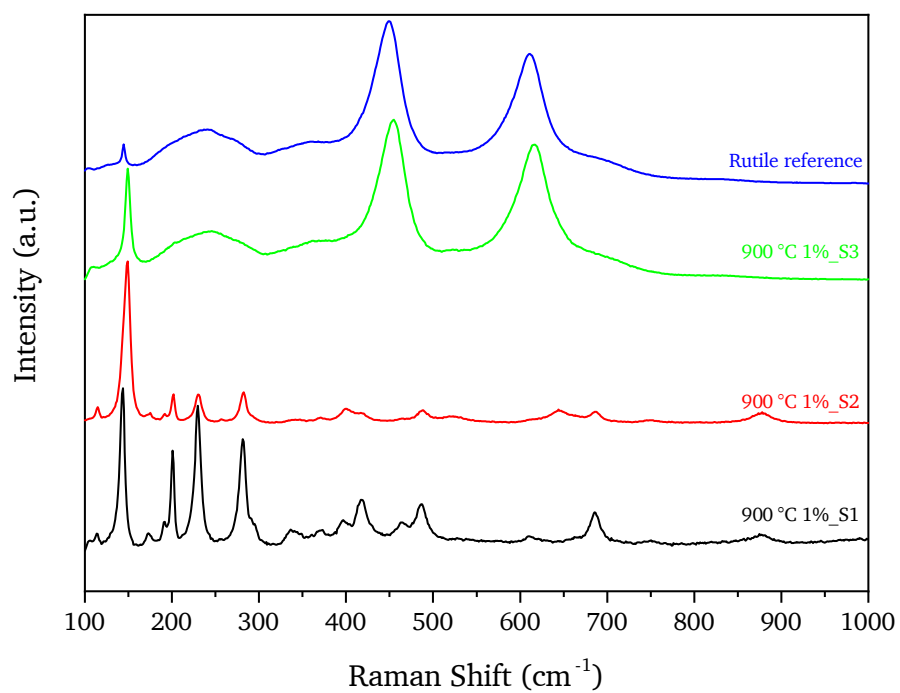
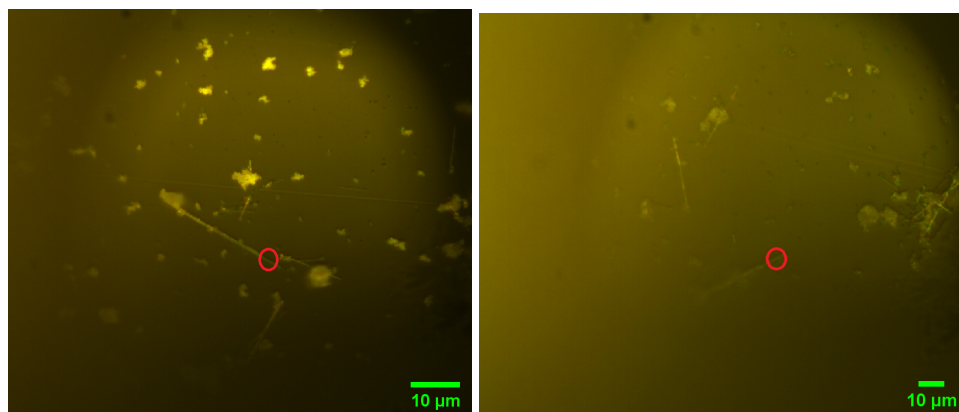


Figure 5.4.: SEM images of TiO₂ particles obtained at 900 °C with 2 h of holding time with a) 1 wt. %, b) 10 wt. %, c) 20 wt. % and d) 50 wt. % of anatase precursor within NaCl. The rutile twin crystal in figure 5.4d is marked by a red circle.

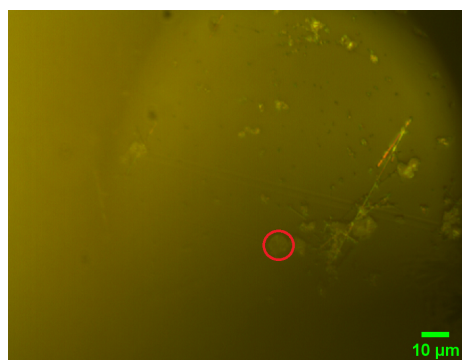


(a) Spot S1, S2 and S3 and rutile reference



(b) Spot S1

(c) Spot S2



(d) Spot S3

Figure 5.5.: a) Raman spectra of the sample obtained at 900 °C with 1 wt. % anatase precursor in NaCl measured on spot b) S1, c) S2 and d) S3. The rutile spectrum of K2900 is added as reference.

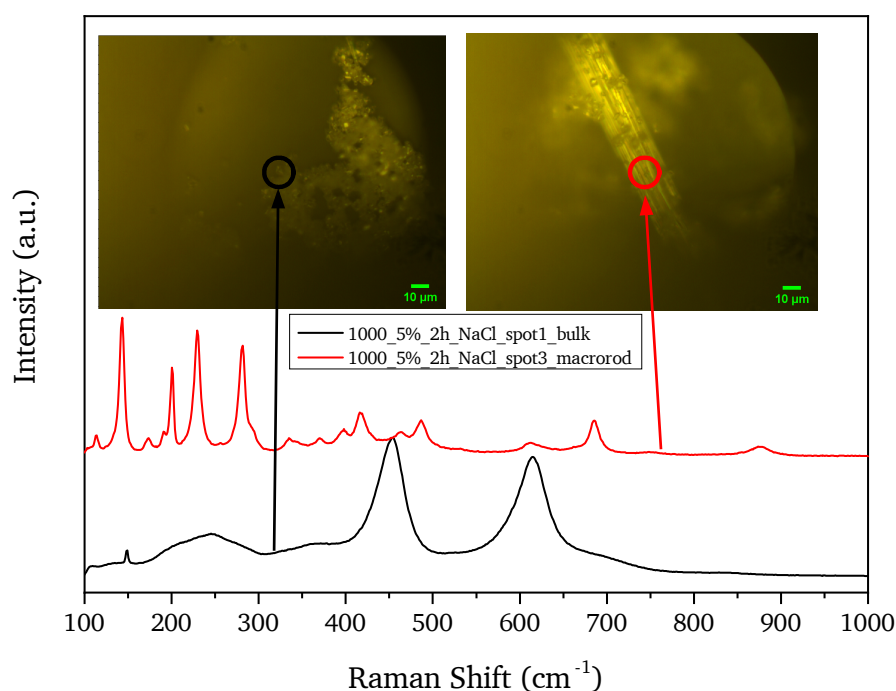


Figure 5.6.: Raman spectra from two spots of the sample obtained by MSS in NaCl with 5 wt. % of titania at 1000 °C.

The presence of different crystal habits in a sample can have several explanations: one is the simple correlation with the ART; there are two phases present, anatase and rutile, which can assume different shapes because the ART is not occurring at identical conditions for all the particles. The different particle size distribution in the DMP, compared to the WCP, is another aspect to consider. By DMP the reactant particles already have an average size $\simeq 100$ nm, being much larger than that of the WCP. This difference is clear at first sight by comparing figure 5.4 with figure 5.31 (see section 5.1.6 on page 84). Additional information is given by the morphology of the samples heat-treated at 820 °C and 850 °C with 10 wt. % of precursor (figure 5.7a and 5.7b). Although the melting point of NaCl is 801 °C, a treatment at temperatures slightly higher than this temperature is not enough for promoting extensive growth of rod-like crystals and their average size is limited to < 1 μm . Only few particles reach sizes $\simeq 5$ μm . At temperature = 900 °C mainly crystals with rod shape are observed whereas the amount of rod-shaped crystal decreases at > 900 °C, at the expense of thicker bipyramidal octahedra with exposed (111) and (110) facets (see the Wulff construction for rutile in figure 3.4 on page 32). A similar trend is found for samples with 20 wt. % of precursor (see figure D.2 in the appendix on page 222). The powder synthesized at 900 °C contains the highest concentration of the rod-like rutile crystals. Increase of the temperature leads to an increase of the the average thickness and a decrease of the length of the rod-like crystals. This effect is more marked at 1100 °C (see figure D.2 c), where the majority of crystals are bipyramidal octahedra with exposed (111) and (110) facets.

To sum up, the variation of the precursor to salt ratio and of the synthesis temperature has a

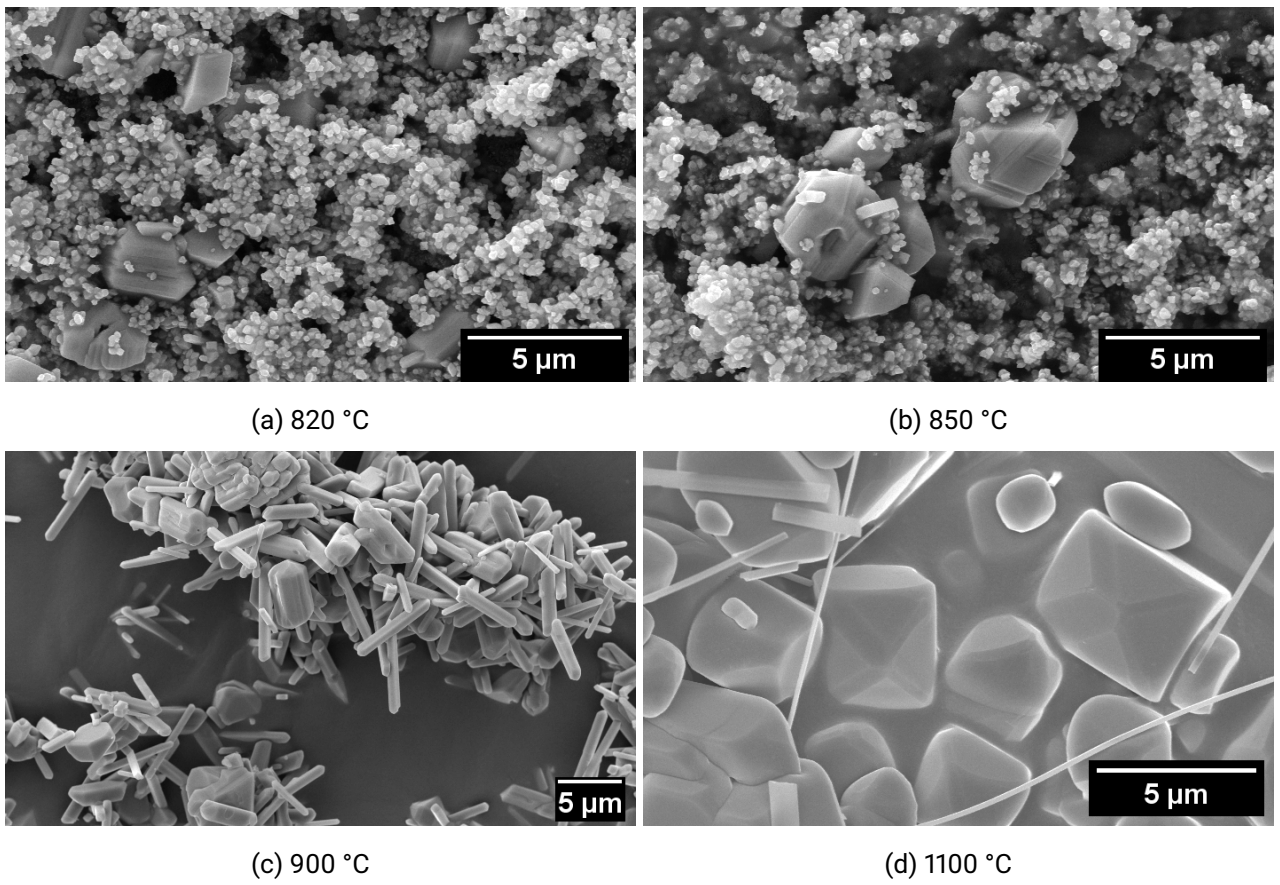


Figure 5.7.: Morphology of titania particles obtained at a) 820, b) 850, c) 900 and d) 1100 °C with 10 wt. % anatase precursor in NaCl, measured by SEM.

decisive influence on the ART. The anatase mass fraction decreases with increasing temperature and increasing wt. % of precursor in the salt mixture. Only in case of precursor concentrations ≥ 10 wt. % and $T \geq 900$ °C the transformation into rutile is complete. Concerning the morphology of the particles, one observes the growth of rod-shaped rutile crystals, typical for MSS with NaCl. The presence of Cl^- ions appears to be decisive for the morphology: Cl^- ions can cap the dangling bonds of the (110) facets of rutile [273], thus favoring the growth along the [001] direction, thereby creating long nano- or microrods. A small amount of NTO crystals is appearing at precursors concentrations < 10 wt. %. This is confirmed by i) Raman measurements, and ii) the reflection at 21.79° of NTO in the XRD experiments. The Raman measurements locally collected on the nanorods (diameter and length are ≤ 500 nm and ≥ 20 μm respectively) allow to uniquely assign this habit to the NTO structure. Rutile structure on the other hand can be attributed to the much shorter (≈ 5 μm) and thicker rods (≥ 500 nm) forming at temperatures ≥ 900 °C and precursor concentrations ≥ 10 wt. %.

5.1.1.2. Phase evolution followed by in-situ high-temperature XRD

A sample with 10 wt. % of anatase precursor has been *in-situ* characterized by XRD up to a temperature of 900 °C in a quartz capillary (see figure 5.8).² The phases detected at room temperature are anatase and NaCl. The cubic NaCl structure has strong reflections at 27.32° , 31.72° and 45.49° (marked with "Cl"). These reflections drift to lower angles with temperature due to the dilatation of the NaCl crystal lattice. NaCl melts at 801 °C explaining the decrease in intensity of all the reflections close to the melting point. The signal (marked with "**") caused by the device setup, is the only signal with unchanged intensity at $T \geq 801$ °C. Anatase's main reflection is localized at 25.28° (labeled with "A") and an additional one is visible at 37.85° . The reflection with the highest intensity belonging to rutile first appears at ≈ 710 °C and is located at 27.38° (labeled with "R"), clearly indicating that the ART starts before the salt matrix reaches the molten state. According to the results for the MSS of samples with 10 wt. % TiO_2 presented in table 5.1 (on page 57), it ends at temperatures ≥ 900 °C (about 100 °C above the melting point of NaCl). Moreover, the persistence of the strongest reflection of both anatase and rutile till 820 °C matches with these data (see table 5.1) and suggests that the titania particles slowly start to dissolve in the molten NaCl. Additionally, an *in-situ* XRD measurement was performed also during the heat-treatment of a sample with 10 wt. % TiO_2 in 0.41 KCl-0.59 LiCl (melting at 352 °C, as reported in table 2.3). This *in-situ* screening also confirmed that no rutile phase is forming at temperatures ≤ 650 °C. Obviously the begin of the ART is not correlated with the melting point of the salt.

²The X-axis in figure 5.8 is limited to the angular interval containing the main reflections of anatase, rutile and NaCl. The quartz reflections appearing above 700 °C are excluded from the diffractogram for graphical convenience.

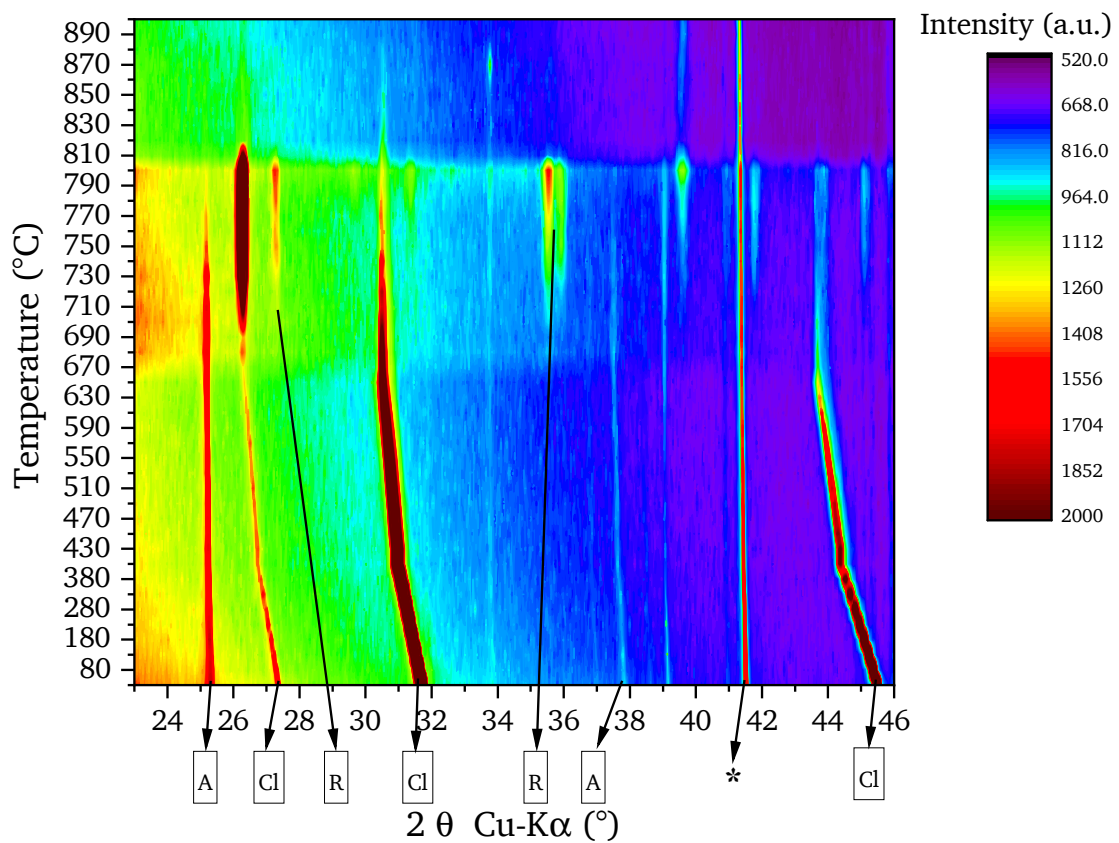


Figure 5.8.: High temperature XRD pattern of NaCl-10 wt. % TiO₂ measured *in-situ* (up to 900 °C). Legend: A = anatase; R = rutile; Cl = NaCl; * = artifact from the device. Note the melting point of NaCl: T = 801 °C.

5.1.2. TiO₂ crystal growth in flux mixtures NaCl-X (X= AlCl₃ · 6 H₂O, KCl, MgCl₂, NaF)

Several binary salt compositions were investigated in order to obtain information about the role of the salt matrix in the growth process of TiO₂ crystals. Among these are mixtures with different cations, or with different anion species. Some of these are symmetrically charged, e.g. NaCl-KCl and NaCl-NaF, others are asymmetrically charged (e.g. NaCl-AlCl₃ and NaCl-MgCl₂) as reported in section 2.1.1 (see table 2.2 on page 9). The molar ratio chosen for the salt composition corresponds in some cases to the eutectic mixture allowing to compare the crystal growth at lower temperatures.

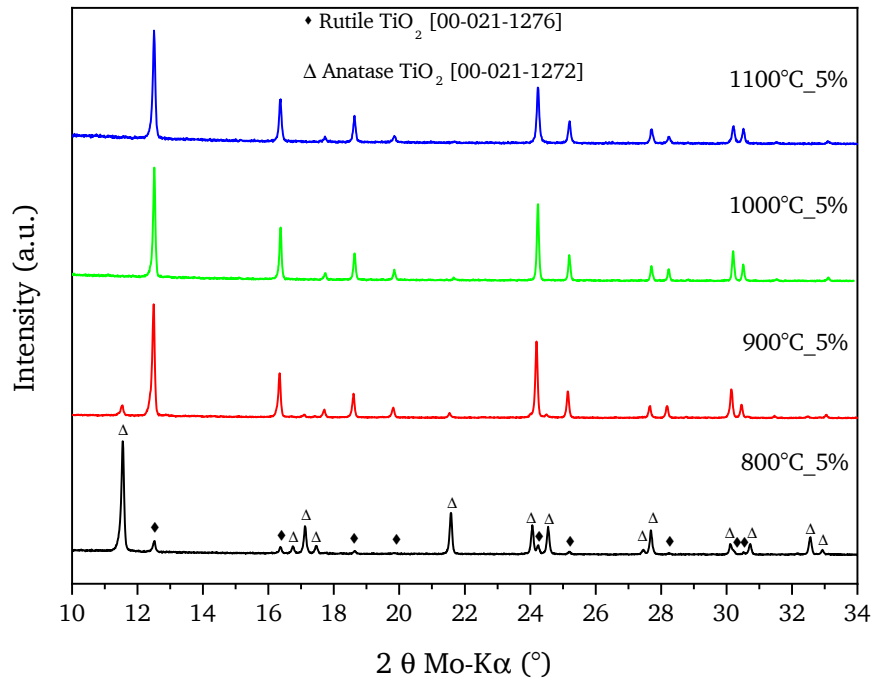
5.1.2.1. NaCl-KCl

The NaCl-KCl salt matrix is interesting for two reasons: i) it introduces a second cation species and ii) it allows molten salt synthesis at lower temperatures compared to pure NaCl. The NaCl-KCl phase diagram with an eutectic point at 650 °C is reported in the appendix (see figure B.1 on page 201). The investigated salt mixtures with their respective melting temperatures are reported in table 2.3 on page 22. All the samples discussed have been synthesized in a 0.5 NaCl-0.5 KCl flux. Figure 5.9 presents the XRD data of the samples with 5 wt. % and 10 wt. % TiO₂ obtained at different temperatures. The ART is complete at 900 °C for 10 wt. % anatase precursor but not for the sample with 5 wt. %. The samples obtained at 800 °C reveal mainly anatase, while the samples heat-treated at 1000 °C and 1100 °C only contain the rutile structure. In comparison to the results obtained with pure NaCl flux, there exists only a small difference in the phase composition indicating that the change of the cation Na⁺ and K⁺ has only minor influence on the ART (see table 5.2). The presence of the K⁺ ion appears to only slightly retard the ART.

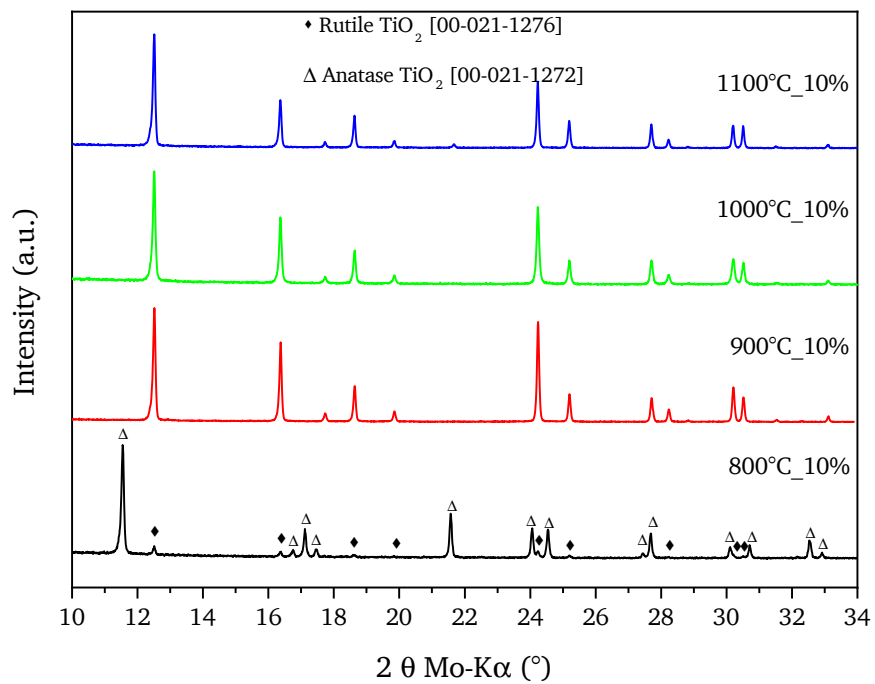
Table 5.2.: Phase composition of samples synthesized in molten 0.5 NaCl-0.5 KCl. Synthesis temperature: 900 to 1100 °C, holding time: 2 hours (A = Anatase, R = Rutile).

Salt molar ratio	Temperature [°C]	wt. % TiO ₂	Phase composition
0.5 NaCl-0.5 KCl	800	5	A, R
0.5 NaCl-0.5 KCl	800	10	A, R
0.5 NaCl-0.5 KCl	900	5	R, A
0.5 NaCl-0.5 KCl	900	10	R
0.5 NaCl-0.5 KCl	1000	5	R
0.5 NaCl-0.5 KCl	1000	10	R
0.5 NaCl-0.5 KCl	1100	5	R
0.5 NaCl-0.5 KCl	1100	10	R

The advantage of conducting a MSS NaCl-KCl at lower temperature than in NaCl alone appears to be not important for the crystal growth, since most of the particles reach an average lengths of \approx 200 nm at 800 °C comparable to that obtained in NaCl at 820 °C (see figure D.3 in the appendix on page 222). As in the NaCl system, the increase of the particle size is evident first at 900 °C (see figure 5.10a and b). The SEM data in figure 5.10c, however, reveal a significant difference with respect to the samples obtained in NaCl alone. The sizes of the particles grown in NaCl-KCl at 1000 °C are slightly bigger than



(a) 5 wt. % TiO_2 in NaCl-KCl



(b) 10 wt. % TiO_2 in NaCl-KCl

Figure 5.9.: XRD patterns of titania samples obtained by MSS in NaCl-KCl eutectic mixture at 800 °C, 900 °C, 1000 °C and 1100 °C with a) 5 and b) 10 wt. % of anatase precursor.

those of the pure NaCl system. Another interesting aspect is the change of the habit with increasing amount of titania precursor (see figure D.4 in the appendix). Rutile rod shaped crystals are not present at 5 wt. % of titania precursor but clearly appear at \geq wt. % 10.

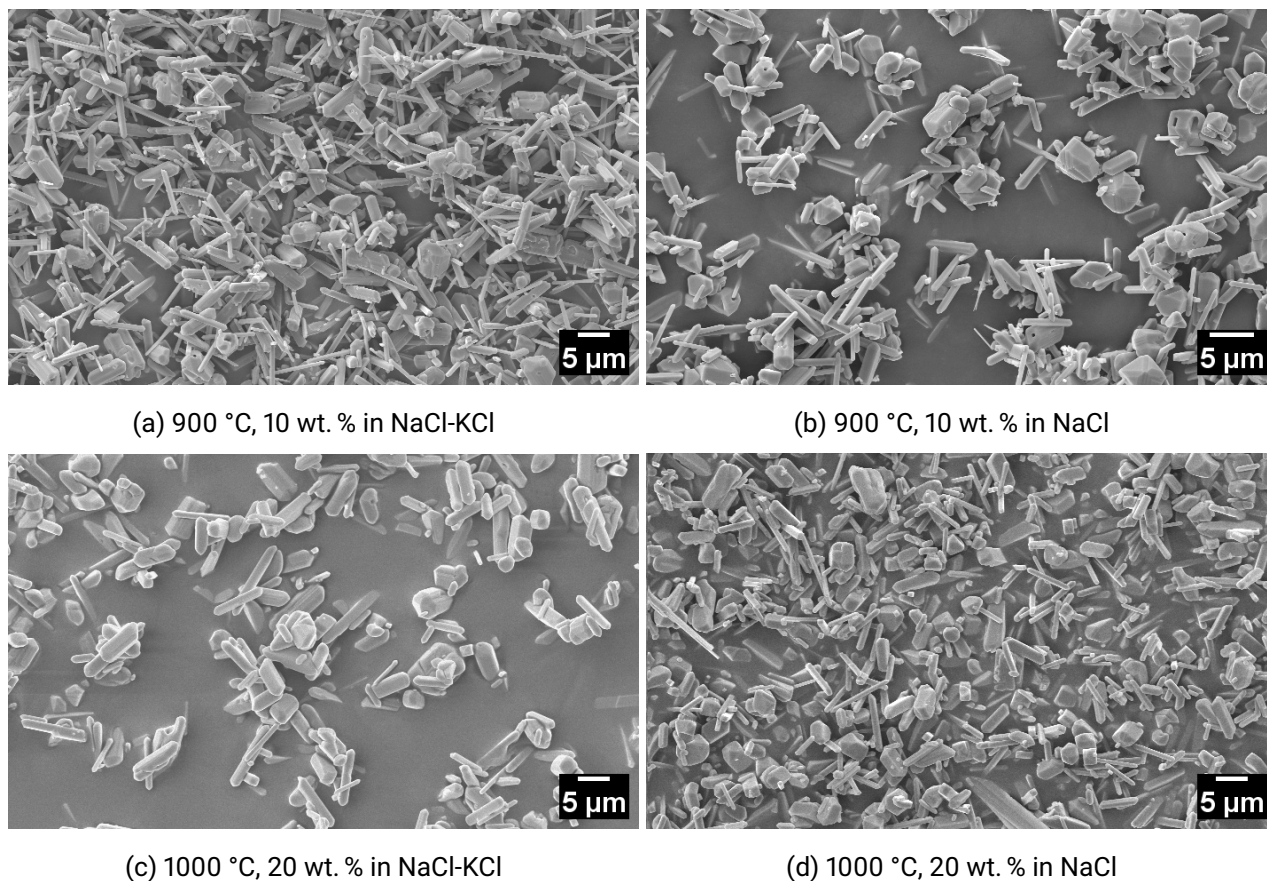


Figure 5.10.: SEM images of titania particles obtained with 10 wt. % of anatase precursor at 900 °C in NaCl-KCl eutectic mixture a) and NaCl b) respectively and with 20 wt. % of anatase precursor at 1000 °C in NaCl-KCl eutectic mixture c) and NaCl d).

5.1.2.2. NaCl-NaF

It is known from literature that fluoride ions interact with the titanium dioxide crystal surfaces in a specific way [30, 34, 179, 180]. Fluoride reverses the relative order of surface energies by acting as "capping agent". Mostly {001} facets are formed in anatase on expense of the {101} facet, adopting the micro-sheet shape (see section 3.1.1 and anatase Wulff construction in figure 3.2 on page 29) [278–283]. On the other hand, the rutile crystal habits change when the most energetic facets {111} and {001} are replaced by the {110} facet (see rutile's Wulff construction in figure 3.4 on page 32) [209, 211, 280, 284].

It is unknown whether the capping effect of F^- occurs in molten salt synthesis (MSS), since the

reported studies on the F^- effect are mainly referring to the wet-chemistry synthesis. Therefore NaF was added as F^- source in MSS and added to NaCl in different amounts to reverse the relative order of surface energies and the crystal growth conditions, respectively. The MSS was performed at 900 to 1100 °C by i) adding a few mol % of NaF (between $\simeq 0.02\%$ and 5.6 %) and ii) by setting the molar ratio of the salt species as 0.33 NaF-0.67 NaCl (close to the eutectic point, see figure B.4 in the appendix).

The XRD diffractograms of the samples heat-treated at 900 °C (see figure 5.11) all reveal the presence of rutile. Moles of NaF are added to the 20 wt. % of TiO_2 up to reaching F/Ti molar ratios of 0.1, 5, 10 and 20 %. The samples with 0.1 and 20 % molar ratio of fluoride are compared with the respective NaCl sample in figure C.5 in the appendix (also plotted in figure 5.2 on page 55). The intensity ratios of the reflections belonging to (002), (310), (301) and (112) planes change by increasing the amount of fluoride in the melt. The most visible change occurs in the reflections assigned to (002) planes (at 27.73°) and to (310) planes (at 28.24°) for the samples with 10 mol % and 20 mol % F^- . These two reflections have different intensities: a higher intensity for the (310) reflection, opposite to the one observed for pure NaCl, figure 5.2 (which has a higher intensity for the (002) reflection). This result can be explained by the habit change of rutile crystals by altering the average plane populations. A very similar trend is observed for the samples heat-treated at 1000 °C. Rutile is in all the samples the main phase but the NTO phase is also formed. Rutile reflection intensities change their ratios by increasing the NaF concentration (see figure C.6 in the appendix). The reflections corresponding to NTO increase in intensity for higher concentrations of NaF, suggesting a direct correlation of NTO growth and F^- concentration. The effect is most clearly seen in the sample with 20 mol % of NaF heat-treated at 1100 °C (see figure C.7 in the appendix).

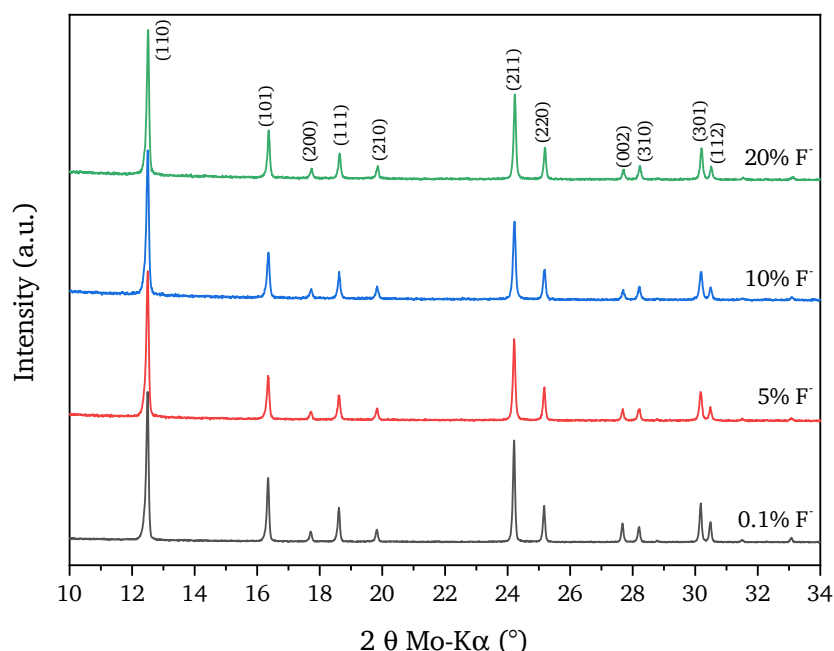


Figure 5.11.: XRD patterns of titania samples obtained by MSS at 900 °C in NaCl/NaF with $\simeq 20$ wt. % of anatase precursor (0.1 %, 5 %, 10 % and 20 % NaF/ TiO_2 mol %).

In accordance with the different ratios of the (002) and (310) reflections, the SEM results presented in figure 5.12 confirm that the crystal habit of rutile is quite different from that observed in a pure NaCl melt at 900 °C (see figure 5.4). Rod-shaped crystals can be found only in a negligible amount, therefore the intensity of the (002) reflection decreases in comparison to the (310) reflection. The bipyramidal octahedron is the main habit and NaF causes the terraced growth with the most prominent exposition of the 111 facet. Figure C.8 in the appendix shows the overlapping of two XRD patterns reported in figure C.5. The reflections with Miller index $l \neq 0$ have lower intensities for the sample heat-treated with NaF than those without NaF. This confirms the strong decrease of the crystal plane population growing perpendicular to the [001] direction. From the morphological point of view, MSS with NaCl-NaF determines the macroscopic appearance more strongly than MSS with NaCl alone, as it can be observed in figure 5.13. No matter which F/Ti ratio was set, the terraced growth is observed

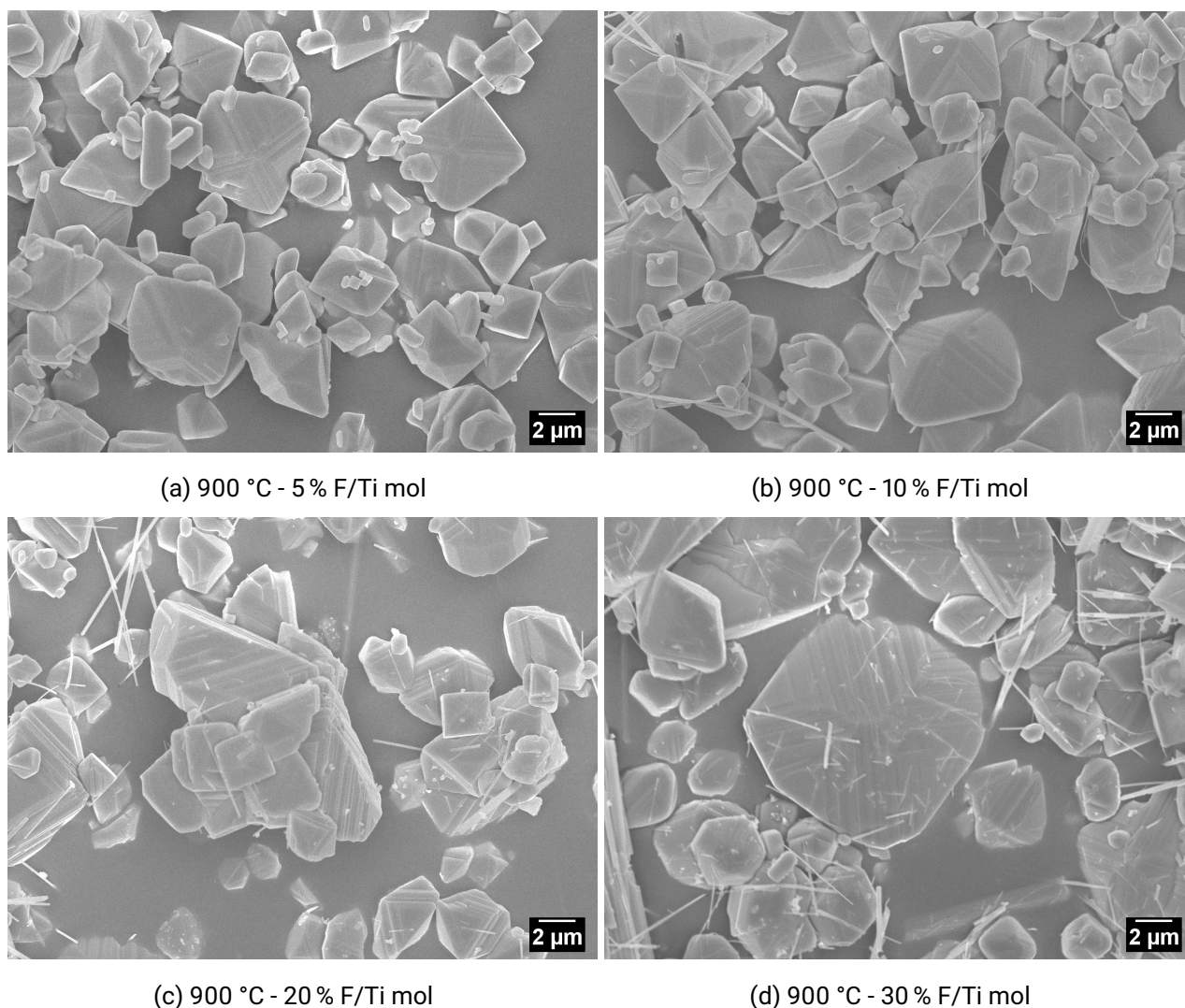


Figure 5.12.: SEM images of titania crystals obtained at 900 °C with 20 wt. % of TiO_2 precursor in NaCl. Additionally were added: a) 5 % b) 10 %, c) 20 % and d) 30 % F/Ti mol.

for most of the crystals synthesized at 900 °C (for a detailed view see figure D.5 in the appendix). By increasing the temperature to 1100 °C, the surfaces become smoother and the terraced texture is not visible anymore (see figure 5.13e).

NaCl-NaF Eutectic mixture Figure B.4 of the appendix (see page 203) presents the phase diagram of the NaF-NaCl salt system. The eutectic point of this mixture is reached at 33 mol % NaF, with a melting point ≈ 700 °C. The MSS performed in the 0.67 NaCl-0.33 NaF eutectic mixture leads to a different phase composition compared to the previously investigated samples with lower NaF content. The XRD data (see figure 5.14) show a strong interaction of NaF with the TiO₂ precursor. Notably, the NTO phase is formed already at 900 °C and a strong preferential orientation of the NTO crystals can be observed from the high intensity of the reflection at 21.79°, corresponding to the (020) plane. Rutile is still the main phase but increasing the temperature to 1000 °C causes the NTO concentration to be higher than rutile. Accordingly, the reflection at 21.79° gains in intensity, dominating all other reflections.

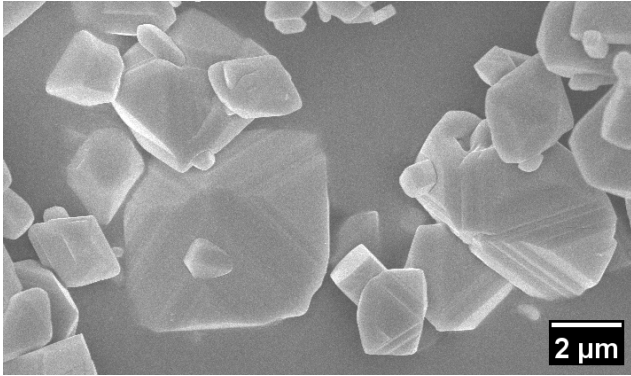
The SEM pictures of figure 5.15 show an impressive formation of micro-rods at 900 °C and 1000 °C with length of several tens of μm . Their diameters are typically $< 1 \mu\text{m}$, but there are many rod-like crystals with a diameter exceeding 10 μm . According to the Lux-Flood theory (see section 2.3.4 on page 23), F⁻ functions as a base and promotes the formation of the NTO structure [39, 160].³ The high concentration of F⁻ ions promotes the reaction of the precursor with the salt matrix by enhancing the solubility of TiO₂ in the molten salt through the formation of TiO₃²⁻ ions. The Rietveld refinement performed on the sample synthesized at 900 °C delivers 54.1 wt. % of NTO and 45.9 wt. % of rutile. Increasing the temperature to 1000 °C leads to an even lower concentration of rutile.

5.1.2.3. NaCl-MgCl₂

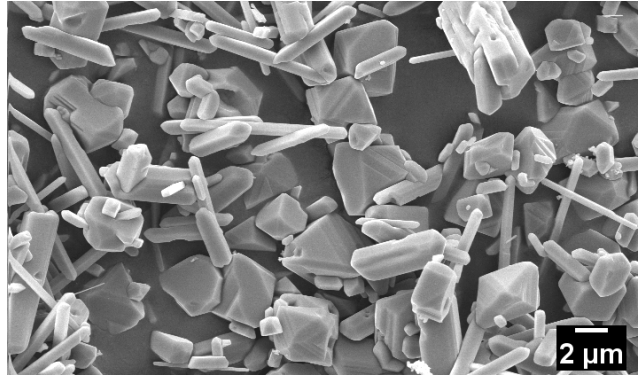
An asymmetrically charged binary salt mixture was investigated next. MgCl₂ has been added to NaCl with a 0.2 molar ratio. This leads to a lower melting point than the one of pure NaCl at 801 °C (the phase diagram of the system can be found in figure B.3).

In case of a sample with 5 wt. % of TiO₂ precursor no change of the phase composition is observed by increasing the synthesis temperature from 900 °C to 1100 °C (see figure 5.16a). The phases forming are MgO (periclase) and MgTiO₃ in this temperature range. No TiO₂ phase can be found. Increasing the anatase precursor to 20 wt. %, however, leads to a substantial change in the phase composition (see figure 5.16b). At 900 °C MgTiO₃ is the main phase, accompanied by MgO and rutile in a negligible amount. Increasing the temperature to 1000 °C leads to the formation of an additional phase, MgTi₂O₅, together with a strongly increased rutile fraction and a decreased MgTiO₃ fraction. MgO is not present anymore. Finally, the MgTi₂O₅ fraction increases with respect to rutile and MgTiO₃ at 1100 °C.

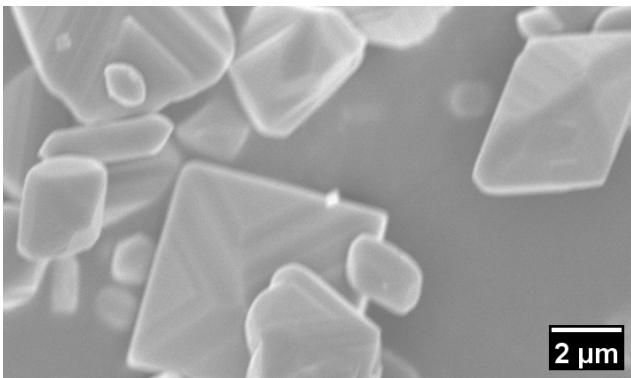
³In the chapter "Acid-Base Effects in Molten Electrolytes" (page 279) B.L. Tremillon gives a clear overview regarding this concept [160].



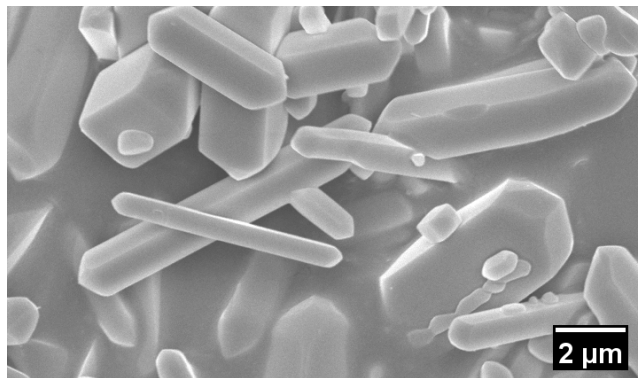
(a) 900 °C - 5 % F/Ti mol



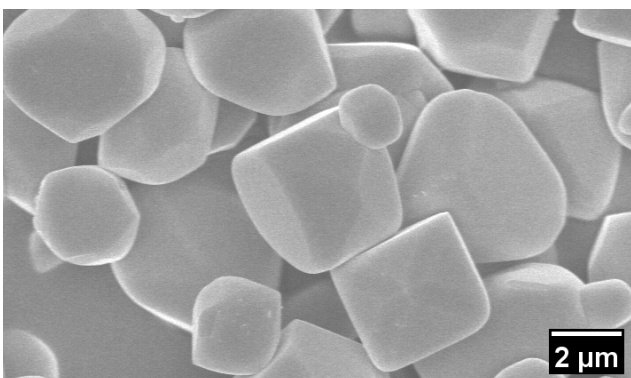
(b) 900 °C in pure NaCl



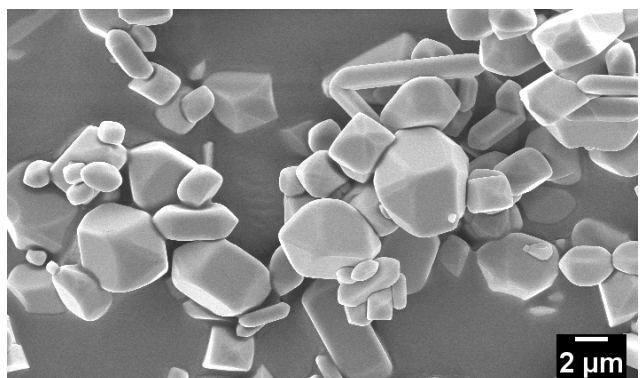
(c) 1000 °C - 5 % F/Ti mol



(d) 1000 °C in pure NaCl



(e) 1100 °C - 5 % F/Ti mol



(f) 1100 °C in pure NaCl

Figure 5.13.: SEM images of titania particles obtained at a) 900, c) 1000 and e) 1100 °C with 20 wt. % TiO_2 in NaCl with the addition of 5 % F/Ti mol. In b), d) and f) the same synthesis temperatures were applied in pure NaCl.

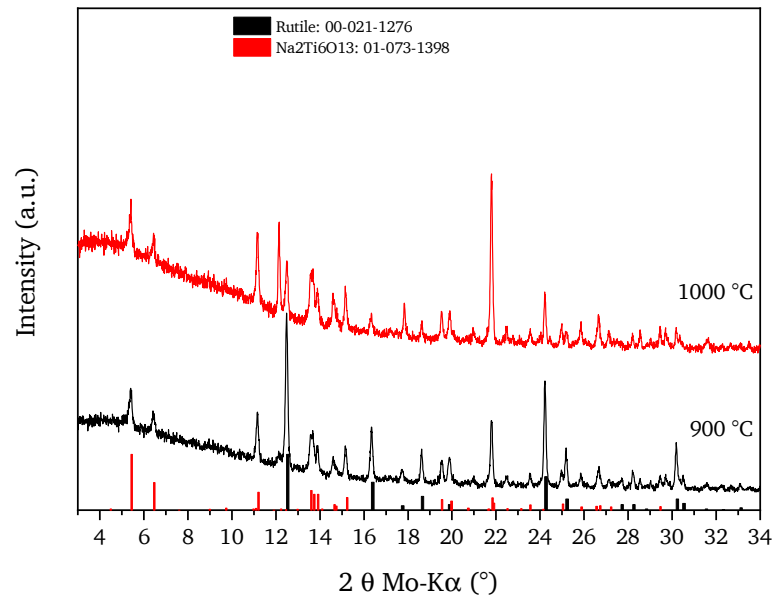
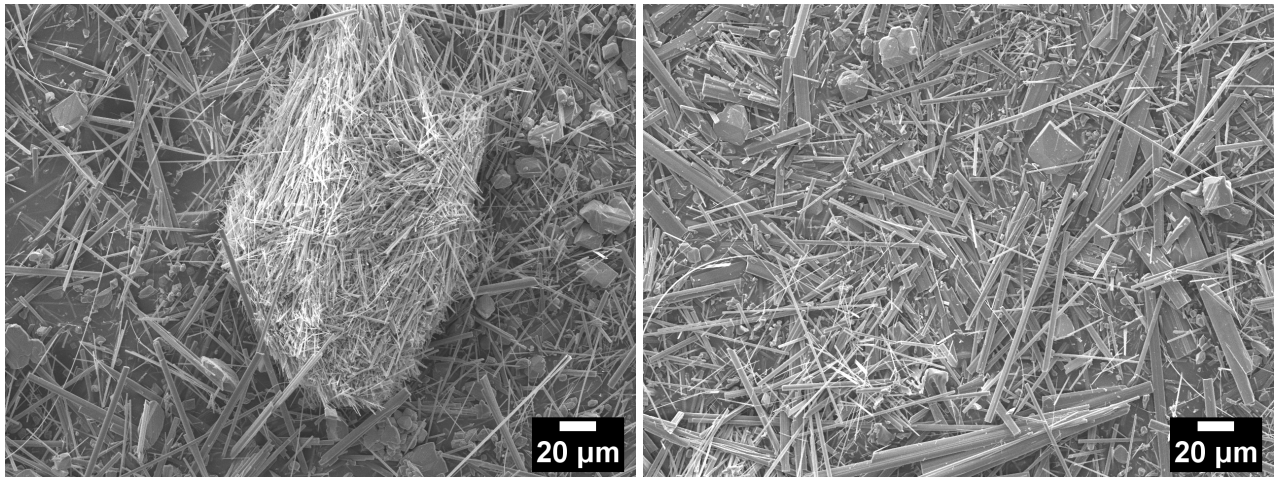


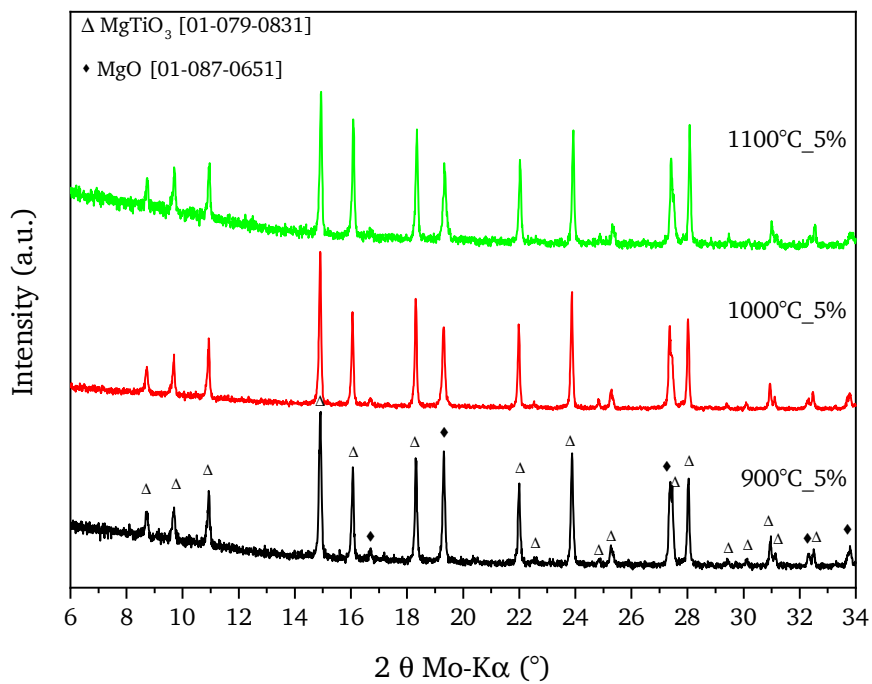
Figure 5.14.: XRD patterns of titania samples obtained by MSS at 900 °C in 0.67 NaCl-0.33 NaF with 10 wt. % of anatase precursor. Reference patterns from the ICDD are reported for comparison.



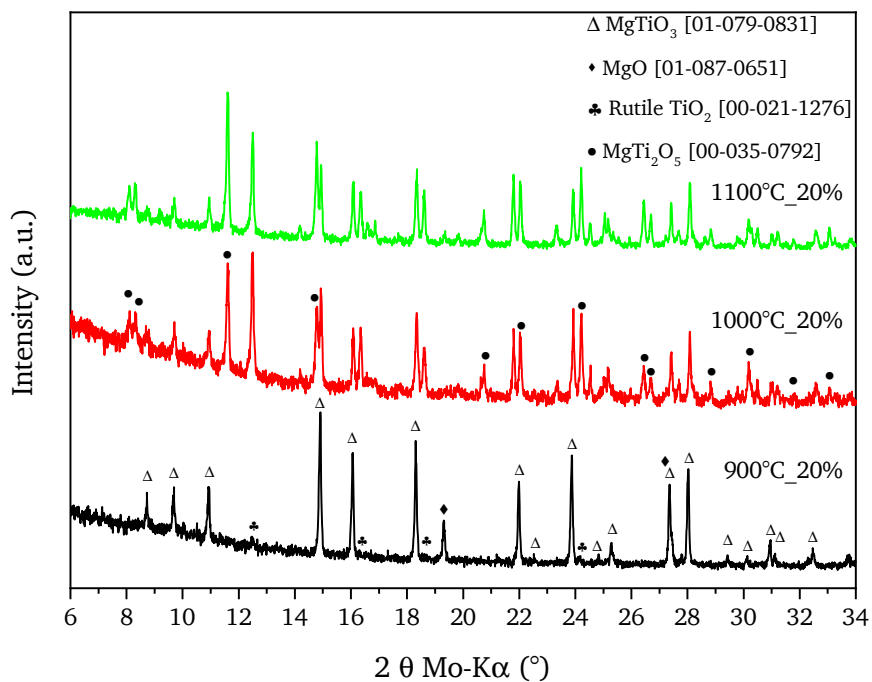
(a) 900 °C in 0.77 NaCl-0.33 NaF

(b) 1000 °C in 0.67 NaCl-0.33 NaF

Figure 5.15.: SEM images of titania crystals obtained in 0.77 NaCl-0.33 NaF eutectic mixture at a) 900 °C and b) 1000 °C with 10 wt. % of TiO_2 precursor.



(a) 5 wt. % TiO₂ in NaCl-MgCl₂



(b) 20 wt. % TiO₂ in NaCl-MgCl₂

Figure 5.16.: XRD patterns of titania samples obtained by MSS in NaCl-MgCl₂ at 900 °C, 1000 °C and 1100 °C with (a) 5 and (b) 20 wt. % of TiO₂ precursor. Reference patterns from the ICDD are listed.

Figure 5.17 shows the morphological changes of a 20 wt. % TiO_2 sample heat-treated at different temperatures. Flake-like particles, almost $1\ \mu\text{m}$ thick, can be observed in the sample heat-treated at $900\ ^\circ\text{C}$. According to the XRD data, rutile and MgTiO_3 coexist at this stage. The flake-like habit can be assigned to the MgTiO_3 phase, as also reported by Kang *et al.* via sol-gel method [285] and by Lou *et al.* [286] (nanoplatelets obtained by synthesis in NaCl-KCl at $600\ ^\circ\text{C}$). A glaring change in the crystal size is reached by increasing the temperature to $1000\ ^\circ\text{C}$ (see also figure D.6 in the appendix). Tetragonal blocks reach side lengths of $40\ \mu\text{m}$ per side and thicknesses $\geq 20\ \mu\text{m}$ with well defined facets (figure 5.17b), which can be assigned to MgTi_2O_5 . Further increase of the temperature leads to the appearance of other types of habit, but also broadens the particle size distribution. This might be explained by the low ratio of MgCl_2 to anatase precursor hindering the formation of the ternary compounds with Ti. The observed habit changes strongly depend on the concentration of anatase precursor. Size and shapes of the particles change significantly (see figure D.7 in the appendix) if the mass fraction of precursor is increased from 5 to 20 wt. % at $900\ ^\circ\text{C}$. By 5 wt. % the average size is $\leq 1\ \mu\text{m}$ with the majority of small particles $\leq 500\ \text{nm}$. By 20 wt. % the flake-like shaped crystals can even reach a diameter $\simeq 10\ \mu\text{m}$.

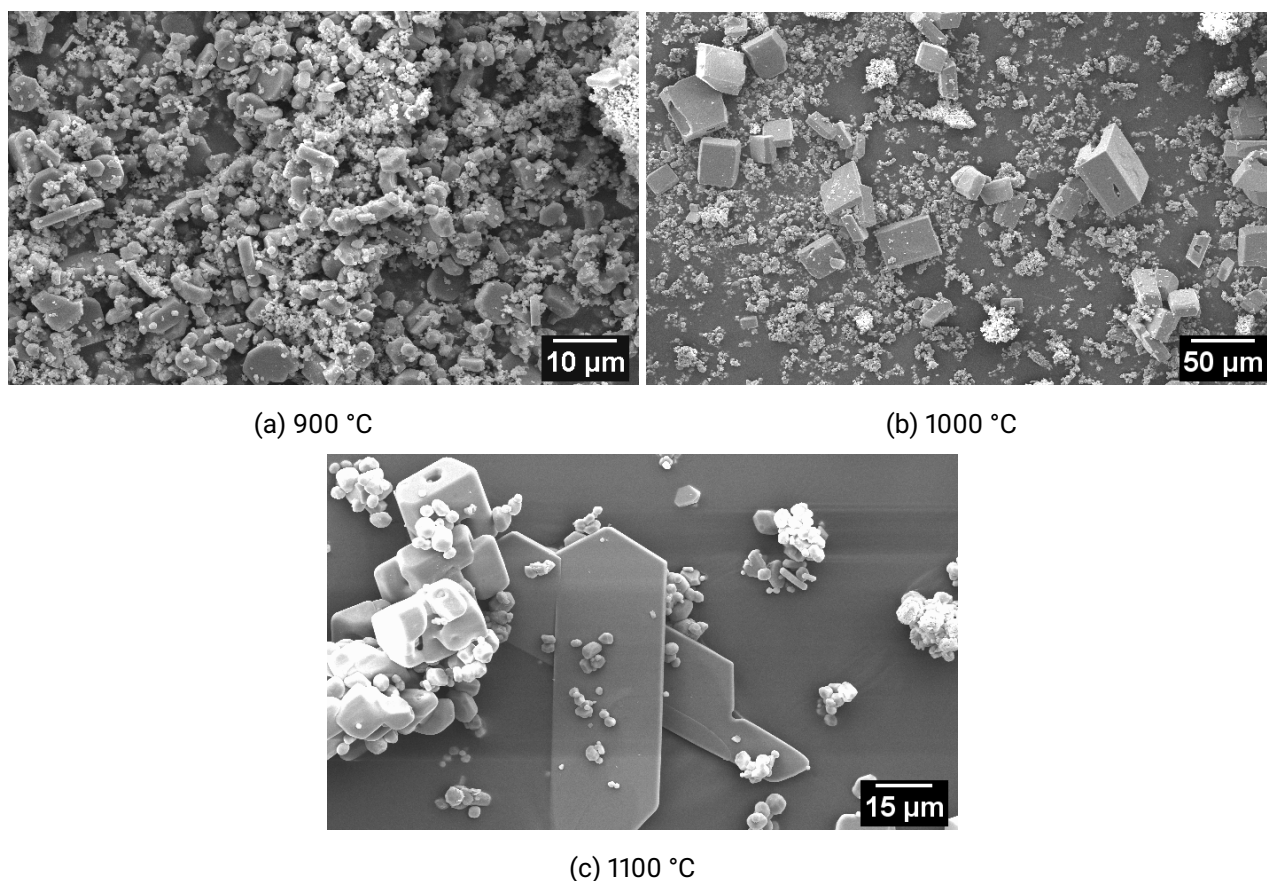


Figure 5.17.: SEM images of titania particles obtained at a) 900, b) 1000 and c) 1100 $^\circ\text{C}$: 20 wt. % TiO_2 in 0.8 NaCl -0.2 MgCl_2 mixture.

Interestingly the MSS in a NaCl-MgCl_2 molten flux provides crystals with a morphology close to

the desired one for the application as pearl luster pigment (PLP). However, some major drawbacks are observed: i) a broad particle size distribution, related to the ii) multiple phases forming and iii) the scarce presence of rutile, meaning that the flake-like particles are not TiO_2 .

5.1.2.4. NaCl- AlCl_3

Further experiments were performed with NaCl- AlCl_3 in different ratios. The lamellar morphology that Al_2O_3 develops in molten salts can be taken as a template for the TiO_2 growth (see figure 2.6) [85, 86]. Therefore, the following salt combinations i) 0.7 NaCl-0.3 AlCl_3 and ii) 0.6 NaCl-0.4 AlCl_3 , have been investigated. Both allow MSS already slightly above 700 °C (see phase diagram in figure B.2). Rutile is the main phase in all 0.7 NaCl-0.3 AlCl_3 samples synthesized in the range 900 to 1100 °C with 10 wt. % of anatase precursor (see figure 5.18 and table 5.3). Additionally, anatase and fractions of a cubic alumina phase (space group $Fd\text{-}3m$ (227)) and corundum are present at 900 °C and 1000 °C. The anatase phase disappears at $T > 900$ °C. Corundum and an orthorhombic Al_2O_3 phase form next to rutile at 1100 °C.

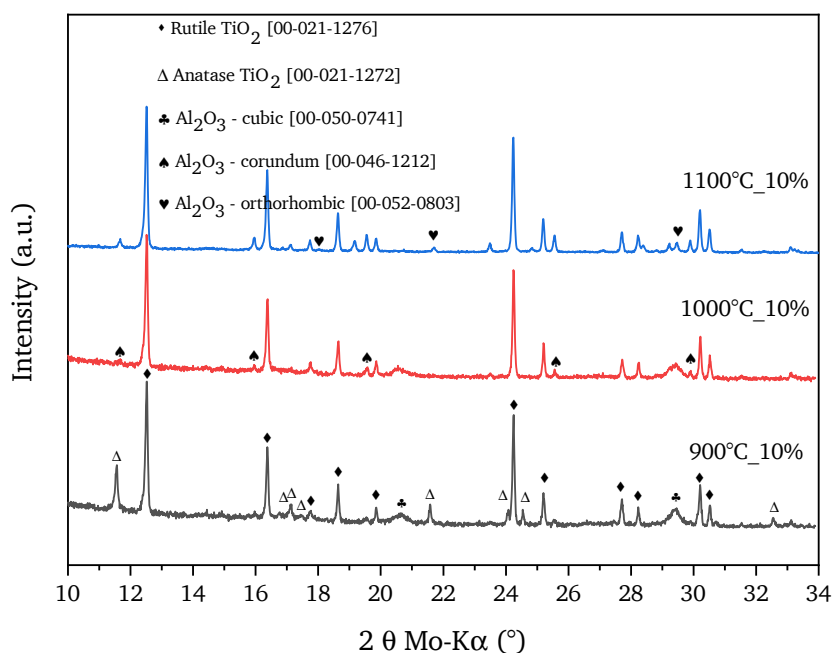


Figure 5.18.: XRD patterns of titania samples obtained by MSS in 0.7 NaCl - 0.3 AlCl_3 mixture with 2 hours holding time and 10 wt. % of titania.

The 0.6 NaCl-0.4 AlCl_3 samples also reveal the presence of rutile as main phase (see table 5.3). The high ratio of AlCl_3 in this sample slows down the ART (see figure C.9 in the appendix), because Al_2O_3 might interact as an oxo-acid upon his formation, since it is accepting the O^{2-} ion [287]. This might be related to the competing formation of (Al_2O_3) in higher concentration with respect to the 0.7 NaCl-0.3 AlCl_3 samples.

Table 5.3.: Phase composition of samples heat-treated in two different NaCl-AlCl₃ ratios. Synthesis temperature: 900 to 1100 °C, 2 hours holding time (A = Anatase, R = Rutile).

Salt molar ratio	wt. % TiO ₂	Temperature [°C]	Phase composition
0.7NaCl-0.3AlCl ₃	10	900	A, R, cubic Al ₂ O ₃ , corundum Al ₂ O ₃
0.7NaCl-0.3AlCl ₃	10	1000	R, cubic Al ₂ O ₃ , corundum Al ₂ O ₃
0.7NaCl-0.3AlCl ₃	10	1100	R, corundum Al ₂ O ₃ , orthorhombic Al ₂ O ₃
0.6NaCl-0.4AlCl ₃	10	900	A, R, cubic Al ₂ O ₃ , corundum Al ₂ O ₃
0.6NaCl-0.4AlCl ₃	10	1100	R, corundum Al ₂ O ₃ , orthorhombic Al ₂ O ₃

The habit of the samples change also changes with the synthesis conditions. The SEM micrographs of the samples obtained in 0.7 NaCl - 0.3 AlCl₃ flux reveal a clear phase segregation. The presence of alumina plates is evident in figure 5.19. Al₂O₃ flakes of the size of 2 μm can be observed in the sample with 10 wt. % at 1000 °C and 1100 °C (see the zoomed views reported in figure D.8 in the appendix). Also, rutile rod-like crystals mixed with the alumina flakes are visible in the sample heat-treated at 1100 °C (see figure 5.19d). Furthermore, cube shaped crystals exist at 1100 °C (see figure 5.19). Unfortunately, this attempt did not lead to morphologies suitable for the PLP application, because mainly Al₂O₃ flakes appear instead of the desired TiO₂ crystals with a similar habit.

5.1.3. KCl-LiCl eutectic mixture with low melting point

The ability of NaF to interact with the crystallization of titania discussed in section 5.1.2.2, motivates the experiments presented in this section. They were performed in the eutectic KCl-LiCl mixture (0.41 KCl-0.59 LiCl) melting at 352 °C (see also table 2.3 on page 22 and the phase diagram in figure B.5 in the appendix). In this way a MSS could be performed at temperatures \ll 900 °C, allowing the investigation of the capping effect of F⁻ on the anatase phase in a low temperature system. Fluorine ions can interfere both with the crystallization of rutile and anatase, strongly affecting the resulting habits. According to the reported studies for rutile [30, 203] and anatase [30, 174, 183], it seems favorable to increase the concentration of anatase (001) facet rather than that of the rutile structure in order to achieve a platelet morphology (see chapter 3, section 3.1 on page 27).⁴ In general, for rutile are reported higher surface energies than for anatase [288, 289]. Therefore, it is of interest to perform the MSS in 0.41 KCl-0.59 LiCl at temperatures \leq 700 °C, in order to analyze the interaction of NaF with the anatase habit formation.

The XRD data in figure 5.20 confirm that the ART in 0.41 KCl-0.59 LiCl with 10 wt. % precursor begins at 700 °C. For lower synthesis temperatures the XRD patterns show only reflections belonging to the anatase phase. This transformation temperature is close to \simeq 710 °C, as assessed by *in-operando* XRD in a pure NaCl melt (see 5.1.1.2 on page 62). The comparison of the SEM pictures in figure 5.21 with the anatase precursor (see figure 5.1 on page 54) shows comparable sizes of the particles

⁴The reported surface energy for rutile's (001) facet is 28.9 meV au⁻² according to Ramamoorthy [203], corresponding to 2.07 J m⁻². In the anatase phase it is estimated to be 0.9 J m⁻² according to [175].

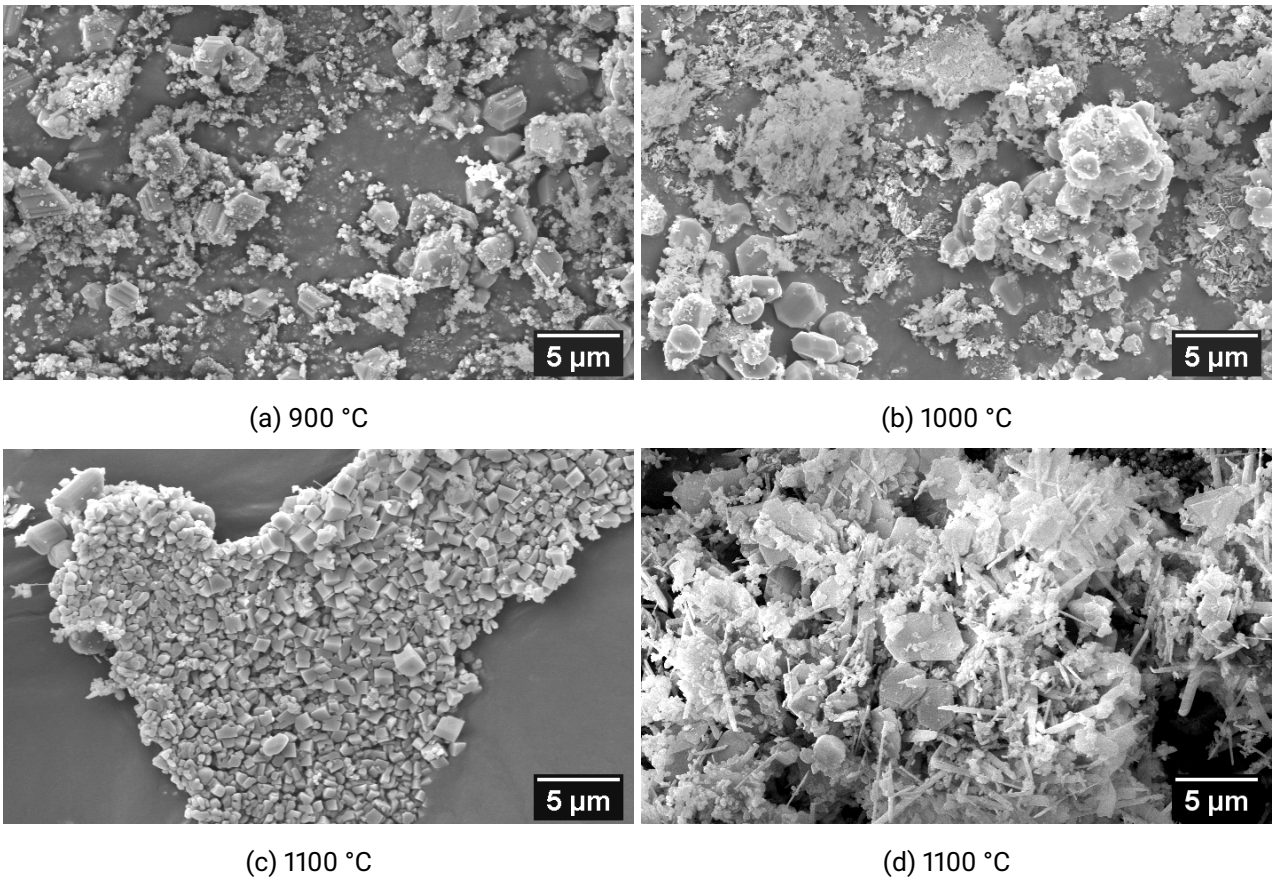


Figure 5.19.: SEM images of titania and alumina particles obtained at a) 900, b) 1000, c) and d) 1100 °C, 10 wt. % TiO_2 in 0.7 NaCl -0.3 AlCl_3 mixture.

for heat-treatment at 400 °C. Increasing the temperature to 500 °C leads to the growth of only a few particles. Most of the particles still have a size of ≈ 100 nm as in the precursor. However, the anatase particles acquire a more defined geometrical shape with marked sides. A change in the habit becomes only evident for samples heat-treated at 600 °C: cube-shaped crystals and bi-pyramidal octahedra are appearing.

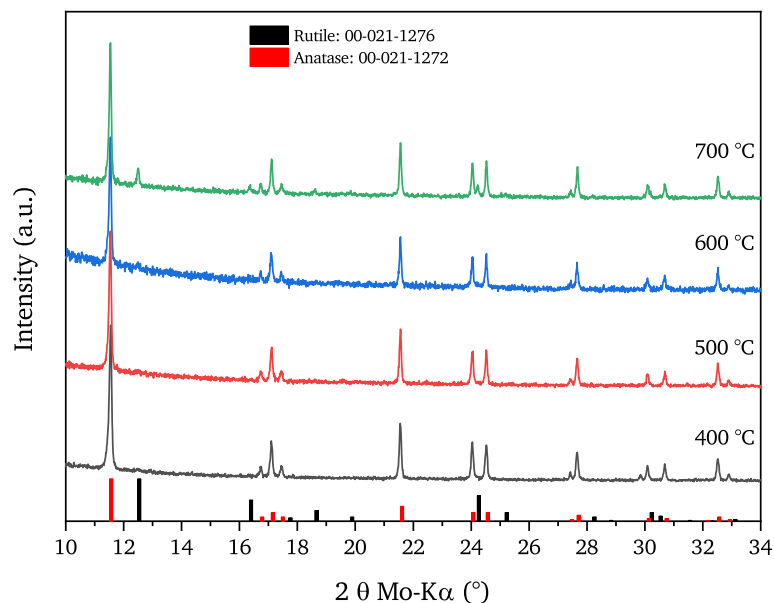


Figure 5.20.: XRD patterns of titania samples obtained by MSS between 400 and 700 °C in 0.41 KCl-0.59 LiCl with 10 wt.% of anatase precursor. Reference patterns from the ICDD are reported for comparison.

The addition of 1, 10 and 20 mol % of NaF to the system does not change the crystallization process. The phase composition of the samples corresponds exactly to that reported for the 0.41 KCl-0.59 LiCl system without the NaF addition reported in figure 5.20 (see the comparison reported in figure C.10 and C.11 in the appendix). As regards the habit, there also exist no remarkable differences (see SEM micrographs in figure 5.22).

In summary, at temperatures < 700 °C the thermal energy appears to be too low to achieve a growth of the particles reaching the micro scale and to observe a well defined habit. Most of the crystals in figure 5.22 keep the shape of a tetragonal bi-pyramid, corresponding to the equilibrium shapes of anatase (see figure 3.2 on page 29) [174] indicating that the addition of F^- has no relevant effect on the crystal habit formation.

5.1.4. Influence of the oxygen partial pressure on the crystal growth in NaCl

Several experiments were performed under argon and pure oxygen flow in order to investigate to which extent the atmosphere above the molten salt defines the ART and the formation of NTO occurring in the

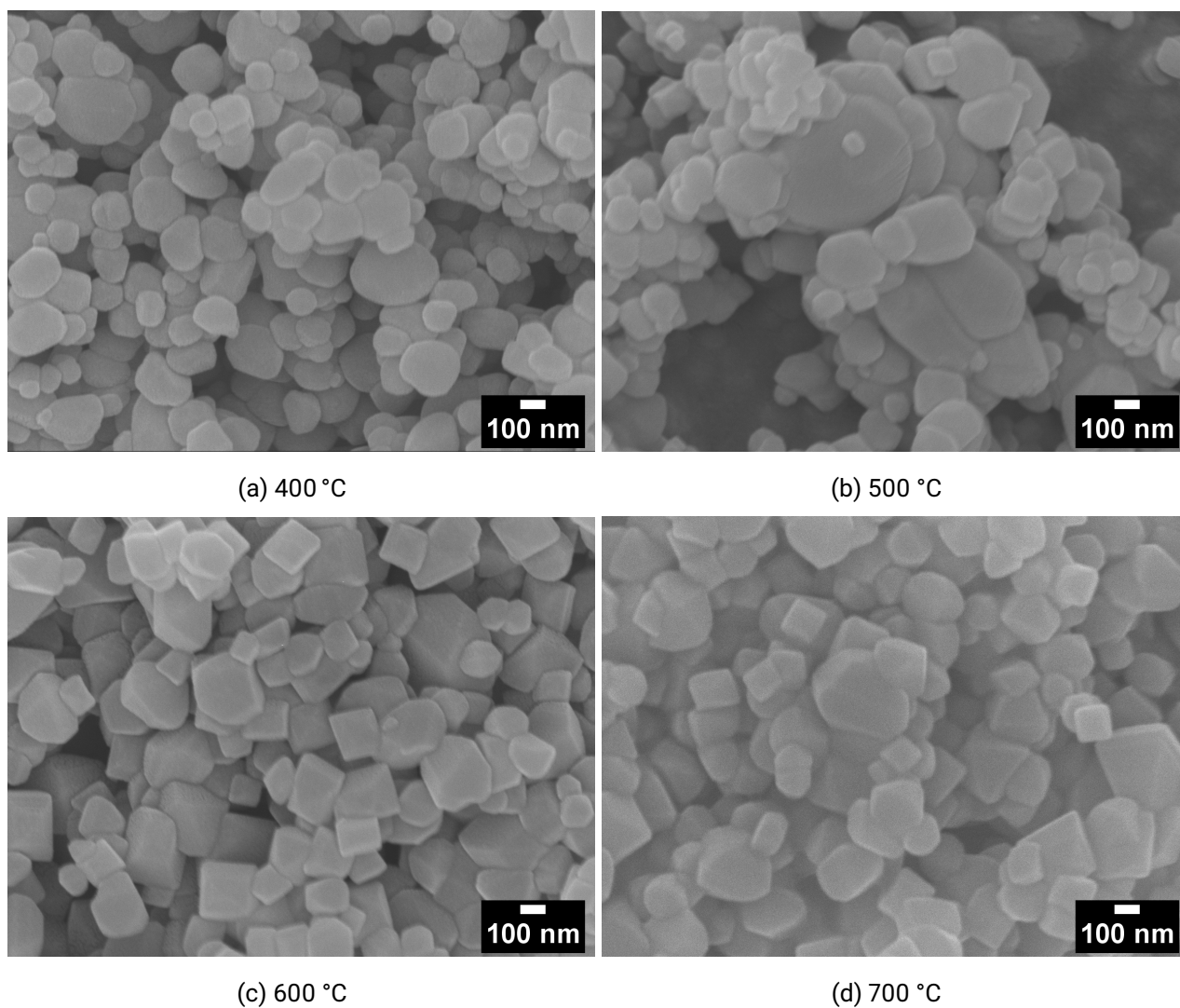
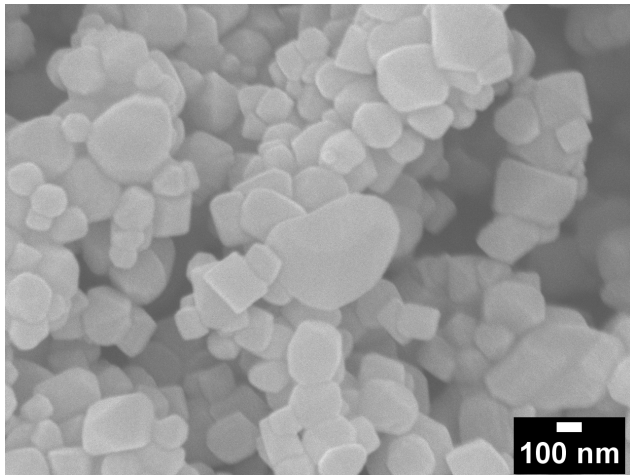
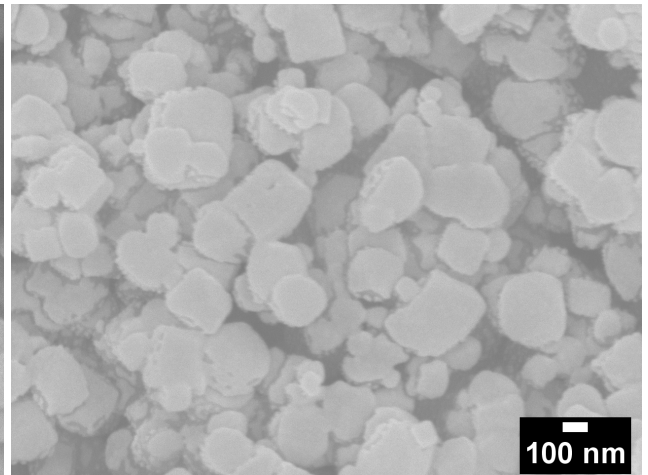


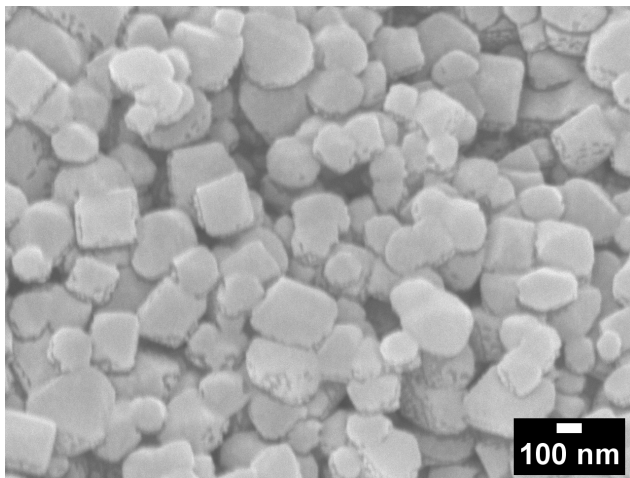
Figure 5.21.: SEM images of titania particles obtained at a) 400, b) 500, c) 600 and d) 700 °C with 10 wt. % TiO_2 precursor in 0.41 KCl-0.59 LiCl.



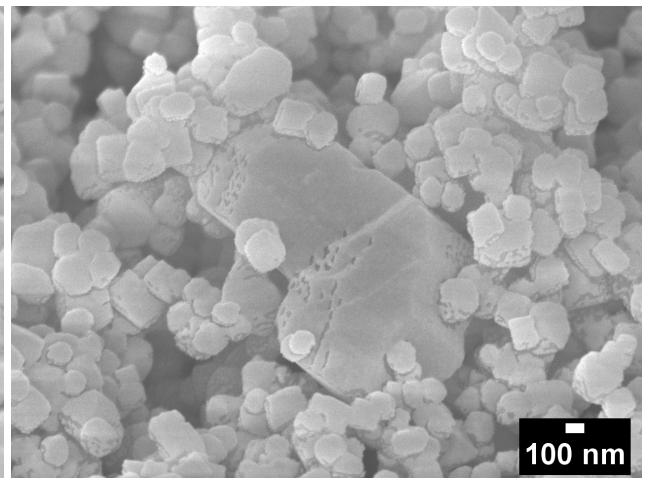
(a) 500 °C with 10 mol % NaF



(b) 500 °C with 20 mol % NaF



(c) 600 °C with 10 mol % NaF

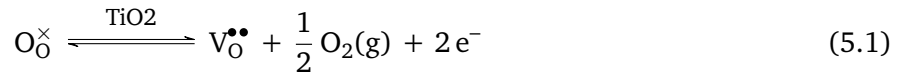


(d) 600 °C with 20 mol % NaF

Figure 5.22.: SEM images of titania particles obtained at a) and b) 500 °C and c) and d) 600 °C with 10 wt. % TiO_2 precursor in 0.41 KCl-0.59 LiCl. a) and c) report the addition of 10 mol % NaF and b) and d) of 20 mol % NaF respect to TiO_2 .

molten NaCl.

Argon atmosphere The impact of a reduced oxygen partial pressure ($\simeq 10^{-2}$ atm) was investigated by a MSS study performed at 900 °C with 1 wt. % of TiO₂ precursor. The XRD results (see figure 5.23) yield rutile as main phase mixed with anatase, as obtained under ambient atmosphere. A difference appears, however, from the main reflection of anatase at 11.53°, which is barely visible under argon flow indicating that the ART is enhanced at low oxygen partial pressure, in accordance with literature postulating a correlation with the concentration of oxygen vacancies ($[V_{\text{O}}^{\bullet\bullet}]$) [290–292]. Thermal annealing in oxygen depleted atmosphere promotes the formation of oxygen vacancies $V_{\text{O}}^{\bullet\bullet}$ [293].



where $\text{O}_{\text{O}}^{\times}$ denotes a (neutral) oxygen atom in the TiO₂ lattice and $\frac{1}{2} \text{O}_2(\text{g})$ oxygen in the gas phase. Accordingly, the equilibrium constant K is given as

$$K = [V_{\text{O}}^{\bullet\bullet}] [e^-]^2 p(\text{O}_2)^{(1/2)} \quad (5.2)$$

which permits to define the concentration of oxygen vacancies as a function of the oxygen partial pressure, equation 5.3.

$$[V_{\text{O}}^{\bullet\bullet}] = K [e^-]^{-2} p(\text{O}_2)^{-(1/2)} \quad (5.3)$$

A clear difference between oxygen depleted and ambient atmosphere is visible in the morphological investigations. The SEM graphs in figure 5.24 show the sample's morphology obtained under argon flow at the same experimental conditions as given in figure 5.4a (under air). The rod-shaped crystals (with a length of at least 20 μm and a diameter ≤ 500 nm) present at ambient atmosphere are not found in the sample heat-treated under argon flow, indicating the suppression of the formation of the NTO structure. This is also the case for the samples synthesized at 1000 °C reported in figure D.9 in the appendix. Probably, the random distribution of $V_{\text{O}}^{\bullet\bullet}$ does not allow directional growth.

Oxygen atmosphere The synthesis under oxygen flow ($\text{O}_2 \geq 99.998$ mol %) was performed at 1100 °C. Figure 5.25 compares the XRD result with the one obtained under ambient condition. Both reveal the presence of the rutile phase. However, the sample heat-treated under ambient atmosphere shows the typical reflection at 21.79° attributable to NTO. All the rutile reflections corresponding to planes with Miller index $l \neq 0$ show a remarkable intensity decrease with O₂ treatment (see figure C.13 in the appendix). Moreover, all the reflection lines are broader under O₂ (see the overlapped diffractograms in figure C.13), indicating that the average particle size is slightly smaller than the one obtained in ambient condition. The SEM graphs in figure 5.26 confirm this result. The long NTO rod-like crystals forming under ambient atmosphere (see also figure 5.7d on page 61) are not present in the sample

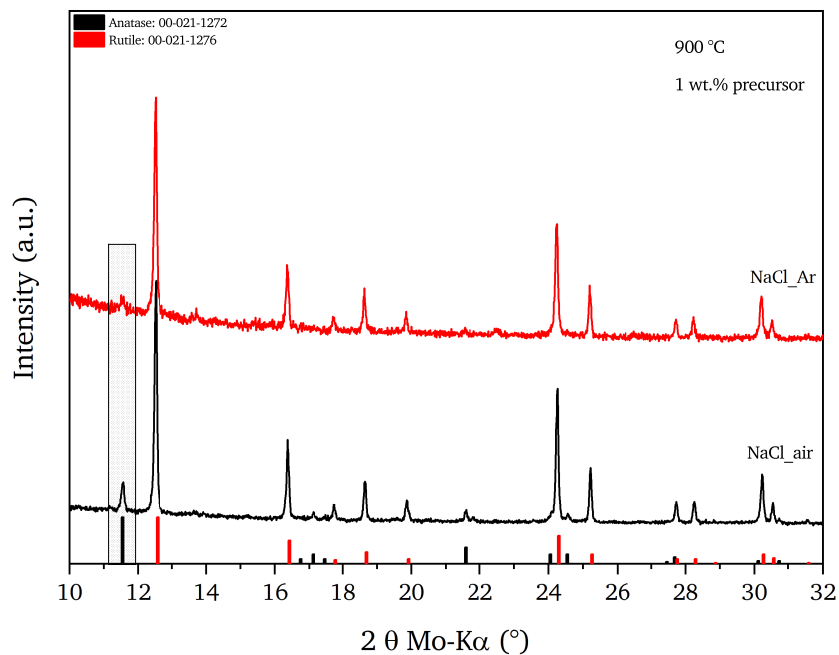
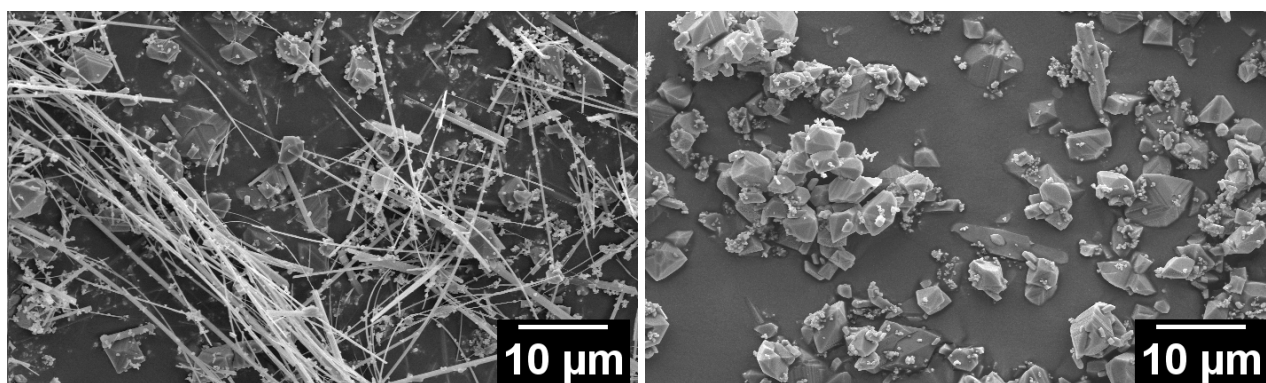


Figure 5.23.: Comparison between samples with 1 wt. % anatase precursor in NaCl heat-treated under ambient atmosphere and under argon at 900 °C; reference patterns from the ICDD are reported for comparison.



(a) 900 °C under ambient atmosphere

(b) 900 °C under pure argon atmosphere

Figure 5.24.: Morphology of titania particles obtained at 900 °C for 1 wt. % anatase precursor in NaCl under: a) ambient atmosphere (same picture as in figure 5.4 a) and b) argon flow, measured by SEM.

treated under higher oxygen activity (see enlargement of figure 5.26 in figure D.10 in the appendix). This also explains the absence of NTO reflections from in figure 5.25. Additionally, a much closer view of the powders in figure D.11 in the appendix, highlights the size difference and the shape features of the sides of the polyhedra.

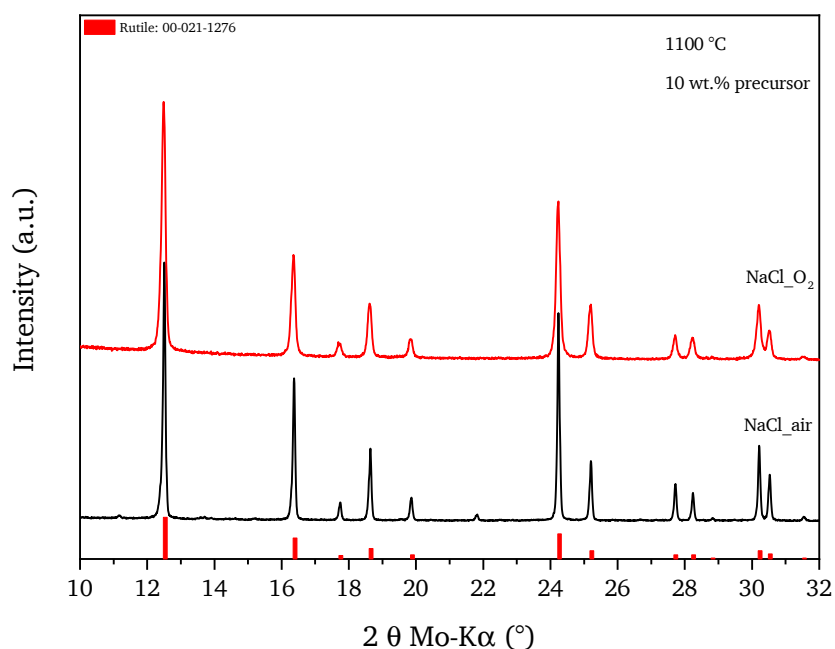


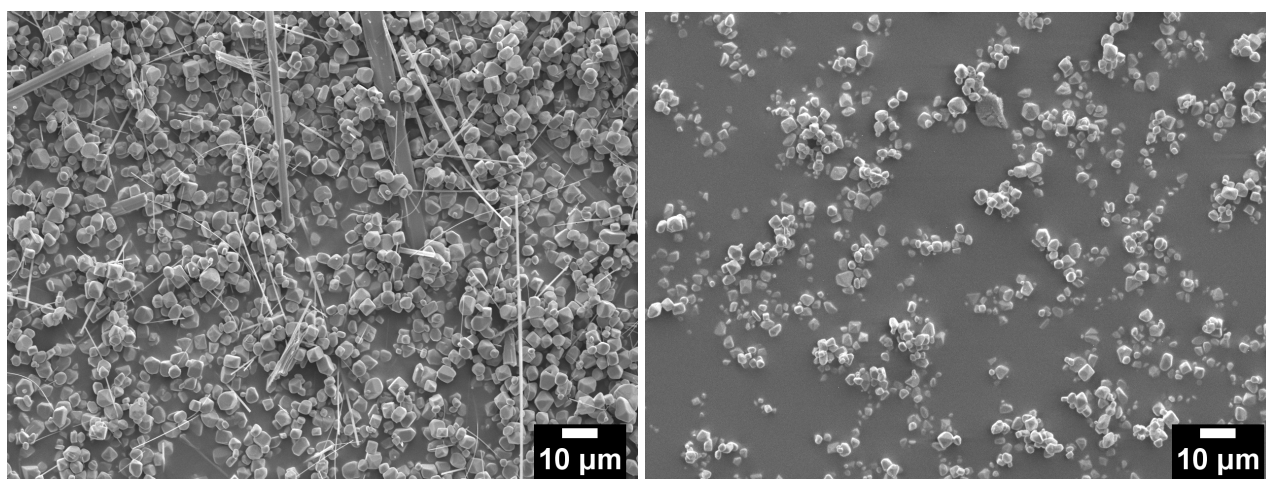
Figure 5.25.: Comparison between samples heat-treated under ambient atmosphere and under O₂ flow at 1100 °C with 10 wt. % anatase precursor in NaCl. A reference pattern from the ICDD is reported for comparison.

A higher oxygen activity in the atmosphere above the molten salt leads to a higher oxygen content in the melt [165, 294], in agreement with Henry's law. The increased concentration of dissolved oxygen has structural and morphological consequences on the crystallization of titania in NaCl. It leads to a less pronounced growth of the particles and decreases the interaction of the reactant with NaCl [160, 287, 295–297]. Accordingly, the capping activity of the chlorine ions may be reduced and, as a consequence, the growth along the [001] direction is suppressed, hindering the formation of the long rod-shaped NTO particles.

5.1.5. Addition of B₂O₃ to NaCl synthesis

According to the L-F theory [127] (see chapter 2, section 2.3.4), the addition of B₂O₃ to a molten salt increases the acidity of the melt and, thus, the solubility of TiO₂ in the melt. This affects the growth and habit formation of rutile. B₂O₃ is an O²⁻ acceptor, therefore also defined "oxoacid". Its interaction with the oxygen anion follows in equation 5.4:





(a) 1100 °C under ambient atmosphere

(b) 1100 °C under pure oxygen atmosphere

Figure 5.26.: Morphology of titania particles obtained at 1100 °C with 10 wt. % anatase precursor in NaCl under: a) ambient atmosphere and b) pure oxygen, measured by SEM.

B_2O_3 reacts with O^{2-} decreasing the oxygen activity in the melt [126, 127, 287]. The increased solubility of titania, due to the removal of oxygen from the crystal lattice, accelerates a transformation of reconstructive type [39, 168, 190, 191]. Figure 5.27 reports the XRD diffractograms of the samples with and without the addition of 0.8 mol % B_2O_3 , heat-treated in air at 900 °C in NaCl with 20 wt. % of anatase precursor. Both match the rutile reference pattern from the ICDD. However, all reflections attributed to rutile planes having Miller indices $l \neq 0$ show a remarkable intensity increase with B_2O_3 addition, indicating an enhanced growth along the 001 axis. Especially the reflections attributed to (101) and to (211) are underlining this result. They have almost identical intensity, being quite close to that of the prominent (110) reflection. The changes observed for the reflection intensities are confirmed with the addition of 1.2 mol % B_2O_3 (see XRD diffractogram in figure C.12).

The SEM data shown in figure 5.28 shed light on the observed deviations of the XRD patterns. The addition of B_2O_3 promotes the growth of the rutile crystals along the [001] direction. Their habit is strongly altered by adding just 0.8 mol %, leading exclusively to the formation of elongated rods with different thicknesses and length depending on the temperature of the heat-treatment. Increasing the temperature from 900 °C to 1100 °C increases the length to $> 5 \mu m$ (till a maximum of 20 μm). Additionally, the habits of the rod-shaped crystals are more faceted in presence of B_2O_3 . The same characteristics are observed with the addition of 1.2 mol % B_2O_3 (see figure D.12 in the appendix). A further confirmation of the enhanced growth of elongated rod-shaped rutile crystals promoted by boron oxide has been found by the B_2O_3 -aided liquid-phase sintering of TiO_2 [298].

An additional experiment was conducted under lower oxygen partial pressure. A sample was heat-treated at 900 °C with the addition of 0.8 mol % of B_2O_3 under argon. Figure 5.29 shows the comparison between the different atmospheres. Depletion of oxygen promotes the growth of needle-like

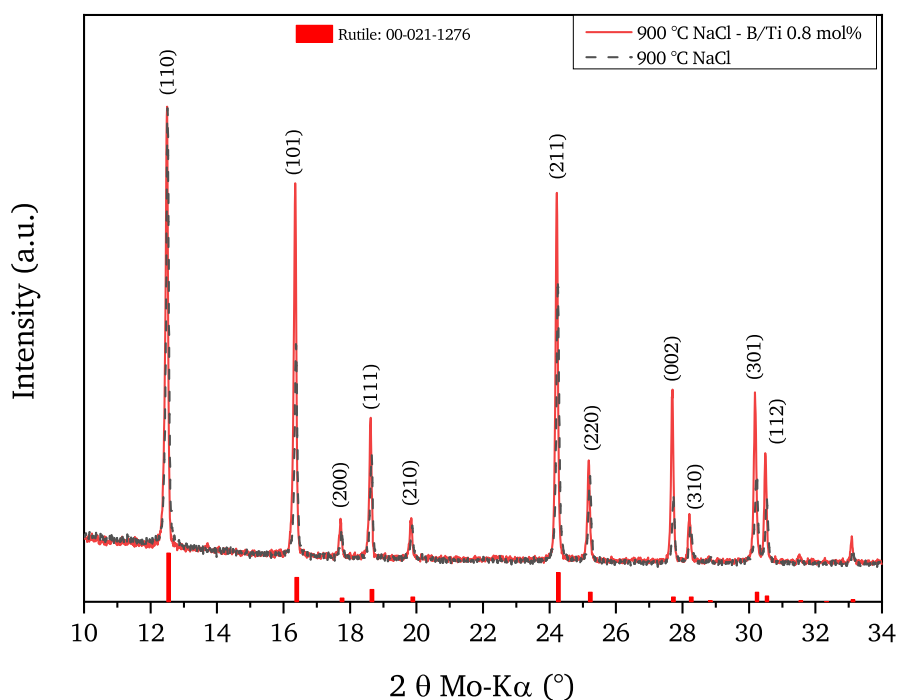
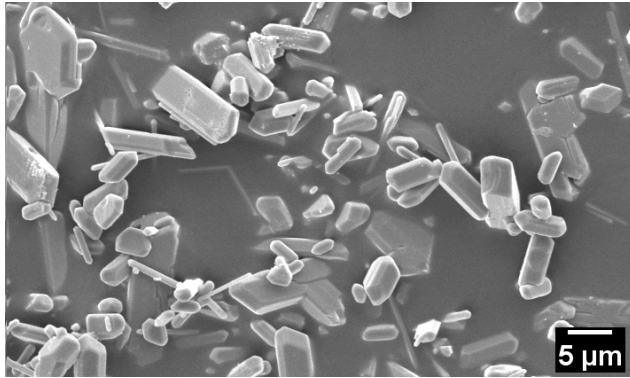


Figure 5.27.: XRD patterns of titania samples obtained by MSS at 900 °C for NaCl/20 wt. % anatase precursor (red dashed line) and the addition of 0.8 mol % B_2O_3 (black solid line). The rutile reference pattern from the ICDD is added at the bottom.

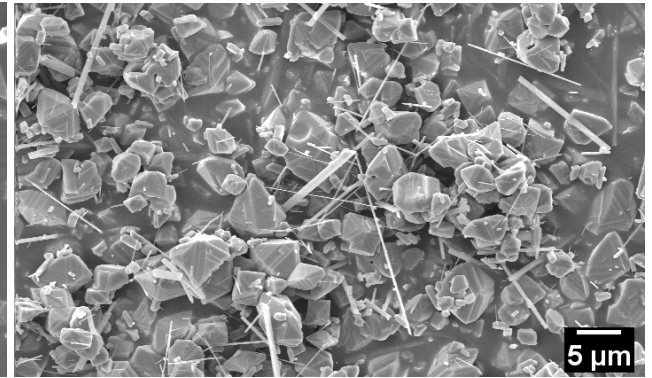
rutile crystals, with length $\approx 10 \mu\text{m}$ and diameters as low as 300 nm. This result further confirms the correlation between the higher solubility of titania precursor — due to the lower O^{2-} activity — and the enhanced growth along the 001 axis of thin and long rutile rod-shaped crystals.

5.1.6. Wet chemical pretreatment in NaCl

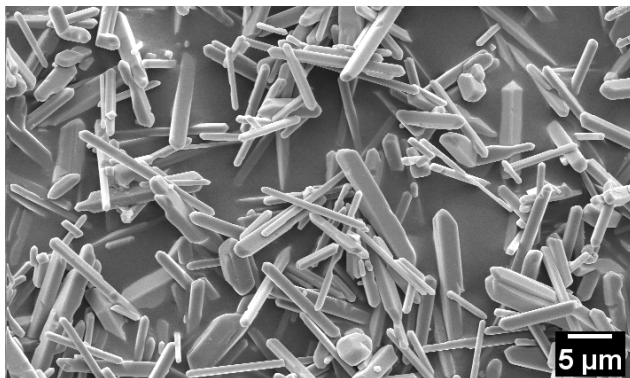
Two different approaches are compared in this section: the dry-mixed preparation (DMP) and the wet chemical preparation (WCP). Both are used for MSS in NaCl. The samples described in this section are exclusively obtained by using the WCP (for the experimental details see chapter 4, section 4.1.2 on page 48). This route substantially differs from the MSS previously described because of the different precursor ($TiCl_4$). The first TiO_2 nucleation process occurs in aqueous solution and is then followed by the addition of NaCl. The comparison between the WCP and DMP permits to evaluate the influence of the precursor particle size and the dispersion degree of the titania particles in the molten salt on the final habit of the product. Figure 5.30 shows the phase composition of four samples obtained by WCP with 5 wt. % $TiCl_4$ precursor and heat-treatment between 850 and 1100 °C in NaCl. The formation of NTO besides rutile is detected already at 850 °C and the presence of both phases is common to all synthesized samples (see the wt. % determined by Rietveld refinement in table 5.4). The different size of the particles, by almost three orders of magnitude (see figure 5.31), is responsible for the lower signal



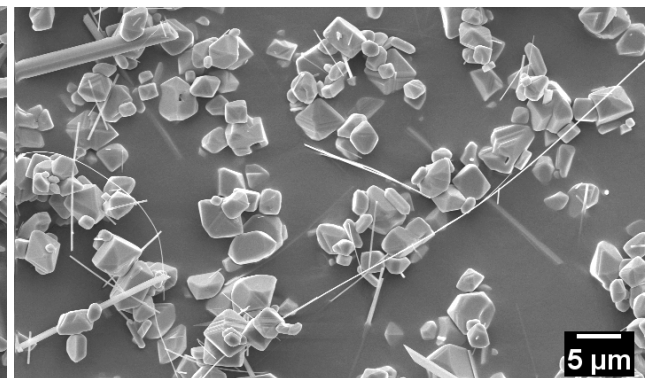
(a) 900 °C, NaCl + 0.8 mol % B₂O₃



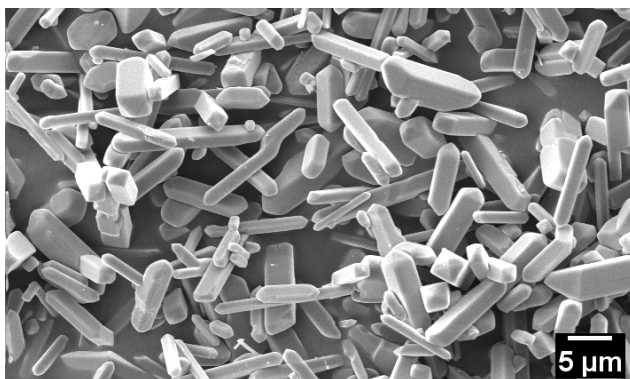
(b) 900 °C NaCl



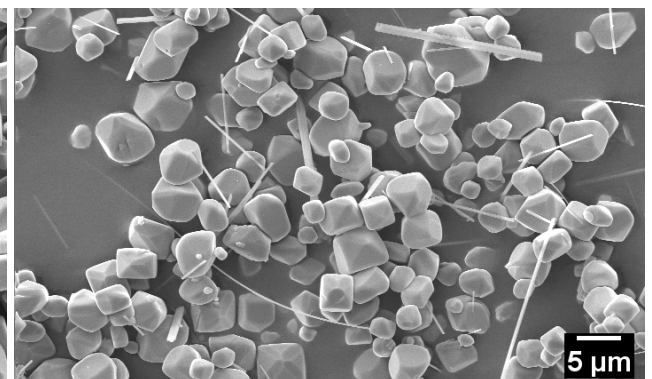
(c) 1000 °C, NaCl + 0.8 mol % B₂O₃



(d) 1000 °C NaCl

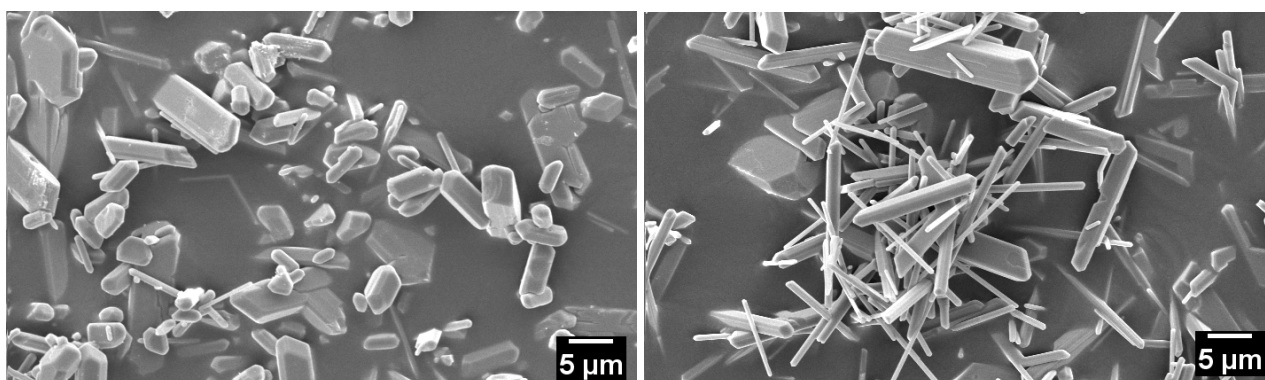


(e) 1100 °C, NaCl + 0.8 mol % B₂O₃



(f) 1100 °C NaCl

Figure 5.28.: SEM images of titania particles obtained at 900 °C, 1000 °C and 1100 °C: 20 wt. % TiO₂ precursor in NaCl (b, d and f) and with the addition of 0.8 mol % B₂O₃ (a, c and e).



(a) 900 °C, 0.8 mol % B₂O₃, ambient atmosphere

(b) 900 °C, 0.8 mol % B₂O₃ under argon

Figure 5.29.: SEM images of titania particles obtained at 900 °C: 20 wt. % TiO₂ precursor in NaCl with the addition of 0.8 mol % B₂O₃ in a) ambient atmosphere and b) under argon.

intensity at temperatures < 1000 °C. These results strongly deviate from those obtained by DMP (see figure 5.3a on page 56). Notably, the lack of anatase (forming by DMP both at 850 °C and 900 °C) is outstanding.

Table 5.4.: Phase composition of samples obtained by MSS in NaCl with 5 wt. % TiCl₄ precursor calculated by Rietveld refinement. Synthesis temperature: 850 to 1100 °C, 2 hours holding time.

Temperature [°C]	TiO ₂ (rutile) [%]	Na ₂ Ti ₆ O ₁₃ [%]	Residual wR [%]
850	94.3	5.7	8.76
900	92.6	7.4	8.59
1000	81.8	18.2	10.30
1100	81.7	18.3	10.48

The morphology of the four samples is shown in figure 5.31. Two habits can be unambiguously identified at all temperatures: rod-shaped and polyhedral particles. Heat-treatment at 850 °C produces the growth of nanorods with a maximum length of $\approx 3 \mu\text{m}$ and an average thickness of $\approx 100 \text{ nm}$. The polyhedral nanoparticles seldom exceed 100 nm. This happens, however, for few particles shaped in the rutile bifrustum. At 900 °C the average diameter of polyhedral nanoparticles is $\approx 130 \text{ nm}$. Drastic changes occur by heat-treatment at 1000 °C. The smallest polyhedral particles reach sizes > 500 nm and there are many reaching the micron scale. Concerning the rod-shaped crystals, the maximum length can exceed 5 μm while the thickness is between 140 nm and 300 nm. Increase of the temperature to 1100 °C causes a further growth of the polyhedral particles (compare figure 5.31c and d). The rod-shaped particles increase beyond 8 μm , as evident in figure 5.31d.

The morphologies obtained by WCP and DMP are directly compared in figure 5.32. The particles obtained by WCP are by about an order of magnitude smaller at the same synthesis temperature. Figure 5.32a clearly shows that the amount of particles reaching the micro scale by WCP is negligible compared

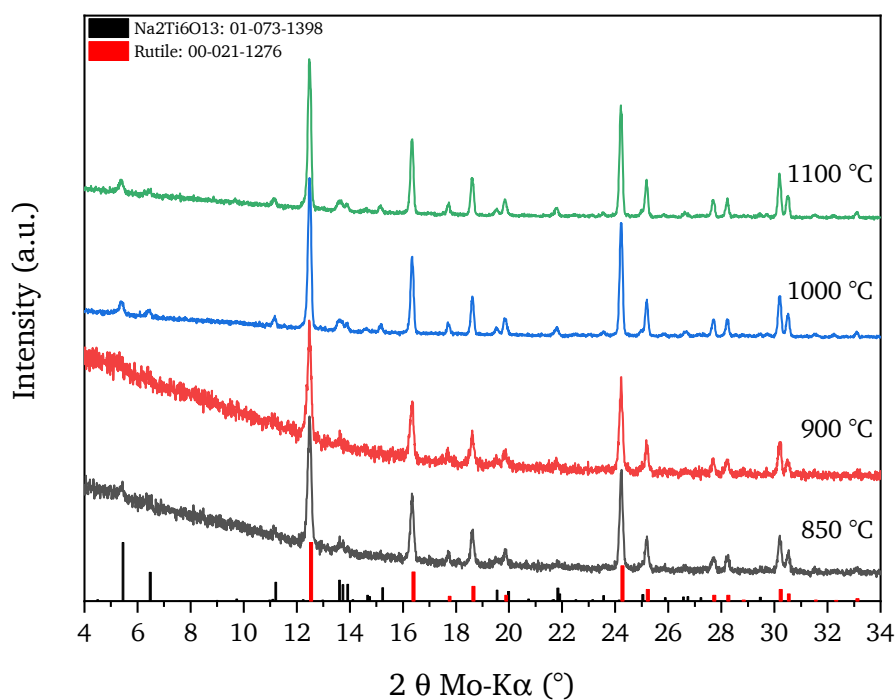


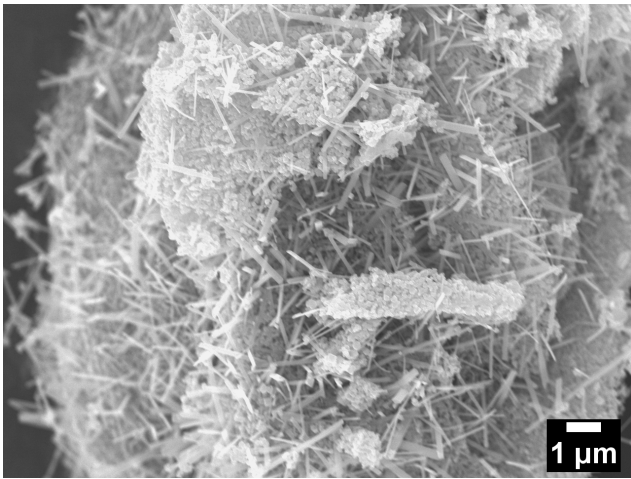
Figure 5.30.: XRD patterns of titania samples obtained by MSS in NaCl with 5 wt. % TiCl_4 as precursor. Reference XRD patterns from the ICDD for anatase and rutile are present at the bottom of the graph.

to the crystals obtained by DMP (see figure 5.32b). Nanorod crystals, coexisting with rutile, appear to be thinner and shorter by WCP than by DMP and exist in a higher concentration. Increasing the temperature to 1000 °C leads to the most noteworthy difference: rod-shaped crystals are only formed by WCP. The nanorod own the habit of the NTO structure. The rutile and NTO habits are also present at 1100 °C as observable in figure D.14 in the appendix.

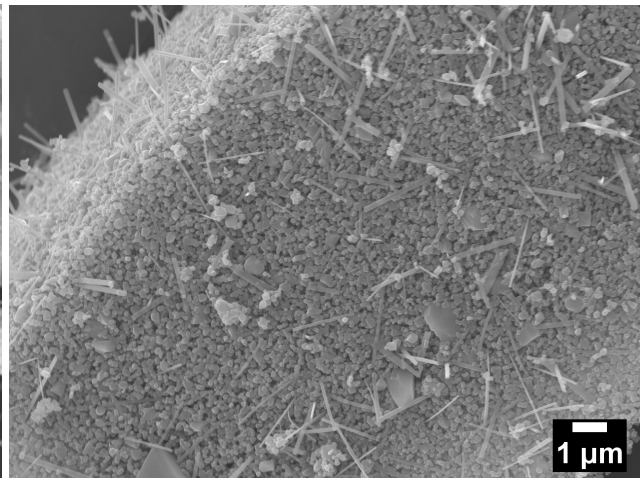
To summarize, the dispersion and homogenization degree reached by WCP is much higher than the one in DMP, leading to quite different results: the ART occurs in different temperature ranges. Anatase is still present at 900 °C by DMP, whereas it vanishes by WCP already at 850 °C. The simple mixture of anatase and NaCl shows differences arising from the oxide to salt ratio and the temperatures at which the treatment is performed. This MSS is simple and time efficient (it skips the nucleation step in wet solution). However, the lower dispersion of the precursor particle in the salt matrix causes a less homogeneous particle size distribution in the melt. The WCP guarantees a more homogeneous particle distribution in the melt than the DMP, since the precursor particles have a much smaller size.

5.1.7. Summary of MSS in chlorides

The results of two different synthesis routes, the DMP with anatase nanoparticles as precursor and the WCP with TiCl_4 as precursor are summarized in this section. The final products differ with respect



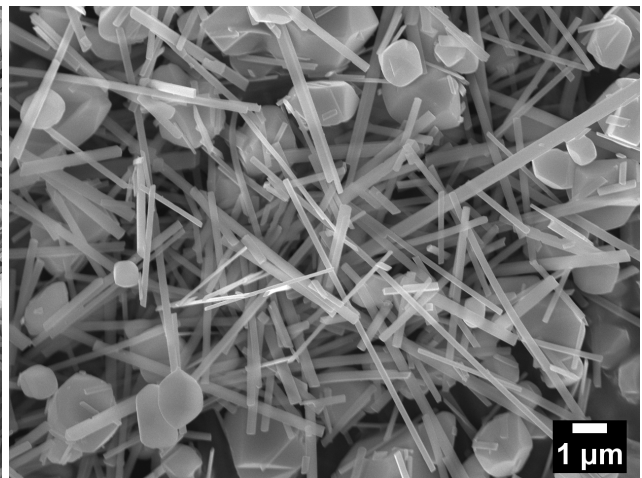
(a) 850 °C



(b) 900 °C

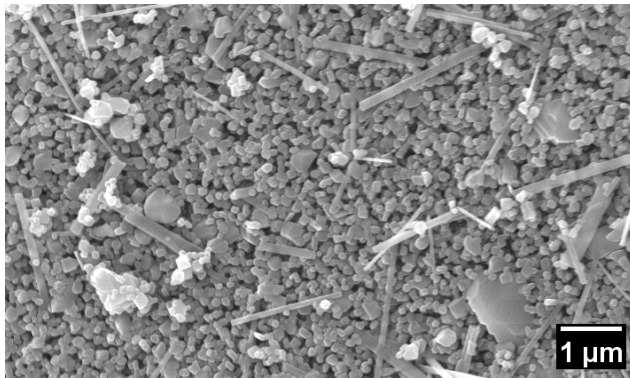


(c) 1000 °C

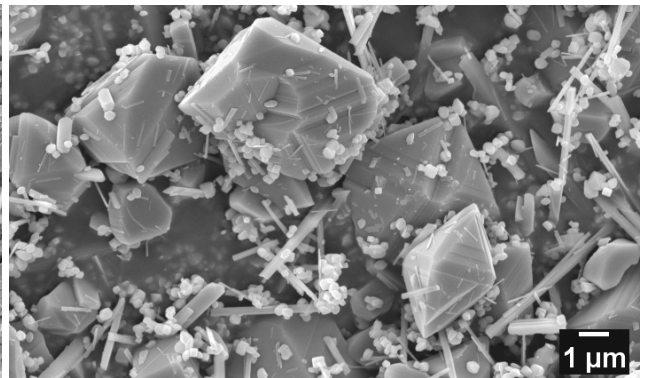


(d) 1100 °C

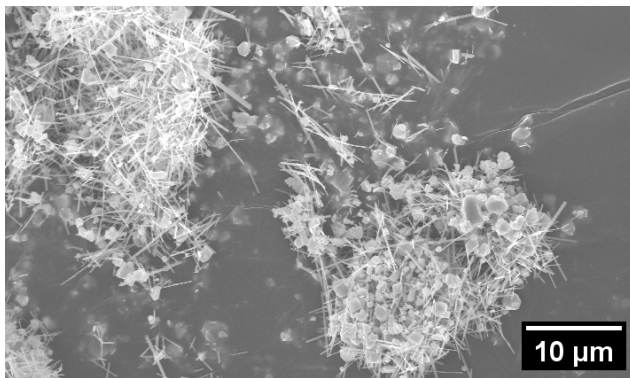
Figure 5.31.: SEM images of titania particles synthesized by MSS in NaCl with 5 wt. % TiCl_4 precursor.



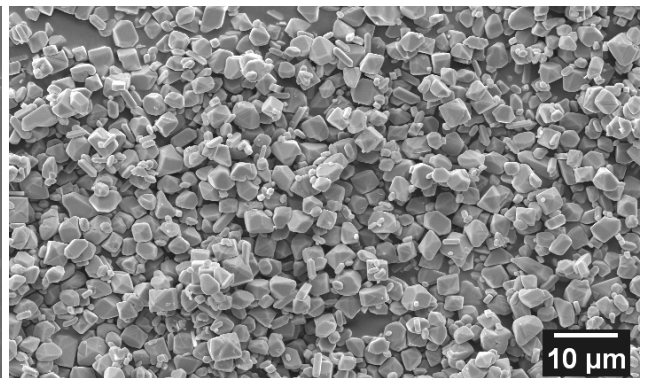
(a) 900 °C WCP



(b) 900 °C DMP



(c) 1000 °C WCP



(d) 1000 °C DMP

Figure 5.32.: SEM images showing the comparison between titania particles obtained in NaCl by WCP (with 5 wt. % TiCl_4 precursor) (figure a and c) and by DMP with 5 wt. % anatase precursor (figure b and d).

to morphology, crystal habit and phase composition. As concerns the DMP, the temperature and the concentration of the precursor are the main parameters determining the product formation (see the graphical summary in figure 5.33). Both define the ART rate in the MSS with NaCl. The ART is complete

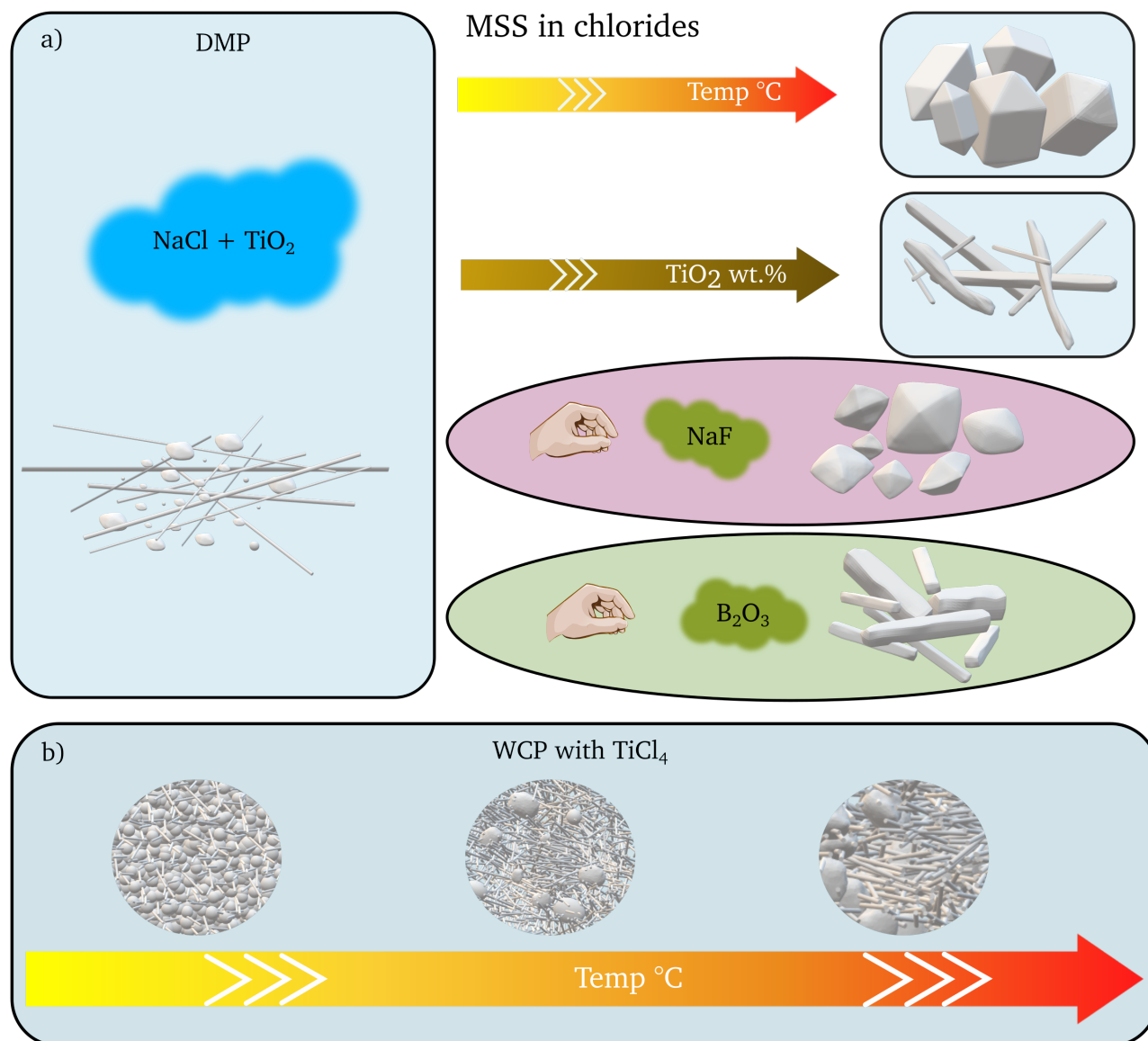


Figure 5.33.: MSS in NaCl: schematic representation of the change of a) the rutile crystals morphology with temperature, precursor concentration, the addition of NaF and B₂O₃ by DMP; b) the rutile and NTO particle size and morphology by WCP with TiCl₄.

at 900 °C only for precursors concentrations ≥ 10 wt. %. At 1100 °C the higher precursor concentration hinders the formation of rod-shaped rutile crystals. The crystal growth has been also investigated in mixed salts (0.5 NaCl-0.5 KCl, 0.8 NaCl-0.2 MgCl₂ and different NaCl-AlCl₃ ratios), showing the formation of crystal structures different from TiO₂ but not leading to any effect on the rutile morphology

advantageous for the application as pearl luster pigment. The most noteworthy changes of the rutile morphology are arising from the addition of NaF. A few mol% of F⁻ ions hinder the formation of rod-shaped rutile crystals and promote the formation of bipyramidal octahedra with the highly reactive 111 facet exposed. As a general trend, the presence of Cl⁻ ions promotes the growth of rutile crystals along the [001] direction (in pure NaCl and in 0.5 NaCl-0.5 KCl), confirming findings from the literature. The 0.41 KCl-0.59 LiCl salt allowed TiO₂ crystallization studies at low temperature (≤ 700 °C). No micrometer sized rutile crystals and no NTO rods are observed.

The oxygen partial pressure as synthesis parameter mainly affects the rate of the ART. Lowering of the pO₂ leads to an increase of the ART rate compared to the same synthesis conditions under ambient atmosphere. Synthesis under pure oxygen hinders the formation of rod-shaped rutile crystals and of NTO nanorods. B₂O₃ added to the salt melt strongly promotes the growth of rod-shaped rutile crystals.

WCP, as second synthesis route, has been performed with 5 wt. % TiCl₄ precursor. The samples differ from those obtained by DMP with respect to the crystal morphology and the structure composition. Anatase is not detected at a temperature of 850 °C, as it is in DMP which reports anatase till 900 °C. Accordingly, the ART is occurring with a different rate. NTO has been found in all the different samples in addition to the (dominant) rutile phase. The crystal size of rutile by WCP is smaller than by DMP. NTO nano-rods are already present at 1000 °C by WCP, but not by DMP.

5.2. Molten salt synthesis of TiO₂ performed in sulfates

5.2.1. TiO₂ crystal growth in Na₂SO₄ flux

Anatase nanopowder of average size $\simeq 100$ nm (see figure 5.1 and table A.1 in the appendix) is mixed with Na₂SO₄ powder in different ratios as precursor (DMP synthesis route) in order to investigate the influence of the SO₄²⁻ ion on the TiO₂ crystal growth. All the samples have been obtained by heating the different mixtures to a given temperature that was kept for two hours (same procedure as reported for chlorides in section 5.1.1 on page 53). The phase composition and the habits of the obtained crystals change with the anatase/Na₂SO₄ ratio and the holding temperature.

According to the X-ray diffractograms (figure 5.34), anatase is the main phase for all the samples heat-treated at 900 °C. The minor rutile fraction — forming at all of the 5 different precursor concentrations — is inversely related to the precursor concentration. At T > 1100 °C only rutile is observed. The phase compositions have been calculated by Rietveld refinement and are reported in table 5.5. Comparison with the data reported for the synthesis performed in NaCl (see figure 5.2), clearly suggests that the SO₄²⁻ anion shows a more retarding effect on the ART than Cl⁻.

Figure 5.35 shows the morphological evolution of TiO₂ samples obtained by increasing the fraction of anatase precursor in Na₂SO₄. There are minimal differences arising between the five samples. Most

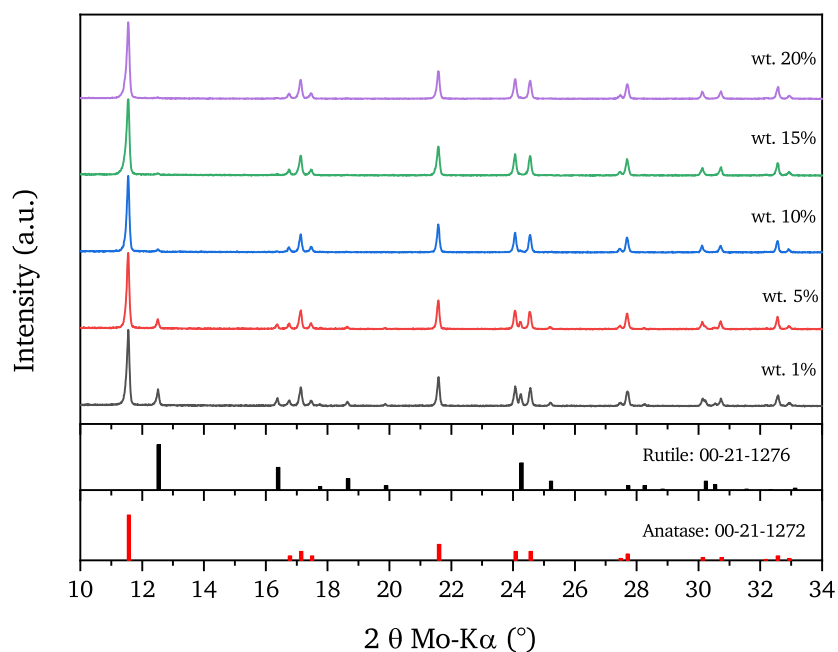


Figure 5.34.: XRD patterns of titania samples obtained by MSS at 900 °C in Na₂SO₄ with 5 different wt. % of anatase precursor (1%, 5%, 10%, 15% and 20%). Reference XRD patterns from the ICDD for anatase and rutile are given at the bottom of the graph.

Table 5.5.: Phase composition of samples after heat-treating different amounts of TiO₂ in Na₂SO₄ in the range 900 °C to 1200 °C calculated by Rietveld refinement (A = Anatase, R = Rutile).

wt. % TiO ₂	900 °C	1000 °C	1100 °C	1200 °C
1	80.3 % A, 19.7 % R	R, A	100 % R	100 % R
5	87.5 % A, 12.5 % R	R, A	100 % R	100 % R
10	96.8 % A, 3.2 % R	R, A	100 % R	100 % R
15	97.2 % A, 2.8 % R	R, A	100 % R	100 % R
20	97.2 % A, 2.8 % R	100 % R	100 % R	100 % R

of the small particles have dimensions varying from 150 nm to 300 nm, indicating a slow crystal growth at 900 °C. Few particles are growing beyond the micro-scale. The higher the amount of titania present in the mixture, the more likely is the appearance of faceted crystals. Such crystals are present in the samples with 15 and 20 wt. % precursor (bipyramidal octahedra are visible in figure 5.35d and 5.35e). The comparison with the samples obtained at 900 °C in pure NaCl (see figure 5.4 on page 58) emphasizes the strong effect that the salt matrix plays on the crystal habit. Notably, needle-shaped crystals — common in the synthesis in NaCl — are absent in Na₂SO₄.

The SEM images of the samples obtained in NaCl and Na₂SO₄ at 900 °C and 1000 °C are presented together in figure 5.36 for comparison (see also figure 5.4 and figure D.2 in the appendix). Obviously, TiO₂ crystals growing in the Na₂SO₄ melt achieve a different shape and size compared to those grown in NaCl. The chloride melt promotes the growth along the [001] axis leading to the formation of needle-shaped crystals [157, 273, 299–301]. The limited growth of the particles in the sulfate environment at 900 °C and the formation of a different habit are a direct consequence of the interaction between the growing TiO₂ crystals and the salt matrix. Na₂SO₄, as an oxygen containing salt species, interacts differently with the surface of TiO₂ particles than NaCl. The SO₄²⁻ ions retard the reordering of the TiO₆ octahedra units and therefore the densification process that occurs during the ART. The results show that the ART, as well as the anisotropical growth of particles, is hindered in the MSS performed in Na₂SO₄. The higher amount of oxygen available in the melt during the MSS slows-down the reconstructive transformation. According to the L-F theory (see section 2.3.4 on page 23), MSS performed in molten oxosalts ensures that the crystallization process proceeds by different interaction between the salt ions and the growing TiO₂ nanoclusters, depending on the dissociation equilibrium of the sulfate anion (see section 2.1.1 and equations 2.5, 2.6 and 2.7). The morphologies achieved in Na₂SO₄ at 900 °C and 1000 °C are therefore caused by a low anisotropic growth in comparison to the anisotropic growth along the <001> direction within molten NaCl (see section 5.1.1). The dependence of the ART on the anion type has been already reported in literature [302]. The ART rate with anion type follows the series Cl⁻ > SO₄²⁻ > PO₄³⁻. This order is confirmed by our MSS experiments, since the chloride based fluxes accelerate the ART in comparison to the sulfate based fluxes. The contraction of the tetragonal unit cell of rutile, that occurs during the phase transformation, is hindered by the size-effect of bulky anions. This correlates with an increasing retarding effect on the ART.

The typical habit for anatase crystals reported in literature [30, 177, 178] — a bipyramid with a varying degree of truncation (*i.e.* a squared bifrustum) — can be also observed by MSS at 900 °C in this work (see figure 5.35a, figure 5.35d and figure 5.35e with a magnification reported in figure D.15 in the appendix). It matches the anatase Wulff construction reported in figure 3.2 on page 29. These MSS results clearly establish the potential role of SO₄²⁻ anions in stabilizing the {001} facets of anatase, reported already for hydrothermal synthesis [30]. In MSS the stability range of the anatase phase is extended to ≈ 1000 °C, as can be seen from figure 5.37. The main reflection of anatase at 11.53° is visible for samples with 1 to 15 wt. % of precursor. The signal intensity of the 20 wt. % sample is presumably below the detection limit of the diffractometer.

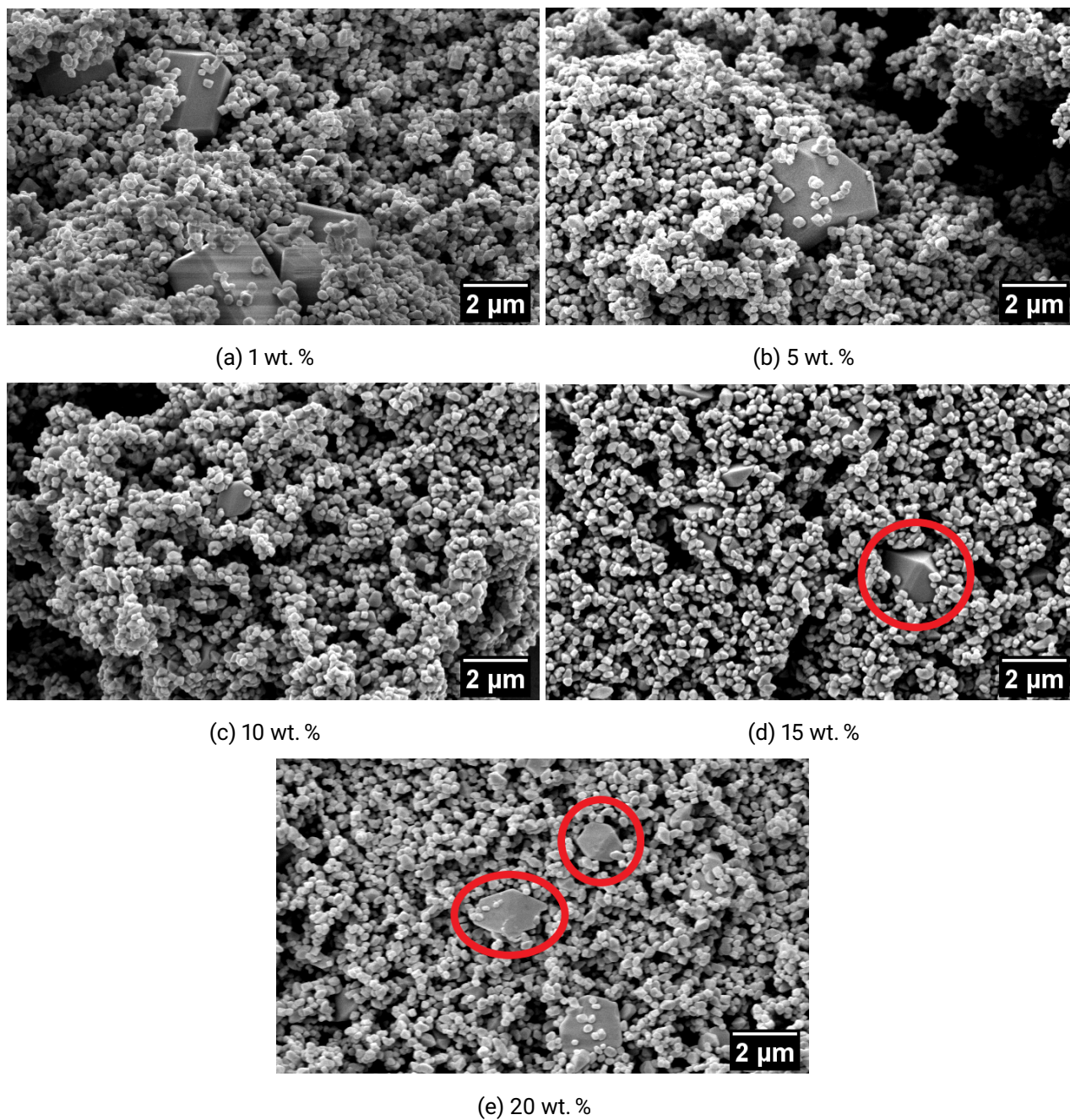


Figure 5.35.: SEM images of TiO_2 particles obtained at $900\text{ }^\circ\text{C}$ and 2 h of holding time: a) 1 wt. %, b) 5 wt. %, c) 10 wt. %, d) 15 wt. %, and e) 20 wt. % of TiO_2 in Na_2SO_4 .

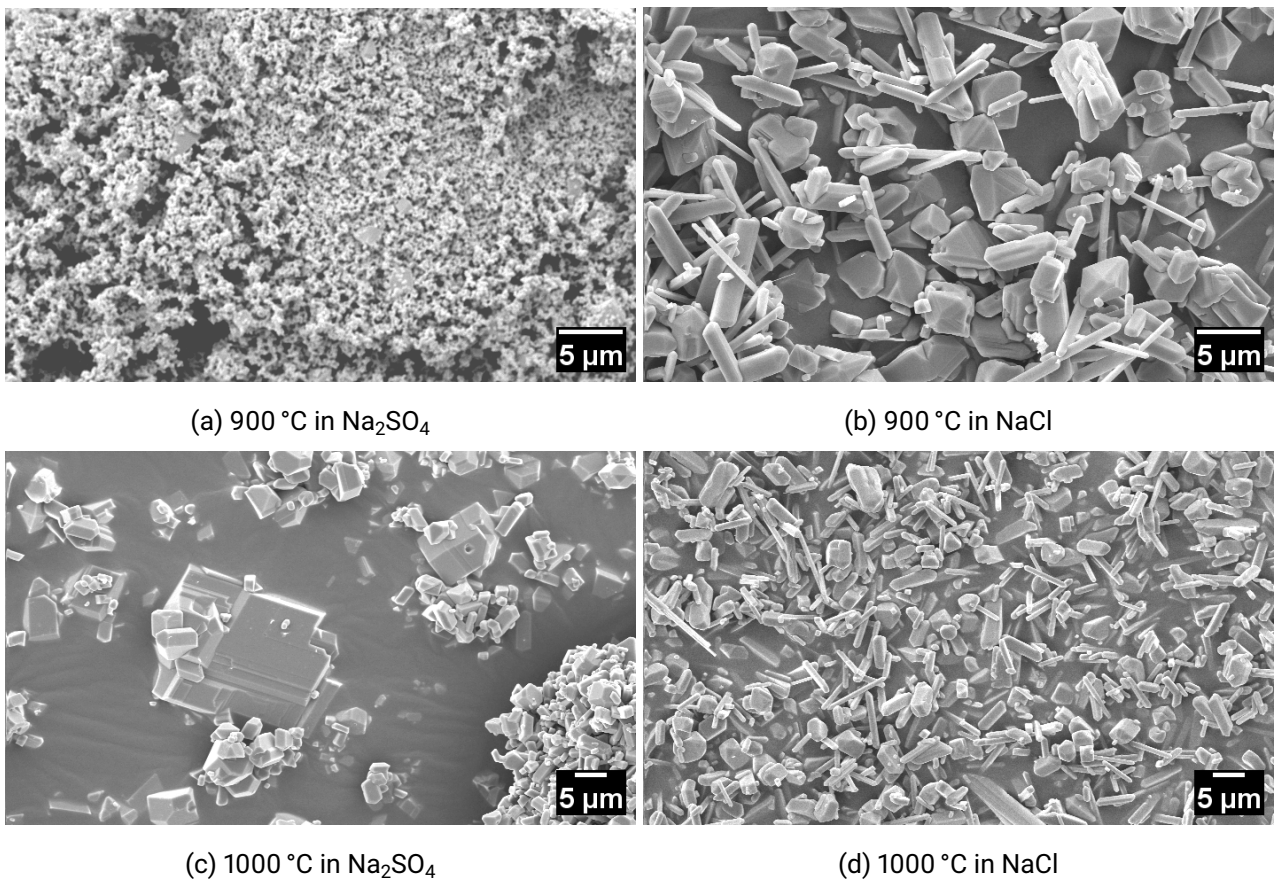


Figure 5.36.: SEM images of TiO₂ particles obtained at 900 °C, 1000 °C and 2 h of holding time with 20 wt. % of precursor in Na₂SO₄ (a and c) and in NaCl (b and d).

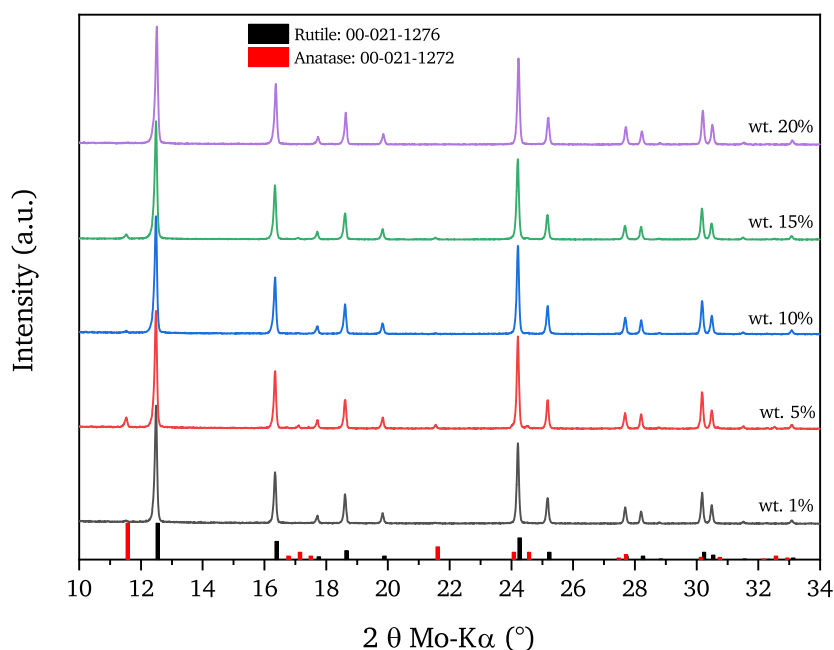


Figure 5.37.: XRD patterns of titania samples obtained by MSS at 1000 °C in Na_2SO_4 with 5 different wt. % of anatase precursor (1%, 5%, 10%, 15% and 20%). Reference XRD patterns from the ICDD for anatase and rutile are given at the bottom of the graph.

Figure 5.38 shows the morphological changes related to the increase of the anatase precursor in the Na_2SO_4 melt at 1000 °C. There is a significantly enhanced crystal growth compared to lower temperatures. The equilibrium shape of rutile — reported in section 3.1.3 (see figure 3.4) — is present in many of the crystals. The higher thermal energy ensures a preferential growth along the $\langle 001 \rangle$ direction. The crystals reach a length $> 5 \mu\text{m}$ (shorter than those achieved in pure NaCl , see figure 5.38b and figure 5.38d). A further increase of the temperature to 1100 °C leads to a complete conversion to rutile and a remarkable increase of the average particle size. All the crystals have lengths $> 5 \mu\text{m}$, no matter of the precursor concentration (see figure C.14 and figure D.16 in the appendix). The habit and the size of the crystals differ, however, within the sample.

5.2.2. TiO_2 crystal growth in Na_2SO_4 - NaCl mixture

5.2.2.1. Na_2SO_4 - NaCl eutectic mixture

MSS was first performed in the eutectic mixture with molar ratio as 0.47 Na_2SO_4 -0.53 NaCl with a melting point of $\approx 625 \text{ °C}$ (see tables 2.3 and 5.6), followed by MSS with higher and lower fractions of NaCl (as listed in table 5.7) in order to analyze the effect of the mixed ions $\text{Cl}^-/\text{SO}_4^{2-}$ on the ART and the habit of titania crystals. For details regarding the phase diagram of NaCl - Na_2SO_4 , see figure B.7 in the appendix (page 204). The concomitant presence of two anion species is not only affecting the ART,

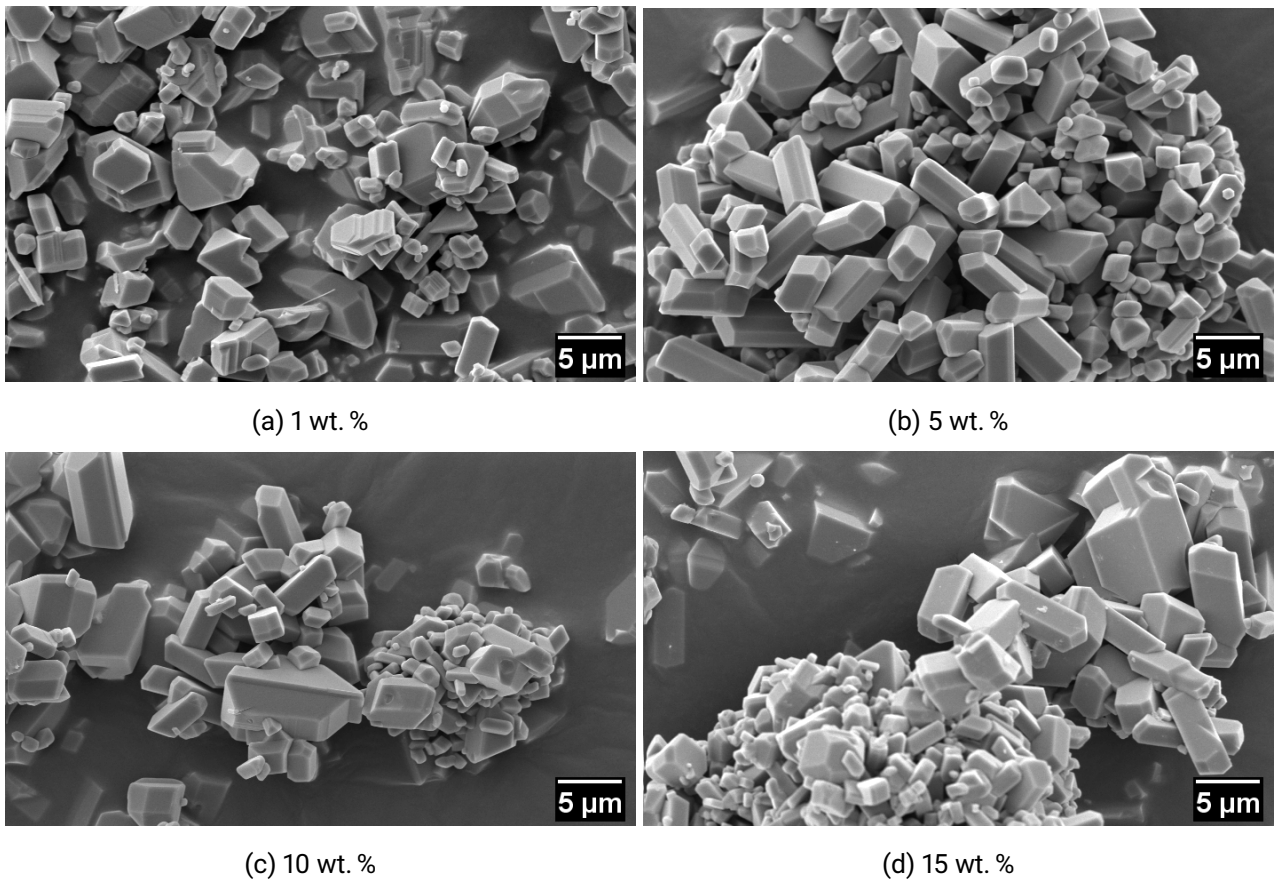


Figure 5.38.: SEM images of TiO₂ particles obtained at 1000 °C and 2 hours of holding time with a) 1 wt. %, b) 5 wt. %, c) 10 wt. % and d) 15 wt. % of anatase precursor in Na₂SO₄.

but also determines the habit of the particles by controlling the surfaces which are activated. All these aspects are discussed in a more comprehensive manner in the next section.

Table 5.6.: Phase composition of samples obtained by DMP in the 0.47 Na₂SO₄-0.53 NaCl eutectic mixture calculated by Rietveld refinement. Synthesis temperature: 900 to 1100 °C and 2 hours holding time.

Temperature [°C]	wt. [%]	TiO ₂ (rutile) [%]	TiO ₂ (anatase) [%]	Residual wR [%]
900	1	92.8	7.2	12.12
900	5	93.7	6.3	8.25
900	10	95.5	4.5	12.43
1000	1	100	0	0
1000	5	100	0	0
1000	10	100	0	0
1100	1	100	0	0
1100	5	100	0	0
1100	10	100	0	0

The binary salt composition has the effect to promote the ART with respect to the sample containing only Na₂SO₄. Figure 5.39 shows the comparison of the XRD patterns obtained from pure NaCl, pure Na₂SO₄ and the eutectic mixture. The result from the eutectic mixture confirms that the ART is enhanced in the presence of Cl⁻, since the main reflection of anatase at 11.53° has a low intensity. At temperatures > 900 °C the ART is complete, as reported in table 5.6. The morphologies of the samples obtained at 900 °C are reported in figure 5.40. The SEM micrographs reveal increased particle dimensions for 1, 5 and 10 wt. %. At the lowest precursor fraction only few particles reach the micron scale (> 5 μm), though being bigger than those obtained in pure Na₂SO₄ flux (> 2 μm). The majority of the crystals is still sized by ≈ 100 nm. The improvement is easier to perceive for 5 and 10 wt. % anatase precursor. Most of the crystals grow to an average size of 5 μm. Small particulates with sizes around 100 nm are in the minority and decrease with increase of the precursor fraction. This direct relation with increasing precursor wt. % can not be observed in a pure Na₂SO₄ flux. Heat-treatment at temperatures higher than 900 °C leads to the formation of only rutile crystals and, accordingly, the habits of the particles changes into rod-shaped crystals. At 1000 °C the particles grown in pure Na₂SO₄ are bigger than those grown in the eutectic mixture (see figure D.17 in the appendix). This is the opposite to what happens at 900 °C. Additionally, small particulates disappear and the average sizes of the crystals increase. The eutectic mixtures with 10 wt. % of precursor promotes the formation of needle-like rutile crystals (see figure D.17d) that reach a length of 10 μm. Figure D.17e and f present the comparison of the MSS performed at 1100 °C in the eutectic mixture and in Na₂SO₄, respectively. The average size of the particles increases in both fluxes in comparison to the 1000 °C samples. However, the habit is more defined in the eutectic mixture. Only very sharp edges are formed in the pure sulfate matrix. As a main result, the comparison between the eutectic mixture and Na₂SO₄ reveals the strongest differences at 900 °C, the lowest temperature investigated.

An *in-situ* XRD characterization up to 850 °C has been performed for the eutectic mixture with 10

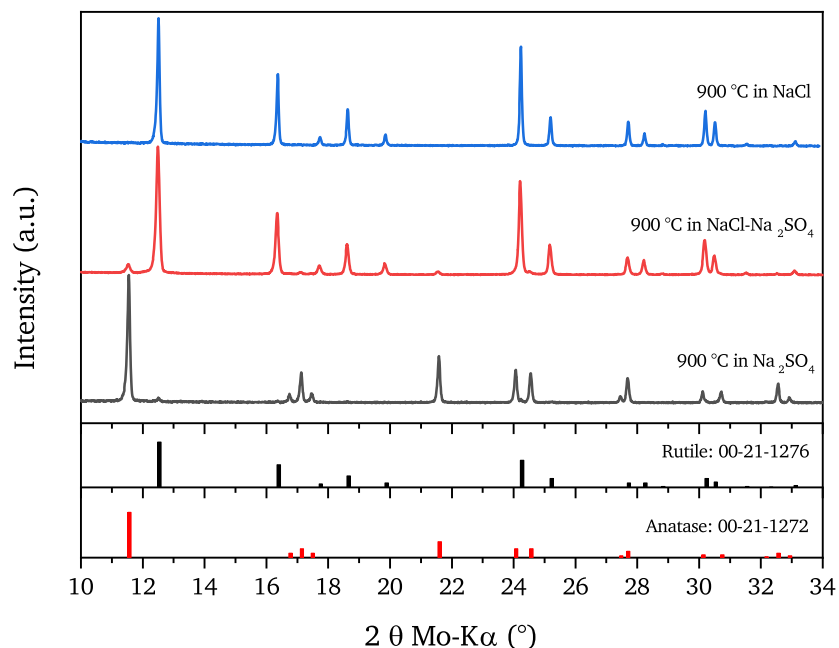


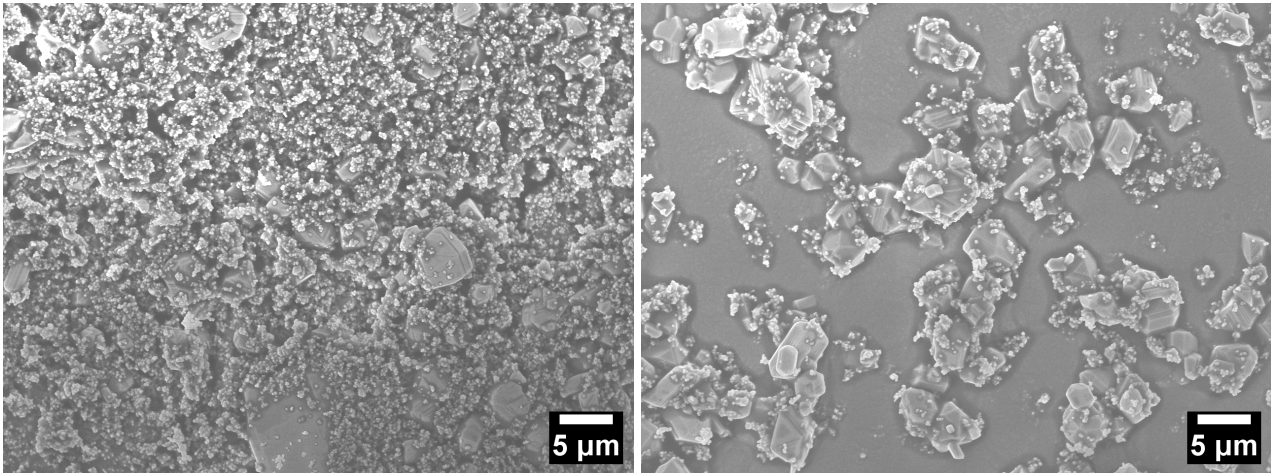
Figure 5.39.: XRD patterns of titania samples obtained by MSS at 900 °C in Na₂SO₄, NaCl and in 0.47 Na₂SO₄-0.53 NaCl with 10 wt. % of precursor. Reference XRD patterns from the ICDD for anatase and rutile are given at the bottom of the graph.

wt. % of anatase precursor (see figure 5.41). The characterization was performed in a quartz capillary.⁵ A partial dissolution of anatase is suggested by the attenuation of its strongest reflection close to the melting point of the eutectic mixture (≈ 625.3 °C, see table 2.3). The ART appears to be independent of the melting point of the salt matrix, since the first reflection belonging to rutile appears at the same temperature found for pure NaCl (at ≈ 710 °C). The Na₂SO₄ reflections (marked with "S") drift to lower angles with temperature due to the dilatation of the lattice, and also show a structural change. This is the phase transition V-I, marked with "SS" at ≈ 243.9 °C [303] that was confirmed from a DTA-TGA performed for pure Na₂SO₄ (see figure 5.84).

5.2.2.2. Effect of non-eutectic Na₂SO₄-NaCl mixtures

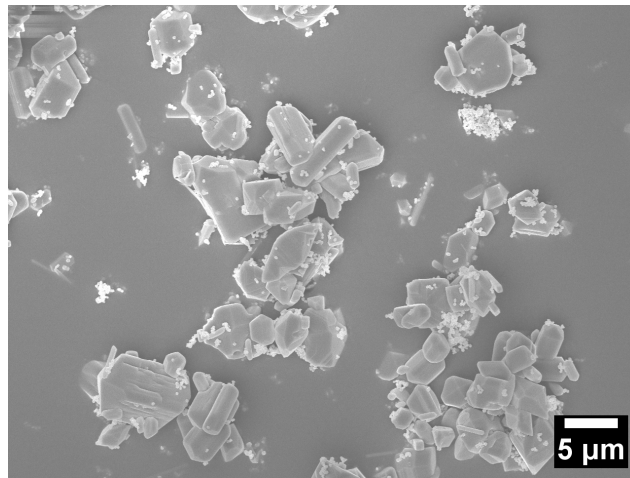
Several other combination of Na₂SO₄-NaCl salts were investigated in order to shed light on the influence of the O²⁻/Cl⁻ ratio — responsible for the basicity of the salt — on the habit formation and the ART. This study was limited to samples heat-treated at 900 °C with 10 wt. % of precursor. Table 5.7 reports the four binary salt mixtures and the results of the Rietveld refinement performed on each diffractogram reported in figure 5.42. Increase of the NaCl weight fraction promotes the ART, since the anatase phase

⁵The X-axis in figure 5.41 is limited to the angular interval containing the main reflections of anatase, rutile and the binary eutectic salt mixture.



(a) 1 wt. %

(b) 5 wt. %



(c) 10 wt. %

Figure 5.40.: SEM images of TiO_2 particles obtained at 900 °C and 2 hours of holding time with a) 1 wt. %, b) 5 wt. % and c) 10 wt. % of TiO_2 in 0.47 Na_2SO_4 -0.53 NaCl .

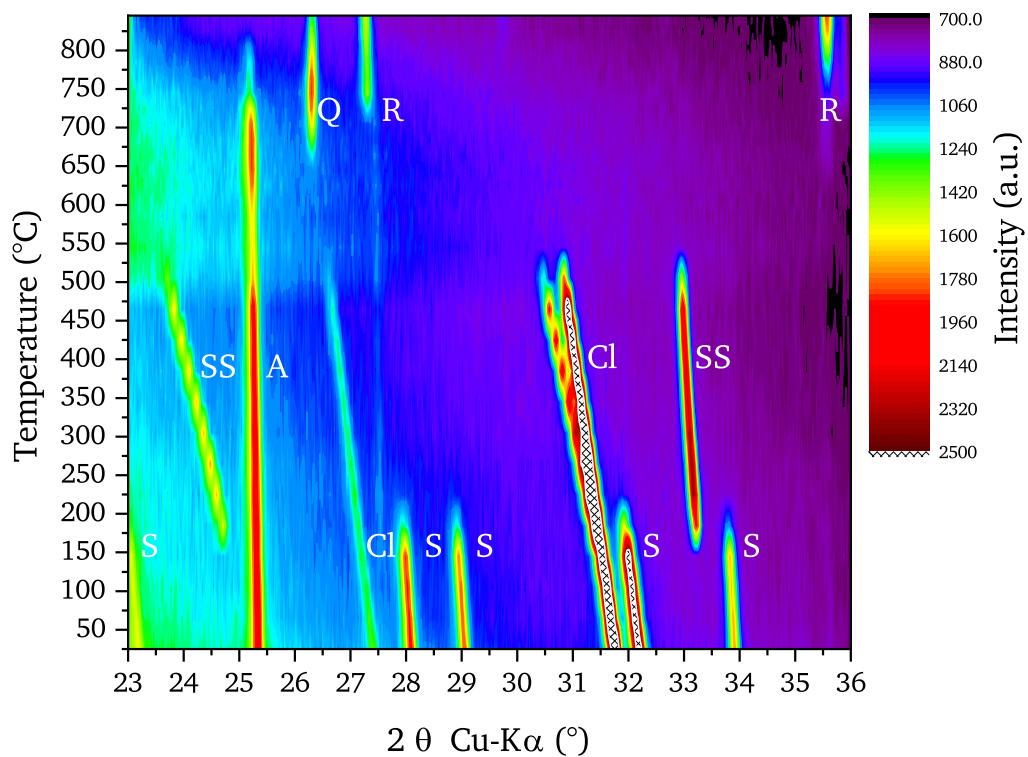


Figure 5.41.: High temperature XRD pattern of 10 wt. % TiO_2 mixed in 0.47 Na_2SO_4 -0.53 NaCl measured *in-situ* (up to 850 °C). Legend: A = anatase; R = rutile; Cl = NaCl ; S = Na_2SO_4 ; SS = Na_2SO_4 V-I; Q = quartz capillary.

decreases (figure 5.42). The impact of the NaCl addition to the salt matrix is evident by comparing the phase composition of pure Na_2SO_4 flux with $0.8 \text{Na}_2\text{SO}_4\text{-}0.2 \text{NaCl}$ flux. In the first case the anatase content is $> 95\%$ while in the second one it is the rutile content being $> 95\%$. The diffractograms differs slightly and the most remarkable feature is the fact that the sample $0.2 \text{Na}_2\text{SO}_4\text{-}0.8 \text{NaCl}$ reports the highest rutile fraction among all the samples.

Table 5.7.: Phase composition of samples obtained by MSS in $\text{NaCl-Na}_2\text{SO}_4$ mixtures by DMP calculated by Rietveld refinement. Synthesis temperature: 900 to 1100 °C and 2 hours holding time.

Temperature [°C]	Salt combination mol %	$\approx T_m$ [°C]	wt. [%]	TiO_2 (rutile) [%]	TiO_2 (anatase) [%]	Residual wR [%]
900	$0.8 \text{Na}_2\text{SO}_4\text{-}0.2 \text{NaCl}$	785	10	95.6	4.4	12.6
900	$0.6 \text{Na}_2\text{SO}_4\text{-}0.4 \text{NaCl}$	689	10	98	2	10.1
900	$0.4 \text{Na}_2\text{SO}_4\text{-}0.6 \text{NaCl}$	652	10	98.2	1.8	9.6
900	$0.2 \text{Na}_2\text{SO}_4\text{-}0.8 \text{NaCl}$	728	10	98	2	13.5

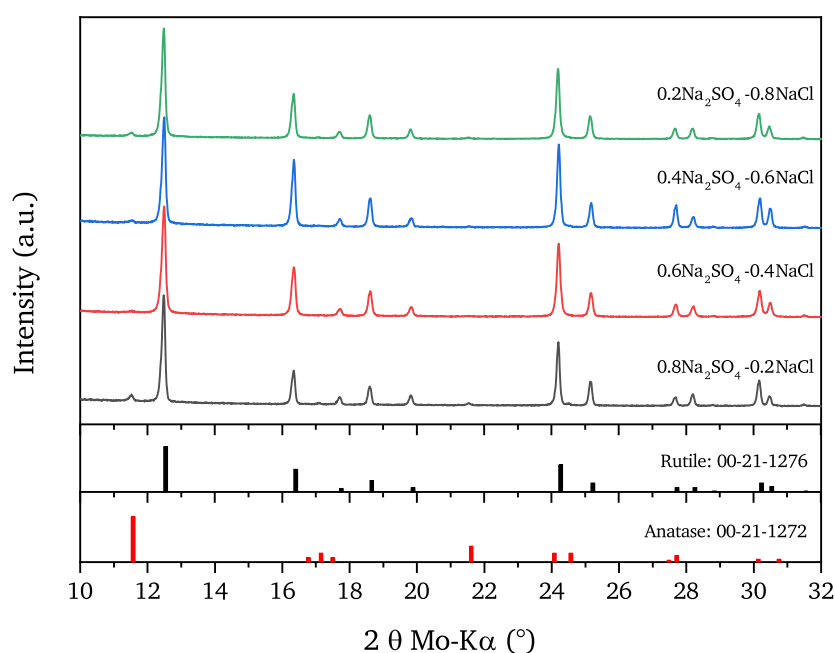


Figure 5.42.: XRD patterns of titania samples obtained by MSS at 900 °C in 4 different $\text{Na}_2\text{SO}_4\text{-NaCl}$ combinations with 10 wt. % of precursor. Reference XRD patterns from the ICDD for anatase and rutile are given at the bottom of the graph.

The strong impact of the Cl^- concentration in the MSS is clearly demonstrated by the morphology change seen in the different $\text{Na}_2\text{SO}_4\text{-NaCl}$ binary salt combinations (see figure 5.43). The SEM graphs provide an important information: the habit of the particles is mainly determined by the Cl^- concentration but not with the synthesis temperature, considering that the melting points of $0.8 \text{Na}_2\text{SO}_4\text{-}0.2 \text{NaCl}$ and of $0.2 \text{Na}_2\text{SO}_4\text{-}0.8 \text{NaCl}$ are quite close. A magnification of the SEM micrographs is given in figure

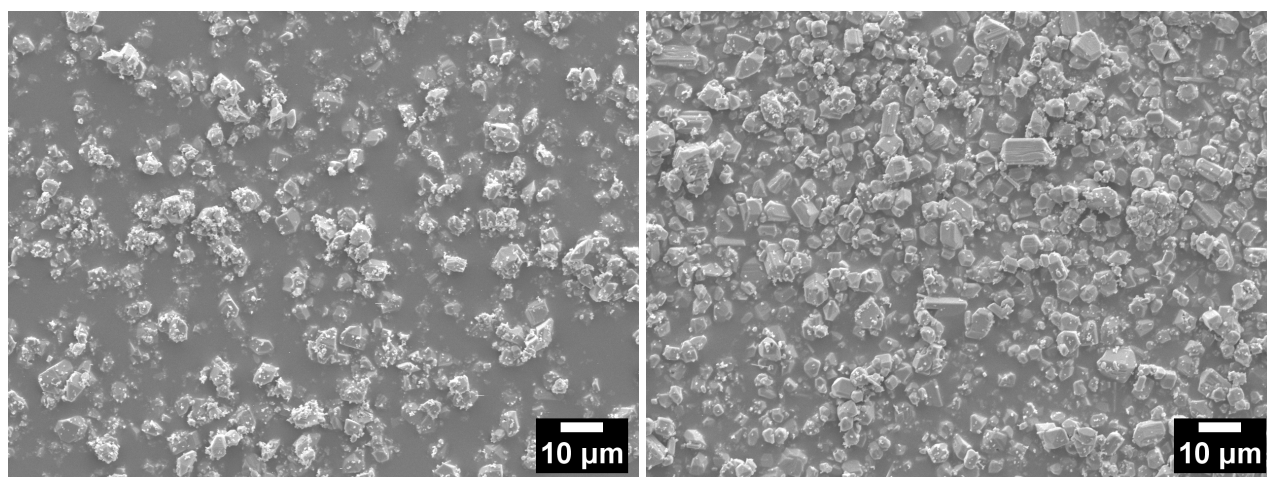
D.18 in the appendix (see page 234). This observation is also valid for 0.6 Na₂SO₄-0.4 NaCl and 0.4 Na₂SO₄-0.6 NaCl. The sample synthesized in Na₂SO₄ (see figure 5.35c) mainly forms anatase crystals with limited dimensions (150 nm - 300 nm). In the 0.8 Na₂SO₄-0.2 NaCl sample the trend is completely reversed, forming mainly rutile crystals with size > 2 μm. Further addition of NaCl increase the average dimensions of the particles (see figure 5.43b), but the most striking changes appear for NaCl fractions ≥ 0.6. Rod-shaped crystals starts to appear at this concentration, indicating that now the Cl⁻ preferentially interacts with the surfaces of the growing rutile crystals. Figure 5.43d shows rod-shaped crystals with a length of ≈ 10 μm. At a NaCl fraction of 0.8 the formation of rod-shaped crystals with lengths ≥ 20 μm occurs. The observed habits highlight the impact of the O²⁻/Cl⁻ ratio on the growth of rutile. The sulfate system creates an acid-base equilibrium regulated by the oxyanion SO₄²⁻. The pO²⁻ of the salt decreases and the mixture becomes more acidic, by increasing the concentration of NaCl in the mixture. Accordingly, the ART is sped-up by higher oxygen vacancy formation in the TiO₂ lattice [296, 304]. This promotes the anisotropic growth of rutile in NaCl. Additionally, halide fluxes are notoriously not so suitable to solvate O²⁻ as oxysulfates [97]. The fact that the transformation is slower in Na₂SO₄ than in NaCl is related to the presence of SO₄²⁻ that limits the formation of oxygen vacancies and results in the dissolution of anatase in form of TiO₃²⁻ [39, 301]. The rising NaCl concentration in the Na₂SO₄ attenuates this effect, paving the way for a faster ART and a more anisotropic growth of crystals.

5.2.3. NaF addition to Na₂SO₄

The addition of NaF in NaCl flux (see section 5.1.2.2 on page 66) causes a substantial morphology change of rutile crystals. This study also gives new insights into the significance of F⁻ for the ART and the habit of the crystals synthesized in a sulfate melt (see phase diagram in figure B.8 on page 205 in the appendix).

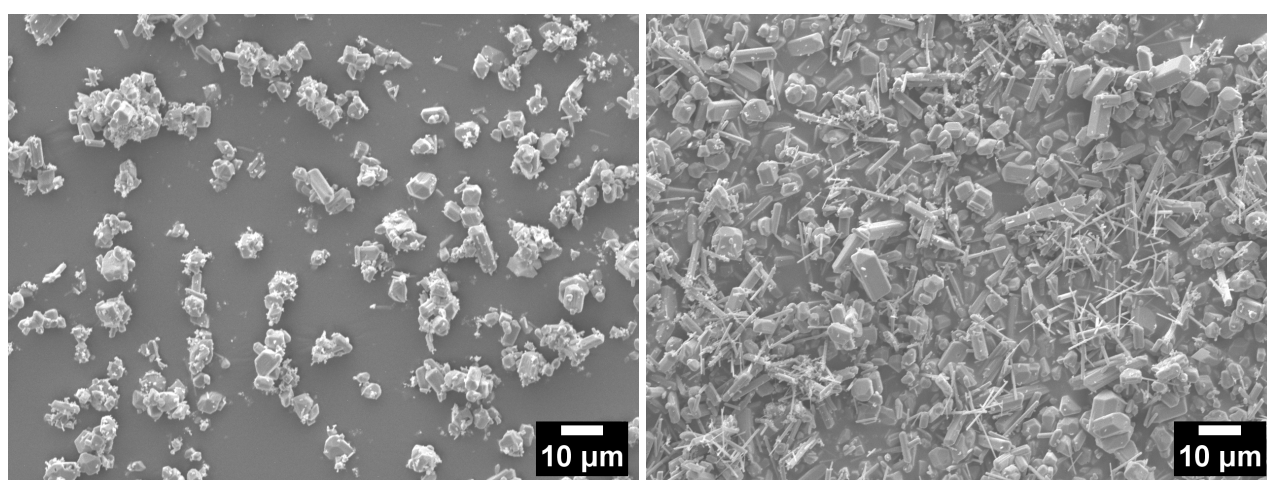
The study was performed by heat-treating 10 wt. % of anatase precursor at 1100 °C in Na₂SO₄ with different concentrations of F⁻. The XRD results in figure 5.44 reveal the structural changes with increasing NaF concentration. For NaF concentration ≤ 5 mol% there is only rutile forming. For concentrations ≥ 10 mol% the NTO phase appears together with rutile. The X-ray line at 21.79° in figure 5.44 belongs to the NTO phase. It grows in intensity by increasing the F⁻ concentration. Another result concerns the rutile phase: two couples of reflections are changing their ratio when increasing the F⁻ concentration. The intensity of the (310) plane is lower than that of the (002) plane for an F⁻ concentration of 0.1 mol%. The intensity difference decreases for [F⁻] = 0.5 mol% till the (310) plane dominates for higher F⁻ concentrations. The same behavior is observed for the (301) with respect to the (112) plane. These changes of the intensity ratios are also seen in NaCl-NaF (see section 5.1.2.2 on page 66) highlighting the habit change caused by the presence of fluorine anions.

The SEM micrographs in figure 5.45 prove the F⁻ effect on the formation of titania crystals. Magnification of the 0.5 mol% NaF micrographs (see figure 5.46b) reveals that the surface of the crystals is not smooth as in the absence of NaF, but reports a slight roughness that is caused by the interaction of



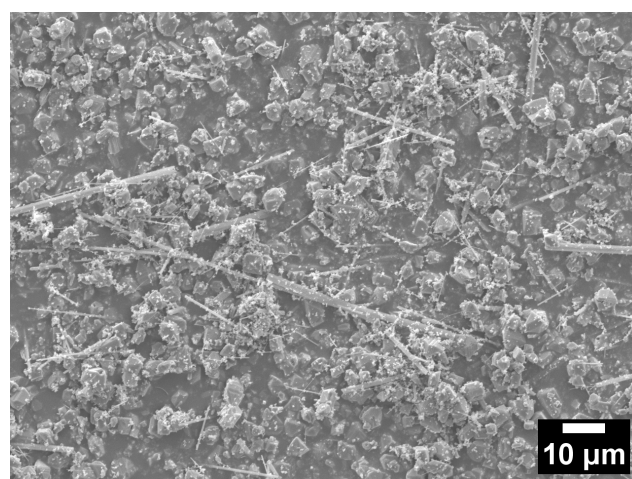
(a) 0.2 NaCl-0.8 Na₂SO₄

(b) 0.4 NaCl-0.6 Na₂SO₄



(c) eutectic 0.53 NaCl-0.47 Na₂SO₄

(d) 0.6 NaCl-0.4 Na₂SO₄



(e) 0.8 NaCl-0.2 Na₂SO₄

Figure 5.43.: SEM images of TiO₂ particles obtained at 900 °C and 2 hours of holding time with 10 wt. % of TiO₂ in: a) 0.2 NaCl-0.8 Na₂SO₄, b) 0.4 NaCl-0.6 Na₂SO₄, c) 0.53 NaCl-0.47 Na₂SO₄, d) 0.6 NaCl-0.4 Na₂SO₄ and e) 0.8 NaCl-0.2 Na₂SO₄.

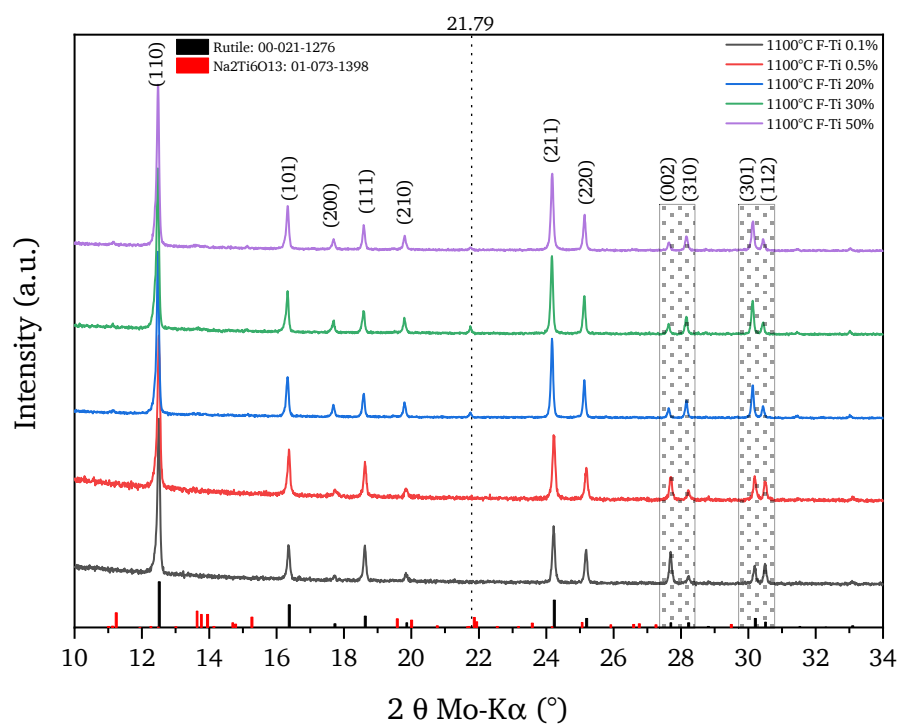


Figure 5.44.: XRD patterns of titania samples obtained by MSS at 1100 °C in Na_2SO_4 , with different moles of NaF added. The precursor amount is 10 wt. %. Reference XRD patterns from the ICDD for $\text{Na}_2\text{Ti}_6\text{O}_{13}$ and rutile are given at the bottom of the graph.

F^- with dangling Ti bonds present on the growing surfaces of the rutile crystals. The first remarkable changes of the habit are visible for the NaF sample with ≥ 5 mol % (figure 5.45c). The crystals start to be shorter — they do not overpass a maximum of $5 \mu\text{m}$ — and develop additional facets that were hidden for lower NaF mol %. The 001 facets, having the highest surface energy of rutile, are no more the privileged growth area. The crystals do not develop along the $\langle 001 \rangle$ direction, since F^- decreases the 001 surface energy, allowing for the formation of new habits. A comparison with the samples obtained at 1100°C in pure Na_2SO_4 (see figure D.16 in the appendix) highlights the role of F^- : additional faces are exposed in the presence of F^- (see figure 5.46 and for comparison figure 5.45). Figure 5.46c and figure 5.46d report the terraced growth, a feature which is also observed for the addition of NaF to NaCl (see figure 5.12 on page 68 and figure D.5 in the appendix on page 224). For the samples heat-treated in NaCl at 1100°C (see figure 5.13) the terraced growth is not visible anymore. Therefore, the interaction of the F^- ions with the rutile lattice is the same independently from the flux used for the synthesis. Only the temperature of the treatment appears to be decisive. For concentrations ≥ 10 mol % NaF the formation of few NTO rods is promoted. The anisotropic habit is clearly visible among the rutile particles (see figure 5.45d, figure 5.45e and figure 5.45f). Additionally, a broadening of the rod-shaped NTO crystals occurs for a concentration ≥ 20 NaF mol %, reaching a width of $\approx 10 \mu\text{m}$ (figure 5.45e and figure 5.45f). Their lengths are $\geq 50 \mu\text{m}$ (see figure D.19 in the appendix). In the case of sulfates, the formation of NTO can be explained by the presence of an intermediate step leading to the TiO_3^{2-} anion, which is the main difference from the MSS in NaCl.

5.2.4. Influence of the oxygen partial pressure on the crystal growth in Na_2SO_4

The impact of the oxygen partial pressure on the MSS has already been presented for the NaCl flux in section 5.1.4 on page 77. In the following the results of similar experiments under argon and pure oxygen are described for Na_2SO_4 .

MSS in Na_2SO_4 under argon atmosphere The X-ray diffractograms of the samples heat-treated at 900°C in Na_2SO_4 at a reduced oxygen partial pressure are plotted in figure 5.47 together with those of NaCl for comparison. The main reflection of the anatase phase has a much stronger intensity for the samples synthesized in Na_2SO_4 . Accordingly, the oxysulfate melt is not promoting the ART with the same intensity as the chloridic one. However, the ratio of the main reflections of the two phases is almost equal to one for the Na_2SO_4 sample heat-treated under argon, revealing the formation of a higher phase fraction of rutile. It has also been observed that the NTO formation is hindered at a reduced $p\text{O}_2$.

Figure 5.48 shows the difference in the habits of the particles formed in Na_2SO_4 under argon and under ambient condition. They reveal a slight decrease of the average size of the nanoparticles under argon flow (on average 200 nm compared to 350 nm under ambient atmosphere). In addition to this, the crystals reaching the micro-size have larger dimensions and some of them also reveal terraced-growth on particles with a side length of $\approx 5 \mu\text{m}$ (marked with a red circle). The crystal growth in Na_2SO_4 is

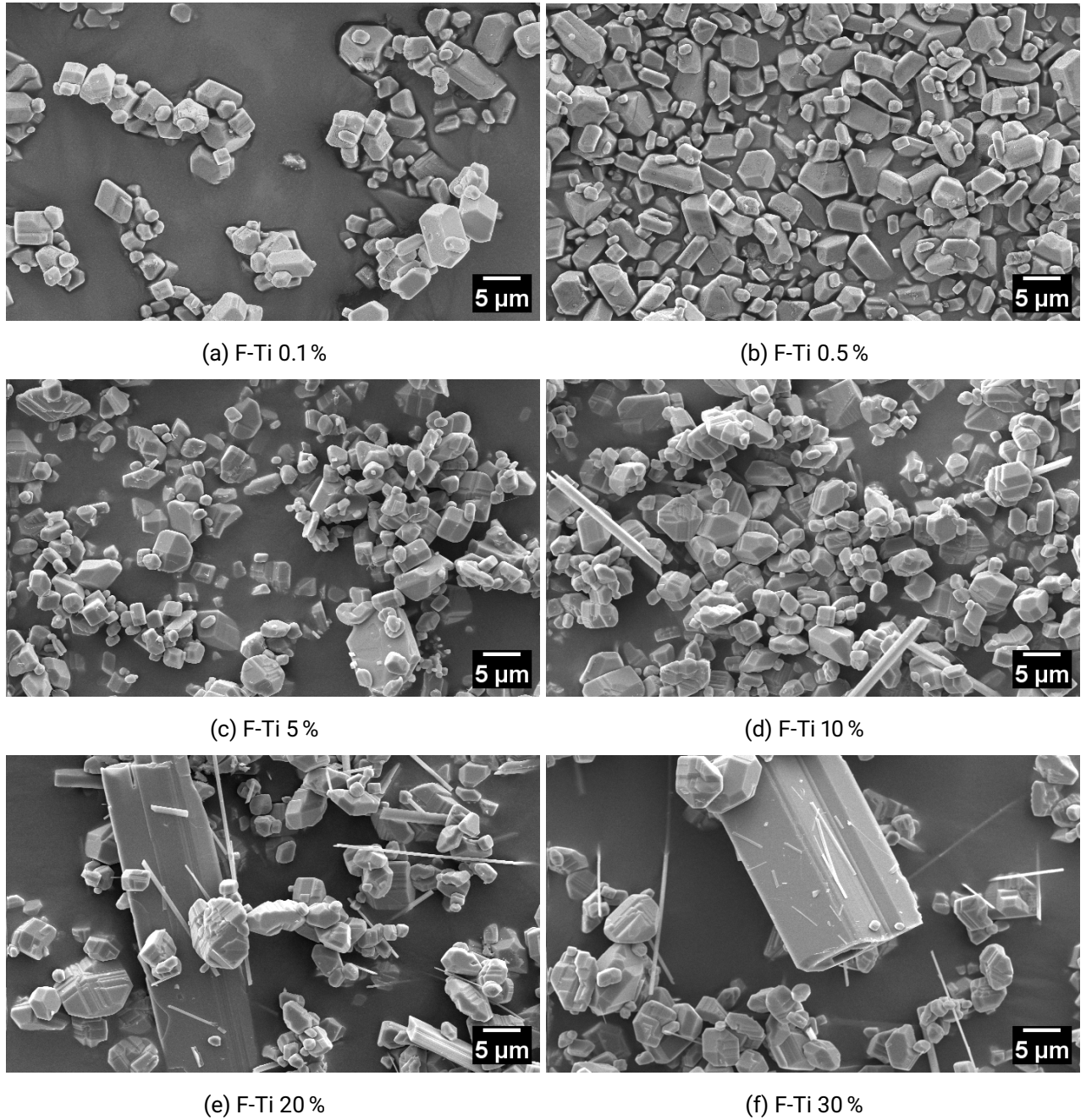


Figure 5.45.: SEM images of TiO₂ particles obtained at 1100 °C and 2 h of holding time, 10 wt. % of TiO₂ with: a) 0.1 NaF mol %, b) 0.5 NaF mol %, c) 5 NaF mol %, d) 10 NaF mol %, e) 20 NaF mol % and f) 30 NaF mol %.

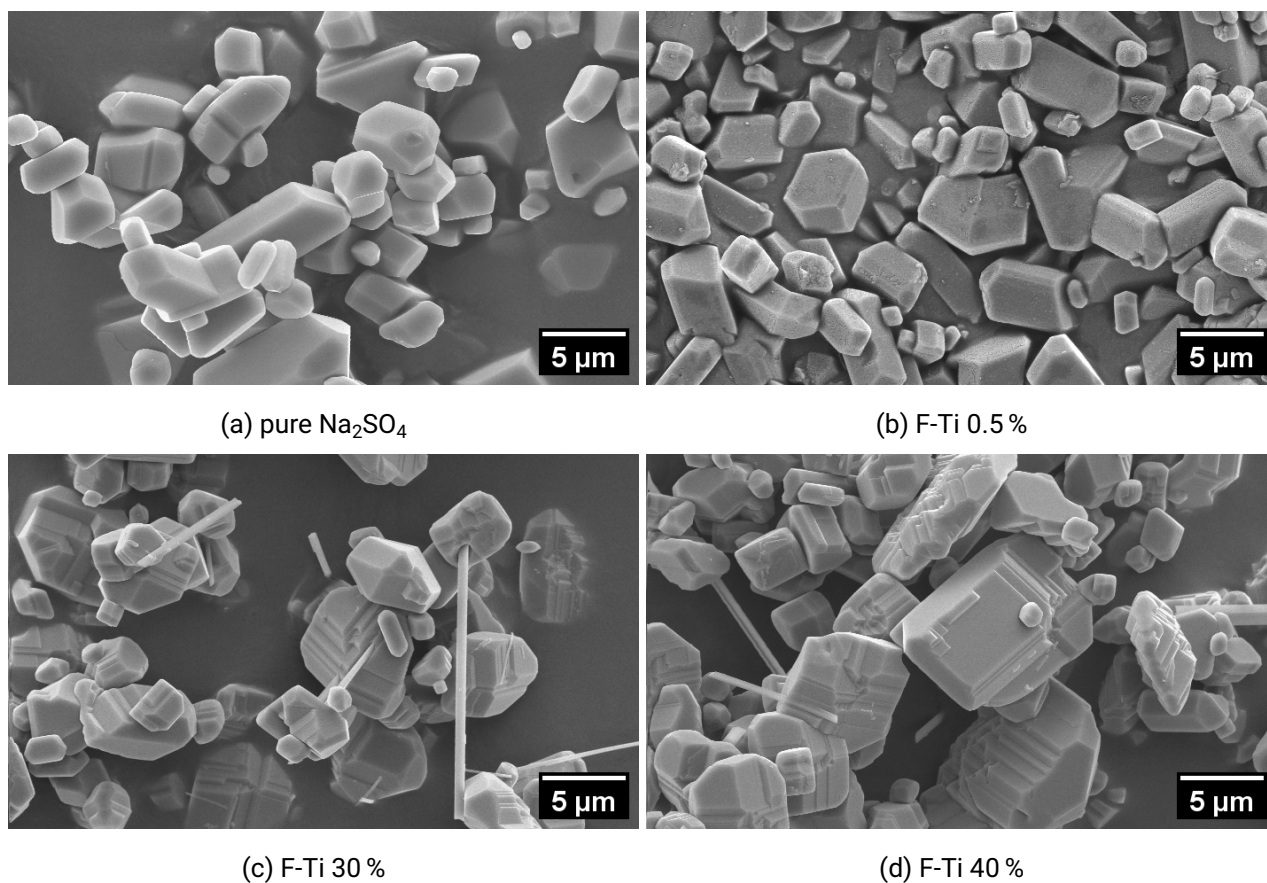


Figure 5.46.: SEM images showing the comparison between a) TiO₂ particles obtained in Na₂SO₄ at 1100 °C, 2 h of holding time and 10 wt. % of anatase precursor and those with the addition of b) 0.5 NaF mol %, c) 30 NaF mol % and d) 40 NaF mol %.

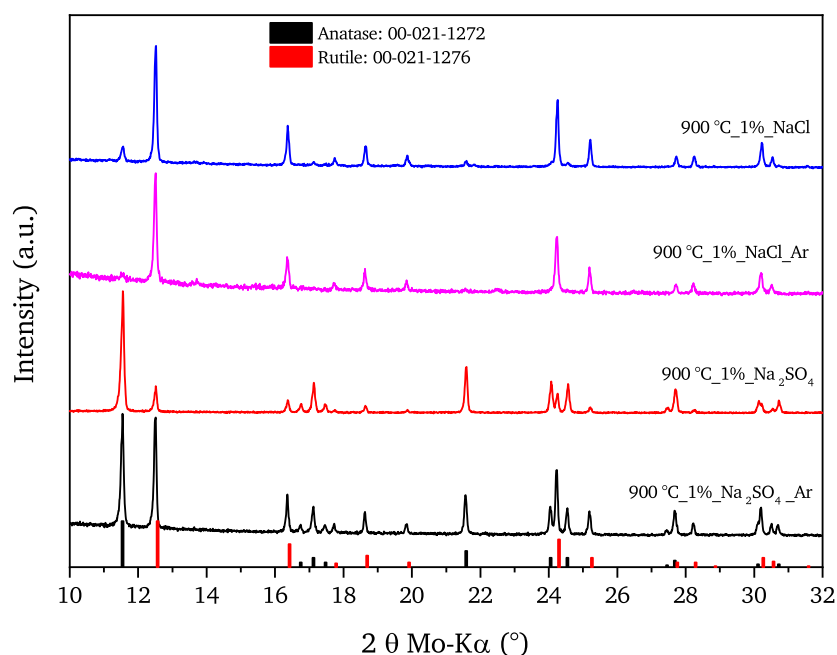
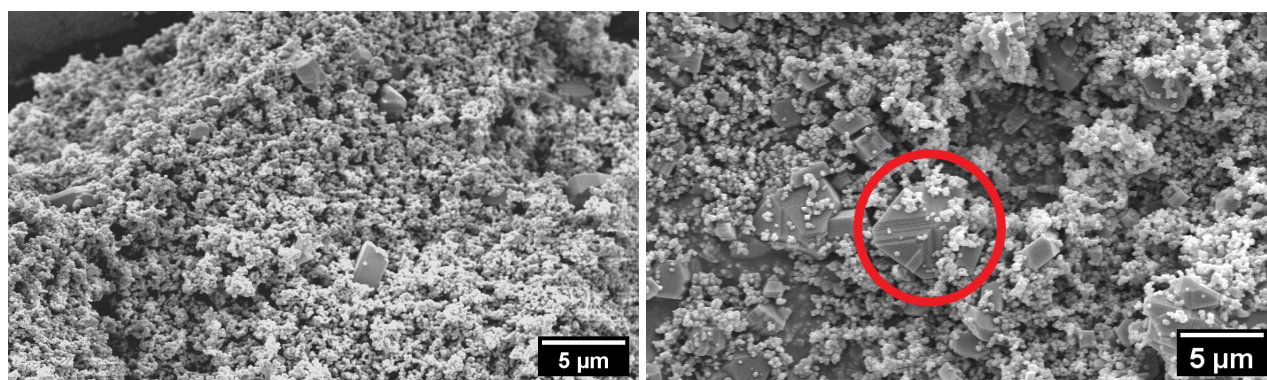


Figure 5.47.: Comparison between samples heat-treated under ambient atmosphere and under argon at 900 °C with 1 wt. % anatase precursor in Na₂SO₄ and NaCl. Reference XRD patterns from the ICDD for anatase and rutile are given at the bottom of the graph.

limited, since most of the small particles do not exceed 500 nm, different from those growing in NaCl that reach $\approx 5 \mu\text{m}$ (see figure 5.24 on page 81).

MSS in Na₂SO₄ under oxygen atmosphere The experiment under O₂ flow was performed at 1100 °C, where the ART is complete, in order to investigate the effect of the oxygen on the rutile habit. The same temperature was also chosen for the investigation in NaCl flux (see figure 5.26). The O₂ flow sets the limit for the solubility of the oxide in the melt. The Na₂SO₄ flux is already providing an environment where the acid-base equilibrium is regulated by the SO₄²⁻ ion (see section 2.3.4 and 2.3.5, equation 2.32), and the basicity is enhanced by the atmosphere with higher partial pressure [159]. Figure 5.49 shows the overlapped diffractograms of the Na₂SO₄ samples obtained in air and oxygen. Both only reveal the presence of the rutile phase. However, as already observed in the study performed in NaCl (see figure C.13), all the rutile reflections corresponding to planes with Miller index $l \neq 0$ show a remarkable intensity decrease under O₂ treatment. This indicates a different growth of the crystal planes. Figure 5.50 reports SEM micrographs of the samples obtained under the two different atmospheres. Red circles mark high-energy facets. For this reason, these crystals assume the habit of a truncated bipyramid, which are not visible in the sample obtained under atmospheric conditions, where many crystals grow along the $\langle 001 \rangle$ direction assuming the rod-shape. Additionally, the SEM micrographs of the crystals grown under higher oxygen partial pressure reveal a narrow distribution of the habits. Comparing the morphologies presented here with those obtained from a NaCl flux (see figure 5.26), a similar change



(a) 900 °C, 1 wt. % under ambient atmosphere

(b) 900 °C, 1 wt. % under argon

Figure 5.48.: SEM images of TiO_2 particles obtained at 900 °C and 2 h of holding time with 1 wt. % of TiO_2 in Na_2SO_4 under: a) ambient atmosphere and b) argon. The terraced growth is highlighted by a red circle.

of the habit is retrieved by heat-treatment under O_2 flow. Another important aspect to mention is the absence of the NTO formation, which on the contrary is present in the samples obtained in NaCl under atmospheric conditions.

5.2.5. Addition of B_2O_3 to the Na_2SO_4 flux

The experiments with B_2O_3 in Na_2SO_4 flux were conducted at 1000 °C and 1100 °C where the transformation into rutile is complete. The addition of 0.1, 0.5, 0.8 and 1.2 mol % of B_2O_3 was investigated for 10 wt. % of anatase precursor in Na_2SO_4 . The diffractograms of all the samples can be found in the appendix (see figures C.15 and C.16 on page 215). Figure 5.51 shows the comparison between the diffractograms of the samples with 0.8 and 1.2 mol % B_2O_3 and the reference sample without B_2O_3 at 1100 °C. All the samples show only the formation of the rutile phase. The diffractograms normalized to the (110) reflection reveal a decrease of the intensities of (101), (211) and (301) with increasing B_2O_3 content. On the contrary, the intensity of the (002) reflection increases by adding B_2O_3 .

Figure 5.52 shows the morphological changes obtained by the addition of 0.5, 0.8 and 1.2 mol % B_2O_3 . The surfaces become rough and at the same time, the sharp edges typical of the rutile crystals get more rounded with the increasing amount of B_2O_3 . An enlarged view of the crystal surfaces is presented in figure D.20 in the appendix. The results for $\text{Na}_2\text{SO}_4/\text{B}_2\text{O}_3$ differ strongly from those of $\text{NaCl}/\text{B}_2\text{O}_3$ (see section 5.1.5 on page 82), where a pronounced preferential growth of the rutile crystals along the [001] direction occurs leading to rod-shaped crystals (see figure 5.28). The presence of the B_2O_3 increases the acidity of the melt according to the chemical reaction described in equation 5.4 (see section 5.1.5 on page 82. This mechanism is developing in an oxysulfate melt and leads thus to different results.

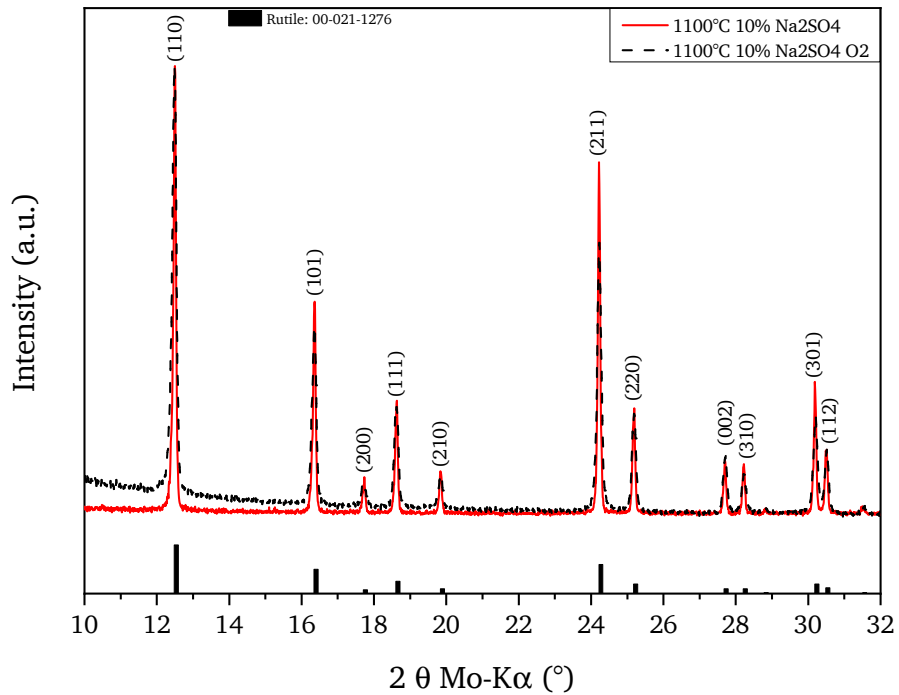
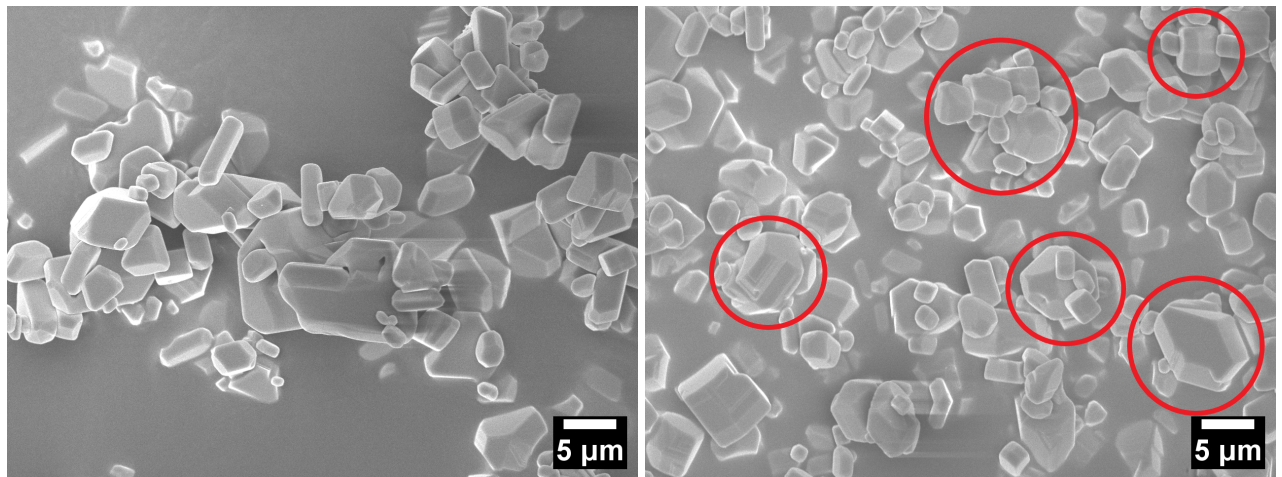


Figure 5.49.: Comparison between samples heat-treated under ambient atmosphere and under O₂ flow at 1100 °C with 10 wt. % anatase precursor in Na₂SO₄. Reference XRD pattern from the ICDD for rutile is given at the bottom of the graph.



(a) 1100 °C, 10 wt. % under ambient atmosphere

(b) 1100 °C, 10 wt. % under O₂ flow

Figure 5.50.: SEM images of TiO₂ particles obtained at 1100 °C and 2 h of holding time in Na₂SO₄ with 10 wt. % of TiO₂ under: a) ambient atmosphere and b) O₂ flow (red circles: truncated bipyramid habit).

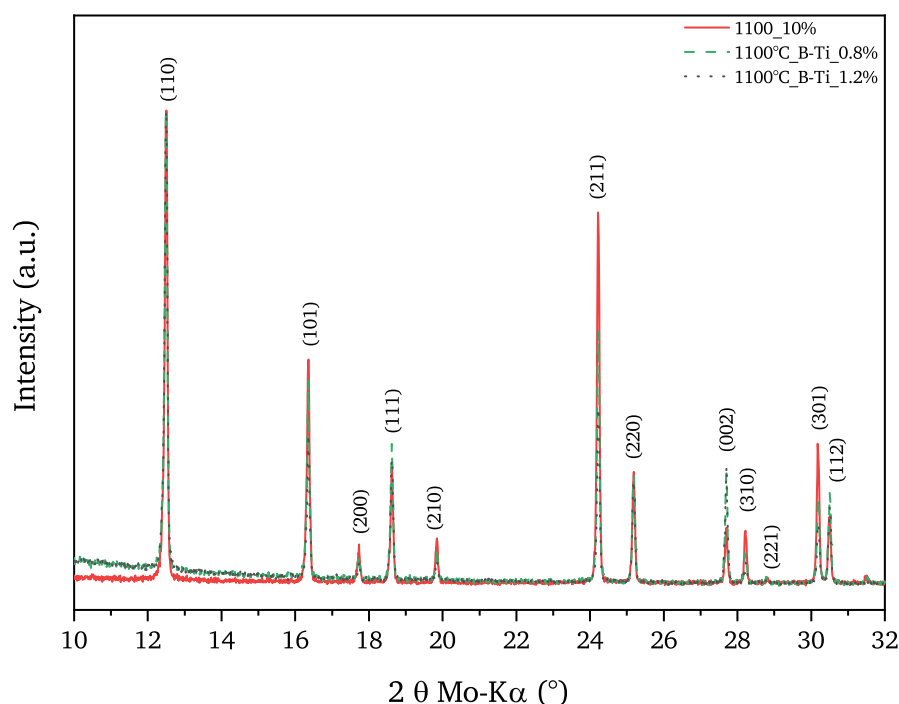


Figure 5.51.: Comparison between samples heat-treated at 1100 °C with 10 wt. % anatase precursor in Na_2SO_4 (red solid line) and the addition of 0.8 (green dashed line) and 1.2 mol % (black dotted line) of B_2O_3 to Na_2SO_4 .

5.2.6. Wet chemical precursor preparation for molten salt synthesis in sulfates

This section reports the results of wet chemical precursor preparation (WCP) and subsequent MSS in a sulfate based flux. The synthesis steps are identical to those presented in section 5.1.6 with TiCl_4 as precursor (for the experimental details see chapter 4, section 4.1.2 on page 48). Only the TiCl_4 precursor is replaced by TiOSO_4 and Na_2SO_4 is chosen as salt matrix. The experiments have been done in order to allow a comparison of the influence of the salt species in the MSS.

5.2.6.1. Wet chemical preparation with TiOSO_4 precursor

Figure 5.53 shows the phase composition of three samples obtained by WCP with ≈ 10 wt. % TiOSO_4 precursor and heat-treatment between 1000 and 1200 °C in Na_2SO_4 . The formation of NTO besides rutile is detected already at 1000 °C and the presence of both phases is confirmed for all applied temperatures (see table 5.8). A comparison with the WCP using TiCl_4 (see table 5.4 on page 86) shows that TiOSO_4 promotes the formation of NTO.

The presence of NTO and the absence of anatase obviously leads to the formation of different crystal habits compared to those achieved by DMP (see figure 5.37 on page 96). The SEM micrographs in figure 5.54 mainly show the formation of rod-shaped crystals and few small particulates. The average

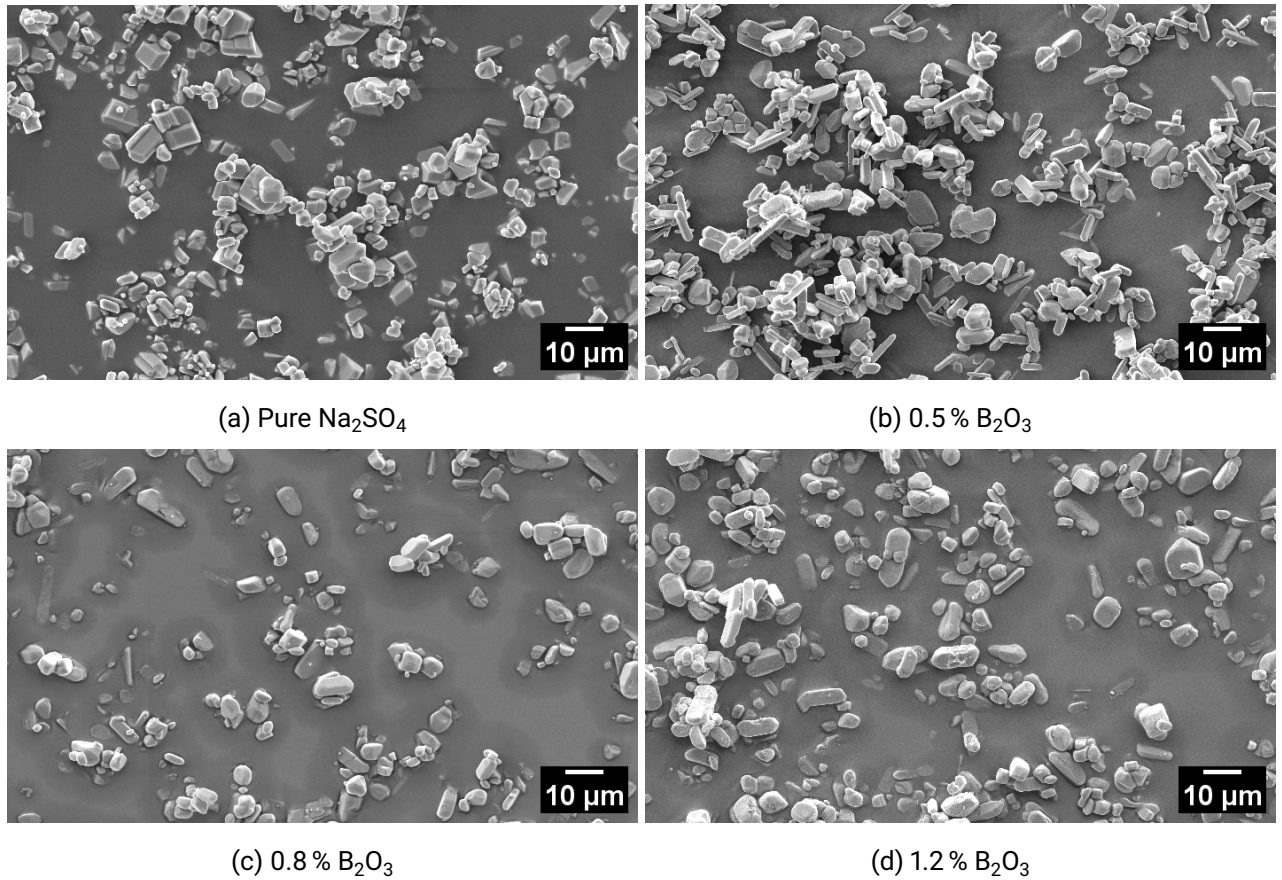


Figure 5.52.: SEM images showing the comparison between TiO₂ particles obtained at 1100 °C and 2 h of holding time, 10 wt. % of TiO₂ with: a) any B₂O₃, b) 0.5 B₂O₃ mol %, c) 0.8 B₂O₃ mol % and d) 1.2 B₂O₃ mol %.

Table 5.8.: Phase composition of samples obtained by WCP at 60 °C in Na₂SO₄ with TiOSO₄ precursor. Synthesis temperature: 1000 to 1200 °C and 2 hours holding time (A = Anatase, R = Rutile, NTO = Na₂Ti₆O₁₃).

TiOSO ₄ Precursor wt. %	850 °C	900 °C	1000 °C	1100 °C	1200 °C
10	-	-	R, NTO	R, NTO	R, NTO
5	A, R, NTO	R, NTO	R, NTO	R, NTO	-

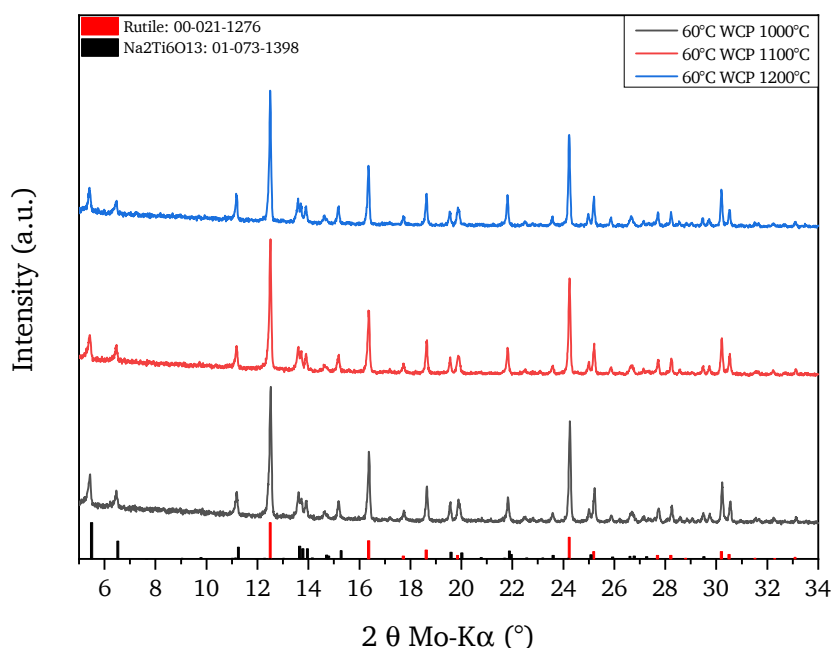
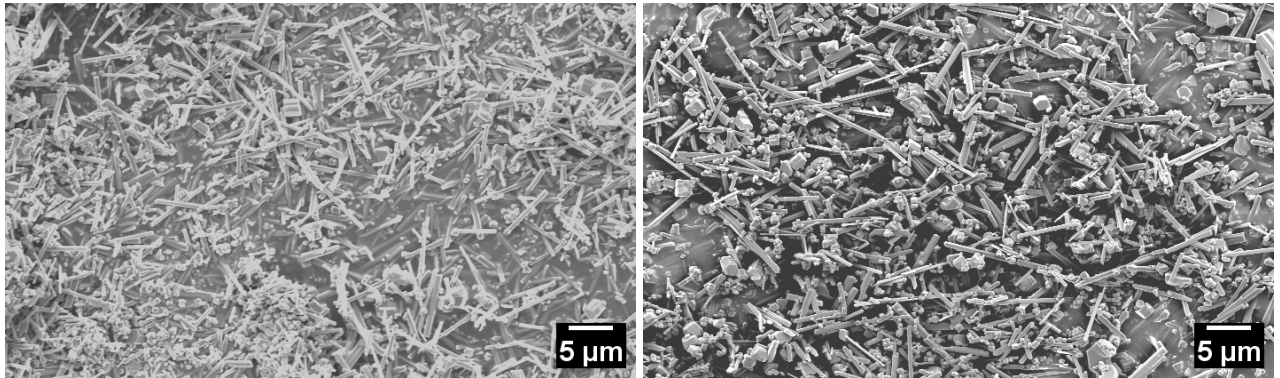


Figure 5.53.: XRD of samples obtained by WCP performed at 60 °C with 10 wt. % TiOSO_4 precursor heat-treated at 1000 °C, 1100 °C and 1200 °C. Reference XRD patterns from the ICDD for $\text{Na}_2\text{Ti}_6\text{O}_{13}$ and rutile are given at the bottom of the graph.

rods length is $\leq 5 \mu\text{m}$, their diameter $\approx 500 \text{ nm}$. The size of the particulates is on the average $\geq 500 \text{ nm}$. There exists a strong difference for the samples obtained by DMP in Na_2SO_4 (see figure 5.38 on page 97, section 5.2.1), since these mainly contain thicker and bulkier rutile crystals (the rods have lengths ranging from 5 to 10 μm and diameters of 2 to 3 μm). The same trend is observed for the samples heat-treated at 1100 °C (see for comparison figure D.16 in the appendix).

The impact of the precursor content on the crystallization process was investigated by decreasing the TiOSO_4 precursor content to 5 wt. %. Figure 5.55 shows the phase composition of four samples obtained by heat-treatments between 850 and 1100 °C in Na_2SO_4 . A precursor content $< 10 \text{ wt. } \%$ causes an increase of the NTO phase fraction with respect to the (decreasing) rutile fraction. The presence of both phases is confirmed for all heat-treatments (see table 5.8). The use of TiOSO_4 as precursor generally promotes the formation of NTO because the oxysulfate system guarantees a higher O^{2-} activity than a pure chloridic system (see for comparison the phase composition of the TiCl_4 WCP in table 5.4 and the XRD diffractograms in figure 5.30 on page 87). In addition, the decrease of the rutile concentration at lower wt. % is opposite to what is observed for the DMP (see section 5.2.1, where the ART is playing the dominant role for the the phase composition, consisting of rutile with few percents of anatase (see figure 5.37).

The TiOSO_4 content has a strong impact on the morphology of the samples. The SEM micrographs in figure 5.56 reveal that most of the crystals develop a rod-shaped habit for the samples with 5 wt. % TiOSO_4 precursor. The rods are thinner and longer than those obtained with 10 wt. % TiOSO_4 . The



(a) 1000 °C, 10 wt. % WCP at 60 °C

(b) 1100 °C, 10 wt. % WCP at 60 °C

Figure 5.54.: SEM images of titania and NTO particles synthesized at a) 1000 °C and b) 1100 °C by MSS in Na_2SO_4 via WCP at 60 °C with 10 wt. % TiOSO_4 precursor.

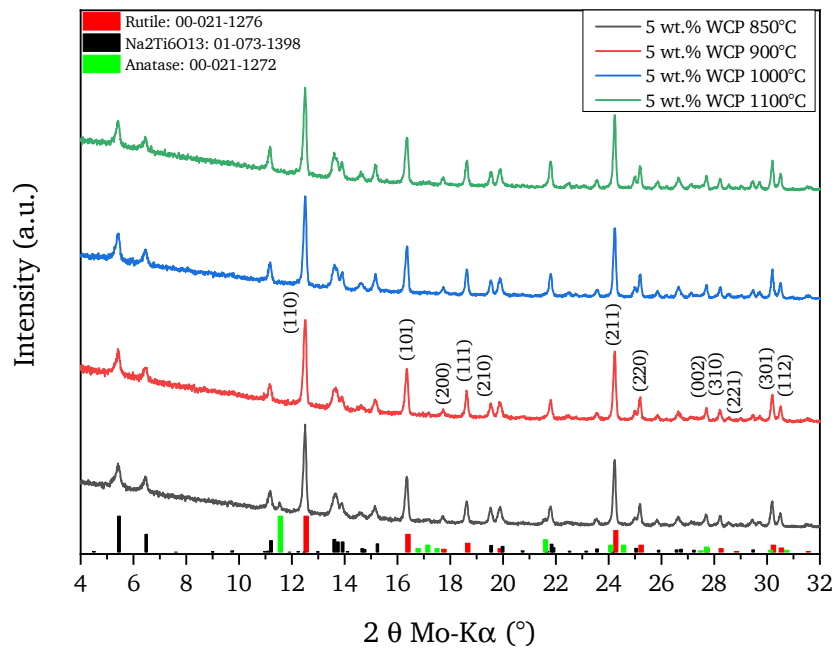
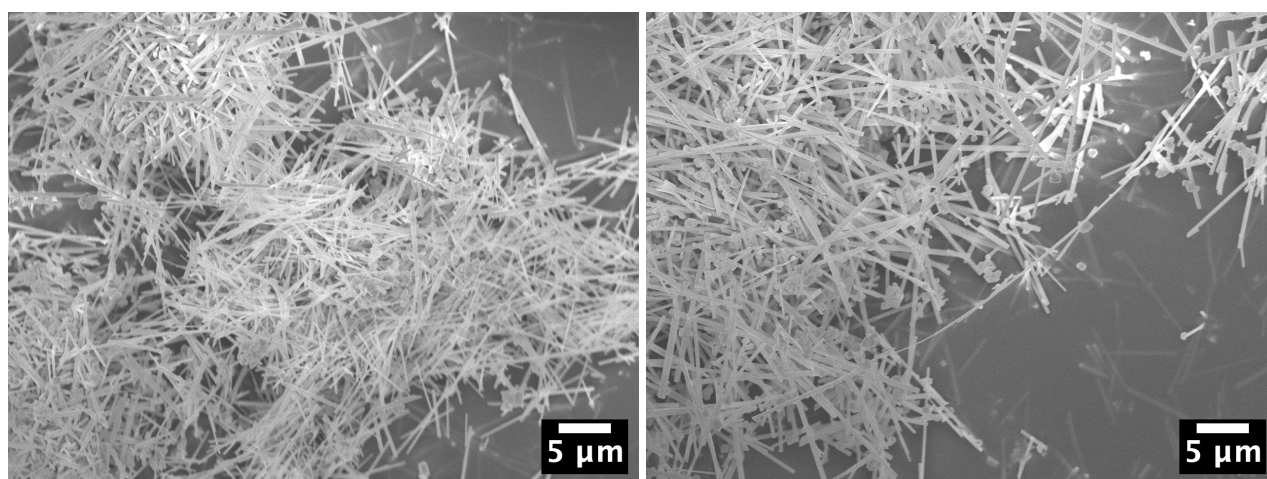


Figure 5.55.: XRD of samples obtained by WCP performed at 60 °C with 5 wt. % TiOSO_4 precursor, heat-treated at 850 °C, 900 °C, 1000 °C and 1100 °C. Reference XRD patterns from the ICDD for $\text{Na}_2\text{Ti}_6\text{O}_{13}$ and rutile are given at the bottom of the graph.

majority of the rods have a diameter ≤ 250 nm (few reach a maximum of 500 nm) and a length ≥ 10 μm , respectively. This is a strong indication of preferential NTO phase formation. In line with this result, few rutile particles with a size ≤ 1 μm are visible (see the magnification in figure D.21 in the appendix) and their concentration is heavily decreased with respect to the 10 wt. % precursor sample (figure 5.54).



(a) 1000 °C, 5 wt. % WCP at 60 °C

(b) 1100 °C, 5 wt. % WCP at 60 °C

Figure 5.56.: SEM images of titania and NTO particles synthesized at a) 1000 °C and b) 1100 °C by MSS in Na_2SO_4 via WCP at 60 °C with 5 wt. % TiOSO_4 precursor.

Next, a WCP at 30 °C (instead of 60 °C) was performed in order to investigate the effect of the precursor preparation temperature on the composition and habit of the final product. The phase composition of the obtained samples is reported in figure 5.57. Evidently, the ratio between rutile and NTO is changed in comparison to that obtained with the precursor prepared at 60 °C (see figure 5.53). A substantial decrease of the rutile fraction is observed. The precipitate obtained at 60 °C reveals a different shape of the reflections and stronger intensities (see figure 5.58) than the precipitate obtained at 30 °C. Thus, the crystallinity and particle size are more defined when the WCP is carried out at a temperature of 60 °C.

Figure 5.59 shows the morphology of the TiO_2 samples obtained by WCP at 30 °C. The decrease of the WCP temperature appears to limit the nucleation of particles, leading to an enhanced formation of NTO at $T = 1000$ °C or 1100 °C. The comparison with figure 5.54 emphasizes the different crystal habits achieved. Much thinner and longer rod-shaped crystals are obtained by the WCP at 30 °C. Additionally, the small particles are not visible anymore, with the exception of few crystals having dimensions $\simeq 4$ μm . WCP at lower temperature appears to hinder the growth of anatase nanocrystals and therefore allows easier titanates formation.

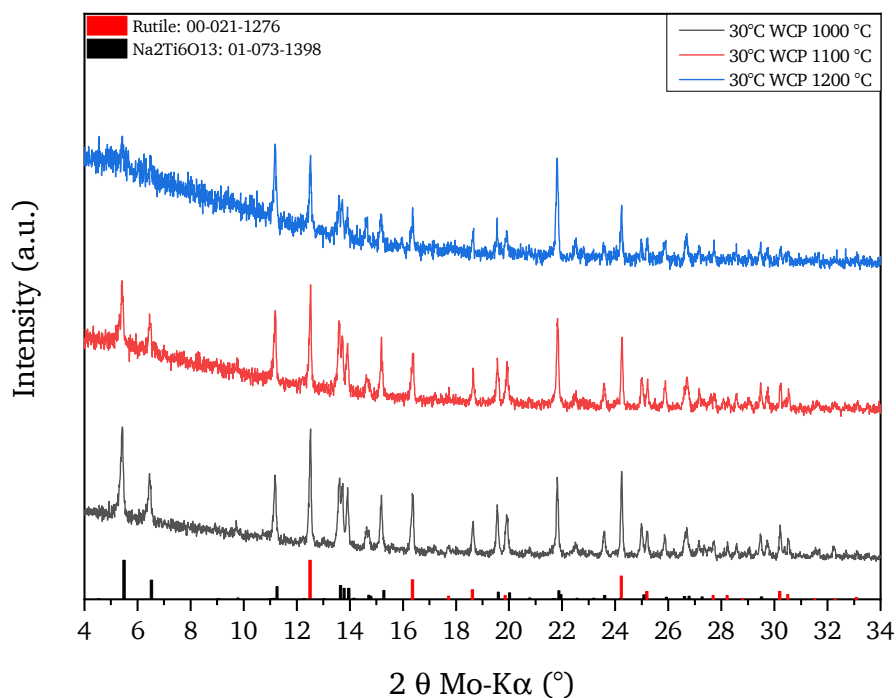


Figure 5.57.: XRD of samples obtained by WCP performed at 30 °C with 10 wt. % TiOSO₄ precursor, heat-treated at 1000 °C, 1100 °C and 1200 °C. Reference XRD patterns from the ICDD for Na₂Ti₆O₁₃ and rutile are given at the bottom of the graph.

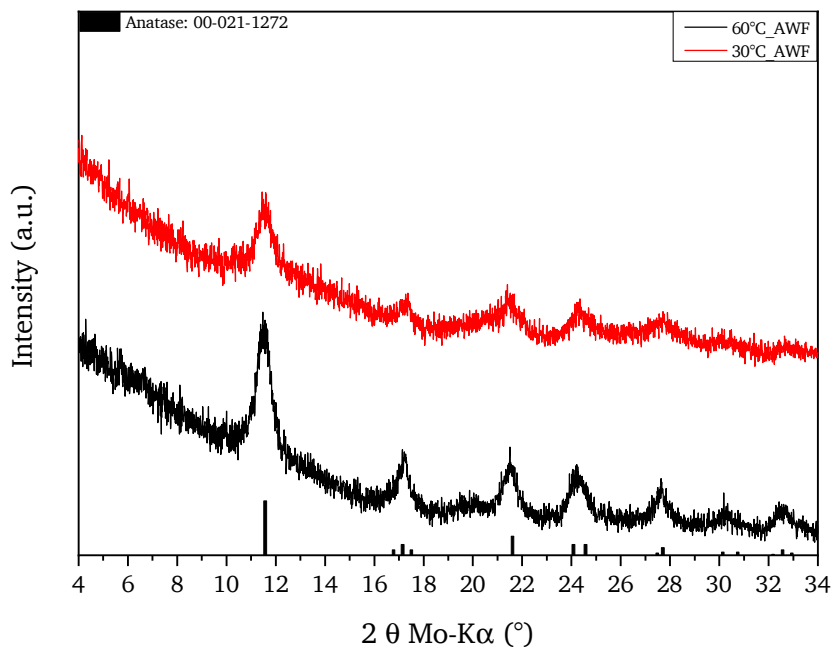
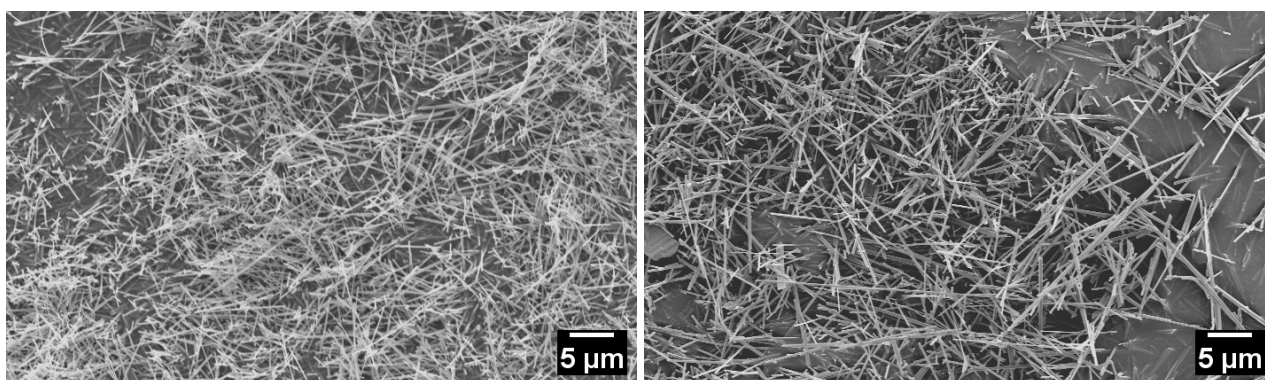


Figure 5.58.: XRD of precipitates obtained by WCP performed at 30 °C and 60 °C with 10 wt. % TiOSO₄ precursor. Reference XRD patterns from the ICDD for anatase is given at the bottom of the graph.



(a) 1000 °C, WCP at 30 °C

(b) 1100 °C, WCP at 30 °C

Figure 5.59.: SEM images of titania and NTO particles synthesized at a) 1000 °C and b) 1100 °C by MSS in Na_2SO_4 via WCP at 30 °C with 10 wt. % TiOSO_4 precursor.

5.2.6.2. Effect of Na_3PO_4 addition in the molten salt synthesis

Na_3PO_4 addition was studied with the aim of promoting the rutile formation in the MSS. Na_3PO_4 is an O^{2-} -ion acceptor (strong Lux-Flood acid) and it changes the reaction equilibrium towards the formation of pure rutile (see chapter 2, section 2.3.4). Its presence in the melt reduces the O^{2-} activity, similar to other phosphate species [39], and stabilizes the anatase phase even up to 1000 °C. The latter is metastable and tends to convert more easily into rutile in a reconstructive way than forming NTO. Figure 5.60 reports the XRD results of samples with 1 mol % of Na_3PO_4 added to 10 wt. % of TiOSO_4 precursor. Rutile is the dominant phase and NTO reflections can be observed next to it. The NTO formation seems to be inhibited by the addition of Na_3PO_4 since its intensity of the reflections decreases when compared to the (same) synthesis conditions without Na_3PO_4 (see figure 5.53 and figure 5.57). This observation is supported by the fact that the NTO reflections disappear by further increasing the concentration of Na_3PO_4 (see figure 5.62).

The addition of Na_3PO_4 causes distinct morphology changes of the crystals synthesized at $1000\text{ °C} < T < 1200\text{ °C}$. Figure 5.61 shows the SEM micrographs of the samples, revealing the lowest concentration of rod-shaped crystals compared to all the previous samples obtained by WCP with TiOSO_4 . Their size is also changed, with lengths exceeding 10 μm and diameters $\geq 500\text{ nm}$. At the same time the amount of polyhedral particulates with a dimension ranging between 2 and 6 μm increased, representing the favored habit of rutile. Increase of Na_3PO_4 makes the changes even more obvious. Figure 5.62 shows the diffractograms of the samples obtained by the addition of 10 wt. % Na_3PO_4 revealing the dominant presence of the rutile phase (see compositions in table 5.9). The NTO reflections barely appear in the sample heat-treated at 1000 °C. The ratio of the reflections belonging to rutile suggests an unusual behavior. The reflections assigned to the (101) and (211) planes have much stronger intensity than they usually have, reaching that of the main (110) reflection. At 1200 °C the (101) intensity becomes even stronger than (110). Thus, a change in the rutile habit is expected.

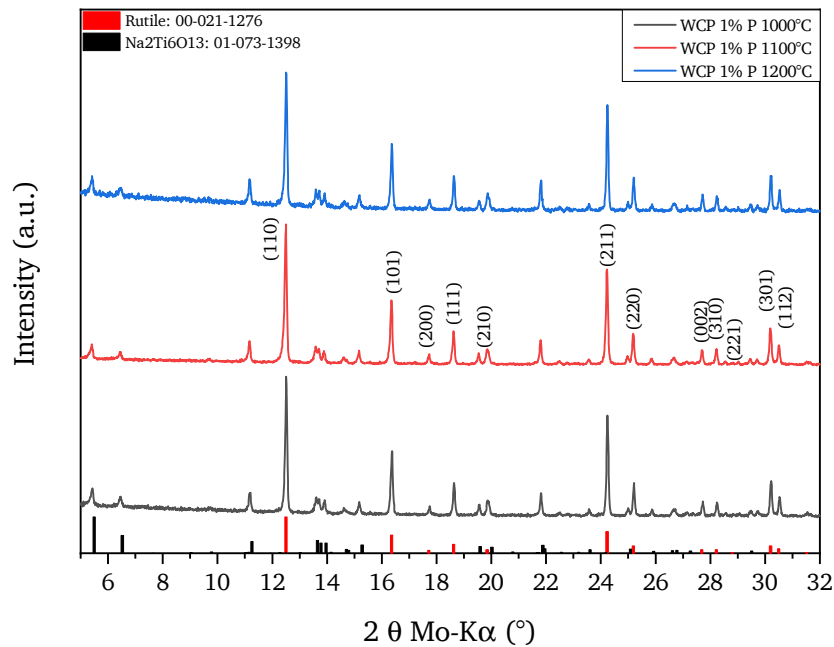
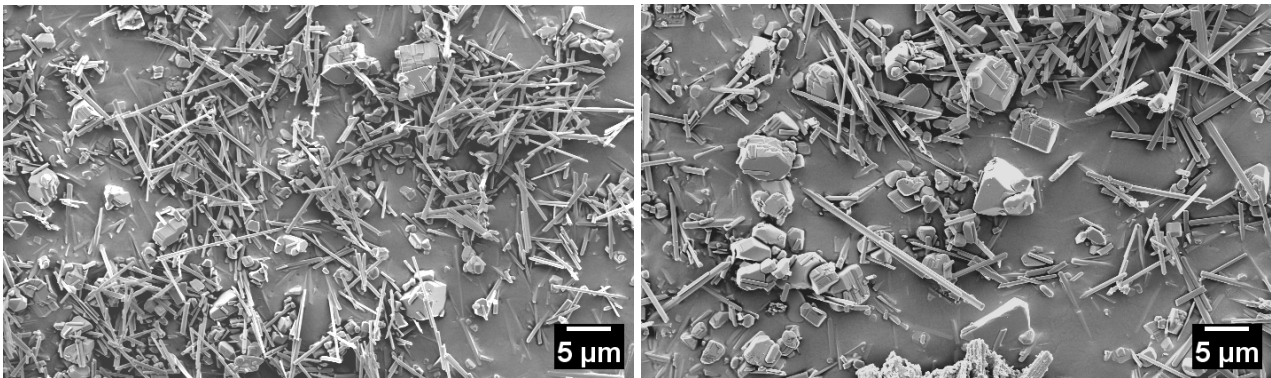


Figure 5.60.: XRD of samples obtained by WCP performed at 60 °C with 10 wt. % TiOSO_4 precursor and the addition of 1 mol % of Na_3PO_4 . The samples were heat-treated at 1000 °C, 1100 °C and 1200 °C. Reference XRD patterns from the ICDD for $\text{Na}_2\text{Ti}_6\text{O}_{13}$ and rutile are given at the bottom of the graph.

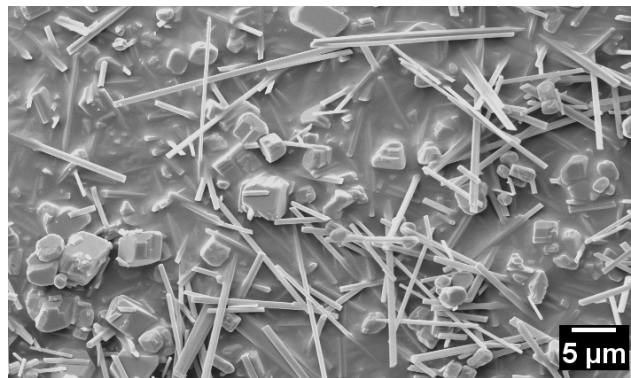
Table 5.9.: Phase composition of samples obtained by WCP in Na_2SO_4 with 10 % TiOSO_4 precursor and the addition of Na_3PO_4 . Synthesis temperature: 1000 to 1200 °C and 2 hours holding time. (R = rutile, NTO = $\text{Na}_2\text{Ti}_6\text{O}_{13}$).

TiOSO_4 Precursor wt. %	Na_3PO_4 mol %	1000 °C	1100 °C	1200 °C
10	1	R, NTO	R, NTO	R, NTO
10	10	R, NTO	R	R



(a) 1000 °C, 1 mol % Na_3PO_4

(b) 1100 °C, 1 mol % Na_3PO_4



(c) 1200 °C, 1 mol % Na_3PO_4

Figure 5.61.: SEM images of samples synthesized at a) 1000 °C, b) 1100 °C and c) 1200 °C by MSS in Na_2SO_4 via WCP with 10 wt. % TiOSO_4 precursor. 1 mol % of Na_3PO_4 was added to the system.

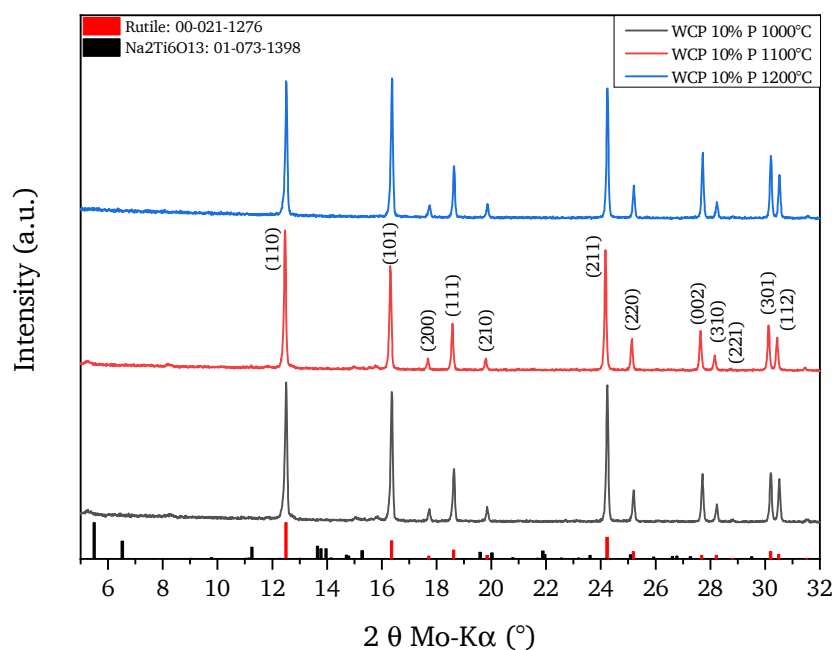
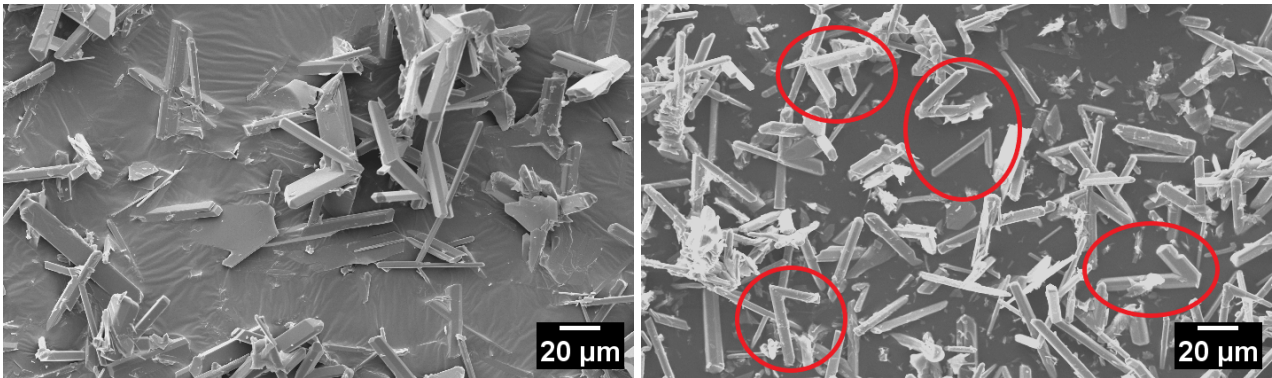


Figure 5.62.: XRD of samples obtained by WCP performed at 60 °C with 10 wt. % TiOSO₄ precursor and the addition of 10 mol % of Na₃PO₄. Heat-treatments performed at: 1000 °C, 1100 °C and 1200 °C. Reference XRD patterns from the ICDD for Na₂Ti₆O₁₃ and rutile are given at the bottom of the graph.

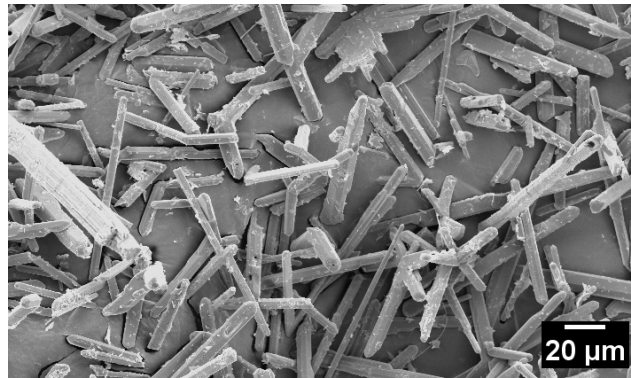
The SEM micrographs shown in figure 5.63 shed light on this aspect. The rod-shaped crystals have increased in size exceeding that obtained by the addition of 1 % of Na₃PO₄ by far. Their length is $\geq 45 \mu\text{m}$ and their diameter increased to 1 to 10 μm . The thickness of the rod-shaped crystals increases with temperature and, in general, the appearance of additional facets is observed. The preferential axial growth of the crystals causes a different reflection ratios in figure 5.62. These are specifically involving planes with Miller index $l \neq 0$ (e.g. (101), (211), (002), (301) and (112)). The rod-shaped crystals can unambiguously be attributed to the rutile phase, the only structure detected by XRD at $T \geq 1000 \text{ }^\circ\text{C}$. It is also possible to observe the formation of V-shaped crystals, especially at 1100 °C (highlighted with red circles), given by the presence of a twin junction (see for more information section 2.3.1 on page 15). This structure can be explained by an OA process during growth [270, 272, 305] or of the ART [192] (see section 3.1.2). Finally, the size reached by these crystals is greater than that of the crystals obtained by the WCP without Na₃PO₄ (see figure 5.54) and by the corresponding WCP with TiCl₄ (see figure 5.31).

Another set of experiments was performed by systematically varying the Na₃PO₄ amount keeping the TiOSO₄ content fixed to 5 wt. % in order to allow i) a consistent comparison with the WCP using 5 wt. % TiCl₄ and ii) the WCP with 5 wt. % TiOSO₄ without Na₃PO₄ addition. The series of experiment was performed by adding 2.7, 5, 10 and 20 mol % of Na₃PO₄ and heat-treating the samples between 900 and 1100 °C. The most noteworthy consequence of the addition of this strong Lux-Flood acid is the stabilization of the anatase phase (see sample compositions in table 5.10). Figure 5.64a presents the



(a) 1000 °C, 10 mol % Na_3PO_4

(b) 1100 °C, 10 mol % Na_3PO_4



(c) 1200 °C, 10 mol % Na_3PO_4

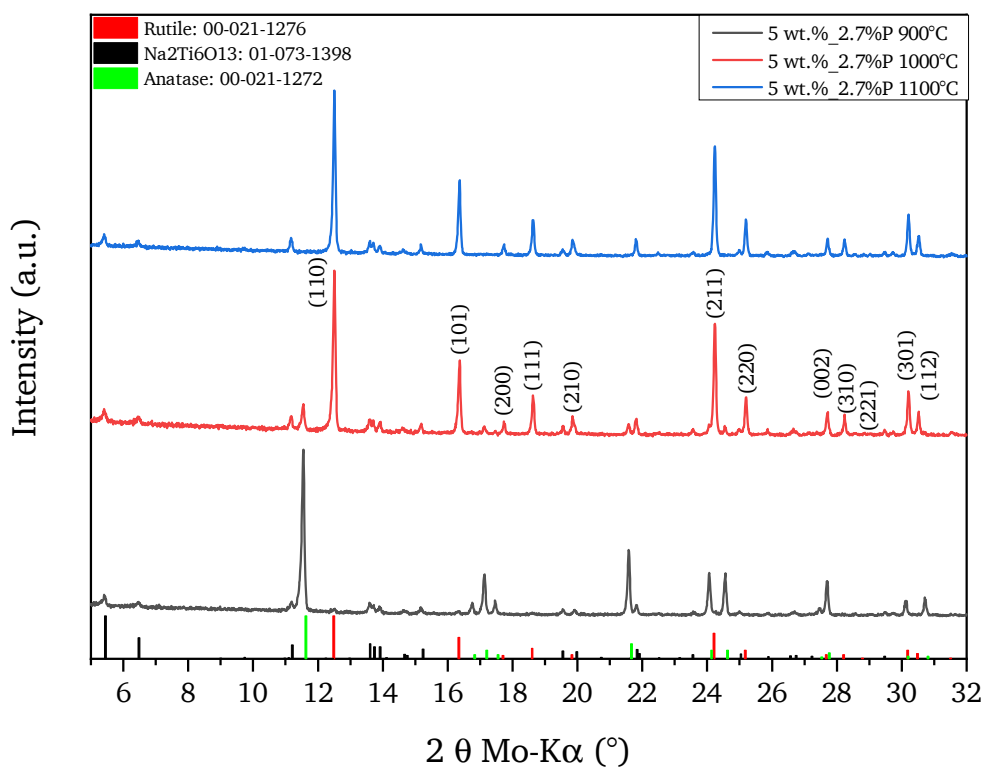
Figure 5.63.: SEM images of samples synthesized by MSS in Na_2SO_4 via WCP with 10 wt. % TiOSO_4 precursor, heat-treated at a) 1000 °C, b) 1100 °C and c) 1200 °C. 10 mol % of Na_3PO_4 were added to the system.

diffractograms of the samples obtained by the addition of 2.7 mol% Na₃PO₄. Heat-treatment at 900 °C creates a high concentration of anatase, dominating some reflections assigned to the NTO phase. The main reflection of rutile is barely visible. Heat-treatment at 1000 °C enhances the ART, but the main reflection for the anatase phase is still clearly visible. The full conversion to rutile is achieved at 1100 °C. The NTO phase is always present at temperatures > 900 °C. Increase of the Na₃PO₄ concentration leads to structural changes. For Na₃PO₄ concentrations ≥ 5 % the NTO phase vanishes (see figures 5.64b, 5.65a and 5.65b). At 900 °C anatase is the only phase present for 5 and 10 % Na₃PO₄ addition. At 20 % there is a sodium titanium phosphate phase forming along with anatase (NaTi₂(PO₄)₃ with code 00-033-1296). The anatase stabilization by the phosphate ion gets clearer by comparing the XRD data of the samples with different Na₃PO₄ concentration and heat-treated at 950 °C and 1000 °C (see figures C.17a and C.17b in the appendix). At 950 °C the main rutile reflection is visible only for 5 mol % Na₃PO₄ and disappears at higher concentrations. This trend is also confirmed by increasing the temperature to 1000 °C. The 2.7 mol % Na₃PO₄ sample contains mainly rutile, and just after an addition of ≈ 5 mol % Na₃PO₄, the ratio anatase to rutile is capsized. Furthermore, NTO is not detected anymore. Rutile is the only phase at 1100 °C for concentrations of Na₃PO₄ ≥ 10 mol %. The sample obtained by the addition of 20 mol % of phosphate reveals an unusual ratio of the rutile reflections. They change their intensities with the (101) reflection being the most intense one, followed by (211) (see figure 5.65b). This feature is similar to what has been already observed for the sample with 10 wt. % TiOSO₄ and the addition of 10 mol % Na₃PO₄ (see figure 5.62 and phase compositions in the tables 5.9 and 5.10).

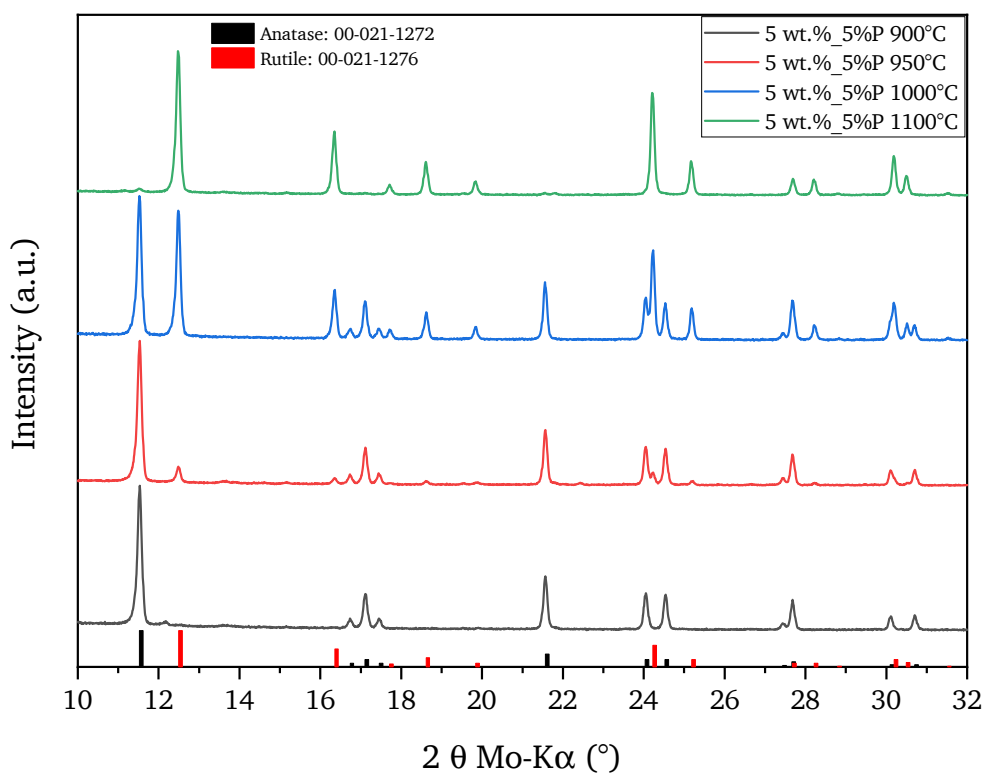
Table 5.10.: Phase composition of samples obtained by WCP in Na₂SO₄ with 5 % TiOSO₄ precursor and the addition of Na₃PO₄. Synthesis temperature: 900 to 1100 °C and 2 hours holding time. (A = anatase, R = rutile, NTO = Na₂Ti₆O₁₃).

TiOSO ₄ Precursor wt. %	Na ₃ PO ₄ mol %	900 °C	950 °C	1000 °C	1100 °C
5	2.7	A, R, NTO	-	R, A, NTO	R, NTO
5	5	A	A, R	A, R	R, A
5	10	A	A	R, A	R
5	20	A	A	R, A	R

Figure 5.66 shows the morphology of the crystals obtained by adding 2.7 mol % of Na₃PO₄. Two habits are mixed, NTO rod-shaped crystals and polyhedral rutile particles. The NTO rods are present in every experiment and their average length varies from ≈ 5 μm at 900 °C up to ≈ 15 μm at 1100 °C. The diameters increase from ≈ 100 nm at 900 °C to a maximum of 1 μm at 1100 °C. The same happens with the rutile particles, having an average size of ≈ 1 μm at 900 °C that increases up to 5 μm at 1100 °C. Concentrations of Na₃PO₄ ≥ 5 mol % lead to the formation of rutile crystals larger than those obtained with 2.7 mol % of Na₃PO₄ at 1000 and 1100 °C (see figure 5.67). The addition of 5 mol % Na₃PO₄ hinders the formation of rod-shaped NTO crystals, favoring anatase (see figure 5.64b). The three samples heat-treated at 1000 °C contain almost equal amounts of rutile and anatase phase. The latter is represented by the small unreacted particulates (see figures 5.67a, c and e). At 1100 °C the particulates disappear in all samples (see figures 5.67b, d and f). At 10 wt. % the formation of rods is much stronger,

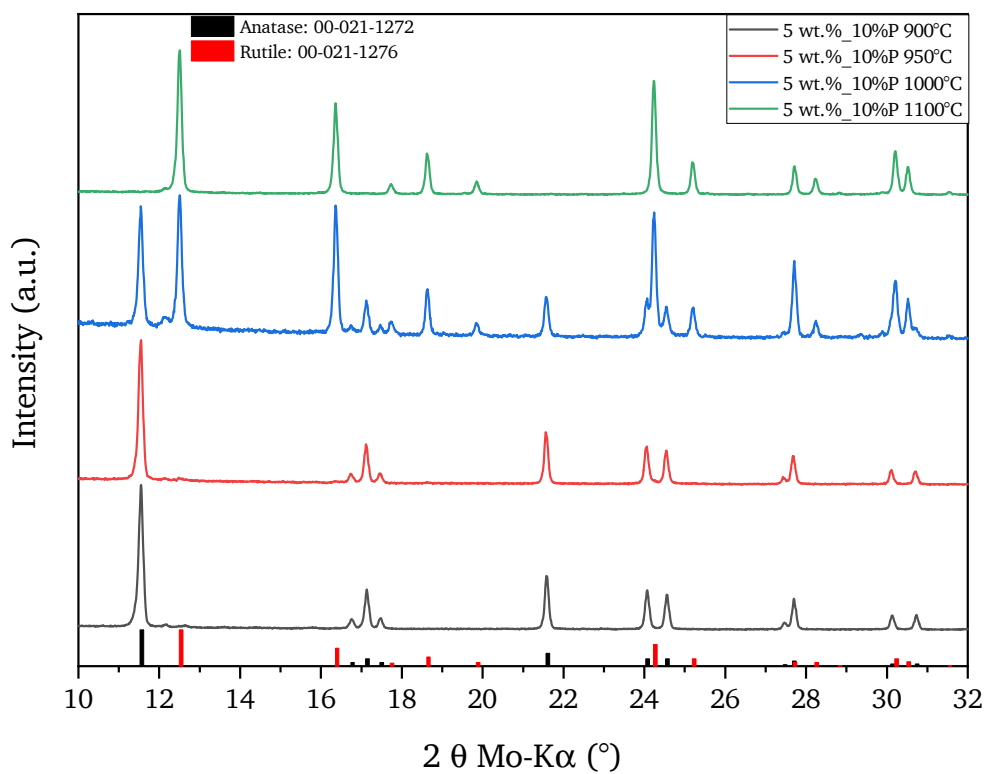


(a) 2.7 % of Na_3PO_4

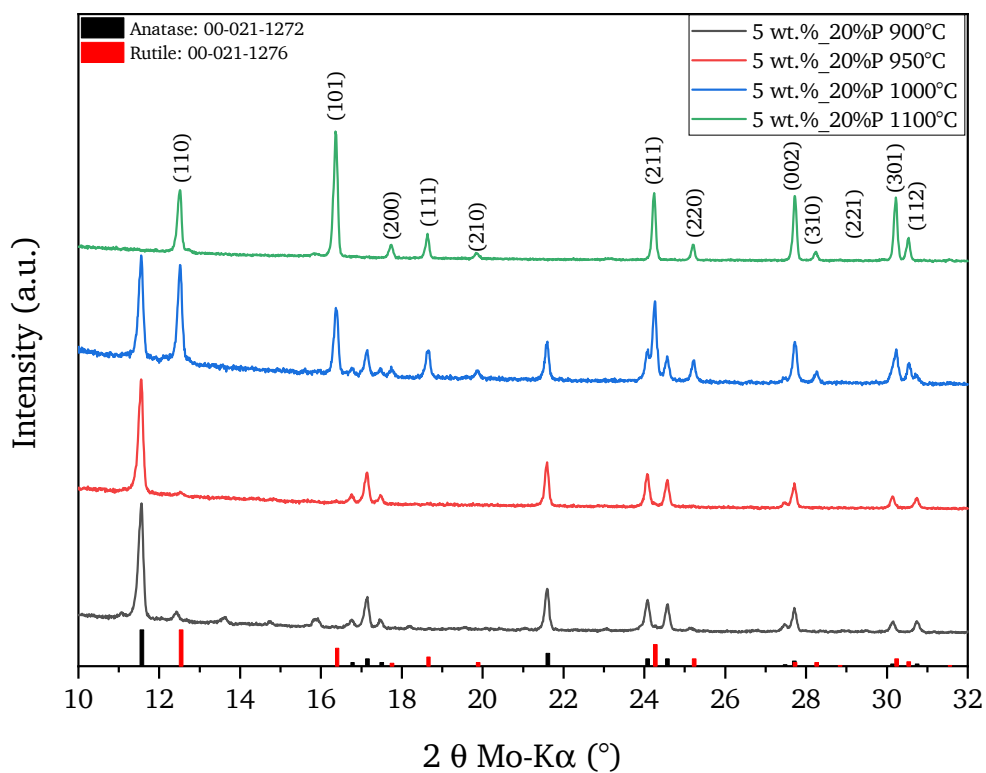


(b) 5 % of Na_3PO_4

Figure 5.64.: XRD of samples obtained by WCP performed at 60 °C with 5 wt. % TiOSO_4 precursor and a) 2.7 % and b) 5 % of Na_3PO_4 . Reference XRD patterns from the ICDD for $\text{Na}_2\text{Ti}_6\text{O}_{13}$, anatase and rutile are given at the bottom of the graph.



(a) 10% of Na_3PO_4



(b) 20% of Na_3PO_4

Figure 5.65.: XRD of samples obtained by WCP performed at 60 °C with 5 wt. % TiOSO_4 precursor and a) 10% and b) 20% of Na_3PO_4 . Reference XRD patterns from the ICDD for anatase and rutile are given at the bottom of the graph.

as well as the trend of forming V-shaped crystals (highlighted by red circles in figure 5.67c), typical for rutile crystallization behavior and observed also for the sample with 10% TiOSO_4 precursor and 10% Na_3PO_4 in figure 5.63. A detailed view of a V-shaped crystal is given in figure D.22 in the appendix. Addition of 20 mol% Na_3PO_4 has a strong influence on the habit formation, since the rod-shaped crystals are then transformed into flat plates whose thickness increases along one axis (see figure 5.67e). They usually assume the typical V-shape, which can gradually change into a triangle (as can be observed in the red marked circles number 1, 2 and 3 in figure 5.67e). The phase composition of the discussed samples is summarized in table 5.10.

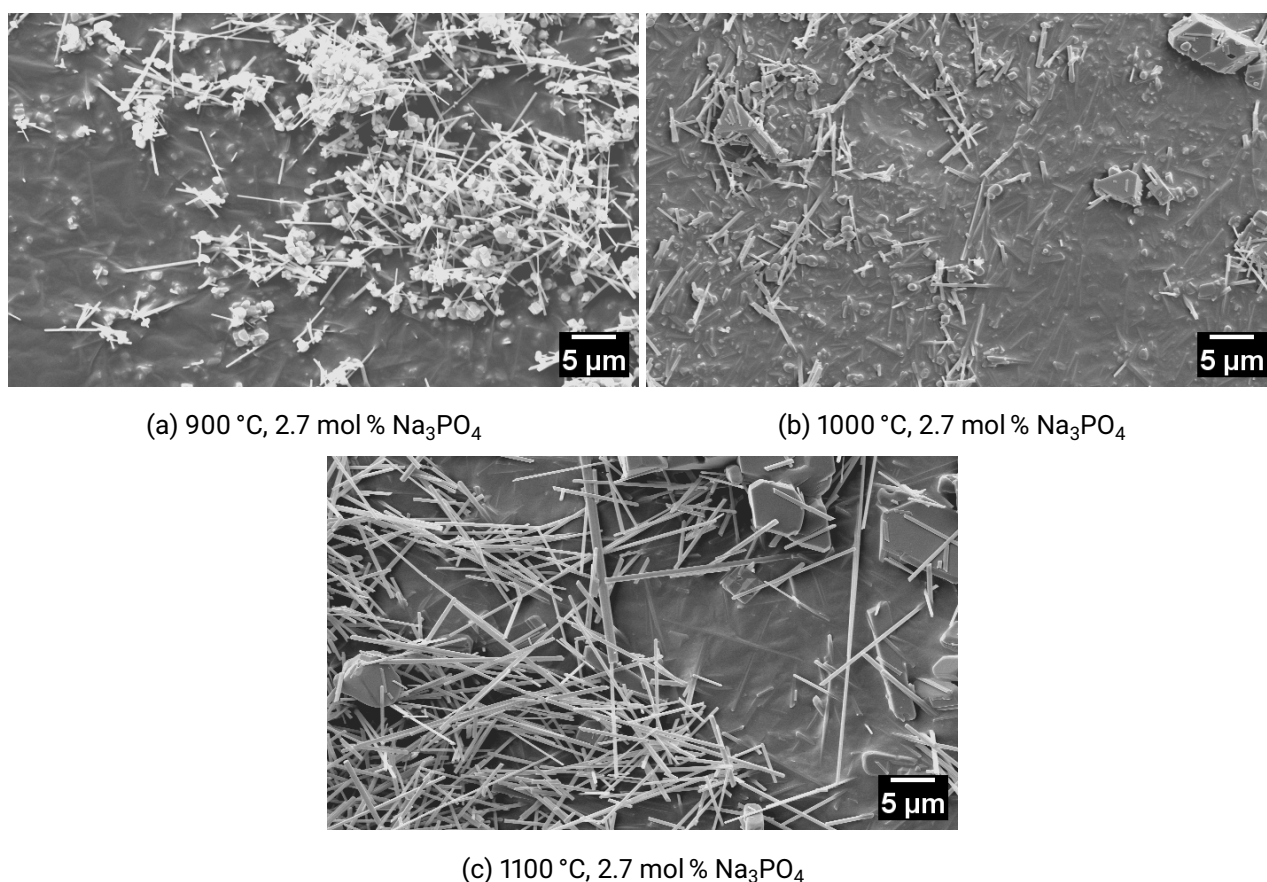
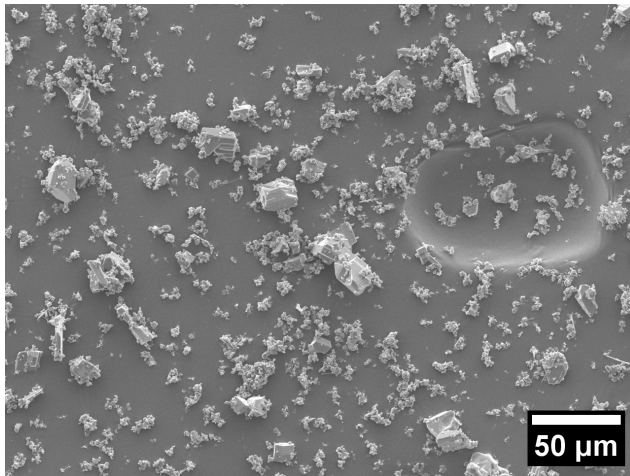
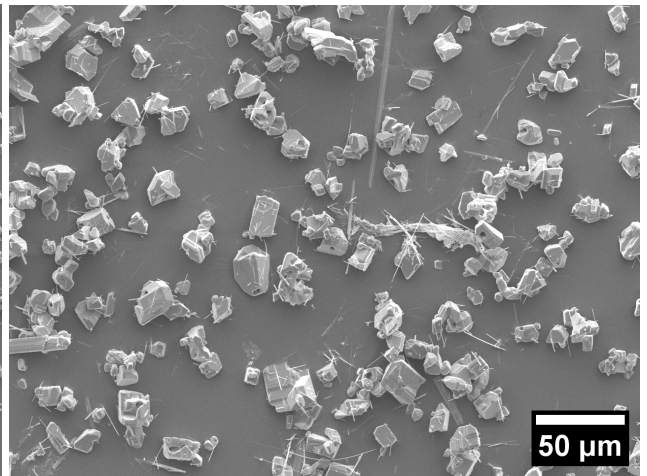


Figure 5.66.: SEM images of samples synthesized at a) 900 °C, b) 1000 °C and c) 1100 °C by MSS in Na_2SO_4 via WCP with 5 wt. % TiOSO_4 precursor. 2.7 mol % of Na_3PO_4 were added to the system.

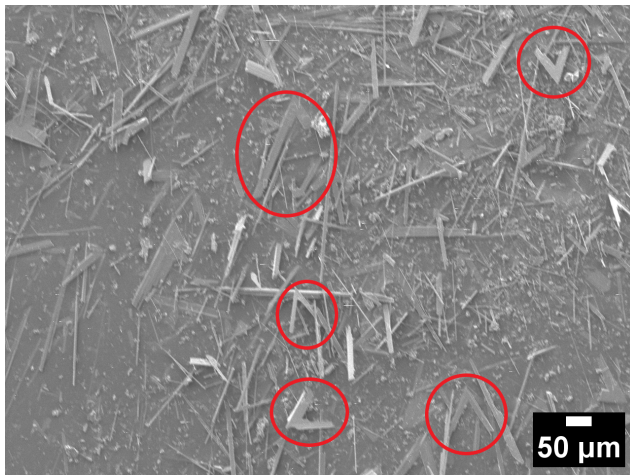
To sum up, strong effects of the Na_3PO_4 addition can be easily observed in the morphology and the phase evolution of the samples. An anisotropic growth is promoted by the depletion of O^{2-} due to the presence of Na_3PO_4 . Strong differences are visible if one compares i) WCP and DMP results (see figure 5.38 and figure D.16) and ii) WCP with the sulfate system and no Na_3PO_4 (see figure 5.56). Small and thick rutile polyhedral particles by DMP ($\approx 5 \mu\text{m}$) and thin and long rutile nano-rods by WCP (exposing preferentially other facets with the addition of Na_3PO_4) stem from a completely



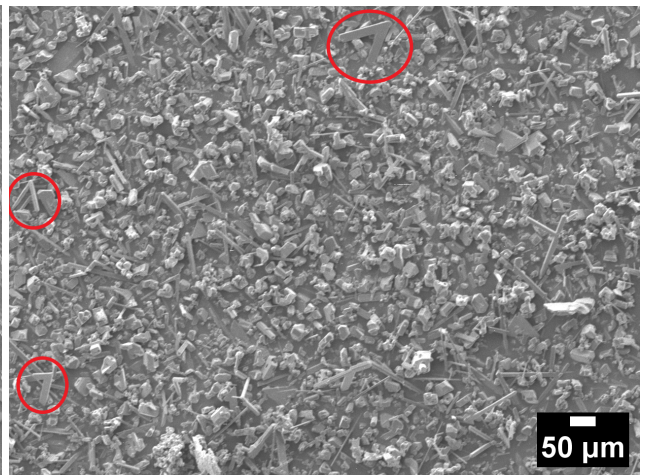
(a) 1000 °C and 5 % Na_3PO_4



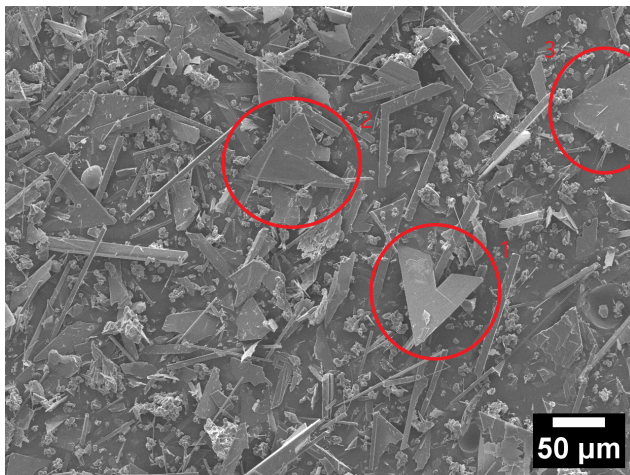
(b) 1100 °C and 5 % Na_3PO_4



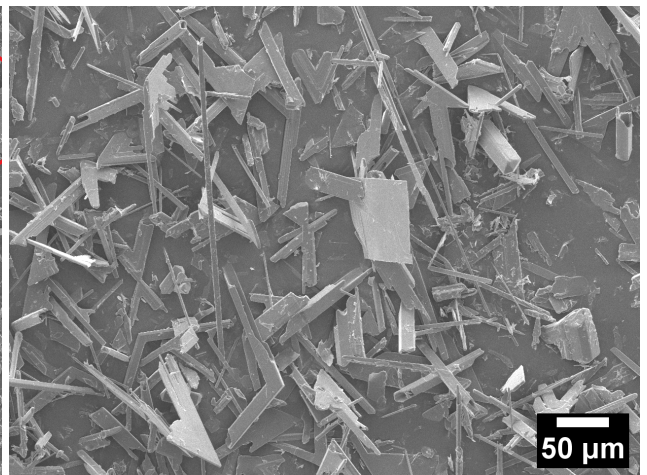
(c) 1000 °C and 10 % Na_3PO_4



(d) 1100 °C and 10 % Na_3PO_4



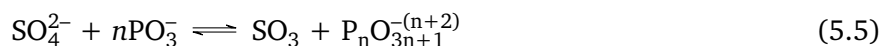
(e) 1000 °C and 20 % Na_3PO_4



(f) 1100 °C and 20 % Na_3PO_4

Figure 5.67.: SEM images of samples synthesized by MSS in Na_2SO_4 at 1000 °C and 1100 °C via WCP with 5 wt. % TiOSO_4 precursor and the addition of respectively 5 % (a and b), 10 % (c and d) and 20 % of Na_3PO_4 (e and f).

changed growth mechanism. Two parameters appear to be important for this habit change: i) the acidic strength $\text{PO}_3^- > \text{TiO}_3^{2-}$ which does not allow the formation of titanates [127]; ii) the Lux-Flood acid-base equilibrium (see equations 2.5 and 2.6 on page 10) is shifted by the presence of a strong acid enhancing the decomposition of sulfate ions according to equation 5.5 [296, 304].



The PO_4^{3-} ion has a marked retardation effect on the ART, in agreement with the findings of [302]. The concomitant effects change the surface energies of the growing TiO_2 crystals, directing the growth differently. Finally, the addition of an oxygen acceptor suppresses the sodium titanate formation. This just happens with 2.7 % of Na_3PO_4 or in total absence of it (the study on the NTO is deepened in section 5.3).

5.2.6.3. Heat-treatment under O_2 flow

The fact that the ART is reconstructive [168] supports the idea that the interaction of oxygen with growing TiO_2 crystals strongly affects the ART and the morphology of the particles. This was already proven by the findings discussed in section 5.1.4 and 5.2.4, respectively. The samples described in this section have been heat-treated under O_2 flow at 1100°C in order to investigate the impact of the O_2 activity on the crystals structure and morphology.

Figure 5.68 and 5.69 present the structural information for the samples with different Na_3PO_4 concentrations, heat-treated at 1100°C under O_2 . All of them reveal the presence of the rutile structure. However, the samples with 10 and 20 wt. % Na_3PO_4 show a clear deviation from the rutile reference pattern (see figure 5.69a and b). This behavior indicates that some planes scatter more than they usually do. All the planes with Miller indices h and $k \neq 0$ decrease in intensity after the heat-treatment under oxygen, indicating an increase of the plane population that directs the growth along the $[001]$ direction. Additionally, the intensity of the planes with Miller index $l \neq 0$ increased. All these changes are commonly due to an anisotropic growth of the crystals.

The results of the XRD studies are confirmed by the SEM micrographs in figure 5.70. Generally, the crystals grown under O_2 flow increase in size. The comparison with the samples obtained by DMP (see figure 5.50) shows that the samples in figure 5.70 doubled their size. This can be attributed to the WCP and the presence of Na_3PO_4 , as well as to the concomitant effect of O_2 . The rutile crystals obtained with 5 wt. % of Na_3PO_4 are revealing a slight change of the habit when changing the atmosphere to O_2 . The irregularly shaped crystals collected under ambient condition get a smoother shape with some particles recalling the shape of a mosaic tile (for a detailed comparison refer to figure D.24 in the appendix). The "mosaic tile"-like crystals are a good candidate for the pearl luster pigment (PLP) application due to the squared and flat surfaces that can facilitate interference effects. The "mosaic tile"-like crystals can reach a maximum length of $35\ \mu\text{m}$. Unfortunately their concentration is low. The changes occurring with

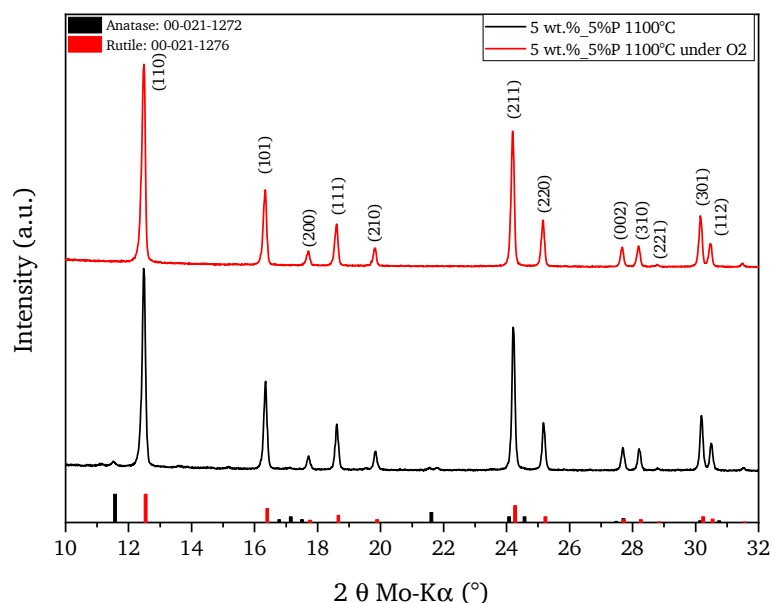


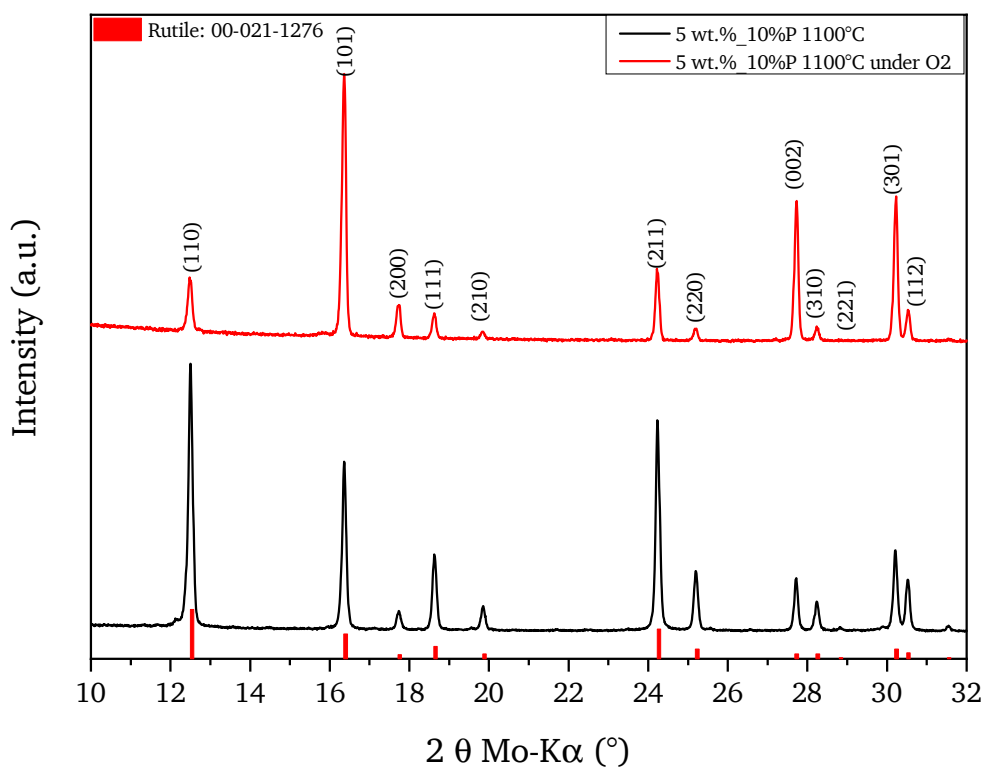
Figure 5.68.: XRD of samples obtained by WCP performed at 60 °C with 5 wt. % TiOSO_4 precursor and the addition of 5 wt. % of Na_3PO_4 . Reference XRD patterns from the ICDD for anatase and rutile are given at the bottom of the graph.

an increase of the oxygen partial pressure are more defined with the addition of 10 wt. % of Na_3PO_4 . In this case the formation of V-shaped crystals with side lengths $\geq 100 \mu\text{m}$ is favored, making 90 % or more of the sample. Finally, the sample with 20 wt. % of Na_3PO_4 reveal a subtle change between the two atmospheres. The habit distribution and the particle size are similar, but the O_2 flow causes the formation of very small particles on top of the V-shaped crystal surfaces (see magnification in figure D.23 in the appendix).

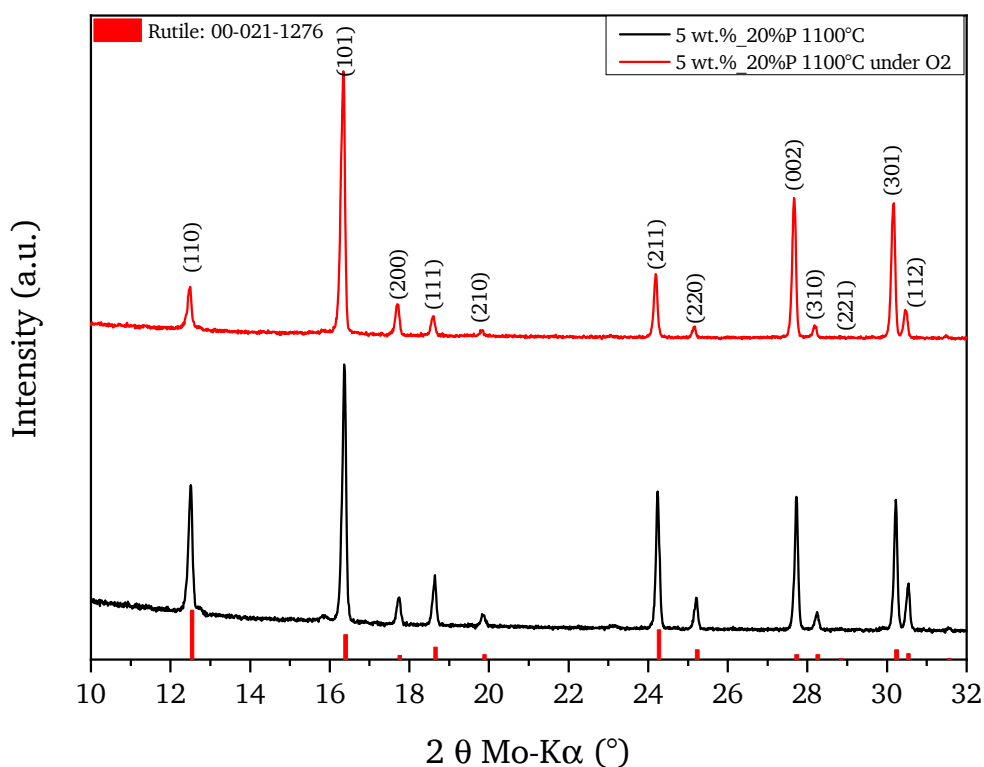
The thermodynamic equilibrium of titania in molten Na_2SO_4 changes if more oxygen is available on top of the surface melt (see equations 2.5, 2.6 and 2.7 in section 2.1.1 (page 10) and equation 2.32 in section 2.3.5 on page 26). The most attractive habit for the PLP is given by the sample obtained at 1100 °C with 5 wt. % of Na_3PO_4 under pure oxygen atmosphere (see figure 5.70b). An additional characterization has been performed by EBSD (see figures D.25 and D.26 in the appendix). This confirms the assumption that the oxygen flow promotes the 001 facet stabilization, inducing the formation of the "mosaic tile"-like habit.

5.2.6.4. Wet chemical preparation at different temperatures and TiCl_4 precursor

As part of the WCP studies in sulfates, an MSS experiment has been performed using 10 wt. % TiCl_4 as precursor in Na_2SO_4 (with the addition of Na_3PO_4). The sample preparation presented in this section differs due to the temperature chosen for the WCP (30 °C, 60 °C and 95 °C, respectively). All samples have been heat-treated at 1100 °C and reveal the presence of a rutile single phase (see figure 5.71).

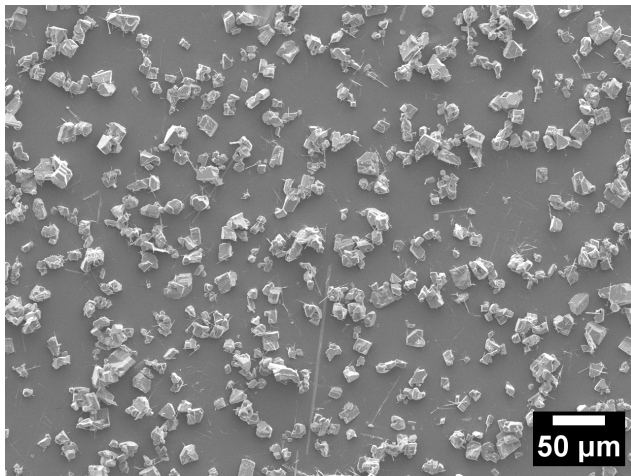


(a) WCP performed at 60 °C with 5 wt. % TiOSO₄ precursor and 10 wt. % of Na₃PO₄

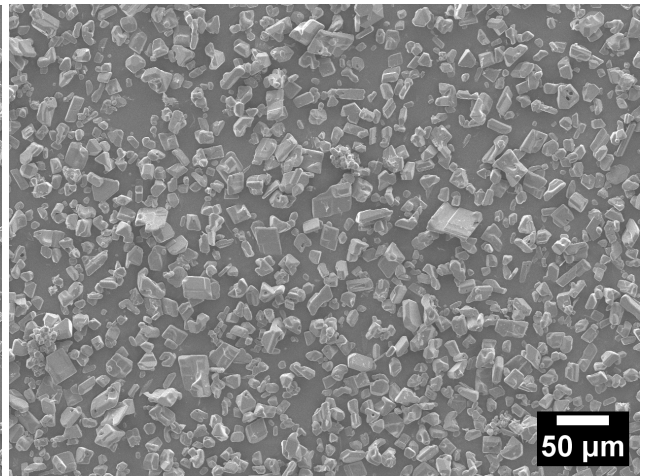


(b) WCP performed at 60 °C with 5 wt. % TiOSO₄ precursor and 20 wt. % of Na₃PO₄

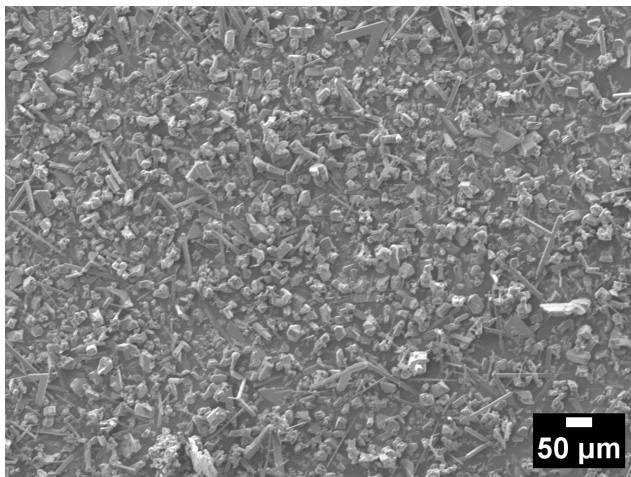
Figure 5.69.: XRD comparison of phases obtained by WCP and heat-treatment at 1100 °C under O₂ flow or ambient condition and the addition of a) 10 % and b) 20 % of Na₃PO₄. Reference XRD patterns from the ICDD for rutile is given at the bottom of the graph.



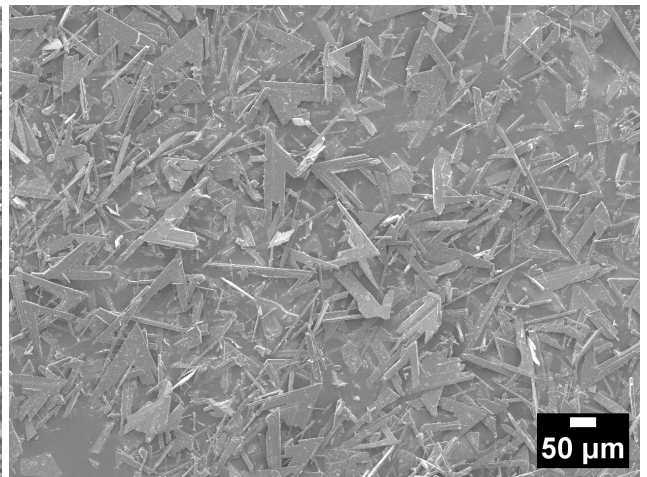
(a) 1100 °C and 5 % Na_3PO_4 under ambient condition



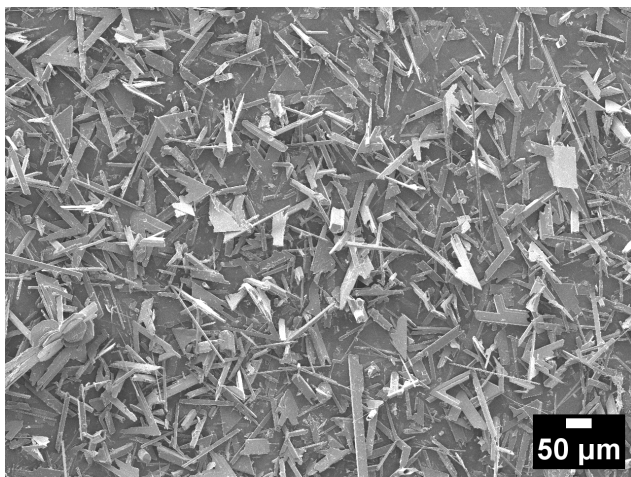
(b) 1100 °C and 5 % Na_3PO_4 under O_2



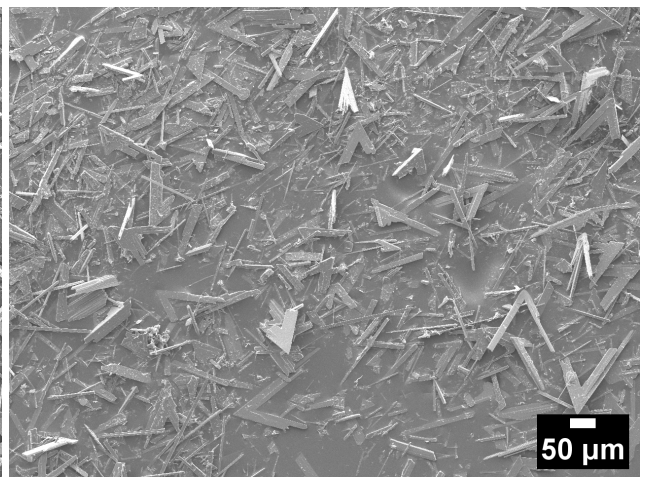
(c) 1100 °C and 10 % Na_3PO_4 under ambient condition



(d) 1100 °C and 10 % Na_3PO_4 under O_2



(e) 1100 °C and 20 % Na_3PO_4 under ambient condition



(f) 1100 °C and 20 % Na_3PO_4 under O_2

Figure 5.70.: SEM images of samples synthesized by MSS under different oxygen partial pressures in Na_2SO_4 at 1100 °C via WCP with 5 wt. % TiOSO_4 precursor and the addition of respectively 5 % (a and b) and 10 % (c and d) of Na_3PO_4 .

There is no difference compared to the sample obtained at 1100 °C using TiOSO_4 as precursor (WCP performed at 60 °C) with the same amount of Na_3PO_4 (see figure 5.62 on page 121).

The temperature chosen for the WCP with TiCl_4 causes differences in the reflections belonging to rutile. The reflections assigned to the (101) and (211) planes have much stronger intensity compared to (110) than they usually have. At 60 °C the intensity ratios are close to the usual ones (with an intensity of (211) almost equal to (110)). At 30 °C and 95 °C the (101) intensity becomes stronger than (110). This suggests that the samples form different rutile habits, due to a fluctuating exposition of crystal facets during growth, causing the intensity variation for some planes.

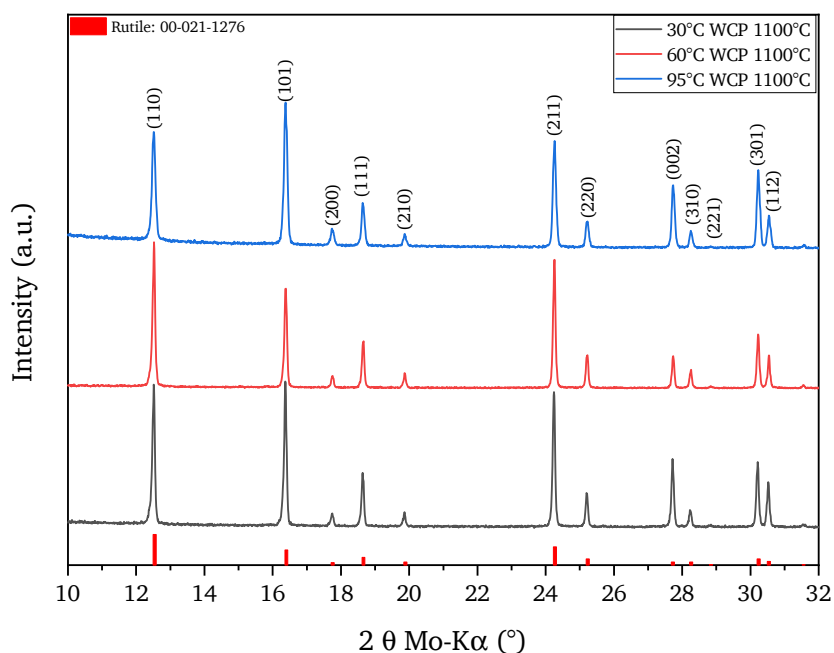


Figure 5.71.: XRD of samples obtained by WCP performed at 30, 60 and 95 °C with 10 wt. % TiCl_4 precursor and the addition of 10 % of Na_3PO_4 to Na_2SO_4 . Reference XRD pattern from the ICDD for rutile is given at the bottom of the graph.

Figure 5.72 reports the habits obtained with the TiCl_4 precursor. The different WCP temperatures are clearly affecting the crystal growth. At 30 °C most of the crystals assume a V-shape. The two rods that merge in a V-shaped crystal can reach lengths of $\approx 200 \mu\text{m}$ and a thickness of $> 20 \mu\text{m}$. Additionally, cavities appear inside the rods. The hollow extremities can be $> 10 \mu\text{m}$, as visible in figure 5.72a. The WCP performed at 60 °C does not lead to hollow rods. The formation of V-shaped crystals is drastically reduced as well as the average dimensions of the crystals. Their length seldom exceeds $50 \mu\text{m}$. Apart from the rod-shaped crystals, the formation of polyhedral particles can be observed. Their size is $\approx 25 \mu\text{m}$. Also the thickness of the rods decreased compared to the sample prepared at 30 °C. It never exceeds $12 \mu\text{m}$. A comparison with a TiOSO_4 WCP performed at 60 °C is given by the sample shown in figure 5.63 on page 122. The changes in the habit and morphology are probably caused by different precipitation reactions at 30 up to 95 °C. However, common to all micrographs the crystal growth

appears to be dominated by the $\langle 001 \rangle$ direction and the formation of twin-junctions resulting in mainly V-shaped rutile crystal.

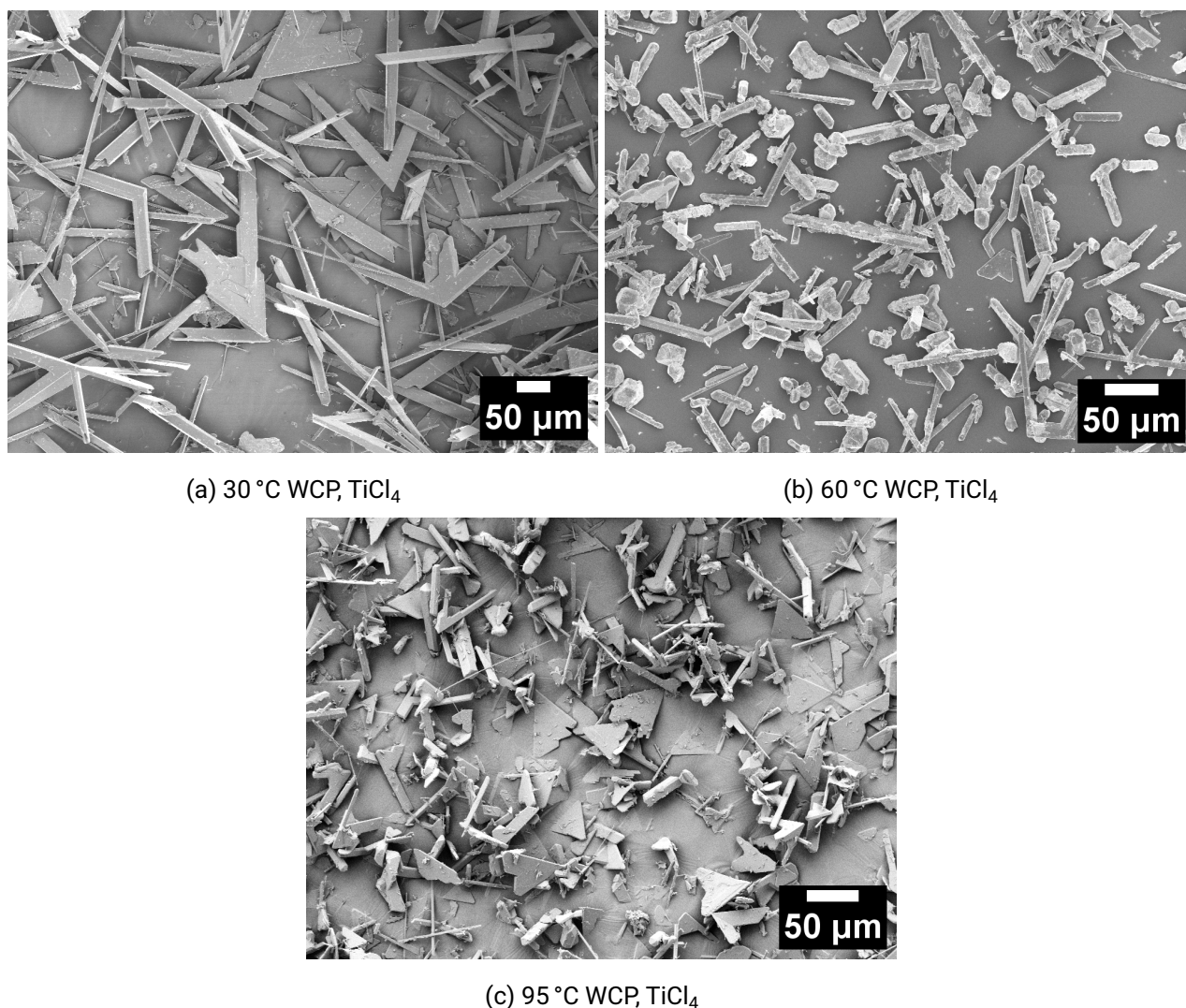


Figure 5.72.: SEM images of samples synthesized by MSS in Na_2SO_4 at $1100\text{ }^\circ\text{C}$ via WCP with 10 wt. % TiCl_4 precursor and the addition of 10 % Na_3PO_4 at a) $30\text{ }^\circ\text{C}$, b) $60\text{ }^\circ\text{C}$ and c) $95\text{ }^\circ\text{C}$.

5.2.7. Summary of MSS in sulfates

The results of the MSS with Na_2SO_4 generally differ from those in NaCl . The precursor preparation method (DMP or WCP) plays a predominant role for the habit formation, morphology and the phase composition (see the graphical summary in figure 5.73). The temperature, the precursor content (in wt. %) and the salt matrix composition are the main factors in DMP. The replacement of Cl^- by the bulky SO_4^{2-} -ion retards the ART. This can be explained by the contraction of the tetragonal unit cell that

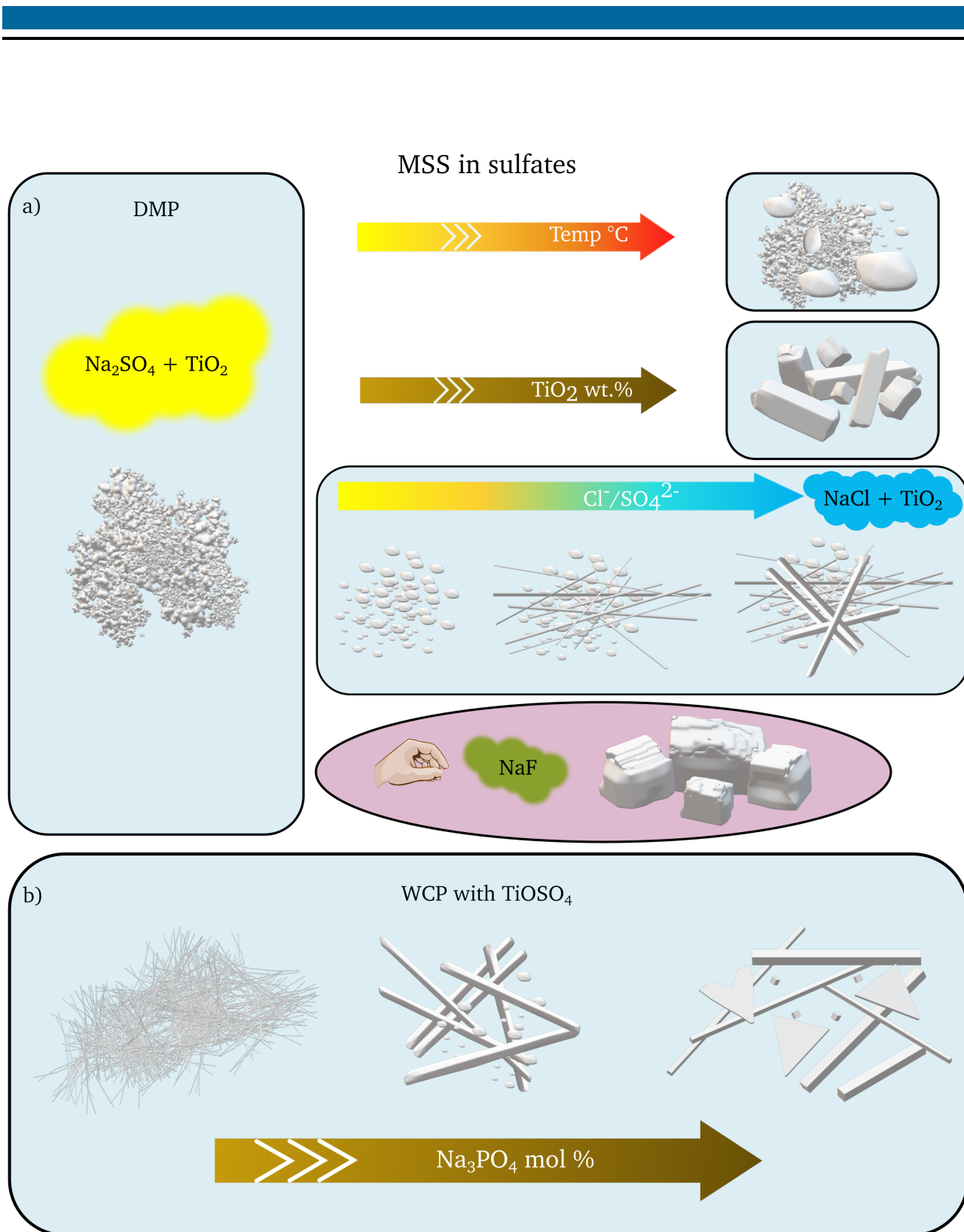


Figure 5.73.: MSS in Na_2SO_4 : schematic representation of the change of a) the TiO_2 crystals morphology with temperature, precursor concentration, the $\text{Cl}^-/\text{SO}_4^{2-}$ ratio and the addition of NaF by DMP; b) the rutile and NTO particle size and morphology by WCP with TiOSO_4 and the addition of Na_3PO_4 .

occurs during the ART [302]. Rutile is not the main phase by MSS in Na_2SO_4 at 900°C , independent of the chosen TiO_2 precursor concentration (exactly the opposite of the MSS in NaCl). Rutile becomes dominant only at a temperature $\geq 1000^\circ\text{C}$. Moreover, the ART rate in sulfates is faster for the lowest precursor concentration (1 wt. % at 900°C), opposite to the behavior observed in chlorides. The rutile crystals are not assuming the rod-shaped morphology typically observed in chlorides. These findings are further supported by the results of the experiments performed in the $\text{NaCl-Na}_2\text{SO}_4$ mixture: increasing the $\text{Cl}^-/\text{SO}_4^{2-}$ ratio leads to a faster ART rate and a higher concentration of rod-shaped crystals. The addition of few mol% of NaF to Na_2SO_4 causes more faceted crystals by terraced growth (see figure 5.46). The B_2O_3 addition influences the surface of the crystals, increasing their roughness. Synthesis in pure oxygen increases the rutile habit and promotes the formation of truncated bipyramid of rutile. Lowering the oxygen partial pressure increases the ART rate, but not at the same extent as in the chloride environment.

Concerning the WCP, the precursor concentration (TiOSO_4 oder TiCl_4), the Na_3PO_4 concentration and the temperature of the precipitation step (60°C vs. 30°C) have a main influence on the resulting samples. Notably, the size of the crystals is affected by the amount of TiOSO_4 precursor. The WCP provides a dominant presence of TiO_2 and strongly enhances the formation of NTO in contrast to the DMP. The addition of Na_3PO_4 — a strong Lux-Flood acid — to 5 wt. % TiOSO_4 strongly retards the ART at 1000°C and hinders the titanate formation. The retardation effect is more evident for high Na_3PO_4 concentrations ($5\% \leq \text{wt. \%} \leq 20\%$), leading to an anatase/rutile ratio > 1 . The Na_3PO_4 presence also determines the rutile habit formation leading to V-shaped crystals for a Na_3PO_4 concentration ≥ 10 wt. %. The WCP with 5 wt. % Na_3PO_4 , heat-treated in pure oxygen at 1100°C , provides the most useful habit for the pearl luster application: "mosaic tile"-like rutile crystals. Higher Na_3PO_4 concentrations only lead to an increased formation of V-shaped rutile crystals. Without the addition of Na_3PO_4 , the NTO phase is a by-product of the MSS. Increasing the pH of the precipitation step by adding NaOH , promotes the pure NTO formation (see following section).

5.3. Molten salt synthesis of sodium titanates in sulfates

According to the experimental findings presented in the sections 5.1 and 5.2, the $\text{Na}_2\text{Ti}_6\text{O}_{13}$ (NTO) phase often appears as a by-product in the MSS performed with the aim of obtaining rutile crystals with a flake morphology suitable to be used as pearl luster pigment (PLP). The potential use of NTO as a high-voltage anode for lithium-ion batteries motivated a deeper investigation of its synthesis via MSS. Hydrothermal or sol-gel synthesis routes are commonly reported in literature (see section 3.3 in chapter 3). The advantage of NTO obtained by MSS via WCP is its unique morphology that, combined with its crystal structure (section 3.3), favors energy-storage applications (see section 5.4).

5.3.1. Influence of the NaOH concentration on the phase composition

The TiO₂ synthesis presented in section 5.2.6.2 reveals that an increased acidity in the salt melt — achieved by Na₃PO₄ addition — inhibits the NTO formation and leads to important changes in the rutile habit. As a consequence, the opposite experimental direction has been followed aiming to exclusively synthesize titanates. Na₂SO₄ was selected as the salt matrix common to all the experiments described in this section. Some parameters, especially the concentration of NaOH added and the synthesis temperature, have been varied to analyze their influence on the final phase composition. Increase of the NaOH concentration leads to an increase of the L-F basicity of the melt (see section 2.3.4) and sufficiently sodium will be available for the formation of NTO. NaOH is used to establish a pH > 7 in the WCP of the Ti-precursor (see chapter 4 for the experimental details). The addition of the hydroxide leads to a NaOH-Na₂SO₄ salt mixture in the subsequent MSS (lowering the melting point of the salt matrix, see phase diagram in figure B.6 in the appendix). The phase compositions are collected in table 5.11 and reveal the change of the titanates crystal structure at high NaOH concentration.⁶

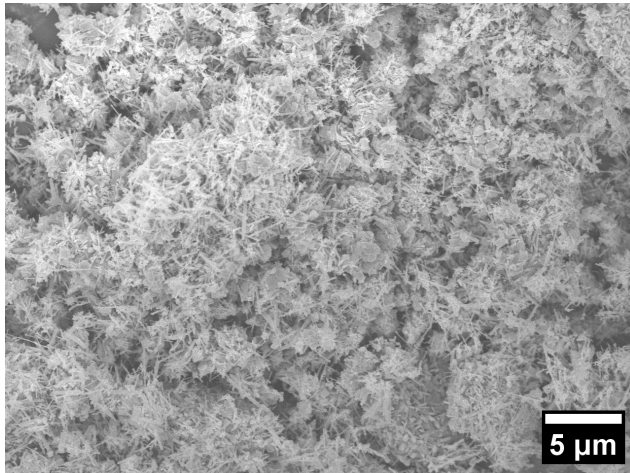
Table 5.11.: Phase composition of samples obtained by WCP of TiOSO₄ at different pH and MSS at 750 °C - 1100 °C. A = Anatase, R = Rutile, NTO = Na₂Ti₆O₁₃, NTO7 = Na₂Ti₃O₇.

pH	wt.% TiO ₂	750 °C	800 °C	850 °C	900 °C	1000 °C	1100 °C
7	5	-	-	NTO, A, R	NTO, R	NTO, R	NTO, R
7	10	-	-	NTO, A, R	NTO, R	NTO, R	NTO, R
7	20	-	-	NTO, A, R	NTO, R	NTO, R	NTO, R
8	5	-	-	NTO, A, R	NTO, A, R	NTO, R	NTO, R
9	5	-	-	NTO, A, R	NTO, R	NTO, R	NTO, R
10	5	-	-	NTO, A, R	NTO, R	NTO, R	NTO, R
10	20	-	-	NTO, A, R	NTO, A, R	NTO, R	NTO, R
10.3	5	NTO	NTO	NTO	NTO	NTO	NTO
11	5	-	-	NTO, NTO7	NTO, NTO7	NTO, NTO7	NTO, NTO7
11	20	-	-	NTO, NTO7	NTO, NTO7	NTO, NTO7	NTO, NTO7
11-eutectic	5	-	NTO, NTO7	-	NTO, NTO7	NTO, NTO7	NTO, NTO7

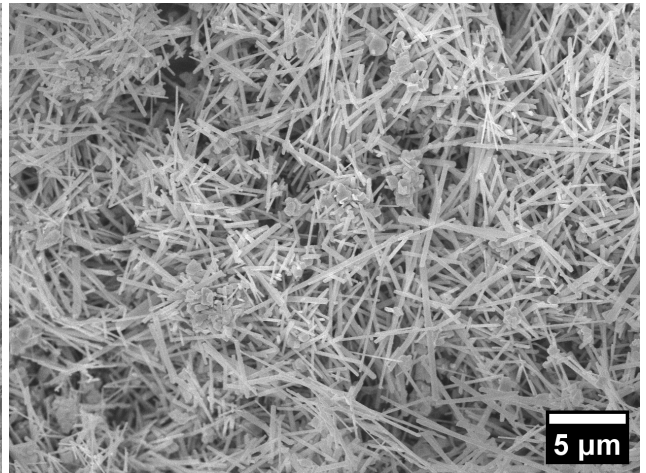
Setting pH = 7 in the WCP with 5 wt. % TiOSO₄ leads to a mixture of rutile and NTO in the MSS at T > 850 °C (see section 5.2.6.1). The rod-shaped NTO particles achieve a smaller size at 850 and 900 °C than at temperatures > 900 °C (see figure 5.74). Especially at 850 °C the particles exhibit a maximum length of ≈ 1 μm, a value that is far from the 10 μm reached at higher temperatures. Moreover, the majority of the rods have a diameter ≤ 200 nm, close to the average value at higher temperature.

An increase of the precursor fraction by reducing the amount of Na₂SO₄ reveals a combination of rutile and NTO for temperatures > 850 °C for both 10 and 20 wt. % TiOSO₄ (see table 5.11 and figure C.18 in the appendix). The anatase content slightly increases with increasing precursor at pH = 7 and 850 °C (see figure C.19 in the appendix). For a pH = 8 a higher content of anatase than rutile results (see figure C.20a in the appendix). The ART is even not terminated at 900 °C showing an anatase reflection with lower intensity than that of rutile.

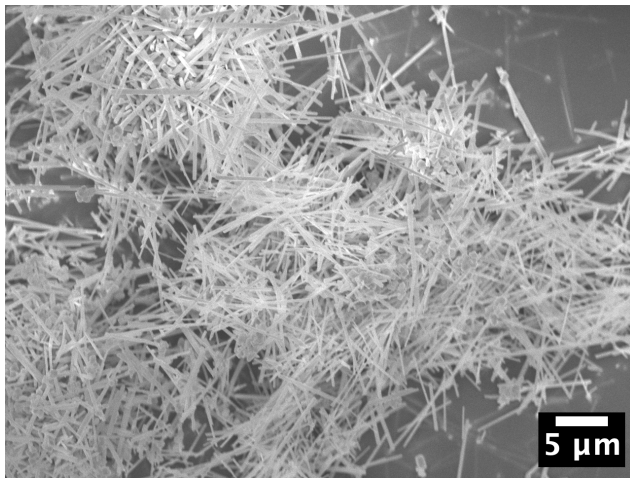
⁶The data reported in table 5.11 are reported in the bachelor thesis of Samira Astrid Kiefer, performed under my supervision in the dispersive solids group.



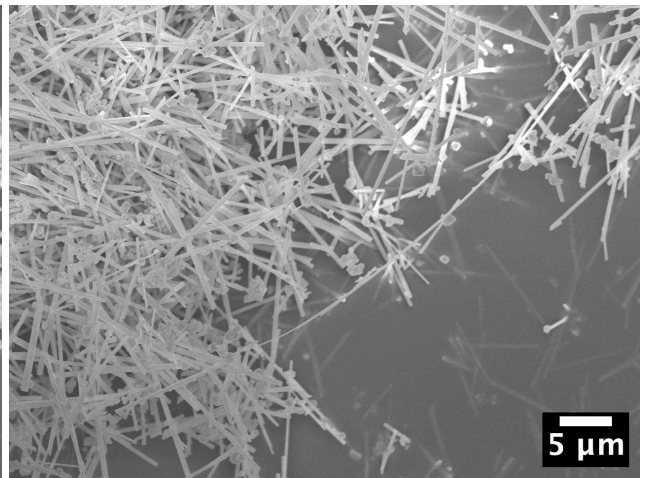
(a) 850 °C; WCP at pH = 7



(b) 900 °C; WCP at pH = 7



(c) 1000 °C; WCP at pH = 7



(d) 1100 °C; WCP at pH = 7

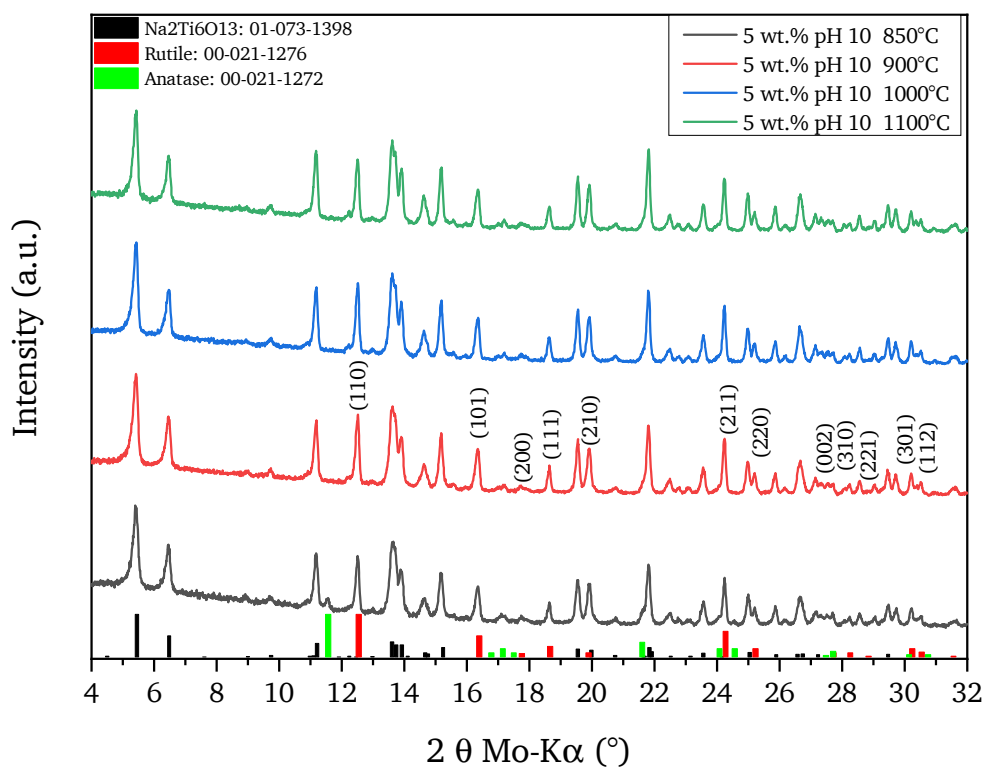
Figure 5.74.: SEM images of titania and NTO particles synthesized by MSS in Na_2SO_4 via WCP with 5 wt. % TiOSO_4 precursor at pH = 7 and heat-treated at a) 850 °C, b) 900 °C, c) 1000 °C and d) 1100 °C.

According to table 5.11 the NTO formation increases with the pH of the WCP and the basicity of the molten salt. A significant change in the phase ratio between rutile and NTO occurs for $\text{pH} \geq 10$, where the NTO becomes the dominant phase (see figure 5.75a). Increase to $\text{pH} = 11$ abruptly alters the phase composition of the samples. The higher amount of NaOH leads to the formation of the $\text{Na}_2\text{Ti}_3\text{O}_7$ and NTO already at 850°C (see figure 5.75b). No rutile or anatase are detected. Only the two titanate phases exist up to $T = 1100^\circ\text{C}$. The temperature increase leads to an increase of the $\text{Na}_2\text{Ti}_3\text{O}_7$ phase content as indicated by the intensity rise of its reflections.

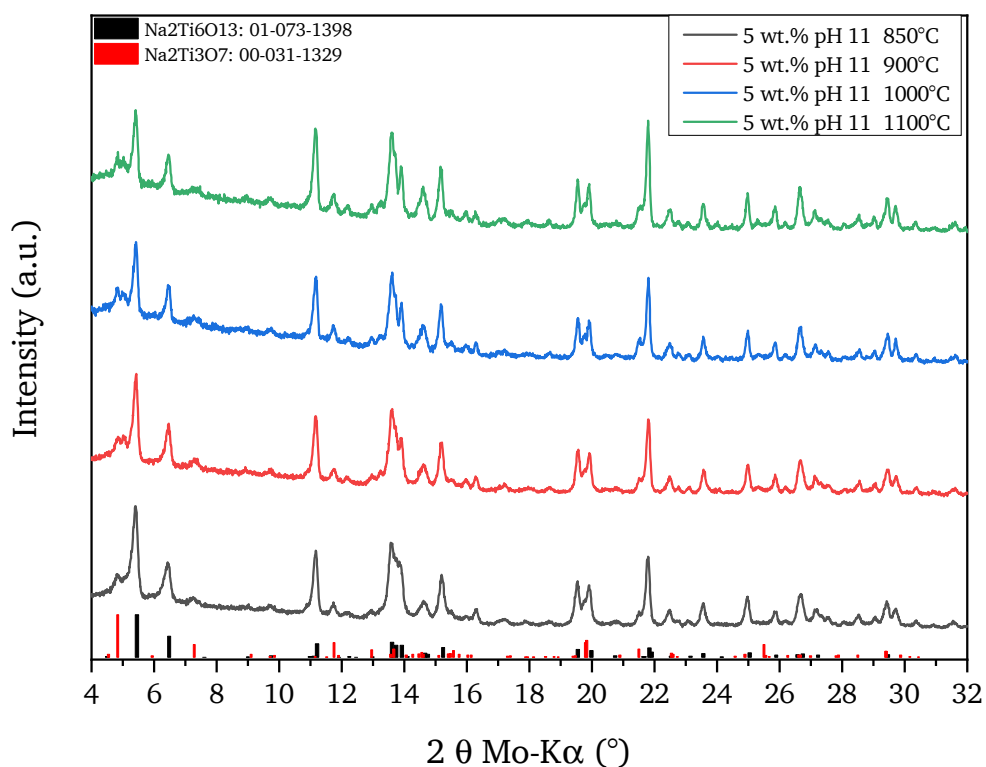
The morphology of the samples exhibit distinct changes with precursor pH and synthesis temperature. The comparison of the batches obtained at $\text{pH} = 7$ and treated at 850°C shows that the morphology depends on the precursor content (see figures 5.76a, 5.76b and 5.76c). Both polyhedral and rod-shaped crystals are present in the three samples. Their sizes and concentrations change with the precursor amount. The polyhedral particles obtained with the 20 wt. % precursor have sides with a length of 500 nm to $1\ \mu\text{m}$. The rod-shaped particles seldom exceed a length of $1\ \mu\text{m}$ and have diameters between 100 nm and 300 nm. At 5 wt. % and 10 wt. % precursor their size is smaller than at 20 wt. %. An increase to temperatures $\geq 1000^\circ\text{C}$ diminishes the precursor influence on the morphology, since all the samples mainly contain rod-shaped particles. From a morphological point of view, the pH increase shifts the product formation towards titanates. This can be observed already at 850°C and 5 wt. % TiOSO_4 (see figures 5.76c, 5.76d and 5.76e). The pH increase from 7 to 10 causes a decrease of the average particle size and an increase of NTO nanorods in comparison to the polyhedral rutile particles. A pH increase from 10 to 11 leads to the formation of shorter nanorods. This could be attributed to the concurrent formation of $\text{Na}_2\text{Ti}_3\text{O}_7$. The comparison between the samples obtained at $\text{pH} = 10$ and $\text{pH} = 11$ and temperatures $\geq 1000^\circ\text{C}$ (see figure 5.77) confirms that the obtained morphology is related to the crystal structure change. At 900°C the sample obtained at $\text{pH} = 11$ shows an enhanced growth of the nanorods, reaching higher lengths. Similarly, at 1000°C the sample with $\text{pH} = 11$ exhibits thinner nanorods and an increase in length. The greatest change can be observed at 1100°C for $\text{pH} = 11$, revealing the formation of belt-shaped crystals whose width can even reach $5\ \mu\text{m}$. This type of growth could be attributed to the formation of the layered titanate $\text{Na}_2\text{Ti}_3\text{O}_7$ (see chapter 3, section 3.3).

A specific case was investigated for the WCP at $\text{pH} = 11$. The addition of NaCl to Na_2SO_4 (0.53 mol NaCl and 0.47 mol Na_2SO_4) leads to a decrease of the melting point to 625°C (see phase diagram in figure B.7 in the appendix and table 2.3), allowing to investigate the titanate formation in the melt at 700°C and 800°C . The XRD data show $\text{Na}_2\text{Ti}_3\text{O}_7$ next to NTO already at 700°C (see figure 5.78). These two phases are the only components up to 1100°C . Note that the diffractogram of the 700°C samples shows less pronounced reflections due to a low degree of crystallinity. The SEM micrographs in figure 5.79 reveal only flakes which already transform at 800°C into nanorods.

The results presented above highlight the changes with the NaOH fraction, from a mixture of mainly rutile and titanates, to a mixture with prevalent sodium titanate, to only sodium titanate and finally a combination of two different sodium titanate structures with a different alkali/Ti atomic ratio. The results can be explained by an increase of "oxobasicity" in the following series of compounds: $\text{TiOSO}_4 <$

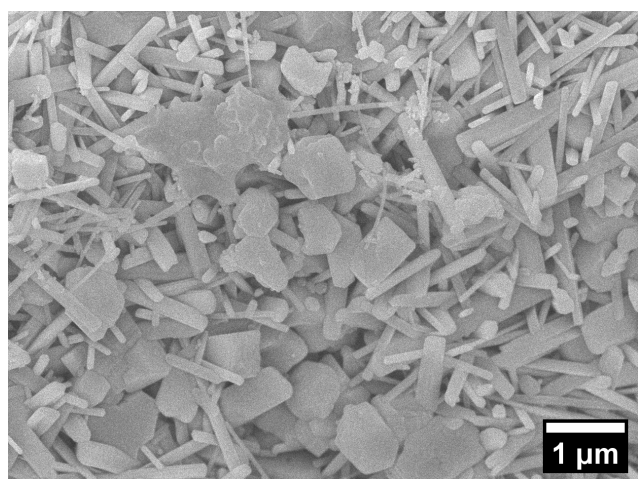


(a) WCP with pH = 10

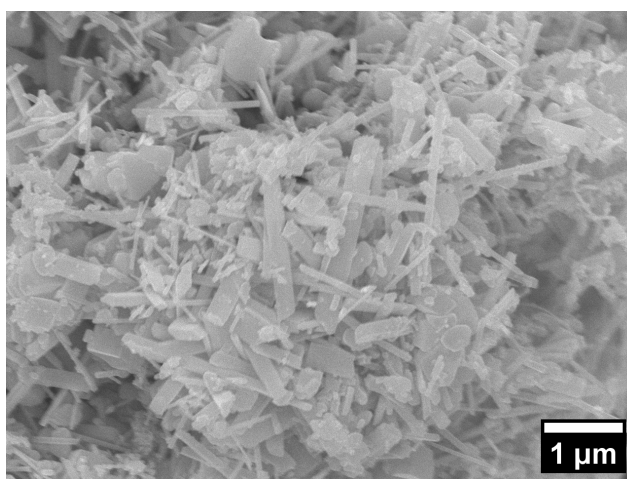


(b) WCP with pH = 11

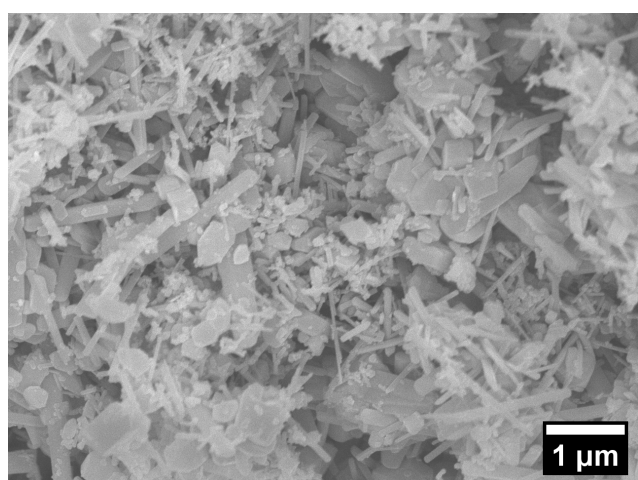
Figure 5.75.: XRD of samples obtained by WCP with a) pH = 10 and b) pH = 11 performed at 60 °C with 5 wt. % TiOSO₄ precursor. Reference XRD patterns from the ICDD for rutile, anatase, NTO and Na₂Ti₃O₇ are given at the bottom of the graph.



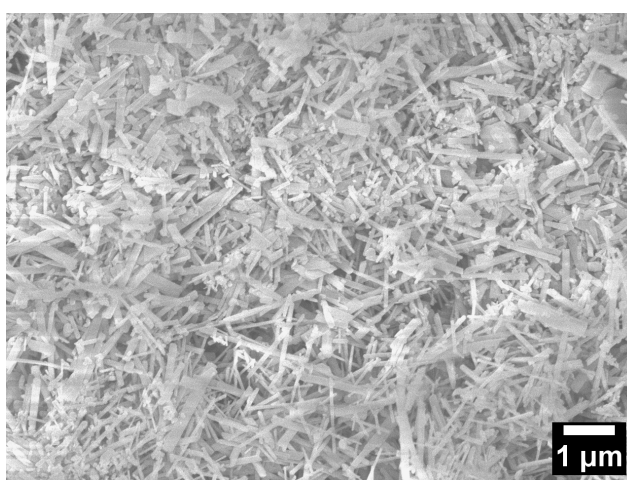
(a) pH = 7; 20 wt. % TiOSO_4



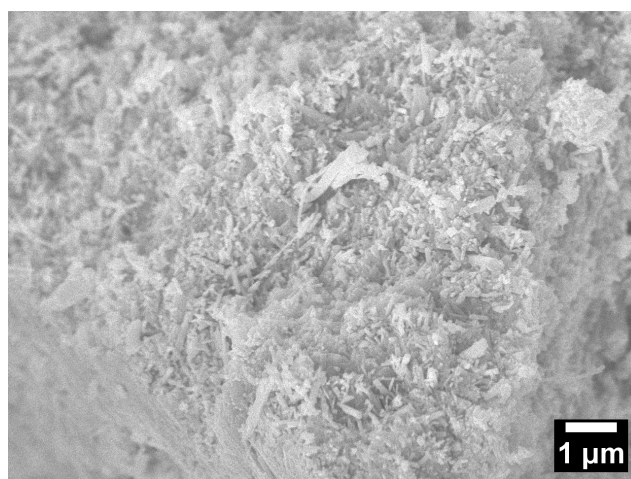
(b) pH = 7; 10 wt. % TiOSO_4



(c) pH = 7; 5 wt. % TiOSO_4

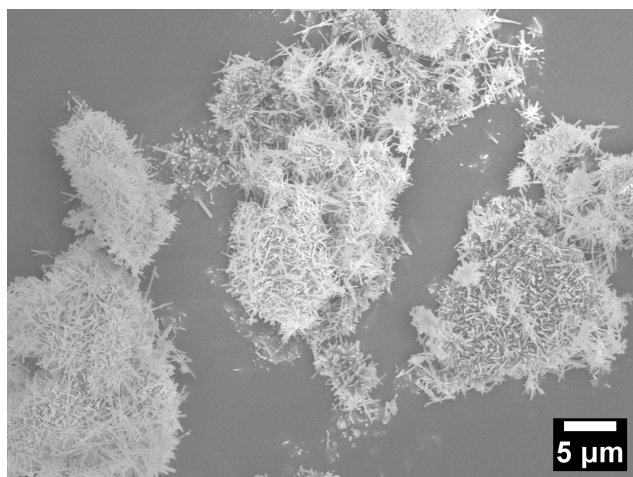


(d) pH = 10; 5 wt. % TiOSO_4

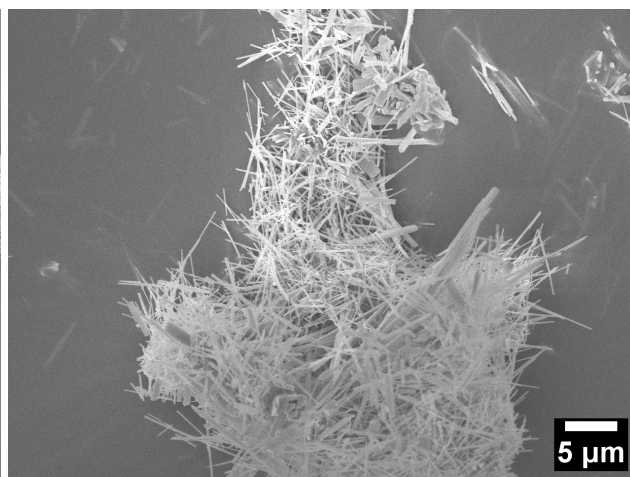


(e) pH = 11; 5 wt. % TiOSO_4

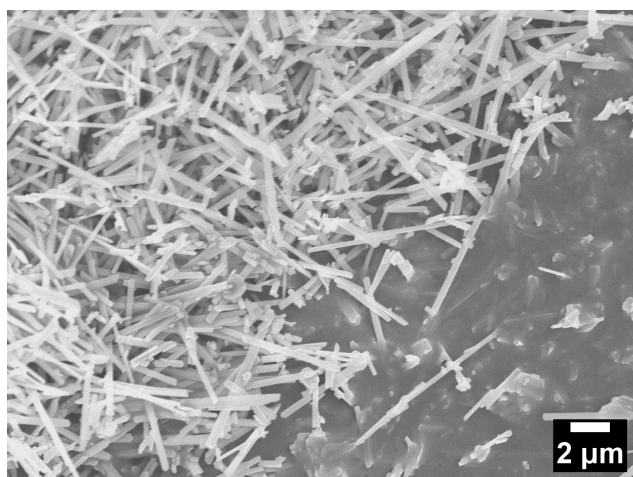
Figure 5.76.: SEM images of samples synthesized by MSS in Na_2SO_4 via WCP with 5, 10 and 20 wt. % of TiOSO_4 precursor at pH = 7, 10 and 11, all heat-treated at 850 °C.



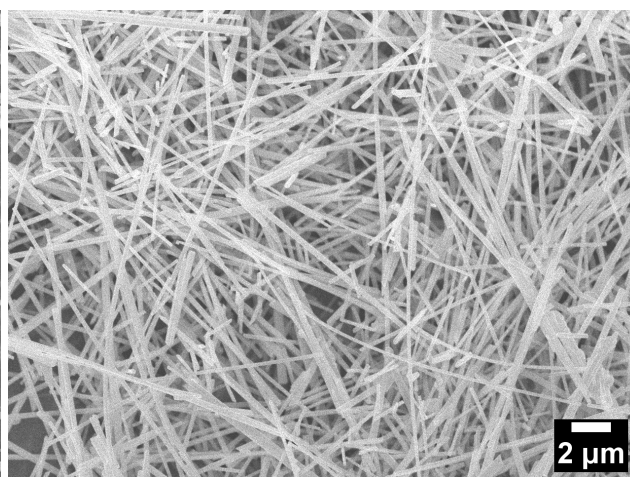
(a) 900 °C; pH = 10



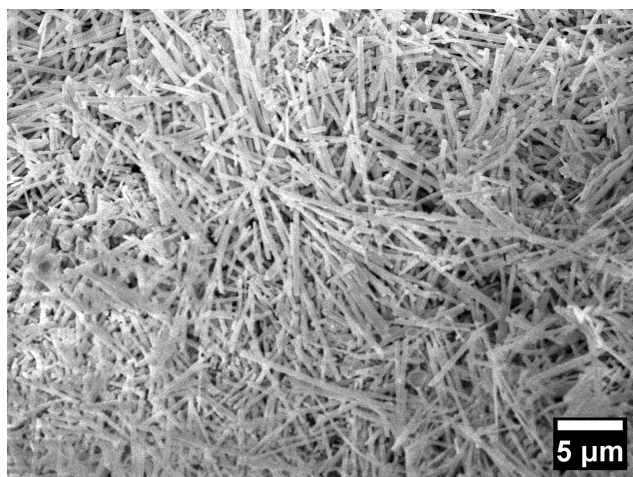
(b) 900 °C; pH = 11



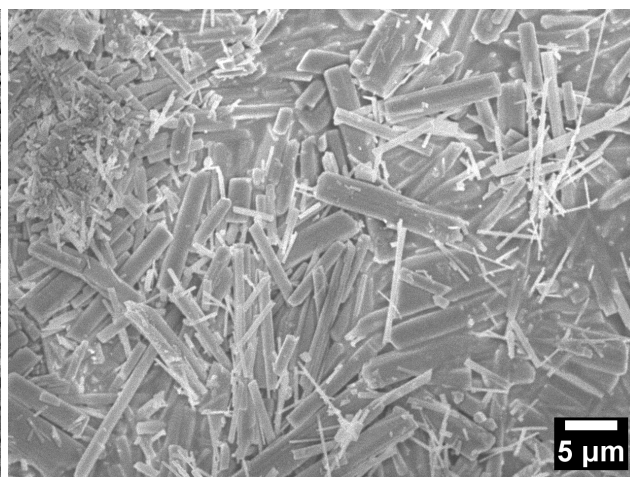
(c) 1000 °C; pH = 10



(d) 1000 °C; pH = 11



(e) 1100 °C; pH = 10



(f) 1100 °C; pH = 11

Figure 5.77.: SEM images of samples synthesized by MSS in Na_2SO_4 via WCP with 5 wt. % TiOSO_4 precursor at pH = 10 and pH = 11 and heat-treated at a) and b) 900 °C, c) and d) 1000 °C and e) and f) 1100 °C.

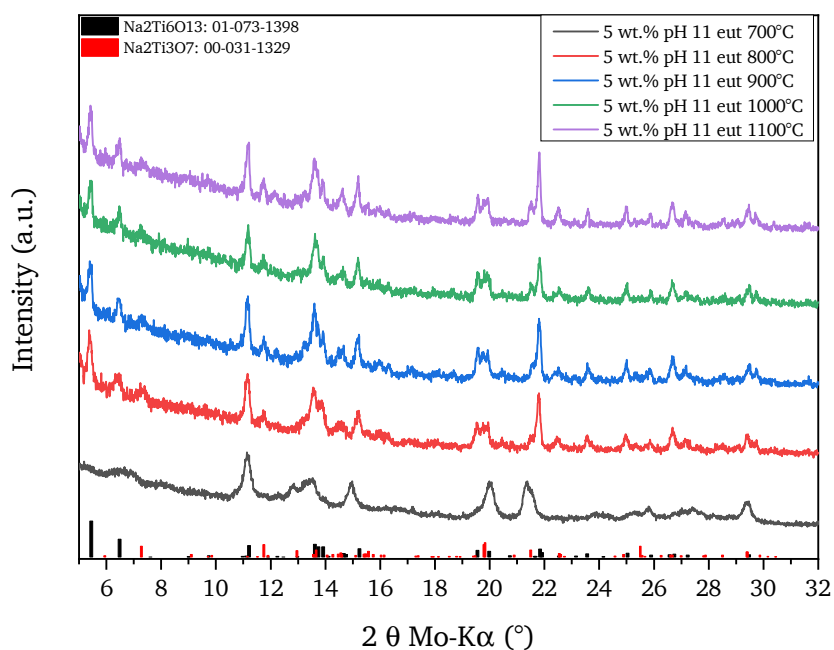


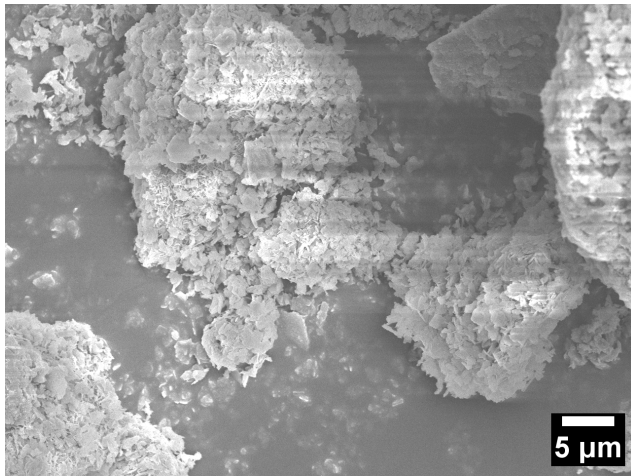
Figure 5.78.: XRD of samples obtained by WCP with pH = 11 performed at 60 °C with 5 wt. % TiOSO₄ precursor in the eutectic mixture 0.53 NaCl-0.47 Na₂SO₄ synthesized at 700 °C < T < 1100 °C. Reference XRD patterns from the ICDD for rutile, anatase, NTO and Na₂Ti₃O₇ are given at the bottom of the graph.

TiO₂ < Alk₂Ti₆O₁₃ < Alk₂Ti₄O₉ < Alk₂Ti₂O₅ < Alk₂TiO₃ ("Alk" = alkali metal) [306]. Accordingly, the oxygen activity in the melt has to be optimized to achieve compounds with high molecular weight. Ti atoms are then increasingly coordinated by O²⁻ ions.

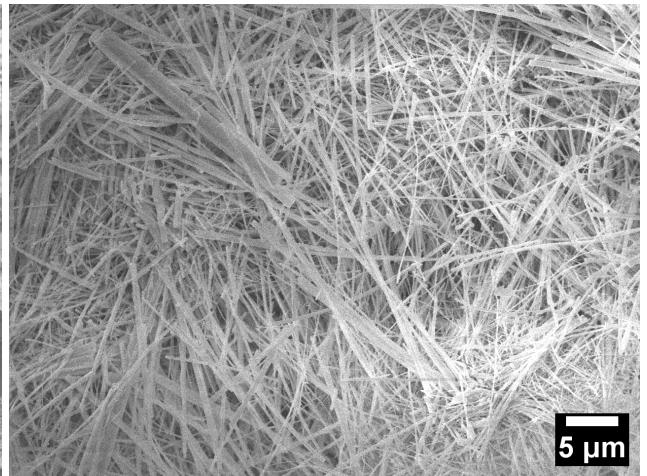
5.3.2. Synthesis of pure Na₂Ti₆O₁₃

Pure Na₂Ti₆O₁₃ has been obtained by WCP at a pH = 10.3 with 5 wt. % of TiOSO₄ at 60 °C and subsequent MSS at 900 °C < T < 1100 °C [307]. The XRD data of the samples are reported in figure 5.80. The addition of NaOH to Na₂SO₄ hinders the formation of rutile as well as anatase. The diffractograms match the ICDD entry (No.: 01-073-1398) for NTO. The samples are named according to the synthesis temperature as NTO-900, NTO-1000 and NTO-1100, respectively. They all reveal an anomaly concerning the (020) reflection at 21.79°. The intensity should be lower than that of the reflections at lower angles. Nevertheless it is close to the intensity reached by the (200) reflection, indicating strong preferential growth along <010> direction.

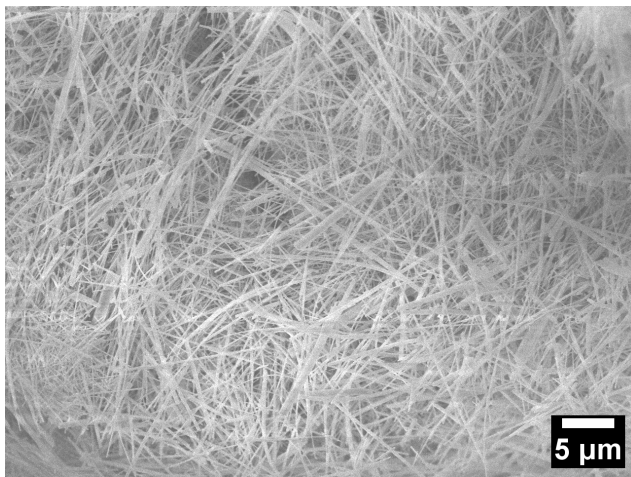
The morphology of the NTO samples is presented by the SEM micrographs in figure 5.81. They reveal a highly anisotropic morphology due to the presence of exclusively nanorods, thereby explaining the enhanced intensity of the (020) reflection (especially for sample NTO-1100). The rod-shaped crystals are organized in cotton-wads like aggregates. Those obtained at 900 °C have a smaller diameter,



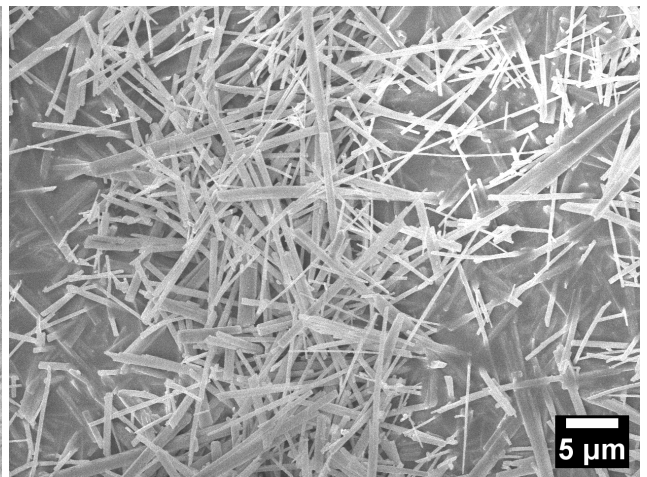
(a) 700 °C



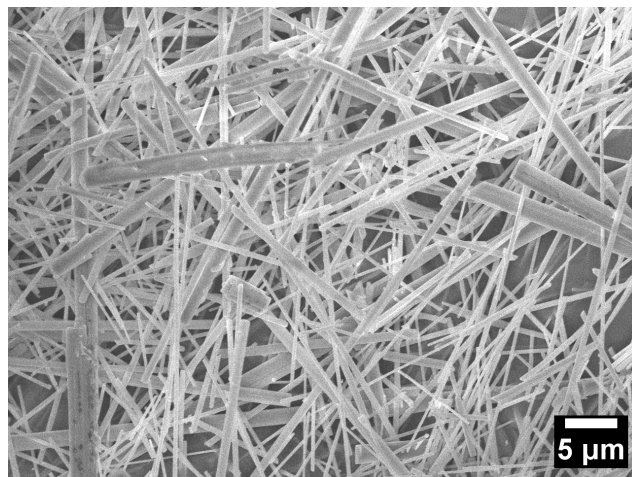
(b) 800 °C



(c) 900 °C



(d) 1000 °C



(e) 1100 °C

Figure 5.79.: SEM images of titanates particles synthesized by MSS in the eutectic mixture 0.53 NaCl-0.47 Na₂SO₄ via WCP with 5 wt. % TiOSO₄ precursor at pH = 11 and heat-treated at a) 700 °C, b) 800 °C, c) 900 °C, d) 1000 °C and e) 1100 °C.

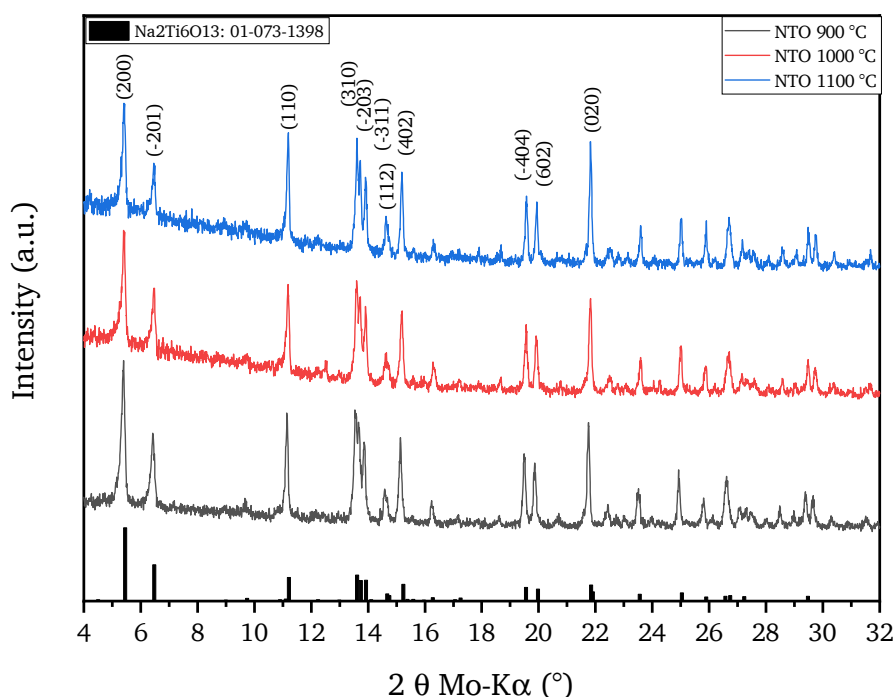


Figure 5.80.: Samples obtained by WCP with pH = 10.3 performed at 60 °C with 5 wt. % TiOSO_4 precursor in Na_2SO_4 . Reference XRD pattern from the ICDD for NTO is given at the bottom of the graph.

≈ 120 nm, than the crystals synthesized at temperatures ≥ 1000 °C (≥ 200 nm). The length of tens of microns, reaching even a maximal value of ≈ 40 μm , is noteworthy.

Electron backscatter diffraction (EBSD) analysis No commonly accepted growth mechanism of NTO nanorods has been reported in the literature. According to Dominko *et al.* [71] the rods grow preferentially along the direction perpendicular and not parallel to the tunnels formed by the edge-sharing octahedra. Pérez-Flores *et al.* [41] considered $\langle 110 \rangle$ as direction along which the rods develop. Cao *et al.* [241] identified the facet $(-2\ 0\ 1)$ as the most exposed one claiming it as responsible for a facilitated Na^+ diffusion through the tunnels. Teshima *et al.* [44, 300] suggested growth along the $\langle 010 \rangle$ direction [44]. In view of these divergent results, an EBSD analysis was performed in order to determine the growth axis and the most exposed facet. Figure 5.82 shows the corresponding EBSD results for a NTO-1100 nanorod (see additional data of NTO-900 and NTO-1100 in figure D.27 in the appendix). The acquired Kikuchi patterns could be unambiguously indexed, clearly indicating that the growth direction of all analyzed nanorods is parallel to the $\langle 010 \rangle$ direction, *i.e.* the short axis of the unit cell (see insert in figure 5.82a). The identification of the top facet is not as straight forward, given that the inclination of the surface cannot be identified as precisely as the orientation of the long axis. However, all analyzed nanorods show crystal orientations with a (101) surface plane (similar to the example shown in figure 5.82a). These results essentially confirm the growth model of Teshima *et al.*

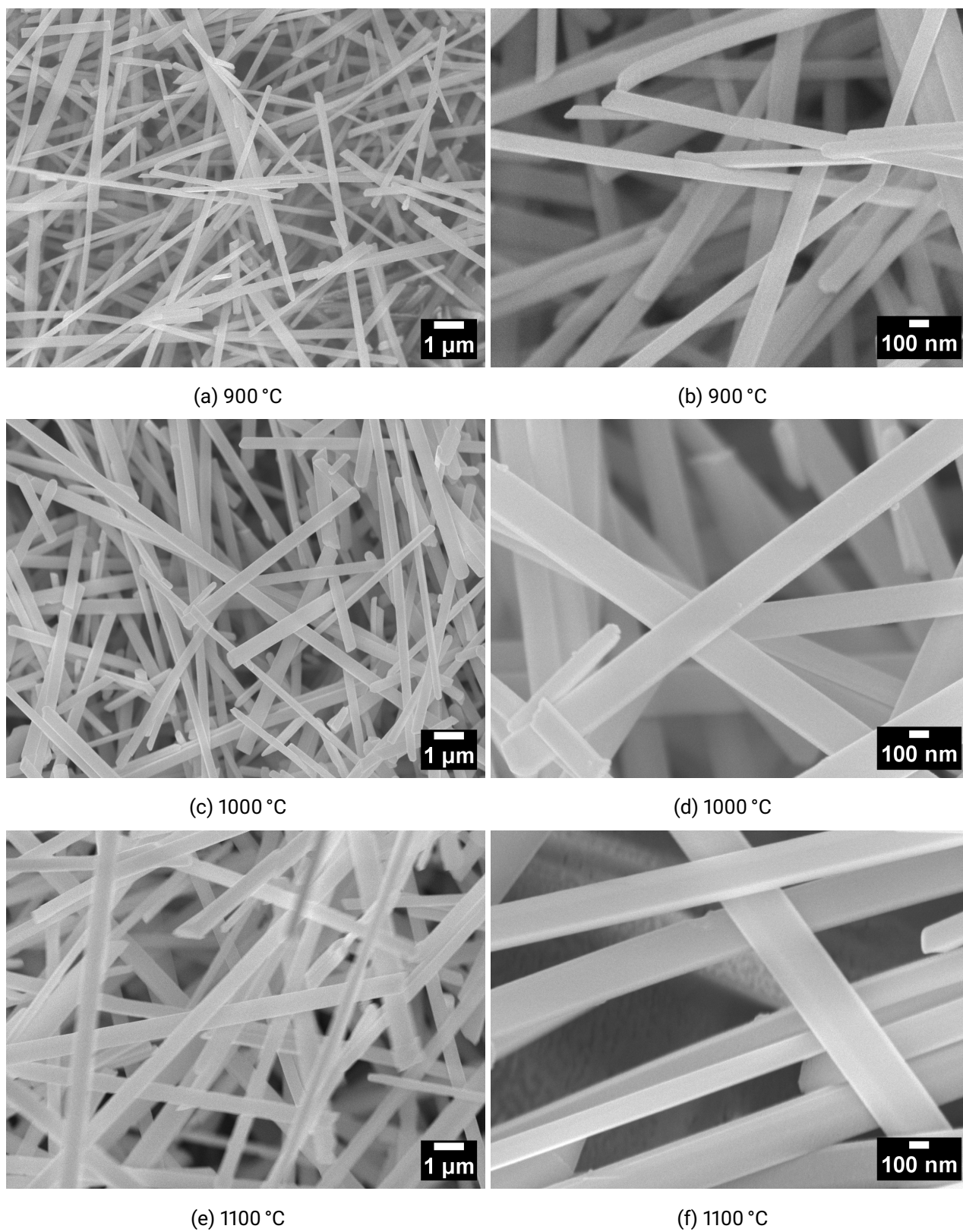


Figure 5.81.: SEM images of $\text{Na}_2\text{Ti}_6\text{O}_{13}$ rod-shaped particles synthesized by MSS in Na_2SO_4 via WCP with 5 wt. % TiOSO_4 precursor at pH = 10.3, heat-treated at a) 900 °C, c) 1000 °C and e) 1100 °C. A magnification of each is reported in b), d) and f) respectively.

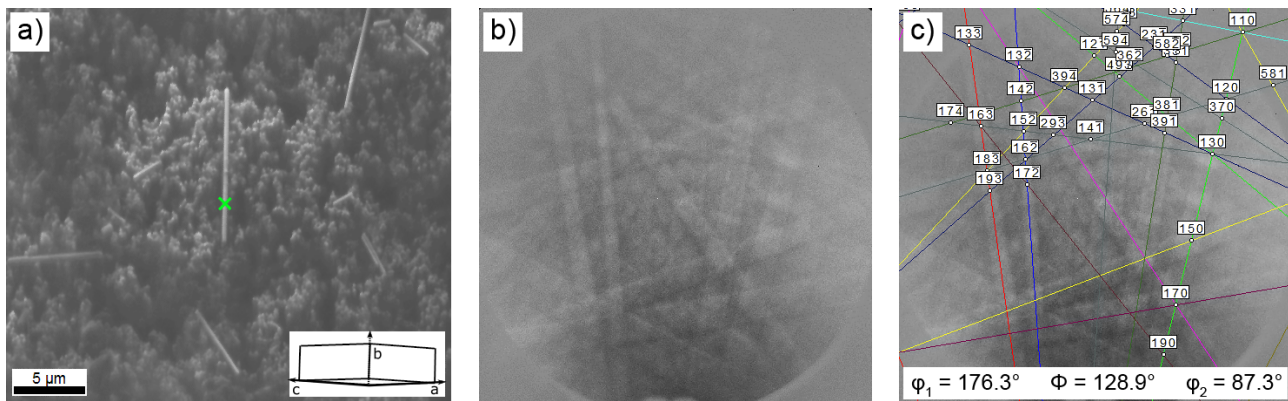


Figure 5.82.: SEM image of NTO-1100 showing nanorods on a carbon pad (a) with raw Kikuchi pattern (b) and indexed pattern with Euler angles (c) acquired at the spot marked by a green cross in (a). The insert in (a) shows the orientation of the unit cell according to the indexed pattern.

HT-XRD analysis The temperature dependent structure evolution during the MSS has been followed by *in-situ* XRD analysis. Figure 5.83 reports the structural changes with temperature. The investigated temperature range is limited by the set-up up to $T = 900^\circ\text{C}$. A quartz capillary is filled with the dried powder (less than 1 mg), sealed and heated up to 900°C . As a main result of the experiment, anatase converts to rutile at $T > 800^\circ\text{C}$. Up to 870°C no transformation to $\text{Na}_2\text{Ti}_6\text{O}_{13}$ can be observed. The reflections belonging to the Na_2SO_4 phase start to shift at temperatures $> 240^\circ\text{C}$ towards smaller angles, because of a structural transformation occurring, also confirmed by DTA results (see following paragraph). The oxygen concentration above the melt is fixed and rather low when heating the sample in the closed capillary (to $\approx 900^\circ\text{C}$). The NTO formation will be suppressed under this condition.

DTA analysis The results of the *in-situ* XRD analysis can be compared with the DTA results in synthetic air (75 mL min^{-1} , see figure 5.84). The DTA reveals two strong endothermic peaks at 243.9°C and 882.1°C . They are attributed to the structural change of Na_2SO_4 [303] (also visible in the phase evolution reported in figure 5.83) and to its melting point. The DTA measurement performed on a pure Na_2SO_4 sample (see red line in figure 5.84), confirms these findings. The structural change of Na_2SO_4 consists of the phase transition V-I, reported in the same range of temperature (also visible in the plot in figure 5.83) [303]. Other endothermic peaks of a lower intensity are recorded at 119.8°C , 517°C and 974.8°C . The first is explained by residual water present in the sample. This is accompanied by a mass loss of 1.2% of total 1.86%. The peak at 517°C is attributed to a solid-state reaction between nanocrystalline anatase and Na_2SO_4 [5], while the one at 974.8°C is ascribed to the evaporation of gaseous species SO_x . According to Sauvet *et al.* [250] the $\text{Na}_2\text{Ti}_6\text{O}_{13}$ crystallization process is exothermic, taking place at a temperature of $\approx 550^\circ\text{C}$ (see the inset in figure 5.84). Considering the different synthesis conditions (solid state sintering applied by [250]), it is possible to attribute the exothermic peak at $\approx 463^\circ\text{C}$ to the formation of $\text{Na}_2\text{Ti}_6\text{O}_{13}$ at lower temperatures by MSS.

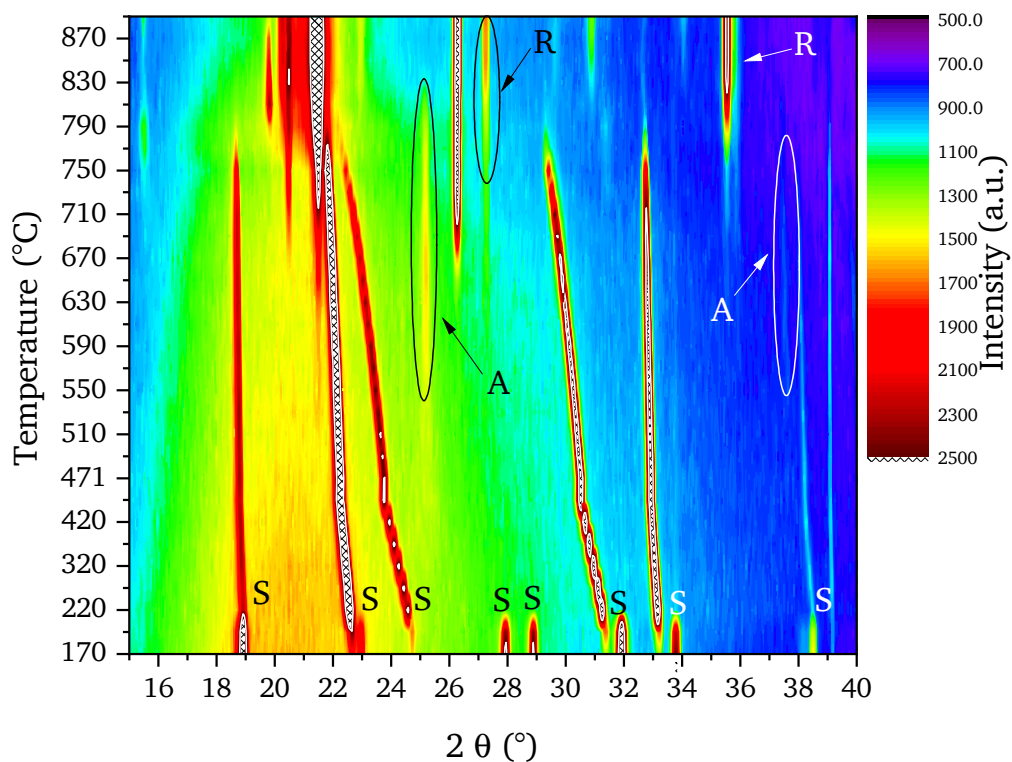


Figure 5.83.: XRD diffractograms recorded *in-situ* during the heat-treatment up to 900 °C of the precursor mixed to Na_2SO_4 . The phases are labeled as follows: S) Na_2SO_4 with the recognizable structural change at $T \approx 240$ °C; A) anatase; R) rutile.

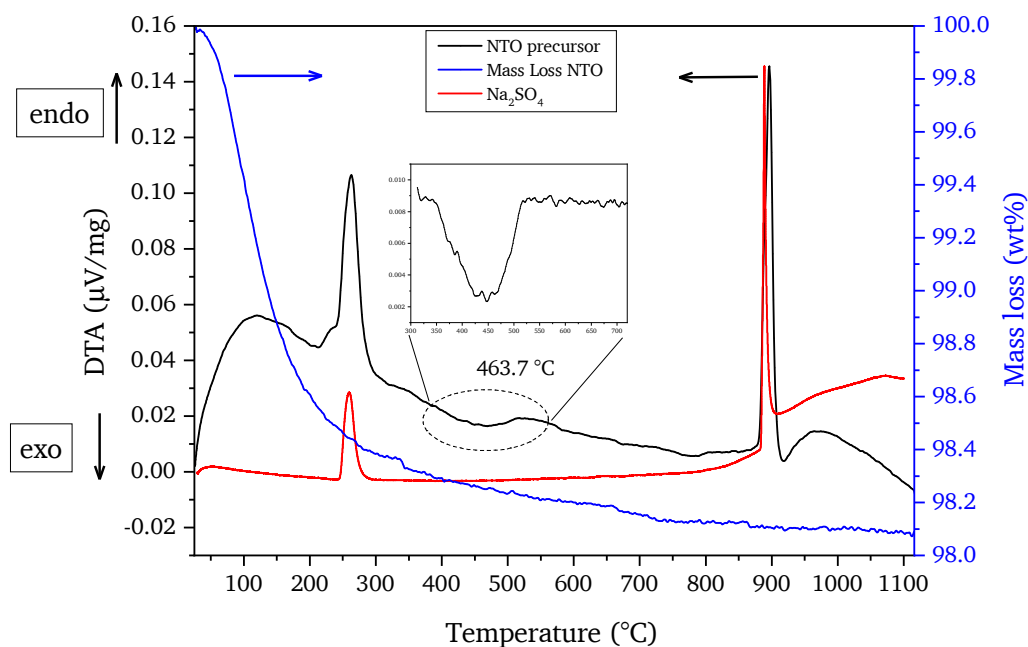


Figure 5.84.: DTA (black line) and TG (blue line) measurement performed on the precursor powder mixed to Na_2SO_4 . The DTA of Na_2SO_4 is reported for comparison (red line). The inset shows a magnification of the exothermic peak at 463.7 °C with baseline correction.

5.3.3. Raman investigation of Na₂Ti₆O₁₃

Figure 5.85 presents the Raman spectra of NTO synthesized by MSS. The Raman data confirm the remarkable purity of the samples since typical peaks denoting the presence of rutile (144.5 cm⁻¹, 241.6 cm⁻¹, 449.9 cm⁻¹ and 610.2 cm⁻¹) and anatase (144.5 cm⁻¹) are absent. The presence of sharp peaks with strong intensity underlines the high crystallinity of the samples. Peaks attributable to Na–O vibrations and Ti–O stretching vibrations are identified at wavenumbers below 400 cm⁻¹ [243]. The peaks at 139 and 683 cm⁻¹ are attributed to Ti–O–Ti bonds (edge-shared TiO₆ octahedra), scaffolding the tunnel structure [241, 243, 308]. For these two peaks we observe a blue shift of about 9 cm⁻¹ with respect to the reported literature data [241]. The Ti–O–Ti bonds in corner-shared TiO₆ octahedra of NTO are reflected by the vibration band at 750 cm⁻¹. The bands in the range 195 to 276 cm⁻¹, characteristic of the Na–Ti–O bond [241], confirm the assignment to NTO. Moreover, the lack of a band at 700 cm⁻¹, typically for Ti–O–H vibrations, proves that the samples are fully dehydrated [243]. Finally, the peak located at 876 cm⁻¹ is assigned to the short Ti–O stretching vibration with low coordination [241, 243, 308–310] indicating that each oxygen atom is bound to at least two Ti atoms [46, 243, 309]. The fact that this peak is increasing by about 80 % with the synthesis temperature suggests a change in the TiO₆ framework. In parallel, the band at 226 cm⁻¹ is decreasing in intensity (about 20 %). For an easier check of these intensity variations, figure E.6 in the appendix includes a break between 320 and 820 cm⁻¹. The decrease of the 226 cm⁻¹ band and the increase of the 876 cm⁻¹ band most likely arise from a simultaneous change of Ti and Na bonds during the MSS.

5.3.4. TEM and EELS investigation of Na₂Ti₆O₁₃

HR-TEM has been performed on the samples NTO-900 and NTO-1100 in order to get more insight into their microstructure. Figure 5.86a shows a bright-field TEM image of NTO-900. The selected area electron diffraction (SAED) pattern shown in figure 5.86b has been taken in the area marked by a red circle. The nanorod is oriented in [0-10] zone-axis orientation and can be indexed using the data of Pérez-Flores *et al.* [228]. Figure 5.86c is a HRTEM phase contrast image of the nanorods. Figure 5.86d is the corresponding fast Fourier transform (FFT) which is well indexed by the structural data of Pérez-Flores *et al.* [228]. Figure D.28a and b in the appendix demonstrate that the FFT pattern of NTO-900 agrees well with JEMS calculations [311] with the structural data input taken from Perez-Flores [228].

Figure 5.87a is a bright-field TEM image of sample NTO-1100. Figure 5.87b presents the SAED pattern of the region marked by the red circle in figure 5.87a. Evidently, the nanorod is oriented along the [001] zone-axis of NTO. The high-resolution phase contrast image (see figure 5.87c) and its corresponding FFT confirm this finding (figure 5.87d). Figures D.28c and d in the appendix reveal a good match between the acquired FFT pattern and the JEMS calculations [311]. Further information about the local structure has been obtained by an atomic resolution STEM high angle annular dark-field (HAADF) Z-contrast image (figure 5.87e). The inset in figure 5.87e exhibits the corresponding

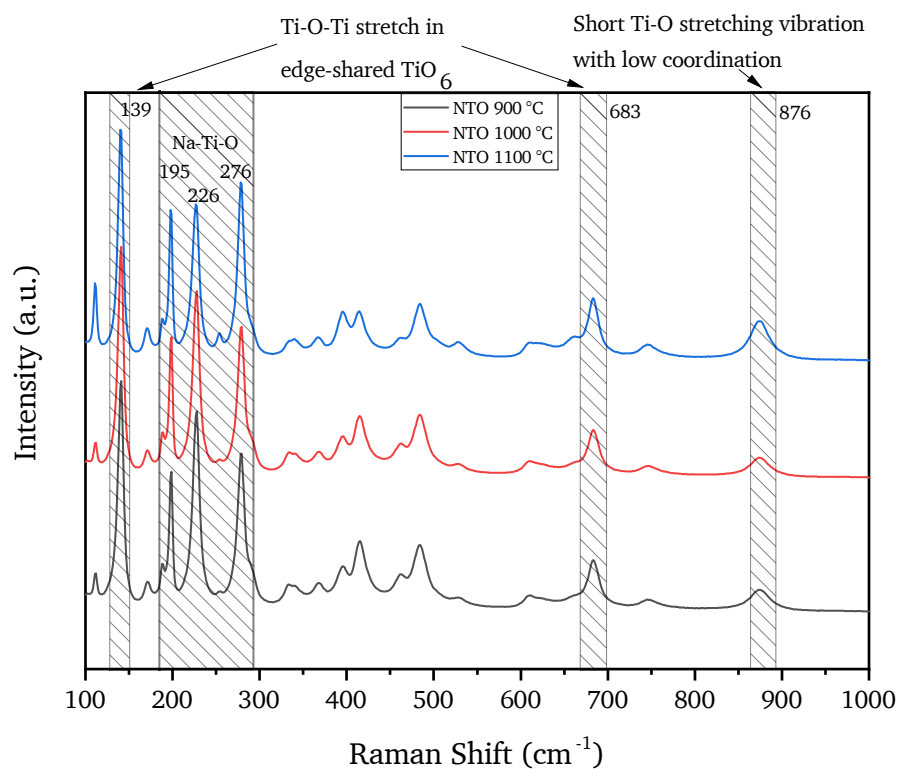


Figure 5.85.: Raman spectra of NTO-900 (black curve), NTO-1000 (red curve) and NTO-1100 (blue curve). The most important bands discussed in the text are shaded and labeled with the respective wavenumber.

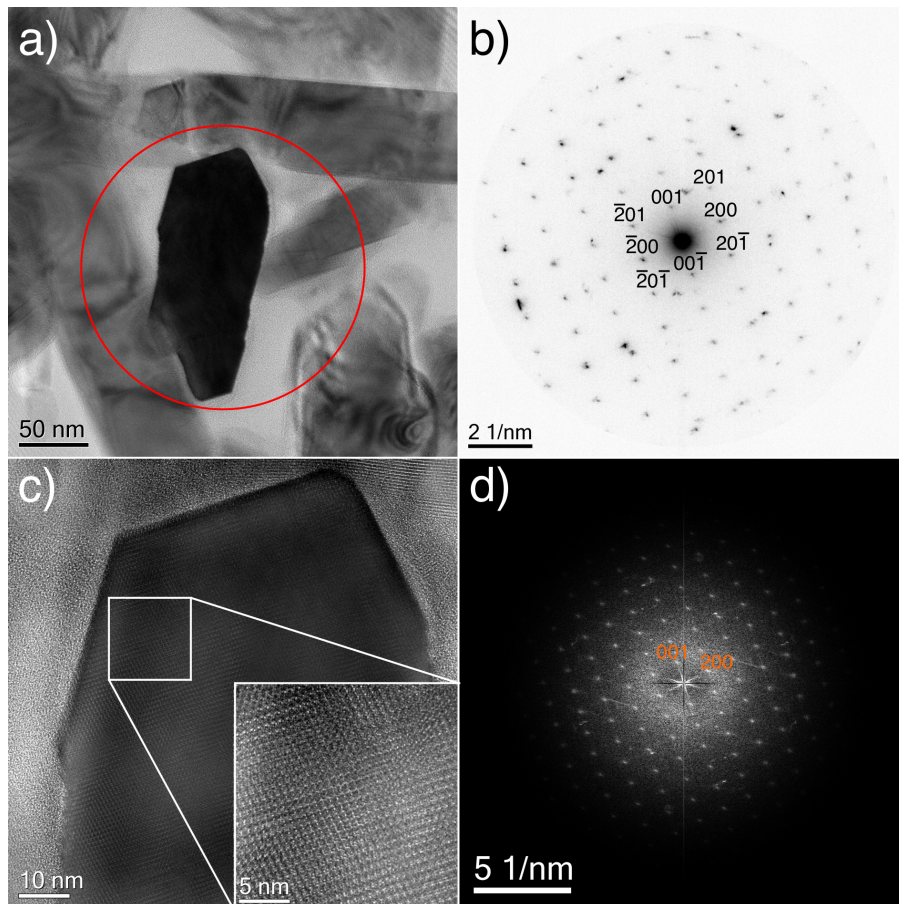


Figure 5.86.: TEM imaging and diffraction in sample NTO-900. a) Bright-field TEM image of an NTO nanorod oriented in $[0-10]$ zone-axis orientation (red circle: SAED aperture) and b) selected area diffraction pattern. c) HRTEM phase contrast image and d) corresponding FFT to c). The inset in c) shows a magnified region of c).

FFT. Part of figure 5.87e is shown as zoomed view in figure 5.87f. The titanium containing columns have a bright contrast due to their larger Z value. Sodium and oxygen are barely recognizable due to the limited spatial resolution and their lower Z value ($Z_{\text{Na}} = 11$ and $Z_{\text{O}} = 8$). An atomic model of NTO, oriented in [001] zone-axis direction, showing Na atoms as green, Ti atoms as red, and O atoms as blue balls has been overlaid for clarity. One immediately recognizes that the bright Ti contrast consists of 3 Ti columns unfortunately lying too close to be separated.

Figure 5.88a shows intensity-normalized low-loss EELS spectra of samples NTO-900 and NTO-1100, embedded in araldite, and of anatase and rutile for comparison (Panepinto *et al.* [312]). The overall electronic structure of both NTO samples is similar to that of rutile or anatase except for the additional Na-L_{2,3} edge present at about 31 eV (see figure 5.88b). Furthermore, both samples exhibit a feature located at about 5-8 eV that is similarly present in rutile and anatase. Launay *et al.* [313] assigned this feature to the transitions from the top of the valence band into the t_{2g} and e_g levels of the Ti d-orbitals in rutile and anatase. This argumentation should also be valid for NTO. Like rutile and anatase, both NTO samples also show two peaks in the energy region of 10-15 eV. The second one located at about 14 eV in rutile is explained by Launay *et al.* [313] by interband transitions originating from specific Ti-O structural units. Further investigations are needed however, to clearly elucidate the differences in the Ti-O bonding of NTO and TiO₂. Figure 5.88c shows core-loss EELS measurements of anatase, rutile, NTO-900, and NTO-1100, respectively. NTO and the two TiO₂ modifications have a number of similarities but also differences in both the Ti-L_{2,3} and the O-K energy loss near edge structure (ELNES). Deconvolution of the EELS spectra presented in figure 5.88c show right above the Ti-L_{2,3} edge onset a slight increase in signal intensity resulting in a difference in the peak-height ratio. This difference is more prominent in the NTO-900 than in the NTO-1100. In addition, the L₃t_{2g} peak is less prominent in NTO than in both TiO₂ modifications. Furthermore, the L₃e_g peak of both rutile and anatase is asymmetric, whereas it is not in NTO. Monochromated EELS measurements of Cheynet *et al.* [314] show that this asymmetry is due to a splitting of the L₃e_g peak into two to three single peaks depending on the actual TiO₂ modification. Also, the L₂ edge exhibits some differences that need to be addressed. The L₂e_g peak of sample NTO-1100 is slightly shifted in energy by about 0.1-0.2 eV to lower energy in comparison to all other Ti-L_{2,3} ELNES peaks in rutile, anatase and NTO-900. The origin of this shift is unclear at present and needs further clarification. Figure 5.88c presents the O-K ELNES of the two NTO samples and of the rutile and anatase reference, besides the Ti-L_{2,3} lines. All the samples have four distinct peaks labeled a, b, c, and d between 530 eV and 545 eV energy-loss. These features are also observed for several mixed-valence titanates e.g. barium titanate [315]. In addition, nanometric effects might alter the O-K ELNES of our material compared to bulk material. As shown by reference [316], the O-K ELNES of TiO₂ nanotubes is smeared out in the energy-loss range of about 536-546 eV. Figure 5.88d shows a magnified view of the O-K ELNES signal of both NTO samples. The O-K edge onset for NTO-1100 is shifted by about 0.2 eV to lower energy compared to that of NTO-900. For sample NTO-900 the peaks c and d of the O-K ELNES are better separable than for the sample NTO-1100. The quantification of the NTO-900 and NTO-1100 data via the Cliff-Lorimer method can be found in table

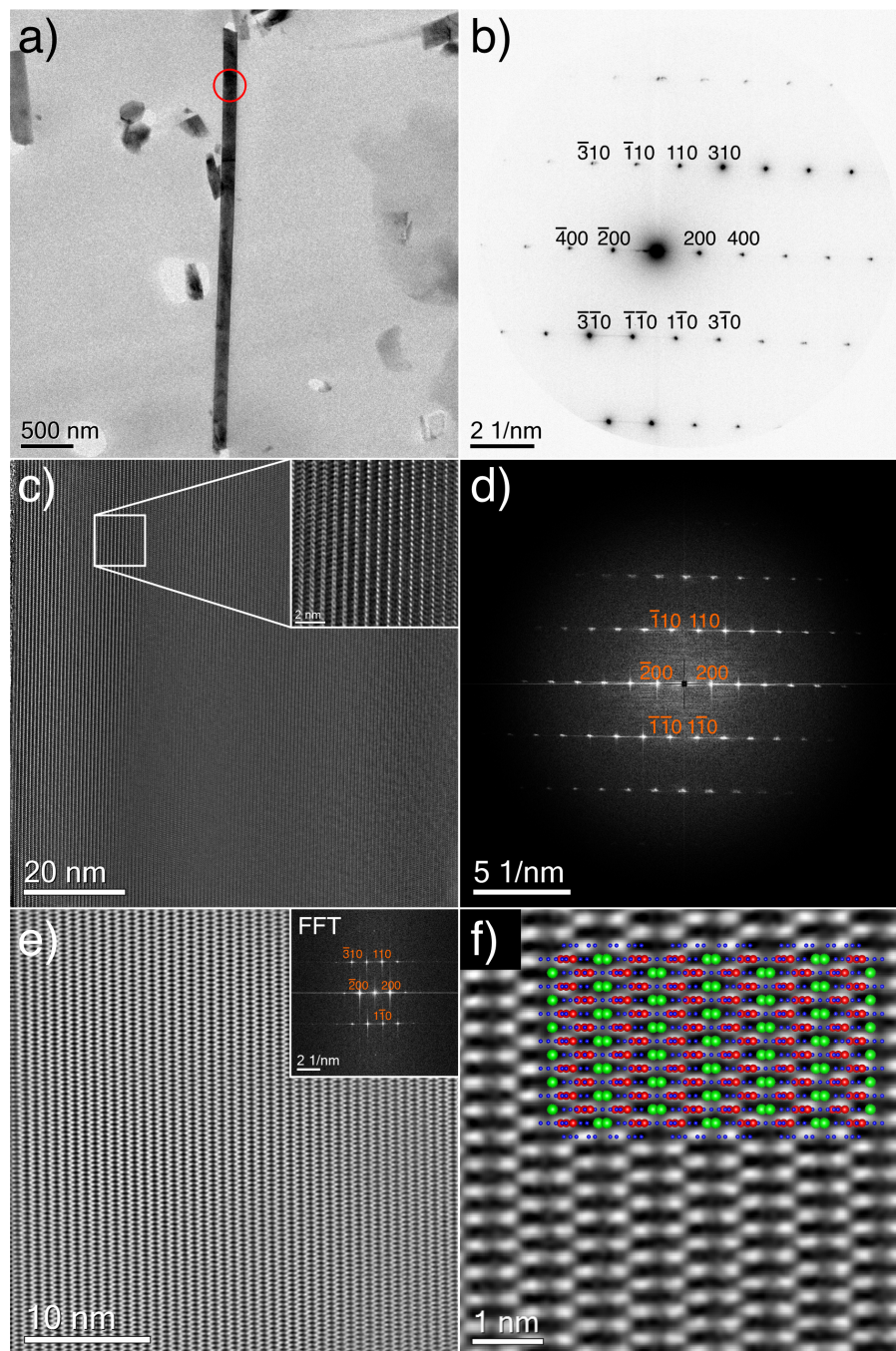


Figure 5.87.: TEM imaging and diffraction in sample NTO-1100. a) Bright-field TEM image of an NTO nanorod oriented in $[001]$ zone-axis orientation (red circle: SAED aperture) and b) selected area diffraction pattern. c) HRTEM phase contrast image and d) corresponding FFT. e) Noise-filtered STEM-HAADF Z-contrast image and f) magnified part of e) with an atomic model of NTO overlaid (Na: green, Ti: red, O: blue).

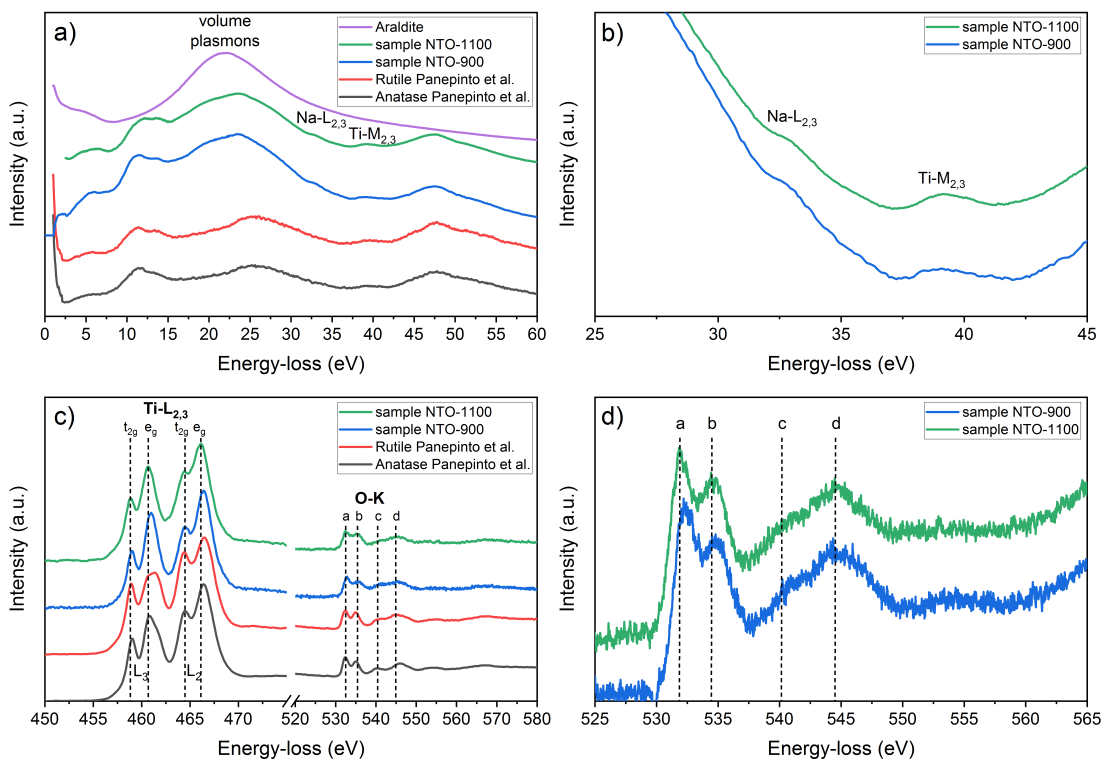


Figure 5.88.: a) Low-loss EELS spectra of rutile [312], anatase [312], sample NTO-900, NTO-1100, and araldite. b) Magnified view of a) to highlight the Na-L_{2,3} and Ti-M_{2,3} edges for sample NTO-900 and NTO-1100, respectively. c) Ti-L_{2,3} and O-K core-loss EELS spectra of rutile [312], anatase [312], sample NTO-900, and NTO-1100. (d) O-K ELNES of sample NTO-900 and NTO-1100, respectively.

5.12. The results essentially agree with the nominal composition presented in the last row of the table. These results — together with the changes seen in the Raman spectra (see figure 5.85) — suggest a slight structural modification in the Ti-O sub-lattice when increasing the synthesis temperature of the NTO sample from 900 °C to 1100 °C. Recent first-principles calculations [317] propose a low binding energy for two-fold coordinated oxygen atoms in the NTO tunnel structure sitting next to an alkali ion. Accordingly, the observed ELNES changes might be due to local rearrangements in the tunnel region near alkali ions. However, further studies are needed to corroborate this finding.

Table 5.12.: Quantification of EDX spectra acquired from a single $\text{Na}_2\text{Ti}_6\text{O}_{13}$ nanorod using the Cliff-Lorimer k-factor method.

Sample	Na [at%]	Ti [at%]	O [at%]
k-factor	0.9432	1.0291	1.0000
NTO-900	8.46 ± 1.93	29.16 ± 5.06	62.38 ± 6.98
NTO-1100	7.10 ± 1.65	33.19 ± 5.95	59.70 ± 7.20
Nominal	9.52	28.57	61.90

5.4. Electrochemical performance of sodium titanates

As discussed in the introduction part and in section 3.3, NTO has a large potential as battery material. There is still research required to identify a viable and safe electrode for Na-based battery. Graphite, commonly used in Li-ion batteries does not form intercalation compounds with sodium [65]. Titanates, however incorporate Na-ions. The electrochemical performance of the titanates synthesized in this work is therefore evaluated. First for the pure NTO, then for comparison also mixtures with rutile and with $\text{Na}_2\text{Ti}_3\text{O}_7$ are investigated.

The electrochemical performance of the NTO nanorods synthesized at 900, 1000 and 1100 °C has been investigated in a half-cell arrangement by galvanostatic cycling with potential limitation (GCPL) in order to determine the lithium and sodium storage capacity, and its stability over time. For the sake of clarity, the results of the two systems, are presented in two separated sections since they involve different aspects of the intercalation.

5.4.1. Galvanostatic cycling with potential limitation vs Li/Li^+

$\text{Na}_2\text{Ti}_6\text{O}_{13}$ electrodes Figure 5.89 shows the cycling performance of the pristine NTO materials obtained at pH = 10.3 and heat-treated at 900, 1000 and 1100 °C for the reversible lithium storage. The highest capacities are recovered by NTO-900, followed by NTO-1000 and NTO-1100. NTO-900 initially recovers 150 mA h g^{-1} and the specific capacity stabilizes at $\approx 100 \text{ mA h g}^{-1}$ for 100 cycles. The coulombic efficiency becomes stable along 100 cycles being $> 99\%$ after the first 15 cycles (NTO-900), 28 cycles (NTO-1000) and 35 cycles (NTO-1100). The performance of the half-cells exceeds that

reported in the literature (90 mA h g^{-1} at 50 mA g^{-1} [240] and 90 mA h g^{-1} at 12.5 mA g^{-1} [231]). For example the NTO material synthesized by Li *et al.* [232] recovers less than 80 mA h g^{-1} at 50 mA g^{-1} after 50 cycles. These literature data belong to NTO samples synthesized with methods different from MSS. They are not leading to the unique NTO nanorods achieved in MSS. Therefore, the improvement of capacity and stability is attributed to the specific MSS preparation step leading to NTO nanorods of high purity and well defined structure.

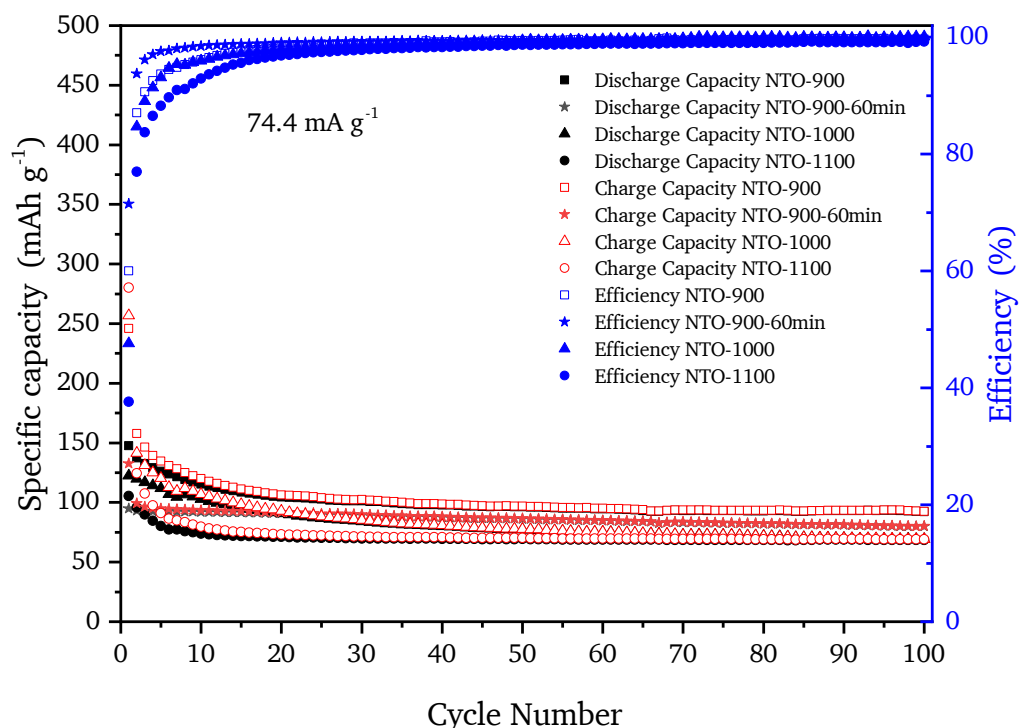


Figure 5.89.: Charge-discharge capacities of NTO-900, NTO-900-60min, NTO-1000 and NTO-1100 electrodes assessed with 74.4 mA/g from 0.01 to 3 V vs. Li/Li^+ with their relative efficiencies.

Figure 5.90 depicts the first cycle's charge (Li^+ -insertion) and discharge (Li^+ -extraction) profiles for NTO-900, NTO-1000, and NTO-1100 at a constant current density of 74.4 mA g^{-1} . There is a substantial impact of the synthesis temperature on the Li insertion/extraction performance (already visible in figure 5.89). The electrodes recover the initial charge capacities of 245, 256 and 280 mA h g^{-1} with the corresponding first coulombic efficiencies of 60, 48 and 38% for NTO-900, NTO-1000, and NTO-1100, respectively. The large irreversible capacities observed within the first cycle can be attributed to: (i) the formation of a solid electrolyte interface (SEI) layer on the nanorods and (ii) irreversible insertion of Li^+ -ions into $\text{Na}_2\text{Ti}_6\text{O}_{13}$. The efficiency loss with increasing synthesis temperature (see blue curves in figure 5.89) results from (i) the change in the active electrode volume arising from the increase in the nanorods thickness and (ii) from changes in the Ti-O bonding and Na bonding inside the tunnel structure, as supported by the results of the Raman (see section 5.3.3) and O-K ELNES studies (as discussed in section 5.3.4).

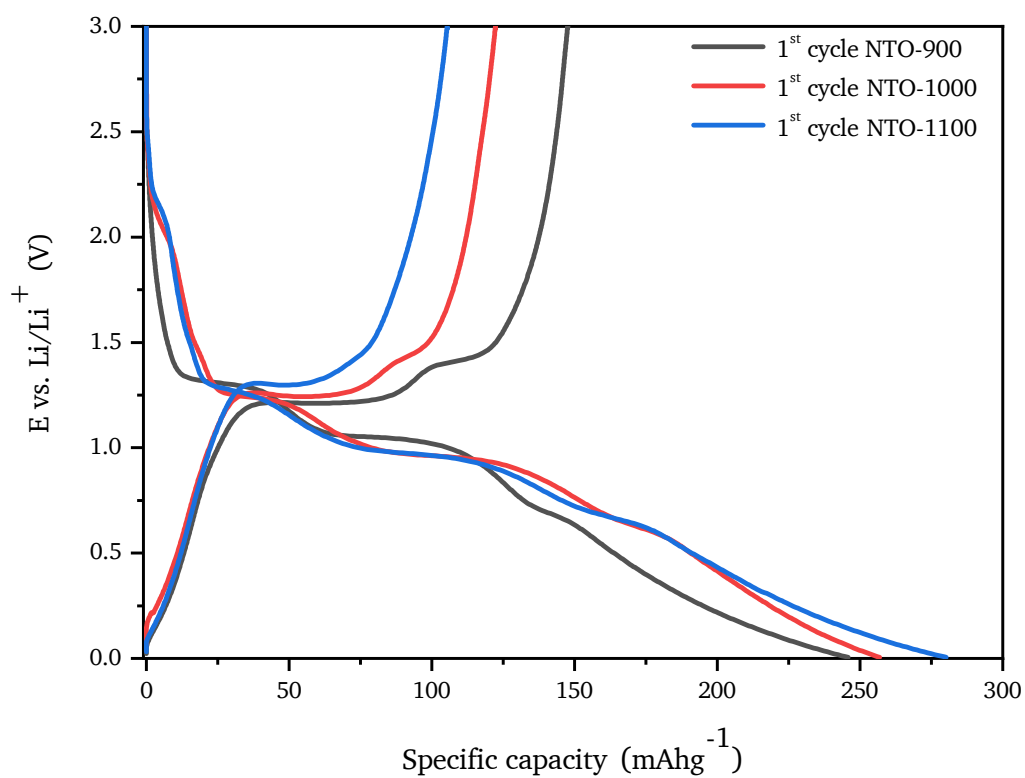


Figure 5.90.: First cycle's charge and discharge profiles of NTO-900, NTO-1000 and NTO-1100 V vs. Li/Li⁺ with 74.4 mA/g.

In agreement with literature [41, 47, 228, 232], reversible lithium insertion leads to two plateaus at 1.3 V and at 1.0 V and a wide slope at around 0.8 V (see figure 5.90). Two plateaus appear at 1.2 V and 1.4 V for NTO-900 and NTO-1000 during the Li extraction process, whereas for NTO-1100 only the plateau at 1.3 V is recorded. Hence, the electrochemical insertion of lithium into NTO can be described by $\text{Na}_2(\text{Ti}^{4+})_6\text{O}_{13} + x\text{e}^- + x\text{Li}^+ \rightarrow \text{Na}_2\text{Li}_x(\text{Ti}^{3+})_6\text{O}_{13}$, where the presence of the two plateaus denotes the insertion of lithium ions at two different sites in the tunnel structure [42, 47]. The region from 0.01 V to 0.4 V is ascribed to irreversible lithium intercalation into the $\text{Na}_2\text{Li}_x\text{Ti}_6\text{O}_{13}$ [245]. Figure 5.90 shows that the lithiation plateaus in the charging step of NTO-900 are better defined than that for NTO-1000 and NTO-1100, indicating more stable intercalation. Furthermore, the first delithiation capacity is remarkably higher for NTO-900 ($147.6 \text{ mA h g}^{-1}$ for NTO-900 vs. the $122.3 \text{ mA h g}^{-1}$ for NTO-1000 and $105.4 \text{ mA h g}^{-1}$ for NTO-1100), that leads to a lower Li irreversible capacity loss at first cycle than for NTO-1000 and NTO-1100. Also, a better resolution of the delithiation profile is seen for the NTO-900 sample with the clearly distinguishable plateaus at 1.2 V and 1.4 V. The subtle differences in the microstructure of the material obtained at lower temperature appear to be responsible for the reversible insertion of two lithium ions (96 mA h g^{-1}). According to Raman and ELNES findings and recent first-principles calculations [317], NTO-900 reveals a lower binding energy for two-fold coordinated oxygen atoms in the tunnel structure, sitting next to the alkali ion. The higher electrochemical performance of the material is in accord with this result.

NTO-900, NTO-1000, and NTO-1100 have all been heat-treated for 2 hours in MSS. A galvanostatic cycling with potential limitation (GCPL) has been measured also for the NTO-900 sample heat-treated only 1 hour (see figure 5.89) to analyze the effect on the Li intercalation. This sample shows clear improvements in terms of efficiency and cyclability, since the first cycle efficiency at 71.47% is higher than any other sample (60, 48 and 38% for NTO-900, NTO-1000 and NTO-1100) and stays stable > 99% after 15 cycles. The decreased holding time leads to a lower first cycle capacity loss of $\approx 37.81 \text{ mA h g}^{-1}$ respect to NTO-900 ($98.25 \text{ mA h g}^{-1}$), NTO-1000 ($134.55 \text{ mA h g}^{-1}$), and NTO-1100 ($174.82 \text{ mA h g}^{-1}$). The specific capacity slightly fades along the 100 cycles, from $99.16 \text{ mA h g}^{-1}$ after 2 cycles to $80.09 \text{ mA h g}^{-1}$ after 100 cycles. In overall this sample shows a lower specific capacity than NTO-900 ($\approx 100 \text{ mA h g}^{-1}$) after 100 cycles, but it is more stable.

Figure 5.91 shows the cyclic voltammetry (CV) measured for sample NTO-900, which includes five lithiation and delithiation cycles measured at $20 \mu\text{V s}^{-1}$ and the sixth one at $10 \mu\text{V s}^{-1}$. The cyclic voltammetry (CV) is measured on the NTO electrode in its pristine state. The first cycle is therefore affected by the typical irreversible process of the SEI formation. Two reduction peaks for the lithium insertion are found at $\approx 1.32 \text{ V}$ and at 1.05 V . This confirms the presence of two intercalation plateaus that are observed in the first cycle capacity over the voltage (see figure 5.90). They originate from the different vacant sites occupied by the Li ions, as suggested in literature [47, 228, 232]. The two lithiation peaks both shift to higher voltages with cycling and loose intensity cycle by cycle. Especially, the intensity of the second intercalation peak becomes lower than the first one from the second lithiation cycle onward. This can be attributed to the completed SEI formation and to a change in the lithiation

steps. Two oxidation peaks are visible in the first cycle at ≈ 1.30 V and 1.40 V. These two peaks merge in the second cycle and then the single oxidation peak shifts towards voltages > 1.40 V. This behavior identifies an E_rE_r mechanism, *i.e.* a reversible two electron transfer process [318]. At first, there is a clear difference in the potential of the two electrochemical steps, and since the second step is thermodynamically more favorable, the peak-to-peak separation decreases till merging in the following cycles. The broadening of the peak together with the intensity decrease indicates a decrease of the NTO conductivity. All these observations might be related to the arrangement of the Li ions by full-lithiation in the voltage range 0-3 V, as described from Li *et al.* [232].⁷ Kuhn *et al.* [47] partially confirmed this, correlating the higher Li occupation of the interstitial sites in the $(\text{Ti}_6\text{O}_{13})^{2-}$ framework with a decrease of the Li mobility and a reduction of the amount of the charge carriers involved in conduction processes.

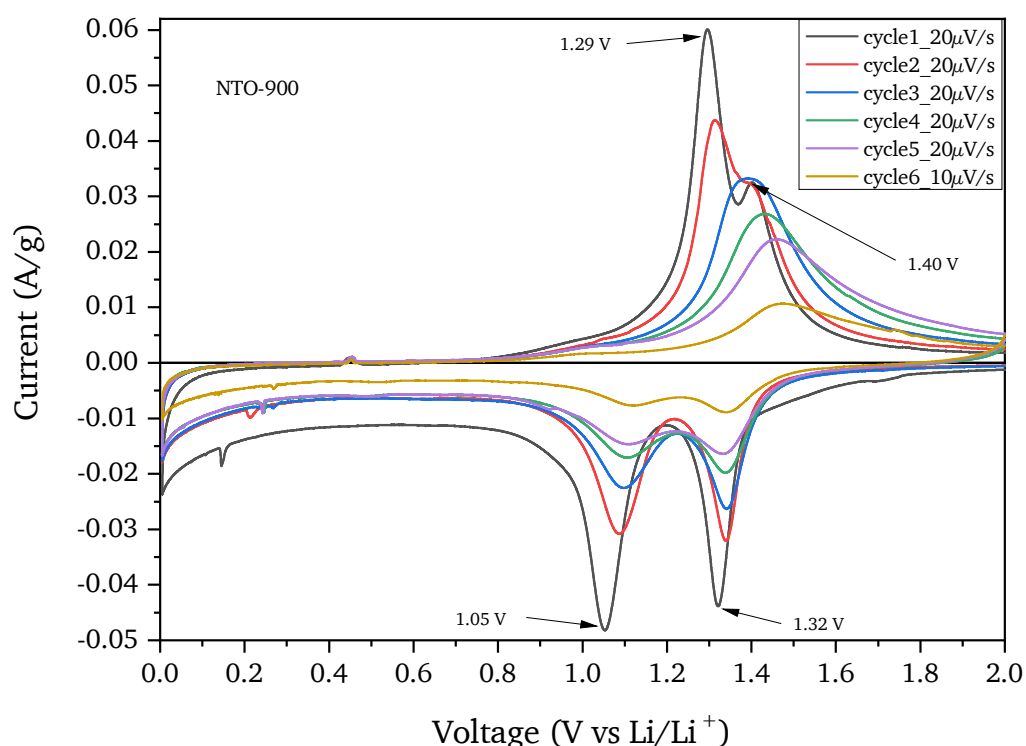


Figure 5.91.: CV performed on sample NTO-900. The half-cell is cycled from 0.01 to 3 V vs. Li/Li^+ at $20 \mu\text{V s}^{-1}$ for 5 cycles and at $10 \mu\text{V s}^{-1}$ during the 6th cycle.

Next, the rate capability of NTO has been determined by cycling the half-cell at different current rates (see figure 5.92). This allows to assess the ability of the anode to generate power even at high current loads, which is possible if the material has a low polarizability, reducing the voltage loss. Sample NTO-900 was cycled between 0.01 and 3 V applying the following loads: 14.85 mA g^{-1} for 5 cycles, 29.7 mA g^{-1} for 10 cycles, 59.4 mA g^{-1} for 20 cycles, 148.5 mA g^{-1} for 20 cycles, 297 mA g^{-1} for 20 cycles, 594 mA g^{-1} for 20 cycles, 1188 mA g^{-1} for 20 cycles and again 14.85 mA g^{-1} for 20 cycles (as indicated

⁷Figure 8 in reference [232] clearly shows the Li-ion occupation of the central crystallographic site 2c and the interstitial crystallographic site 4i for potentials > 1.0 V and of the 2d and another 4i site for potentials > 1.0 V.

in figure 5.92). Such loads correspond to the rates C/20, C/10, C/5, C/2, C, 2C, 4C considering the theoretical capacity of NTO as equal to 297 mA h g^{-1} [232]. Comparing the specific capacity after the fifth cycle ($174.83 \text{ mA h g}^{-1}$ at 14.85 mA g^{-1}) with the $168.3 \text{ mA h g}^{-1}$ delivered with the same applied load after 116 cycles (14.85 mA g^{-1}), it is clear that the material recovered $\approx 96\%$ of the initial reversible capacity. Additionally, by doubling the applied current density, the overpotential for NTO-900 is quite limited, denoting a weak polarization during the charge and discharge process. Finally, NTO-900 shows a good rate capability and reveals an outstanding cycling stability at a high-rate of 1188 mA g^{-1} . The observed features confirm that NTO is electrochemically stable.

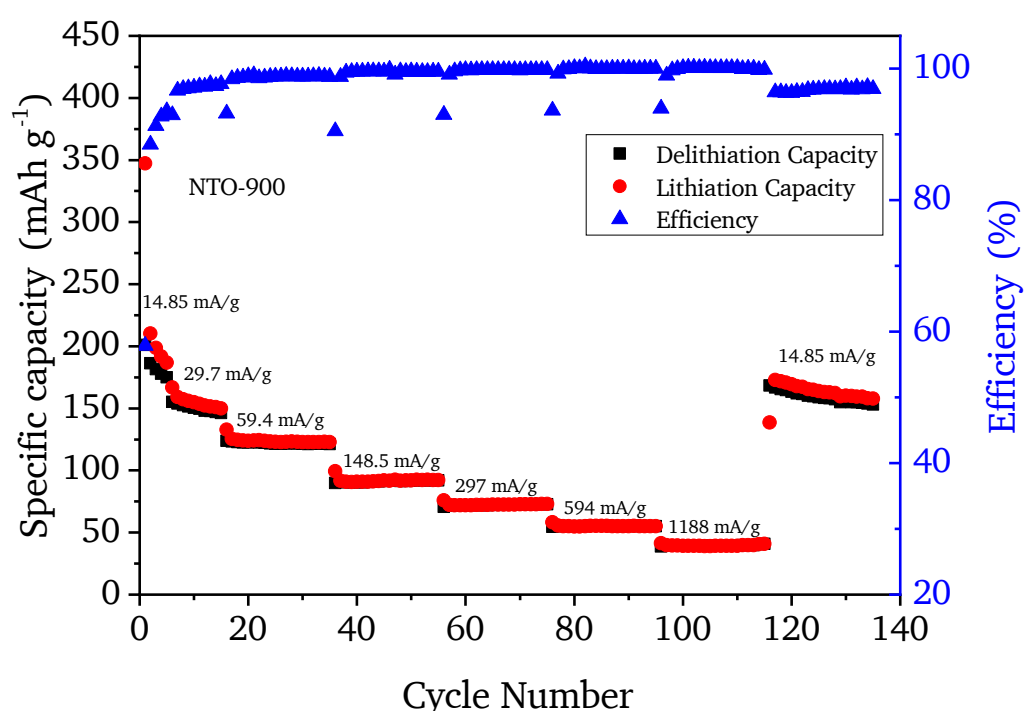


Figure 5.92.: Rate capability of NTO-900 measured from 0.01 to 3 V vs. Li/Li^+ with different applied rates. The reference for the rate is a theoretical capacity of 297 mA h g^{-1} .

The rate capability of sample NTO-1000 is reported for comparison (see figure 5.93). In this case lower currents were applied for a series of cycles, namely C/20 for the first 5 cycles, then C/10 for 10 cycles, C/5 for 20 cycles, C/2 for 50 cycles, C for 50 cycles and finally again C/20 for 5 cycles (the applied currents are 18.6 mA g^{-1} , 32.7 mA g^{-1} , 74.4 mA g^{-1} , 186 mA g^{-1} and 372 mA g^{-1} , respectively). The fading of the specific capacity is faster in NTO-1000 even though the first lithiation capacity of NTO-1000 is higher than that of NTO-900 achieved at a similar current density ($\approx 420 \text{ mA h g}^{-1}$ vs 349 mA h g^{-1}). After 60 cycles NTO-1000 maintains a specific capacity of $\approx 47 \text{ mA h g}^{-1}$ at 186 mA g^{-1} compared to $\approx 73 \text{ mA h g}^{-1}$ delivered by NTO-900 at 297 mA g^{-1} . This trend confirms the results of the GCPLs (see figure 5.89). Nonetheless, the NTO-1000 sample delivers $110.53 \text{ mA h g}^{-1}$ after 137 cycles, recovering $\approx 80\%$ of the initial reversible capacity obtained at the fifth cycle ($136.79 \text{ mA h g}^{-1}$), with the final applied load being equal to the first one. The comparison of the rate capabilities of NTO-900

and NTO-1000 confirms that a highest initial specific capacity is achieved from the sample synthesized at higher temperature. However, the final capacity and the stability at higher rates are enhanced for NTO-900.

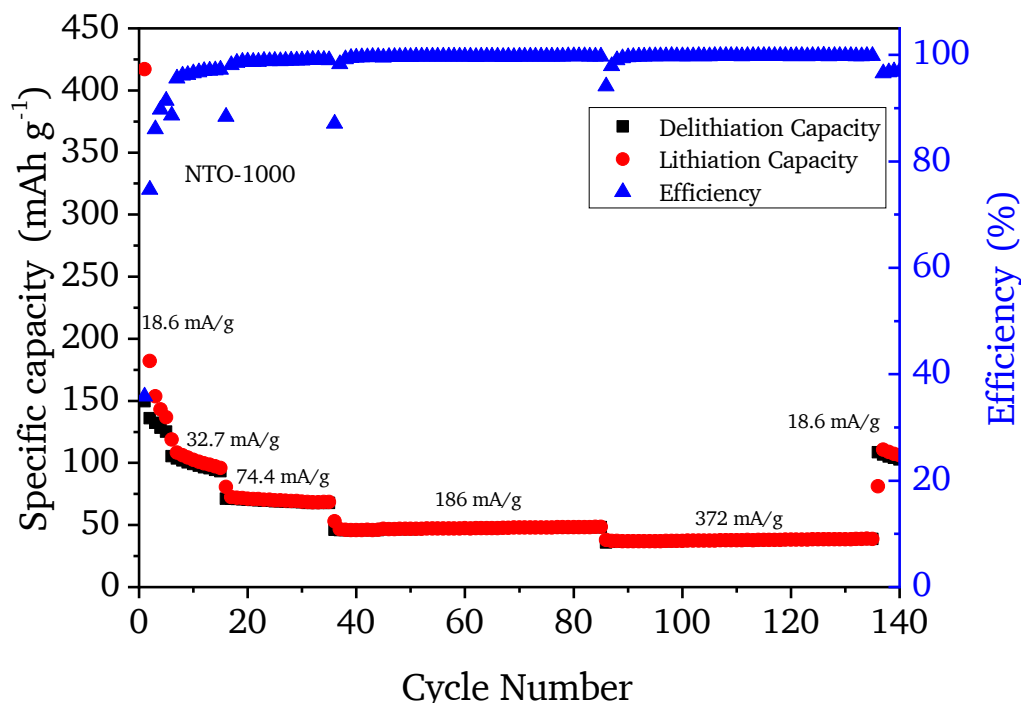


Figure 5.93.: Rate capability of NTO-1000 measured from 0.01 to 3 V vs. Li/Li⁺ with different rates. The reference for the rate is the theoretical capacity of graphite: 372 mA h g⁻¹.

Na₂Ti₆O₁₃/Na₂Ti₃O₇ hybrid electrodes GCPLs were measured for some of the electrodes produced by WCP performed at pH values ≥ 7 (see section 5.3.1 and table 5.11) to assess their electrochemical performances with respect to that of pure NTO electrode. Samples synthesized at pH < 10 contain mixtures of the NTO, anatase and rutile. All these samples deliver a stable specific capacity over 100 cycles, at 74.4 mA g⁻¹ ranging between ≈ 55 mA h g⁻¹ and 20 mA h g⁻¹. The sample prepared at pH = 10 and 900 °C — a mixture of NTO and rutile, but with a higher NTO fraction than the samples at pH < 10 — delivers a capacity of ≈ 96.3 mA h g⁻¹ in the first cycle and 68.19 mA h g⁻¹ after 100 cycles. The efficiency of ≈ 72.4 % in the first cycle, rises to 97.1 % already after 5 cycles and is > 99 % after 25 cycles. From the structural point of view, the most interesting samples are mixtures of Na₂Ti₆O₁₃ - Na₂Ti₃O₇ obtained at pH = 11. Figure 5.94 shows the comparison of the samples obtained with 5 and 20 wt. % TiOSO₄ precursor (from 850 to 1100 °C). The sample heat-treated at 850 °C delivers the highest specific capacity for 100 cycles (≈ 95.12 mA h g⁻¹ in the first cycle and 46.86 mA h g⁻¹ after 100 cycles). The efficiency is ≈ 73.5 % after the first cycle, rises to 97.18 % after 9 cycles and is > 99 % after 35 cycles. Hence an increase of the synthesis temperature causes a steady decrease of the specific capacities. The two samples synthesized with 20 wt. % precursor deliver lower capacities than those with 5 % (\approx

58 mA h g⁻¹ in the first cycle and 27.84 mA h g⁻¹ after 100 cycles). This correlates with the volume changes by the bigger particles achieved at 900 °C with 20 wt. % of precursor (see figure 5.95).

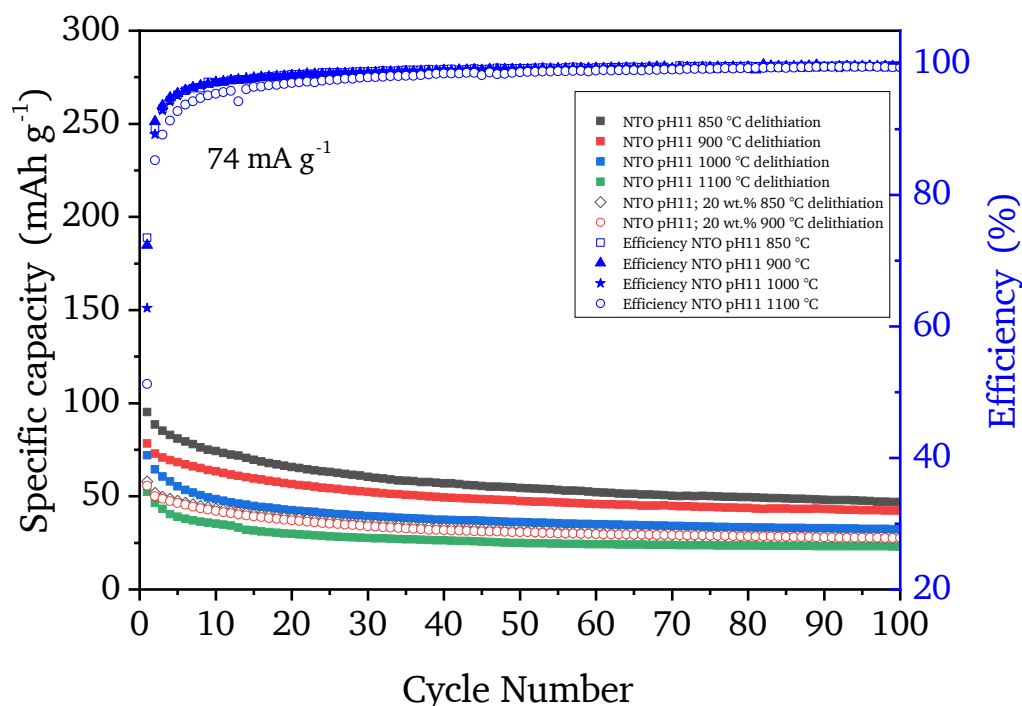
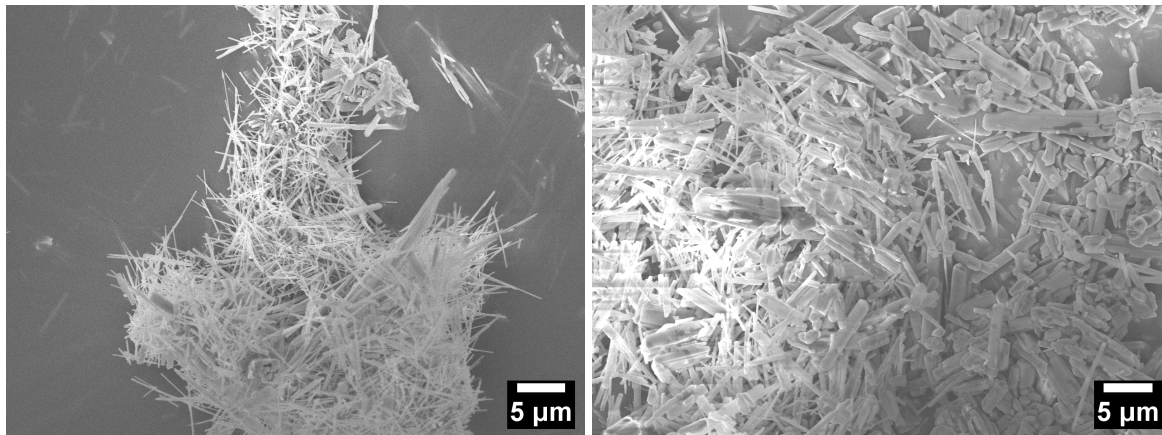


Figure 5.94.: Charge-discharge capacities of Na₂Ti₆O₁₃/Na₂Ti₃O₇ electrodes heat-treated at different temperatures and with 5 and 20 wt. % precursor. The cells were cycled from 0.01 to 3 V vs. Li/Li⁺ with 74.4 mA/g.

Comparing all the above mentioned samples a higher NTO concentration in the electrode material delivers a higher capacity. Therefore, samples obtained at pH = 10 are delivering higher specific capacities than those at pH = 7, 8 and 9, but do not equalize those of pure NTO.

An additional electrochemical investigation has been performed on the samples obtained at pH = 11 in the NaCl-Na₂SO₄ eutectic mixture (see figures 5.78 and 5.79 in section 5.3.1). The GCPLs in figure 5.96 reveal the correlation of the capacities with the synthesis temperature. The best performance is delivered by the sample heat-treated at 700 °C (≈ 149.36 mA h g⁻¹ in the first cycle and 50.54 mA h g⁻¹ after 100 cycles). This is comparable to the performances achieved by the sample synthesized at pH = 11 in Na₂SO₄ system at 850 °C (see figure 5.94). The efficiency, at ≈ 59.15 % in the first cycle, rises to 97.1 % already after 7 cycles and is > 99 % after 42 cycles.

Rutile-dominated Na₂Ti₆O₁₃ electrodes The electrochemical performance of the sample resulting from the WCP in TiCl₄ (see section 5.1.6, figure 5.31) and heat-treated at 900 °C in NaCl matrix has been investigated in order to highlight the advantages of the NTO structure over titania based anodes. The rutile-based electrode (rutile concentration > 80 %, see table 5.4)) was cycled between 0.005 V and



(a) 900 °C; 5 wt. %

(b) 900 °C; 20 wt. %

Figure 5.95.: SEM images of titanates particles synthesized by MSS in Na_2SO_4 via WCP with a) 5 and b) 20 wt. % TiOSO_4 precursor at pH = 11 and heat-treated at 900 °C.

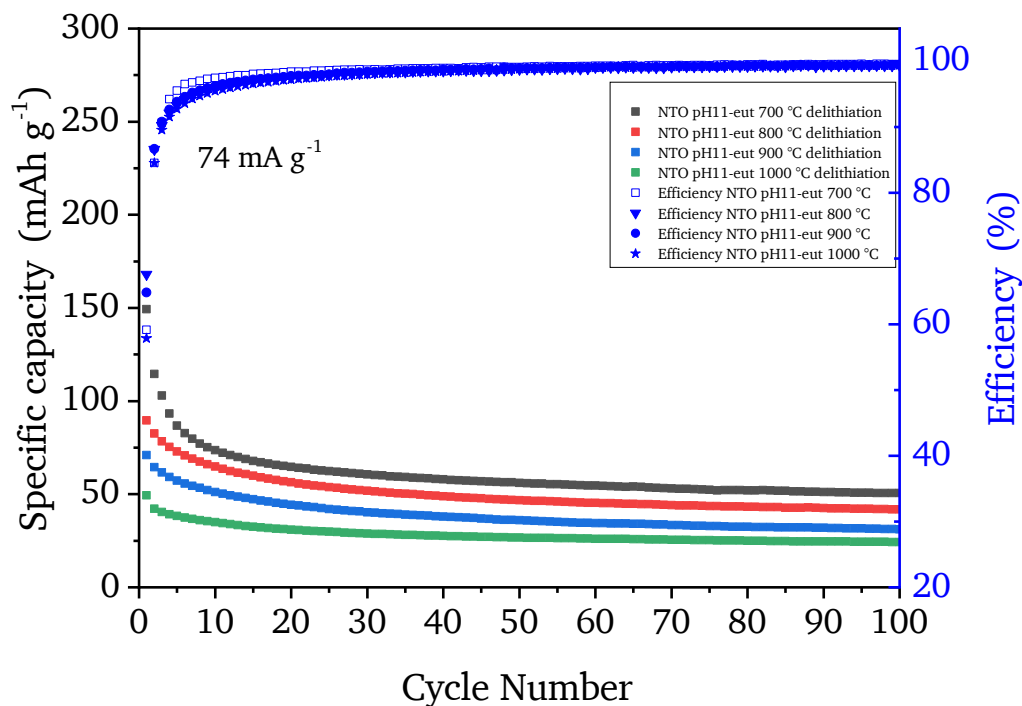


Figure 5.96.: Charge-discharge capacities of $\text{Na}_2\text{Ti}_6\text{O}_{13}/\text{Na}_2\text{Ti}_3\text{O}_7$ electrodes heat-treated at different temperatures in the $\text{NaCl-Na}_2\text{SO}_4$ eutectic mixture. The cells were cycled from 0.01 to 3 V vs. Li/Li^+ with 74.4 mA/g.

3 V at 74.4 mA g^{-1} and the data are reported in figure 5.97. It shows that rutile is also electrochemically active towards Li, but that the performance is not comparable to that of pure NTO. The first charging cycle achieves $\approx 180 \text{ mA h g}^{-1}$ but it suffers from a high irreversible Li loss leading to a discharge capacity of $\approx 72.5 \text{ mA h g}^{-1}$ with only 40 % efficiency. The second cycle's efficiency increases to 89.15 % for a discharge capacity of $\approx 69.02 \text{ mA h g}^{-1}$, resulting in less than 50 % of the capacity recovered by NTO-900 (see figure 5.89) and performing even worse than NTO-1000 and NTO-1100.

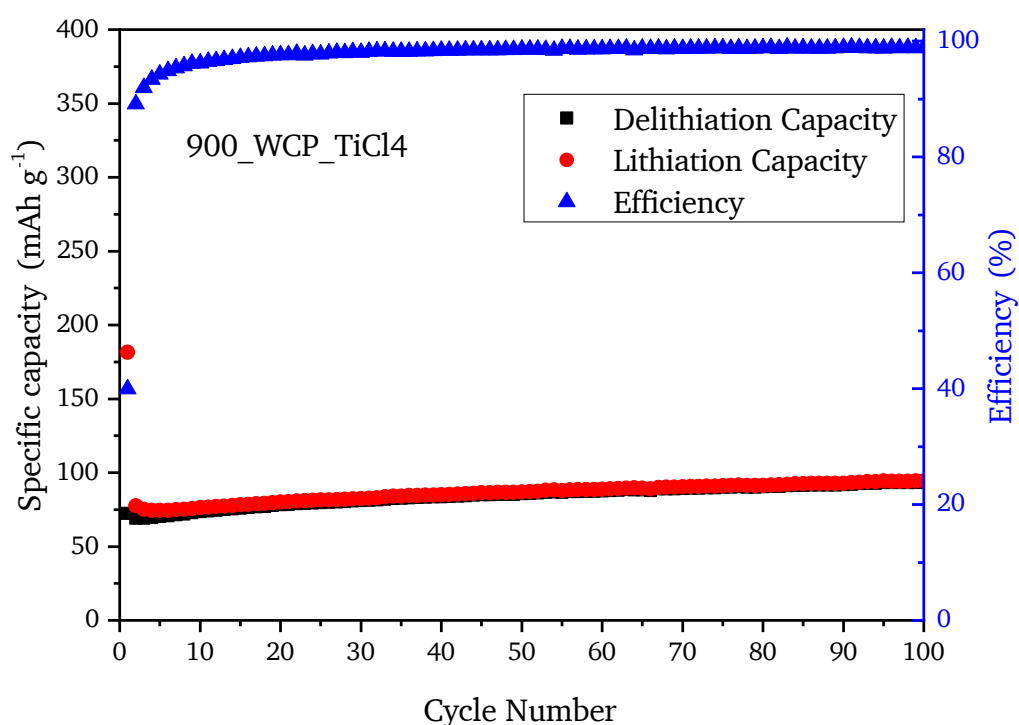


Figure 5.97.: Charge-discharge capacities per cycle and corresponding efficiency of a rutile-dominated NTO sample, synthesized by WCP with TiCl_4 precursor, assessed with 74.4 mA/g from 0.01 to 3 V vs. Li/Li^+ .

Figure 5.98 shows the comparison of the first charging/discharging cycle measured for NTO-900 and the rutile-based electrode. Rutile stores $\approx 180 \text{ mA h g}^{-1}$ in the first cycle, or $\approx 60 \text{ mA h g}^{-1}$ less than NTO-900. Its first reversible delithiation delivers 93.4 mA h g^{-1} less than NTO-900. Additionally, the second lithiation of rutile is $\approx 100 \text{ mA h g}^{-1}$ lower than the first one, reporting a higher first-cycle Li loss than NTO. The comparison among the lithiation profiles of the two samples reveals a difference in the intercalation process. The plateau present at $\approx 1.3 \text{ V}$ for NTO-900 is not forming for the rutile-based anode, which instead suffers a steep decrease converging to the second plateau of NTO-900 ($\approx 1.05 \text{ V}$).

To shed light on this mechanism, a CV was measured in order to locate the reduction and oxidation peaks of the rutile-dominated electrode (see figure 5.99). The two most intense reduction peaks (at 1.31 V and 1.06 V) are close to the values reported for NTO-900 in figure 5.91 (1.32 V and 1.05 V). They indicate the high contribution of NTO to the Li intercalation. Just a small electrochemical activity (<

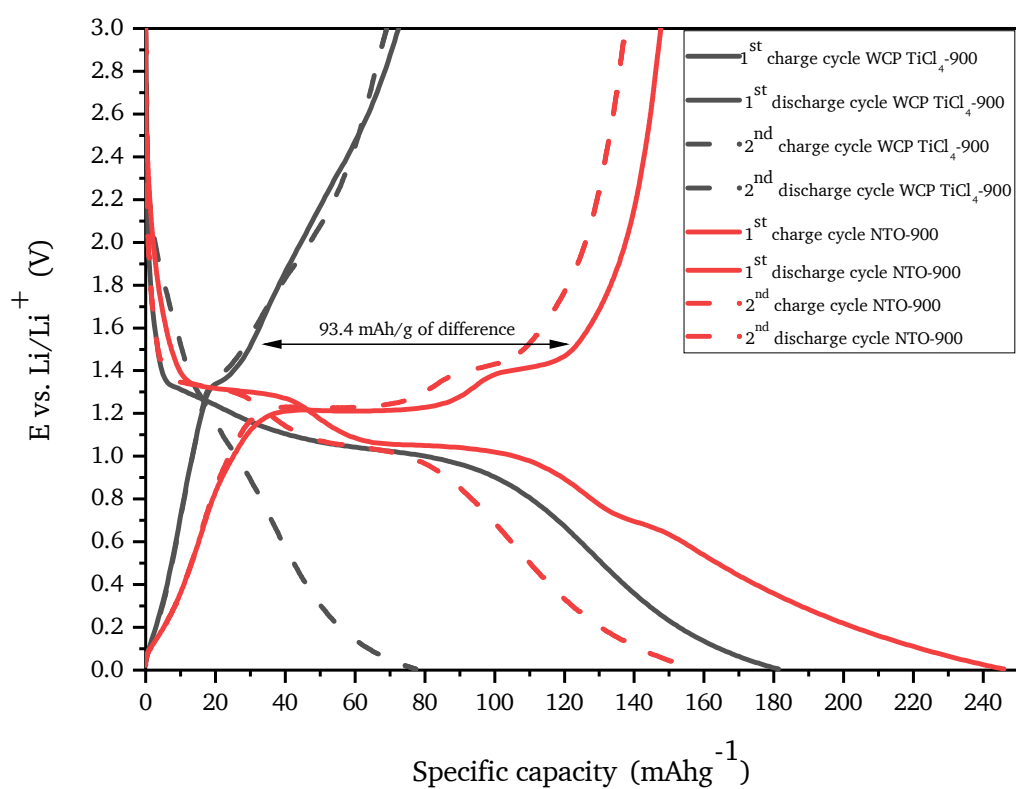


Figure 5.98.: First and second cycle's charge and discharge profiles of the sample obtained by WCP of TiCl_4 precursor in NaCl, cycled from 0.01 to 3 V vs. Li/Li^+ with 74.4 mA/g. The first and second cycles of NTO-900 are added for comparison.

0.005 A g⁻¹) is detected at 1.7 V, a potential that tags the reduction of TiO₂. The irreversible capacity loss due to the SEI formation is clearly visible at potentials < 1 V. As concerns the oxidation reactions, the main peaks in the first cycle are at 1.31 V and 1.40 V. These potentials are close to those of the pure NTO phase (at 1.29 V and 1.40 V), confirming the electrochemical activity of the minor NTO phase. The current increase at 1.89 V indicates an additional oxidation reaction addressable to the TiO₂ phase. The oxidation/reduction peaks belonging to NTO decrease in intensity from the second cycle on and the two oxidation peaks start to merge in one. Additionally, the CV shows the formation of a new broad oxidation/reduction peak visible after the second cycle. This might be an indication of a structural transformation occurring after the first lithiation (1.89 V), providing a high Li loss of ≈ 100 mA h g⁻¹. This result confirms the recent findings in literature, ascribing the first-cycle capacity loss to an irreversible structural transformation of rutile into quasi-stoichiometric cubic LiTiO₂ [319].

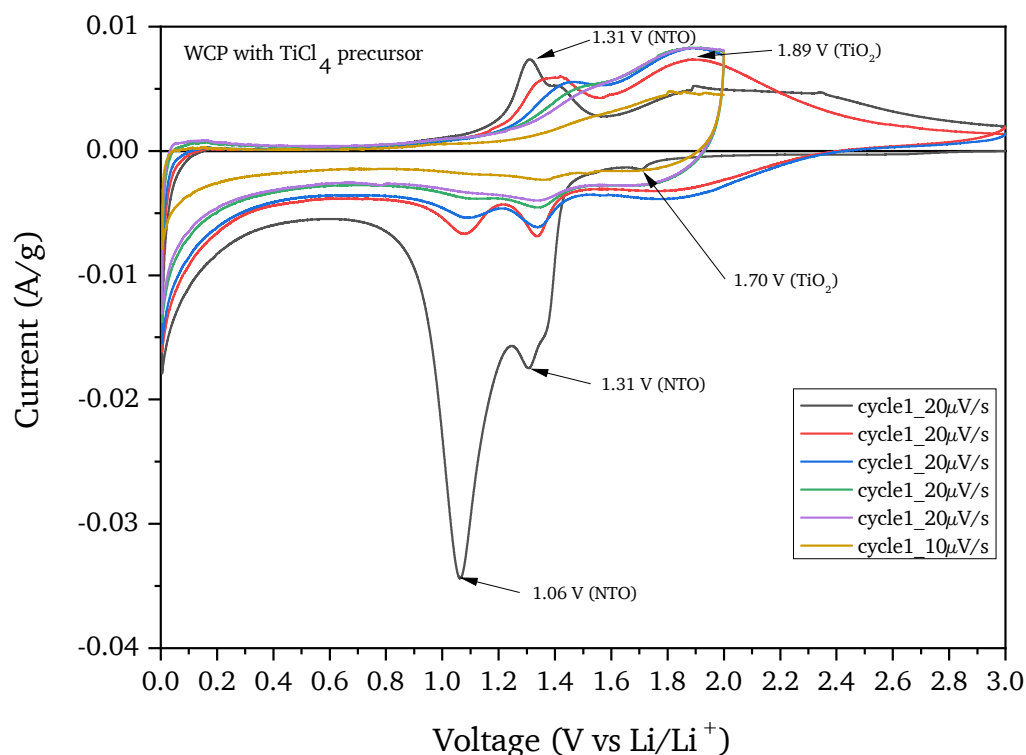


Figure 5.99.: CV of a combination of rutile and NTO phase, obtained by the WCP with 5% of TiCl₄ precursor.

All these results lead to the conclusion that rutile mixed to the NTO phase has the detrimental effect to decrease the overall specific capacity of the anode. Nevertheless, the importance of the dimensions and the morphology of the rutile particles for the improvement of its specific capacity has to be reaffirmed once more here. A large amount of data presented in previous publications correlate the improved capacities with nanosized particles and the morphology [48, 320–324]. As a matter of fact, the size of the rutile particles cycled in this work — ≤ 200 nm (see figure D.29 in the appendix) — might have been the limiting factor for the electrochemical performances.

5.4.2. Galvanostatic cycling with potential limitation vs Na/Na⁺

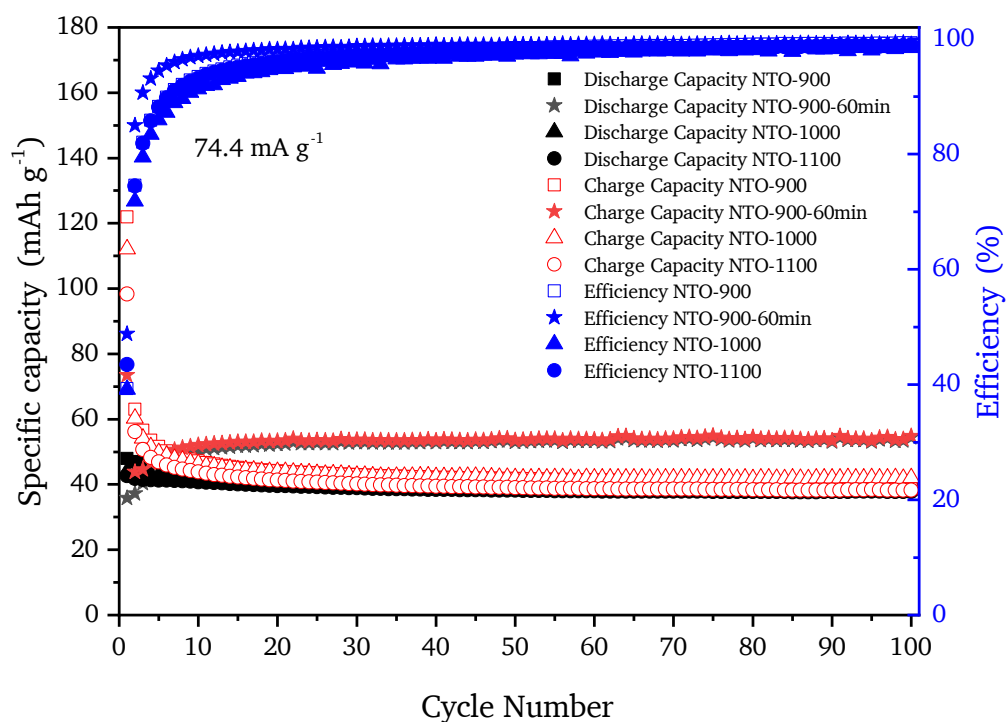
The electrochemical cycling of the NTO samples in the Na-based half-cells is presented in figure 5.100a. Only a small difference in the electrochemical performance among NTO-900, NTO-1000 and NTO-1100 is found. Initial discharge capacities of ca. 45 mA h g⁻¹ are recorded, stabilizing at around 40 mA h g⁻¹ after 100 cycles. The coulombic efficiency is > 98 % within 35 to 100 cycles. These results for a pristine NTO anode present a substantial improvement over the previous works of Rudola *et al.* [72] and Cech *et al.* [237] (both reporting 30 mA h g⁻¹ at 49.5 mA g⁻¹) using other synthesis methods than MSS. The latter reference shows 20 cycles of unstable Na-ion capacity with about similar initial values, but underperforming in terms of stability with respect to NTO-900. Further comparison with literature values from Cao *et al.* [241] and Zhang *et al.* [243] is difficult, because of the rather different electrode preparation and cycling conditions. Nevertheless, their results confirm that NTO could be a valid anode material for sodium ion batteries.

Figure 5.100b showcases the first cycle's charge (Na⁺ insertion) and discharge (Na⁺ extraction) profiles for NTO-900, NTO-1000, and NTO-1100 at a constant current density of 74.4 mA g⁻¹. The electrodes in sodium assembly provide initial discharge and charge capacities of 122, 112 and 98 mA h g⁻¹ for NTO-900, NTO-1000 and NTO-1100, with corresponding coulombic efficiencies of about 50 to 40 %. The large irreversible capacities observed over the first cycle are attributed to: (i) the formation of a SEI layer on the nanorods and (ii) the irreversible insertion of several Na⁺ ions into Na₂Ti₆O₁₃ at potentials lower than 0.3 V, reaching Na₆Ti₆O₁₃ as demonstrated by Shen and Wagemaker [247]. The comparison with the first de-lithiation cycles shows that NTO-900 has both the highest sodiation and desodiation capacity.

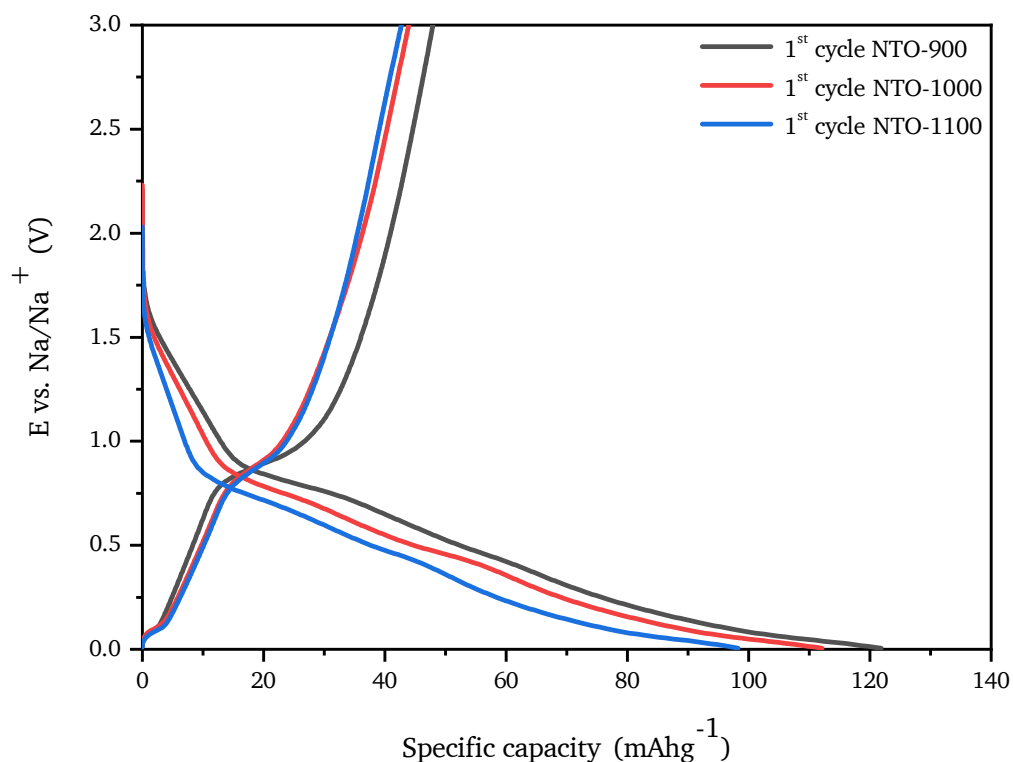
Sodium insertion produces one plateau at ≈ 0.8 V followed by a wide slope (see figure 5.100b). A distinct plateau at ca. 0.9 V appears for all the investigated materials during the extraction of sodium [241]. Similar to lithium, the electrochemical insertion of sodium into Na₂Ti₆O₁₃ above 0.3 V can be described by Na₂(Ti⁴⁺)₆O₁₃ + xe⁻ + xNa⁺ → Na₂Na_x(Ti³⁺)₆O₁₃, with one distinct plateau signifying the reversible insertion/extraction of one sodium ion. The region from 0.01 to 0.4 V is dominated by the irreversible sodium intercalation yielding Na_{2+x}Ti₆O₁₃. There is no significant difference in the insertion/extraction potential vs. capacity curves recorded for the NTO samples synthesized at different temperatures, as it is the case for NTO cycled vs. Li (see figure 5.90).

The samples NTO-900, NTO-1000, and NTO-1100 were all heat-treated for 2 hours. Figure 5.100a shows also the GCPL of the NTO-900 sample heat-treated only for 1 hour. The decreased holding time leads to a lower first cycle capacity loss and the efficiency is > 98 % already after 16 cycles. The specific capacity steadily increases along the 100 cycles, from 43.8 mA h g⁻¹ after 2 cycles to 54.82 mA h g⁻¹ after 100 cycles. A similar behavior was observed already in literature [241], and explained by a larger interlayer spacing present in the NTO structure beneficial for an improved Na de-intercalation.

Figure 5.101 shows the CV measurement performed on NTO-900 at 200 μV s⁻¹ for five cycles. The



(a) GCPLs of different NTO samples



(b) First cycle's profiles

Figure 5.100.: a) Charge-discharge capacities of NTO-900, NTO-900-60min, NTO-1000 and NTO-1100 assessed with 74.4 mA/g from 0.01 to 3 V vs. Na/Na⁺ with their relative efficiencies. b) First cycle's charge and discharge profiles of NTO-900, NTO-1000 and NTO-1100 from 0.01 to 3 V vs. Na/Na⁺.

data are collected on the electrode in its pristine state. The first cycle clearly demonstrate the effect of the SEI formation that disappears after the second cycle. The main sodiation/reduction peak is shifting from 0.68 V of the first cycle to ≈ 0.72 V for the following cycles. The desodiation/oxidation peak is much more stable shifting from 0.94 V at the first cycle to ≈ 0.96 V in the following cycles. At about 0.1 V there is an oxidation peak appearing that might be related to the deintercalation of additional Na ions which are intercalated in the NTO structure when the cutoff voltage is set to 0 V as reported by Wagemaker *et al.* [247]. This peak is also found but not further commented by reference [241]. The current increase of both oxidation and reduction peaks after the first cycles suggests an improved Na-ion diffusion kinetic [241].

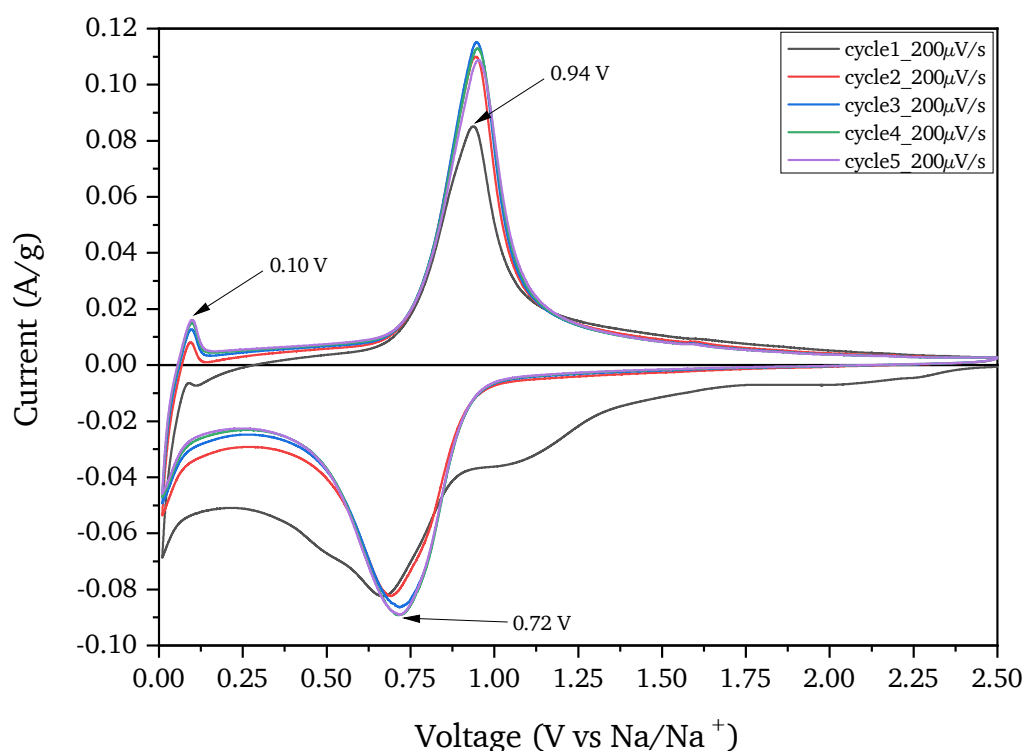


Figure 5.101.: CV performed on sample NTO-900. The half-cell is cycled from 0.01 to 3 V vs. Na/Na⁺ at $200 \mu\text{V s}^{-1}$ for 5 cycles and at $10 \mu\text{V s}^{-1}$ during the 6th cycle.

In this study, the Na insertion tests are limited to pure NTO, since rutile is not active towards sodium [72] and the hybrid electrode $\text{Na}_2\text{Ti}_6\text{O}_{13}/\text{Na}_2\text{Ti}_3\text{O}_7$ shows no remarkable results. To finalize the investigation on the Na insertion, also a rate capability measurement on NTO-900 is reported in figure 5.102. It shows that the electrode can deliver an initial capacity of 100 mA h g^{-1} at a low current density of 18.6 mA g^{-1} . At each of the following applied current densities (32.7 mA g^{-1} , 74.4 mA g^{-1} , 186 mA g^{-1} and 372 mA g^{-1}) the decrease of the specific capacity is minimal and highlights the high rate capability of the titanates. This is further confirmed by the specific capacity delivered after 133 cycle, close to that of the second cycle ($\approx 38 \text{ mA h g}^{-1}$).

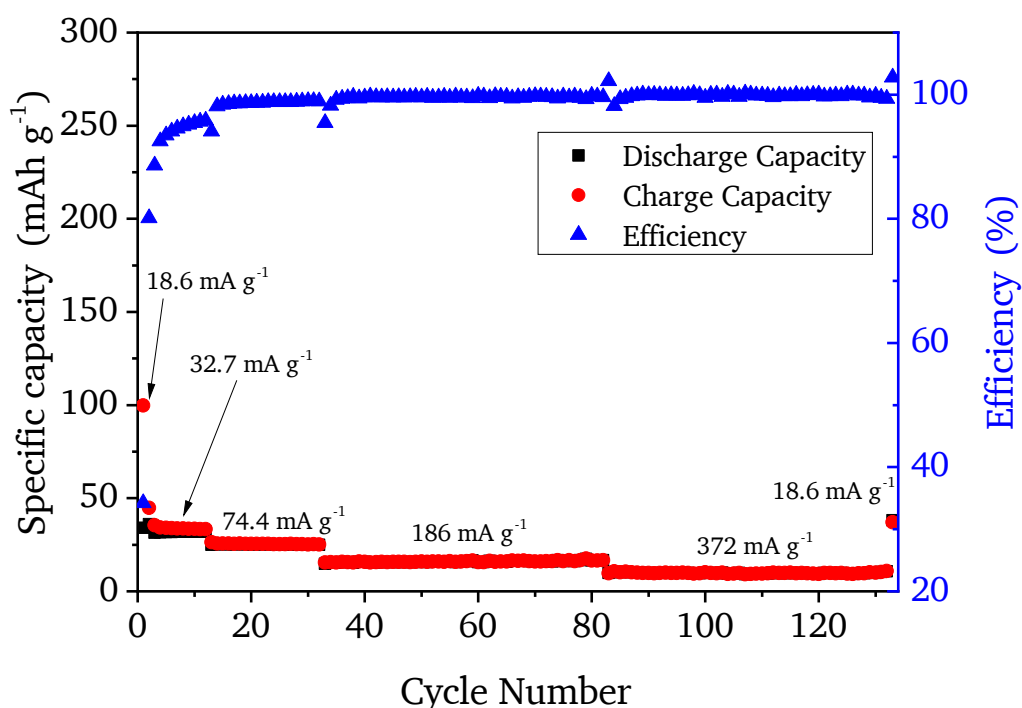


Figure 5.102.: Rate capability of NTO-900 measured from 0.01 to 3 V vs. Na/Na⁺ with different applied rates. The reference for the rate is a theoretical capacity of 297 mA h g⁻¹.

In conclusion, the sample NTO-900 delivers more than 100 and 50 mA h g⁻¹ of stable Li- and Na-storage capacity, respectively. The extraordinary electrochemical performance is rationalized by the high purity of the elongated NTO nanorods facilitating the insertion and diffusion of lithium and sodium ions. Further enhancement of the Li storage capacities can be obtained by carbon-coating of the NTO, as reported in reference [245]. The capacity value given above corresponds to more than the half of that of Li₄Ti₅O₁₂ spinel oxide, which is currently the most promising Ti-containing battery material (capacity of 175 mA h g⁻¹ and long cycle life [325]). Taking into account the cheap starting materials, NTO-900 synthesized by MSS is a competitive battery material in particular for stationary applications where the size/mass of the battery is not considered as a serious obstacle. Moreover, referring to the capacities of graphitic carbon (100 mA h g⁻¹ of NTO-900 vs 360 mA h g⁻¹ of graphite), one should consider the different densities, namely 3.41 g cm⁻³ vs 2.2 g cm⁻³ [326]. This leads to a volumetric energy density of around 340 mA h cm⁻³ for NTO-900, which is slightly less than half of that of graphite with 790 mA h cm⁻³, underlining again the significance of the research on NTO-based anode materials. Additionally, the NTO performance is noteworthy considering that the ion diffusion occurs in the rigid lattice of a zero-strain material. Last but not least, the high-voltage at which the de-intercalation processes occurs reduces the known safety concerns related to the lithium ion batteries [327, 328]. Especially for the Na-ion batteries, only few materials have been identified to date as useful anode (see figure 5.103), motivating research on other new materials.

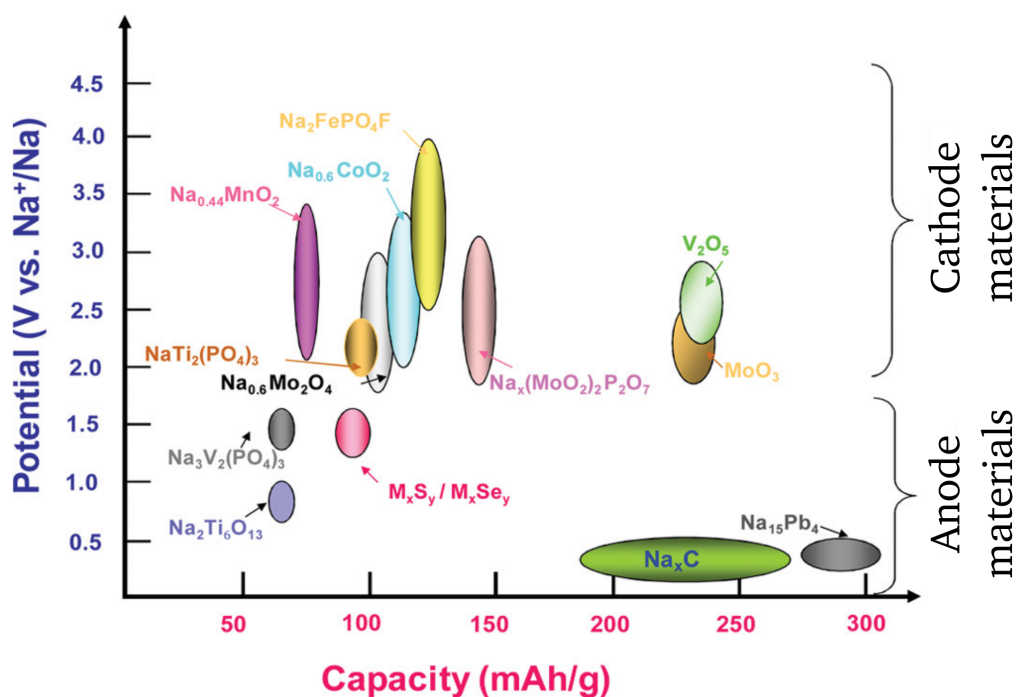


Figure 5.103.: Potential Na/Na⁺ vs. specific capacity plot classifying materials having been reported to exhibit reversible sodium insertion (reprinted with permission from [234]. Copyright © 2011 American Chemical Society.)

6. Conclusion and outlook

The crystal growth of TiO_2 and sodium titanates by MSS has been thoroughly investigated in this thesis. Mainly chlorides and sulfates have been used as high-temperature solvents. The influence of the MSS parameters on the composition, structure, habit and morphology was studied by varying the precursor concentration in the salt, the atmosphere above the melt and the heat-treatment. Finally, a strategy to obtain either pure rutile or pure NTO by MSS was developed.

Rutile is the dominant phase at temperatures $\geq 900^\circ\text{C}$ and the rod-shaped habit is promoted in chloridic environment (summarized in 5.1.7). Increase of the precursor concentration accelerates the ART (complete at 900°C for precursor concentration wt. % ≥ 10) and influences the crystal habit (see figure 5.4 at 900°C , page 58). The amount of rod-shaped crystals decreases for > 10 wt. % precursor for temperatures $> 900^\circ\text{C}$. The addition of a few mol % NaF to NaCl changes their growth direction thereby strongly affecting the habit of the rutile crystals. The rod-shaped crystals transform into bipyramidal octahedra and 111 facets appear in the habit (see figure 5.13, page 70). The ART was sped-up at a low oxygen partial pressure of 10^{-2} in argon. Higher partial pressures hinder the formation of rod-shaped crystals. However, the addition of B_2O_3 increases the acidity of the melt and promotes the rod-shaped habit formation (see figure 5.28, page 85). MSS in sulfates (summarized in section 5.2.7) provides an oxygen rich melt in comparison to the chloride system. As a consequence, the ART is retarded, the habit deviates from the rod-shaped morphology and the particle size is low (at 900°C). NaF addition, investigated at 1100°C to achieve larger particle sizes, triggers the appearance of additional facets by terraced growth, while the B_2O_3 addition roughen the surface of the crystals. Synthesis in pure oxygen promotes the formation of rutile crystals with a truncated bifrustum habit. Lowering the oxygen partial pressure increases the ART rate, but not at the same extent as in the chloridic environment. Increasing the acidity (*i.e.* reducing the O^{2-} activity) of the melt generally leads to a higher oxide dissolution, which has the effect of increasing the ART rate and the formation of rod-shaped habits.

The general trends observed by DMP, are confirmed by WCP. The use of a Ti-containing precursor (TiOSO_4 or TiCl_4) in place of anatase nanoparticles provides a faster ART rate with TiCl_4 precursor in NaCl melt (anatase absent at $T \geq 850^\circ\text{C}$, see figure 5.30). The ART is slightly slower with TiOSO_4 precursor in Na_2SO_4 melt (anatase in traces at $T = 850^\circ\text{C}$, see figure 5.55). The higher solubilities of these precursors in the salt matrix facilitate the formation of NTO (observed in chlorides and enhanced in sulfates). Concerning the morphology of the samples, the Raman investigation unequivocally attributes

the rod-shaped habit to the NTO phase and the polyhedral particles to the rutile phase. The Na_3PO_4 addition to the precursor TiOSO_4 markedly retards the ART, effects the size and morphology of rutile (5.67), and hinders the $\text{Na}_2\text{Ti}_6\text{O}_{13}$ formation. The addition of NaOH to the TiOSO_4 precursor, regulating the pH of the solution, strongly changes the phase composition. A $\text{Na}_2\text{Ti}_6\text{O}_{13}$ /rutile composition is obtained at neutral pH, a pure $\text{Na}_2\text{Ti}_6\text{O}_{13}$ phase at a pH = 10.3 and a $\text{Na}_2\text{Ti}_6\text{O}_{13}/\text{Na}_2\text{Ti}_3\text{O}_7$ composition at pH = 11. The control of the pH of the precursor permits to obtain NTO nanorods of high aspect ratio in a large yield. To the best of our knowledge, NTO nanorods with a length of $\approx 40 \mu\text{m}$, a diameter $\approx 250 \text{ nm}$ and a narrow particle size distribution have not been reported yet. The high aspect ratio can be explained by the direct formation of $\text{Na}_2\text{Ti}_6\text{O}_{13}$ in the MSS and the preferential growth along the $\langle 010 \rangle$ direction.

As regards the applications, the morphologies obtained for rutile, are partially fulfilling the requirements for the production of PLPs. Especially the rod-shaped crystals generate a glittering effect due to the high rutile refractive index, but create a rough surface once randomly mixed to the lack and applied on a surface. The "mosaic tile"-like rutile crystal morphology, obtained under pure oxygen flow, strongly generate a less rough surface, but their iridescent effect is limited by the crystal thickness. Concerning NTO, nano-rods obtained with the high-aspect ratio due to an extensive growth along the $\langle 010 \rangle$ direction, show attractive electrochemical performance. EBSD and HRTEM investigations have confirmed this crystal growth direction. Half-cells with NTO, $\text{Na}_2\text{Ti}_6\text{O}_{13}/\text{Na}_2\text{Ti}_3\text{O}_7$ and rutile as anode materials have been cycled vs Li^+/Li and vs Na^+/Na . The performance of these anode materials follows the series NTO nanorods > NTO/ $\text{Na}_2\text{Ti}_3\text{O}_7$ > rutile. The enhanced electrochemical performance of the pure NTO nanorods can be rationalized by the high purity and the high aspect ratio (maximum of 400) not yet reported in literature. The unique open tunnel structure of NTO facilitates the sodium (and lithium) transport along the $\langle 010 \rangle$ direction of the TiO_6 octahedral framework. The recovered capacities 100 mA h g^{-1} (Li) and 40 mA h g^{-1} (Na) at 74.4 mA g^{-1} after 100 cycles, strongly depend on the synthesis temperature. Increase of the temperature to $1100 \text{ }^\circ\text{C}$ lowers the capacities by $\approx 20 \%$. This effect can be explained by i) the volume change with temperature and ii) an alteration in Ti–O bonding and Na bonding inside the tunnel structure. The Ti-L_{2,3} and the O-K ELNES lines of NTO-1100, investigated by EELS, show a shift by about 0.2 eV to lower energy in comparison to NTO-900, indicating a slight change in the Ti–O bonding. Raman data agree with this finding. To date, only a few insertion electrode materials are reported displaying reversible Na-ion uptake, anode materials being in particular scarce. The high capacity and the remarkable structural stability of the NTO nanorods qualify them as promising materials for large-scale energy storage applications in future grid technologies.

Outlook Although the present work clarified many aspects of the growth of titania and titanates crystals in molten salts, by establishing a clear relation between phase formation, crystal habit and sample morphologies, future research should focus on the following topics:

- a better habit tunability by WCP, e.g. by control of the basicity of the molten salt.

-
- a systematic study of the dependence on the oxygen partial pressure/defect density of Ti^{3+} ($\text{V}_\text{O}^{\bullet\bullet}$).
 - CFE by testing other additives than NaF, B_2O_3 .
 - modeling of the crystal growth process in molten salts to identify the interactions at the single facets.

In order to enhance the performance of the promising NTO material in LIBs and in SIBs, studies should be concentrated on:

- the Ti–O bonding and Na bonding inside the NTO tunnel structure at different synthesis conditions.
- relationship between the electrochemical properties and the synthesis conditions of NTO, notably the effect of the holding time.
- carbon coating of the nanorods.

Bibliography

1. Liu, X., Fehler, N. & Antonietti, M. *Salt melt synthesis of ceramics, semiconductors and carbon nanostructures*. *Chem. Soc. Rev.* **42**, 8237–65. ISSN: 1460-4744. doi:10.1039/c3cs60159e (2013).
2. Li, Z., Zhang, S. & Lee, W. E. *Molten salt synthesis of zinc aluminate powder*. *J. Eur. Ceram. Soc.* **27**, 3407–3412. ISSN: 09552219. doi:10.1016/j.jeurceramsoc.2007.02.195 (2007).
3. Mugavero, S. J., Gemmill, W. R., Roof, I. P. & zur Loye, H. C. *Materials discovery by crystal growth: Lanthanide metal containing oxides of the platinum group metals (Ru, Os, Ir, Rh, Pd, Pt) from molten alkali metal hydroxides*. *J. Solid State Chem.* **182**, 1950–1963. ISSN: 00224596. doi:10.1016/j.jssc.2009.05.006 (2009).
4. Kimura, T. in *Adv. Ceram. - Synth. Charact. Process. Specif. Appl.* (ed Sikalidis, C.) 75–100 (InTechOpen, Rijeka, 2011). ISBN: 978-953-307-505-1. doi:10.5772/20472.
5. He, H., Yao, W., Wang, C., Feng, X. & Lu, X. *Morphology-Controlled Synthesis of Sodium Hexa-Titanate Nanowhiskers by Changing Evaporation Rate of NaCl – KCl Molten Salts*. *Ind. Eng. Chem. Res.* **52**, 15034–15040. doi:10.1021/ie402630h (2013).
6. Mann, A. K., Fu, J., Desantis, C. J. & Skrabalak, S. E. *Spatial and temporal confinement of salt fluxes for the shape-controlled synthesis of Fe₂O₃ nanocrystals*. *Chem. Mater.* **25**, 1549–1555. ISSN: 08974756. doi:10.1021/cm3038087 (2013).
7. Boltersdorf, J., King, N. & Maggard, P. A. *Flux-mediated crystal growth of metal oxides: Synthetic tunability of particle morphologies, sizes, and surface features for photocatalysis research*. *CrystEngComm* **17**, 2225–2241. ISSN: 14668033. doi:10.1039/c4ce01587h (2015).
8. Gupta, S. K. & Mao, Y. *A review on molten salt synthesis of metal oxide nanomaterials: Status, opportunity, and challenge*. *Prog. Mater. Sci.* **117**, 100734. ISSN: 00796425. doi:10.1016/j.pmatsci.2020.100734 (2021).
9. Gupta, S. K. & Mao, Y. *Recent Developments on Molten Salt Synthesis of Inorganic Nanomaterials: A Review*. *J. Phys. Chem. C* **125**, 6508–6533. ISSN: 19327455. doi:10.1021/acs.jpcc.0c10981 (2021).
10. Yoon, K. H., Cho, Y. S. & Kang, D. H. *Molten salt synthesis of lead-based relaxors*. *J. Mater. Sci.* **33**, 2977–2984. ISSN: 00222461. doi:10.1023/A:1004310931643 (1998).
11. Rørvik, P. M. *et al.* *Influence of volatile chlorides on the molten salt synthesis of ternary oxide nanorods and nanoparticles*. *Inorg. Chem.* **47**, 3173–3181. ISSN: 00201669. doi:10.1021/ic702207a (2008).
12. Billik, P., Caplovicová, M. & Caplovic, L. *Mechanochemical-molten salt synthesis of Na₂Ti₆O₁₃ nanobelts*. *Mater. Res. Bull.* **45**, 621–627. ISSN: 00255408. doi:10.1016/j.materresbull.2010.01.009 (2010).

13. Xu, C.-Y. *et al.* Molten salt synthesis of $\text{Na}_2\text{Ti}_3\text{O}_7$ and $\text{Na}_2\text{Ti}_6\text{O}_{13}$ one-dimensional nanostructures and their photocatalytic and humidity sensing properties. *CrystEngComm* **15**, 3448. ISSN: 1466-8033. doi:10.1039/c3ce27092k (2013).
14. Chen, J. A single-source molten salt synthesis of rod-shape $\text{Na}_2\text{Ti}_6\text{O}_{13}$ crystals. *Ceram. Int.* **41**, 9018–9023. ISSN: 02728842. doi:10.1016/j.ceramint.2015.03.240 (2015).
15. Zhou, X., Zhong, D., Luo, H., Pan, J. & Zhang, D. $\text{Na}_2\text{Ti}_6\text{O}_{13}$ @ TiO_2 core-shell nanorods with controllable mesoporous shells and their enhanced photocatalytic performance. *Appl. Surf. Sci.* **427**, 1183–1192. ISSN: 01694332. doi:10.1016/j.apsusc.2017.08.149 (2018).
16. Liu, B. *et al.* Large-Scale Synthesis of Transition-metal Doped TiO_2 Nanowires with Controllable Overpotential. *J. Am. Chem. Soc.* **135**, 9995–9998 (2013).
17. Einarsrud, M.-A. & Grande, T. 1D oxide nanostructures from chemical solutions. *Chem. Soc. Rev.* **43**, 2187–2199. ISSN: 0306-0012. doi:10.1039/C3CS60219B (2014).
18. Mao, Y., Park, T. J., Zhang, F., Zhou, H. & Wong, S. S. Environmentally friendly methodologies of nanostructure synthesis. *Small* **3**, 1122–1139. ISSN: 16136810. doi:10.1002/smll.200700048 (2007).
19. Maile, F. J., Pfaff, G. & Reynders, P. Effect pigments—past, present and future. *Prog. Org. Coatings* **54**, 150–163. ISSN: 03009440. doi:10.1016/j.porgcoat.2005.07.003 (Nov. 2005).
20. Yang, M.-C., Lee, Y.-Y., Xu, B., Powers, K. & Meng, Y. S. TiO_2 flakes as anode materials for Li-ion-batteries. *J. Power Sources* **207**, 166–172. ISSN: 03787753. doi:10.1016/j.jpowsour.2012.01.155 (June 2012).
21. Bai, S., Wang, L., Li, Z. & Xiong, Y. Facet-Engineered Surface and Interface Design of Photocatalytic Materials. *Adv. Sci.* **4**, 1–26. ISSN: 21983844. doi:10.1002/advs.201600216 (2017).
22. Wang, S., Liu, G. & Wang, L. Crystal Facet Engineering of Photoelectrodes for Photoelectrochemical Water Splitting. *Chem. Rev.* **119**, 5192–5247. ISSN: 15206890. doi:10.1021/acs.chemrev.8b00584 (2019).
23. Xu, T. *et al.* Syntheses of nano/submicrostructured metal oxides with all polar surfaces exposed via a molten salt route. *Cryst. Growth Des.* **9**, 192–196. ISSN: 15287483. doi:10.1021/cg8002096 (2009).
24. Yu, S. *et al.* Ionic liquid assisted chemical strategy to TiO_2 hollow nanocube assemblies with surface-fluorination and nitridation and high energy crystal facet exposure for enhanced photocatalysis. *ACS Appl. Mater. Interfaces* **6**, 10283–10295. ISSN: 19448252. doi:10.1021/am5016809 (2014).
25. Wang, X. *et al.* Molten Salt Flux Synthesis, Crystal Facet Design, Characterization, Electronic Structure, and Catalytic Properties of Perovskite Cobaltite. *ACS Appl. Mater. Interfaces* **10**, 28219–28231. ISSN: 19448252. doi:10.1021/acsami.8b08621 (2018).
26. Susman, M. D. *et al.* Synthesis of NiO Crystals Exposing Stable High-Index Facets. *Angew. Chemie* **132**, 1–6. ISSN: 0044-8249. doi:10.1002/ange.202003390 (2020).
27. Phillips, L. G. & Barbano, D. M. The Influence of Fat Substitutes Based on Protein and Titanium Dioxide on the Sensory Properties of Lowfat Milks. *J. Dairy Sci.* **80**, 2726–2731. ISSN: 00220302. doi:10.3168/jds.S0022-0302(97)76234-9 (Nov. 1997).
28. Diebold, U. The surface science of titanium dioxide. *Surf. Sci. Rep.* **48**, 53–229. ISSN: 01675729. doi:10.1016/S0167-5729(02)00100-0 (Jan. 2003).
29. Winkler, J. *Titanium Dioxide*, 128 (Vincentz Network, Hannover, 2003).

-
30. Liu, G. *et al.* Titanium dioxide crystals with tailored facets. *Chem. Rev.* **114**, 9559–9612. ISSN: 15206890. doi:10.1021/cr400621z (2014).
 31. Wang, F. *et al.* First-principles atomistic Wulff constructions for an equilibrium rutile TiO₂ shape modeling. *Appl. Surf. Sci.* **436**, 989–994. ISSN: 01694332. doi:10.1016/j.apsusc.2017.12.050 (2018).
 32. Liu, L. *et al.* Anion-assisted synthesis of TiO₂ nanocrystals with tunable crystal forms and crystal facets and their photocatalytic redox activities in organic reactions. *J. Phys. Chem. C* **117**, 18578–18587. ISSN: 19327447. doi:10.1021/jp4064774 (2013).
 33. Ong, W.-J., Tan, L.-L., Chai, S.-P., Yong, S.-T. & Mohamed, A. R. Highly reactive {001} facets of TiO₂-based composites: synthesis, formation mechanism and characterization. *Nanoscale* **6**, 1946–2008. ISSN: 2040-3372. doi:10.1039/c3nr04655a (2014).
 34. Chen, W., Kuang, Q., Wang, Q. & Xie, Z. Engineering a high energy surface of anatase TiO₂ crystals towards enhanced performance for energy conversion and environmental applications. *RSC Adv.* **5**, 20396–20409. ISSN: 2046-2069. doi:10.1039/C5RA00344J (2015).
 35. Roy, B., Ahrenkiel, S. P. & Fuierer, P. A. Controlling the size and morphology of TiO₂ powder by molten and solid salt synthesis. *J. Am. Ceram. Soc.* **91**, 2455–2463. ISSN: 00027820. doi:10.1111/j.1551-2916.2008.02456.x (2008).
 36. Roy, B. & Fuierer, P. A. Influence of sodium chloride and dibasic sodium phosphate salt matrices on the anatase-rutile phase transformation and particle size of titanium dioxide powder. *J. Am. Ceram. Soc.* **93**, 436–444. ISSN: 00027820. doi:10.1111/j.1551-2916.2009.03415.x (2010).
 37. Reddy, M. V. *et al.* Low temperature molten salt synthesis of anatase TiO₂ and its electrochemical properties. *Solid State Ionics* **262**, 120–123. ISSN: 01672738. doi:10.1016/j.ssi.2013.11.030 (2014).
 38. Peining, Z. *et al.* TiO₂ nanoparticles synthesized by the molten salt method as a dual functional material for dye-sensitized solar cells. *RSC Adv.* **2**, 5123. ISSN: 2046-2069. doi:10.1039/c2ra00041e (2012).
 39. Beyene, A. M., Baek, C., Jung, W. K., Ragupathy, P. & Kim, D. K. Understanding the role of oxygen ion (O²⁻) activity in 1-D crystal growth of rutile TiO₂ in molten salts. *CrystEngComm* **20**, 487–495. ISSN: 1466-8033. doi:10.1039/C7CE01807J (2018).
 40. Garnier, S., Bohnke, C., Bohnke, O. & Fourquet, J. L. Electrochemical intercalation of lithium into the ramsdellite-type structure of Li₂Ti₃O₇. *Solid State Ionics* **83**, 323–332. ISSN: 01672738. doi:10.1016/0167-2738(96)00002-1 (1996).
 41. Pérez-Flores, J. C., Kuhn, A. & García-Alvarado, F. Synthesis, structure and electrochemical Li insertion behaviour of Li₂Ti₆O₁₃ with the Na₂Ti₆O₁₃ tunnel-structure. *J. Power Sources* **196**, 1378–1385. ISSN: 03787753. doi:10.1016/j.jpowsour.2010.08.106 (2011).
 42. Ling, C. & Zhang, R. Anomalously high Na⁺ and low Li⁺ mobility in intercalated Na₂Ti₆O₁₃. *Phys. Chem. Chem. Phys.* **19**, 10036–10041. ISSN: 1463-9076. doi:10.1039/c7cp01138e (2017).
 43. Zulueta, Y. A., Geerlings, P., Tielens, F. & Nguyen, M. T. Lithium- and sodium-ion transport properties of Li₂Ti₆O₁₃, Na₂Ti₆O₁₃ and Li₂Sn₆O₁₃. *J. Solid State Chem.* **279**, 120930. ISSN: 00224596. doi:10.1016/j.jssc.2019.120930 (2019).
 44. Teshima, K. *et al.* Environmentally Friendly Growth of Highly Crystalline Photocatalytic Na₂Ti₆O₁₃ Whiskers from a NaCl Flux. *Cryst. Growth Des.* **8**, 465–469. ISSN: 1528-7483. doi:10.1021/cg070341p (Feb. 2008).

-
45. Teshima, K. *et al.* Highly crystalline, idiomorphic $\text{Na}_2\text{Ti}_6\text{O}_{13}$ whiskers grown from a NaCl flux at a relatively low temperature. *Eur. J. Inorg. Chem.* **2010**, 2936–2940. ISSN: 14341948. doi:10.1002/ejic.200901175 (2010).
 46. Shirpour, M., Cabana, J. & Doeff, M. New materials based on a layered sodium titanate for dual electrochemical Na and Li intercalation systems. *Energy Environ. Sci.* **6**, 2538. ISSN: 1754-5692. doi:10.1039/c3ee41037d (2013).
 47. Kuhn, A. *et al.* Comprehensive investigation of the lithium insertion mechanism of $\text{Na}_2\text{Ti}_6\text{O}_{13}$ anode material for Li-ion batteries. *J. Mater. Chem. A* **6**, 443–455. ISSN: 2050-7488. doi:10.1039/C7TA09150H (2018).
 48. Hasa, I., Hassoun, J. & Passerini, S. Nanostructured Na-ion and Li-ion anodes for battery application: A comparative overview. *Nano Res.* **3**, 12274. ISSN: 1998-0124. doi:10.1007/s12274-017-1513-7 (2017).
 49. Xu, Y. *et al.* High-power sodium titanate anodes; a comparison of lithium vs sodium-ion batteries. *J. Power Sources* **408**, 28–37. ISSN: 03787753. doi:10.1016/j.jpowsour.2018.10.038 (2018).
 50. Tarvydas, D., Tsiropoulos, I. & Lebedeva, N. Li-ion batteries for mobility and stationary storage applications : scenarios for costs and market growth. doi:doi/10.2760/87175 (Publications Office, European Commission, Joint Research Centre, 2018).
 51. Guo, S., Yi, J., Sun, Y. & Zhou, H. Recent advances in titanium-based electrode materials for stationary sodium-ion batteries. *Energy Environ. Sci.* **9**, 2978–3006. ISSN: 1754-5692. doi:10.1039/C6EE01807F (2016).
 52. Hwang, J.-Y., Myung, S.-T. & Sun, Y.-K. Sodium-ion batteries: present and future. *Chem. Soc. Rev.* **46**, 3529–3614. ISSN: 0306-0012. doi:10.1039/C6CS00776G (2017).
 53. Chen, L. *et al.* Readiness Level of Sodium-Ion Battery Technology: A Materials Review. *Adv. Sustain. Syst.* **1700153**, 37. ISSN: 23667486. doi:10.1002/adsu.201700153 (2018).
 54. Hasa, I. *et al.* Challenges of today for Na-based batteries of the future: From materials to cell metrics. *J. Power Sources* **482**, 228872. ISSN: 03787753. doi:10.1016/j.jpowsour.2020.228872 (2021).
 55. Bugga, R. V. & Smart, M. C. Lithium Plating Behavior in Lithium-Ion Cells. *ECS Trans.* **25**, 241–252. ISSN: 1938-6737. doi:10.1149/1.3393860 (2010).
 56. Williard, N., He, W., Hendricks, C. & Pecht, M. Lessons learned from the 787 dreamliner issue on Lithium-Ion Battery reliability. *Energies* **6**, 4682–4695. ISSN: 19961073. doi:10.3390/en6094682 (2013).
 57. Fordham, E. J., William, W. & Allison, M. *Safety of Grid Scale Lithium-ion Battery Energy Storage Systems* (2021).
 58. Dunn, B., Kamath, H. & Tarascon, J. M. Electrical energy storage for the grid: A battery of choices. *Science* **334**, 928–935. ISSN: 10959203. doi:10.1126/science.1212741 (2011).
 59. Solomon, A. A., Child, M., Caldera, U. & Breyer, C. How much energy storage is needed to incorporate very large intermittent renewables? *Energy Procedia* **135**, 283–293. ISSN: 18766102. doi:10.1016/j.egypro.2017.09.520 (2017).
 60. Delmas, C. Sodium and Sodium-Ion Batteries: 50 Years of Research. *Adv. Energy Mater.* **8**, 1703137. ISSN: 16146840. doi:10.1002/aenm.201703137 (2018).

-
61. Zhang, H., Hasa, I. & Passerini, S. *Beyond Insertion for Na-Ion Batteries: Nanostructured Alloying and Conversion Anode Materials*. *Adv. Energy Mater.* **8**, 1702582. ISSN: 16146840. doi:10.1002/aenm.201702582 (2018).
 62. Huang, Y. *et al.* *Electrode Materials of Sodium-Ion Batteries toward Practical Application*. *ACS Energy Lett.* **3**, 1604–1612. ISSN: 23808195. doi:10.1021/acsenergylett.8b00609 (2018).
 63. Liu, T. *et al.* *Exploring competitive features of stationary sodium ion batteries for electrochemical energy storage*. *Energy Environ. Sci.* **12**, 1512–1533. ISSN: 17545706. doi:10.1039/c8ee03727b (2019).
 64. Okamoto, Y. *Density functional theory calculations of alkali metal (Li, Na, and K) graphite intercalation compounds*. *J. Phys. Chem. C* **118**, 16–19. ISSN: 19327447. doi:10.1021/jp4063753 (2014).
 65. Moriwake, H., Kuwabara, A., Fisher, C. A. & Ikuhara, Y. *Why is sodium-intercalated graphite unstable?* *RSC Adv.* **7**, 36550–36554. ISSN: 20462069. doi:10.1039/c7ra06777a (2017).
 66. Sangster, J. *C-Na (Carbon-Sodium) System*. *J. Phase Equilibria Diffus.* **28**, 571–579 (2007).
 67. Stevens, D. A. & Dahn, J. R. *High Capacity Anode Materials for Rechargeable Sodium-Ion Batteries*. *J. Electrochem. Soc.* **147**, 1271. ISSN: 0013-4651. doi:10.1149/1.1393348 (2000).
 68. Wenzel, S., Hara, T., Janek, J. & Adelhelm, P. *Room-temperature sodium-ion batteries: Improving the rate capability of carbon anode materials by templating strategies*. *Energy Environ. Sci.* **4**, 3342–3345. ISSN: 17545692. doi:10.1039/c1ee01744f (2011).
 69. Palomares, V., Casas-Cabanas, M., Castillo-Martínez, E., Han, M. H. & Rojo, T. *Update on Na-based battery materials. A growing research path*. *Energy Environ. Sci.* **6**, 2312–2337. ISSN: 17545692. doi:10.1039/c3ee41031e (2013).
 70. Dominko, R. *et al.* *Reversible lithium insertion into Na₂Ti₆O₁₃ structure*. *Electrochem. commun.* **8**, 673–677. ISSN: 13882481. doi:10.1016/j.elecom.2006.02.017 (2006).
 71. Dominko, R., Dupont, L., Gaberšček, M., Jamnik, J. & Baudrin, E. *Alkali hexatitanates-A₂Ti₆O₁₃ (A = Na, K) as host structure for reversible lithium insertion*. *J. Power Sources* **174**, 1172–1176. ISSN: 03787753. doi:10.1016/j.jpowsour.2007.06.181 (2007).
 72. Rudola, A., Saravanan, K., Devaraj, S., Gong, H. & Balaya, P. *Na₂Ti₆O₁₃: a potential anode for grid-storage sodium-ion batteries*. *Chem. Commun.* **49**, 7451. ISSN: 1359-7345. doi:10.1039/c3cc44381g (2013).
 73. Maisch, R. & Weigand, M. *Perlglanzpigmente* Second, 70 (verlag moderne industrie, 1992).
 74. Wang, L. & Sasaki, T. *Titanium Oxide Nanosheets: Graphene Analogues with Versatile Functionalities*. *Chem. Rev.* **114**, 9455–9486. ISSN: 1520-6890. doi:10.1021/cr400627u (Apr. 2014).
 75. Alessandri, I. *et al.* *Sol-gel synthesis and characterization of lamellar mesostructured titania films*. *Mater. Sci. Eng. C* **25**, 560–564. ISSN: 09284931. doi:10.1016/j.msec.2005.07.006 (Dec. 2005).
 76. Sasaki, T., Nakano, S., Yamauchi, S. & Watanabe, M. *Fabrication of Titanium Dioxide Thin Flakes and Their Porous Aggregate*. *Chem. Mater.* **9**, 602–608. ISSN: 0897-4756. doi:10.1021/cm9604322 (Feb. 1997).
 77. Nakagawa, K. *et al.* *Synthesis and Characterization of Surface-Functionalized Layered Titanate Nanosheets Using Lamellar Self-Assembly as a Template*. *Eur. J. Inorg. Chem.* **2012**, 2741–2748. ISSN: 14341948. doi:10.1002/ejic.201101136 (June 2012).

-
78. Bloom, H. *The Chemistry of Molten Salts* (eds Plane, R. A. & Sienko, M. J.) 184 (W. A. BENJAMIN, INC., New York, 1967).
 79. Schmalzried, H. *Chemical Kinetics of solids* (VHC Verlagsgesellschaft mbH, Weinheim, 1995).
 80. Gaune-Escard, M. & Haarberg, G. M. *Molten Salts Chemistry and Technology* First, 1–600. ISBN: 9781118448847. doi:10.1002/9781118448847 (John Wiley & Sons, Ltd., 2014).
 81. Bugaris, D. E. & Zur Loye, H. C. *Materials discovery by flux crystal growth: Quaternary and higher order oxides. Angew. Chemie - Int. Ed.* **51**, 3780–3811. ISSN: 14337851. doi:10.1002/anie.201102676 (2012).
 82. Tiano, A. L., Koenigsmann, C., Santulli, A. C. & Wong, S. S. *Solution-based synthetic strategies for one-dimensional metal-containing nanostructures. Chem. Commun.* **46**, 8093–8130. ISSN: 1359-7345. doi:10.1039/c0cc01735c (2010).
 83. Noureldine, D., Anjum, D. H. & Takanabe, K. *Flux-assisted synthesis of SnNb₂O₆ for tuning photocatalytic properties. Phys. Chem. Chem. Phys.* **16**, 10762–10769. ISSN: 14639076. doi:10.1039/c4cp00654b (2014).
 84. Xue, P., Wu, H., Lu, Y. & Zhu, X. *Recent progress in molten salt synthesis of low-dimensional perovskite oxide nanostructures, structural characterization, properties, and functional applications: A review. J. Mater. Sci. Technol.* **34**, 914–930. ISSN: 10050302. doi:10.1016/j.jmst.2017.10.005 (2018).
 85. Zhang, S., Jayaseelan, D. D., Bhattacharya, G. & Lee, W. E. *Molten salt synthesis of magnesium aluminate (MgAl₂O₄) spinel powder. J. Am. Ceram. Soc.* **89**, 1724–1726. ISSN: 00027820. doi:10.1111/j.1551-2916.2006.00932.x (2006).
 86. Jayaseelan, D. D., Zhang, S., Hashimoto, S. & Lee, W. E. *Template formation of magnesium aluminate (MgAl₂O₄) spinel microplatelets in molten salt. J. Eur. Ceram. Soc.* **27**, 4745–4749. ISSN: 09552219. doi:10.1016/j.jeurceramsoc.2007.03.027 (2007).
 87. Ye, J., Zhang, S. & Lee, W. E. *Novel low temperature synthesis and characterisation of hollow silicon carbide spheres. Microporous Mesoporous Mater.* **152**, 25–30. ISSN: 13871811. doi:10.1016/j.micromeso.2011.11.059 (2012).
 88. Ye, J., Thackray, R. P., Lee, W. E. & Zhang, S. *Microstructure and rheological properties of titanium carbide-coated carbon black particles synthesised from molten salt. J. Mater. Sci.* **48**, 6269–6275. ISSN: 00222461. doi:10.1007/s10853-013-7424-4 (2013).
 89. Ye, J., Zhang, S. & Lee, W. E. *Molten salt synthesis and characterization of SiC coated carbon black particles for refractory castable applications. J. Eur. Ceram. Soc.* **33**, 2023–2029. ISSN: 09552219. doi:10.1016/j.jeurceramsoc.2013.02.011 (2013).
 90. Li, L., Deng, J., Chen, J. & Xing, X. *Topochemical molten salt synthesis for functional perovskite compounds. Chem. Sci.* **7**, 855–865. ISSN: 2041-6520. doi:10.1039/C5SC03521J (2016).
 91. Fu, J., Hou, Y., Liu, X., Zheng, M. & Zhu, M. *A construction strategy of ferroelectrics by the molten salt method and its application in the energy field. J. Mater. Chem. C* **8**, 8704–8731. ISSN: 2050-7526. doi:10.1039/d0tc01924k (2020).
 92. Huang, Z., Zhang, H. & Zhang, S. *Growth of well-developed LaOCl microplates by chloride salt-assisted method. CrystEngComm* **19**, 2971–2976. ISSN: 1466-8033. doi:10.1039/C7CE00549K (2017).

-
93. Moriya, Y., Takata, T. & Domen, K. *Recent progress in the development of (oxy)nitride photocatalysts for water splitting under visible-light irradiation*. *Coord. Chem. Rev.* **257**, 1957–1969. ISSN: 00108545. doi:10.1016/j.ccr.2013.01.021 (2013).
 94. Hojamberdiev, M. *et al.* *NH₃-Assisted Flux Growth of Cube-like BaTaO₂N Submicron Crystals in a Completely Ionized Nonaqueous High-Temperature Solution and Their Water Splitting Activity*. *Cryst. Growth Des.* **15**, 4663–4671. ISSN: 1528-7483. doi:10.1021/acs.cgd.5b00927 (2015).
 95. Hojamberdiev, M., Yamaguchi, A., Yubuta, K., Oishi, S. & Teshima, K. *Fabrication of La₂Ti₂O₇ crystals using an alkali-metal molybdate flux growth method and their nitridability to form LaTiO₂N crystals under a high-temperature NH₃ atmosphere*. *Inorg. Chem.* **54**, 3237–3244. ISSN: 1520510X. doi:10.1021/ic502862t (2015).
 96. Kodera, M., Katayama, M., Hisatomi, T., Minegishi, T. & Domen, K. *Effects of flux treatment on morphology of single-crystalline BaNbO₂N particles*. *CrystEngComm* **18**, 3186–3190. ISSN: 14668033. doi:10.1039/c5ce02335a (2016).
 97. Cortese, A. J. *et al.* *Oxygen anion solubility as a factor in molten flux crystal growth, synthesis, and characterization of four new reduced lanthanide molybdenum oxides: Ce_{4.918(3)}Mo₃O₁₆, Pr_{4.880(3)}Mo₃O₁₆, Nd_{4.910(3)}Mo₃O₁₆, and Sm_{4.952(3)}Mo₃O₁₆*. *Cryst. Growth Des.* **16**, 4225–4231. ISSN: 15287505. doi:10.1021/acs.cgd.6b00201 (2016).
 98. Arney, D., Watkins, T. & Maggard, P. A. *Effects of particle surface areas and microstructures on photocatalytic H₂ and O₂ production over PbTiO₃*. *J. Am. Ceram. Soc.* **94**, 1483–1489. ISSN: 00027820. doi:10.1111/j.1551-2916.2010.04262.x (2011).
 99. Fuoco, L., Rodriguez, D., Peppel, T. & Maggard, P. A. *Molten-salt-mediated syntheses of Sr₂FeReO₆, Ba₂FeReO₆, and Sr₂CrReO₆: Particle sizes, B/B' site disorder, and magnetic properties*. *Chem. Mater.* **23**, 5409–5414. ISSN: 08974756. doi:10.1021/cm202545z (2011).
 100. Choi, J., King, N. & Maggard, P. A. *Metastable Cu(I)-niobate semiconductor with a low-temperature, nanoparticle-mediated synthesis*. *ACS Nano* **7**, 1699–1708. ISSN: 19360851. doi:10.1021/nn305707f (2013).
 101. Boltersdorf, J., Zoellner, B., Fancher, C. M., Jones, J. L. & Maggard, P. A. *Single- and Double-Site Substitutions in Mixed-Metal Oxides: Adjusting the Band Edges Toward the Water Redox Couples*. *J. Phys. Chem. C* **120**, 19175–19188. ISSN: 19327455. doi:10.1021/acs.jpcc.6b05758 (2016).
 102. Boltersdorf, J. *et al.* *Flux Synthesis, Optical and Photocatalytic Properties of n-type Sn₂TiO₄: Hydrogen and Oxygen Evolution under Visible Light*. *Chem. Mater.* **28**, 8876–8889. ISSN: 15205002. doi:10.1021/acs.chemmater.6b02003 (2016).
 103. O'Donnell, S., Hamilton, A. & Maggard, P. A. *Fast Flux Reaction Approach for the Preparation of Sn₂TiO₄: Tuning Particle Sizes and Photocatalytic Properties*. *J. Electrochem. Soc.* **166**, H3084–H3090. ISSN: 0013-4651. doi:10.1149/2.0141905jes (2019).
 104. *Industrial Inorganic Pigments* Third (eds Buxbaum, G. & Pfaff, G.) 288 (WILEY-VCH, 2005).
 105. Dash, A., Vaßen, R., Guillon, O. & Gonzalez-Julian, J. *Molten salt shielded synthesis of oxidation prone materials in air*. *Nat. Mater.* **18**, 465–470. ISSN: 14764660. doi:10.1038/s41563-019-0328-1 (2019).
 106. Dash, A., Sohn, Y. J., Vaßen, R., Guillon, O. & Gonzalez-Julian, J. *Synthesis of Ti₃SiC₂ MAX phase powder by a molten salt shielded synthesis (MS³) method in air*. *J. Eur. Ceram. Soc.* **39**, 3651–3659. ISSN: 1873619X. doi:10.1016/j.jeurceramsoc.2019.05.011 (2019).

-
107. Lantelme, F., Turq, P., Quentrec, B. & Lewis, J. W. *Application of the molecular dynamics method to a liquid system with long range forces (Molten NaCl)*. *Mol. Phys.* **28**, 1537–1549. ISSN: 13623028. doi:10.1080/00268977400102791 (1974).
 108. Sundermeyer, W. *Fused Salts and Their Use as Reaction Media*. *Angew. Chemie Int. Ed. English* **4**, 222–238. ISSN: 0570-0833. doi:10.1002/anie.196502221 (1965).
 109. Janz, G. J. *Molten Salts Handbook*, 588 (Academic Press Inc., New York - London, 1967).
 110. Blander, M. *Molten Salt Chemistry* (ed Blander, M.) 775 (Interscience Publishers, 1964).
 111. Lantelme, F. & Turq, P. *The role of Coulomb forces in the properties of ionic liquids*. *J. Chem. Phys.* **81**, 5046–5052. ISSN: 00219606. doi:10.1063/1.447492 (1984).
 112. Freyland, W. *Coulombic Fluids - Bulk and Interfaces*, 5–44. ISBN: 978-3-642-17778-1. doi:10.1007/978-3-642-17779-8 (Springer-Verlag Berlin Heidelberg, 2011).
 113. Salanne, M., Simon, C., Turq, P., Ohtori, N. & Madden, P. A. in *Molten Salts Chem.* (eds Lantelme, F. & Groult, H.) 1st ed., 1–16 (Elsevier Inc., Oxford, 2013). ISBN: 9780123985385. doi:10.1016/B978-0-12-398538-5.00001-9.
 114. Kenney, C. N. *Molten Salt Catalysis of Gas Reactions*. *Catal. Rev. Sci. Eng.* **11**, 197–224. ISSN: 15205703. doi:10.1080/01614947508079985 (1975).
 115. Parshall, G. W. *Catalysis in Molten Salt Media*. *J. Am. Chem. Soc.* **94**, 8716. ISSN: 13846566. doi:10.1023/A:1024235221365 (1972).
 116. Emons, H. H. & Voigt, W. *Zur Chemie geschmolzener Salze*. *Sitzungsberichte der Akademie der Wissenschaften der DDR / N* **No. 15** (Akademie-Verlag, 1981).
 117. Lovering, D. G. & Gale, R. J. *Molten Salt Techniques* (Plenum Press, New York and London, 1983).
 118. *Crystal Growth Technology* (eds Byrappa, K. & Ohachi, T.) 590. ISBN: 0815514530 (Andrew [u.a.], Norwich, New York, 2003).
 119. Burton, W. K., Cabrera, N., Frank, F. C. & Mott, N. F. *The growth of crystals and the equilibrium structure of their surfaces*. *Philos. Trans. R. Soc. London. Ser. A, Math. Phys. Sci.* **243**, 299–358. doi:10.1098/rsta.1951.0006 (June 1951).
 120. Myers-Beaghton, A. K. & Vvedensky, D. D. *Generalized Burton-Cabrera-Frank*. *Phys. Rev. A* **44** (1991).
 121. Woodruff, D. P. *How does your crystal grow? A commentary on Burton, Cabrera and Frank (1951) 'The growth of crystals and the equilibrium structure of their surfaces'*. *Philos. Trans. R. Soc. A Math. Phys. Eng. Sci.* **373**. ISSN: 1364503X. doi:10.1098/rsta.2014.0230 (2015).
 122. Uwaha, M. *Introduction to the BCF theory*. *Prog. Cryst. Growth Charact. Mater.* **62**, 58–68. ISSN: 09608974. doi:10.1016/j.pcrysgrow.2016.04.002 (2016).
 123. Elwell, D. & Scheel, H. J. *Crystal Growth from High-Temperature Solutions*, 634. ISBN: 0-12-237550-8 (Academic Press Inc., London, 1975).
 124. Sunagawa, I. *Growth and morphology of crystals*. *Forma* **14**, 147. ISSN: 10290338. doi:10.1080/01411599308210261 (1999).
 125. Bennema, P. *et al.* *Crystal growth and morphology: New developments in an integrated Hartman-Perdok-connected net-roughening transition theory, supported by computer simulations*. *Cryst. Growth Des.* **4**, 905–913. ISSN: 15287483. doi:10.1021/cg034182v (2004).
 126. Lux, H. *Säuren und Basen im Schmelzfluss: die Bestimmung der Sauerstoffionen-Konzentration*. *Z. Elektrochem* **45**, 303–309 (1939).

-
127. Flood, H. & Förland, T. *The acidic and basic properties of oxides. Acta Chem. Scand* **1**, 592–604. ISSN: 0001-5393. doi:10.3891/acta.chem.scand.01-0592 (1947).
 128. Mao, C., Wang, G., Dong, X., Zhou, Z. & Zhang, Y. *Low temperature synthesis of Ba_{0.70}Sr_{0.30}TiO₃ powders by the molten-salt method. Mater. Chem. Phys.* **106**, 164–167. ISSN: 02540584. doi:10.1016/j.matchemphys.2007.06.052 (2007).
 129. Arendt, R. H., Rosolowski, J. H. & Szymaszek, J. W. *Lead zirconate titanate ceramics from molten salt solvent synthesized powders. Mater. Res. Bull.* **14**, 703–709. doi:http://dx.doi.org/10.1016/0025-5408(79)90055-2 (1979).
 130. Gaune-Escard, M. & Seddon, K. R. *Molten Salts and Ionic Liquids: Never the Twain?* ISBN: 9780471773924. doi:10.1002/9780470947777 (2010).
 131. Donnay, J. D. H. & Harker, D. *A New Law of Crystal Morphology Extending the Law of Bravais. Am. Miner.* **22**, 446. ISSN: 0003-004X (1937).
 132. Lovette, M. A. *et al. Crystal shape engineering. Ind. Eng. Chem. Res.* **47**, 9812–9833. ISSN: 08885885. doi:10.1021/ie800900f (2008).
 133. Susman, M. D., Pham, H. N., Datye, A. K., Chinta, S. & Rimer, J. D. *Factors Governing MgO(111) Faceting in the Thermal Decomposition of Oxide Precursors. Chem. Mater.* **30**, 2641–2650. ISSN: 15205002. doi:10.1021/acs.chemmater.7b05302 (2018).
 134. Zhang, S. *et al. Growth habit control of ZnO single crystals in molten hydrous alkali solutions. J. Cryst. Growth* **336**, 56–59. ISSN: 00220248. doi:10.1016/j.jcrysgro.2011.09.027 (2011).
 135. Li, W. J., Shi, E. W., Zhong, W. Z. & Yin, Z. W. *Growth mechanism and growth habit of oxide crystals. J. Cryst. Growth* **203**, 186–196. ISSN: 00220248. doi:10.1016/S0022-0248(99)00076-7 (1999).
 136. Li, W., Shi, E., Chen, Z. & Yin, Z. *Coordination polyhedron growth mechanism model and growth habit of crystals. Sci. China, Ser. B Chem.* **44**, 123–136. ISSN: 10069291. doi:10.1007/BF02879530 (2001).
 137. White, E. A. & Brightwell, J. *The growth of ruby crystals from solution in molten lead fluoride. Chem. Ind.* **39**, 1662 (1965).
 138. White, E. A. & Wood, J. D. *The growth of highly perfect alumina platelets and other oxides by solvent vapour transport. J. Mater. Sci.* **9**, 1999–2006. ISSN: 00222461. doi:10.1007/BF00540549 (1974).
 139. Li, W. J., Shi, E. W. & Yin, Z. W. *Growth habit of rutile and α -Al₂O₃ crystals. J. Cryst. Growth* **208**, 546–554. ISSN: 00220248. doi:10.1016/S0022-0248(99)00419-4 (2000).
 140. Kim, B. Y. *et al. Effect of salt on crystal growth of plate-like alumina particles by molten-salt method. Korean Chem. Eng. Res.* **53**, 603–608. ISSN: 22339558. doi:10.9713/kcer.2015.53.5.603 (2015).
 141. Billik, P., Čaplovičová, M., Čaplovič, L. & Horváth, B. *Mechanochemical-molten salt synthesis of α -Al₂O₃ platelets. Ceram. Int.* **41**, 8742–8747. ISSN: 02728842. doi:10.1016/j.ceramint.2015.03.095 (2015).
 142. Chang, Y., Wu, J., Zhang, M., Kupp, E. & Messing, G. L. *Molten salt synthesis of morphology controlled α -alumina platelets. Ceram. Int.* **43**, 12684–12688. ISSN: 02728842. doi:10.1016/j.ceramint.2017.06.150 (2017).

-
143. Pfaff, G. & Reynders, P. *Angle-Dependent Optical Effects Deriving from Submicron Structures of Films and Pigments*. *Chem. Rev. (Washington, D. C.)* **99**, 1963–1981. ISSN: 1520-6890. doi:10.1021/cr970075u (July 1999).
 144. Pfaff, G. *High Performance Pigments*, 77 (Wiley- VCH, Weinheim, 2002).
 145. Chen, H. *et al.* *The influence of different titanium sources on flaky α - Al_2O_3 prepared by molten salt synthesis*. *Ceram. Int.* **41**, 12288–12294. ISSN: 02728842. doi:10.1016/j.ceramint.2015.06.054 (2015).
 146. Sunagawa, I. in *Morphol. Crystals, Part B* (ed Sunagawa, I.) 509–587 (Terra Sci. Pub., Tokyo, 1987).
 147. Lux, H. *Reaktionen im Schmelzfluß VI. Gleichgewichte im System $\text{Na}_2\text{O-TiO}_2$* . *Z. Elektrochem* **53**, 45–47 (1949).
 148. Kimura, T., Takahashi, T. & Yamaguchi, T. *Preparation and characteristics of Ni-ferrite powders obtained in the presence of fused salts*. *J. Mater. Sci.* **15**, 1491–1497. ISSN: 00222461. doi:10.1007/BF00752130 (1980).
 149. Burke, J. E. *Some factors affecting the rate of grain growth in metals*. *Trans. AIME* **180**, 73 (1949).
 150. Danek, V. & Matiasovsky, K. *Preparation of Double Oxides in Ionic Melts*. *Z. Anorg. Allg. Chem.* **584**, 207–216 (1990).
 151. Rahaman, M. N. *Ceramic processing and sintering* (Marcel Dekker, New York [u.a.], 1995).
 152. Penn, R. L. & Banfield, J. F. *Morphology development and crystal growth in nanocrystalline aggregates under hydrothermal conditions: Insights from titania*. *Geochim. Cosmochim. Acta* **63**, 1549–1557. ISSN: 00167037. doi:10.1016/S0016-7037(99)00037-X (1999).
 153. Wang, F., Richards, V. N., Shields, S. P. & Buhro, W. E. *Kinetics and mechanisms of aggregative nanocrystal growth*. *Chem. Mater.* **26**, 5–21. ISSN: 08974756. doi:10.1021/cm402139r (2014).
 154. Sui, N., Duan, Y., Jiao, X. & Chen, D. *Large-Scale Preparation and Catalytic Properties of One-Dimensional α/β - MnO_2 Nanostructures*. *J. Phys. Chem. C* **113**, 8560–8565. doi:10.1021/jp810452k (2009).
 155. Tiano, A. L. *et al.* *Toward a reliable synthesis of strontium ruthenate: Parameter control and property investigation of submicrometer-sized structures*. *Chem. Mater.* **23**, 3277–3288. ISSN: 08974756. doi:10.1021/cm1029497 (2011).
 156. Shoemaker, D. P. *et al.* *Understanding fluxes as media for directed synthesis: In situ local structure of molten potassium polysulfides*. *J. Am. Chem. Soc.* **134**, 9456–9463. ISSN: 00027863. doi:10.1021/ja303047e (2012).
 157. Xiao, X., Hayashi, F., Yubuta, K., Selloni, A. & Teshima, K. *Effects of Alkali Cations and Sulfate/Chloride Anions on the Flux Growth of {001}-Faceted β - Li_2TiO_3 Crystals*. *Cryst. Growth Des.* **17**, 1118–1124. ISSN: 15287505. doi:10.1021/acs.cgd.6b01504 (2017).
 158. Hayashi, Y., Kimura, T. & Yamaguchi, T. *Preparation of rod-shaped BaTiO_3 powder*. *J. Mater. Sci.* **21**, 757–762 (1986).
 159. Fukumoto, M., Suzuki, T., Sano, M., Hirade, M. & Kara, M. *Solubility of metal oxides under control of basicity by electrolysis in fused Na_2SO_4* . *Mater. Trans.* **45**, 2994–2998. ISSN: 13459678. doi:10.2320/matertrans.45.2994 (2004).
 160. *Molten Salt Chemistry* 1st ed. (eds Mamantov, G. & Marassi, R.) 525. ISBN: 978-90-277-2483-0. doi:https://doi.org/10.1007/978-94-009-3863-2 (Springer, Dordrecht, 1987).

-
161. Stein, A., Keller, S. W. & Mallouk, T. E. *Turning Down the Heat : Design and Mechanism in Solid-State Synthesis* Published by : American Association for the Advancement of Science *Turning Down the Heat : Design and Mechanism in Solid State Synthesis*. *Science* **259**, 1558–1564 (1993).
162. Tremillon, B. & Doisneau, R. G. *Propriétés chimiques et électrochimiques dans les hydroxydes alcalins fondus*. *J. Chim. Phys.* **71**, 1379–1387 (1974).
163. Zarubitskii, O. G. *The Electrochemistry of Hydroxide Melts*. *Russ. Chem. Rev.* **49**, 536–548. ISSN: 0036-021X. doi:10.1070/rc1980v049n06abeh002486 (1980).
164. Lux, H., Kuhn, R. & Niedermaier, T. *Reaktionen und Gleichgewichte in Alkalihydroxydschmelzen. III Peroxydgleichgewichte*. *Z. Anorg. Allg. Chem.* **298**, 285 (1959).
165. Zheng, H. et al. *Bi/Bi₂O₃ sensor for quantitation of dissolved oxygen in molten salts*. *J. Adv. Ceram.* **7**, 1–4. ISSN: 22278508. doi:10.1007/s40145-017-0250-4 (2018).
166. Bartholomew, R. F. & White, W. B. *Growth of the intermediate oxides of titanium from borate fluxes under controlled oxygen fugacities*. *J. Cryst. Growth* **6**, 249–252. ISSN: 00220248. doi:10.1016/0022-0248(70)90075-8 (1970).
167. Samsonov, G. *The Oxide Handbook* (IFI/Plenum Press, New York, 1982).
168. Hanaor, D. a. H. & Sorrell, C. C. *Review of the anatase to rutile phase transformation*. *J. Mater. Sci.* **46**, 855–874. ISSN: 00222461. doi:10.1007/s10853-010-5113-0 (2011).
169. Finnegan, M. P., Zhang, H. & Banfield, J. F. *Phase stability and transformation in titania nanoparticles in aqueous solutions dominated by surface energy*. *J. Phys. Chem. C* **111**, 1962–1968. ISSN: 19327447. doi:10.1021/jp063822c (2007).
170. Zhang, H. & Banfield, J. F. *Understanding Polymorphic Phase Transformation Behavior during Growth of Nanocrystalline Aggregates: Insights from TiO₂*. *J. Phys. Chem. B* **104**, 3481–3487. ISSN: 1520-6106. doi:10.1021/jp000499j (2000).
171. Burdett, J. K., Hughbanks, T., Miller, G. J., Smith, J. V. & Richardson, J. W. *Structural-Electronic Relationships in Inorganic Solids: Powder Neutron Diffraction Studies of the Rutile and Anatase Polymorphs of Titanium Dioxide at 15 and 295 K*. *J. Am. Chem. Soc.* **109**, 3639–3646. ISSN: 15205126. doi:10.1021/ja00246a021 (1987).
172. Momma, K. & Izumi, F. *VESTA 3 for three-dimensional visualization of crystal, volumetric and morphology data*. *J. Appl. Crystallogr.* **44**, 1272–1276. doi:10.1107/S0021889811038970 (2011).
173. Howard, C. J., Sabine, T. M. & Dickson, F. *Structural and thermal parameters for rutile and anatase*. *Acta Crystallogr. Sect. B* **47**, 462–468. ISSN: 16005740. doi:10.1107/S010876819100335X (1991).
174. Lazzeri, M., Vittadini, A. & Selloni, A. *Structure and energetics of stoichiometric TiO₂ anatase surfaces*. *Phys. Rev. B - Condens. Matter Mater. Phys.* **63**, 1554091–1554099. ISSN: 01631829. doi:10.1103/PhysRevB.63.155409 (2001).
175. Lazzeri, M., Vittadini, A. & Selloni, A. *Erratum: Structure and energetics of stoichiometric TiO₂ anatase surfaces [Phys. Rev. B 63, 155409 (2001)]*. *Phys. Rev. B - Condens. Matter Mater. Phys.* **65**, 119901. ISSN: 1550235X. doi:10.1103/PhysRevB.65.119901 (2002).
176. Vittadini, A., Selloni, A., Rotzinger, F. P. & Grätzel, M. *Structure and energetics of water adsorbed at TiO₂ anatase (101) and (001) surfaces*. *Phys. Rev. Lett.* **81**, 2954–2957. ISSN: 10797114. doi:10.1103/PhysRevLett.81.2954 (1998).

-
177. Barnard, A. S. & Zapol, P. *Predicting the energetics, phase stability, and morphology evolution of faceted and spherical anatase nanocrystals*. *J. Phys. Chem. B* **108**, 18435–18440. ISSN: 15206106. doi:10.1021/jp0472459 (2004).
 178. Barnard, A. S. & Curtiss, L. A. *Prediction of TiO₂ nanoparticle phase and shape transitions controlled by surface chemistry*. *Nano Lett.* **5**, 1261–1266. ISSN: 15306984. doi:10.1021/nl050355m (2005).
 179. Yang, H. G. *et al.* *Anatase TiO₂ single crystals with a large percentage of reactive facets*. *Nature* **453**, 638–641. ISSN: 00280836. doi:10.1038/nature06964 (2008).
 180. Selloni, A. *Anatase shows its reactive side*. *Nat. Mater.* **7**, 613–615 (2008).
 181. Menzel, R. *et al.* *Determining the morphology and photocatalytic activity of two-dimensional anatase nanoplatelets using reagent stoichiometry*. *Chem. Mater.* **25**, 2137–2145. ISSN: 08974756. doi:10.1021/cm400785z (2013).
 182. Liu, G., Yu, J. C., Lu, G. Q. M. & Cheng, H.-M. *Crystal facet engineering of semiconductor photocatalysts: motivations, advances and unique properties*. *Chem. Commun. (Camb)*. **47**, 6763–6783. ISSN: 1359-7345. doi:10.1039/c1cc10665a (2011).
 183. Lai, Z. *et al.* *Low temperature solvothermal synthesis of anatase TiO₂ single crystals with wholly {100} and {001} faceted surfaces*. *J. Mater. Chem.* **22**, 23906–23912. ISSN: 09599428. doi:10.1039/c2jm34880b (2012).
 184. Hu, Y., Tsai, H.-L. & Huang, C.-L. *Phase transformation of precipitated TiO₂ nanoparticles*. *Mater. Sci. Eng. A* **344**, 209–214. ISSN: 09215093. doi:10.1016/S0921-5093(02)00408-2 (Mar. 2003).
 185. Carp, O., Huisman, C. L. & Reller, a. *Photoinduced reactivity of titanium dioxide*. *Prog. Solid State Chem.* **32**, 33–177. ISSN: 00796786. doi:10.1016/j.progsolidstchem.2004.08.001 (2004).
 186. Hirano, M., Nakahara, C., Ota, K., Tanaike, O. & Inagaki, M. *Photoactivity and phase stability of ZrO₂-doped anatase-type TiO₂ directly formed as nanometer-sized particles by hydrolysis under hydrothermal conditions*. *J. Solid State Chem.* **170**, 39–47 (2003).
 187. Matthews, A. *The crystallization of anatase and rutile from amorphous titanium dioxide under hydrothermal conditions*. *Am. Mineral.* **61**, 419–424 (1976).
 188. Ghosh, T. B., Dhabal, S. & Datta, a. K. *On crystallite size dependence of phase stability of nanocrystalline TiO₂*. *J. Appl. Phys.* **94**, 4577–4582. ISSN: 00218979. doi:10.1063/1.1604966 (2003).
 189. Zhang, H. & Banfield, J. F. *Thermodynamic analysis of phase stability of nanocrystalline titania*. *J. Mater. Chem.* **8**, 2073–2076. ISSN: 09599428. doi:10.1039/a802619j (1998).
 190. R. D. Shannon, J. a. P. *Topotaxy in the Anatase-Rutile Transformation*. *Am. Mineral.* **49**, 1707–1717. ISSN: 0003-004X (1964).
 191. Shannon, R. D. & Pask, J. a. *Kinetics of the Anatase-Rutile Transformation*. *J. Am. Ceram. Soc.* **48**, 391–398. ISSN: 1551-2916. doi:10.1111/j.1151-2916.1965.tb14774.x (1965).
 192. Gouma, P. I. & Mills, M. J. *Anatase-to-Rutile Transformation in Titania Powders*. *J. Am. Ceram. Soc.* **84**, 619–622. ISSN: 00027820. doi:10.1111/j.1151-2916.2001.tb00709.x (Mar. 2001).
 193. Reidy, D., Holmes, J. & Morris, M. *The critical size mechanism for the anatase to rutile transformation in TiO₂ and doped-TiO₂*. *J. Eur. Ceram. Soc.* **26**, 1527–1534. ISSN: 09552219. doi:10.1016/j.jeurceramsoc.2005.03.246 (Jan. 2006).

-
194. Lee, G. H. & Zuo, J.-M. *Growth and Phase Transformation of Nanometer-Sized Titanium Oxide Powders Produced by the Precipitation Method*. *J. Am. Ceram. Soc.* **87**, 473–479. ISSN: 00027820. doi:10.1111/j.1551-2916.2004.00473.x (Mar. 2004).
195. Shi, Z. M., Yan, L., Jin, L. N., Lu, X. M. & Zhao, G. *The phase transformation behaviors of Sn²⁺ doped Titania gels*. *J. Non. Cryst. Solids* **353**, 2171–2178. ISSN: 00223093. doi:10.1016/j.jnoncrysol.2007.02.048 (2007).
196. Kumar, K. N. P., Fray, D. J., Nair, J., Mizukami, F. & Okubo, T. *Enhanced anatase-to-rutile phase transformation without exaggerated particle growth in nanostructured titania-tin oxide composites*. *Scr. Mater.* **57**, 771–774. ISSN: 13596462. doi:10.1016/j.scriptamat.2007.06.039 (2007).
197. Qi, B., Wu, L., Zhang, Y., Zeng, Q. & Zhi, J. *Low-temperature and one-step synthesis of rutile TiO₂ aqueous sol by heterogeneous nucleation method*. *J. Colloid Interface Sci.* **345**, 181–186. ISSN: 00219797. doi:10.1016/j.jcis.2010.01.030 (2010).
198. Vargas, S., Arroyo, R., Haro, E. & Rodriguez, R. *Effects of cationic dopants on the phase transition temperature of titania prepared by the sol-gel method*. *J. Mater. Res.* **14**, 3932 (1999).
199. Ihara, T., Miyoshi, M., Iriyama, Y., Matsumoto, O. & Sugihara, S. *Visible-light-active titanium oxide photocatalyst realized by an oxygen-deficient structure and by nitrogen doping*. *Appl. Catal. B Environ.* **42**, 403–409. ISSN: 0926-3373. doi:http://dx.doi.org/10.1016/S0926-3373(02)00269-2 (2003).
200. Janes, R., Knightley, L. J. & Harding, C. J. *Structural and spectroscopic studies of iron (III) doped titania powders prepared by sol-gel synthesis and hydrothermal processing*. *Dye. Pigment.* **62**, 199–212. ISSN: 01437208. doi:10.1016/j.dyepig.2003.12.003 (2004).
201. Riyas, S., Krishnan, G. & Mohan Das, P. *Anatase–rutile transformation in doped titania under argon and hydrogen atmospheres*. *Adv Appl Ceram* **106**, 255–264 (2007).
202. Yin, H. *et al.* *Hydrothermal synthesis of nanosized anatase and rutile TiO₂ using amorphous phase TiO₂*. *J. Mater. Chem.* **11**, 1694–1703. ISSN: 09599428. doi:10.1039/b008974p (2001).
203. Ramamoorthy, M., Vanderbilt, D. & King-Smith, R. D. *First-principles calculations of the energetics of stoichiometric TiO₂ surfaces*. *Phys. Rev. B* **49**, 16721–16727. ISSN: 01631829. doi:10.1103/PhysRevB.49.16721 (1994).
204. Zhao, B., Lin, L. & He, D. *Phase and morphological transitions of titania/titanate nanostructures from an acid to an alkali hydrothermal environment*. *J. Mater. Chem. A* **1**, 1659–1668. ISSN: 2050-7488. doi:10.1039/C2TA00755J (2013).
205. Leidich, P., Linker, O., Panthöfer, M. & Tremel, W. *Synthesis of single crystalline sub-micron rutile TiO₂ rods using hydrothermal treatment in acidic media*. *CrystEngComm* **16**, 8486–8491. ISSN: 1466-8033. doi:10.1039/C4CE00971A (2014).
206. Zheng, Z., Xie, W., Lim, Z. S., You, L. & Wang, J. *CdS sensitized 3D hierarchical TiO₂/ZnO heterostructure for efficient solar energy conversion*. *Sci. Rep.* **4**, 5721. ISSN: 2045-2322. doi:10.1038/srep05721 (2014).
207. Zhang, M., Chen, T. & Wang, Y. *Insights into TiO₂ polymorphs: Highly selective synthesis, phase transition, and their polymorph-dependent properties*. *RSC Adv.* **7**, 52755–52761. ISSN: 20462069. doi:10.1039/c7ra11515f (2017).
208. Barbosa, M., Fabris, G. & Ferrer, M. M. *Computational Simulations of Morphological Transformations by Surface Structures: The case of Rutile TiO₂ phase*. *Mater. Res.* **20**, 920–925 (2017).

-
209. Lai, Z. *et al.* A new insight into regulating high energy facets of rutile TiO₂. *J. Mater. Chem. A* **1**, 4182–4185. ISSN: 20507488. doi:10.1039/c3ta00188a (2013).
210. Wu, H. *et al.* Controllable synthesis of rutile titania with novel curved surfaces. *CrystEngComm* **17**, 7254–7257. ISSN: 14668033. doi:10.1039/c5ce01283j (2015).
211. Sosnowchik, B. D. *et al.* Titanium dioxide nanoswords with highly reactive, photocatalytic facets. *Nanotechnology* **21**. ISSN: 09574484. doi:10.1088/0957-4484/21/48/485601 (2010).
212. Chen, J. S. & Lou, X. W. Unusual rutile TiO₂ nanosheets with exposed (001) facets. *Chem. Sci.* **2**, 2219. ISSN: 2041-6520. doi:10.1039/c1sc00307k (2011).
213. Tasker, P. W. The stability of ionic crystal surfaces. *J. Phys. C Solid State Phys.* **12**, 4977 (1979).
214. LaFemina, J. Total energy computations of oxides surface reconstructions. *Crit. Rev. Surf. Chem.* **3**, 297 (1994).
215. Wang, R. *et al.* Light-induced amphiphilic surfaces. *Nature* **388**, 431–432. ISSN: 00280836. doi:10.1038/41233 (1997).
216. Charlton, G. *et al.* Relaxation of TiO₂ (110)-(1x1) Using Surface X-Ray Diffraction. *Phys. Rev. Lett.* **78**, 495–498. doi:10.1103/PhysRevLett.78.495 (1997).
217. Zschack, P., Cohen, J. B. & Chung, Y. W. Structure of the TiO₂(100) 1 × 3 surface determined by glancing angle X-ray diffraction and low energy electron diffraction. *Surf. Sci.* **262**, 395–408. ISSN: 0039-6028. doi:http://dx.doi.org/10.1016/0039-6028(92)90136-T (1992).
218. Muscat, J., Harrison, N. M. & Thornton, G. Effects of exchange, correlation, and numerical approximations on the computed properties of the rutile TiO₂ (100) surface. *Phys. Rev. B* **59**, 2320–2326. doi:10.1103/PhysRevB.59.2320 (1999).
219. Völz, H. G. Advanced methods of testing the optical properties of pigments. *Prog. Org. Coatings* **2**, 1–34. ISSN: 0300-9440. doi:http://dx.doi.org/10.1016/0300-9440(73)80014-1 (1973).
220. Jaenicke, W. No Title. *Z. Elektrochem* **60**, 163 (1956).
221. Völz, H. G. No Title. *DEFAZET- Dtsch. Farben Z.* **31**, 469 (1977).
222. Völz, H. G., Kämpf, G., Fitzky, H. G. & Klaeren, A. No Title. *ACS Symp. Ser.* **151**, 163 (1981).
223. Glausch, R., Kieser, M., Maisch, R., Pfaff, G. & Weitzel, J. *Special Effect Pigments*, 152 (Vincentz Verlag, Hannover, 1998).
224. Bäumer, W. No Title. *Farbe + Lack* **79**, 747 (1973).
225. Pfaff, G., Franz, K. D., Emmert, N. & Nitta, K. in *Ullmann's Encycl. Ind. Chem. Pigment. Inorg.* 6th. Chap. 4.3 (VHC Verlagsgesellschaft, Weinheim, 1998).
226. Kittel, J. & Spille, L. *Lehrbuch der Lacke und Beschichtungen, Band 5: Pigmente, Füllstoffe und Farbmeterik* 3rd (S. Hirzel Verlag, Stuttgart, 2003).
227. Li-hui, Z. & Qing-wei, H. Morphology control of α-Al₂O₃ platelets by molten salt synthesis. *Ceram. Int.* **37**, 249–255. ISSN: 02728842. doi:10.1016/j.ceramint.2010.09.021 (Jan. 2011).
228. Pérez-Flores, J. C. *et al.* Insight into the channel ion distribution and influence on the lithium insertion properties of hexatitanates A₂Ti₆O₁₃ (A = Na, Li, H) as candidates for anode materials in lithium-ion batteries. *Dalt. Trans.* **41**, 14633–42. ISSN: 1477-9234. doi:10.1039/c2dt31665j (2012).

-
229. Kataoka, K. *et al.* Ion-Exchange Synthesis, Crystal Structure, and Electrochemical Properties of $\text{Li}_2\text{Ti}_6\text{O}_{13}$. *Chem. Mater* **23**, 2344–2352. doi:10.1021/cm103678e (2011).
230. Shannon, R. D. Revised Effective Ionic Radii and Systematic Studies of Interatomic Distances in Halides and Chalcogenides. *Acta Crystallogr.* **A32**, 751–767. ISSN: 1573904X. doi:10.1023/A:1018927109487 (1976).
231. Zhang, X. K. *et al.* Synthesis, conversion, and comparison of the photocatalytic and electrochemical properties of $\text{Na}_2\text{Ti}_6\text{O}_{13}$ and $\text{Li}_2\text{Ti}_6\text{O}_{13}$ nanobelts. *J. Alloys Compd.* **631**, 171–177. ISSN: 09258388. doi:10.1016/j.jallcom.2015.01.102 (2015).
232. Li, P. *et al.* Synthesis of $\text{Na}_2\text{Ti}_6\text{O}_{13}$ nanorods as possible anode materials for rechargeable lithium ion batteries. *Electrochim. Acta* **187**, 46–54. ISSN: 00134686. doi:10.1016/j.electacta.2015.11.057 (2016).
233. Chandel, S. *et al.* Hierarchically nanorod structured $\text{Na}_2\text{Ti}_6\text{O}_{13}/\text{Na}_2\text{Ti}_3\text{O}_7$ nanocomposite as a superior anode for high-performance sodium ion battery. *J. Electroanal. Chem.* **877**, 114747. ISSN: 15726657. doi:10.1016/j.jelechem.2020.114747 (2020).
234. Senguttuvan, P., Rousse, G., Seznec, V., Tarascon, J. M. & Palacín, M. R. $\text{Na}_2\text{Ti}_3\text{O}_7$: Lowest voltage ever reported oxide insertion electrode for sodium ion batteries. *Chem. Mater.* **23**, 4109–4111. ISSN: 08974756. doi:10.1021/cm202076g (2011).
235. Ni, J. *et al.* Superior Sodium Storage in $\text{Na}_2\text{Ti}_3\text{O}_7$ Nanotube Arrays through Surface Engineering. *Adv. Energy Mater.* **6**. ISSN: 16146840. doi:10.1002/aenm.201502568 (2016).
236. Lübke, M. *et al.* High power layered titanate nano-sheets as pseudocapacitive lithium-ion battery anodes. *J. Power Sources* **305**, 115–121. ISSN: 03787753. doi:10.1016/j.jpowsour.2015.11.060 (2016).
237. Cech, O., Castkova, K. & Chladil, L. Synthesis and characterization of $\text{Na}_2\text{Ti}_6\text{O}_{13}$ and $\text{Na}_2\text{Ti}_6\text{O}_{13}/\text{Na}_2\text{Ti}_3\text{O}_7$ sodium titanates with nanorod-like structure as negative electrode materials for sodium. *J. Energy Storage* **14**, 391–398. ISSN: 0888-5885. doi:10.1021/acs.iecr.6b01867 (2017).
238. Wu, C. *et al.* Design and Synthesis of Layered $\text{Na}_2\text{Ti}_3\text{O}_7$ and Tunnel $\text{Na}_2\text{Ti}_6\text{O}_{13}$ Hybrid Structures with Enhanced Electrochemical Behavior for Sodium-Ion Batteries. *Adv. Sci.* **5**, 1800519. ISSN: 21983844. doi:10.1002/advs.201800519 (2018).
239. Pradeep, A. *et al.* Electrochemically stable and very high ‘Rate-capable’ bi-phase Na-titanate based composite anodes for Na-ion batteries. *Electrochim. Acta* **362**, 137122. ISSN: 00134686. doi:10.1016/j.electacta.2020.137122 (2020).
240. Zhang, H., Gao, X. P., Li, G. R., Yan, T. Y. & Zhu, H. Y. Electrochemical lithium storage of sodium titanate nanotubes and nanorods. *Electrochim. Acta* **53**, 7061–7068. ISSN: 00134686. doi:10.1016/j.electacta.2008.05.036 (2008).
241. Cao, K. *et al.* $\text{Na}_2\text{Ti}_6\text{O}_{13}$ Nanorods with Dominant Large Interlayer Spacing Exposed Facet for High-Performance Na-Ion Batteries. *Small* **12**, 2991–2997. ISSN: 16136829. doi:10.1002/smll.201600845 (2016).
242. Du, X. *et al.* Green ball dianthus-like $\text{Na}_2\text{Ti}_6\text{O}_{13}$ as high-rate performance anode for sodium-ion batteries. *J. Alloys Compd.* **721**, 100–105. ISSN: 09258388. doi:10.1016/j.jallcom.2017.05.306 (2017).
243. Zhang, Q., Zhang, T., Wei, Y., Zhai, T. & Li, H. Removing structural water from sodium titanate anode towards barrier-free ion diffusion for sodium ion batteries. *J. Mater. Chem. A* **5**, 18691–18697. ISSN: 2050-7488. doi:10.1039/C7TA05217K (2017).

-
244. Zhang, Y. *et al.* Sodium titanate cuboid as advanced anode material for sodium ion batteries. *J. Power Sources* **305**, 200–208. ISSN: 03787753. doi:10.1016/j.jpowsour.2015.11.101 (2016).
245. Liao, J.-Y. *et al.* Substantially enhanced rate capability of lithium storage in $\text{Na}_2\text{Ti}_6\text{O}_{13}$ with self-doping and carbon-coating. *RSC Adv.* **8**, 8929–8936. ISSN: 2046-2069. doi:10.1039/C8RA00468D (2018).
246. Fagundes, N. G. *et al.* Novel and simple way to synthesize $\text{Na}_2\text{Ti}_6\text{O}_{13}$ nanoparticles by sonochemical method. *Solid State Sci.* **88**, 63–66. ISSN: 12932558. doi:10.1016/j.solidstatesciences.2018.11.014 (2019).
247. Shen, K. & Wagemaker, M. $\text{Na}_{2+x}\text{Ti}_6\text{O}_{13}$ as Potential Negative Electrode Material for Na-Ion Batteries. *Inorg. Chem.* **53**, 8250–8256. ISSN: 0020-1669. doi:10.1021/ic5004269 (2014).
248. Ho, C.-K., Li, C.-Y. V. & Chan, K.-Y. Scalable Template-Free Synthesis of $\text{Na}_2\text{Ti}_3\text{O}_7/\text{Na}_2\text{Ti}_6\text{O}_{13}$ Nanorods with Composition Tunable for Synergistic Performance in Sodium-Ion Batteries. *Ind. Eng. Chem. Res.* **55**, 10065–10072. ISSN: 0888-5885. doi:10.1021/acs.iecr.6b01867 (2016).
249. Wu, C. *et al.* Insight into the Origin of Capacity Fluctuation of $\text{Na}_2\text{Ti}_6\text{O}_{13}$ Anode in Sodium Ion Batteries. *ACS Appl. Mater. Interfaces* **9**, 43596–43602. ISSN: 1944-8244. doi:10.1021/acsami.7b11507 (2017).
250. Sauvet, A.-L., Baliteau, S., Lopez, C. & Fabry, P. Synthesis and characterization of sodium titanates $\text{Na}_2\text{Ti}_3\text{O}_7$ and $\text{Na}_2\text{Ti}_6\text{O}_{13}$. *J. Solid State Chem.* **177**, 4508–4515. ISSN: 00224596. doi:10.1016/j.jssc.2004.09.008 (2004).
251. Wang, H. Y. *et al.* Long life anode material sodium titanate synthesized by a moderate method. *Mater. Lett.* **186**, 326–329. ISSN: 18734979. doi:10.1016/j.matlet.2016.10.027 (2017).
252. Wang, J. *et al.* $\text{Na}_2\text{Ti}_6\text{O}_{13}$ Coated with Carbon Produced by Citric Acid as an Anode Material in Sodium Ion Batteries. *J. Electrochem. Soc.* **167**, 090539. ISSN: 1945-7111. doi:10.1149/1945-7111/ab8fd6 (2020).
253. Teshima, K. *et al.* Growth of $\text{Na}_2\text{Ti}_6\text{O}_{13}$ whiskers from the high-temperature solutions of NaCl-TiO₂ system. *J. Ceram. Soc. Japan* **115**, 230–232. doi:no (2007).
254. Zhen, L., Xu, C. Y., Wang, W. S., Lao, C. S. & Kuang, Q. Electrical and photocatalytic properties of $\text{Na}_2\text{Ti}_6\text{O}_{13}$ nanobelts prepared by molten salt synthesis. *Appl. Surf. Sci.* **255**, 4149–4152. ISSN: 01694332. doi:10.1016/j.apsusc.2008.11.003 (2009).
255. Li, H., Wang, K., Li, W., Cheng, S. & Jiang, K. Molten salt electrochemical synthesis of sodium titanates as high performance anode materials for sodium ion batteries. *J. Mater. Chem. A* **3**, 16495–16500. ISSN: 2050-7488. doi:10.1039/C5TA03250D (2015).
256. Chiba, Y., Koizumi, D., Saito, M. & Motohashi, T. Structural design of alkali-metal titanates: Electrochemical growth of $\text{KxTi}_8\text{O}_{16}$, $\text{Na}_{2+x}\text{Ti}_6\text{O}_{13}$, and $\text{Li}_{2+x}\text{Ti}_3\text{O}_7$ single crystals with one-dimensional tunnel structures. *CrystEngComm* **21**, 3223–3231. ISSN: 14668033. doi:10.1039/c9ce00362b (2019).
257. Rietveld, H. The crystal structure of some alkaline earth metal uranates of the type M_3UO_6 . *Acta Crystallogr.* **20**, 508–513. ISSN: 0365-110X (Apr. 1966).
258. Rietveld, H. Line profiles of neutron powder-diffraction peaks for structure refinement. *Acta Crystallogr.* **22**, 151–152. ISSN: 0365-110X (Jan. 1967).

-
259. Toby, B. H. & Von Dreele, R. B. *GSAS-II: The genesis of a modern open-source all purpose crystallography software package. J. Appl. Crystallogr.* **46**, 544–549. ISSN: 00218898. doi:10.1107/S0021889813003531 (2013).
260. Toby, B. H. & Dreele, R. B. V. *What's new in GSAS-II. Powder Diffr.* **29**, 1–6. ISSN: 0885-7156. doi:10.1017/S0885715614000736 (2014).
261. Mccusker, L. B., Dreele, R. B. V., Cox, D. E., Loue È R D, D. & Scardi, P. *Rietveld refinement guidelines. J. Appl. Cryst* **32**, 36–50. ISSN: 0021-8898. doi:10.1107/S0021889898009856 (1999).
262. Caglioti, G., Paoletti, A. & Ricci, F. P. *Choice of collimators for a crystal spectrometer for neutron diffraction. Nucl. Instruments* **3**, 223–228. ISSN: 0369643X. doi:10.1016/0369-643X(58)90029-X (1958).
263. Zhang, H. & Banfield, J. F. *New kinetic model for the nanocrystalline anatase-to-rutile transformation revealing rate dependence on number of particles. Am. Mineral.* **84**, 528–535. ISSN: 0003004X (1999).
264. Spurr, R. A. & Myers, H. *Quantitative Analysis of Anatase-Rutile Mixtures with an X-Ray Diffractometer. Anal. Chem.* **29**, 760–762. ISSN: 15206882. doi:10.1021/ac60125a006 (1957).
265. Penn, R. & Banfield, J. F. J. *Oriented attachment and growth, twinning, polytypism, and formation of metastable phases: Insights from nanocrystalline TiO₂. Am. Mineral.* **83**, 1077–1082. ISSN: 0003004X (1998).
266. Wang, G. & Li, G. *Titania from nanoclusters to nanowires and nanoforks. Eur. Phys. J. D* **24**, 355–360. ISSN: 14346060. doi:10.1140/epjd/e2003-00172-y (2003).
267. Sabyrov, K., Adamson, V. & Penn, R. L. *Two-step phase transformation of anatase to rutile in aqueous suspension. en. CrystEngComm* **16**, 1488. ISSN: 1466-8033. doi:10.1039/c3ce41820k (Jan. 2014).
268. Daneu, N., Rečnik, A., Schmid, H. & Mader, W. *Atomic structure and formation mechanism of (101) rutile twins from Diamantina (Brazil). Am. Mineral.* **99**, 612–624. ISSN: 0003-004X. doi:10.2138/am.2007.2634 (2014).
269. Jordan, V., Javornik, U., Plavec, J., Podgornik, A. & Rečnik, A. *Self-assembly of multilevel branched rutile-type TiO₂ structures via oriented lateral and twin attachment. Sci. Rep.* **6**, 1–13. ISSN: 20452322. doi:10.1038/srep24216 (2016).
270. Penn, R. L. & Banfield, J. *Imperfect Oriented Attachment: Dislocation Generation in Defect-Free Nanocrystals. Science* **281**, 969–971. ISSN: 1095-9203. doi:10.1126/science.281.5379.969 (1998).
271. Zhou, Y. & Fichtorn, K. a. *Microscopic view of nucleation in the anatase-to-rutile transformation. J. Phys. Chem. C* **116**, 8314–8321. ISSN: 19327447. doi:10.1021/jp301228x (2012).
272. Penn, R. L. & Soltis, J. A. *Characterizing crystal growth by oriented aggregation. CrystEngComm* **16**, 1409–1418. ISSN: 14668033. doi:10.1039/c3ce41773e (2014).
273. Ke, T.-Y., Peng, C.-W., Lee, C.-Y., Chiu, H.-T. & Sheu, H.-S. *{110}-exposed rutile titanium dioxide nanorods in photocatalytic performance. en. CrystEngComm* **11**, 1691. ISSN: 1466-8033. doi:10.1039/b902299f (Aug. 2009).
274. Wang, C., Shao, C., Liu, Y. & Li, X. *Water - Dichloromethane interface controlled synthesis of hierarchical rutile TiO₂ superstructures and their photocatalytic properties. Inorg. Chem.* **48**, 1105–1113. ISSN: 00201669. doi:10.1021/ic8018138 (2009).

275. Roy, B., Fuierer, P. a. & Aich, S. *Photovoltaic performance of dye sensitized solar cell based on rutile TiO₂ scaffold electrode prepared by a 2 step bi-layer process using molten salt matrices*. *Mater. Lett.* **65**, 2473–2475. ISSN: 0167577X. doi:10.1016/j.matlet.2011.05.050 (2011).
276. Sedlacik, M., Mrlik, M., Kozakova, Z., Pavlinek, V. & Kuritka, I. *Synthesis and electrorheology of rod-like titanium oxide particles prepared via microwave-assisted molten-salt method*. *Colloid Polym. Sci.* **291**, 1105–1111. ISSN: 0303402X. doi:10.1007/s00396-012-2834-4 (2013).
277. Zhao, Z., Tian, J., Sang, Y., Cabot, A. & Liu, H. *Structure, synthesis, and applications of TiO₂ nanobelts*. *Adv. Mater.* **27**, 2557–2582. ISSN: 15214095. doi:10.1002/adma.201405589 (2015).
278. Dozzi, M. V. & Selli, E. *Specific Facets-Dominated Anatase TiO₂: Fluorine-Mediated Synthesis and Photoactivity*. *Catalysts* **3**, 455–485. ISSN: 2073-4344. doi:10.3390/catal3020455 (2013).
279. Miao, J. & Liu, B. *Anatase TiO₂ microspheres with reactive {001} facets for improved photocatalytic activity*. *RSC Adv.* **3**, 1222–1226. ISSN: 2046-2069. doi:10.1039/C2RA22312K (2013).
280. Yang, S. *et al.* *Titania single crystals with a curved surface*. *Nat. Commun.* **5**, 5355. ISSN: 2041-1723. doi:10.1038/ncomms6355 (2014).
281. Zhang, B. *et al.* *Formation and evolution of the high-surface-energy facets of anatase TiO₂*. *J. Phys. Chem. C* **119**, 6094–6100. ISSN: 19327455. doi:10.1021/acs.jpcc.5b00087 (2015).
282. Bellardita, M., Garlisi, C., Venezia, A. M., Palmisano, G. & Palmisano, L. *Influence of fluorine on the synthesis of anatase TiO₂ for photocatalytic partial oxidation: Are exposed facets the main actors?* *Catal. Sci. Technol.* **8**, 1606–1620. ISSN: 20444761. doi:10.1039/c7cy02382k (2018).
283. He, Y. *et al.* *Anatase TiO₂ single crystals with dominant {0 0 1} facets: Synthesis, shape-control mechanism and photocatalytic activity*. *Appl. Surf. Sci.* **444**, 267–275. ISSN: 01694332. doi:10.1016/j.apsusc.2018.03.069 (2018).
284. Zhang, J. *et al.* *One-step synthesis of rutile nano-TiO₂ with exposed {1 1 1} facets for high photocatalytic activity*. *J. Alloys Compd.* **632**, 133–139. ISSN: 09258388. doi:10.1016/j.jallcom.2015.01.170 (2015).
285. Kang, H., Wang, L., Xue, D., Li, K. & Liu, C. *Synthesis of tetragonal flake-like magnesium titanate nanocrystallites*. *J. Alloys Compd.* **460**, 160–163. ISSN: 09258388. doi:10.1016/j.jallcom.2007.06.054 (2008).
286. Lou, H. & Wang, L. *A novel method to synthesize well-dispersed MgTiO₃ nanoplatelets*. *Mater. Lett.* **155**, 91–93. ISSN: 18734979. doi:10.1016/j.matlet.2015.04.106 (2015).
287. Bernard Trémillon. *DIAGRAMMES D'EQUILIBRE POTENTIEL-ACIDITE (E-pO²⁻) DANS LES SELS ET HYDROXYDES ALCALINS FONDUS*. *Pure Appl. Chem.* **25**, 395–428. doi:10.1351/pac197125020395 (1971).
288. Ranade, M. R. *et al.* *Energetics of nanocrystalline TiO₂*. *Proc. Natl. Acad. Sci. U. S. A.* **99**, 6476–6481. ISSN: 00278424. doi:10.1073/pnas.251534898 (2002).
289. Levchenko, A. A., Li, G., Boerio-Goates, J., Woodfield, B. F. & Navrotsky, A. *TiO₂ stability landscape: Polymorphism, surface energy, and bound water energetics*. *Chem. Mater.* **18**, 6324–6332. ISSN: 08974756. doi:10.1021/cm061183c (2006).
290. Pan, X. & Ma, X. *Phase transformations in nanocrystalline TiO₂ milled in different milling atmospheres*. *J. Solid State Chem.* **177**, 4098–4103. ISSN: 00224596. doi:10.1016/j.jssc.2004.08.017 (2004).

-
291. Nowotny, M. K., Sheppard, L. R., Bak, T. & Nowotny, J. *Defect engineering of titanium dioxide*. *J. Phys. Chem. C* **112**, 5275–5300. ISSN: 0004881X (2008).
292. Ali, B., Rumaiz, A. K., Ozbay, A., Nowak, E. R. & Ismat Shah, S. *Influence of oxygen partial pressure on structural, transport and magnetic properties of Co doped TiO₂ films*. *Solid State Commun.* **149**, 2210–2214. ISSN: 00381098. doi:10.1016/j.ssc.2009.09.011 (2009).
293. Pan, X., Yang, M.-Q., Fu, X., Zhang, N. & Xu, Y.-J. *Defective TiO₂ with oxygen vacancies: synthesis, properties and photocatalytic applications*. *Nanoscale* **5**, 3601–14. ISSN: 2040-3372. doi:10.1039/c3nr00476g (2013).
294. Volkovich, V. A., Griffiths, T. R., Fray, D. J. & Thied, R. C. *A new method for determining oxygen solubility in molten carbonates and carbonate-chloride mixtures using the oxidation of UO₂ to uranate reaction*. *J. Nucl. Mater.* **282**, 152–158. ISSN: 00223115. doi:10.1016/S0022-3115(00)00427-X (2000).
295. Littlewood, R. *Diagrammatic Representation of the Thermodynamics of Metal-Fused Chloride Systems*. *J. Electrochem. Soc.* **109**, 525. ISSN: 00134651. doi:10.1149/1.2425462 (1962).
296. Nishikata, A., Numata, H. & Tsuru, T. *Electrochemistry of molten salt corrosion*. *Mater. Sci. Eng. A* **146**, 15–31. ISSN: 09215093. doi:10.1016/0921-5093(91)90265-0 (1991).
297. Singh, N. B. *Preparation of metal oxides and chemistry of oxides ions in nitrate eutectic melt*. *Prog. Cryst. Growth Charact. Mater.* **44**, 183–188. ISSN: 09608974. doi:10.1016/S0960-8974(02)00016-5 (2002).
298. Wallot, J., Reynders, P. & Rödel, J. *Liquid-phase sintering of nanocrystalline titania doped with boron oxide: Bulk versus thin film*. *J. Am. Ceram. Soc.* **91**, 3856–3863. ISSN: 00027820. doi:10.1111/j.1551-2916.2008.02770.x (2008).
299. Jiang, Z. Y. *et al.* *Molten salt route toward the growth of ZnO nanowires in unusual growth directions*. *J. Phys. Chem. B* **109**, 23269–23273. ISSN: 15206106. doi:10.1021/jp054566r (2005).
300. Teshima, K. *et al.* *Environmentally friendly growth of layered K₄Nb₆O₁₇ crystals from a KCl flux*. *Eur. J. Inorg. Chem.*, 4687–4692. ISSN: 14341948. doi:10.1002/ejic.200700493 (2007).
301. Sudare, T., Kawaura, D., Yubuta, K., Hayashi, F. & Teshima, K. *Growth of {100}-faceted NaFeTiO₄ crystals with a tunable aspect ratio from a NaCl-Na₂SO₄ binary flux*. *CrystEngComm* **20**, 873–878. ISSN: 14668033. doi:10.1039/c7ce01876b (2018).
302. Rao, C. N., Turner, A. & Honig, J. M. *Some observations concerning the effect of impurities on the anatase-rutile transition*. *J. Phys. Chem. Solids* **11**, 173–175. ISSN: 00223697. doi:10.1016/0022-3697(59)90056-3 (1959).
303. Rasmussen, S. E., Jørgensen, J. E. & Lundtoft, B. *Structures and Phase Transitions of Na₂SO₄*. *J. Appl. Crystallogr.* **29**, 42–47. ISSN: 00218898. doi:10.1107/S0021889895008818 (1996).
304. Burrows, B. W. & Hills, G. J. *Electrochemical studies of molten alkali sulphates*. *Electrochim. Acta* **15**, 445–458. ISSN: 00134686. doi:10.1016/0013-4686(70)87004-9 (1970).
305. Ivanov, V. K., Fedorov, P. P., Baranchikov, A. Y. & Osiko, V. V. *Oriented attachment of particles: 100 years of investigations of non-classical crystal growth*. *Russ. Chem. Rev.* **83**, 1204–1222. ISSN: 0036-021X. doi:10.1070/RC2009v078n07ABEH004015 (2014).
306. Afanasiev, P. *Molten salt syntheses of alkali metal titanates*. *J. Mater. Sci.* **41**, 1187–1195. ISSN: 00222461. doi:10.1007/s10853-005-3656-2 (2006).

-
307. De Carolis, D. M. *et al.* Towards a Greener and Scalable Synthesis of $\text{Na}_2\text{Ti}_6\text{O}_{13}$ Nanorods and Their Application as Anodes in Batteries for Grid-Level Energy Storage. *Energy Technol.* **9**, 2000856. ISSN: 21944296. doi:10.1002/ente.202000856 (2021).
308. Liu, H. *et al.* A Raman spectroscopic and TEM study on the structural evolution of $\text{Na}_2\text{Ti}_3\text{O}_7$ during the transition to $\text{Na}_2\text{Ti}_6\text{O}_{13}$. *J. Raman Spectrosc.* **41**, 1331–1337. ISSN: 03770486. doi:10.1002/jrs.2561 (2010).
309. Bamberger, C. E. & Begun, G. M. Sodium Titanates: Stoichiometry and Raman Spectra. *J. Am. Ceram. Soc.* **70**, C–48–C–51. ISSN: 15512916. doi:10.1111/j.1151-2916.1987.tb04963.x (1987).
310. Su, Y., Balmer, M. L. & Bunker, B. C. Raman spectroscopic studies of silicotitanates. *J. Phys. Chem. B* **104**, 8160–8169. ISSN: 15206106. doi:10.1021/jp0018807 (2000).
311. <https://www.jems-swiss.ch/>.
312. Panepinto, A. *et al.* Synthesis of Anatase (Core)/Rutile (Shell) Nanostructured TiO_2 Thin Films by Magnetron Sputtering Methods for Dye-Sensitized Solar Cell Applications. *ACS Appl. Energy Mater.* **3**, 759–767. ISSN: 25740962. doi:10.1021/acsaem.9b01910 (2020).
313. Launay, M., Boucher, F. & Moreau, P. Evidence of a rutile-phase characteristic peak in low-energy loss spectra. *Phys. Rev. B - Condens. Matter Mater. Phys.* **69**, 035101. ISSN: 1550235X. doi:10.1103/PhysRevB.69.035101 (2004).
314. Cheynet, M., Pokrant, S., Irsen, S. & Krüger, P. New fine structures resolved at the ELNES Ti- $L_{2,3}$ edge spectra of anatase and rutile: Comparison between experiment and calculation. *Ultramicroscopy* **110**, 1046–1053. ISSN: 03043991. doi:10.1016/j.ultramicro.2010.03.001 (2010).
315. Höche, T. *et al.* Synthesis and characterization of mixed-valence barium titanates. *Philos. Mag.* **83**, 165–178. ISSN: 1478-6435. doi:10.1080/0141861021000028367 (Jan. 2003).
316. Gloter, A., Ewels, C., Umek, P., Arcon, D. & Colliex, C. Electronic structure of titania-based nanotubes investigated by EELS spectroscopy. *Phys. Rev. B - Condens. Matter Mater. Phys.* **80**, 035413. ISSN: 10980121. doi:10.1103/PhysRevB.80.035413 (2009).
317. Kanchanawarin, J. *et al.* Local structure of stoichiometric and oxygen-deficient $\text{A}_2\text{Ti}_6\text{O}_{13}$ ($A = \text{Li}, \text{Na}, \text{and K}$) studied by X-ray absorption spectroscopy and first-principles calculations. *J. Appl. Phys.* **124**, 155101. ISSN: 10897550. doi:10.1063/1.5052032 (2018).
318. Bard, A. J. & Faulkner, L. R. *Electrochemical Methods: Fundamentals and Applications* Second Edi, 864. ISBN: 978-0-471-04372-0 (JOHN WILEY & SONS, INC., 2001).
319. Díaz-Carrasco, P., Duarte-Cárdenas, A., Kuhn, A. & García-Alvarado, F. Understanding the high performance of nanosized rutile TiO_2 anode for lithium-ion batteries. *J. Power Sources* **515**, 230632. ISSN: 0378-7753. doi:https://doi.org/10.1016/j.jpowsour.2021.230632 (2021).
320. Kuhn, A., Amandi, R. & García-Alvarado, F. Electrochemical lithium insertion in TiO_2 with the ramsdellite structure. *J. Power Sources* **92**, 221–227. ISSN: 03787753. doi:10.1016/S0378-7753(00)00530-9 (2001).
321. Jiang, C., Honma, I., Kudo, T. & Zhou, H. Nanocrystalline rutile TiO_2 electrode for high-capacity and high-rate lithium storage. *Electrochem. Solid-State Lett.* **10**, 127–129. ISSN: 10990062. doi:10.1149/1.2712041 (2007).
322. Bach, S., Pereira-Ramos, J. P. & Willman, P. Investigation of lithium diffusion in nano-sized rutile TiO_2 by impedance spectroscopy. *Electrochim. Acta* **55**, 4952–4959. ISSN: 00134686. doi:10.1016/j.electacta.2010.03.101 (2010).

-
323. Chen, J. S. & Lou, X. W. *The superior lithium storage capabilities of ultra-fine rutile TiO₂ nanoparticles.* *J. Power Sources* **195**, 2905–2908. ISSN: 03787753. doi:10.1016/j.jpowsour.2009.11.040 (2010).
324. McNulty, D., Carroll, E. & O'Dwyer, C. *Rutile TiO₂ Inverse Opal Anodes for Li-Ion Batteries with Long Cycle Life, High-Rate Capability, and High Structural Stability.* *Adv. Energy Mater.* **7**. ISSN: 16146840. doi:10.1002/aenm.201602291 (2017).
325. Jung, H. G., Jang, M. W., Hassoun, J., Sun, Y. K. & Scrosati, B. *A high-rate long-life Li₄Ti₅O₁₂ / Li[Ni_{0.45}Co_{0.1}Mn_{1.45}]O₄ lithium-ion battery.* *Nat. Commun.* **2:516**. ISSN: 20411723. doi:10.1038/ncomms1527 (2011).
326. Jain, A. *et al.* *Commentary: The materials project: A materials genome approach to accelerating materials innovation.* *APL Mater.* **1**, 011002. ISSN: 2166532X. doi:10.1063/1.4812323 (2013).
327. Huang, S. Y., Kavan, L., Exnar, I. & Grätzel, M. *Rocking Chair Lithium Battery Based on Nanocrystalline TiO₂ (Anatase).* *J. Electrochem. Soc.* **142**, L142–L144. ISSN: 0013-4651. doi:10.1149/1.2048726 (1995).
328. Eftekhari, A. *Lithium-Ion Batteries with High Rate Capabilities.* *ACS Sustain. Chem. Eng.* **5**, 2799–2816. ISSN: 21680485. doi:10.1021/acssuschemeng.7b00046 (2017).
329. Roy, B. & Aich, S. *Synthesis of Mixed-Phase TiO₂ Powders in Salt Matrix and Their Photocatalytic Activity.* *Mater. Manuf. Process.* **31**, 1628–1633. ISSN: 15322475. doi:10.1080/10426914.2015.1117627 (2016).
330. Zhang, Y.-h. & Reller, A. *Phase transformation and grain growth of doped nanosized titania.* *Mater. Sci. Eng. C* **19**, 323–326 (2002).

Acknowledgments

I would like to begin by expressing my gratitude for the joint venture between the “Surface Solution” department of the company Merck KGaA and the Dispersive Solids group (Material Science Department, TU Darmstadt). Without it, this PhD project would not have been possible. To my supervisor and *Doktorvater* Prof. Ralf Riedel I can extend nothing less than my deepest appreciation. Thank you for teaching me the critical evaluation of scientific work, for believing in my abilities and for guiding me, an aspect of tremendous importance in the final stages of this work. Thank you for your support in times of need!

I thank Dr. Carsten Plüg and Dr. Carsten Handrosch (Merck KGaA) for giving me the opportunity to participate in this project and for the financial support of the organization. I am especially thankful to Dr. Handrosch, my co-supervisor, for introducing me to the world of pigments and for the many scientific discussions.

I would like to thank Prof. Wolfgang Donner for accepting to be the co-referee of my PhD thesis, for the fruitful scientific discussions and for giving me access to his laboratories. I also thank Prof. Anke Weidenkaff and Prof. Christina Roth for consenting to be my examiners.

Words cannot express my thankfulness to apl. Prof. Norbert Nicoloso for the inspiring and open discussions, and his enormous generosity with his time when I encountered problems. I owe him a lot and it was a pleasure to learn from him.

Special thanks go to Dr. Magdalena Grackzyk-Zajac and Dr. Dragoljub Vrankovic for the extensive support during my introduction to battery research. Your passion for science had a powerful influence on me and I am proud to consider you friends. Thank you Magda for being there whenever I needed it!

I would like to express my appreciation to the following collaborators and colleagues for their technical assistance and constructive advice during this project: Prof. Leopoldo Molina-Luna, Dr. Michael Dürschnabel and Dr. Enrico Bruder.

The year I spent in the laboratories of the surface solution department at Merck allowed me to meet many wonderful people: Nicole Haferkorn, Lydia Zelonka, Anja Kilian, Jörn Beck, Christoph Münch, Tanja Delp, Joachim Duschek, Jürgen Hartmann, Andrea Heyland and Oliver Eichner. A special mention goes to Lukas Hamm, Johann Bauer and Sebastian Lehmann. I would like to thank you for the scientific and moral support. It was greatly appreciated at the time and is fondly remembered.

Further thanks are due to: Jean-Christophe Jaud for his assistance in carrying out measurements, for answering any scientific concerns related to crystallography and for the diverting conversations; Claudia Fasel for her ability to solve any technical problem and for productive scientific discussions, thank you also for being my hiking buddy in Kleinwalsertal and for the many funny moments we shared; thanks to Ulrike Kunz for the microscopy investigations. For their indispensable mechanical and electrical know-how, I have to mention: Michael Weber, Daniel Isaia, Andreas Hönl and Stephan Diefenbach.

Being a member of the Dispersive Solids group gave me the opportunity to meet many great colleagues from whom I learned a lot, among them PD Dr. Leonore Wiehl (sharing with me her knowledge on Rietveld refinement and GSAS II), Dr. Isabel Gonzalo de Juan, PD Dr. Emanuel Ionescu and Dr. Gabriela Mera. Thank you for your teachings and for sharing your experience. Many colleagues were also really important to me during my time in the group. Their support was invaluable and I am privileged to count them as friends: thanks to Dr. Benjamin Juretzka and Alexander Kempf for being great office mates (and running partner); thanks to Dr. Ying Zhan, Dr. Fangtong Xie, Dr. Felix Rosenburg, Dr. Christina Stabler and Dr. Mathias Storch for your encouragements and trust; thanks to Marco Melzi d'Eril and Dr. Emmanuel Ricohermoso III for your invaluable graphic design skills and to Jan Bernauer as the only one who shared my passion for football. I also want to thank Dr. Yao Feng, Dr. Qingbo Wen, Dr. Xingmin Liu, Nan Chai, Dr. Cong Zhou, Yongchao Chen, Wei Li, Honghong Tian, Fangmu Qu, Sefa Akca, Siri Gani, Samuel Kredel, Dharma Teppala Teja and Alexander Ott. Thanks for being there and for the pleasant moments we shared.

Over the course of my doctorate, I have had the pleasure of supervising and working with several students: Samira Kiefer, Ashaduzzaman Khan, Laura Feldmann, Adnan Ibrahim, Robert Phillips, Eunjong Ko, Chao Li, Wonkyoung Oh and Rishabh Kumar. Each of them has been a great enrichment for me. At this juncture, I would especially like to thank Samira, Laura, Robert and Adnan for the strong support and some contributions to this work. It was a pleasure to be part of your development.

A brief message to my friends in Rome, Darmstadt and the many spread all over the world. Thank you. I also want to thank the CrossFit Kampfgeist team, who helped a lot during this last year.

To my family, parents, grandparents and my brother: thank you for your unyielding support through each step of my life. I am the man I am because of it and I could not have undertaken this journey without you.

Finally, Francesca and Daphne, the patience you showed while waiting for the submission of this thesis was admirable. You gave me the strength to conclude this work and love and support all at every turn. I love you two (soon to be three) with all my heart. I cannot wait to see our family growing.

A. List of chemicals

Table A.1.: List of the chemicals used for the synthesis of TiO₂ and sodium titanates powders.

Chemical	Company	Art. Num	Purity degree	CAS-number
TiO ₂ (anatase)	Kronos	K1002	≥ 99 %	13463-67-7
TiOSO ₄	Sigma Aldrich	14023-1KG	technical	13825-74-6
TiCl ₄	Merck	208566	24.8 wt. % TiO ₂	7550-45-0
Na ₂ SO ₄ anhydrous	Sigma Aldrich	106645-1KG	EMPROVE®	7757-82-6
NaOH 32 %	Sigma Aldrich	1.05587.2500	EMPLURA®	1310-73-2
Na ₃ PO ₄	Sigma Aldrich	342483-2.5KG	ACS reagent, ≥ 98 %	7601-54-9
KCl	Sigma Aldrich	P9541-500G	≥ 99 %	7447-40-7
NaCl	Roth	3957.1	≥ 99.5 %, p.a., ACS	7647-14-5
LiCl	Roth	6698.3	≥ 99 %, p.a., ACS	7447-41-8
NaF	Roth	P756.1	≥ 99 %, p.a., ACS	7681-49-4
B ₂ O ₃	Alfa Aesar	89964.22	98.99 %	1303-86-2
MgCl ₂	Sigma Aldrich	M9272-1KG	ACS reagent, 99.0-102.0 %	7791-18-6
AlCl ₃	Sigma Aldrich	101084	EMPROVE®	7784-13-6
Collodion solution	Sigma Aldrich	102644	4 %	9004-70-0
Isoamyl acetate	Sigma Aldrich	W205508-1KG-K	≥ 95 %	123-92-2

B. Phase Diagrams

All the phase diagrams listed in this section are taken from the website https://www.crct.polymtl.ca/fact/documentation/FS_All_PDs.htm.¹

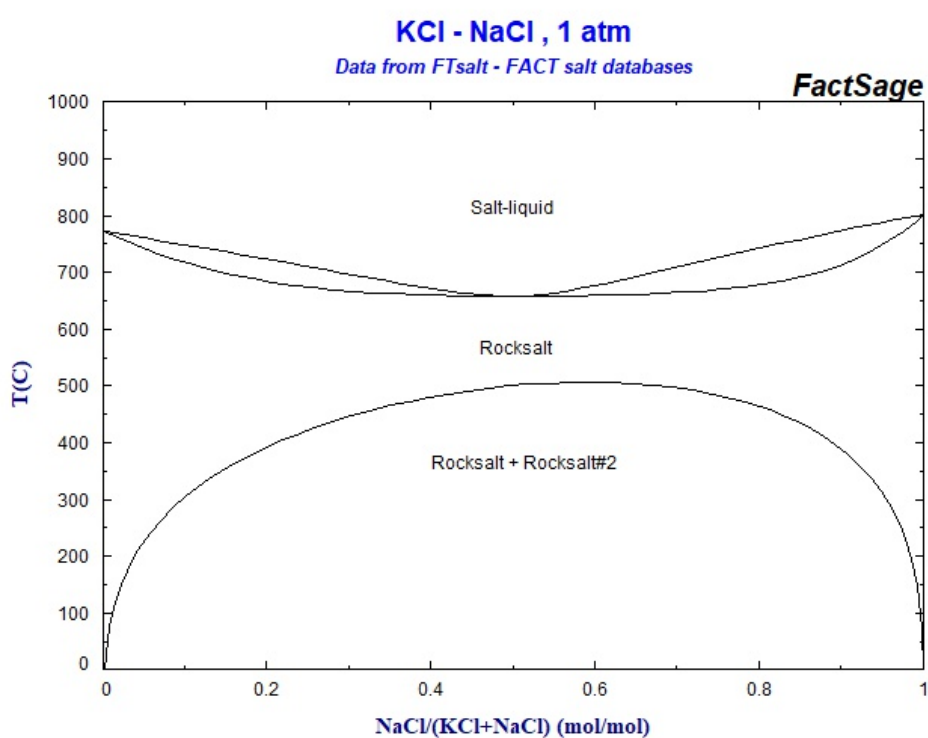


Figure B.1.: Phase diagram of the KCl-NaCl binary mixture.

¹Last time browsed on March 13, 2023

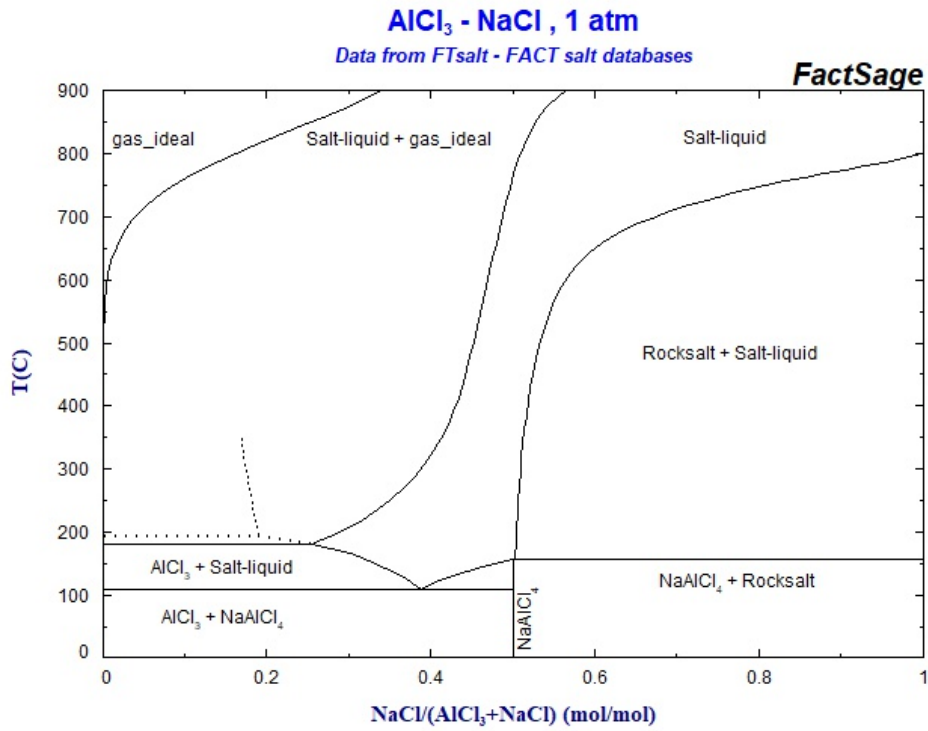


Figure B.2.: Phase diagram of the AlCl₃-NaCl binary mixture.

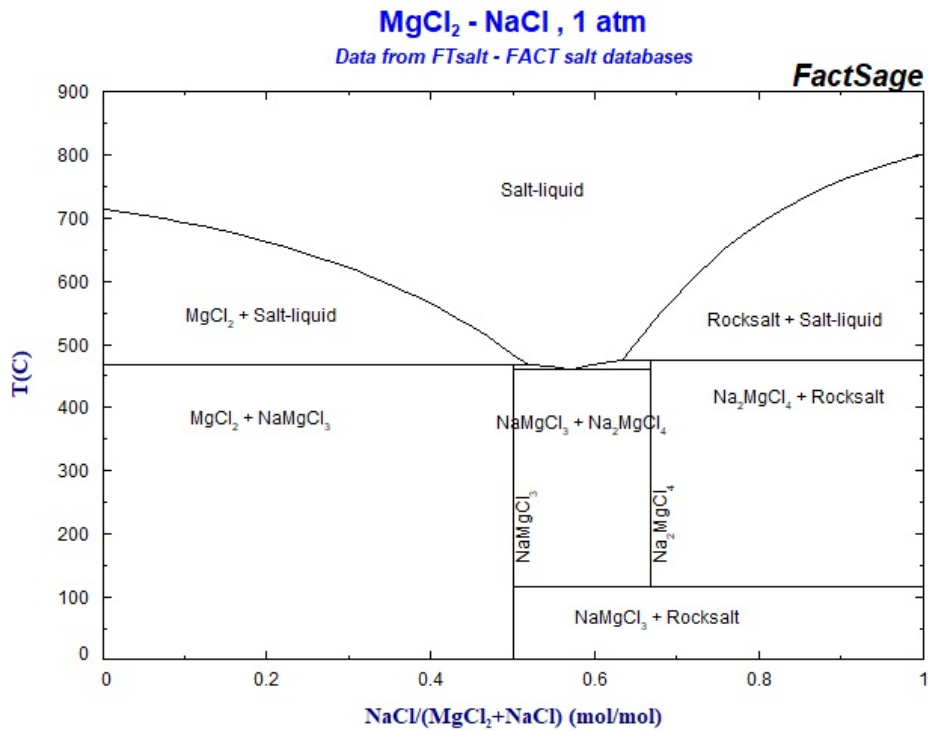


Figure B.3.: Phase diagram of the MgCl₂-NaCl binary mixture.

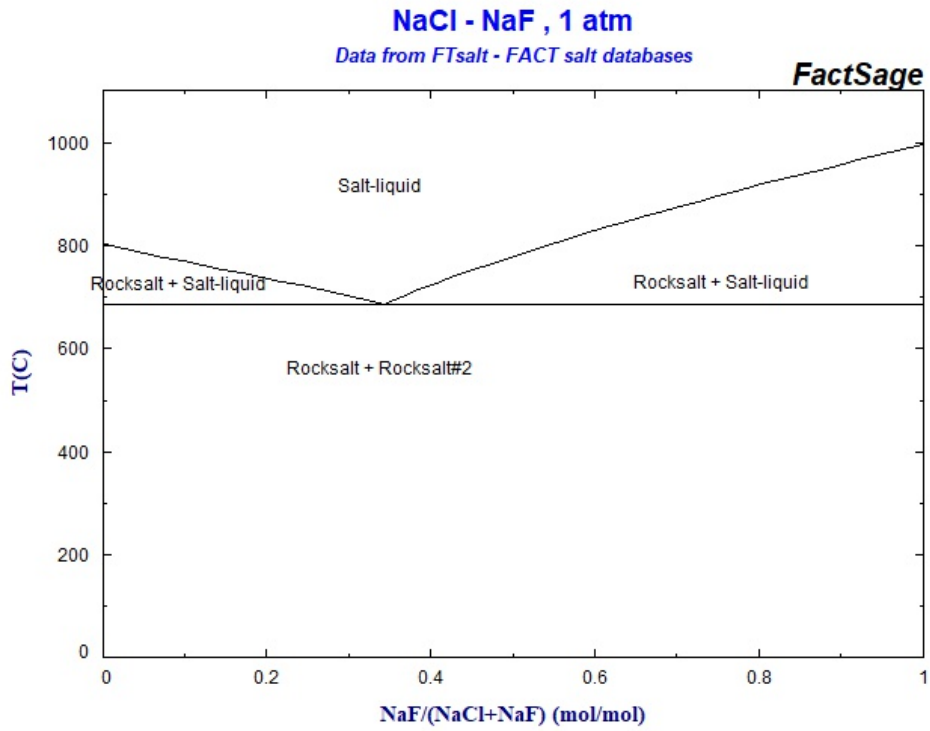


Figure B.4.: Phase diagram of the NaCl-NaF binary mixture.

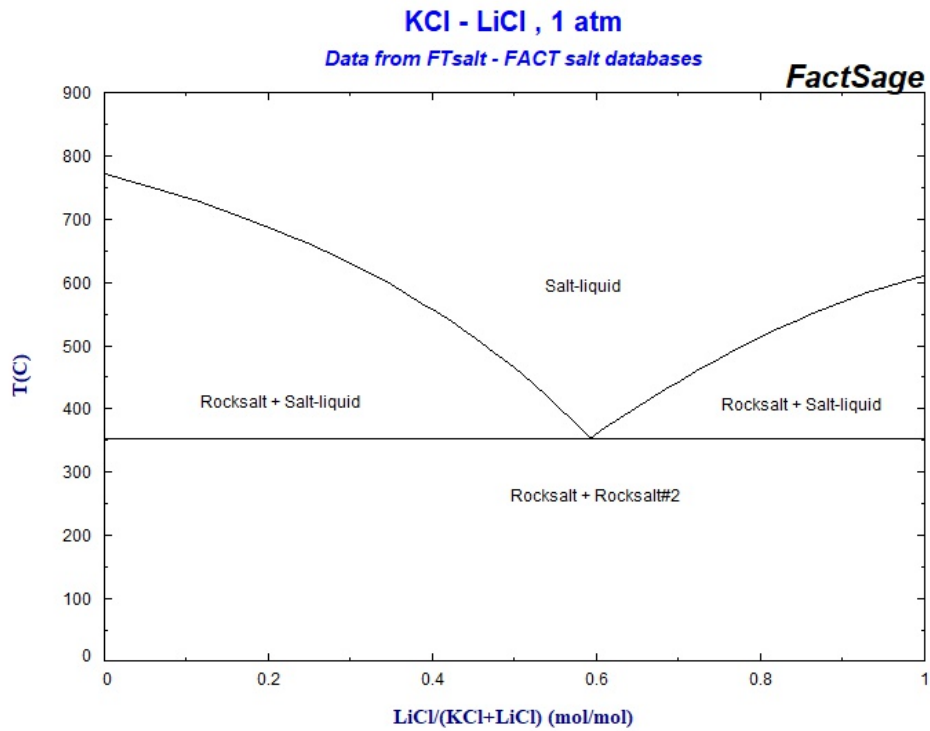


Figure B.5.: Phase diagram of the KCl-LiCl binary mixture.

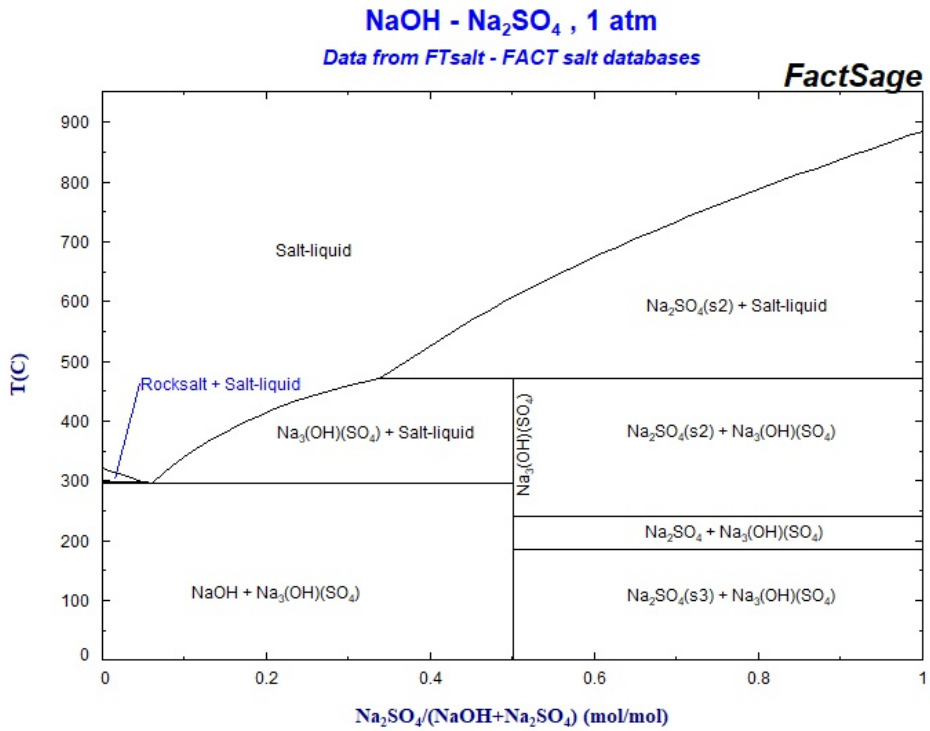


Figure B.6.: Phase diagram of the NaOH-Na₂SO₄ binary mixture.

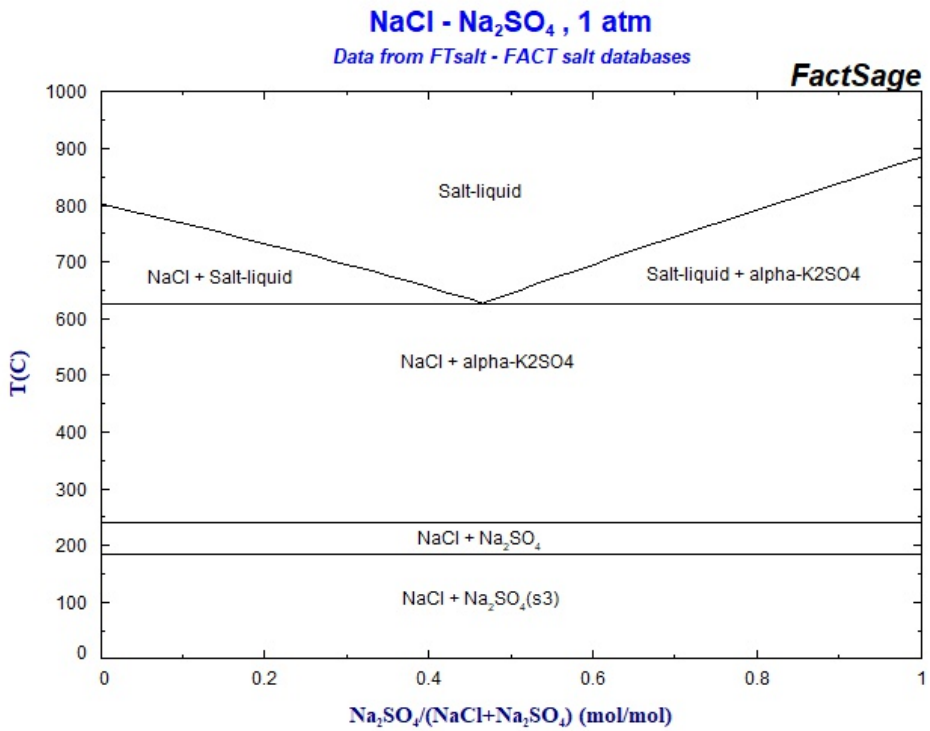


Figure B.7.: Phase diagram of the NaCl-Na₂SO₄ binary mixture.

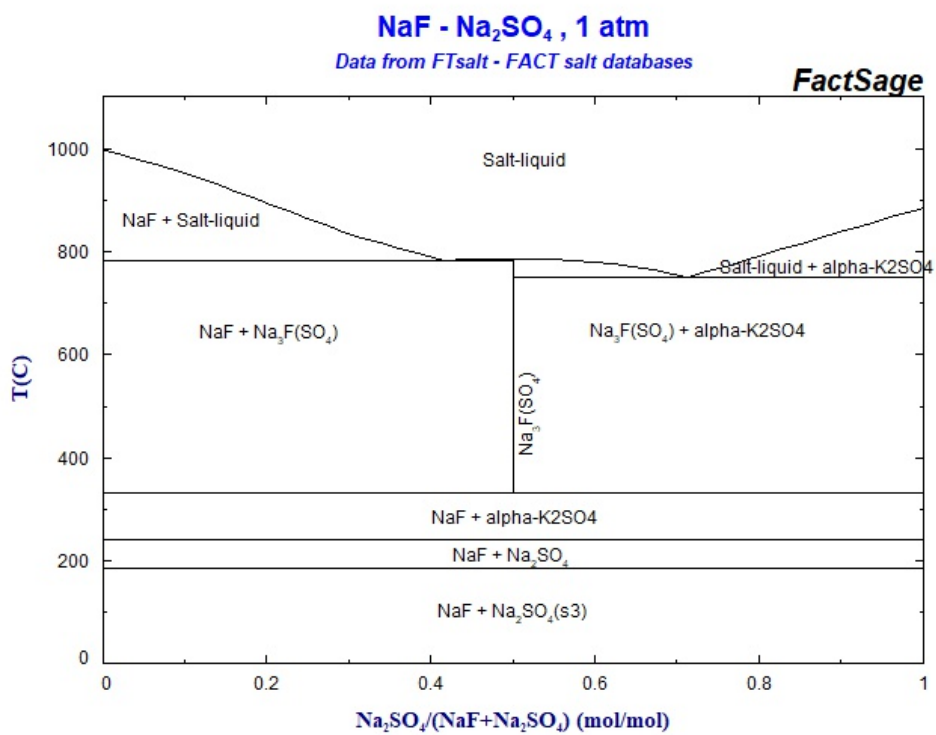


Figure B.8.: Phase diagram of the NaF-Na₂SO₄ binary mixture.

C. Additional XRD Data

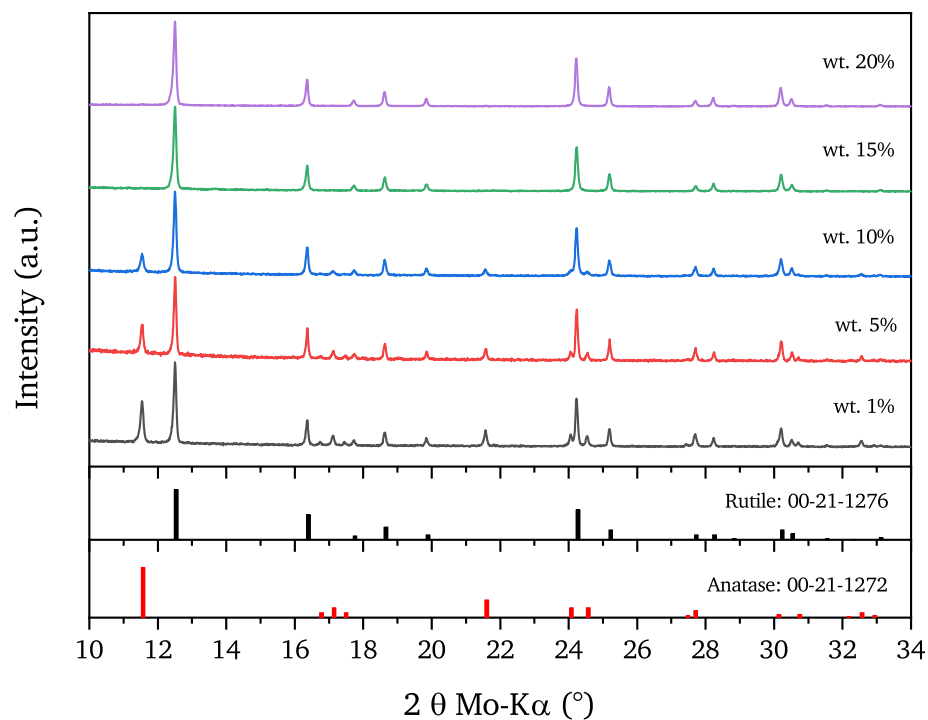


Figure C.1.: XRD patterns of a series of tests of titania samples obtained by MSS at 900 °C by mixing always 1 g of anatase precursor with 5 different NaCl masses (99 g, 19 g, 9 g, 5.67 g and 4 g).

Weight fraction determined by Spurr's equation

Roy *et al.* [36, 329] and other researchers [186] calculated the weight fractions based on Spurr's equation [264], where W_R is the rutile fraction and $I_A(101)$ and $I_R(110)$ are the integrated intensities of the anatase (101) and the rutile (110) reflections, respectively (see equation C.1).

$$W_R = \frac{1}{1 + 1.26 \left(\frac{I_A(101)}{I_R(110)} \right)} \quad (\text{C.1})$$

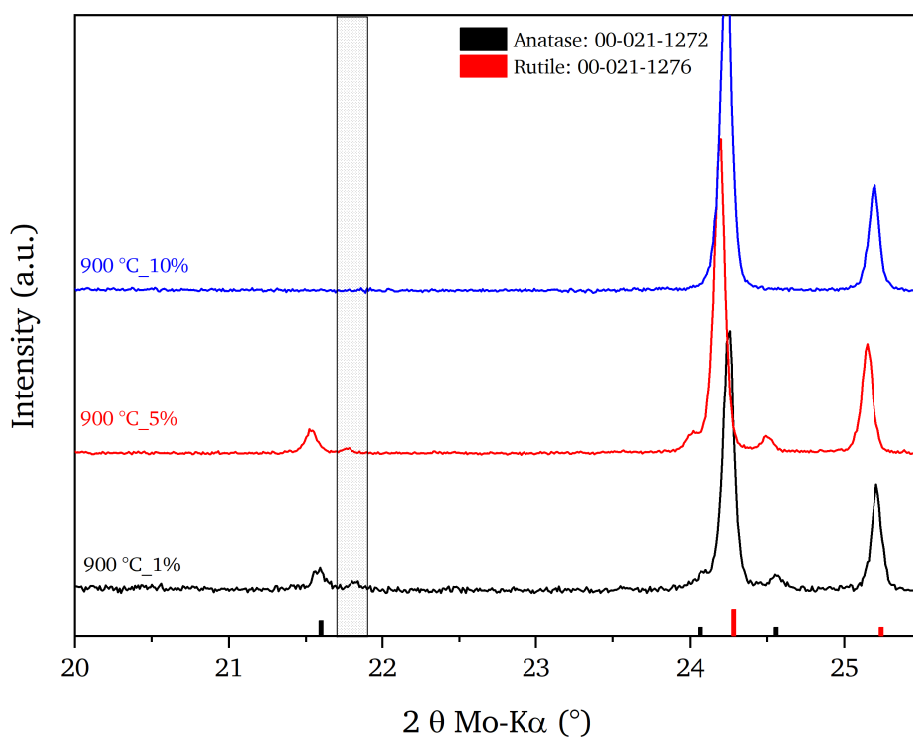


Figure C.2.: Magnification of XRD patterns reported in figure 5.2 on page 55. The marked area highlights the presence of a reflection belonging to NTO phase at 21.79° .

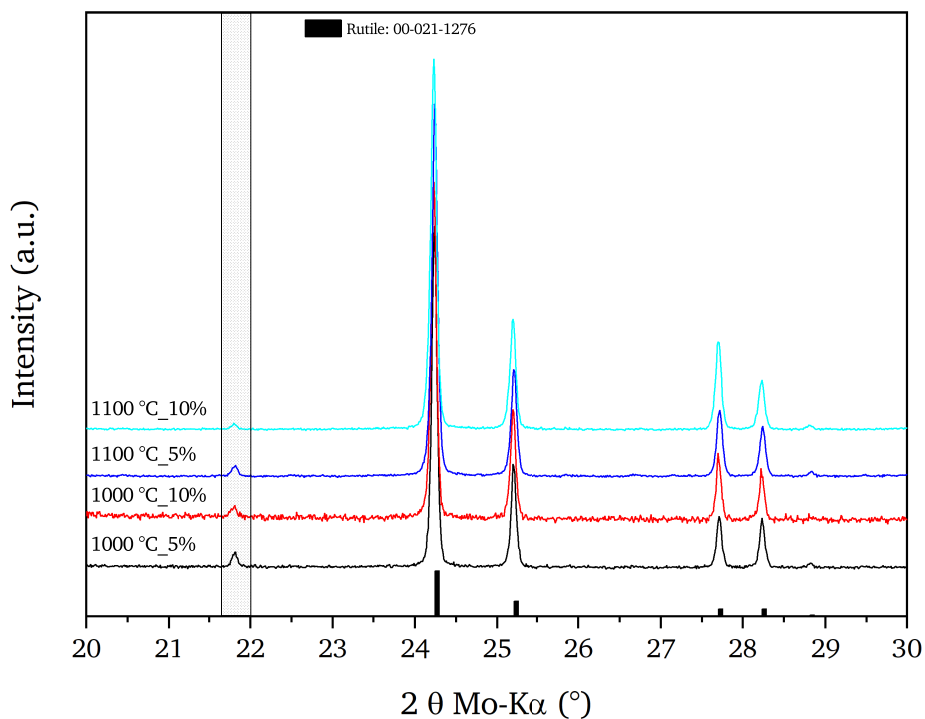


Figure C.3.: Magnification of four XRD patterns reported in figure 5.3 on page 56. The reflection belonging to NTO phase at 21.79° is highlighted.

This is an empirically determined formula, in which many factors can affect the reflection's intensities and thus the accuracy of the result (e.g. lattice distortion, preferred orientation or morphology, encapsulation, degree of crystallinity). Especially the different grain size between the two coexisting phases might alter the result of the Spurr equation, considering that the transition to rutile is correlated to a significant grain growth [330]. Table C.1 reports the phase compositions calculated by Spurr' equation of the same samples reported in table 5.1 on page 57 determined by Rietveld refinement in order to have a comparison with the phase compositions. It is important to mention that this method can not be applied to samples containing NTO.

Table C.1.: Phase composition of samples after heat-treating different amounts of TiO₂ in 25 g of NaCl in the range 820 °C to 1100 °C (A = Anatase, R = Rutile, NTO = Na₂Ti₆O₁₃) and 2 hours of holding time calculated by Spurr's equation.

wt. % TiO ₂	820 °C	850 °C	900 °C	1000 °C	1100 °C
1	n/a	n/a	18.27 % A, 81.73 % R	n/a	n/a
5	n/a	85.74 % A, 14.26 % R	15.06 % A, 84.94 % R	R, NTO	n/a
10	87.32 % A, 12.68 % R	77.48 % A, 22.52 % R	100 % R	R, NTO	R, NTO
15	n/a	n/a	100 % R	n/a	n/a
20	n/a	n/a	100 % R	100 % R	R, NTO
50	n/a	n/a	100 % R	n/a	n/a

Table C.2.: Phase composition of samples obtained by heat-treating 1 g of TiO₂ mixed in different NaCl amounts at 900 °C (A = Anatase, R = Rutile) and 2 hours of holding time calculated by Spurr's equation.

wt. % TiO ₂	NaCl mass [g]	900 °C
1	99	43.40 % A, 56.60 % R
5	19	37.59 % A, 62.41 % R
10	9	25.88 % A, 74.12 % R
15	5.67	100 % R
20	4	100 % R

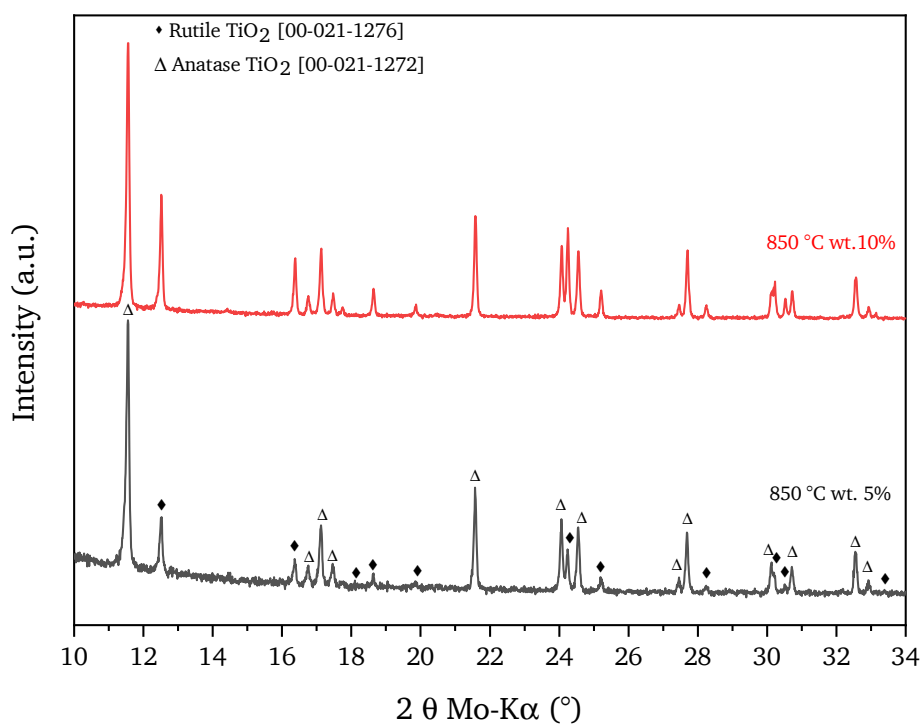


Figure C.4.: XRD patterns of titania samples obtained by MSS in NaCl with 5 and 10 wt. % of titania at 850 °C.

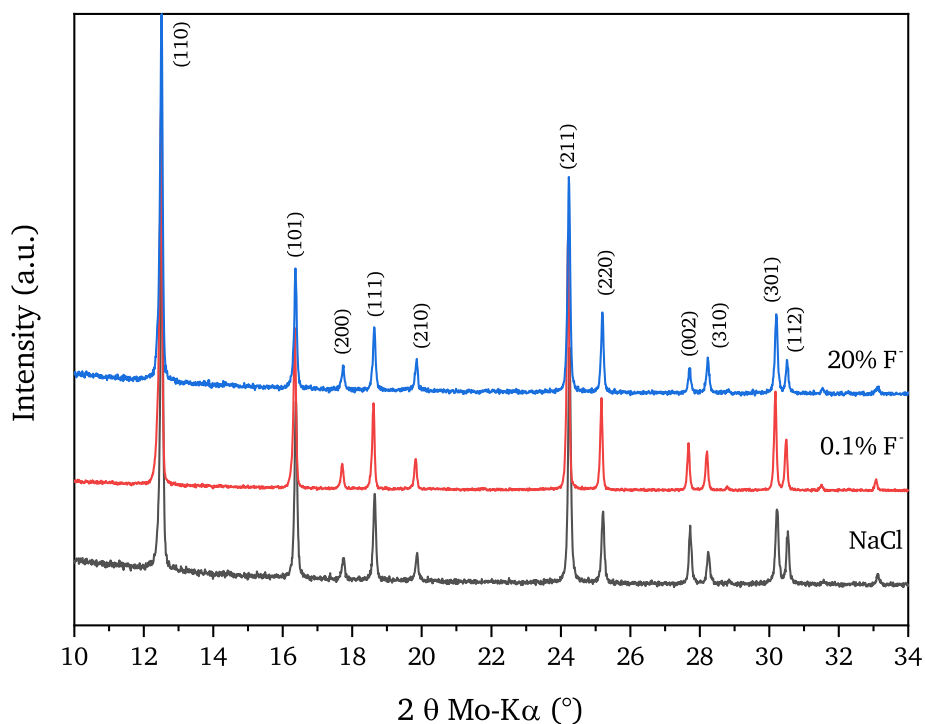


Figure C.5.: XRD patterns of titania samples obtained by MSS at 900 °C in NaCl with \approx 20 wt. % of anatase precursor first without the addition of NaF and with different mol % of NaF (0.1% and 20%).

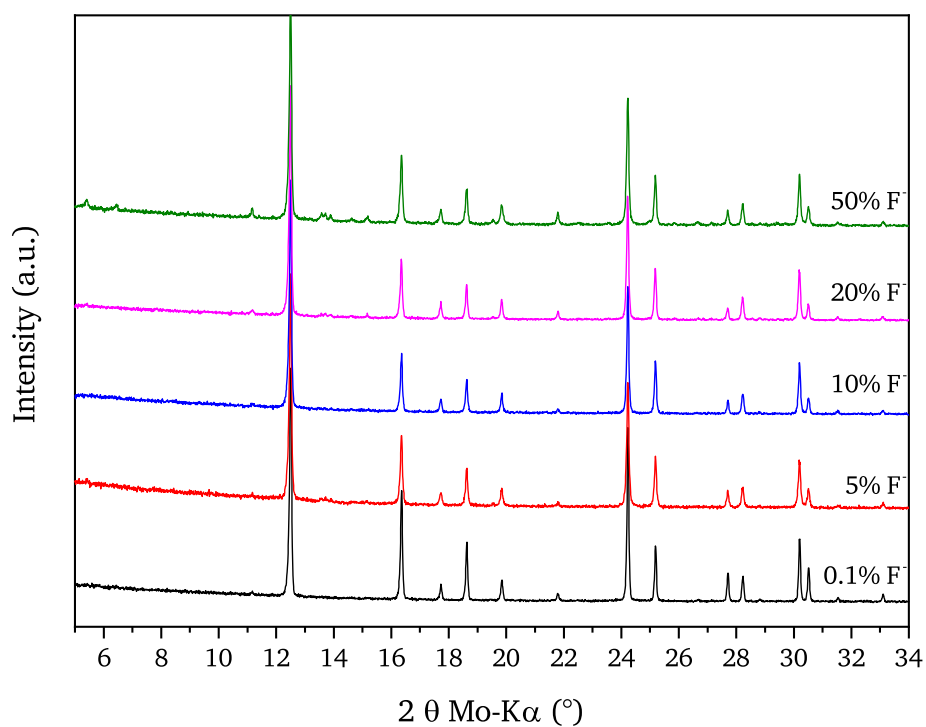


Figure C.6.: XRD patterns of titania samples obtained by MSS at 1000 °C in NaCl with \simeq 20 wt. % of anatase precursor and the addition of different mol % of NaF (0.1% to 50%).

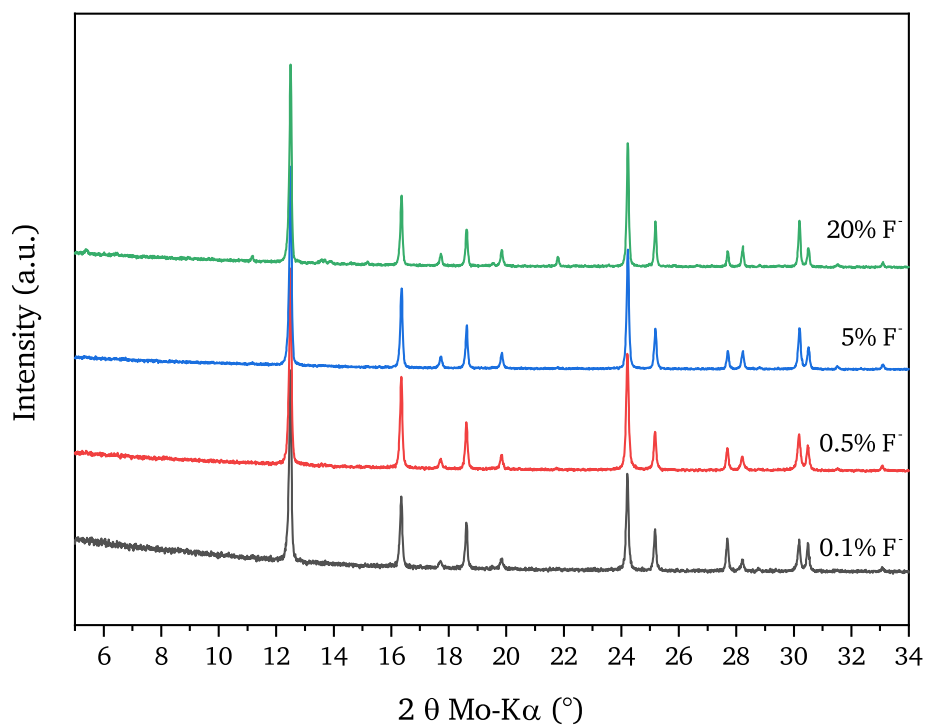


Figure C.7.: XRD patterns of titania samples obtained by MSS at 1100 °C in NaCl with \simeq 20 wt. % of anatase precursor and the addition of different mol % of NaF (0.1% to 20%).

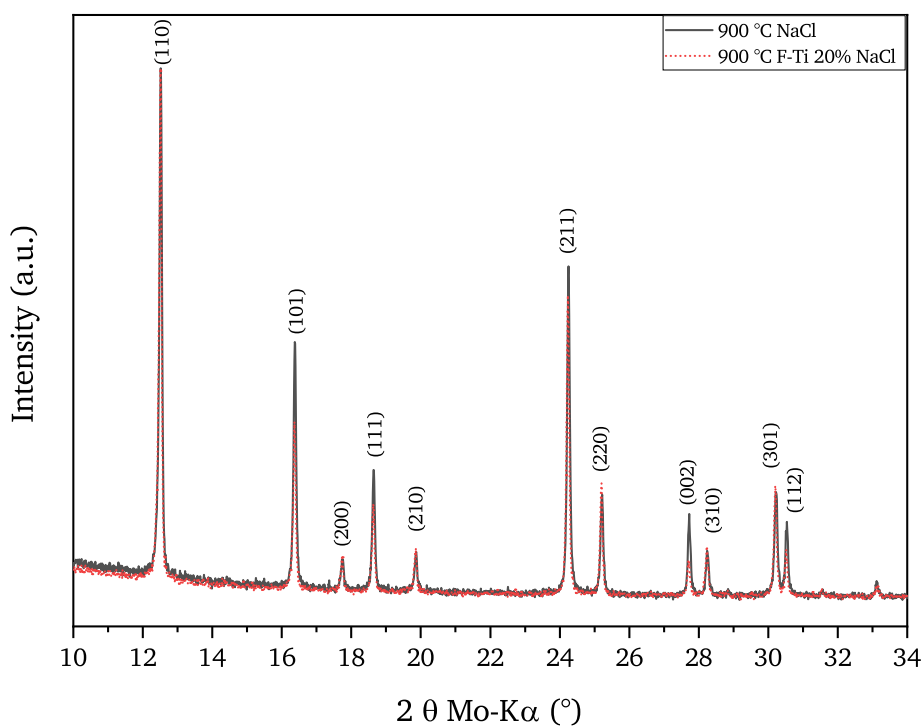


Figure C.8.: XRD patterns of titania samples obtained by MSS at 900 °C with \approx 20 wt. % of anatase precursor in pure NaCl and with the addition of 20 mol % of NaF.

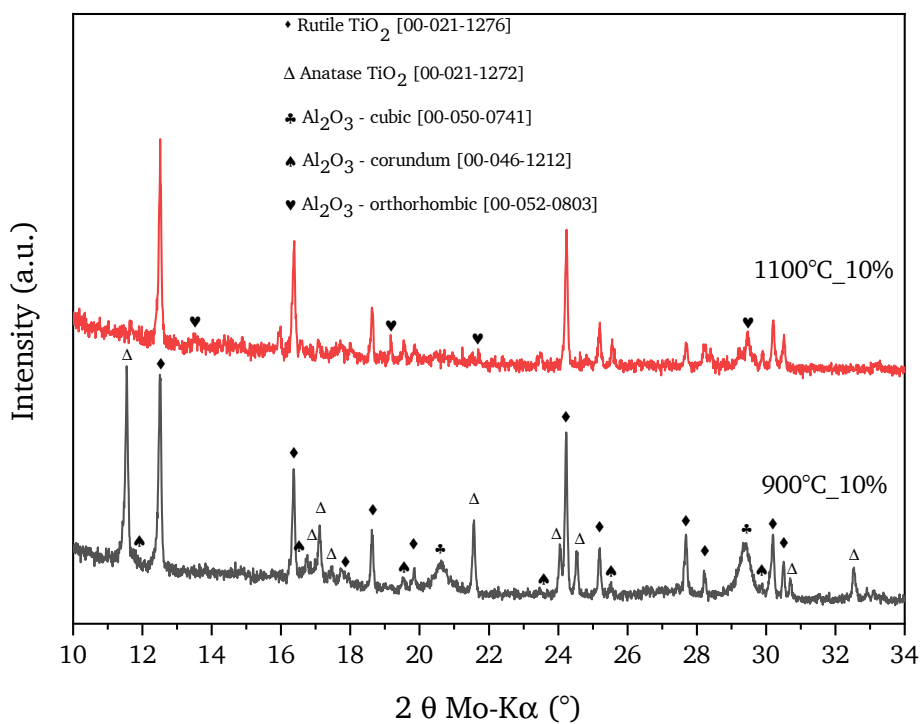


Figure C.9.: XRD patterns of titania samples obtained by MSS in 0.6 NaCl - 0.4 AlCl₃ mixture with 2 hours holding time and 10 wt. % of titania.

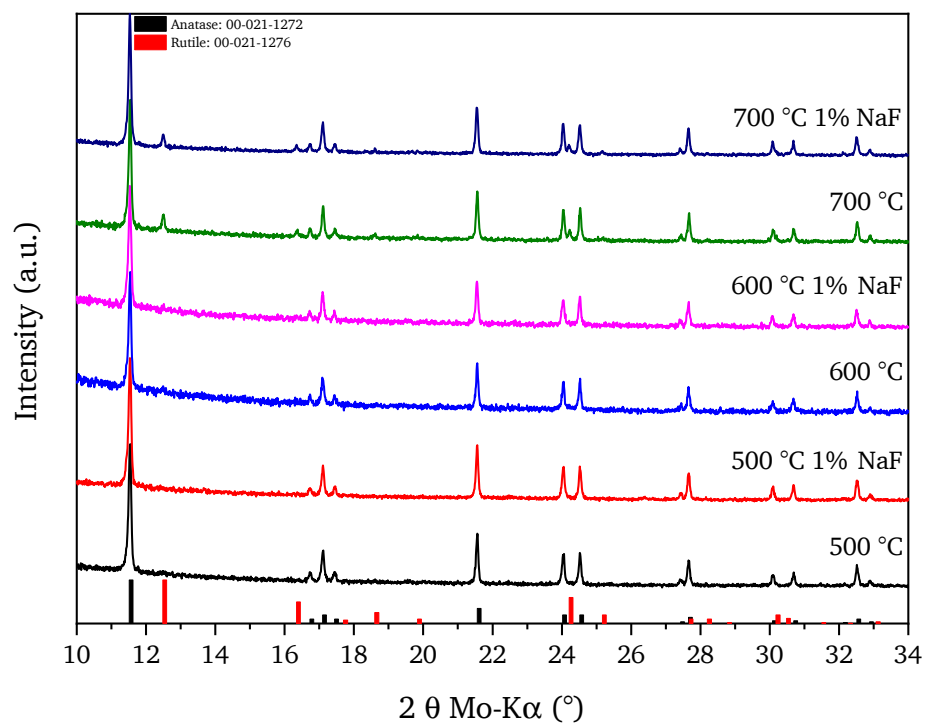


Figure C.10.: XRD patterns of titania samples obtained by MSS between up to 700 °C in 0.41 KCl-0.59 LiCl with 10 wt. % of anatase precursor and with and without the addition of 1 mol % NaF.

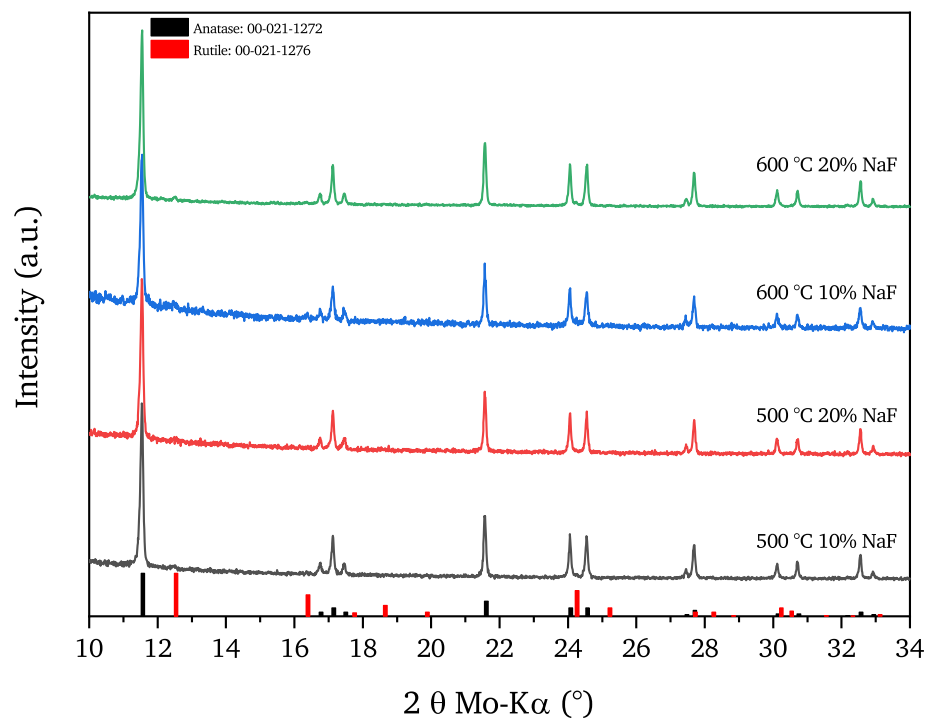


Figure C.11.: XRD patterns of titania samples obtained by MSS at 500 and 600 °C in 0.41 KCl-0.59 LiCl with 10 wt. % of anatase precursor and the addition of 10 and 20 mol % NaF.

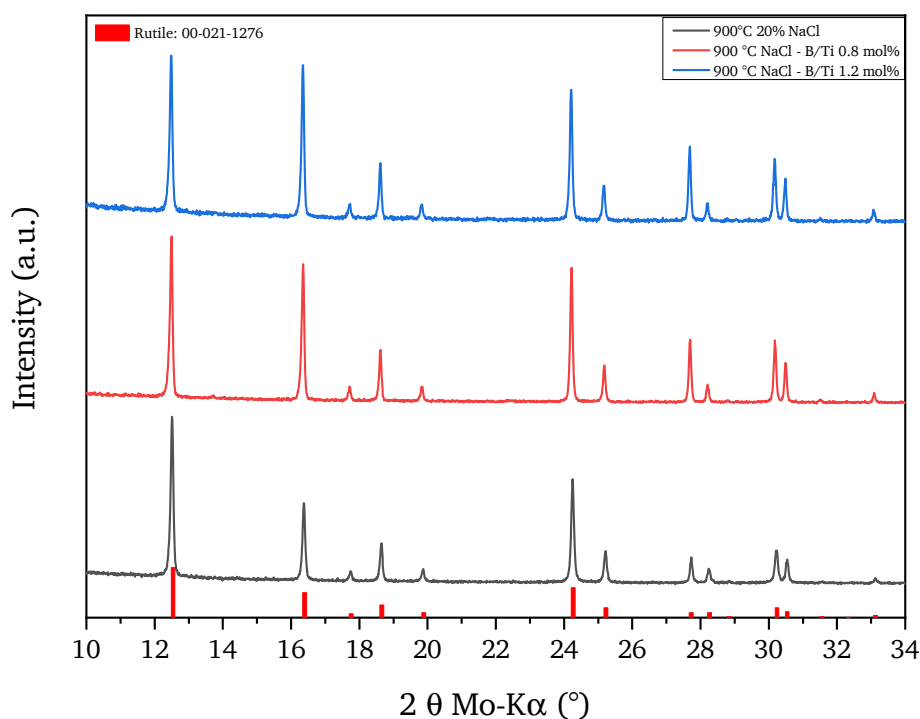


Figure C.12.: XRD patterns of titania samples obtained by MSS at 900 °C in NaCl, 20 wt. % anatase precursor and the addition of 0.8 mol % and 1.2 mol % B₂O₃.

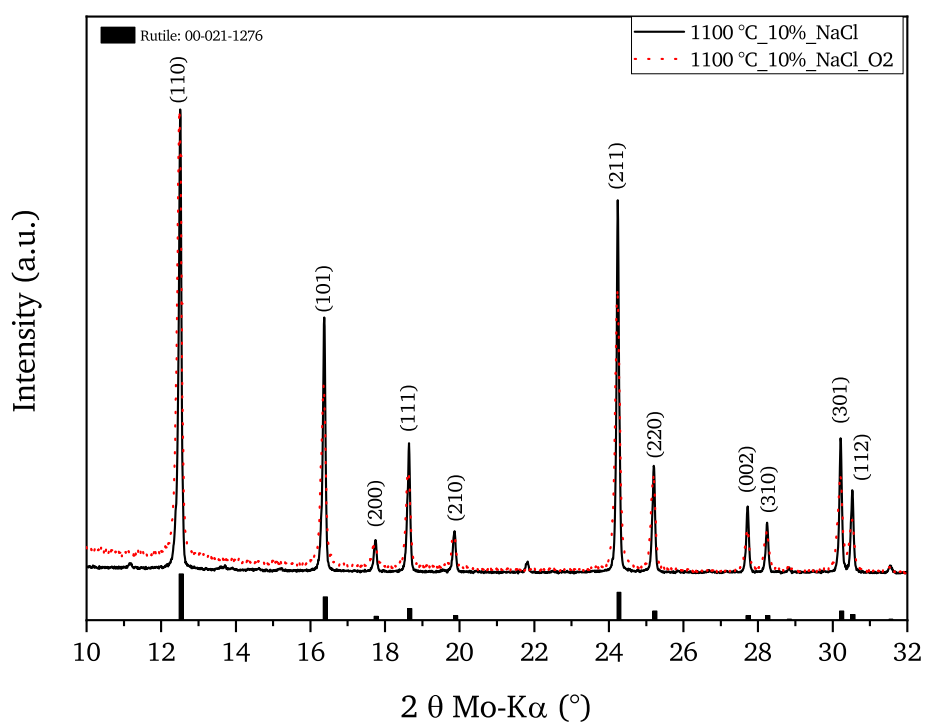


Figure C.13.: Overlapped view of the diffractograms reported in figure 5.25, heat-treatment under ambient atmosphere and under O₂ flow at 1100 °C with 10 wt. % anatase precursor in NaCl. A reference pattern from the ICDD is reported for comparison.

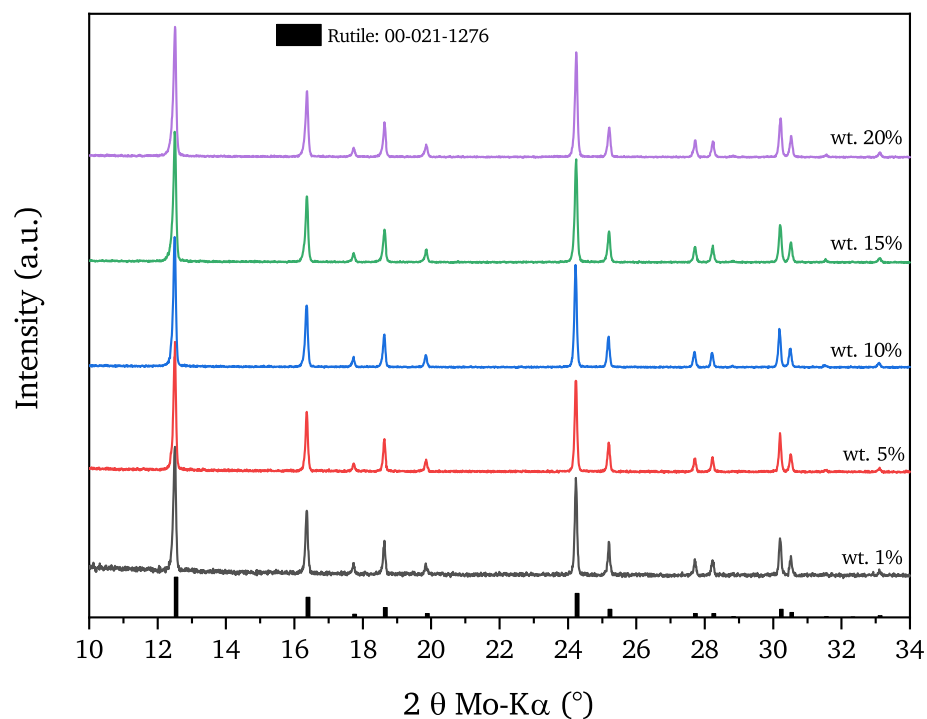


Figure C.14.: Samples heat-treated at 1100 °C with different wt. % anatase precursor in Na_2SO_4 . A reference pattern from the ICDD is reported for comparison.

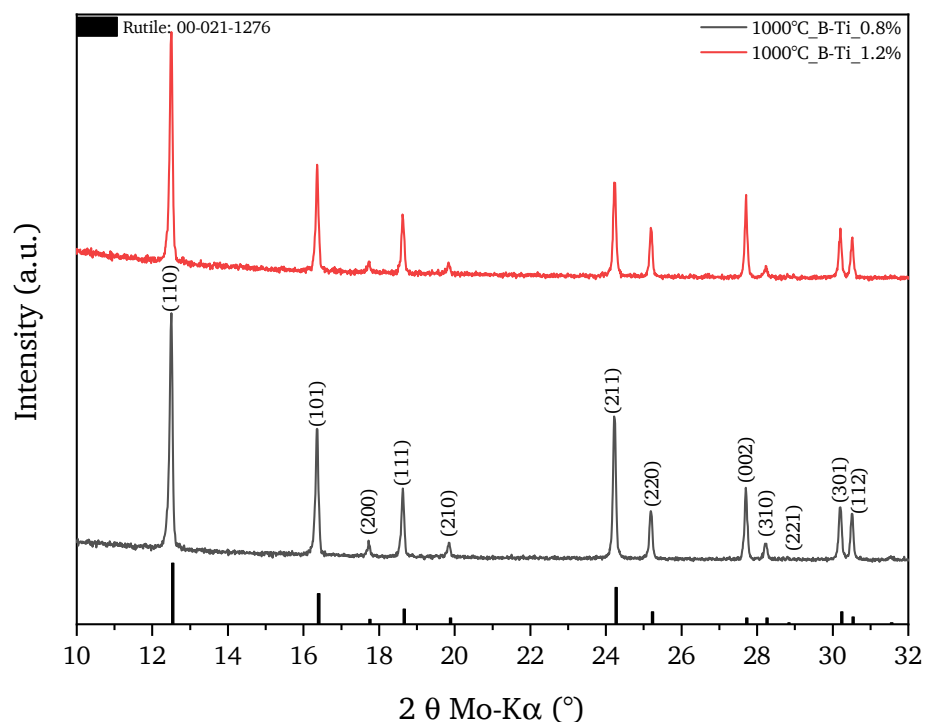


Figure C.15.: Samples heat-treated at 1000 °C with 10 wt. % anatase precursor in Na_2SO_4 with the addition of 0.8 and 1.2 mol % of B_2O_3 . Reference patterns from the ICDD are reported for comparison.

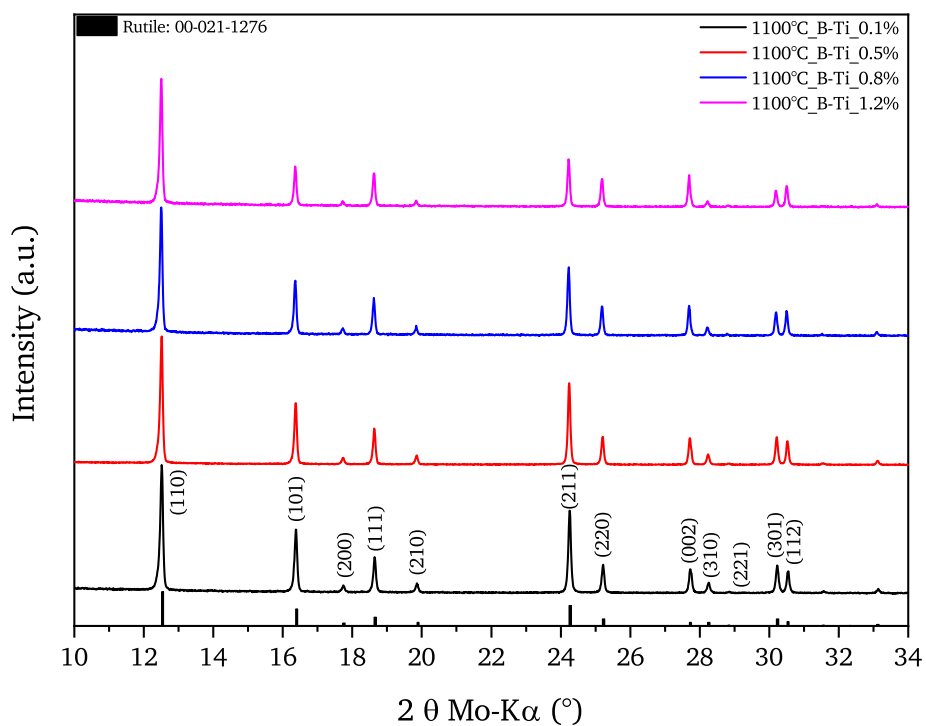
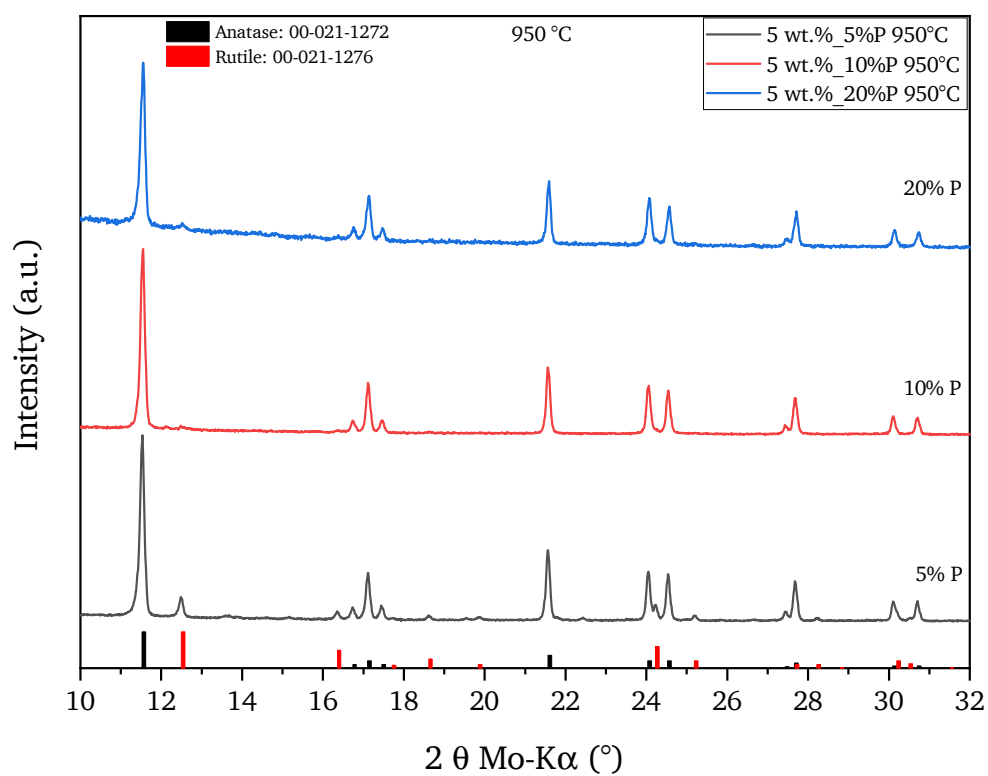
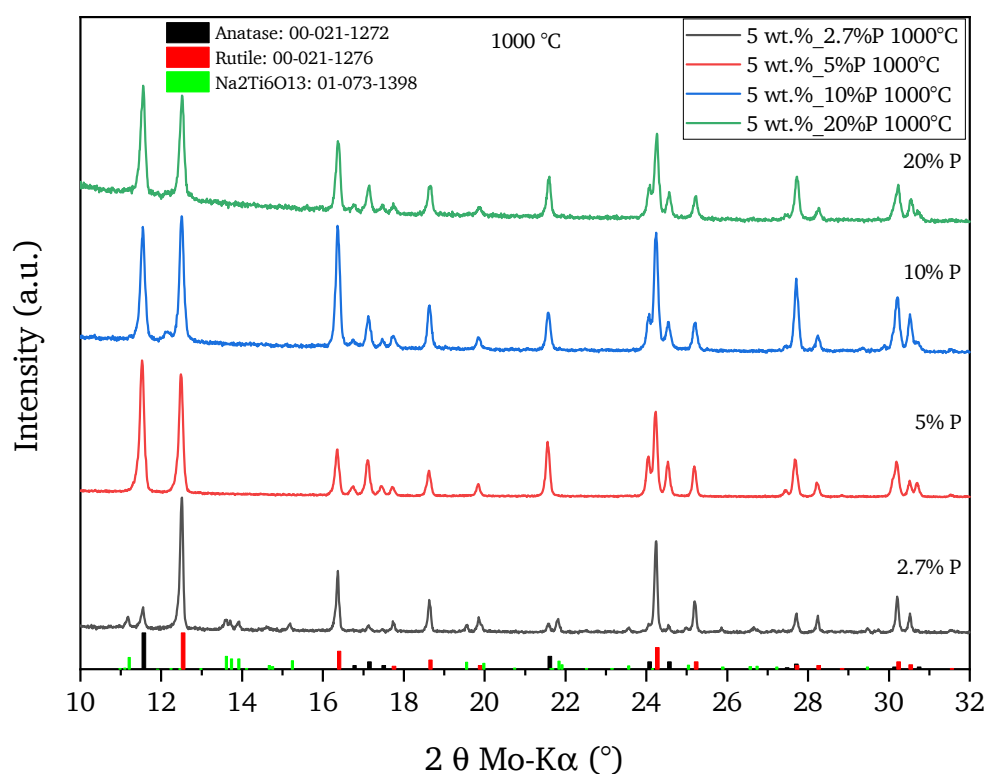


Figure C.16.: Samples heat-treated at 1100 °C with 10 wt. % anatase precursor in Na_2SO_4 with the addition of 0.1, 0.5, 0.8 and 1.2 mol % of B_2O_3 .

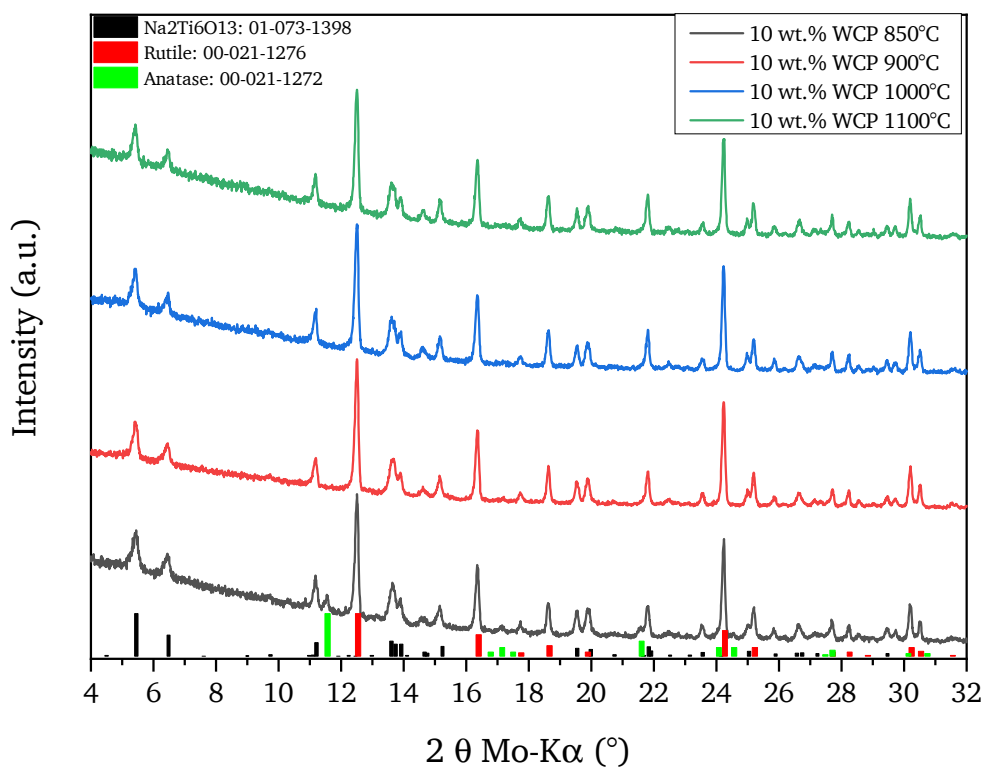


(a) 950 °C

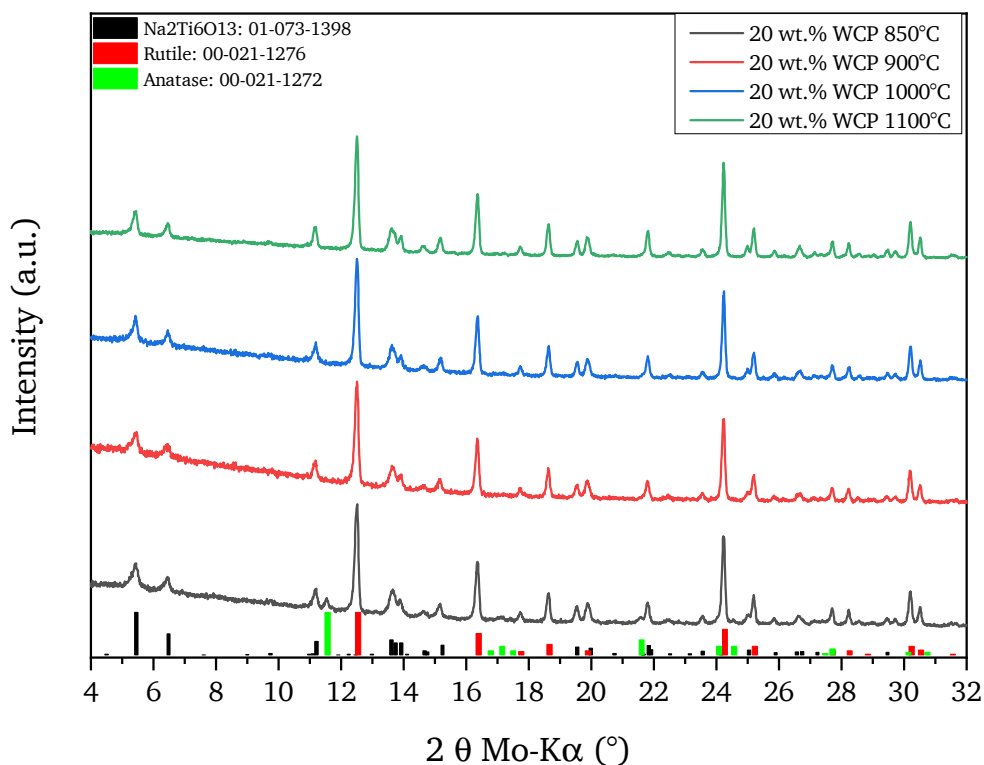


(b) 1000 °C

Figure C.17.: XRD comparison of samples obtained with 5 wt. % TiOSO_4 precursor and different Na_3PO_4 concentrations at a) 950 °C and b) 1000 °C. Reference XRD patterns from the ICDD for $\text{Na}_2\text{Ti}_6\text{O}_{13}$, anatase and rutile are given at the bottom of the graph.



(a) WCP performed at 60 °C with 10 wt. % TiOSO₄



(b) WCP performed at 60 °C with 20 wt. % TiOSO₄

Figure C.18.: Comparison of phases obtained by WCP with a) 10 % and b) 20 % of TiOSO₄. Reference XRD patterns from the ICDD for rutile, anatase and NTO are given at the bottom of the graph.

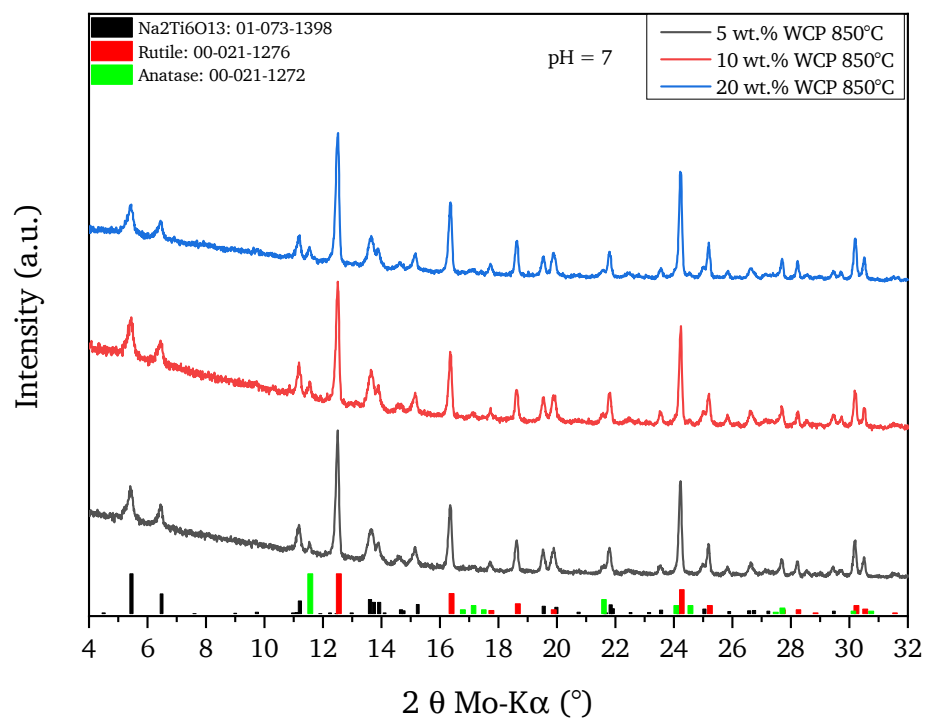
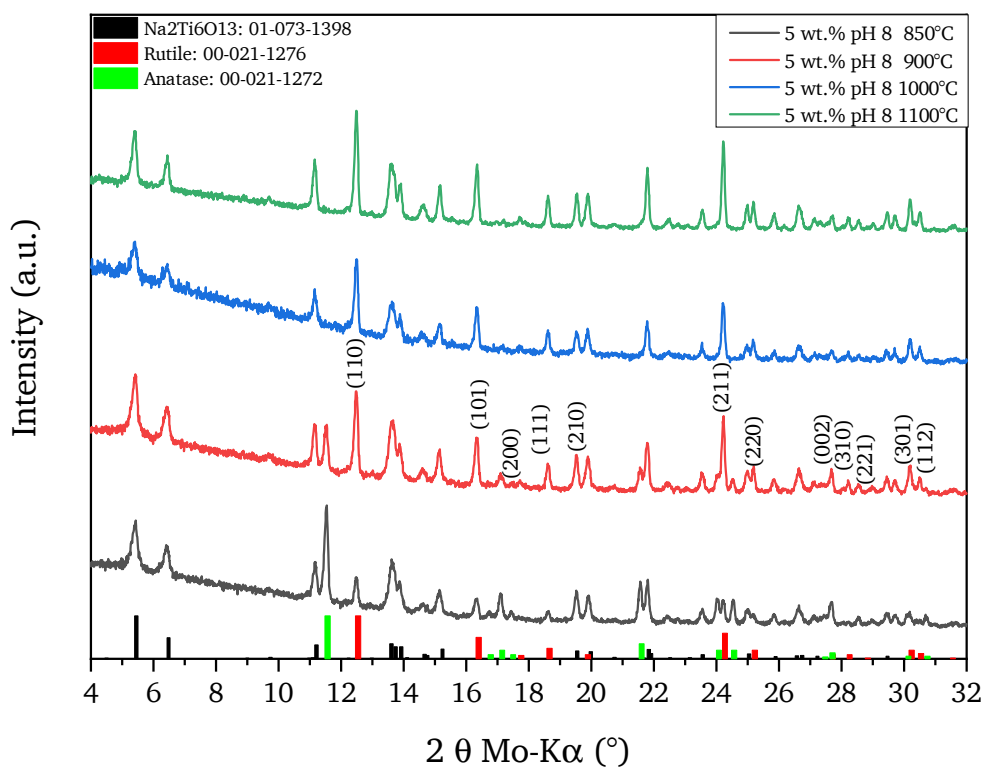
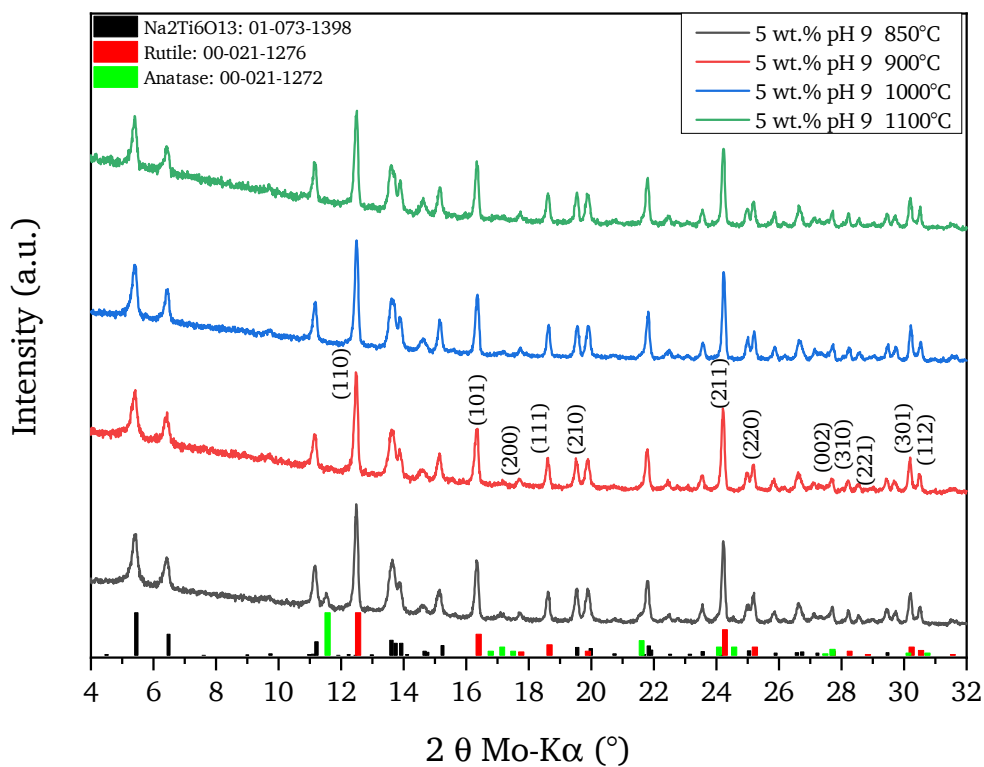


Figure C.19.: Comparison of samples obtained by WCP performed at 60 °C with 5, 10 and 20 wt. % TiOSO_4 precursor in Na_2SO_4 at pH = 7, heat-treated at 850 °C.



(a) WCP with pH = 8



(b) WCP with pH = 9

Figure C.20.: Comparison of samples obtained by WCP performed at 60 °C with 5 wt. % TiOSO₄ and a pH of a) 8 and b) 9. Reference XRD patterns from the ICDD for rutile, anatase and NTO are given at the bottom of the graph.

D. Additional SEM results

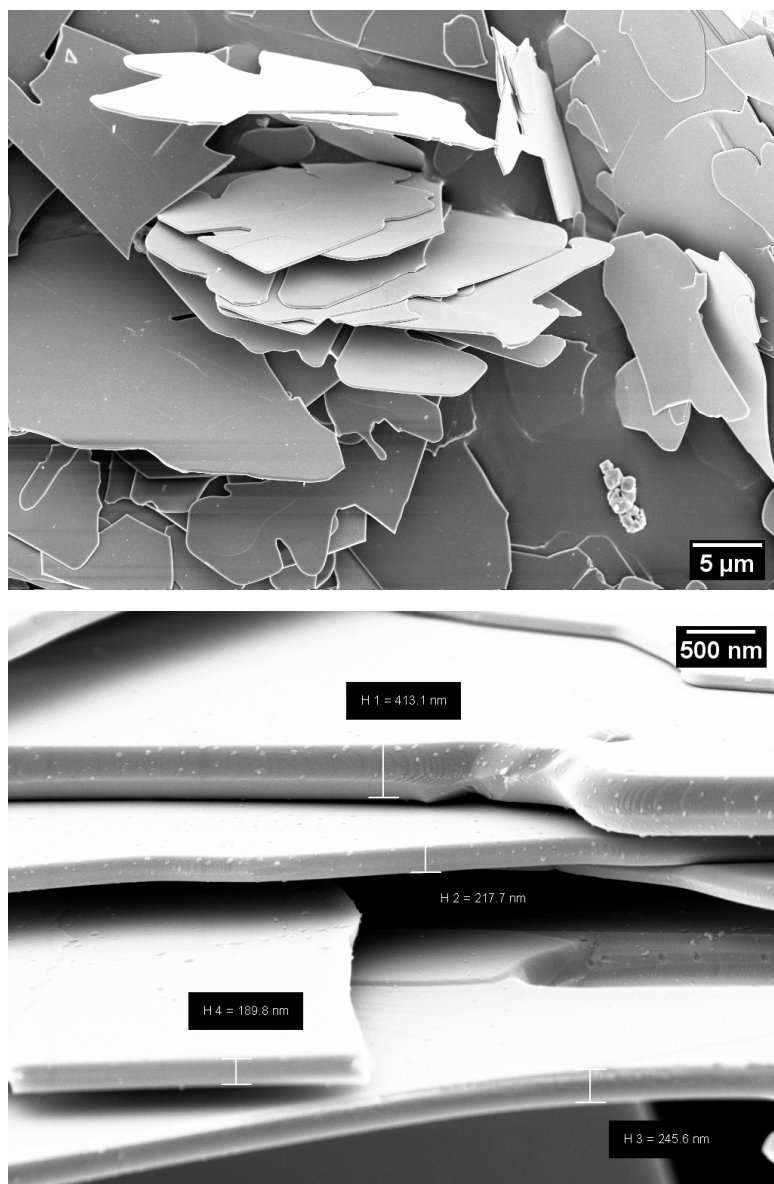


Figure D.1.: SEM images showing the magnifications of the alumina flakes obtained via MSS reported in figure 2.10.

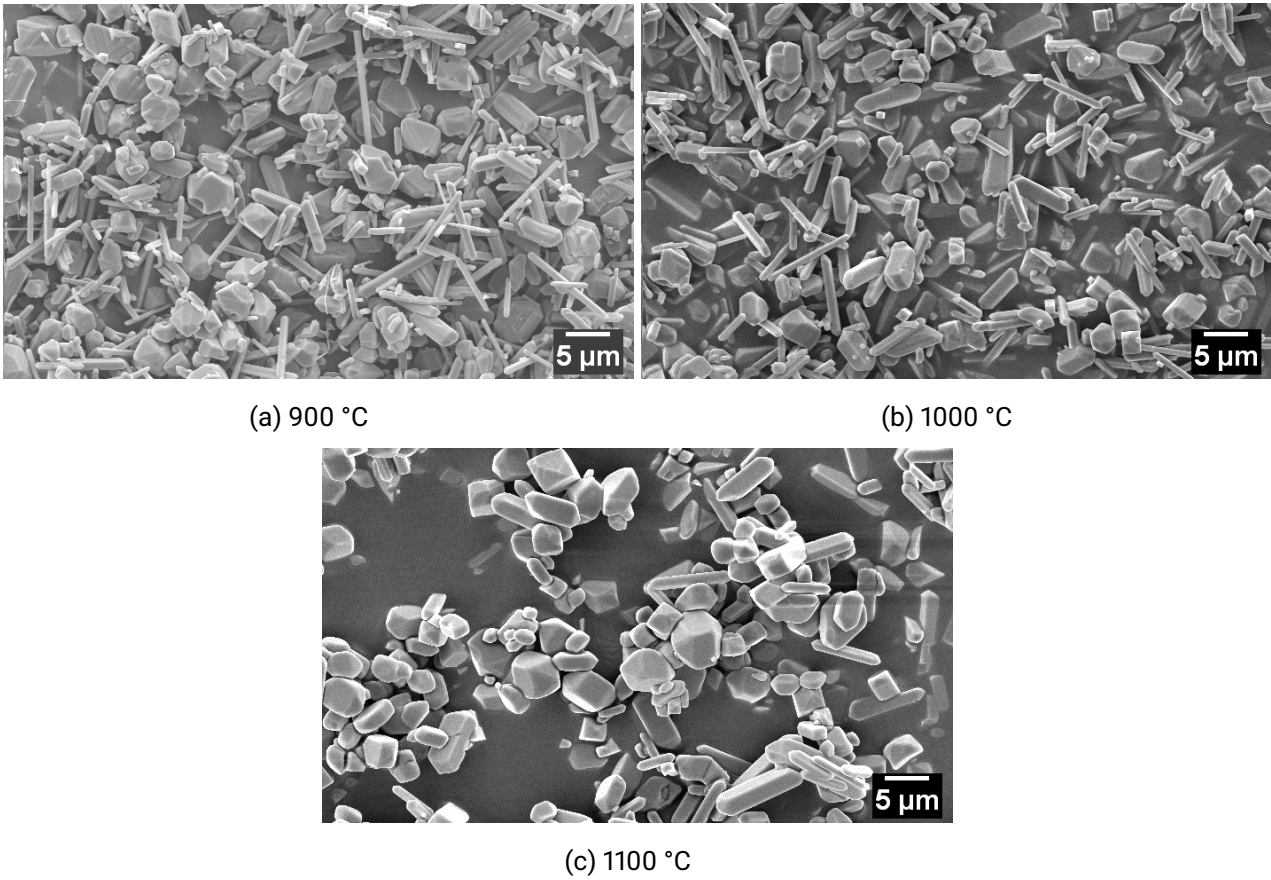


Figure D.2.: SEM images of rutile particles obtained at a) 900, b) 1000 and c) 1100 °C with 20 wt. % anatase precursor in NaCl.

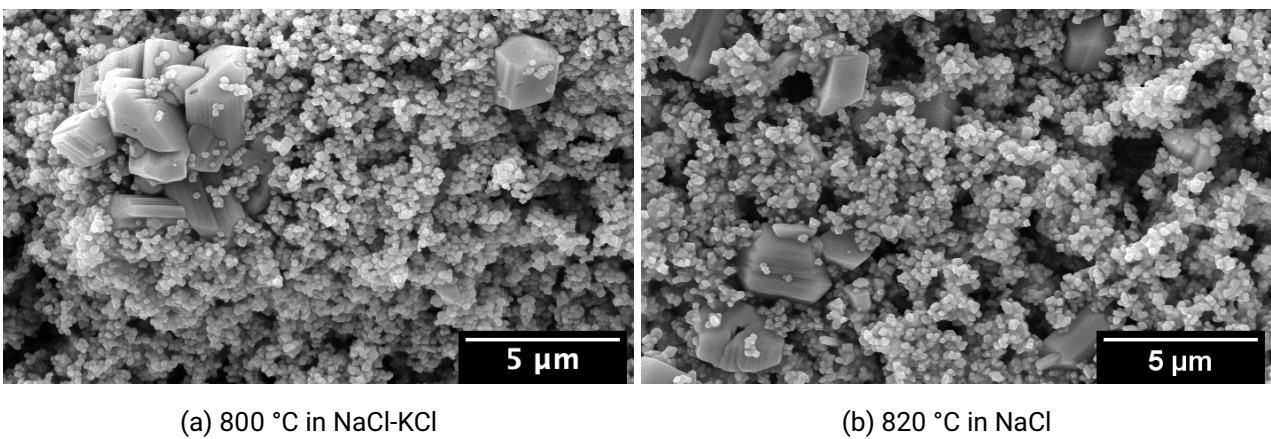
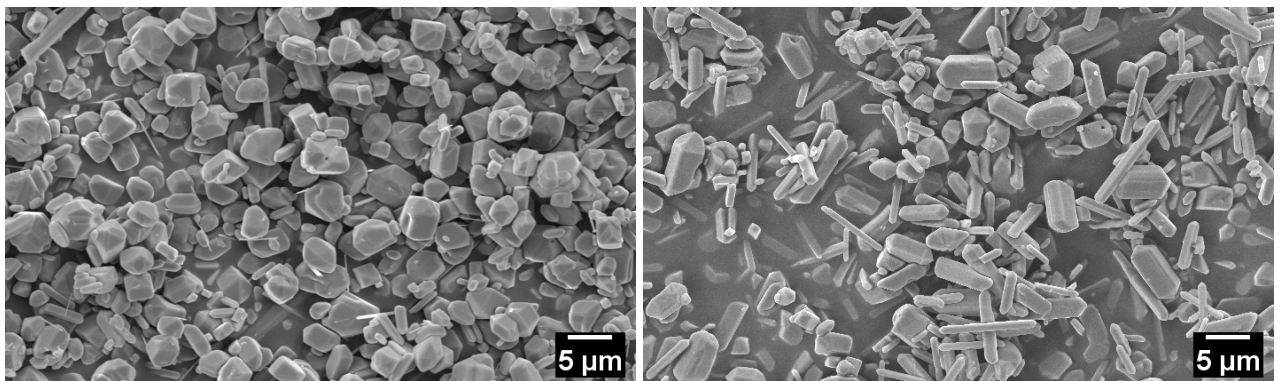
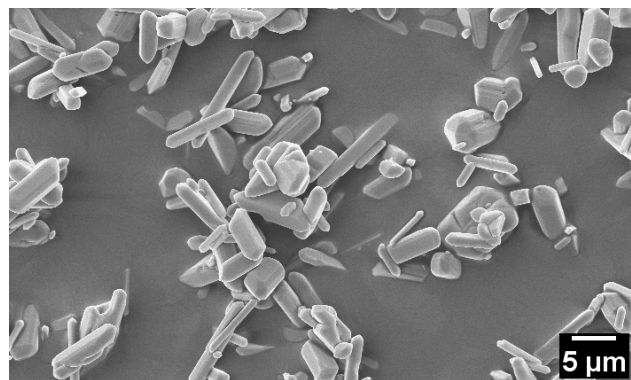


Figure D.3.: SEM images of titania particles obtained with 10 wt. % of anatase precursor at 800 °C in NaCl-KCl eutectic mixture a) and at 820 °C in NaCl b).



(a) 1000 °C and 5 wt. %

(b) 1000 °C and 10 wt. %



(c) 1000 °C and 20 wt. %

Figure D.4.: SEM images of titania particles obtained at 1000 °C in NaCl-KCl eutectic mixture with 5 wt. % a), 10 wt. % b) and 20 wt. % c) of anatase precursor respectively.

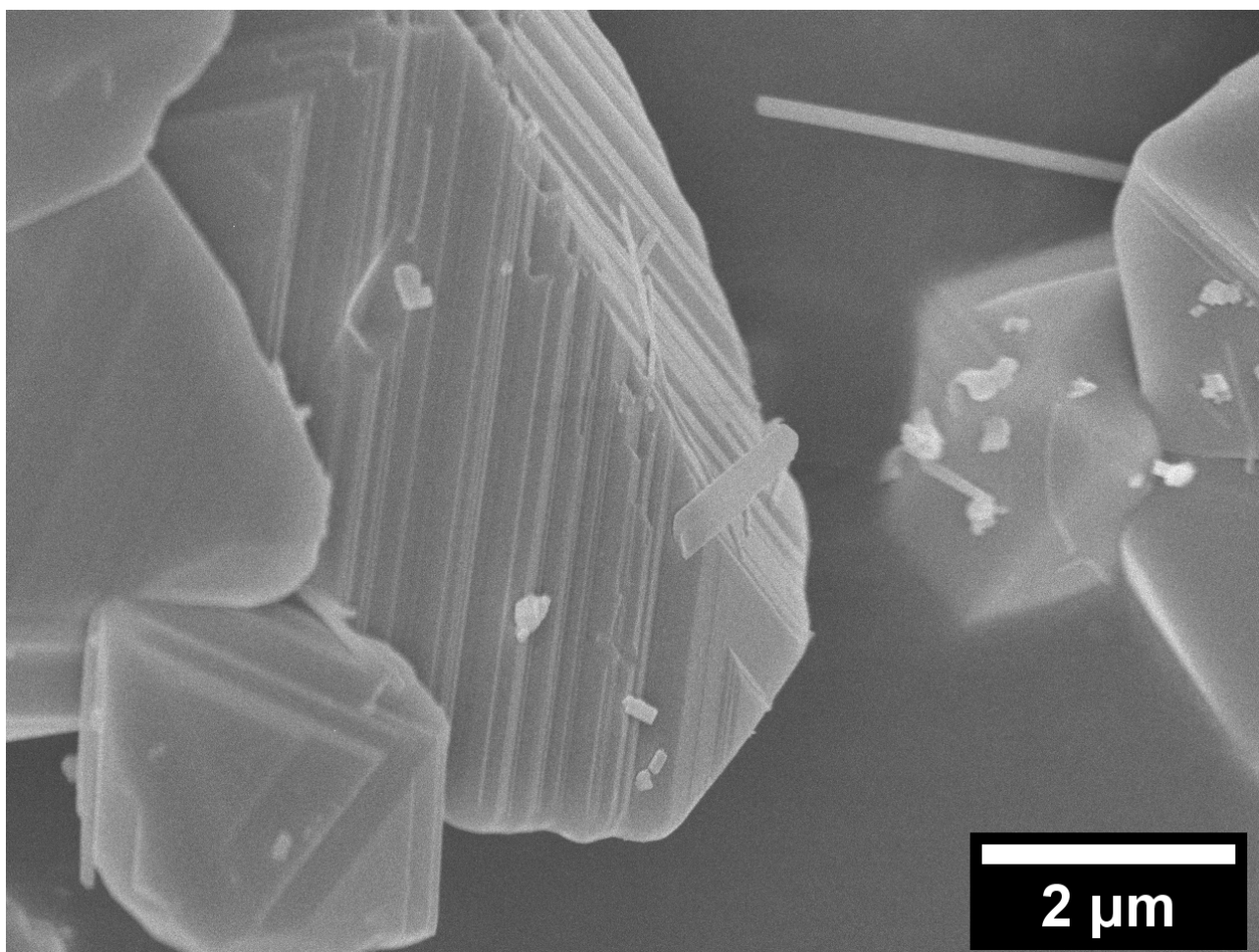
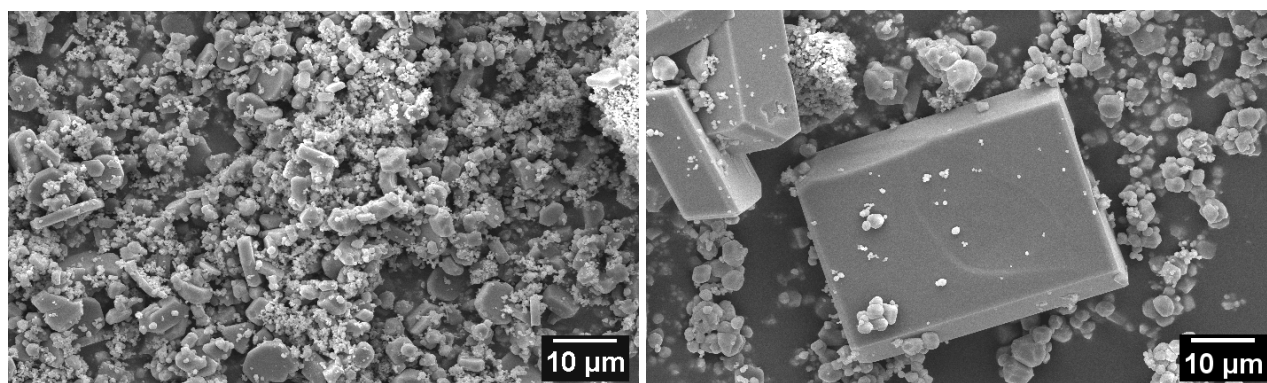


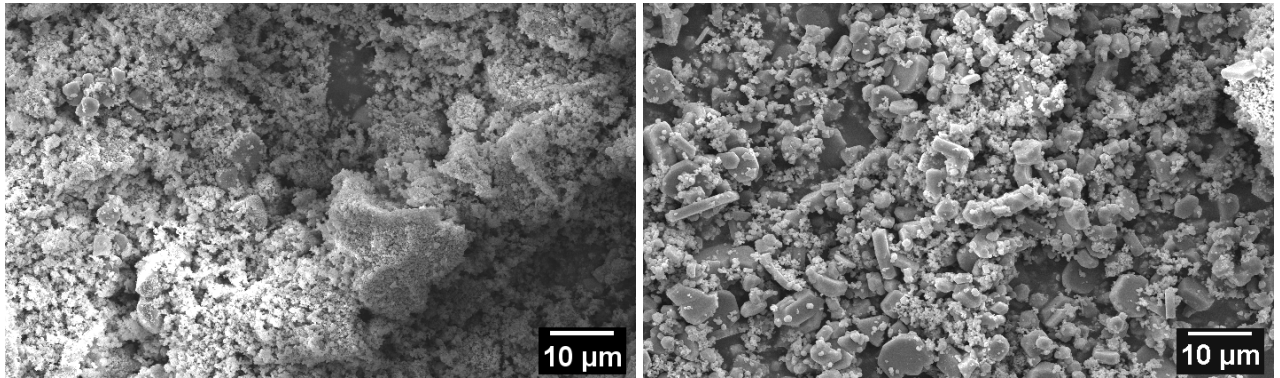
Figure D.5.: SEM image of a detailed view of the terraced growth on titania crystals obtained at 900 °C with 20 wt. % of TiO_2 precursor in NaCl with 20 % F/Ti mol.



(a) 900 °C, 20 wt. %

(b) 1000 °C, 20 wt. %

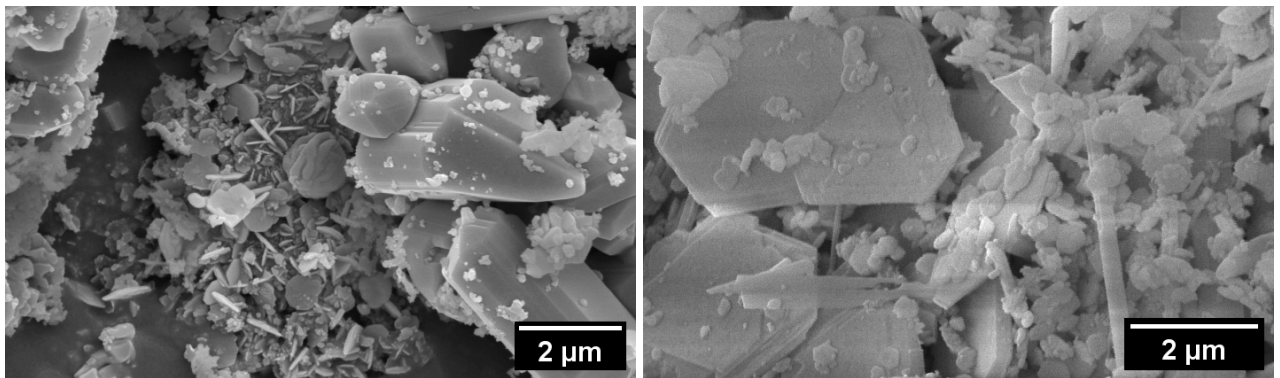
Figure D.6.: SEM images showing the size comparison between titania particles obtained at 900 a) and b) 1000 °C: 20 wt. % TiO_2 in 0.8NaCl-0.2MgCl₂ mixture.



(a) 900 °C, 5 wt. %

(b) 900 °C, 20 wt. %

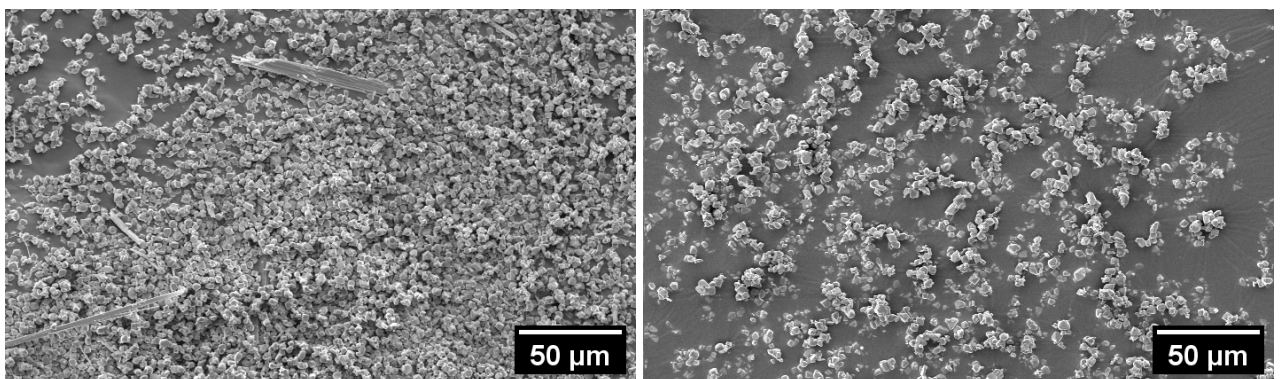
Figure D.7.: SEM images of titania particles obtained at 900 °C with 5 wt. % a) and 20 wt. % b) of TiO_2 in $0.8\text{NaCl}-0.2\text{MgCl}_2$ mixture.



(a) 1000 °C, 10 wt. %

(b) 1100 °C, 10 wt. %

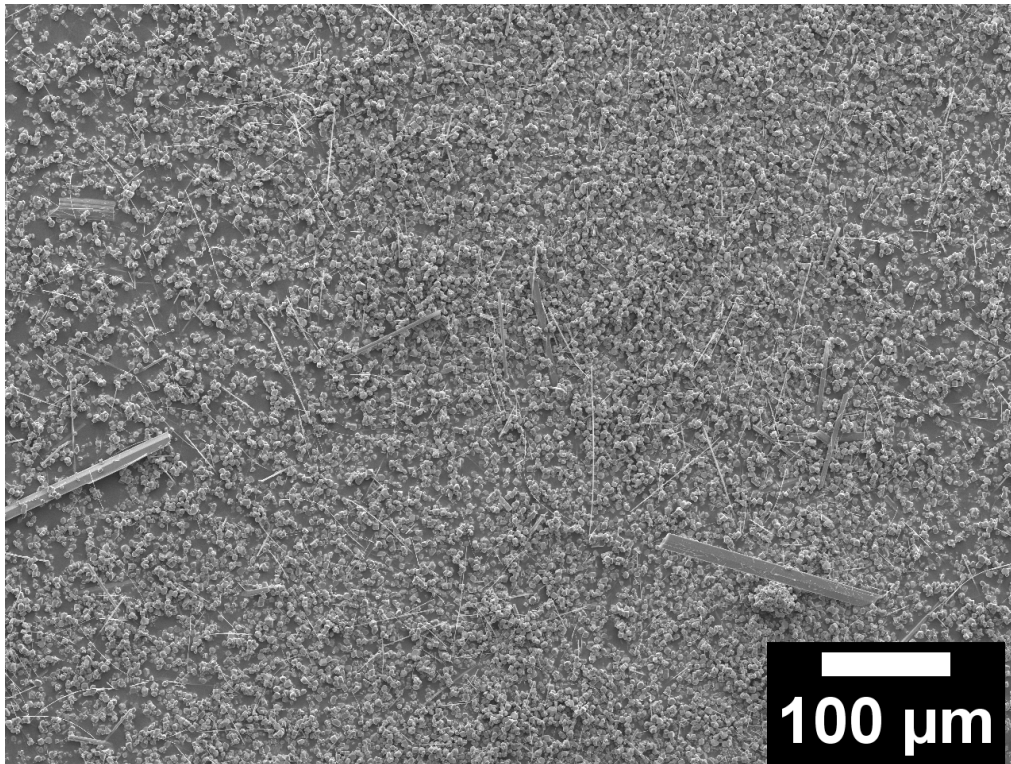
Figure D.8.: SEM images of alumina flakes mixed to rutile crystals (10 wt. % TiO_2 in $0.7\text{NaCl}-0.3\text{AlCl}_3$ mixture): a) magnification of figure 5.19b and b) magnification of figure 5.19d.



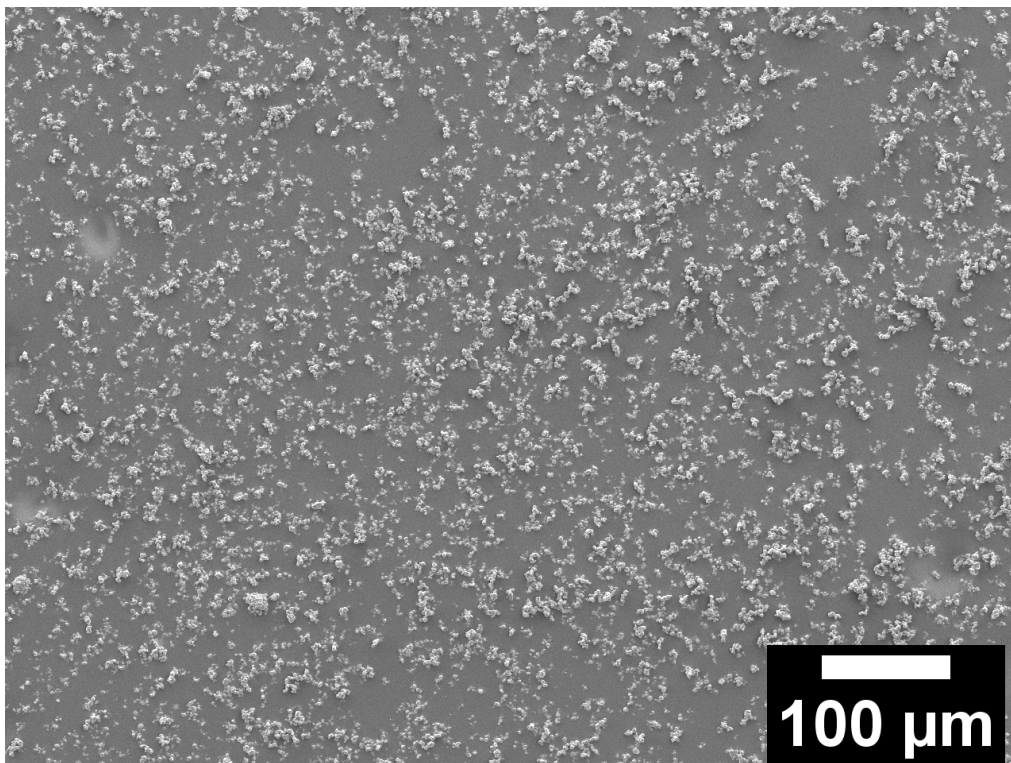
(a) 1000 °C under ambient atmosphere

(b) 1000 °C under pure argon atmosphere

Figure D.9.: SEM images showing the morphology of titania particles obtained at 1000 °C with 1 wt. % anatase precursor in NaCl under a) ambient atmosphere and b) under argon flow.

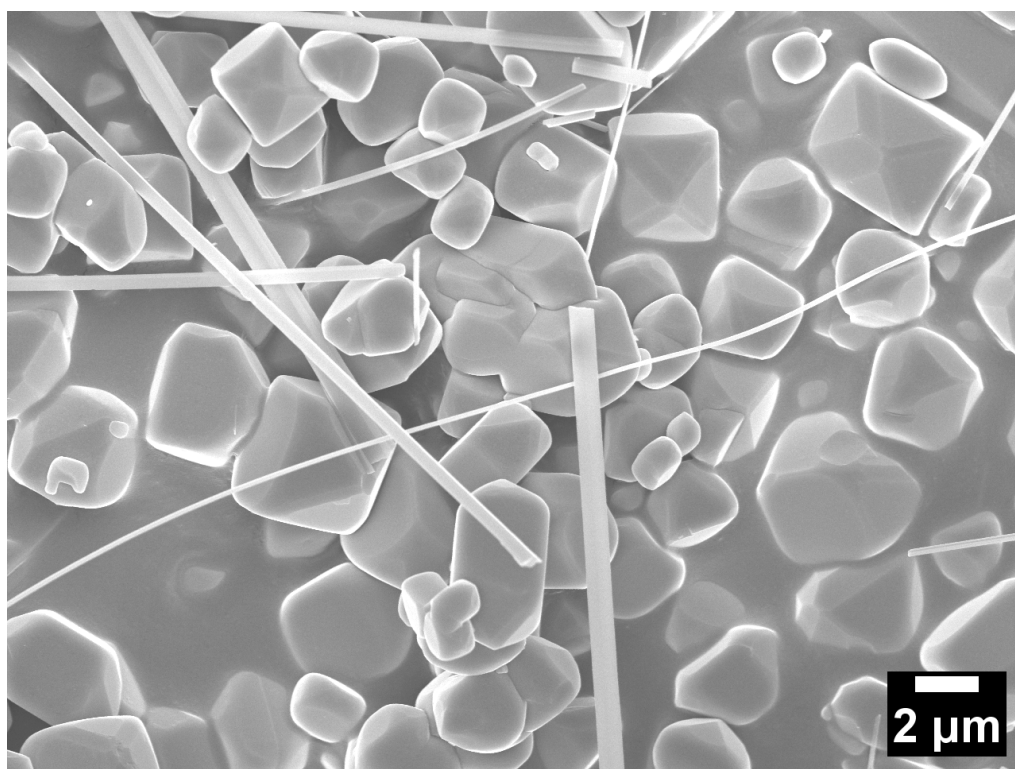


(a) 1100 °C under ambient atmosphere

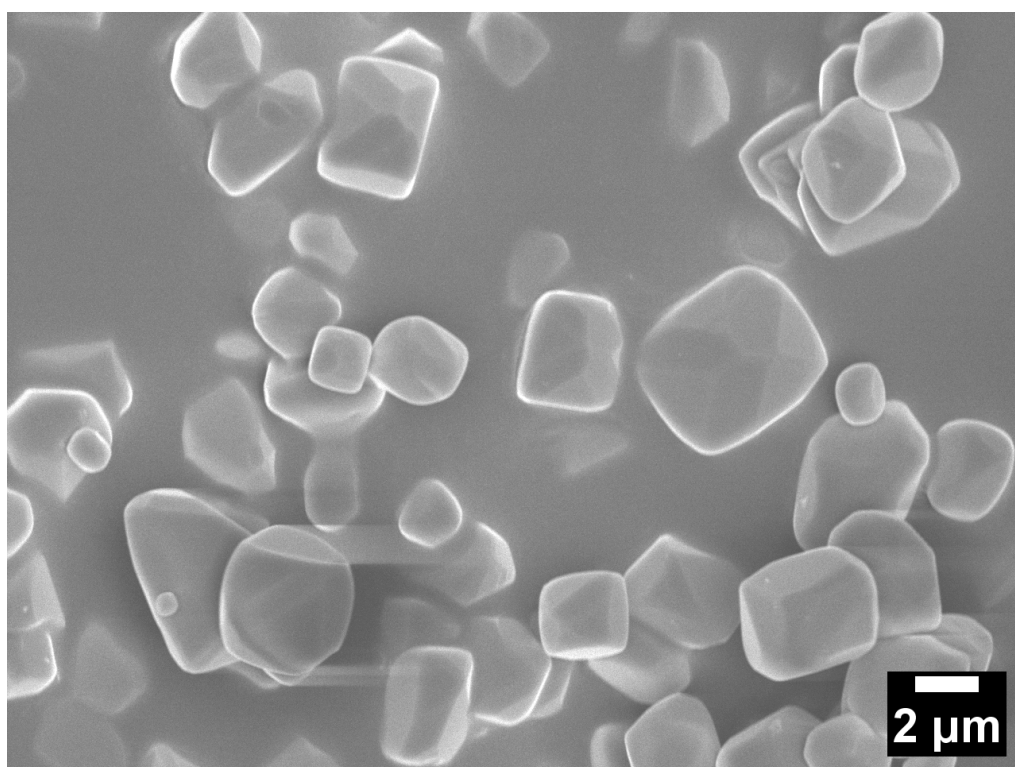


(b) 1100 °C under pure oxygen atmosphere

Figure D.10.: Larger view of the samples reported in figure 5.26 on page 83. Morphology of titania particles obtained at 1100 °C with 10 wt. % anatase precursor in NaCl under: a) ambient atmosphere and b) under pure oxygen, measured by SEM.

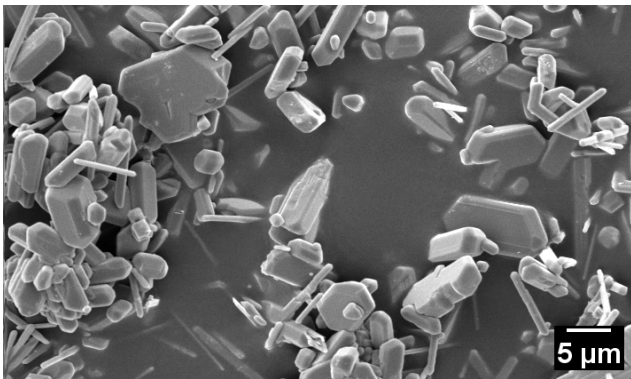


(a) 1100 °C under ambient atmosphere

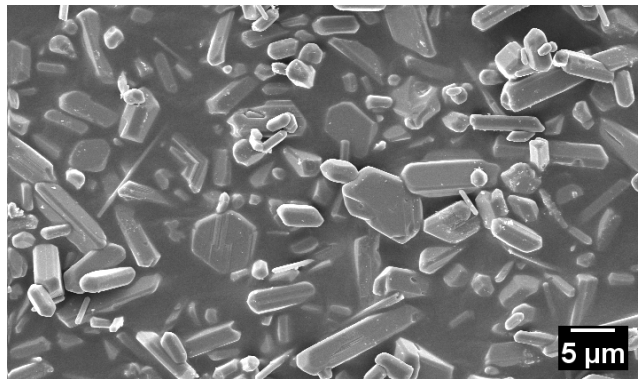


(b) 1100 °C under pure oxygen atmosphere

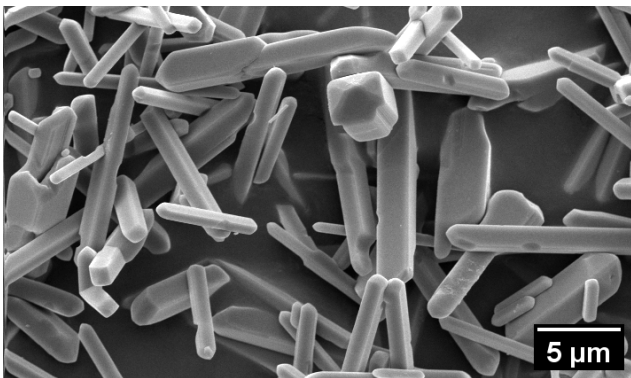
Figure D.11.: SEM images showing the morphology of titania particles obtained at 1100 °C with 10 wt. % anatase precursor in NaCl under: a) ambient atmosphere and b) pure oxygen. Enlarged view of the samples reported in figure 5.26.



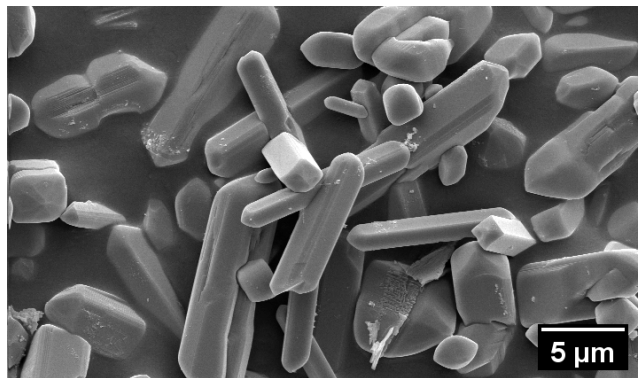
(a) 900 °C, NaCl + 0.8 mol % B₂O₃



(b) 900 °C, NaCl + 1.2 mol % B₂O₃

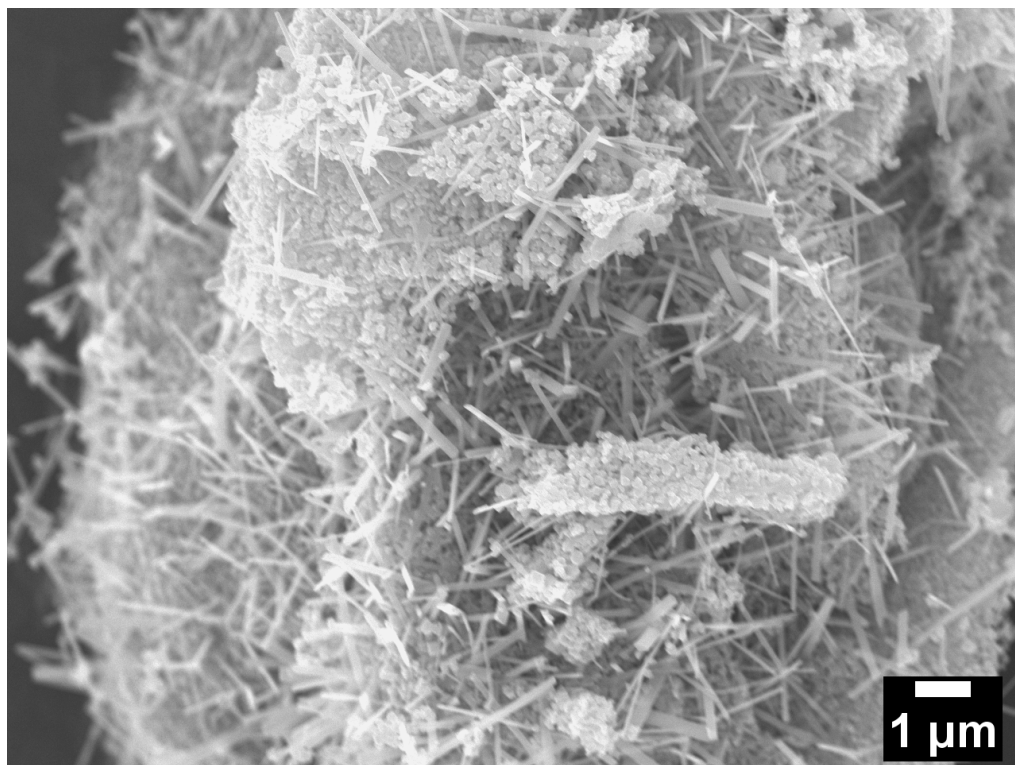


(c) 1000 °C, NaCl + 0.8 mol % B₂O₃

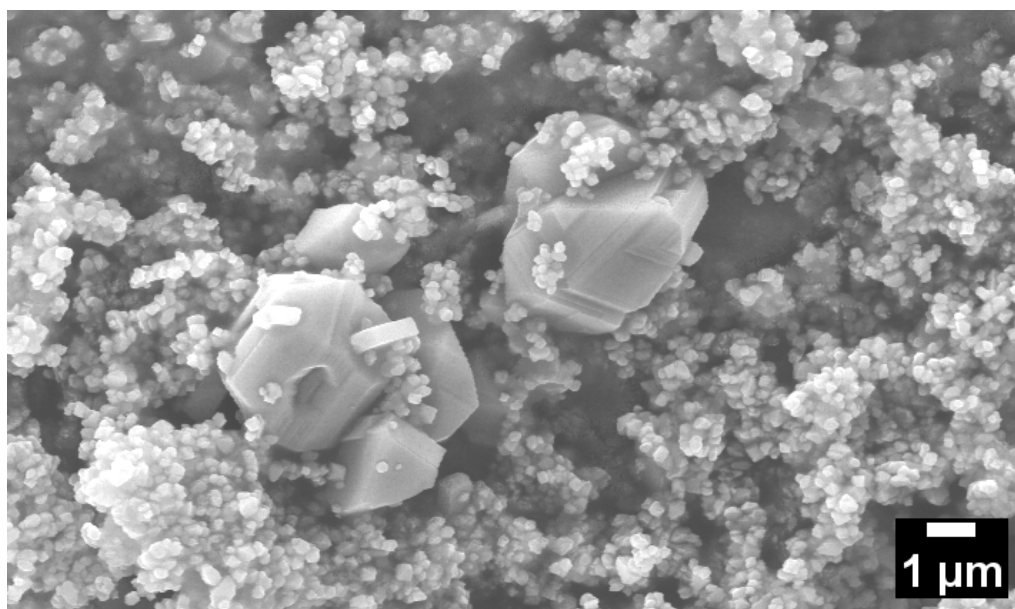


(d) 1000 °C, NaCl + 1.2 mol % B₂O₃

Figure D.12.: SEM images of titania particles obtained at 900 °C and 1000 °C: 20 wt. % TiO₂ precursor in NaCl with the addition of 0.8 mol % (a and c) and 1.2 mol % B₂O₃ (b and d).

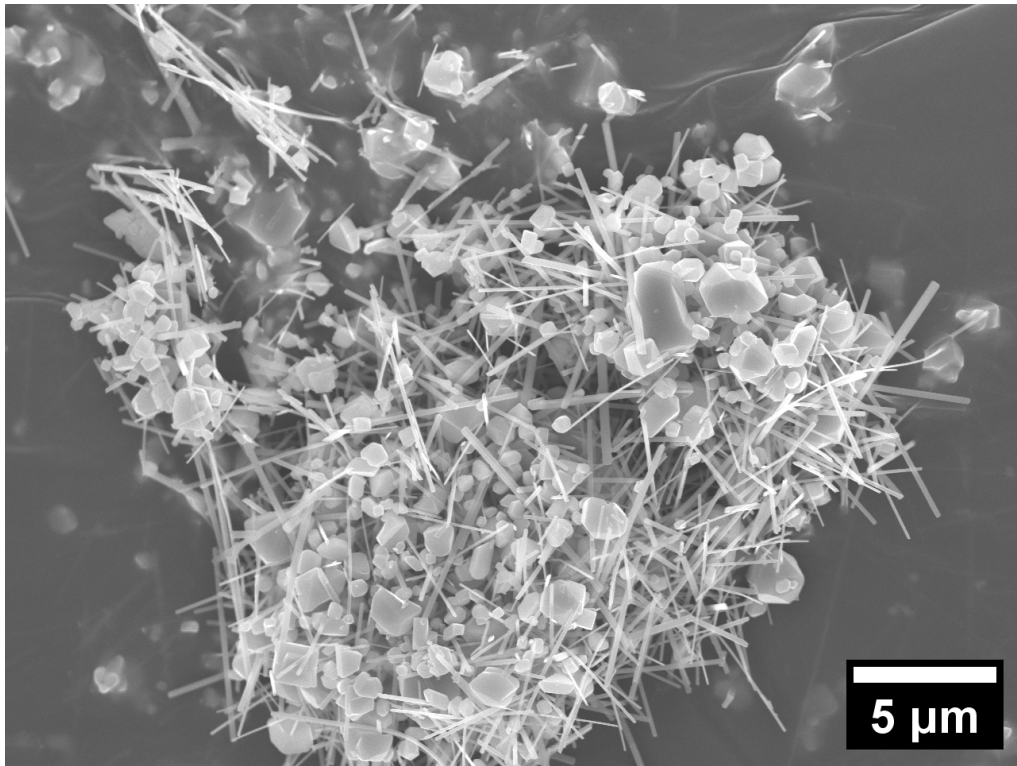


(a) 850 °C WCP

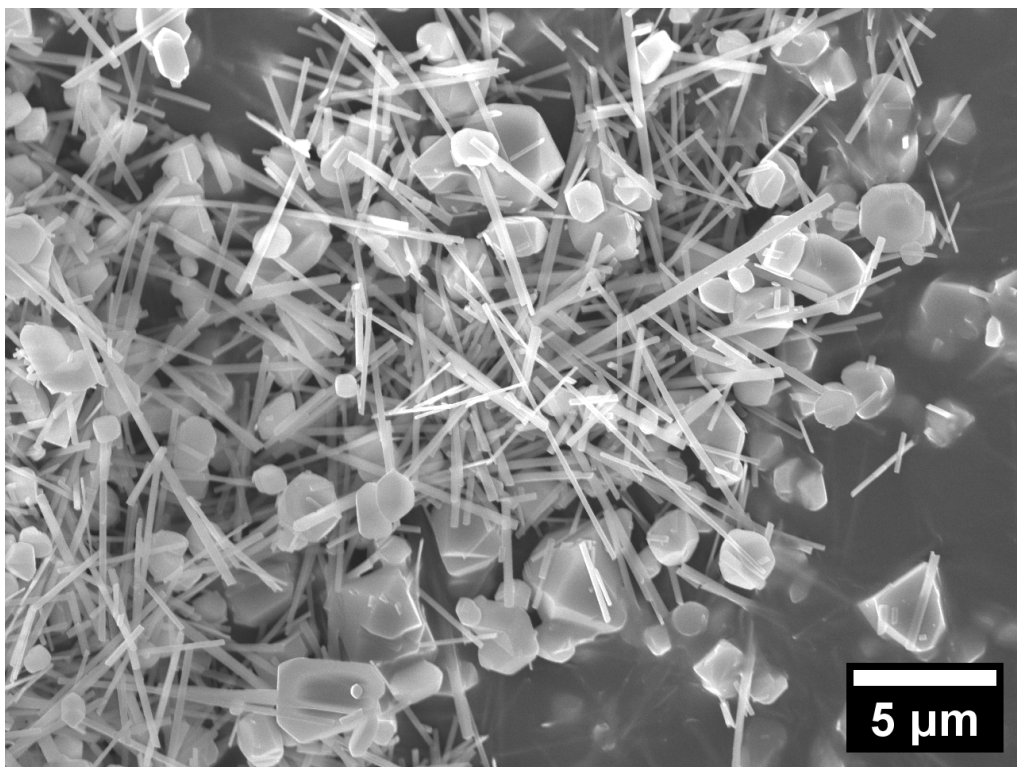


(b) 850 °C DMS

Figure D.13.: SEM images of samples obtained in NaCl by WCP with 5 wt. % TiCl_4 precursor (figure a) and by DMS (figure b) at 850 °C.



(a) 1000 °C WCP



(b) 1100 °C WCP

Figure D.14.: SEM images of titania and NTO particles obtained in NaCl by WCP (with 5 wt. % TiCl_4 precursor) at 1000 °C (figure a) and 1100 °C (figure b).

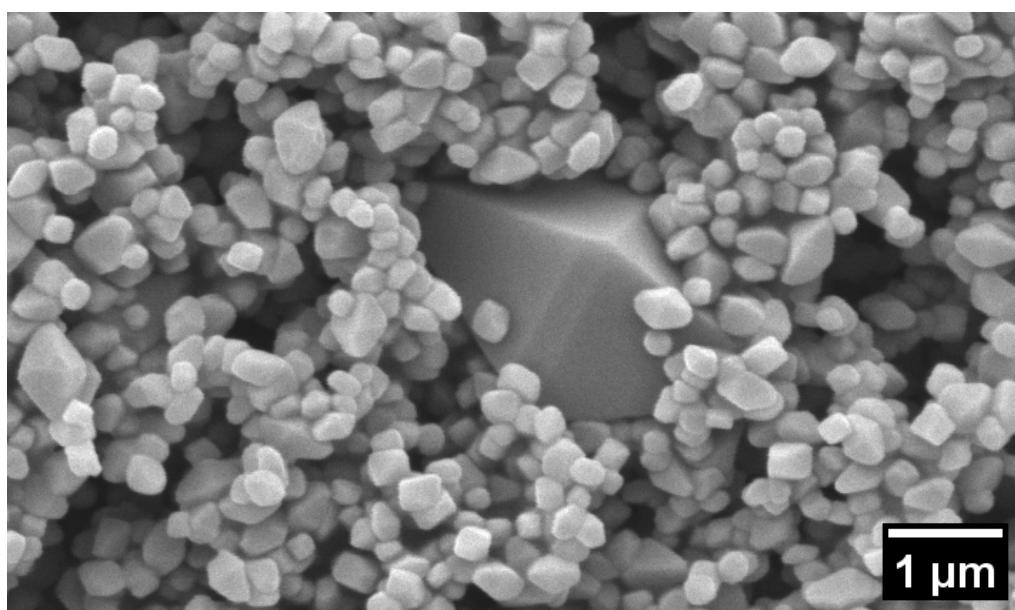


Figure D.15.: SEM image showing the enlarged view of the sample reported in figure 5.35d, with the typical bifrustum morphology of anatase particles: MSS at 900 °C with 15 wt. % precursor in Na_2SO_4 .

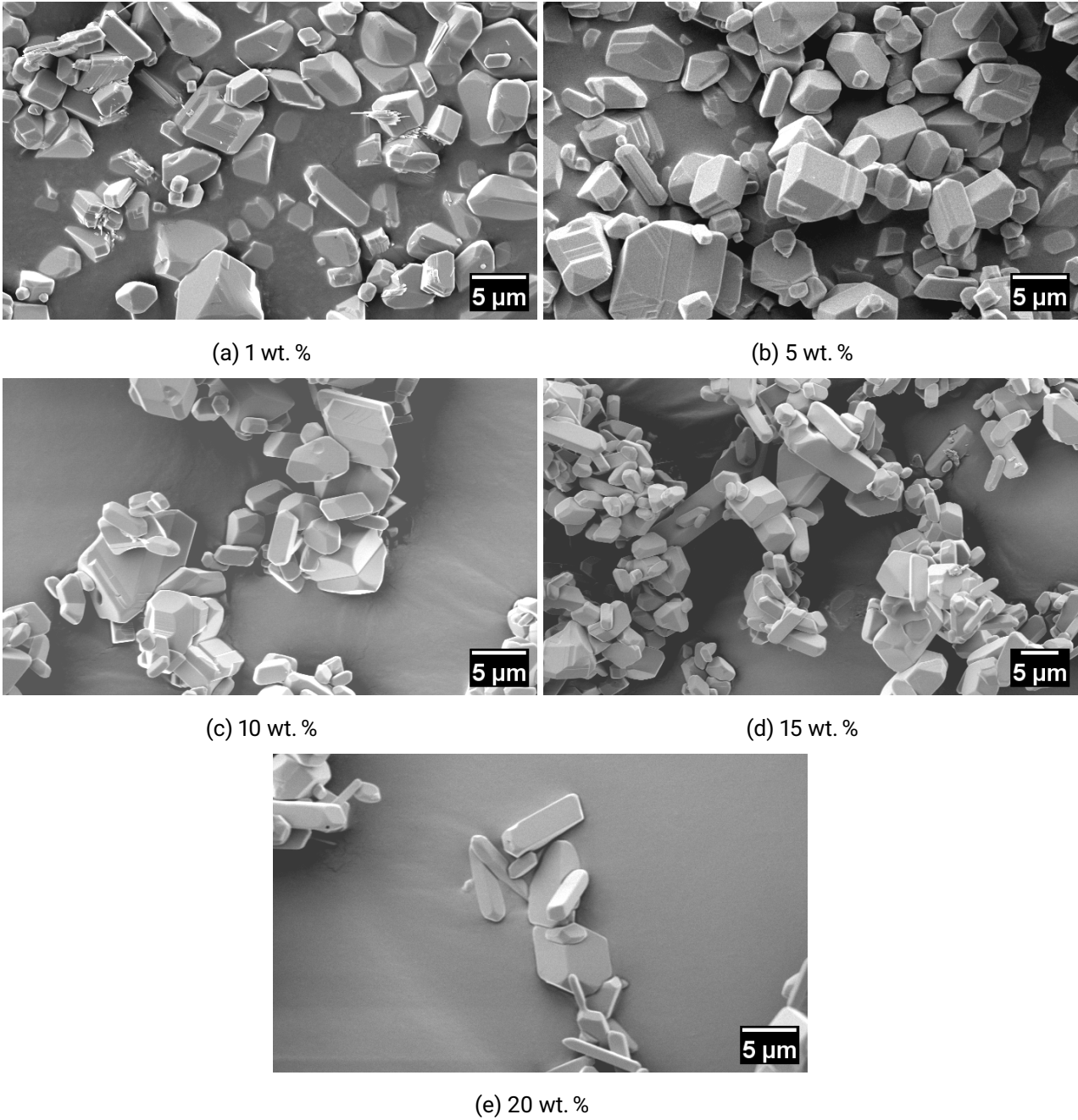
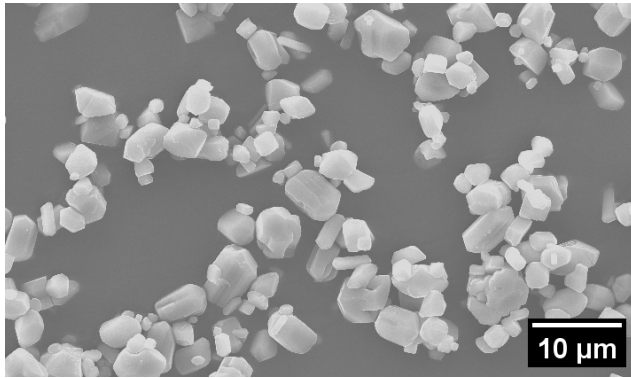
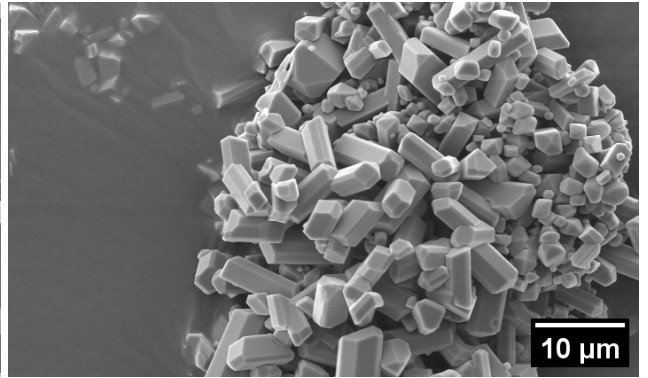


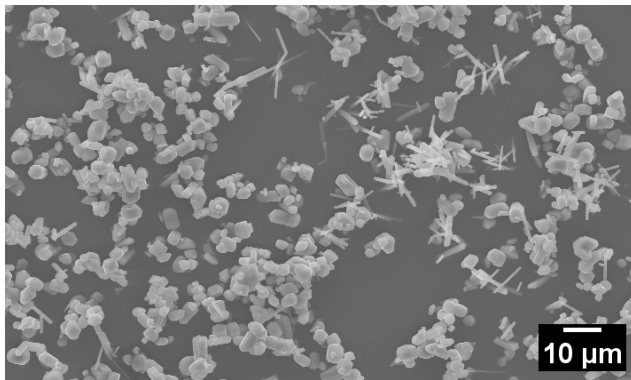
Figure D.16.: SEM images of TiO₂ particles obtained at 1100 °C with 2 hours of holding time with a) 1 wt. %, b) 5 wt. %, c) 10 wt. %, d) 15 wt. % and e) 20 wt. % of TiO₂ in Na₂SO₄.



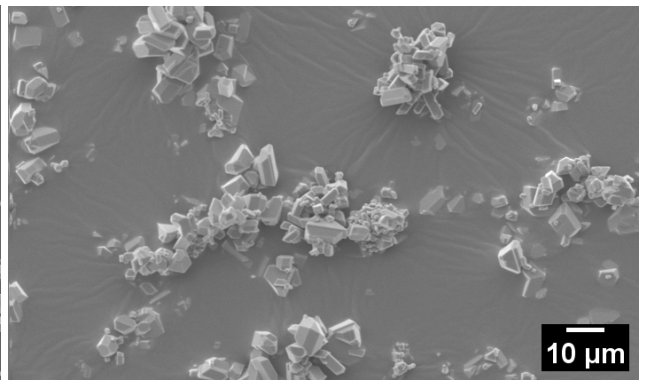
(a) 1000 °C, 5 wt. % in 0.47 Na₂SO₄-0.53 NaCl



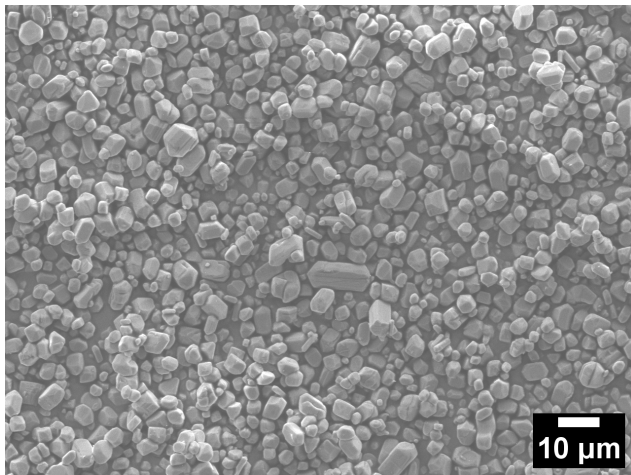
(b) 1000 °C, 5 wt. % in Na₂SO₄



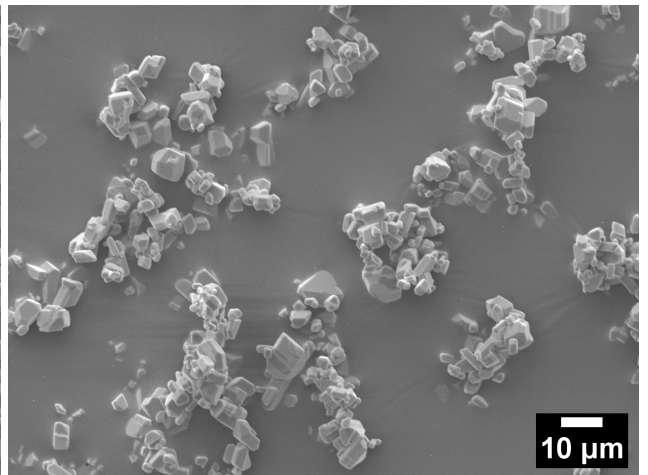
(c) 1000 °C, 10 wt. % in 0.47 Na₂SO₄-0.53 NaCl



(d) 1000 °C, 10 wt. % in Na₂SO₄

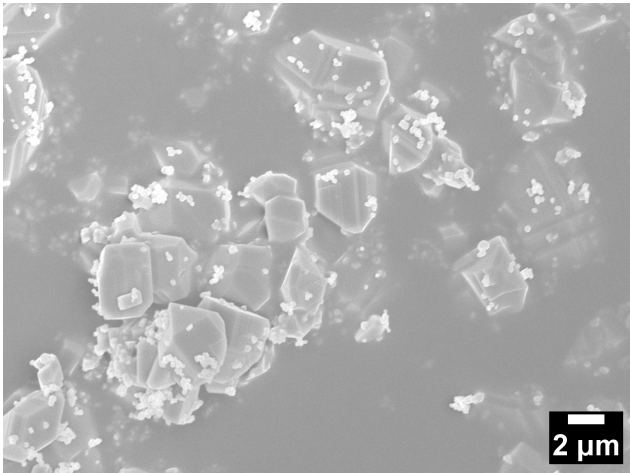


(e) 1100 °C, 10 wt. % in 0.47 Na₂SO₄-0.53 NaCl

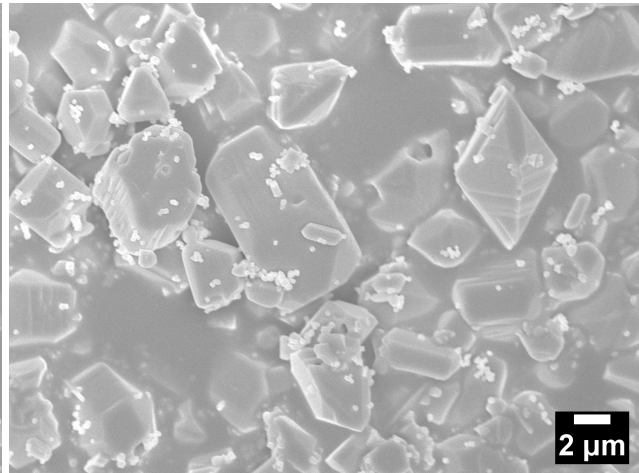


(f) 1100 °C, 10 wt. % in Na₂SO₄

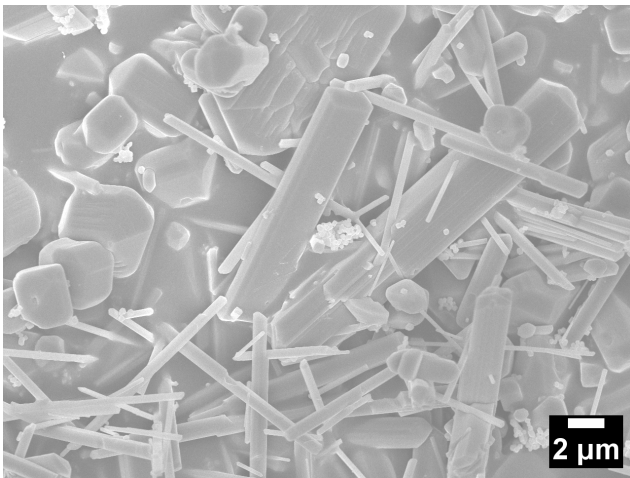
Figure D.17.: SEM images of TiO₂ particles obtained at 1000 °C with 2 hours of holding time with a) 5 wt. % and c) 10 wt. % TiO₂ precursor in 0.47 Na₂SO₄-0.53 NaCl and b) 5 wt. % and d) 10 wt. % of TiO₂ precursor in Na₂SO₄. e) and f) report 10 wt. % of TiO₂ precursor at 1100 °C in 0.47 Na₂SO₄-0.53 NaCl and Na₂SO₄, respectively.



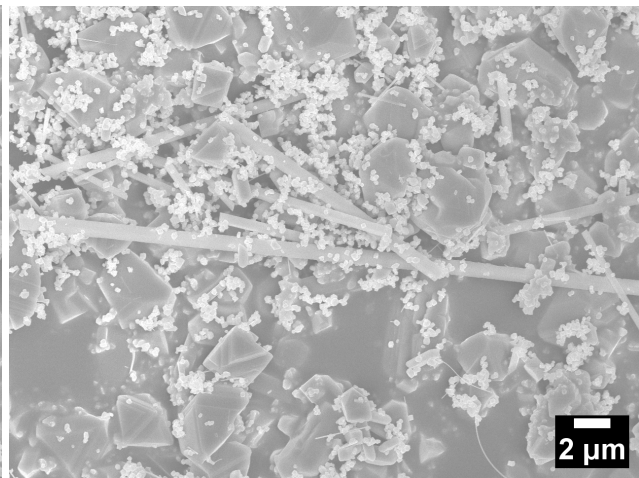
(a) 0.2 NaCl-0.8 Na₂SO₄



(b) 0.4 NaCl-0.6 Na₂SO₄

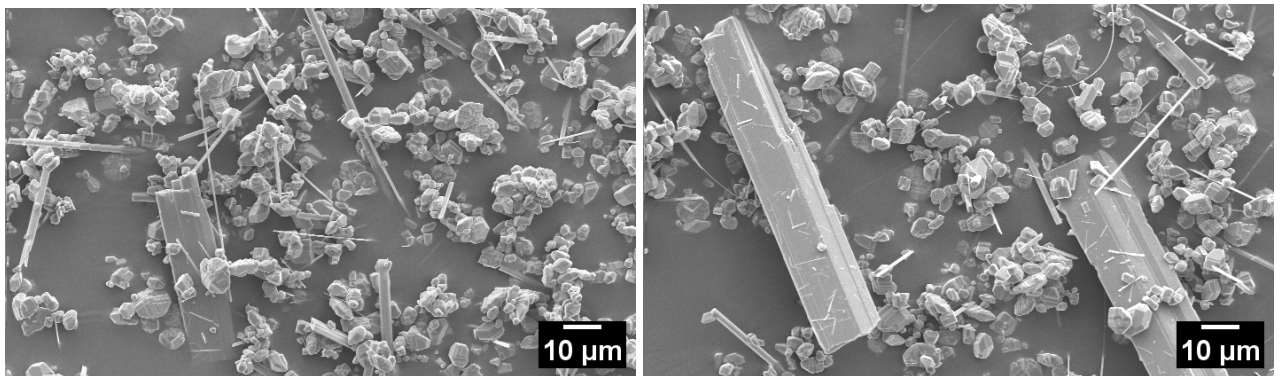


(c) 0.6 NaCl-0.4 Na₂SO₄



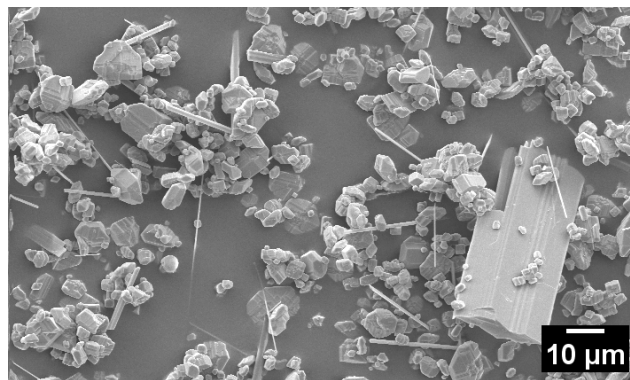
(d) 0.8 NaCl-0.2 Na₂SO₄

Figure D.18.: SEM images showing the magnification of figure 5.43. TiO₂ particles obtained at 900 °C, 2 hours of holding time with 10 wt. % of TiO₂ in: a) 0.2 NaCl-0.8 Na₂SO₄, b) 0.4 NaCl-0.6 Na₂SO₄, c) 0.6 NaCl-0.4 Na₂SO₄ and d) 0.8 NaCl-0.2 Na₂SO₄.



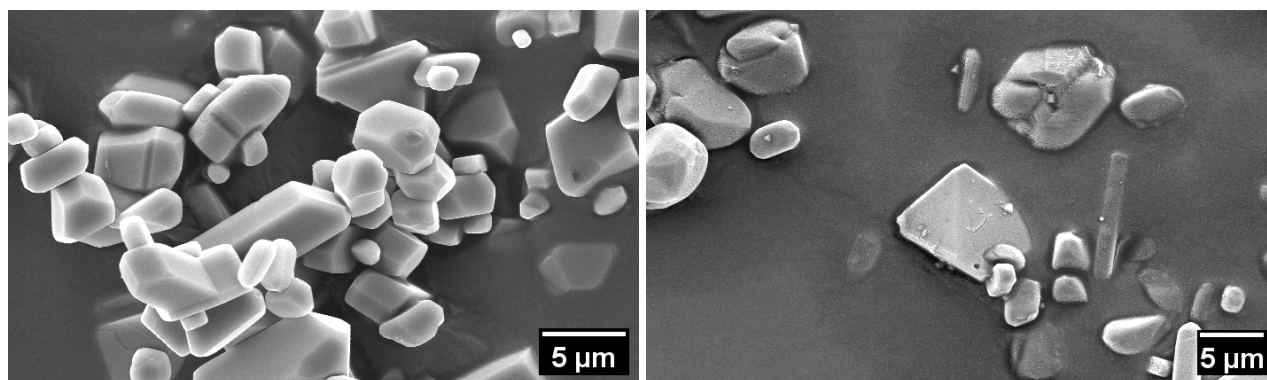
(a) F-Ti 20 %

(b) F-Ti 30 %



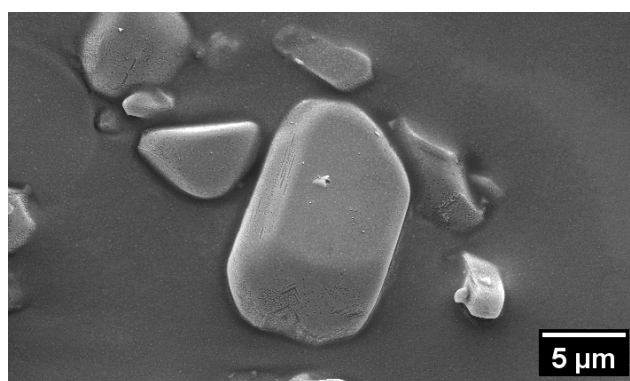
(c) F-Ti 40 %

Figure D.19.: SEM images showing a broader view on TiO_2 particles and $\text{Na}_2\text{Ti}_6\text{O}_{13}$ "micro-belts" obtained at 1100°C , 2 hours of holding time and 10 wt. % of TiO_2 with the addition of a) 20 NaF mol %, b) 30 NaF mol % and c) 40 NaF mol %.



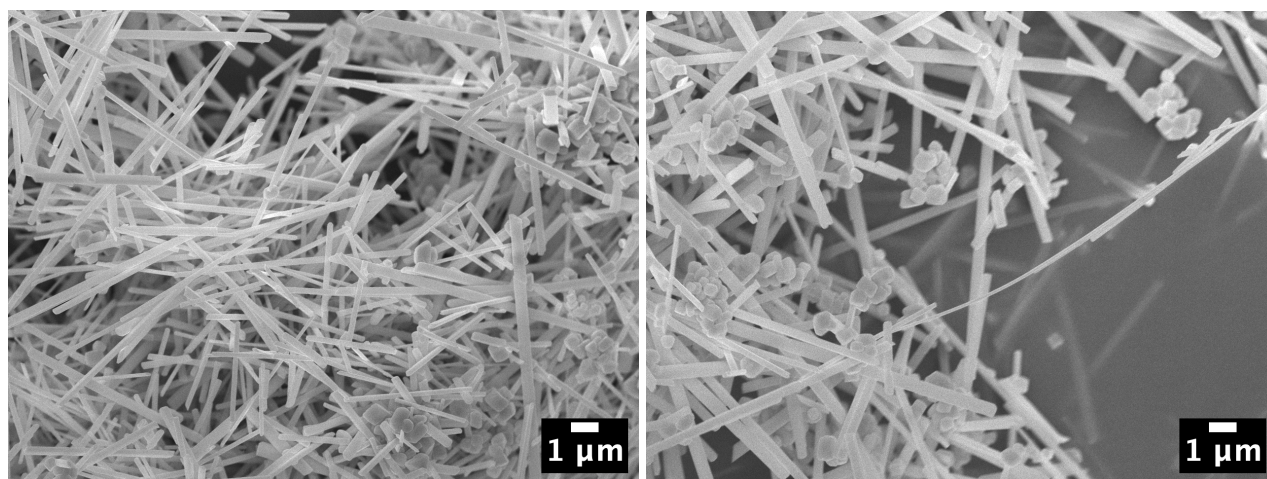
(a) Pure Na_2SO_4

(b) 0.8 % B_2O_3



(c) 1.2 % B_2O_3

Figure D.20.: SEM images showing the enlarged view of figure 5.52: a) TiO_2 particles obtained at $1100\text{ }^\circ\text{C}$, 2 hours of holding time and 10 wt. % of TiO_2 , b) with the addition of 0.8 B_2O_3 mol % and c) with the addition of 1.2 B_2O_3 mol %.



(a) $1000\text{ }^\circ\text{C}$, 5 wt. % WCP TiOSO_4 at $60\text{ }^\circ\text{C}$

(b) $1100\text{ }^\circ\text{C}$, 5 wt. % WCP TiOSO_4 at $60\text{ }^\circ\text{C}$

Figure D.21.: SEM images showing the zoomed view of the particles in figure 5.56, synthesized by MSS in Na_2SO_4 heat-treated at a) $1000\text{ }^\circ\text{C}$ and b) $1100\text{ }^\circ\text{C}$.

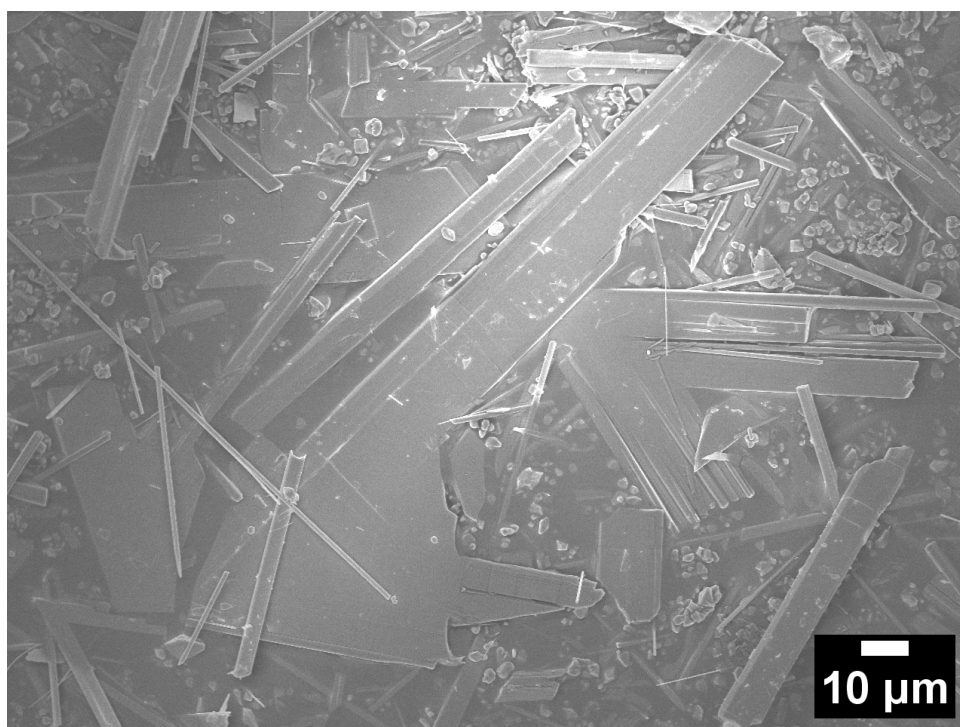


Figure D.22.: SEM image showing the zoomed view of a V-shaped crystal in figure 5.67c, synthesized by WCP in Na_2SO_4 heat-treated at $1000\text{ }^\circ\text{C}$ and with the addition of 10 % of Na_3PO_4 .

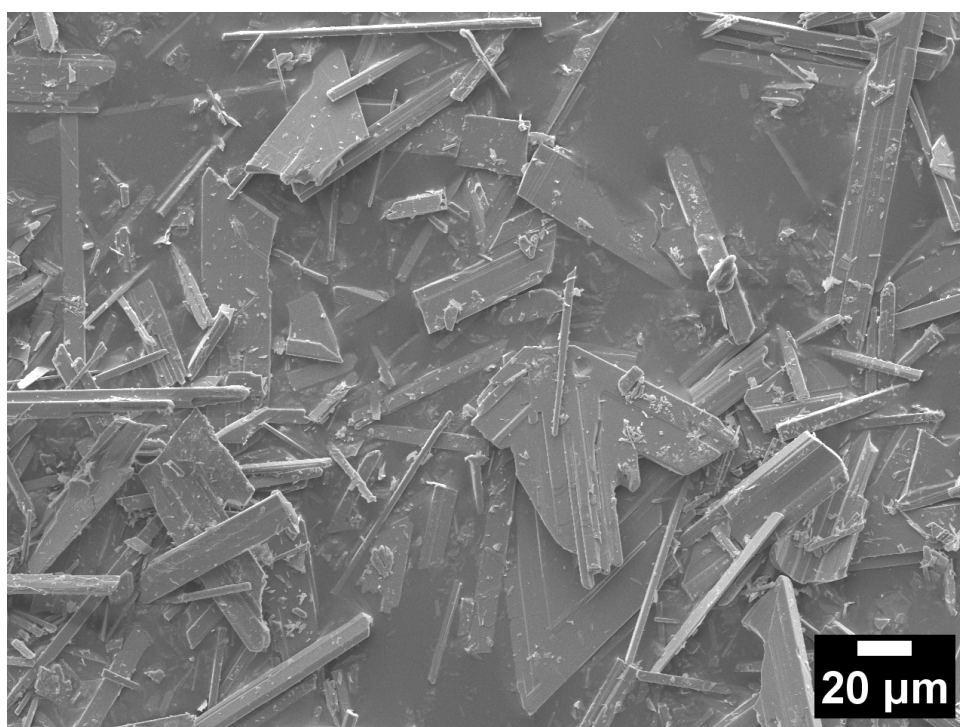
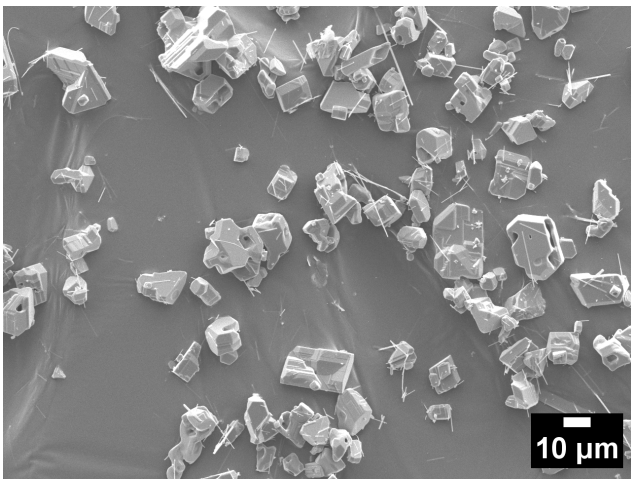
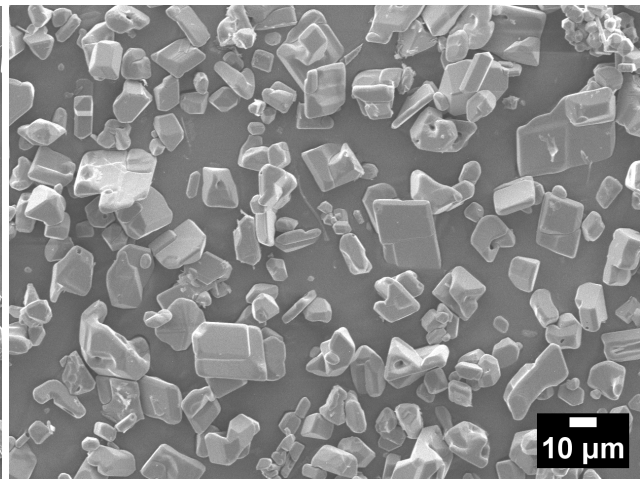


Figure D.23.: SEM image showing the zoomed view of crystals in figure 5.70f, synthesized by WCP in Na_2SO_4 heat-treated under O_2 flow at $1100\text{ }^\circ\text{C}$ and with the addition of 20 % of Na_3PO_4 .



(a) 1100 °C, 5 wt. % WCP under ambient condition



(b) 1100 °C, 5 wt. % WCP under oxygen flow

Figure D.24.: SEM images showing the zoomed view of the particles in figure 5.70a and b, synthesized by MSS in Na_2SO_4 under a) ambient condition and b) oxygen flow.

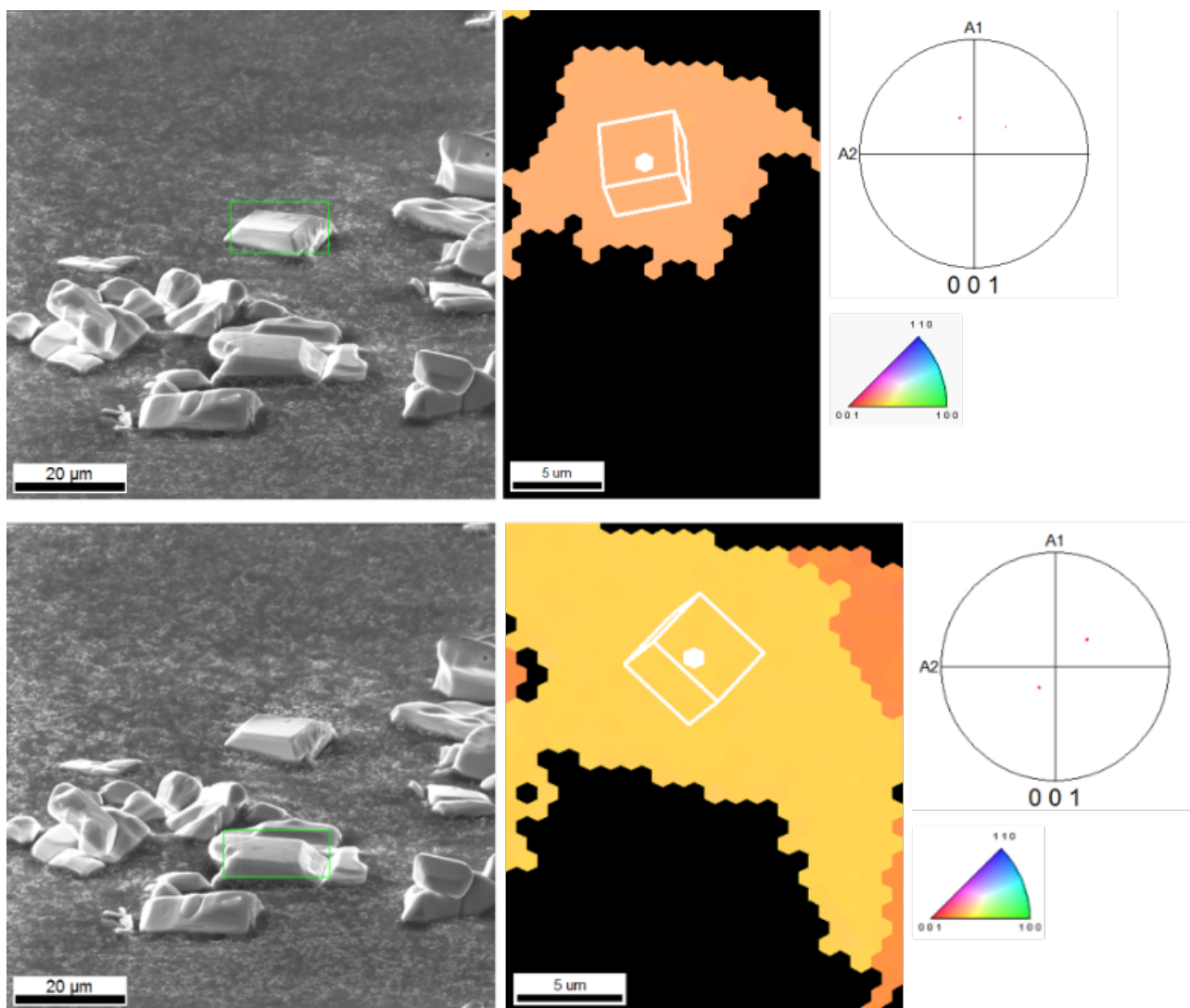


Figure D.25.: EBSD data of samples obtained by MSS under pure oxygen flow in Na_2SO_4 at 1100 °C via WCP with 5 wt. % TiOSO_4 precursor and the addition of 5 % Na_3PO_4 .

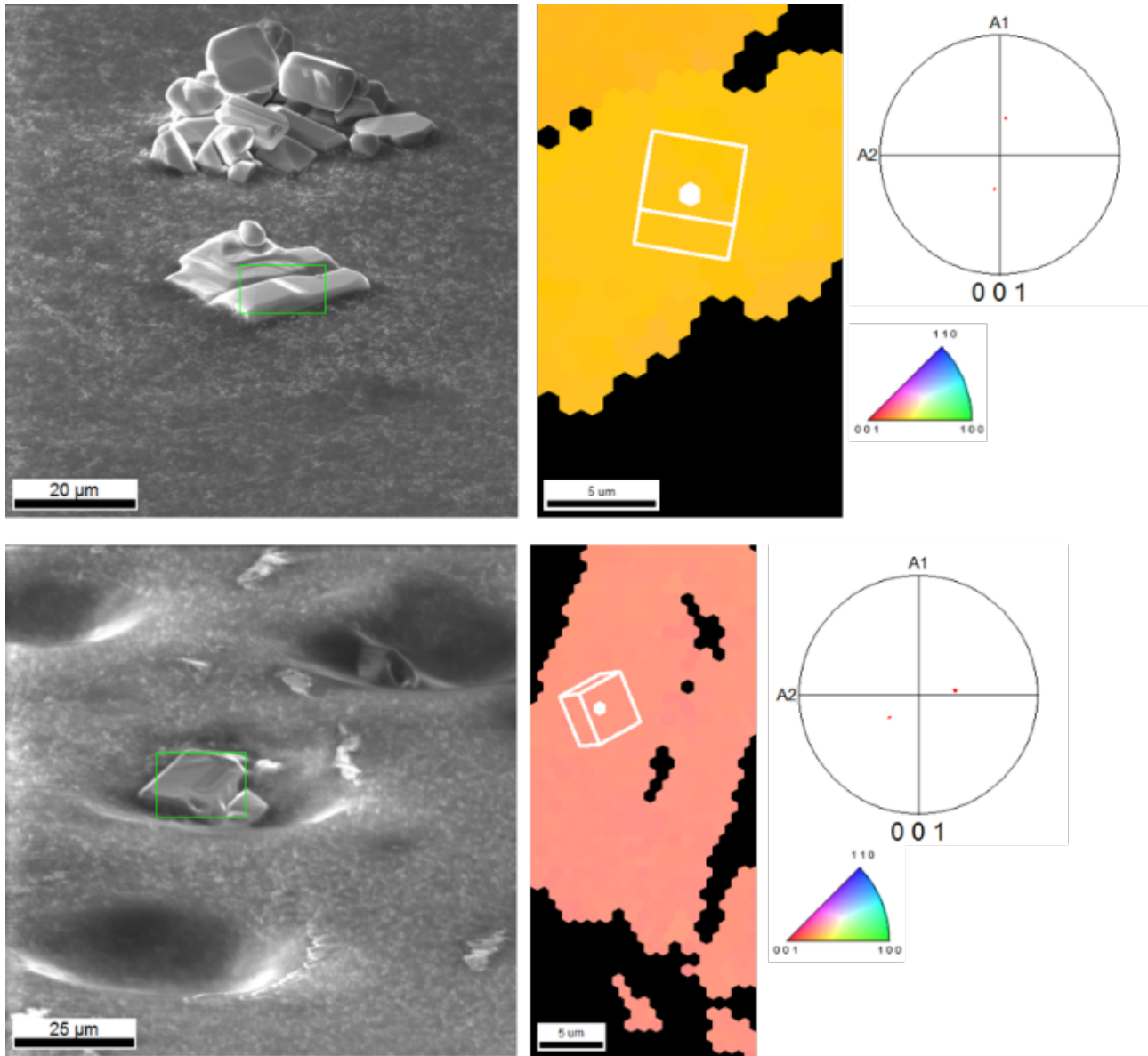
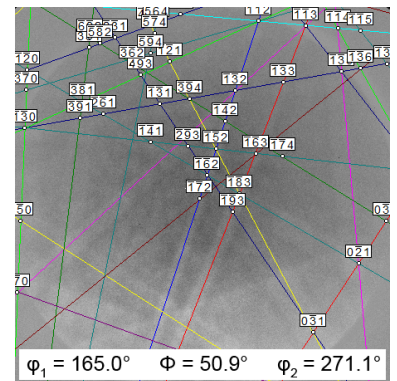
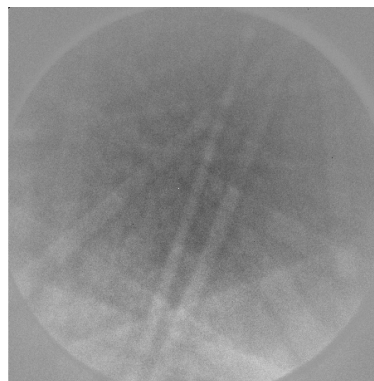
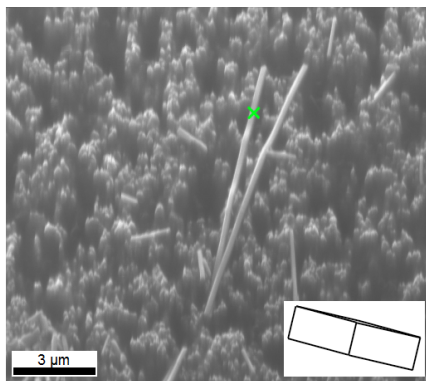


Figure D.26.: Additional EBSD data of samples obtained by MSS under pure oxygen flow in Na_2SO_4 at $1100\text{ }^\circ\text{C}$ via WCP with 5 wt. % TiOSO_4 precursor and the addition of 5 % Na_3PO_4 .

NTO-900



NTO-1100

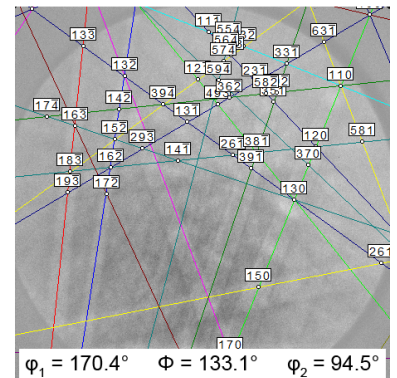
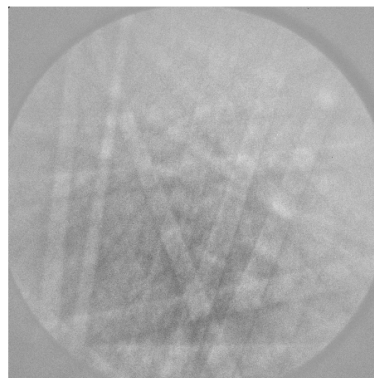
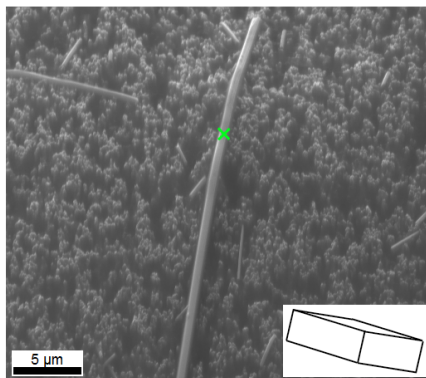


Figure D.27.: EBSD data of samples NTO-900 (top) and NTO-1100 (bottom). The representation follows the pattern described in figure 5.82.

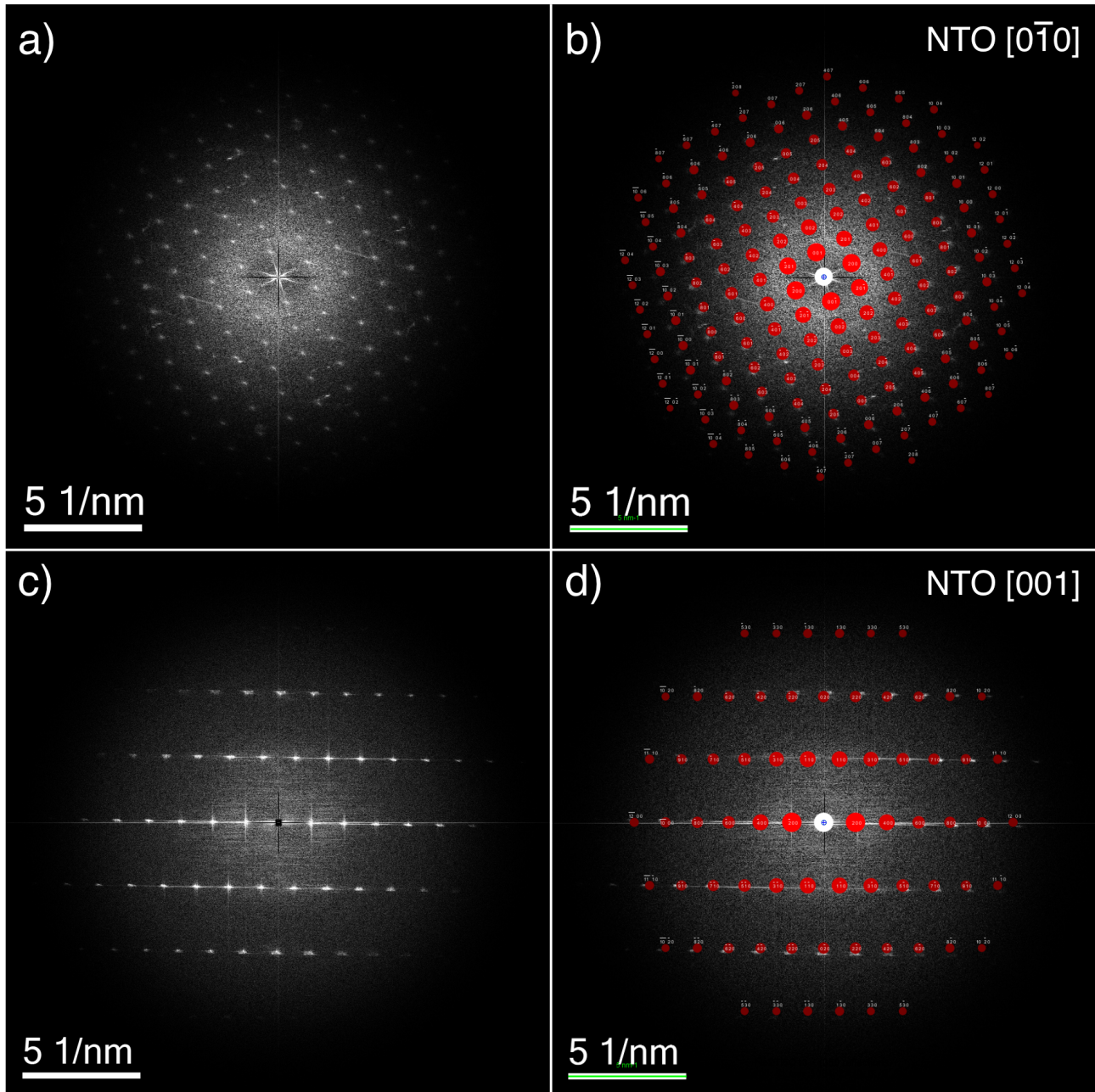


Figure D.28.: Comparison of FFTs calculated from HRTEM images with calculated NTO spot patterns for samples NTO-900 a) and b) and NTO-1100 c) and d), respectively.

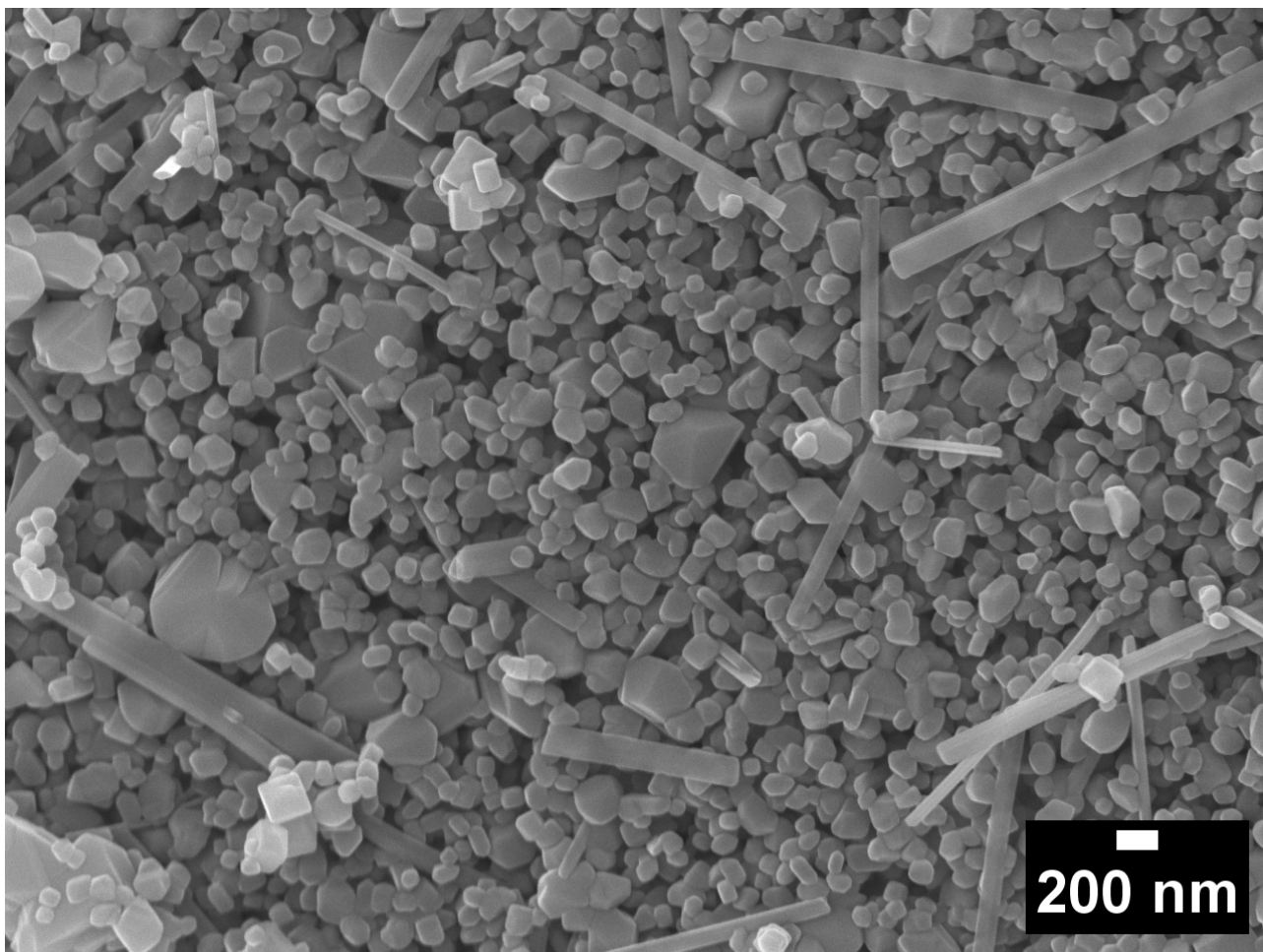


Figure D.29.: SEM image of rutile and NTO particles obtained in NaCl by WCP (with 5 wt. % TiCl_4 precursor) at 900 °C.

E. Additional Raman results

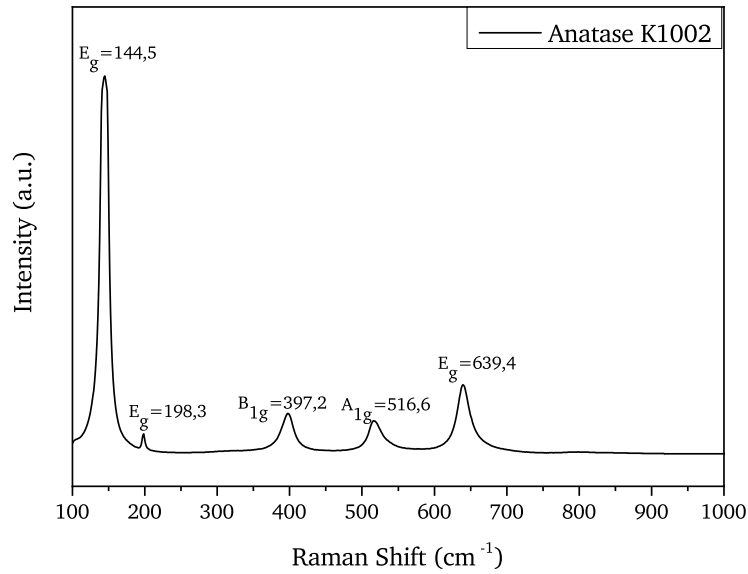


Figure E.1.: Raman reference spectrum of anatase (Kronos K1002).

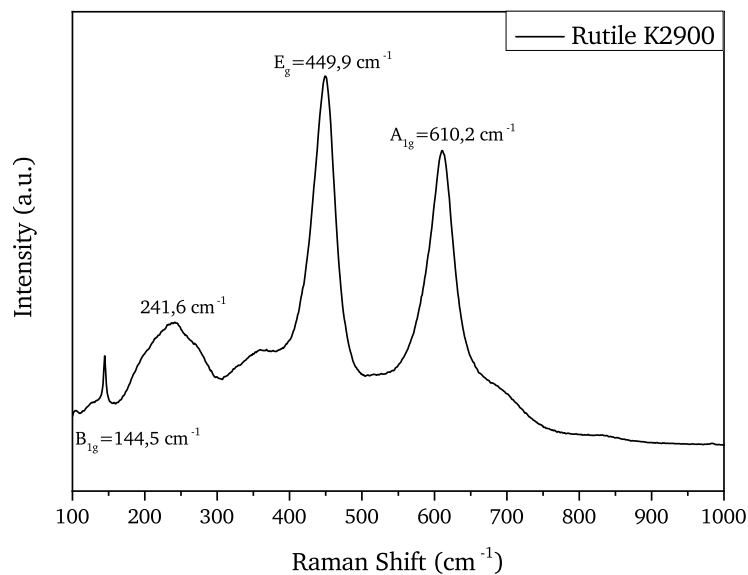


Figure E.2.: Raman reference spectrum of Rutile (Kronos K2900).

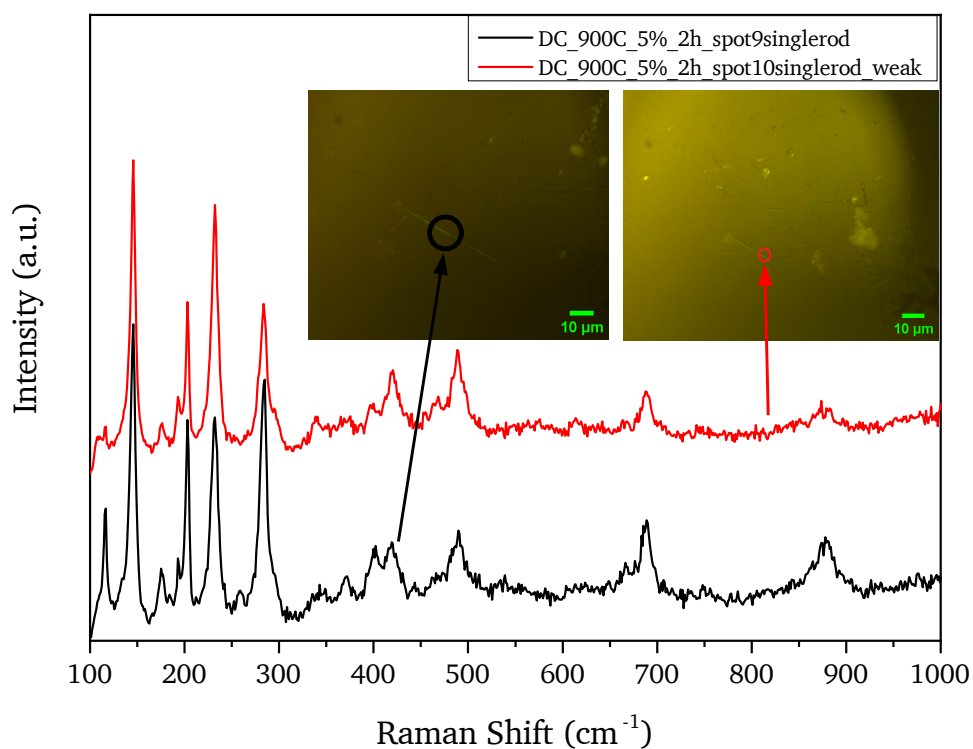


Figure E.3.: Raman spectra from two spots of the sample obtained by MSS in NaCl with 5 wt. % of titania at 900 °C.

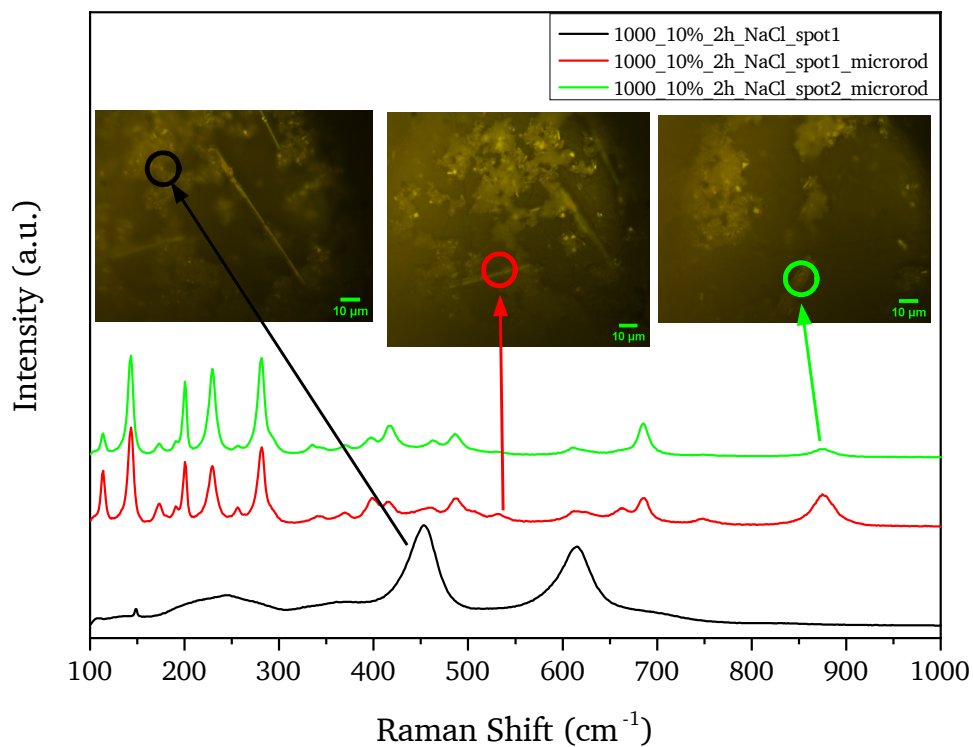


Figure E.4.: Raman spectra from three spots of the sample obtained by MSS in NaCl with 10 wt. % of titania at 1000 °C.

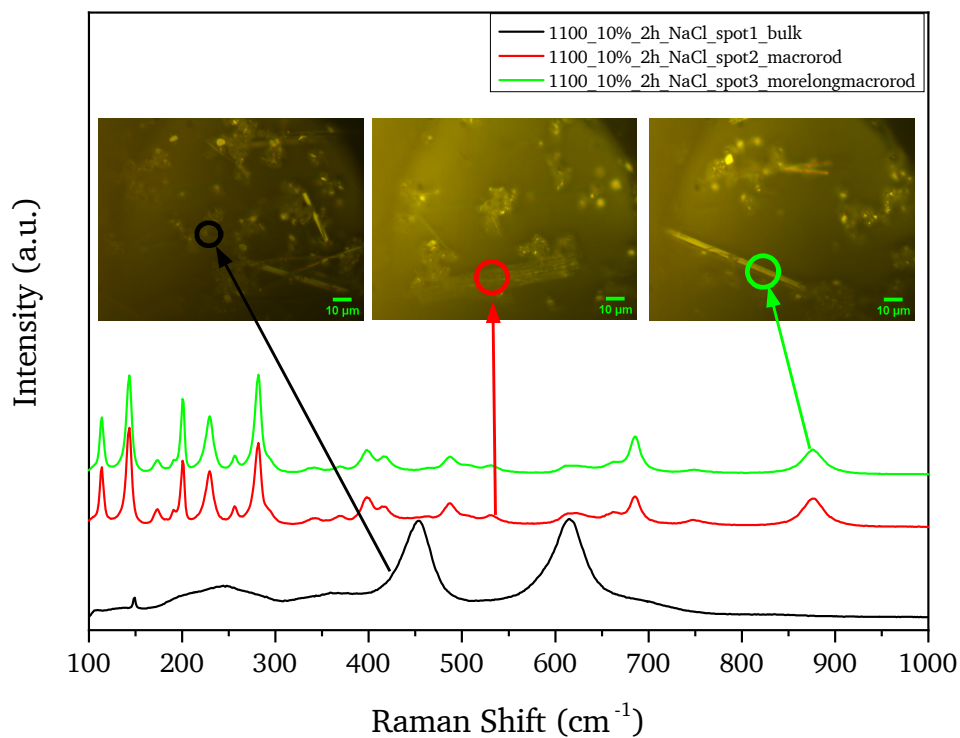


Figure E.5.: Raman spectra from three spots of the sample obtained by MSS in NaCl with 10 wt. % of titania at 1100 °C.

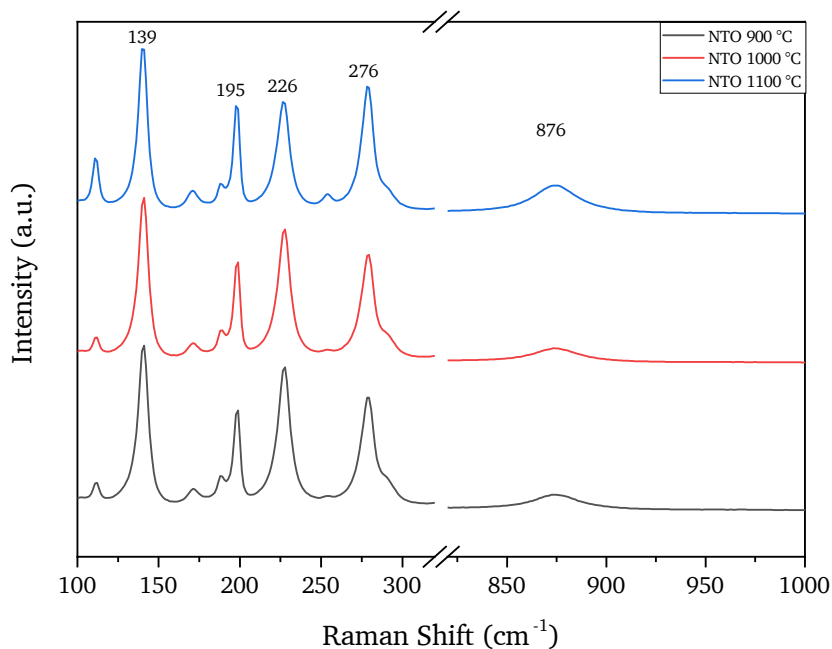


Figure E.6.: Enlarged view of figure 5.85, obtained with a break in the Raman shift. This allows a detailed view on the intensity variations in the Raman measurements depending on the temperature.

F. List of publications

Results from the present work were partly disseminated in the following journal:

- **Dario M. De Carolis**, Dragoljub Vrankovic, Samira A. Kiefer, Enrico Bruder, Michael Thomas Dürschnabel, Leopoldo Molina-Luna, Magdalena Graczyk-Zajac and Ralf Riedel, Towards a Greener and Scalable Synthesis of $\text{Na}_2\text{Ti}_6\text{O}_{13}$ Nanorods and Their Application as Anodes in Batteries for Grid-Level Energy Storage. *Energy Technol.*, **2021**, 9, 2000856. doi:10.1002/ente.202000856.

G. Curriculum Vitae

Personal Data

Name: Dario Mariano De Carolis

Academic Education

10/2015 – present Ph.D. candidate in Materials Science, TU Darmstadt, Darmstadt, Germany

04/2015 M. Sc. in Material Science, TU Darmstadt, Darmstadt, Germany

07/2011 B. Sc. in Material Science, Università degli Studi di Tor Vergata, Rome, Italy

Professional Experience

since 05/2020 Reuse and recycling of lithium-ion batteries (Re2LiB), financed by Hessen Agentur GmbH, TU Darmstadt, Darmstadt, Germany

since 09/2015 PhD project in cooperation with Merck KGaA, Merck KGaA and TU Darmstadt, Darmstadt, Germany

since 09/2015 Graduate research assistant, Department of Material Science, TU Darmstadt, Darmstadt, Germany

10/2014 – 04/2015 Industrial internship with master thesis, Merck KGaA, Darmstadt, Germany

02/2014 – 04/2014 Industrial internship, Schott AG, Mainz, Germany

05/2008 – 09/2009 Side jobs during B. Sc., ONE GROUP SRL, Rome, Italy